ANNUAL REPORT

OF THE

INSTITUTE OF PHYSICS

ACADEMIA SINICA

1974

Published by

The Institute of Physics, Academia Sinica

Nankang, Taipei, Taiwan, Republic of China

August 1975

中央研究院物理研究所集刊

編輯委員會

本集刊每年在八月出版一次

非　賣　品

中　央　研　究　院

物理研究所集刊

第　五　卷

發行人：吳　　大　　猷

編輯者：中央研究院物理研究所集刊編輯委員會

出版者：中央研究院物理研究所　臺北市南港區

印刷者：崇　文　企　業　有　限　公　司

電　話：3710220，3312608

中華民國六十四年八月出版

中央研究院物理研究所集刊

第五卷

中央研究院物理研究所印行

CONTENTS 目錄

ANNUAL REPORT OF THE INSTITUTE OF PHYSICS,
ACADEMIA SINICA, 1974

Boltzmann's H Theorem and the Loschmidt and the Zermelo Paradoxes

Ta-You Wu
Statistical Physics Laboratory
State University of New York at Buffalo

ABSTRACT

The Umkehreinwand of Loschmidt and the Wiederkehreinwand of Zermelo have been re-examined. The former paradox depends on the argument that for a dynamical system, upon the reversal of the velocities of all the molecules, the H function retraces its sequence of values so that $\frac{dH}{dt}$ will change its sign. The latter paradox depends on the argument that the H function return infinitely close to its value after a Poincaré quasi-period and therefore cannot be decreasing all the time.

While the main contention of the two paradoxes is correct that the H theorem is inconsistent with classical dynamical laws, the arguments there can be considerably simplified and the "paradoxes" answered more directly. If the distribution fuction $f(q_k, p_k, t)$ is governed by an equation which is time-reversal invariant (as the Liouville equation for a closed dynamical system), then it can be shown immediately that

$$\frac{dH}{dt} = 0, \quad H = \text{constant}.$$

In this case, both paradoxes disappear, but together with them, the $\frac{dH}{dt} < 0$ part of the H theorem also has disappeared, i.e., there is no second law of thermodynamics.

If $f(q_k, p_k, t)$ is governed by an equation which is not time-reversal invariant (such as the Boltzmann equation, or the Master Equation

for Markovian processes), then (1) there is no argument for f and H(t) to retrace their sequence of value upon the reversal of all the velocities of the system, (2) there is no quasi-period in which f and H(t) return to their earlier values. In this case, both paradoxes disappear also, but then one must go beyond classical dynamics in order to maintain the H theorem.

I. Introduction

The H theorem states that the H function defined by

$$H(t) = \int f(q_k, p_k, t) \ln f(q_k, p_k, t) \, dq_k dp_k \tag{1}$$

where $q_k, p_k = q_1, \ldots, q_n, p_1, \ldots, p_k$, satisfies the relation

$$\frac{dH(t)}{dt} \leq 0. \tag{2}$$

The paradoxes of Loschmidt (1876) and of Zermelo (1896) are the most famous of many discussions of the theorem. The former argues as follows:

Consider a system A whose phase (q_k, p_k) passes through the points $P_1, P_2, P_3 \ldots$ of the Γ space at time $t_1, t_2, t_3 \ldots$ According to (2), we have

$$H_A(t_1) \geqslant H_A(t_2) \geqslant H_A(t_3) \ldots, \quad t_1 < t_2 < t_3 \ldots \tag{3}$$

Consider another system B which differs from A only in having all the velocities opposite to those of A, i.e.,

$$q'_k = q_k, p_k' = - p_k$$

The phase (q'_k, p'_k) of B passes through the points $\ldots P'_3, P'_2, P'_1$ at time $t'_3 \; t'_2 \; t'_1 \ldots$ P'_n and P_n are corresponding points in the sense that

$$P_n = (q_K, p_K), \quad P'_n = (q_K, -p_K) \tag{4}$$

and according to (1).

$$H_A(t_n) = H_B(t'_n), \tag{5}$$

and from (3)

$$H_B(t'_1) \geqslant H_B(t'_2) \geqslant H_B(t'_3) \ldots\ldots, \; t'_3 < t'_3 < t'_1 \ldots. \tag{6}$$

which means

$$\frac{dH_B}{dt} \geqslant 0. \tag{7}$$

This is contradictory to (2).

The Zermelo (1896) argument is as follows: According to Poincaré's ergodic theorem, the phase (q_k, p_K) comes back infinited near any given initial point in the Γ space after a sufficiently long time, the quasiperiod T, and the trajectory passes through points $P'_1, P'_2, P'_3 \ldots$ infinitely close to $P_1, P_2, P_3 \ldots$ at t_1+T, $t_2+T, t_3+T, \ldots$ Zermelo argues that

$$H(t_1+T) = H(t_1), \quad H(t_2+T) = H(t_2), \text{ etc.} \tag{8}$$

so that there is the paradox that H has kept on decreasing according to (3) and yet after a quasi-period gets back to an earlier value (8).

These and other criticisms of the H theorem in the original form have led Boltzmann to reinterpret the theorem on a probability basis. Thus the Stosszahlansatz in the boltzmann equation is interpreted as giving an overwhelmingly large probability for H to decrease, and fluctuations in which H increases are allowed but are not explicitly contained in the Boltzmann equation.

The many discussions on the H theorem have been summarized by the Ehrenfests (1911), Tolman (1935) and ter Haar (1954, 1955). Ehrenfests in particular discuss the fluctuations of H in discrete steps due to molecular collisions.

II. Comments on the Loschmidt and Zermelo Paradoxes

On looking back at these two famous paradoxes, it seems that these criticisms can be answered in a more basis way. Consider first the nature of the equation that governs the variation of $f(q_k, p_k, t))$ with time.

If the equation

$$\frac{df}{dt} = I(f) \tag{9}$$

is invariant with respect to time reversal, that is the transformation

$$t \to -\tau, f(q_k, p_k, t) \to f(q_k - p_k - t) = \bar{f}(qk, p_k, \tau) \tag{10}$$

transforms (9) into

$$\frac{df}{dt} = I(\bar{f}), \tag{11}$$

then it can be shown that $I(f) = 0$ and therefore *

$$\frac{dH}{dt} = 0, \text{ or } H = \text{constant}. \tag{12}$$

For a closed system governed by classical dynamical laws, equation (9) with $I(f) = 0$ is the Liouville equation for which (12) can be obtained immediately.

If $f(q_K, p_K, t)$ is governed by an equation which is invariant under the velocity reversal operation, i.e.,

$$p_K \to -p_K, \quad f(q_K, p_K, t) \to f(q_K, -p_K, t) \equiv \bar{f}(q_K, p_K, t), \tag{13}$$

$$\frac{df}{dt} = I(f) \to \frac{d\bar{f}}{dt} = I(\bar{f}), \quad H(|f) \to H(|\bar{f}) = H(|f),$$

then it can immediately be seen that

$$\frac{dH(|\bar{f})}{dt} = \frac{dH(|f)}{dt} \tag{14}$$

Invariance with respect to velocity-reversal must be assumed in any plausible theory which is to apply to all possible velocities for the molccules. The Boltzmann equation, for example, satisfies this invariance requirement. The time-reversal invariance is, however, a much stronger condition and is not satisfied by the Boltzmann equation.

With these general considerations, we are in a position to examine the two paradoxes. Consider the Loschmidt criticism.

(i) If $f(q_K, p_K, t)$ is governed by a time-reversal invariant equation (9) and (11), then we simply have (12)

$$\frac{dH}{dt} = 0$$

and H is a constant, so that the inequality (7) disappears, together with the $\frac{dH}{dt} < 0$ part of the H theorem $\frac{dH}{dt} \leq 0$, i. e., there is no law of entropy increase.

(ii) If $f(q_K, p_K, t)$ is governed by a velocity-reversal invariant equation (13), then we must have (14), i.e, if

$$\frac{dH(\ |\ f)}{dt} \leq 0,$$

the velocity-reversed system must also have

$$\frac{dH(\ |\ \bar{\bar{f}})}{dt} \leq 0. \qquad (15)$$

(iii) The basis (5) of the paradox is fallacious, if $\frac{dH}{dt} \neq 0$, the equatiCn governing $f(q_K, p_K, t)$ cannot be time-reversal invariant, and reversing the velocities will not cause f to retrace its sequence of values even when the phase (q'_k, p'_k) passes through $P'_3, P'_2, P'_1 \ldots\ldots$ at $t'_3 < t'_2 < t'_1 \ldots$ where P_n and P'_n correspond as in (4). $f(q_K, p_K, t)$ changes not only in value, but also in the functional form, with time and in an irreversible manner (since the equation $\frac{\partial f}{\partial t} = I(f)$ is not re-

versible). Without (5), there is no paradox.

Consider next the Zermelo paradox. Here again: Either (i) $f(q_K, p_K, t)$ is governed by a time-reversal invariant equation, in which case we have (12) and H is a constant so for this case, (8) is valid, but the paradox of H decreasing and getting back to an earlier value after a quasi-period disappears, or (ii) $f(q_K, p_K, t)$ is governed by an irreversible or stochastic equation in which case f changes in time both in value and in functional form*, and in general there is no quasi-period after which $f(q_K, p_K, t)$ and H(t) return to their earlier value. In this case, the relations (8) are not true and there is again no paradox. But then $\frac{dH}{dt} \leq 0$ is not a consequence of dynamical laws.

---

*Footnote (equ. (12))

The proof of (12) is as follows. Upon velocity reversal, $p \longrightarrow -p$, let us denote

$$f(q,p,t) \longrightarrow f(q,-p,t) \equiv f'(q,p,t). \tag{a}$$

Equation (a) must hold for arbitrary velocities, i.e.,

$$\frac{df}{dt} = I(f) \rightarrow \frac{\partial f'}{\partial t} = I(f') \tag{b}$$

or

$$I(f) \rightarrow I(f') \tag{c}$$

Upon t reversal, we have (10) which can be expressed as

$$f(q,p,t) \rightarrow f(q,-p,-t) = f'(q,p,-\tau) = f(q,p,\tau) \tag{d}$$

By hypothesis, (9) is invariant with respect to t reversal,

$$\frac{df}{dt} = I(f) \rightarrow \frac{d\bar{f}}{dt} = I(\bar{f}) \tag{e}$$

i.e.,

$$I(f) \rightarrow = I(\bar{f}) \tag{f}$$

*the velocity distribution of a gas may start with any arbitrary initial function and approach the Maxwell distribution in time.

Let the t revarsal be made at $t = \tau = 0$. Then (d) gives

$$\bar{f}(q,p,o) = f'(g,p,o) \tag{g}$$

so that at $t = \tau = 0$, (f) gives

$$I(f(q,p,o)) \longrightarrow -I(f'(q,p,o)) \tag{h}$$

Comparison with (e) gives

$$I(f) = 0. \tag{i}$$

III. Concluding Remarks

To sum up, we believe that the many involved discussions of the H theorem can be simplified with our present understandings.

(i) On classical dynamical laws, a closed dynamical system can have only

$$H = \text{constant},$$

i.e., there is no law of increasing entropy. This is the contention of Loschmidt and Zermelo. The arguments in the two paradoxes are greatly simplified by the general result (12).

(ii) The $f(q_K, p_K, t)$ in the H function (1) satisfying the H theorem (2) cannot be governed by an equation which is a consequence of reversible dynamical laws; it could be an equation based on general probability assumptions (for example, the Smoluchowski assumption the Markovian processes leading to the Master equation, or the Fokker-Planck equation) or on specific probability assumptions (such as the Boltzmann equation), or on other assumptions. In such cases, the contentions (5) and (8) in the paradoxes are not valid.

(iii) In the face of these paradoxes and other criticisms, Boltzmann later interpreted the H theorem (2) on probability basis, that is, whenever H is above its minimum value, it has an overwhelmingly large probability to decrease, but an increase of H due to molecular collisions are not absolutely ruled out. In the particular case of the Boltzmann equation, the Stosszahlansatz gives this large probability

and (5) and (8) are not relevant.

(iv) The really significant refinement of the original form of the H theorem is Boltzmann's later probability interpretation and the implied extension to include fluctuations. Recently Fox and Uhlenbeck (1969) have suggested the addition of a fluctuation term to the Boltzmann equation. Lee and Wu (1973), starting with the Liouville equation in the form of the B-B-G-K-Y hierarchy, have obtained such a fluctuation term on statistical consideration of the many-particle correlations, From a Boltzmann equation with fluctuation, one obtains immediately an H function which decreases with time in the main but has fluctuations.

References

Ehrenfest, P. & T., (1911) Article in Enzyklopadie der Wessenschaflin IV, (32), English translation, Cornell University Press (1959).

Fox, R. F. and Uhlenbeck, G. E., (1969). Contributions to the Theory of Non-equilibrium Thermodynamics, (Dissertation), Rockefeller University, New York.

ter Haar, D., (1954). Elements of Statistical Mechanics, Rinehart, N. Y. App. I

ter Harr, D. (1955). Review of Modern Phys. 27, 289

Lee, Paul S. and Wu, T. Y., (1973), Intern. J. Theor. Phys. 7, 267

Loschmidt. L. (1867). Sitznngsberichte der Akademie der Wissenschaften in Wien 73, 139; 73, 67

Tolman, R. C. (1935) Principles of Statistical Mechanics, Oxford University Press

Zermelo, E. (1896) Ann. Physik 57, 485; 59, 793

ANNUAL REPORT OF THE INSTITUTE OF PHYSICS,
ACADEMIA SINICA, 1974

ANGULAR CORRELATION STUDIES OF THE 1518, 1800 keV $^{27}Al(p,\gamma)^{28}Si$ RESONANCES*

江紀成　　林爾康
G.C. KIANG, E.K. LIN

INSTITUTE OF PHYSICS, ACADEMIA SINICA

Abstract

The E_p=1518 keV and 1800 keV resonance, corresponding to the 13,051 keV and 13,321 keV states of ^{28}Si have been studied by the directional correlation method. The spin parity of the two resonances was proposed to be 2^+ and 1^+ respectively. The decayed γ-ray emitted from E_p=1518 keV and 1800 keV resonance to the 1.78 MeV level of ^{28}Si were found to be in mixing mode as $2^+(2,3)2^+(2)0^+$ and $1^+(2,3)2^+(2)0^+$. The intensity mixing ratio of E2 to M3 are 22.8% and 65% respectively.

* Work performed at the Physics Center at Tsing Hua Univ. and support by the National Science Council

ANNUAL REPORT OF THE INTITUTE OF PHYSICS,
ACADEMIA SINICA, 1974

The Level Structure of ^{64}Zn Through the ^{63}Cu (p, γ) ^{64}Zn Reaction*

林爾康　　王建萬　　江紀成
C.C. Hsu, E.K. Lin, C.W. Wang, G.C.Kiang,
Y.C. Liu, and M.C. Wang

National Tsing Hua University and Academia Sinica
Hsinchu, Taiwan, China

*Work performed at the Physics Research Center in Hsinchu, and supported by the National Science Council.

This paper has been published in Chinese Journal of Physics Vol. 13 No. 2, 1975.

Summary

The excited states of the ^{64}Zn nucleus was investigated in the $^{63}Cu(p,\gamma)^{64}Zn$ reaction. By means of the Ge(Li)-NaI(Tl) coincidence measurement the level scheme of ^{64}Zn was established and for a number of levels the spin-parity assignments were suggested on the basis of the measured γ-branching ratios. The theoretical calculation in the framework of the conventional shell model was compared with the experimental result and discussed.

ANNUAL REPORT OF THE INSTITUTE OF PHYSICS,
ACADEMIA SINICA, 1974

ANGULAR CORRELATION STUDIES OF THE 1518, 1800 keV $^{27}Al(p,\gamma)^{28}Si$ RESONANCES*

江紀成　　林爾康
G.C. KIANG, E.K. LIN

INSTITUTE OF PHYSICS, ACADEMIA SINICA

The E_p=1518 keV [illegible] nce, corresponding to the 13,051 keV and 13,3[illegible] [illegible] Si have been studied by the directional correlation method. The spin parity of the two resonances was proposed to be 2^+ and 1^+ respectively. The decayed γ-ray emitted from E_p=1518 keV and 1800 keV resonance to the 1.78 MeV level of ^{28}Si were found to be in mixing mode as $2^+(2,3)2^+(2)0^+$ and $1^+(2,3)2^+(2)0^+$. The intensity mixing ratio of E2 to M3 are 22.8% and 65% respectively.

* Work performed at the Physics Center at ,Tsing Hua Univ. and support by the National Science Council

ANNAUL REPORT OF THE INSTITUTE OF PHYSICS,
ACADEMIA SINICA, 1974

Energy Levels and Transitions in ^{71}As from (p, γ) Reaction on ^{70}Ge*

Y. C. Liu, T. H. Hsu, E. K. Lin, P. K. Tseng and C. W. Wang

Tsing Hua University, Academia Sinica and Taiwan University
Hsinchu, Taiwan, Republic of China

Abstract

The ^{70}Ge(p, γ)^{71}As reaction has been investigated in the energy range from E_p=1.0 to 2.5 MeV. Excitation function was obtained for the reaction over this energy region. High-resolution measurements of the de-excitation γ-rays from this reaction have been made at E_p= 2.434 and 2.030 MeV by using a 50 cm^3 Ge(Li) detector. The energy levels of ^{71}As up to 2947 KeV excitation and γ-ray branching ratios were determined; several new levels are proposed. The Q value for this reaction was also determined.

* Work performed at the Physical Research Center and supported by the National Science Council of the Republic of China.
This paper has been published in Journal of The Physical Society of Japan, Vol. 39, No. 1 July, 1975.

I. Introduction

In past years the (p,γ) reaction on the medium-weight nuclei of A-70 has rarely been experimentally studied at protons of energy less than 3 MeV. The main difficulities are those: (1) the cross section is small, and (2) in many cases it is not possible to resolve individual resonances. The usual techniques of resonance spectroscopy cannot be used. However, the recent (p,γ) experiments[1] on the A-90 nuclei indicate that it is also possible to investigate the nuclei of A-70 via (p,γ) reactions with portons of energy less than 3 MeV. We have successfully carried out the $^{74}Ge(p,\gamma)^{75}As$ experiment and have reported the results in a recent paper[2].

Very few energy levels of As isotopes have been previously well established[3-10]. The theoretical studies of the odd-even As isotopes have been performed by several authors hnd teyh attempt to understand the level spectra in terms of the model with single particle-core coupling[11] and so called coriolis-coupling model[12-13] have met only with limited success. They could not predict correctly even the ground state spin of ^{71}As. Therefore, it is worthwhile to study experimentally and to get more information about the energy levels of the As isotopes.

This paper is the second one of a series describing experimental investigations on the energy levels of the As isotopes from (p,γ) reaction, and in this paper we reported the results of the measurements on the $^{70}Ge(p,\gamma)^{71}As$ reaction.

II. Experimental Procedure

Isotopically enriched germanium of 91.4% (^{70}Ge) was evaporated from a tantalium boat on a 99.9% gold backing of 0.4mm in thickness of the prepared targets were between 3 and 30 $\mu g/cm^2$. A specially designed traget chamber[14] with a continuously moving

target holder was used. The target was bombarded by protons from the 3 MeV Van de Graaff accelerator at Tsing Hua University. The beam energies were calibrated with several well-known resonances in the ^{27}Al(p,γ)^{28}Si reaction before and after the experiment. The energy resolution of the proton beam was about 1 keV and the beam current was about 3-5 μA.

The excitation function was obtained by using a 3" x 3" NaI(Tl) detector at a fixed angle of 90° to the incident beam. The γ-ray spectra were taken by a 50 cm^3 Ge(Li) detector of the resolution 2.3 keV at 1.333 MeV. Both detectors were covered with a 2 mm Pb shield to prevent high-intensity low-energy γ-rays. The experimental method is essentially the same as that used in Ref. 2 except there have been improvements in reducing the background by taking coincidence spectra measurement. Two detectors as mentioned above, which were mounted directly opposite to each other at 90° to the beam direction, were used for the coincidence spectra measurement. The coincidence data were obtained when pulses from the Ge(Li) detector are in coincidence with pulses from the NaI(Tl) detector gated at energies corresponding to $E_\gamma > 3$MeV. The resolving time of the whole system was 100 n sec.

The γ-ray energies of the spectra were calibrated by the standard source γ-rays, the 6.131-MeV γ decay of ^{16}O from the ^{19}F(p,$\alpha\gamma$)^{16}O reaction, and the 511-keV energy differences between full energy, single escape and double escape peaks. The relative efficiency of the detector was determined using the method described in Ref. 15. Proper corrections were made for γ-ray absorption of the target chamber and the lead absorber.

III. Result and Discussion

1. Excitation function and γ-ray spectrum

Excitation functions were studied from E_p=0.970 to 2.470 MeV for γ-ray energy of $E_\gamma > 4.5$ MeV. $3.0 < E_\gamma < 4.5$ MeV and $1.5 < E_\gamma < 3.0$ MeV, respectively, typical result is shown in fig. 1. Measurements were repeated several times, generally resulting in a reproduction of the original data points to within acceptable statistical deviation. A total of 149 resonances was observed in the energy region between E_p=0.976 and 2.466 MeV. In order to investigate E_p dependence of the density of the resonance levels, the number of resonances in each 100-keV interval was plotted against E_p, and is shown in Fig. 2. It is seen that the number of resonances appears to increase with energy. This implies that the states being excited are not strongly overlapped, because strongly overlapping resonances give rise to fluctuations whose average spacing does not change with excitation energy.

The observed high-energy γ-ray spectra at E_p=2.430 MeV is shown in fig. 3. All of the peaks higher than 4 MeV, with the exception of those from ^{16}O 6.131 MeV γ decay, are the product of the decay of the ^{71}As resonances. Figure 4 shows the coincidence spectrum at E_p=2.035 MeV which was obtained in a 36-h period. In order to construct the decay scheme, it was assumed that the strong high-energy γ-rays are all due to primary γ transitions from the resonance level. This assumption was justified by considering the energy dependence of the decay process for the primary and secondary transitions[16], and also by the observation of the γ-rays produced in the ^{72}Ge(p,γ)^{73}As and ^{74}Ge(p,γ)^{75}As reactions[17,2] where all observed high-energy γ-rays are found feeding to well-known low-energy levels.

2. Energy levels and decay scheme of ^{71}As

The decay scheme of ^{71}As extracted from the coincidence data is shown in fig. 5. A summary of the energy level determinations from the present investigation is presented in Table I. Only two

energy levels of ^{71}As were reported[3] before 1968. Broman and Rosner[4] have observed 11 energy levels of ^{71}As below 2674 keV in the ^{70}Ge(^{3}He,d)^{71}As reaction experiment and Hundelshausen[5] has measured 5 energy levels from the radioactive decay of ^{71}Se. In this work we found more energy levels, our results agree well with these data. Eight levels observed at energies of 924, 1007, 1467, 1940, 1609, 2360, 2488, and 2947 keV are new, they have not been reported previously. Some individual discussion of the levels are given as follows:

Ground states: The ground state of ^{71}As is known to have $J=5/2$ in contrast to the $J=3/2^-$ assignment for those of ^{73}As, ^{75}As and ^{77}As. According to the spherical shell model, 38 neutrons in ^{71}As form a semi-closed shell and the 33rd proton should be in the $f_{5/2}$ orbit. The deformation treatment of As isotopes by Sholz and Malik[12] and Imanishi et al[13]. might not be applicable for ^{71}As nucleus.

145-keV state: This state was found both in the (^{3}He,d) reaction[4] and the decay of ^{71}Se nucleus[5], its spin and parity were proposed to be $3/2^-$. In a previous investigation of the ^{74}Ge(p,γ)^{75}As reaction[2], we noted that for low energy (p,γ) reaction of even-even nuclei the spins of resonance states are mainly $2/1^+$ and the γ-ray branching ratios from the resonance state to the lower states with small spin are larger. The fact that the measured branching ratio in this experiment is very large for the 145-keV state supports the $3/2^-$ assignment.

510-keV state: This state was observed in the (^{3}He,d) reaction[4] but not in the ^{71}Se decay[5] because of the annihilation r-ray mixing. Its existence is confirmed in the present work from observation of the resonance to this state transition.

830-keV state: This state was found in the (^{3}He,d) work[4]. However, in the ^{71}Se decay experiment[5], the 978-keV state was proposed in-

stead of this state. According to our data, the 830-keV state was identified. We observed the 830-keV γ-ray as well as the transition from the resonance to the 830-keV state, but not to the 978-keV state. It seems that the 978-keV γ-ray observed in the ^{71}Se decay[5] would be the transition γ-ray from 1490-keV state to 410-keV state.

Other states: The 924-keV state is a new one which has not been reported in the previous works[4,5]. From the measured γ-ray spectra in the present experiment, we observed the high-energy r-rays corresponding to the transition from the resonance to the 924-keV state, and also observed its subsequent decays to the 510-, 145-keV and ground states. This indicates the existance of a state at 924 keV.

The 1243-keV state which was not observed in the (^{3}He,d) reaction[4] was found in the ^{71}Se decay[5]. It was also observed in the present experiment. From the logft value deduced in the ^{71}Se decay, Hundelschausen[5] assigned the 1243- and 870-keV states to be $3/2^-$, $5/2^-$ or $7/2^-$. It is seen from Table I that the measured branching ratios for the resonance to the 870-and 1243-keV states are 5.1% and 4.4%, respectively. Comparing these values with the measured branching ratios for the states with spins of (1/2, 3/2) known previously[4,5], we can exclude the $7/2^-$ possibility for the 870-and 1243-keV states, they are most likely states with spin of 3/2 or 5/2.

Similarly, from the measured branching ratios for the 510-, 991-, 1510-, 1490- and 1609-keV states, we suggest that the 991-keV state and two new levels at 1490-and 1609-keV may have spin values of 1/2 or 3/2.

3. Q value

The Q value of the ^{70}Ge(p, γ)^{71}As reaction was determined by averaging the sum of the primary and secondary γ-ray energies through intermediate state. Precise energy determination yields a measured value of 4519±5 keV, in reasonable agreement with the

value of 4538±158 keV given in Ref. 18 and of 4.622±8 KeV in Ref. 3.

IV. Conclusions

We have experimentally investigated both $^{70}Ge(p,\gamma)^{71}As$ and $^{74}Ge(p,\gamma)^{75}As$ reactions at low bombarding energies in the present work and a previous work[2]. Many energy levels of ^{71}As and ^{75}As were proposed, and their decay schemes were constructed. The γ-ray yields are large enough to make the investigation feasible. It is clear that with the (p, γ) reaction on the medium-weight nuclei A-70. especially when the neutron exit channel is closed, it is possible to obtain useful informations on the level structure of these nuclei.

Acknowledgement

The authros wish to express their sincere thanks to all members of the THU Van de Graaff accelerator group for their generous assistance.

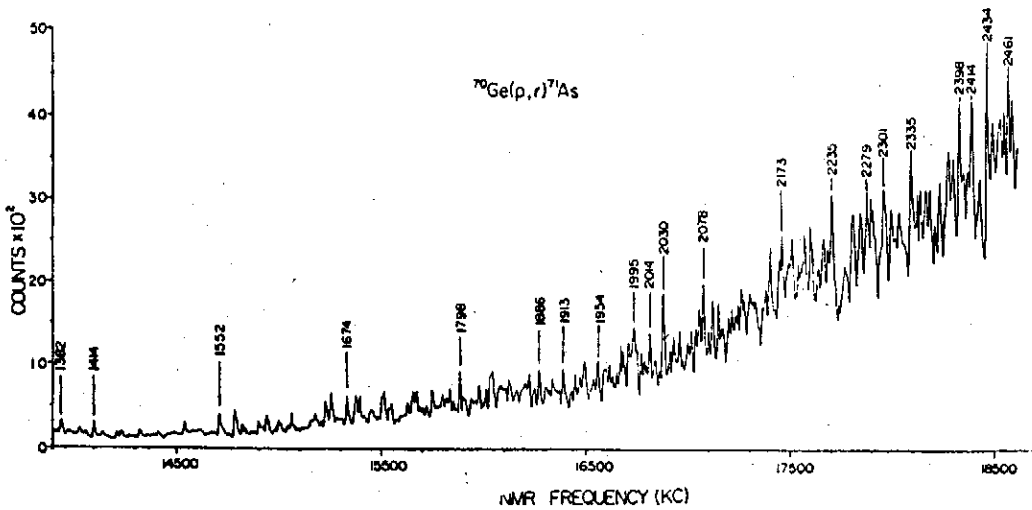

Fig. 1 Excitation function for $^{70}Ge(p,\gamma)^{71}As$ reaction over the energy region E_p=1.3 to 2.5 MeV. Numbers over peaks refer to resonant energy.

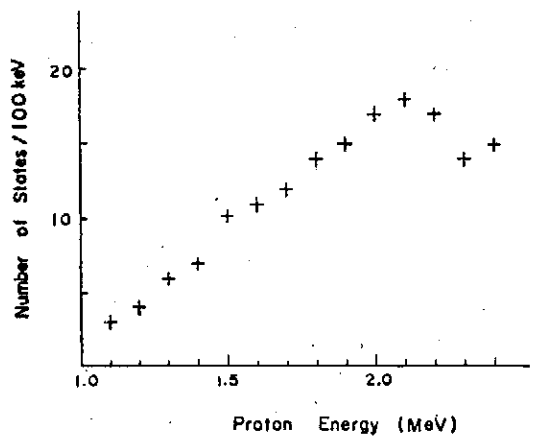

Fig. 2 Number of resonances for $^{70}Ge(p,\gamma)^{71}As$ in each 100 keV interval versus E_p, over the range 1.0 to 2.4 MeV.

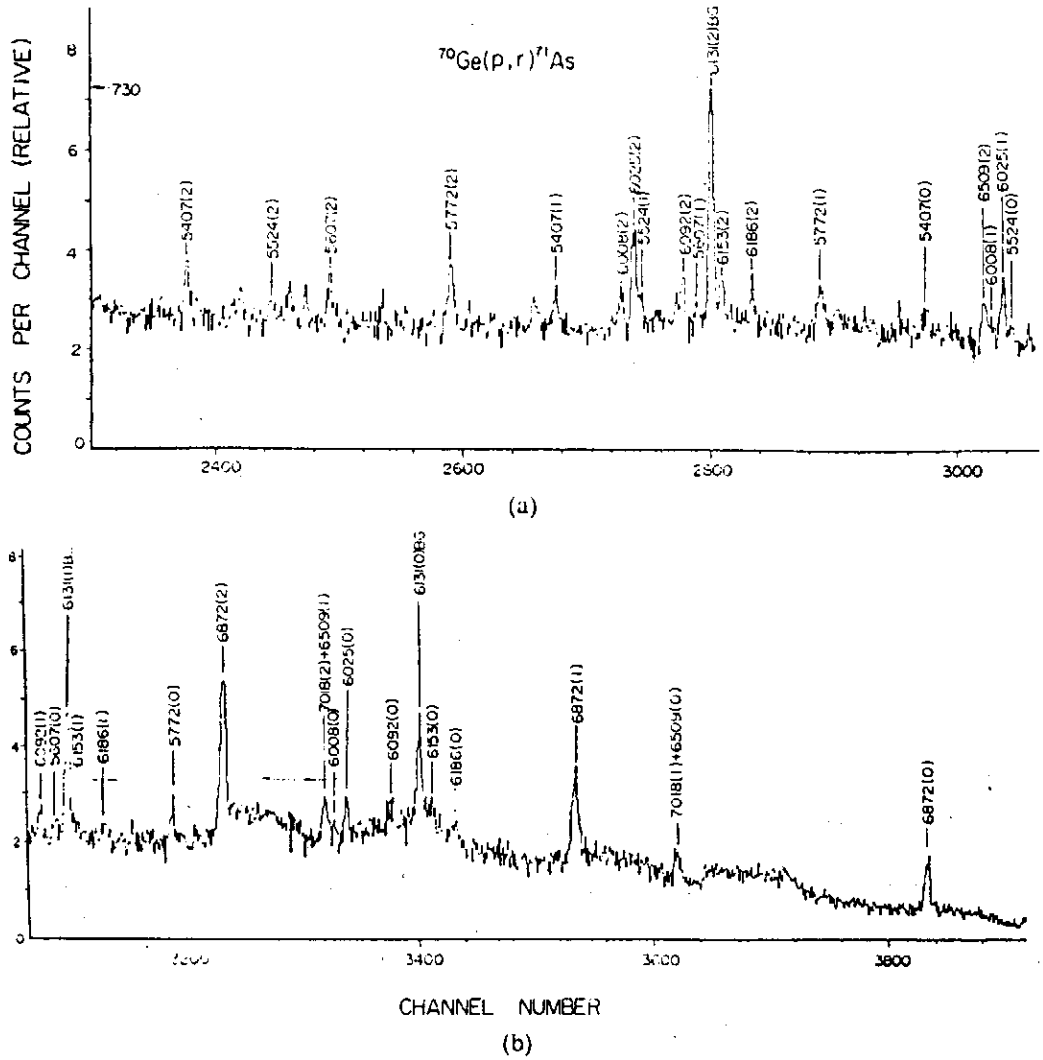

Fig. 3 The gamma-ray spectrum of ^{70}Ge(p,r)^{71}As reaction at E_p=2434 keV. Numbers over peaks refer to gamma-ray energy. (0) (1) (2) refer to the full-energy, single-escape and double-escape peaks respectively.

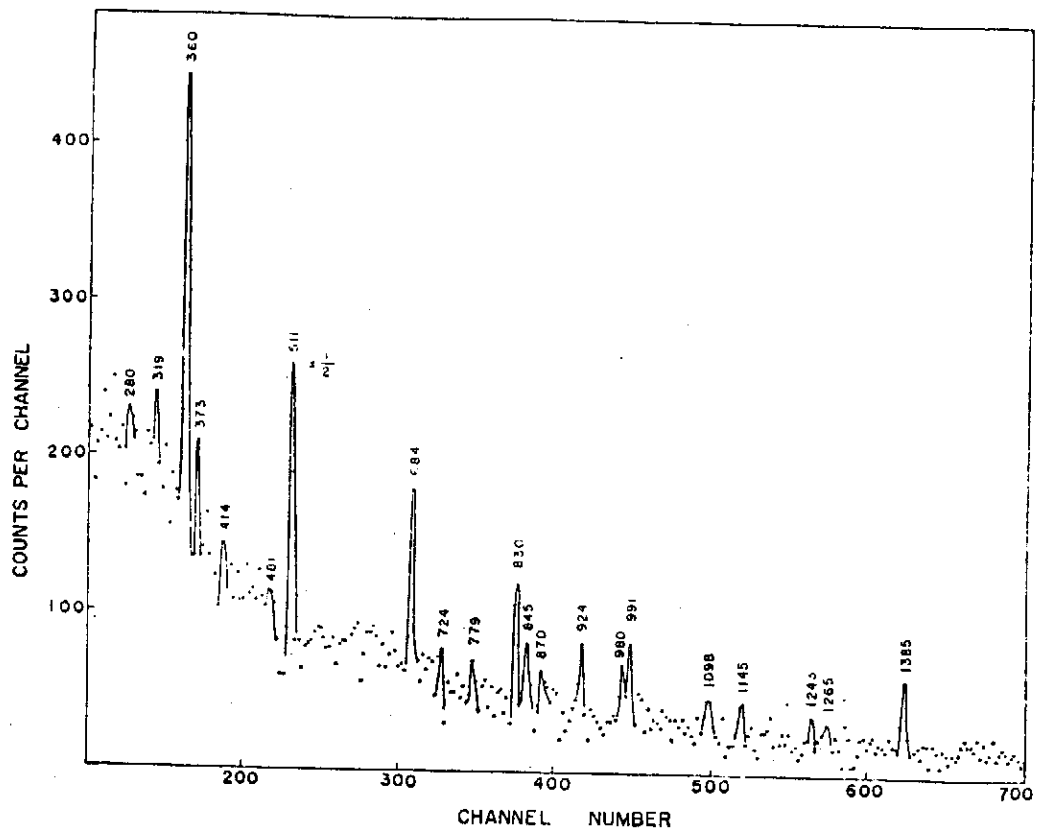

Fig. 4 $^{70}Ge(p,\gamma)^{71}As$ coincidence spectrum at E_p=2030 keV. numbers over peaks refer to gamma-ray energy.

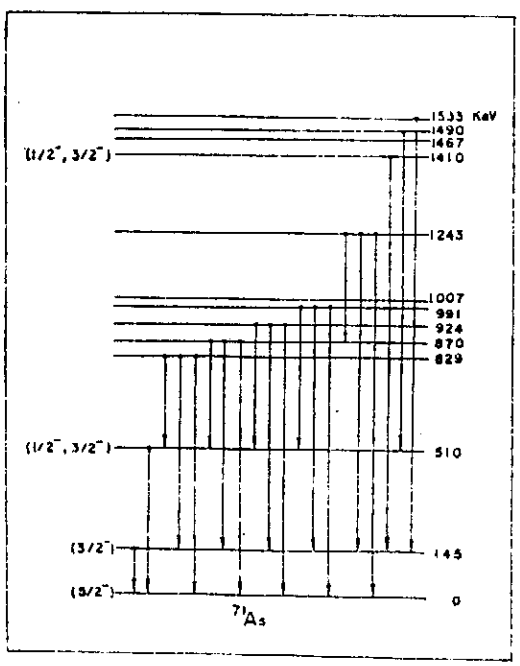

Fig. 5 Deacy scheme of ^{71}As extracted from the coincidence data shown in Fig. 4.

References

1. C.J. Umbarger, C.A. close, W.L. Sievers and R.C. Bearse, Phys. Rev. C, 3, (1971) 199.
2. C.W. Wang, Y.C. Liu, E.K. Lin, C.C. Hsu and G.C. Kiang, Phys. Rev. C, March (1974)
3. Nucl. Data, Edited by K. Way B1-6 (1966)
4. L. Broman and B. Rosner, Nucl. Phys. A114 (1968) 237
5. Ulrich Frhr. V. Hundelshausen, Z. Physik 225 (1969) 125
6. P. van der Merwe, E. Barnard, J.A.M. de Villiers, J. Malan an J. Tepel, Proceedings of the International Conference on Nuclear Physics. Edited by J. de Boer and H. J. Mang (North-Holland/American Elsevier 1973), p. 215
7. R. Moreh and O. Shahal, Phys. Rev. 188 (1969) 1765
8. R. M. Wilenzick, V.R. Dave and J.A. Nelson, Phys. Rev. C, 4, (1971) 2126.
9. D.P. Donnelly, J.J. Reidy and M.L. Wedenbeck, Nucl. Phys. A112 (1968) 145
10. R.D. Meeker and A.B. Tucker Nucl. Phys. A157 (1970) 337
11. R.L. Robinson, F.K. McGowan, P.H. Stelson and W.T. Milner, Nucl. Phys. A104 (1967) 401
12. W. Scholz and F.B. Malik, Phys. Rev. 176 (1968) 1355
13. N. Imanishi, M. Sakisaka and F. Fukuzawa, Nucl. Phys. A125 (1959) 626
14. T.H. Hsu, P.K. Tseng, E.K. Lin and Y.C. Liu, Nucl. Inst. Method 106 (1973) 513
15. F.C. Young, A.S. Figuera and G. Pfeufer, Technical Report 71-013, University of Maryland
16. G.A. Bartholomew, Ann. Rev. Nucl. Sci. 11 (1961) 259
17. Y.C. Liu et al. to be published
18. U C R L - 5419

Table 1

Gamma energies, branching ratios and level energies in ^{71}As from ^{70}Ge(p,γ)^{71}As reaction

High E_γ (keV)	Branching Ratio (%)[a]	Energy Level (keV)			Spin and Parity
		Present	(^{3}He,d)[b]	^{71}Se decay[c]	
6620	1.0	145±2	145±15	0	$5/2^-$
6474	23.1	145±2	145±15	147.2	$(3/2^-)$[b]
6110	5.7	510±2	505±15	...	$(1/2^-, 3/2^-)$[b]
5791	5.0	820±2	826±15	...	
5750	5.1	870±2	869±15	871.1	$(3/2^-, 5/2^-)$[c,d]
5696	3.5	924±2	...	...	
...	...	...	...	978.4	
5629	7.7	991±2	992±15	...	$(1/2,3/2)$[d]
5613	5.6	1007±3	...	...	
...	...	....	1128±20	...	
5377	4.4	1243±4	...	1243.2	$(3/2^-, 5/2^-)$[c,d]
5210	6.4	1410±4	1416±20		$(1/2^-, 3/2)$[v]
5153	1.0	1467±4	...		
5130	7.1	1490±5	...		$(1/2,3/2)$[d]
5087	2.5	1533±5	1536±20		
5011	5.7	1609±5	...		$(1/2,3/2)$[d]
4646	2.2	1974±5	1966±20		
...	...	...	2305±20		
4260	4.3	2360±5	...		
3132	1.0	2488±5	...		
3963	4.5	2657±5	2674±20		
3673	4.2	2947±5			

a) measured at E_p = 2.030 MeV

b) ref. 18

c) ref. 19

d) suggested from present work.

Role of Seniority Number in Shell-Model Calculations*

M. C. Wang (王明建), H. C. Chiang (蔣亨進)
S. T. Hsieh (謝世哲), and E. K. Lin (林爾康)

Department of Physics, National Tsing Hua University,
Hsinchu, Taiwan

(Received 21 February 1975)

The shell-model calculations for copper isotopes are carried out with seniority number restriction. The role of seniority number is discussed. The calculations show that the low-seniority number restriction is an effective way to reduce the size of model space.

* This paper has been published in Chinese Journal of Physics, Vol. 13, No. 1, April, 1975.

ANNUAL REPORT OF THE INSTITUTE OF PHYSICS,
ACADEMIA SINICA, 1974

Optical Wave Attenuation in Thin Films*

N. T. Liang, Shou-yih Wang and M. T. Jahn
Department of Physics, National Tsing Hua University
Hsinchu, Taiwan

Abstract

Ion-exchanged wave guides with $AgNo_3$ as salt and microscope slide as substrate have been prepared. Coupling techniques for prism-film coupler have been attained. Mode spectra of the ion-exchange wave guide and another PVP film were observed. Two simple apparatus of measuring index of refraction have been developed using the Abbe refractometry and features of the Brewster angle. Attenuation constant was determined with a He-Ne laser using direct method in which the CdS photodetector with narrow slit was allowed to contact the waveguide and measure the intensity at each position. The mode dependence of attenuation was determined with a 10W Argon ion laser using the well known 2-prism coupling arrangement. Computer analysis has also been done.

I. Introduction

The field of the guided wave in thin film has recently become very interesting due to its increasingly high potential in both academic and practical aspects. The properties of the wave propagation and control such as coupling of the wave in and out etc., are thus of

* Sponsored by the National Science Council, Rep. of China.

fundamental importance. The study of attenuation of the optical waves in thin films against various losses forms in particular the primary but vital part of understanding the thin film guided waves.

In this report we describe in secton II our set-up of the experiment which includes both coupling of a laser light into and out of a thin film. In section III we report the experimental results of an ion-exchange waveguide and film of polyvinyl pyrylidone (PVP hence -forth). In section IV we describe briefly some simple apparatus which we made by ourselves for determination of refractive index and effective thickness of wave-guiding layer. In section V the attenuation and its dependence on the waveguiding modes are presented and finally in section VI we will summarize and discuss.

II. Experimental arrangement and method

As shown in Fig. 1, an incident laser light was led to focus on the prism at the right hand side. The laser used was a He-Ne model 155 of Spectra-Physics with its output wavelength at 6328 $\mathring{A}$. The prisms are of 45^{o}-45^{o}-90^{o} type having index of refraction $n_3 = 1.778$ at 6328$\mathring{A}$. The waveguide was a Ag^{+} ion layer in an ordinary microscope slide glass made by the usual ion-exchange process[1]. In the second experiment we made on a quartz plate a film of Polyvinyl pyrylidone which is just the Polariod print coater. The method of making it was simply to apply a film of the Polariod print coater to a quartz glass. The rotator allows the incident angle of the laser light to the prism to vary. This effectively changes the angle θ_3 for the synchronization condition[2].

$$n_3 \sin\theta_3 = n_1 \sin\theta_1 \qquad (1)$$

which is necessary for the reinforcement of the guided waves.

The method of the prism-film coupling by way of the evanescent field consists of three key points, viz., cleaness of the prism and the film, tightness of the adjustable screw and the proper height or

position of the incident light on the prism. With these in mind, the coupling work should be easily done. The coupling of the laser light into and out of the PVP film is shown in Fig. 2, a photo plate taken as the couplings were being made.

Coupling of a laser light into an optical wave guide may be made via either one of the four well known methods, viz., prism-film coupling, grating coupling, taper coupling and edge illumination. The main coupling scheme we performed was the prism-film method. However, we did succeed in a taper coupling with an ion-exchanged sodalime glass which had been made by the IBM Co. in the States. We suspect that the taper had been formed unexpectedly during its ion-exchange process which simply could not avoid leaving some kind of taper in the end of an ion layer. We found 3 modes propagating in the ion layer while the taper coupling was made.

The coupling techniques could be developed easily when the laser light paths in the prism were followed clearly. The coupling occurd when the light path from the prism base parallel to the wave guide to the prism face perpendicular to the film became vanishing. The light spot which produced the evanescent field was found not directly opposite to the tip of the clamping screw where the waveguide should contact the prism. This was actually due to coupling between prism and non-uniform air film which is well known for its high coupling efficiency. Slight vertical movement of laser light around the coupling position may clearly enhance the coupling efficiency.

III. Ion exchange film and PVP film

Similar to Fig. 2, we observed the coupling into and out of an ion exchange waveguide which was made in our laboratory by inserting an ordinary microscope slide glass into a $AgNO_3$ melt in a pyrax glass beaker at some $300^{\circ}C$ for one and half hours. The light coupled out of the film into the prism at the left hand side was allowed to fall on a screen to exhibit the structure of the modes. We found the

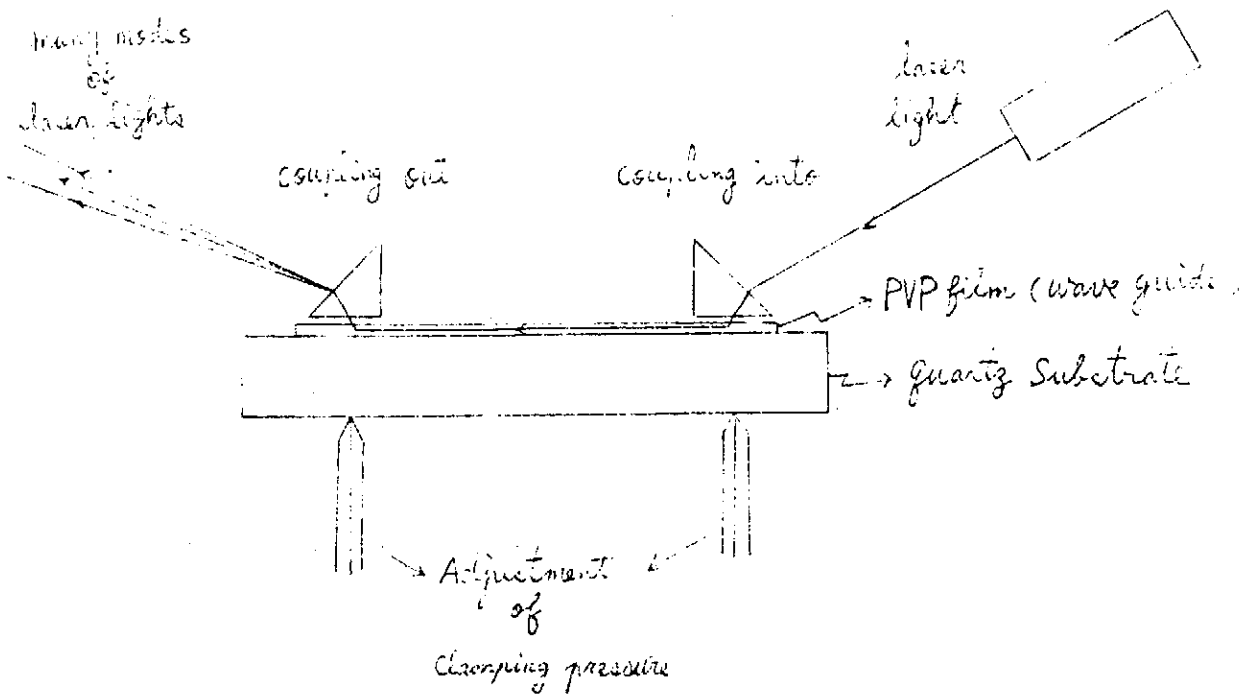

Fig 1. Prism-Film Coupler

mode structure containing eight vertical lines at approximately equal separation. Quantitative explainations of the mode structure can be made by computer analysis.

For the PVP film which we prepared here as mentioned above we obtained the picture of Fig. 2 showing very clearly the guided wave as being coupled in and out. The mode structure of the PVP film exhibiting 6 lines. The pattern may be compared to the Fig. 1 of Ref. 2 and Fig. 2 of Ref. 3 although their film was sputtered ZnO powder on glass with the C-axes of the crystallities oriented within a cone of 5^{o} from the film normal. The quantitative analysis of the mode structure needs again digital computer programming.

IV. Various self-made apparatus and measurement of refractive index

In the following we describe briefly those simple apparatus which we made by ourselves:

(1) A simple goniameter has been designed and manufactured with a rotating circular disk of 8 inches in diameter and with venier subdivisions. The angular positions can be read from the venier to within 3 minutes of one degree. This setting-up is very useful for determining the propagation constants at which the waveguide allows the laser light to propagate.

(2) A new design based on the well known Abbe Refractometry has been prepared. It enabled us to measure the index of refraction of our prisms, substrate and films. Further it can be employed to measure the refractive index of liquid films. In fact, it can be constructed independently as a cheap but powerful index meter. The accuracy of refractive index could be pushed to the third place to the right of the decimal point if focussing and collimating problems are carefully treated. Another method of measuring refractive index was also developed very successfully based on vanishing reflected light of TM polarization at the Brewster angle.

(3) Construction of a new electric furnace has been completed specially for the ion-exchange process of making thin-film waveguides. The temperature distribution can be made uniform and constant over a long period of time. It can also be adjusted to provide a constant gradient of temperature distribution along the axial direction of the cylindrical furnace. We have made an Ag^+ ion-exchange glass waveguide which exhibited gradual change in the thickness of the Ag^+ ion layer along the longest side of the glass. Its feature was that the higher orders of mode of the wave propagation occured with the shorter length of the streak of light in the waveguide.

Upon Completion of the above constructions we were prepared to

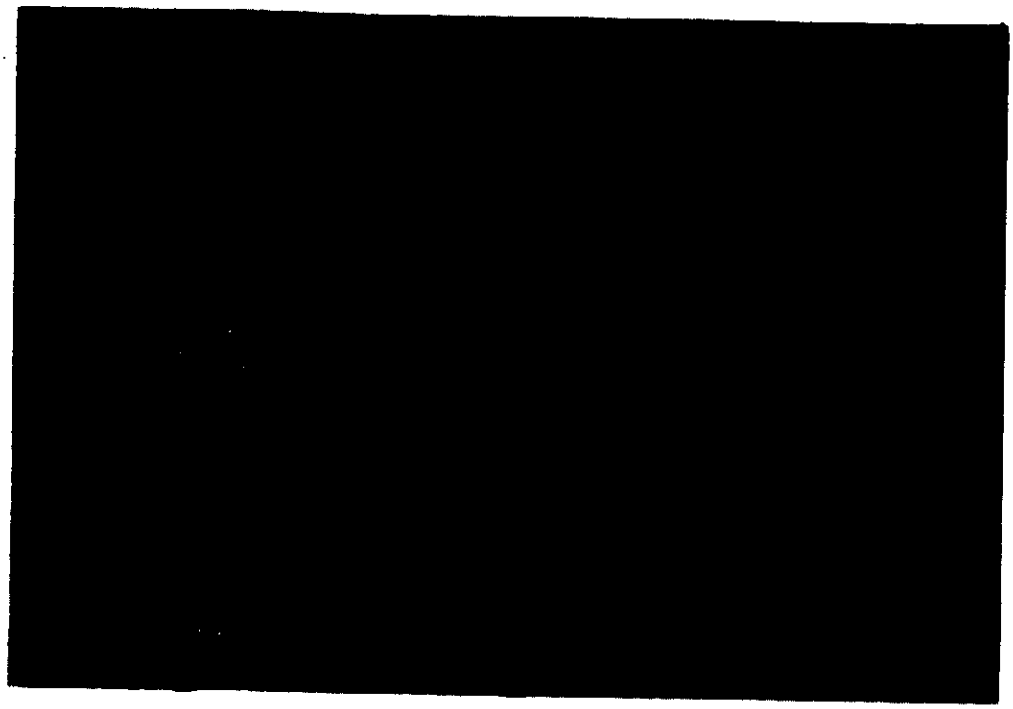

Fig 2.

Fig 3.

read the angular positions at which the coupling of light wave into the waveguide occured. These angular positions can be converted into propagation constants N via the following equation:

$$N = \sin \alpha_m \cos \epsilon + (n_p^2 - \sin^2 \alpha_m)^{1/2} \sin \epsilon$$

where α_m , ϵ and n_p are the angular distance of mode m, the angle of the coupling prism (here $\epsilon = 45^\circ$) and the refractive index of the prism respectively. Based on these observed propagation constants we proceeded to determine the parameters of our ion—exchanged films, namely, the index of refraction n_1 and the effective thickness of the ion-exchange film on its substrate.

Determination of the effective thickness of the Ag^+ layer which was assumed uniformly distributed just like a wave-guiding thin film on a glass substrate has been tried with the help of the Tsing-Hua IBM 1130 digital computer. To check the computer program we have programmed and used the computer to plot the film thickness versus the propagation constant for a family of curves corresponding to various orders of propagation modes for all TE polarization. The plot, shown in Fig. 4 is checked for TE modes perfectly to that of the original paper of reference 3.

In this figure is a plot of thin film thickness W against the propagation constant Beta/K for substrate index n_o=2.19, film index n_1= 3.275 and laser light wavelength λ = 10.6 micron. This reproduces the original plot appeared in Ref. 3 for TE modes, showing that our computer work being correct. In order to see the difference between TE and TM modes we also calculated and plotted the corresponding TM modes which are not available in Ref. 3.

The results of the waveguide parameters which we obtained by fitting the computer data to our experimental values of propagation constants of various modes were estimated to be: n_1 = 1.595 as the

film index of refraction and W = 1.39 micron as the effective thickness of the Ag^+ ion film.

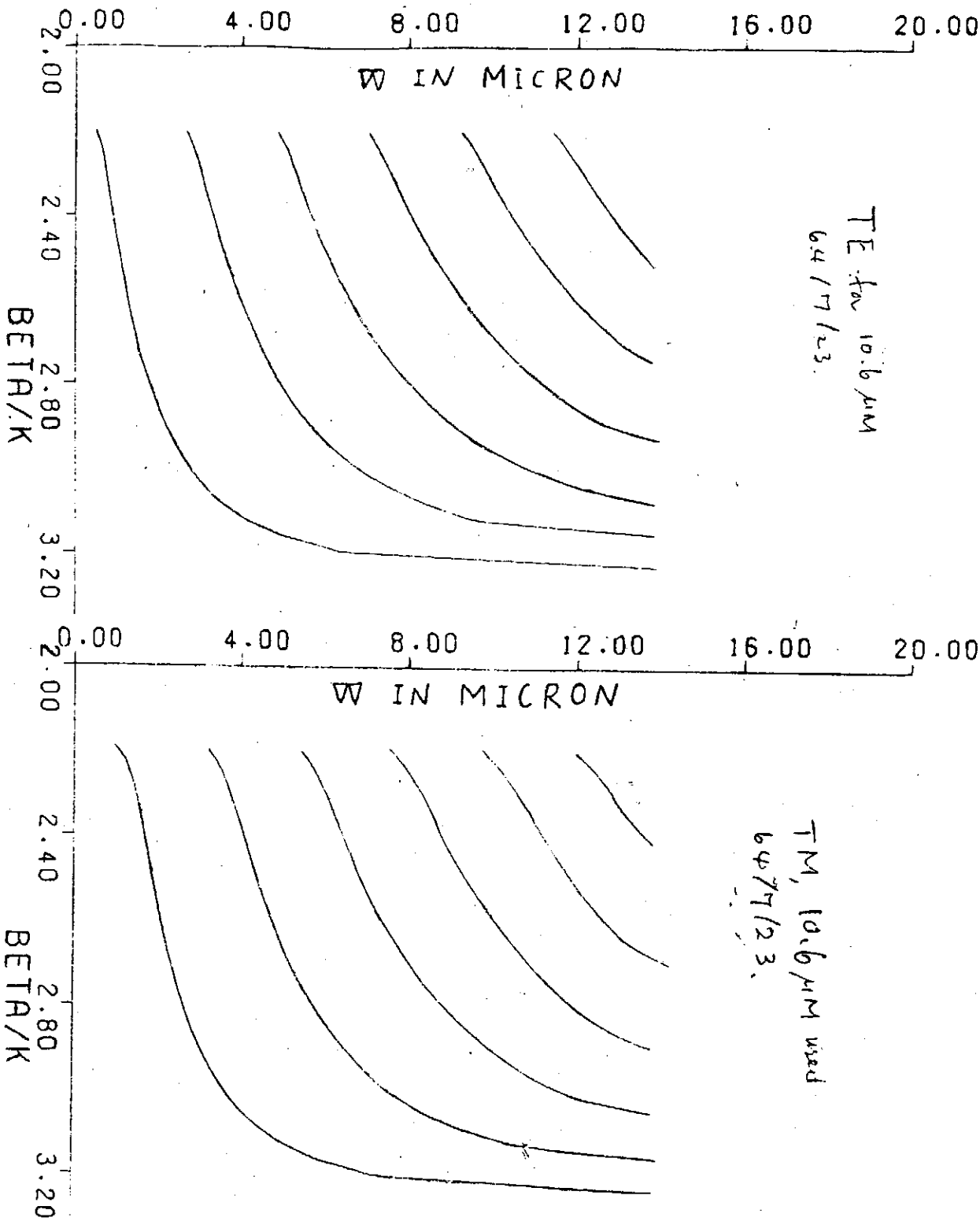

Fig 4.

V. Attenuation Measurement

Three methods are known for measuring the attenuation, namely, the direct method, optical imaging method and the two-prism coupling method. Due to the weak intensity as observed from the streak of light in the waveguide the optical imaging method appeared not workable. By the direct method we mean to place the CdS photoresistor (with a slit in front) almost in contact with the waveguide and measure the intensity at various positions. Since this method does not affect the coupling conditions, it was employed to determine the attenuation constant along the waveguide. A Keithley 610B electrometer was used to yield an electric signal from the CdS detector which was converted as light intensity via the characteristic CdS curve, i.e., a log-log plot of resistance R in ohms versus the intensity I in foot candles. The relation between the CdS resistance R and the intensity I on the CdS was obtained via the characteristic curve from the manufacturing company:

$$\ln R = -1.078 \ln I + 8.530$$

which has been assumed good and used for our CdS resistors.

During the measurement using the direct method with a low cost 0.5 mw He-Ne gas laser we found that the intensity of laser output subjected to fluctuation to about 10 percent. Cooling by an electric fan was found to reduce the intensity fluctuation to about 5% with random but longer periods. To overcome this difficulty we split by reflection the laser light with a glass plate as a reference signal and kept the transmitted light of about 90% of the unsplit intensity as the main signal through the wave guide. The two signals respectively of the two branches were arranged to feed in an x-y recorder so that the slope of the curve (a straight line) of the main signal versus the reference signal as plotted in the x-y recorder should be independent of the fluctuation. However, since the range of the fluctuation was

rather small, the value of the mentioned slope were not readable. We then only plotted the reference signal against time in the x-y recorder and used the plot to monitor the laser intensity and perform correctinn when necessary. With this monitor arrangement we took the data of the resistance of the reference signal E_x, on a Keithley 610C electrometer and those of the main signal, $E_y(x)$, on a Keithley 610B electrometer. The ratio of intensity of the main signal $I_4(x)$ to that of the reference signal I_2 can be expressed from the CdS characteristic:

$$I_4(x) / I_2 = \left(\frac{E_x}{E_y(x)} \right)^{1/1.078}$$

where $I_4(x)$ and $E_y(x)$ depend on the position x along the streak of light. We read E_x and $E_y(x)$ and calculated $I_4(x)$ in unit of the constant I_2 for 5 positions separated by 4mm between two neighboring positions. From the set of $I_4(x)$ which should be independent of the laser fluctuations we obtained for M=0, TE mode in the IBM Ag^+ ion-exchanged waveguide an average attenuation constant $\alpha = 1.0\ cm^{-1}$ where the intensity, I_2, of the light in the waveguide was described as

$$I(x) = \text{constant}\ e^{-\alpha x}$$

The mode dependence of attenuation constant can be obtained if we associate a mode index m to α as α_m. Thus, the intensity of guided light of mode m becomes

$$I_m(x) = C_1\ e^{-\alpha_m x}, \quad \text{for TE or TM,}$$

where C_1 is a constant (equal to $e^{8.53}$ for the CdS under consideration). Suppose we write the above equation for the nth mode and Combine these with the resistance-intensity relation rewritten as

$$R = e^{8.53} / I^{1.078}$$

we obtain readily.

$$\alpha_m = \alpha_n - \frac{1}{1.078x} \ln \left(\frac{R_n}{R_m} \right)$$

in which R_n, R_m and x are respectively CdS resistance for n^{th}, m^{th} modes and the distance along the length of the waveguide. In an experiment using the facility of Argon ion laser at 5145 Å wavelength with automatic feedback control of output intensity we used the 2-prism coupling method as shown in Fig. 1. We found four modes in the IBM ion-exange waveguide for the green laser light whereas we had only three modes for the He-Ne red source. This was as expected. For each of the modes at a fixed separation x between the 2 prism we read the resistance value from the 610B meter.

For example, for x=1.395 cm we took four readings for the four modes. In this way we started with our previous value α_o=1.0 cm^{-1} for m=0, (TE modes unless otherwise stated), we calculated α_1 from the above formula. Similarly α_2 and α_3 were calculated. For three more separations x we again obtained the α_i's. The average $\bar{\alpha}_i$ obtained from these data were

$$\bar{\alpha}_o = 1.00 \quad cm^{-1}$$

$$\bar{\alpha}_1 = 1.33 \quad cm^{-1}$$

$$\bar{\alpha}_2 = 1.84 \quad cm^{-1}$$

$$\bar{\alpha}_3 = 2.27 \quad cm^{-1}$$

VI. Discussions

The monotonic increase in $\bar{\alpha}_i$ was reasonable because of the monotonic increase in the number of boundary scatterings[5] of the zigzag light of higher mode. The $\bar{\alpha}_o$ would represent the volume at-

tenuation in the waveguide. As is well known, one advantage of ion-exchange waveguide is among others smaller loss due to scattering by the smoother boundaries of the ion layer in constrast to the sharply defined boundaries of an ordinary waveguide with its light guiding film deposited on a substrate.

Several other phenomena need mention. The $AgNO_3$ used in our experiment was of low cost grade made by a Japanese Co. with specification of 99.7% purity. The ion-exchange waveguide yielded red light when a green laser light from the Argon ion laser was coupled in it. We believe that this red light might be created from a fluorescence of some impurities like iron, etc., contained in the ion layer. We also note that we used a pyrax glass beaker instead of a platinum cup.

The intensities encountered in the attenuation measurement by the so-called direct method were so weak that the noise due to reflection or scattering at our clothes appeared to affect the data seriously. Thus we did this experiment very carefully and checked from time to time for any type of source of noises. The resistance across the CdS measuring the light intensity in the waveguide was up to the order 10^8 ohms which was close to the upper limit usable for the CdS. The times needed for the meter pointer to settle were much longer for the high resistance region especially after turning on the light for changing the position of the CdS detector. The 60 cps fluctuation in the He-Ne laser light intensity was also observed in the plot of the x-y recorder. It was found very clear in the weak intensity or high resistance branch but was not observable in the reference branch of much higher intensity.

Acknowledgement

The authors are indebted to Dr. D.M. Huang for his stimulating and helpful discussions. Thanks are also extended to him and Dr.

H. Chang for using their Argon ion laser facility and some optical components. We are again very grateful to Miss S. Liu for her computer programming work.

References

1. T. G. giallorenzi, E.J. West, R. Kirk, R. Ginther, and R. A. Andrews. Applied optics Vol. 12, No. 6, P. 1240 (1973)
2. P.K. Tien, R. Ulrich and R.J. Martin, Applied Physics Letters, Vol. 14, No. 9, p. 291.
3. P.K. Tien and R. Ulrich, Journal of the Optical Society of America, Vol. 60, No. 10, p. 1325.
4. Eq. (15) of reference (2).
5. P.K. Tien, Appl. Opt. 10, 2395 (1971).

RADIATIVE PROTON CAPTURE STUDY OF THE GIANT DIPOLE RESONANCE IN ^{55,57}CO

J. V. Maher and L. Meyer-Schutzmeister
Argonne National Laboratory, Argonne, Illinois 60432
and
E. L. Sprenkel Segel
Illinois Institute of Technology, Chicago, Illinois 60616
and
Argonne National Laboratory, Argonne, Illinois 60439
and
D. von Ehrenstein, R. J. Nemanich, and G. C. Kiang
Northern Illinois University, DeKalb, Illinois 60115
and
Argonne National Laboratory, Argonne, Illinois 60439
and
J. F. Tonn
Northerwestern University, Evanston, Illinois 60201
and
R. E. Segel
Northwestern University, Evanston, Illinois 60201
and
Argonne National Laboratory, Argonne, Illinois 60439

Extensive yield-curve and angular-distribution measurements have been made for the $^{54}Fe(\rho, \gamma_0)$ and the $^{56}Fe(\rho, \gamma_0)$ reactions. Both hield curves clearly show the envelope of the giant-dipole resonance. The giant resonance appears to be broader in ^{57}Co and this is attributed to a greater isospin splitting and to the fact that proton emission from the two isospin components is expected to be more nearly euqal. In both cases the angular distributions appear to be somewhat different for the two T compenents with the difference greater in ^{57}Co.

[NUCLEAR REACTIONS $^{54}Fe(\rho, \gamma_0)$, E_p=4.75-16.80 MeV, $^{56}Fe(\rho, \gamma_0)$ E_p=4.65-17.40 MeV, measured $\sigma(E_p)$, $\sigma(\theta)$ at many E_p values. Deduced for (γ, ρ_0) $\sigma(E_\gamma, \theta)$ in giant dipole resonance of $^{55,57}Co$.]

INTRODUCTION

Much of the knowledge of the structure within the giant-dipole resonance comes from radiative-capture experiments. One of the important structures is the splitting of the giant resonance in all but self-conjugate nuclei into two isospin components. The observation of this splitting has been reported in a number of nuclei[1] with protoncapture experiments playing a major role in the identification of the isospin components. A theoretical expression for the variation of the energy splitting with mass number and ground-state isospin has been developed[2] that appears to agree with most of the experimental data.[1] In the present work we examine isospin effects further by studying proton radiative capture through the giant resonance in two closely spaced isotopes.

In nuclei with but a small neutron excess, the gamma-ray absorption strength can be expected to divide between the two isospin components in the ratio $T_> : T_< = 1:T$ since an E1 gamma ray is pure

isovector.[3] Neutron emission is forbidden from $T_>$ states except for decays to analog states. On the other hand, both proton and neutron decay are allowed from the $T_<$ part of the giant resonance and therefore the strength will be divided between these two channels. Alpha emission from the $T_<$ states is also possible but is small even in lighter nuclei[4] and is likely to be further inhibited by the Coulomb barrier in nuclei as heavy as Co. Table 1 gives the expected division of the total gamma-ray strength under the assumption that the (γ, n) and (γ, p) reactions take up the entire reaction cross section. Using the expressions given in Table I, for the (γ, p) reaction in T = $\frac{1}{2}$ ^{55}Co, $T_>$: $T_<$ = 5:1 while in ^{57}Co this ratio is 1.51. These ratios illustrate that the (γ, p) reaction emphasizes the $T_>$ component of the giant diploe resonance. In the present work it is, of course, not all protons but just the ground-state protons that were studied and the fraction of the total (γ, p) strength to the ground state can be expected to vary. Thus, the ratios given above can only be considered to be indicative and are not firm predictions.

Studies of self - conjugate nuclei have revealed the puzzling phenomenon that the gamma-ray angular distributions vary very little with energy even when the yield curve is rich in structure and shows violent variations with energy.[5] While there is extensive angular-distribution data on the self-conjugate nuclei, little such data has been reported on the nuclei where two isospin components are expected. In the present work therefore, in each isotope we have taken angular distributions at a large number of points spanning the entire energy region studied.

YIELD CURVES

The experimental arrangement was similar to that used in other radiative capture experiments that have been done at Argonne.[5] In the present work the gamma rays were detected by two NaI(Tl)

crystals, each 25 cm in diameter and 30 cm thick. Pileup was suppressed by circuitry that has been described previously[6]; the rest of the electronics was conventional. Targets were rolled iron foils whose thickness totalled about 2 mg cm^{-2}. The ^{54}Fe targets were enriched to 97.7%, while for the ^{56}Fe the enrichment was nearly 100%. Typical pulse-height spectra are shown in Figs. 1 and 2. In both ^{55}Co and ^{57}Co only the ground state is separated from other levels by as much as 1 MeV and therefore only the ground-state transition was studied.

Yield curves as a function of proton energy with the crystals at 90° to the incident beam were taken in 50-keV steps. For the ^{54}Fe (p, γ_0)^{55}Co reaction, the $4.75 \leq E_p \leq 16.80$ MeV range was covered when ^{56}Fe was bombarded the range was from 4.65 to 17.40 MeV. Applying the principle of detailed balance, the yield curves for the ^{55}Co(γ, p_0)^{54}Fe and ^{57}Co(γ, p_0)^{56}Fe reactions have been determined and these are shown in Figs. 3 and 4.

Both curves clearly show a giant-resonance envelope upon which considerable structure in superimposed. While in neither curve is there a clear indication of a splitting into two components, the entire pattern is consistent with isopsin splitting with the expected behavior. Specifically, it is quite reasonable that for these rather low T nuclei the width of each T component is greater than the energy difference between them, and therefore the two envelopes are not resolved. For T = $\frac{1}{2}$ ^{55}Co, as explained above, the ^{55}Co(γ,p) reaction should be dominated by the $T_>$ part. In T = $\frac{1}{2}$ ^{57}Co where the (γ, p) would be expected to be more nearly equally distributed between the two components, the energy splitting should also be greater. The ^{55}Co(γ,p_0) yield curve can be interpreted as being dominated by a T = $\frac{1}{2}$ giant resonance centered at about 19.2 MeV with a smaller amount of T = $\frac{1}{2}$ strength centered at about 17 MeV. The ^{57}Co(γ,p_0) curve can be said to have the T = $\frac{5}{2}$ strength centered at about 20.4 MeV and the T = $\frac{1}{2}$ strength centered in the region of

17.2 MeV. In both cases the relative intensity of the two isospin components, which can only be very roughly estimated, appears to be consistent with the ratios derived from Table I, and the energy splittings are in agreement with the prescription given by Akyuz and Fallieros.[2]

When averaged over the fine structure, the maximum ^{55}Co(γ, p_0) cross section is about $2\frac{1}{2}$ times as great as the maximum ^{57}Co(γ, p_0) cross section. Both yield curves show a giant resonance above a nonresonant yield of about 12 μb sr. Some of the useful information that can be extracted from the yield curves is given in Table II.

Only a very small fraction ($<1\%$) of the giant dipole resonance in either ^{55}Co or ^{57}Co goes into the ground-state proton channel. While a trend of less and less of the total strength in proton emission to the ground state as the atomic number is increased is to be expected,[6] the strengths found here are considerably less than that observed in the ^{60}Ni(γ, p_0) reaction.[7] An explanation can be found if it is remembered that both ^{55}Co and ^{57}Co contain a proton hole in the $f_{7/s}$ shell. Removal of a valence proton will leave, in effect, the configuration $(f_{7/2})^{-2}$ with four possible spin values of which only one, 0^+, is that of the ground state of the residual nucleus. On the other hand, ^{60}Ni, like most other nuclei in which the (γ, p_0) reaction has been studied, is even-even with all nucleons paired. Removal of an $f_{7/2}$ proton from ^{60}Ni must have a $\frac{1}{2}^-$ residual nucleus and this is the spin of the ground state of ^{59}Co. Generalizing the above argument, which is admittedly crude and contains oversimplifications, leads to the conclusion that there will be a tendency for the (γ, p_0) yield to be larger in even-even nuclei than in odd-Z nuclei

A statistical analysis was made of the yield curves using the methods given by Ericson[8] and previously applied to (p,γ) data.[9] The autocorrelation function

$$R(e) = \left\langle \left(\frac{\sigma(E)}{\langle\sigma\rangle} - i \right) \left(\frac{\sigma(E+\varepsilon)}{\langle\sigma\rangle} - i \right) \right\rangle \qquad (1)$$

was computed for both yield curves. Figure 5 shows the autocorrelation function obtained for the $^{54}Fe(p, \gamma_0)$ reaction. In both cases a rather small mean square deviation (R(0)), ~4% for $^{54}Fe(p, \gamma_0)$ and ~2% for $^{56}Fe(p, \gamma_0)$ was found. Using a 2-MeV averaging interval in the determination of the average cross section, the characteristic c.m. coherence widths Γ=43 keV for $^{54}Fe(p, \gamma_0)$ and 33keV for $^{56}Fe(p, \gamma_0)$ were found. Both are less than the 48-keV step size, which means that they are in reality only upper limits. Compound level widths much less than 50 keV are what would be expected for nuclei in this mass region excited to 20 MeV. Because the effective energy resolution which was essentially determined by the target thickness was large compared to Γ, the fluctuations were damped and the smaller mean-square deviation found for the $^{56}Fe(p, \gamma)$ yield curve might be due to Γ being smaller in ^{57}Co.

One of the main reasons for performing the statistical analysis was to search for intermediate structure. To this end R(0) was computed as a function of the averaging interval. If there is a significant intermediate-structure component, R(0) should rise, plateau, and then continue to rise.[9] No such behaviour is present (Fig. 6) and it is thus concluded that if there is a significant intermediate srtucture, in each case it must be less than about 100 keV wide.

ANGLUAR EISTRIBUTIONS

For the $^{54}Fe(p, \gamma_0)$ reaction, angular distributions were taken every 500 keV from 7.5 to 17.0 MeV and in somewhat smaller, irregular steps down to 4.90 MeV. In the $^{56}Fe(p, \gamma_0)$ study, angular distributions were taken every 500 keV from 6.0 to 16.5 MeV and also at 16.90 MeV. In both cases a five-point (30^o, 60^o, 90^o, 120^o, 150^o) angular distribution was taken with each crystal and the results were averaged. The distributions were expressed as the usual Legendre polynomial sum: $W(\theta) = A_0[1 + \sum_{n=1}^{4} a_n P_n(\cos\theta)]$. The coef-

ficients that were extracted from the data are shown in Fig. 7 for ^{54}Fe(p, γ_0) and in Fig. 8 for ^{56}Fe(p, γ_0).

Except perhaps at the lowest energies, below the giant resonance region, the coefficient a_4 in the ^{54}Fe(p, γ_0) reaction is indistiguishable from zero. The coefficient a_3 is also near zero throughout, possibly starting to go negative at the high-energy end. These nul or nearly nul results for the higher coefficients are, of course, expected if dipole radiation is to be dominant. The coefficient a_2 seems to average to zero below the main giant resonance, to be slightly positive on the low side of the main peak and slightly negative on the high side. It is noteworthy that the energy where a_2 changes sign, $E_\gamma \approx 18$ MeV, is just about the point where the speculations about the yield curve put the dividing line between the $T_<$ and the $T_>$ part of the giant resonance. Finally, a_1 is slightly positive throughout, reflecting the forward peaking that is usually observed in photonuclear reactions.

In the ^{56}Fe(p, γ_0) reaction the coefficients a_1, a_3 and a_4 exhibit a behavior that is similar to their behavior in the ^{54}Fe(p, γ_0) reaction. While it is true that a_4 appears to be positive throughout, the effect is small-$\overline{a_4} \approx 0.06$ in the giant resonance region-and probably attributable to experimental error. The coefficient a_2 is also somewhat similar in the two reactions, but the effects in the ^{56}Fe(p, γ_0) reaction are more pronounced. Here a_2 is positive on the low side of the giant resonance, reaching a value of about 0.35 at $E_\gamma \approx 16.5$ MeV, and then becomes slightly negative throughout the middle and upper part of the region. The crossover is at about 18.5 MeV which again is in the region where it is thought that $T_>$ starts to dominate.

Although the effects are small in both cases, the data does seem to indicate a systemtaic difference in the angular distributions through the $T_<$ and $T_>$ parts of the giant - dipole resonance. Furthermore, the difference is more pronounced in ^{57}Co than it is in ^{55}Co. That the pattern of angular distributions observed in the pre-

sent work is at least qualitatively in accord with expectations, follows from considering which excitations contribute to each isospin component. A schematic picture applicable to any nucleus with a neutron excess is shown in Fig. 9 where it can be seen that while all excitations that have a $T_>$ component also have a $T_<$ one, there are some excitations that contribute only to $T_<$. As the neutron excess increases so does the fraction of pure $T_<$ excitations and it is this phenomenon that gives rise to the deviation from the simple isospin-Clebsch-Gordan coefficients in the division of strength between the two isospin components.[10]

Where the neutron excess (and hence T) is small, the configurations of the two isospin components are similar and this may be the reason that the angular distributions show only a rather small change in going from the lower to the upper part of the giant-resonance region. The change is greater in $T = \frac{1}{2}$ ^{57}Co than it is in $T = \frac{1}{2}$ ^{55}Co and this too is in accord with the theoretical picture. It should be remembered that no such systematic variation of the gamma-ray angular distributions has been observed in any of the many self-conjugate nuclei that have been studied.[5]

Finally we note that while both yield curves show rapid fluctuations, the angular distributions, and in particular the coefficient a_2, do not show strong variations on a similar energy scale. This behavior is reminiscent of that observed in the self-conjugate nuclei where the angular distributions are nearly constant throughout the entire giant-resonance region.

SUMMARY

The yield curves and angular distributions obtained for the ^{54}Fe(p, γ_0) and ^{56}Fe(p, γ_0) all support the picture of a giant resonance split into two isospin components with the energy splitting and relative strengths in accordance with the theoretical expectations.

Neither the splitting nor the partition of strength is more than very roughly determined in the present work, but both do seem to show the correct behavior with increasing T_z. Perhaps the best identification of the two components comes in the angular distribution data where it appears that there is a small but significant change in the gamma-ray angular distribution in passing from the $T_<$ to the $T_>$ region. Why the further fragmentation (which the structure in the yield curve assures must be taking place) does not lead to major variations in the angular distributions, remains a mystery.

REFERENCES AND FOOTNOTES

+Work performed under the auspices of the U.S. Atomic Energy Commission.

[1]P. Paul, J. F. Amann, and K. A. Snover, Phys. Rev. Lett. 27, 1013 (1971); P. Paul, Int. Conf. on Photonuelear Reactions and Applications. ed. B. L. Berman (USAEC, Oak Ridge, 1973) p. 407.

[2]R. O. Akyuz and S. Fallieros, Phys. Rev. Lett. 27, 1016 (1971).

[3]M. Gell-Mann and V. L. Telegdi, Phys. Rev. 91, 169 (1953).

[4]L. Meyer-Schutzmeister, Z. Vager, R. E. Segel, and P. P. Singh, Nucl. Phys. A108, 180(1968).

[5]R. C. Allas, S. S. Hanna, L. Meyer-Schutzmeister, R. E. Segel, P. P. Singh, and Z. Vager, Phys. Rev. Lett. 13, 628(1964); R. E. Segel, Int. Conf. on Photonuclear Reactions and Applications, ed. B. L. Berman (USAEC, Oak Ridge, 1973) p. 899.

[6]R. E. Segel, Z. Vager, L. Meyer-Schutzemister, P. P. Singh, and R. G. Allas, Nucl. Phys. 93, 31 (1967).

[7]E. M. Diener, J. F. Amann, P. Paul, and S. L. Blatt, Phys. Rev. C3, 2302 (1971).

[8]T. Ericson, Ann. of Phys. 23, 290 (1963).

[9]P. P. Singh, R. E. Segel, L. Meyer-Schutzmeister, S. S. Hanna, and R. G. Allas, Nucl. Phys. 65, 577 (1965).

[10]S. Fallieros and B. Goulard, Nucl. Phys. A147, 593(1970); M. H. Macfarlane, Proc. of the Conf. on Isobaric Spin in Nuclear Physics, Tallabassee, Fla., ed. J. D. Fox and D. Robson, (Academic Press, 1966) p. 383.

TABLE I. Division of total E1 gamma-ray strength under the assumtpion that only the (γ,n) and (γ,p) reactions contribute significantly and that decay through analog states can be ngelected.

	$T_<$	$T_>$
(γ,n)	$\frac{2T}{4T+3}$	0
(γ,ρ)	$\frac{T(2T+i)}{(T+i)(4T+3)}$	$\frac{1}{T+i}$

TABLE II. Integrated strengths in the ^{55}Co(r,p0) and ^{57}Co(γ,p_0) yield curves. Strengths are given in MeV-mb.

	^{55}Co(γ,p_0)	^{57}CO(γ,p_0)
Area under main resonance	2.59	1.04
$\int \sigma$ dE over entire range studied	5.27	2.98
Classical dipole sum (=60 $\frac{NZ}{A}$)	825	853

FIGURE CAPTIONS

Fig. 1. Pulsc-height spectrum from a 25-cm diameter 30-cm thick NaI(T1) crystal showing the ground-state gamma ray from the $^{54}Fe(p,r)$ reaction. The spectrum was taken at a bombarding energy of 14.650 MeV with the crystal at 90° to the incident beam.

Fig. 2. Upper end of the pulse-height spectrum from the $^{56}Fe(p,r_0)$ reaction at $\theta = 90^{\circ}$, E_p=13,000 MeV.

Fig. 3. Yield curve at 90° for the $^{55}Co(r,p_0)^{54}Fe$ reaction obtained by applying detailed balance to the $^{54}Fe(p,r_0)$ measured cross sections.

Fig. 4. Yield curve at 90° for the $^{57}Co(r,p_0)$ reaction.

Fig. 5. Autocorrelation function computed for the $^{54}Fe(p,r_0)$ yield curve. In obtaining the average cross section anaveraging interval of 2.25 MeV was used.

Fig. 6. Mean-square deviation vs. averaging interval for the $^{56}Fe(p,r_0)$ yield curve.

Fig. 7. Coefficients obtained when the $^{54}Fe(p,r_0)$ angular distributions are expressed as a sum of Legendre polynomials.

Fig. 8. Angular distribution coefficients for the $^{56}Fe(p,r_0)$ reaction.

Fig. 9. Shell-model schematic showing isospin of various particle-hole excitations.

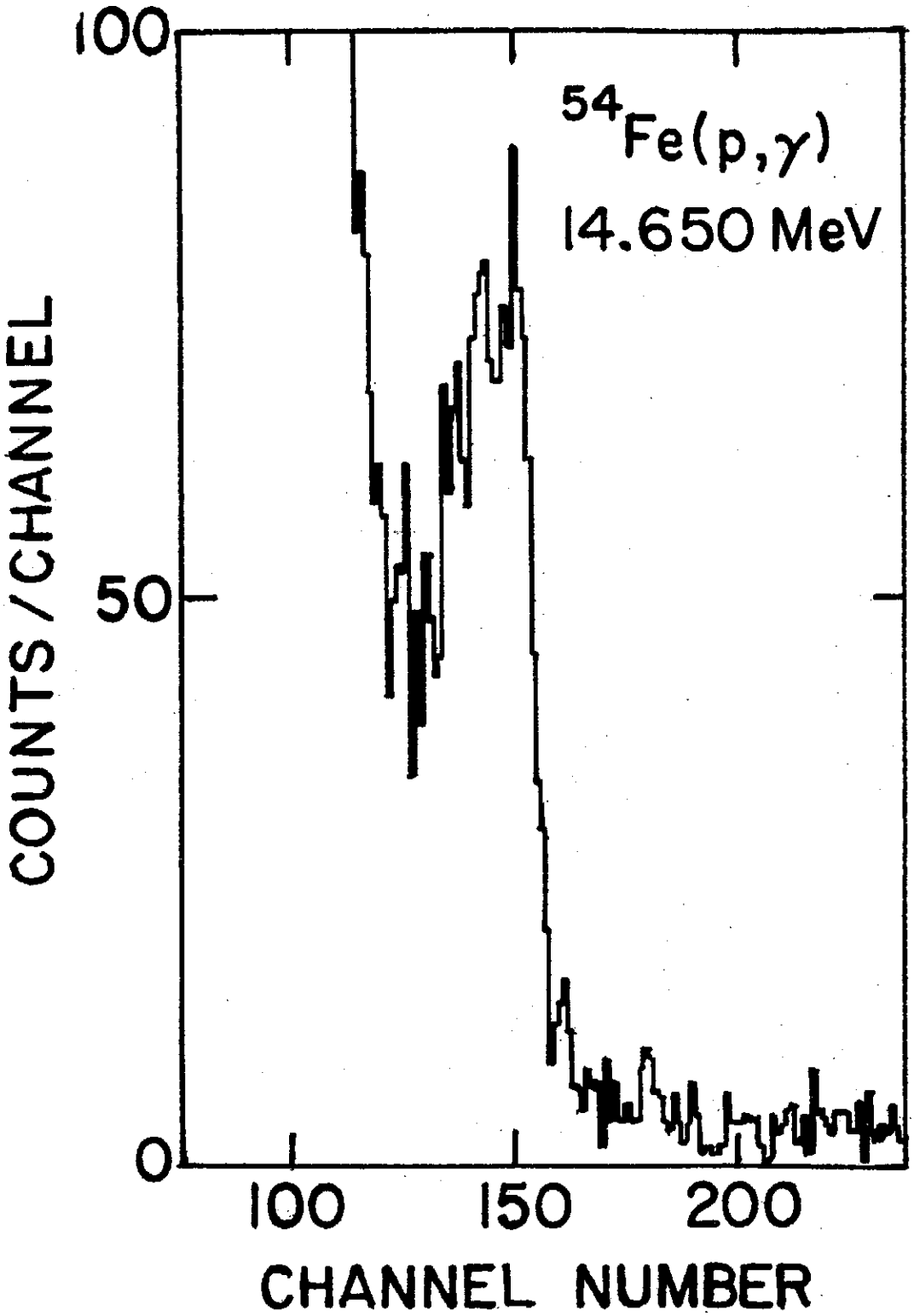

Fig 1. Neg. No. 209-3547:PHG-12081

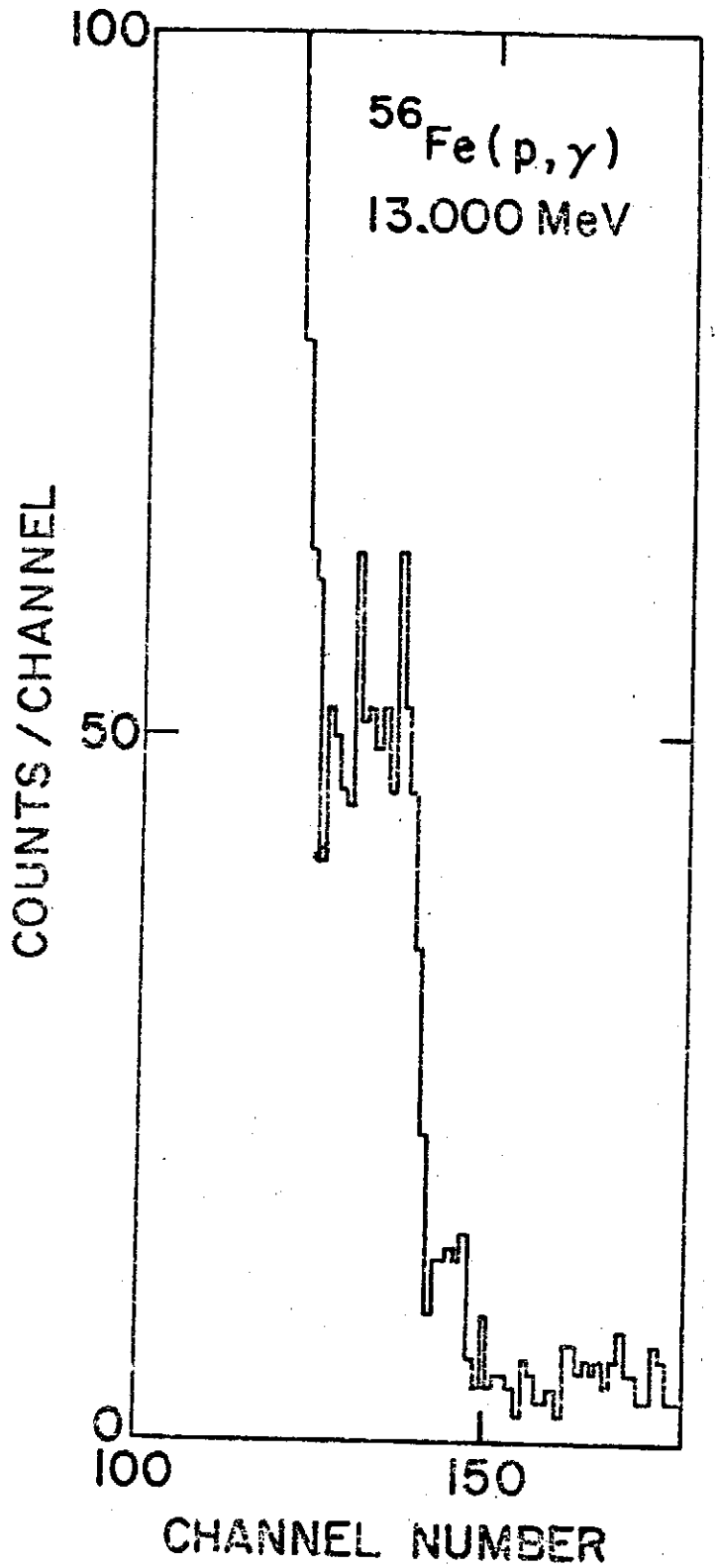

Fig 2. Neg. No. 209-3546:PHG-12080

RADIATIVE PROTON CAPTURE STUDY OF THE GIANT DIPOLE RESONANCE IN ^{55,57}CO

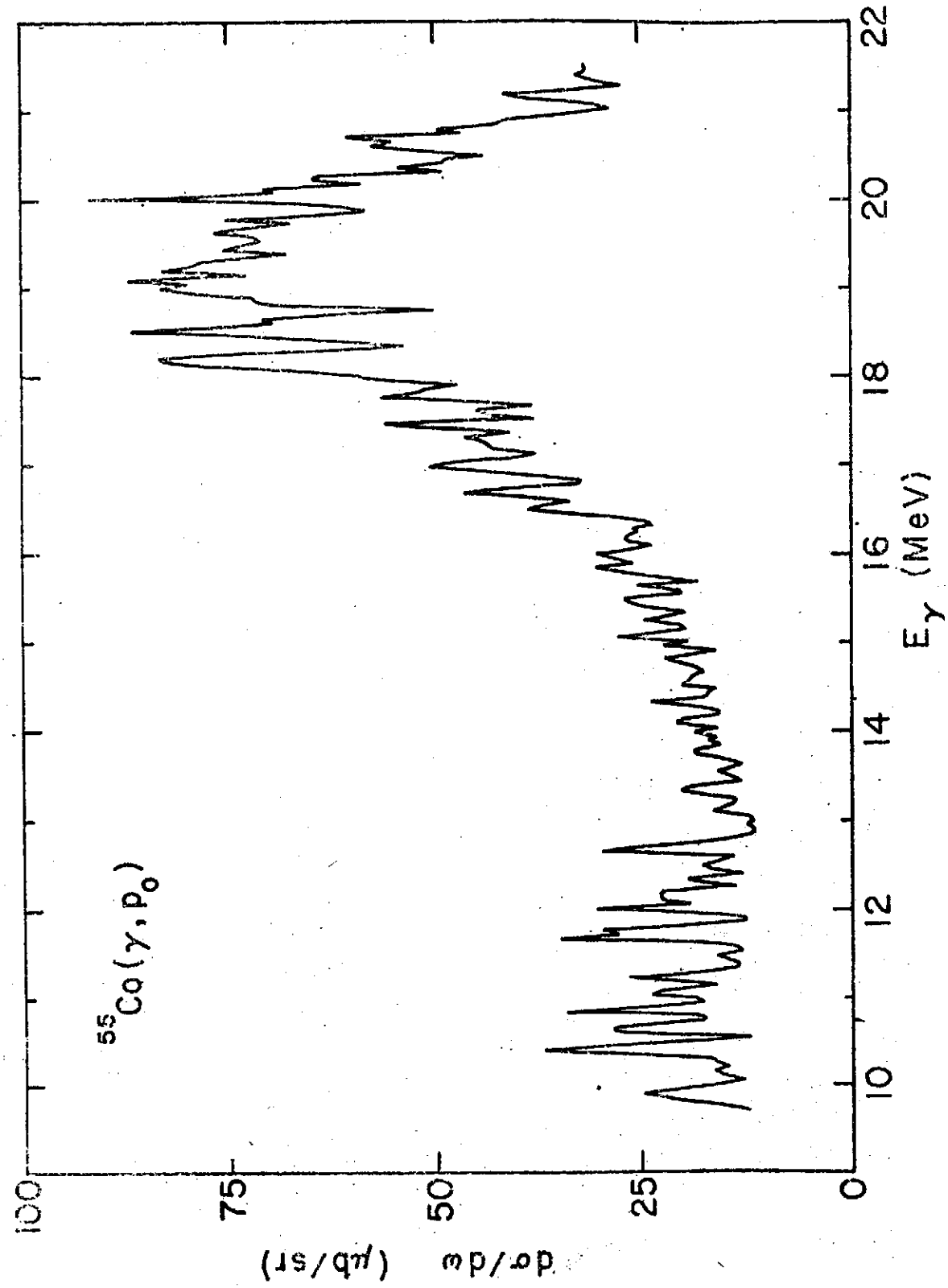

Fig 3. Neg. No. 209-3542:PHG-12076

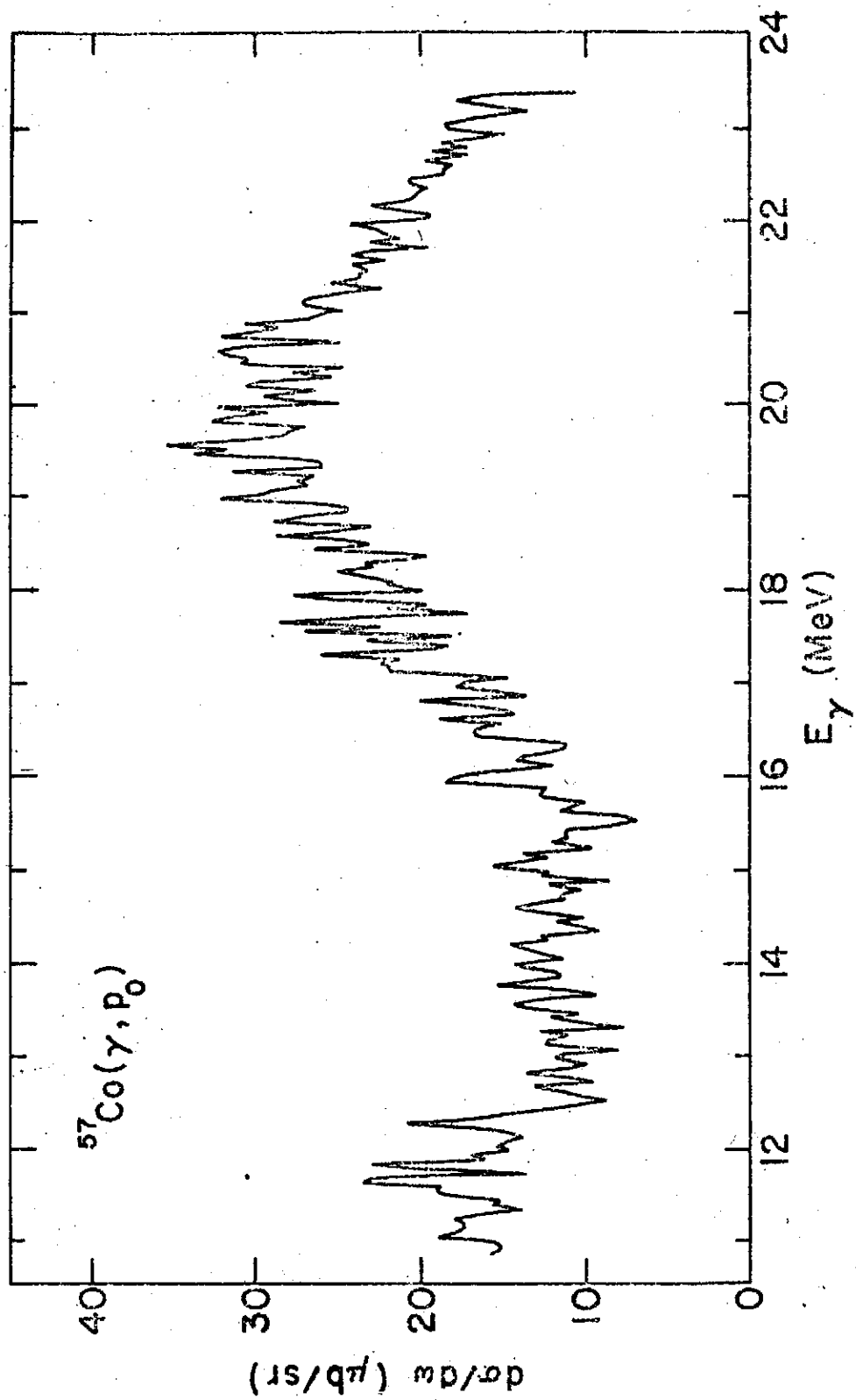

Fig 4. Neg. No. 209-3544:PHG-12078

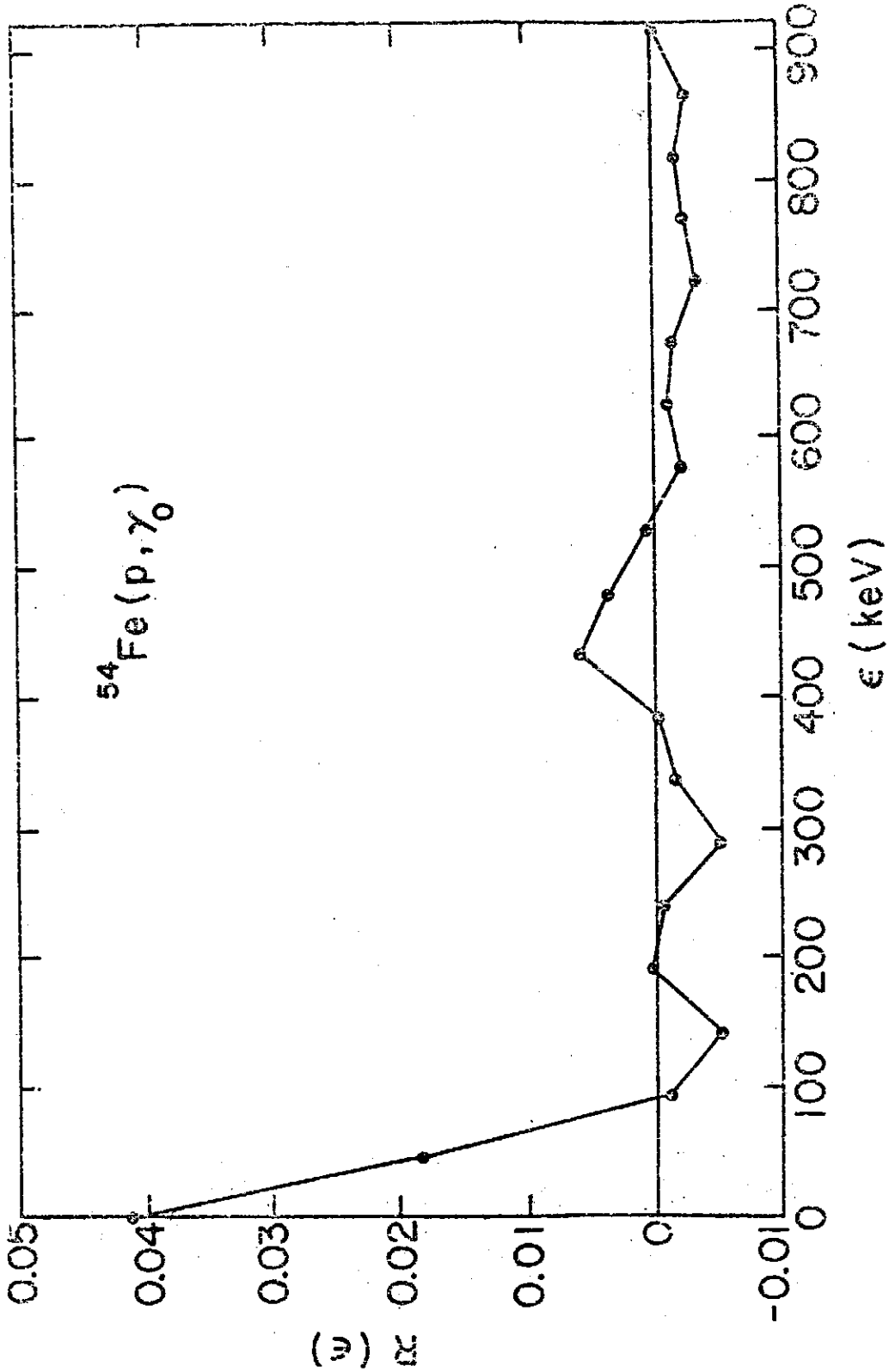

Fig 5. Neg. No. 209-3550:PHG-12084

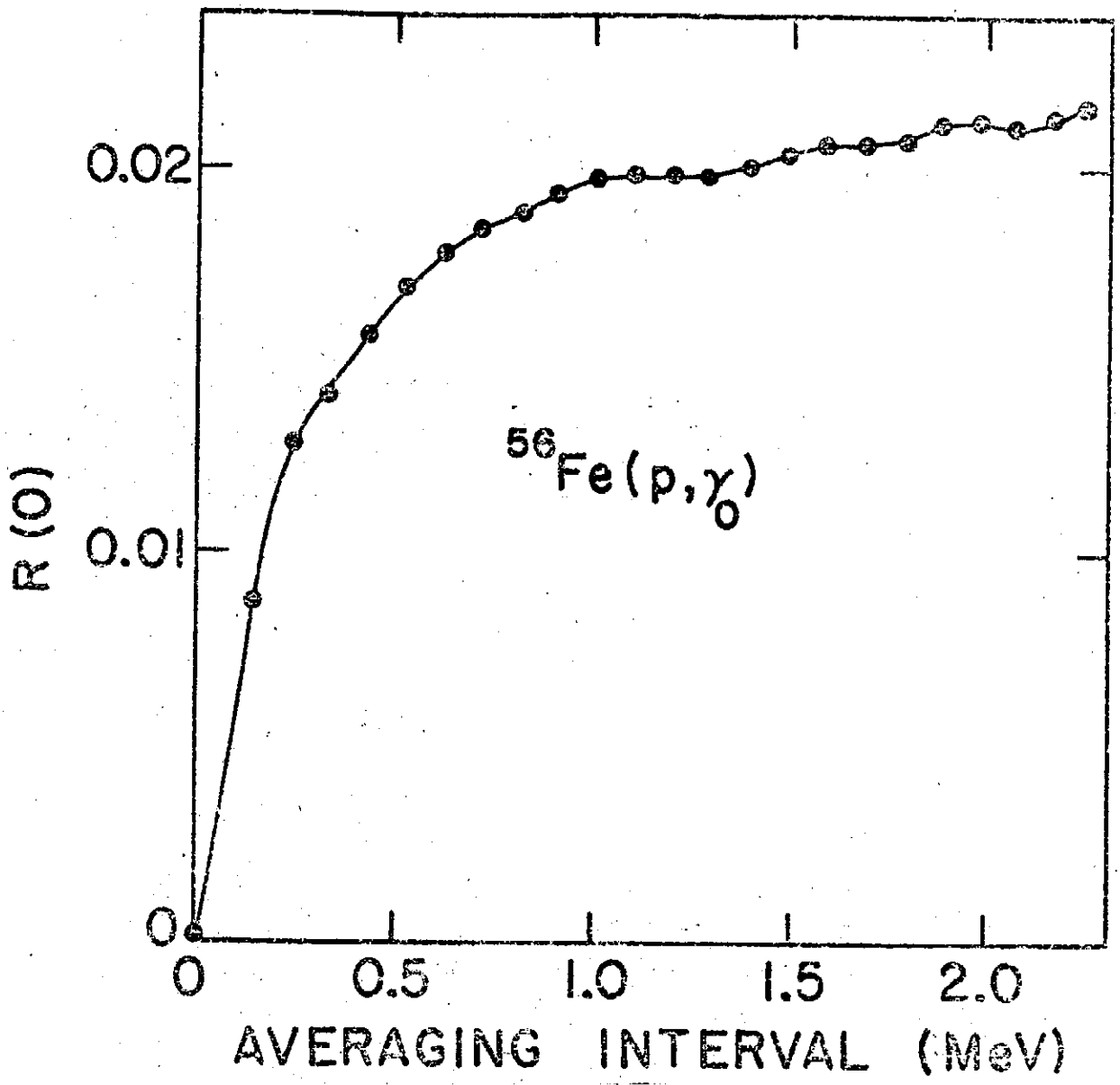

Fig 6. Neg. No. 209-3543:PHG-12077

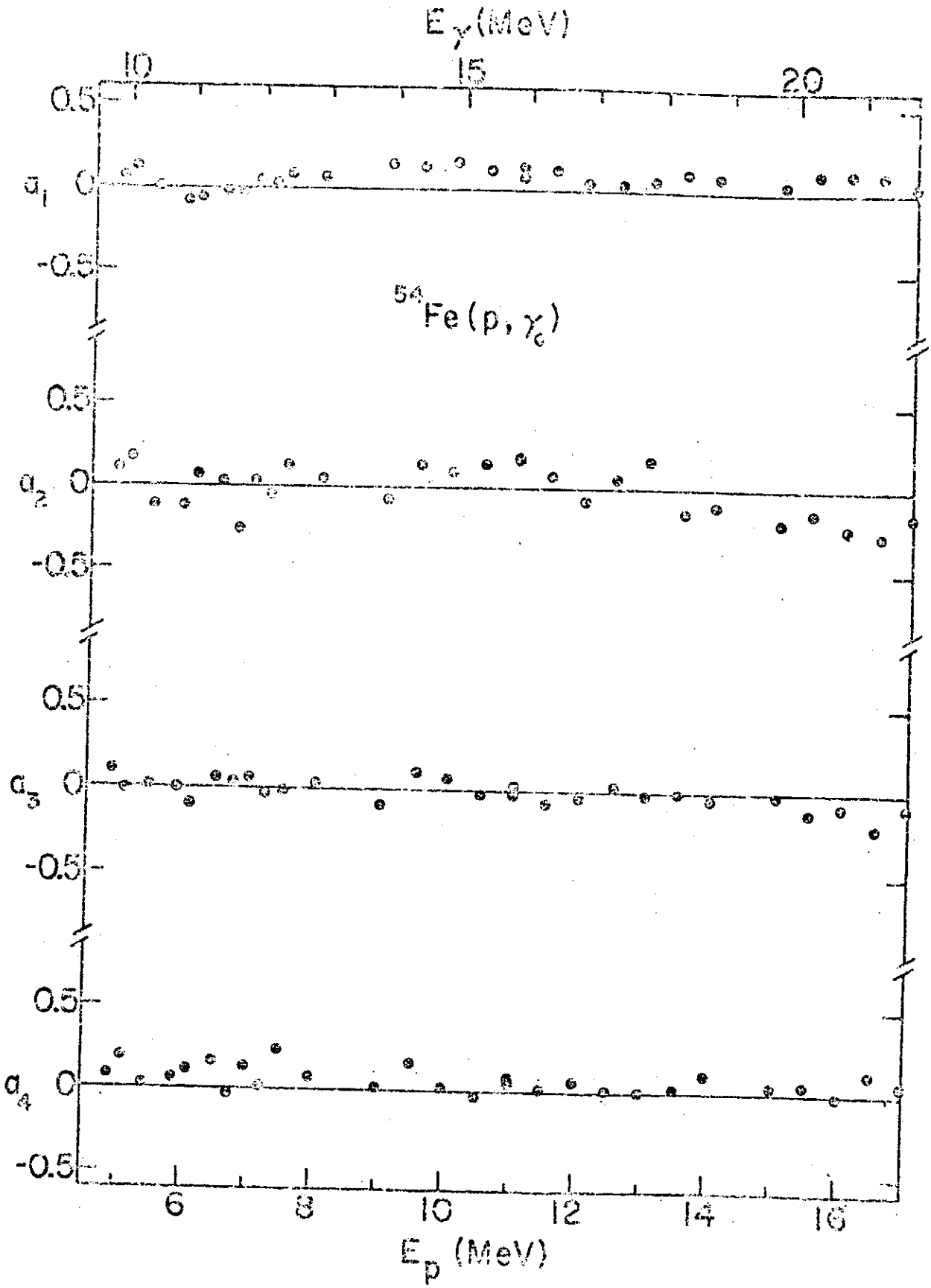
E_γ(MeV)
10
15
20
0.5
a_1 0
-0.5
^{54}Fe(p, γ_c)
0.5
a_2 0
-0.5
0.5
a_3 0
-0.5
0.5
a_4 0
-0.5
6
8
10
12
14
16
E_p (MeV)

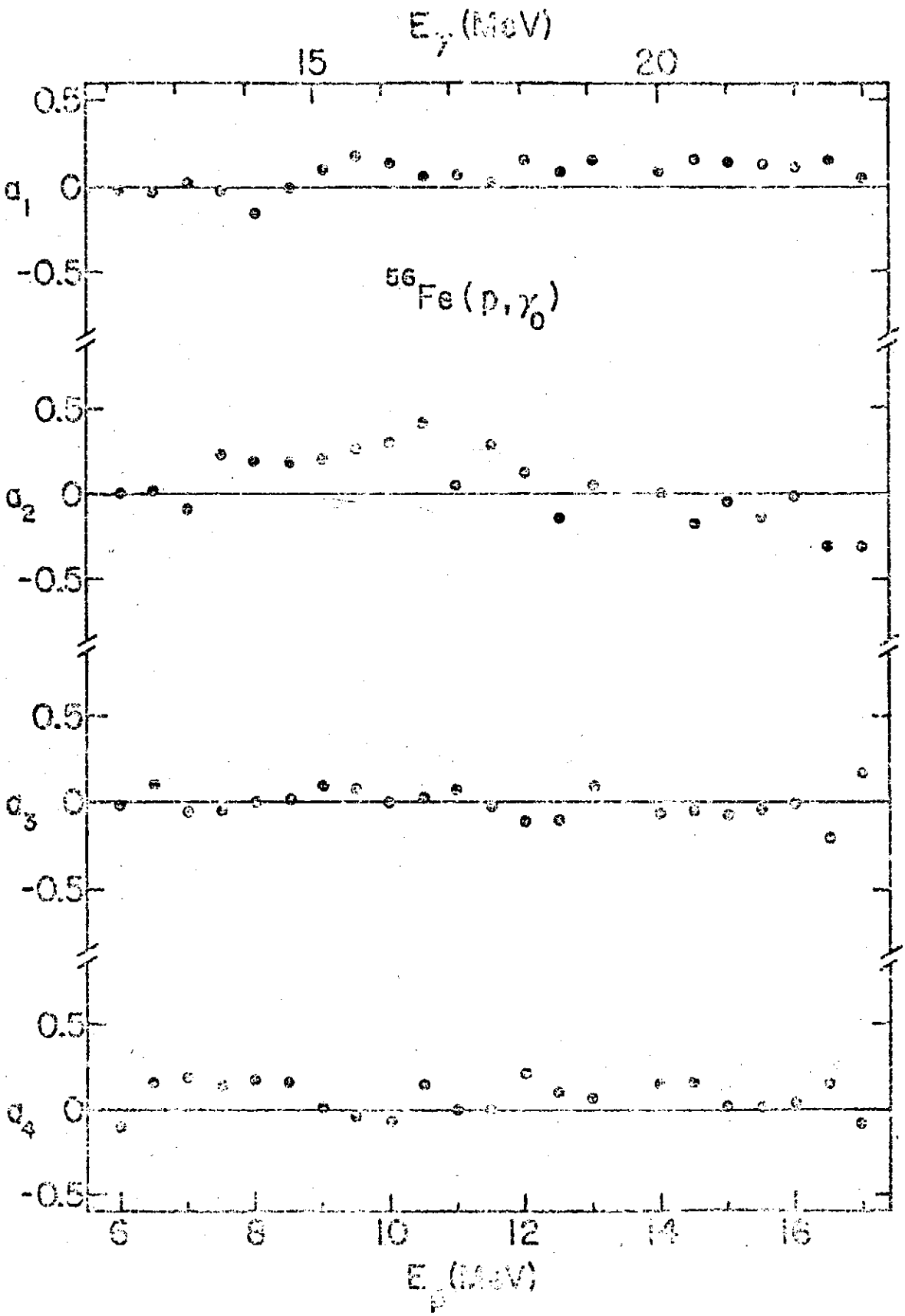
E_γ (MeV)
15
20
0.5
a_1 0
-0.5
$^{56}Fe(p,\gamma_0)$
0.5
a_2 0
-0.5
0.5
a_3 0
-0.5
0.5
a_4 0
-0.5
6
8
10
12
14
16
E_p (MeV)

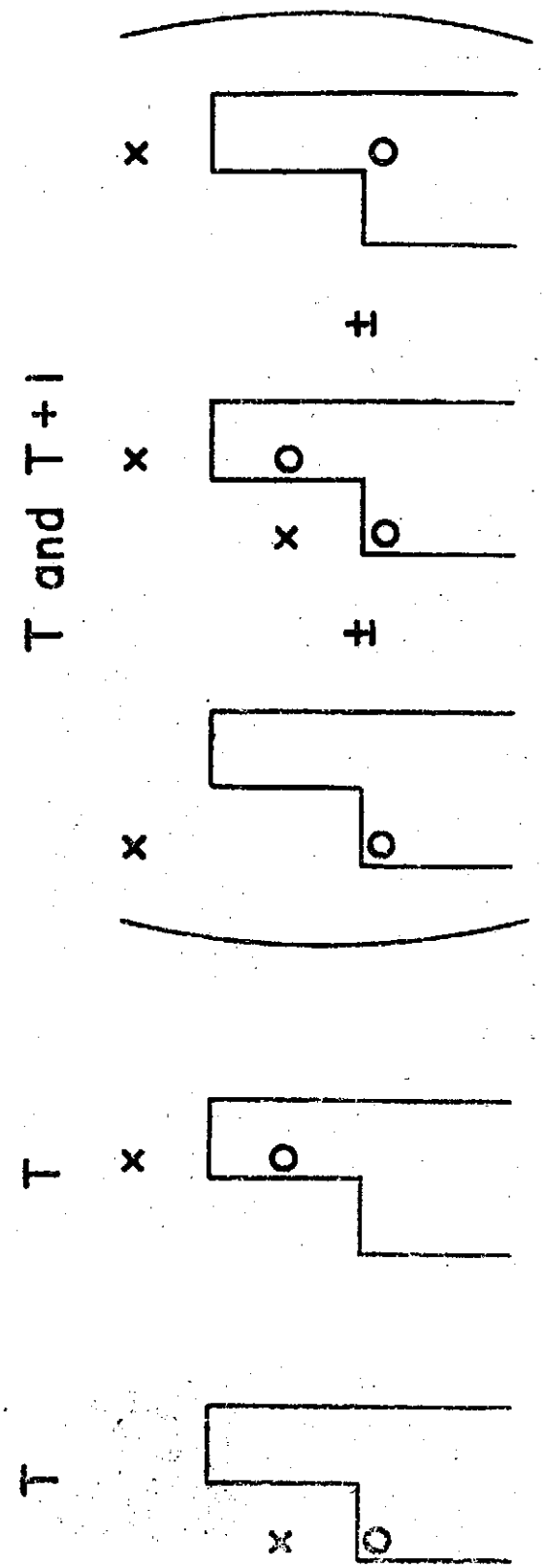

Fig 9. Neg. No. 209-3560:PHG-12096

ANNUAL REPORT OF THE INSTITUTE OF PHYSICS,
ACADEMIA SINICA, 1974

A Simple Computer Program for Automatic Gamma-Ray Spectra Analysis

（江紀成） （王建萬）
G. C. Kiang C. W. Wang* and L. L. Kiang
Institute of Physics, Academia Sinica
and
National Tsing Hua University

Abstract

A simple PORTRAN IV program SPAN-3 designed to analysis gamma ray spectrum is described. It uses a line shape consisting one or two gaussians and a guadratic background together to provide a precise fit to the singlet or doublet gamma ray peaks. An automatic peak searching and identifying subroutine KLOCP is also detailed described. Tihs program has been used on IBM 1130 small computer with very good results.

I. Introduction

The increasing usage of large-volume, high resolution Ge(Li) detectors for the gamma detection with large memory multichannel analyzer, the volume and quality of the gamma spectral data have increased enormously. The need for an automatic method for the gamma spectra analysis is clearly in evidence. To develope such a computer program performing automatic gamma spectrum analysis not only has the advantage of saving analysis time but also improving the analysis accuracy. Generally, a computer program used for automatic gamma spectra analysis the fololwing requirements might be concerned:

---

* Now at University of Maryland, Maryland, U.S.A.

automatic gamma spectra analysis the following requirements might be concerned:

(1). The program should be able to handle the data measured under a whole varity experimental conditions, including variable system gain, runing time and detectors of different size and quality.

(2). The program should be able to search the peaks from the spectrum, locate the peaks positions, and identify the multiplet of each peak without the priori knowledge of the spectral components.

(3). The analysis should include the estimation of the goodness of fit, and the propable errors.

(4). The results of analysis should include the gamma ray energy, intensity and background intensity of each peak.

Recently, a number of computer programs have been written for analysis the gamma ray spectra[1-5]. Robinson[2], Connelly and Black[4], Routti[4], etc. already have developed very good programs. Slavic and Bingulac[1] reported a simple but efficient method for automatic gamma spectra analysis. Based on the data comparision, Slavic and Bingulac's program not only could automatically searching the peaks in the spectrum but also identifying the multiplets of the peaks. However, since several hundred peaks usually appear in the gamma ray spectrum from (p, γ) reaction[10,11] most of those programs are either considerable complex or need a big computer with large memory capacities. Which are not available in the van de Graaff group, Academia Sinica and National Tsing Hua University.

In order to perform the automatic gamma spectra analysis by means of a small computer such as IBM 1130, a FORTRAN IV program SPAN is presented in this paper. Program SPAN was designed to fullfill the general requirements and analysis the whole spectrum once a time. The details will be discribed in the following sections.

II. Method of Analysis

II-1. Peak Searching Procedure

In general a typical gamma ray spectrum consists of a slowly decreasing background with peaks.[3] To locate these peaks in the spectrum a data comparision method could be used. The basic concept of peak searching procedure is based on the two assumptions: (1) The peak is symmetry (2) In the region of the spectrum where the peak rises from the bottom up to the top, the content of the successive channels N_{i-1} and N_i have the relationship as

$$N_i > N_{i-1} \tag{1}$$

Based on the two simple principles mentioned above a subroutine KLOCP has been designed for searching the peaks from a gamma ray spectrum and determining whether the peak is signlet or doublet automatically.

Any peak in the spectrum can be characterized by the following values: I1, I2, IB, IG, ISTA and IEND. Where I1 and I2 are the first and last channel that satisfy the condition $N_i > N_{i-1}$. IB is the channel number (I1-1), or defined as the bottom of the peak. The value of IG, for the kth peak, could be defined as

$$IG_k = I2_k - I1 + 1, \tag{2}$$

which is a value appoximately corresponding to the FWHM. According to the symmetry assumption, the start point and the end point of the kth peak $ISTD_k$ could be defined as

$$\begin{aligned} ISTA_k &= I2_k - IG_k - 1 \\ IEND_k &= I2_k + IG_k + 1 \end{aligned} \tag{3}$$

These relationships could be seen from Fig. 1.

Usually, the shape of the peak in a gamma ray spectrum is pretty obvious in comparision with the fluctuation or other effects. How-

ever, since the very high background in the low energy part and low background in the high energy part of the gamma ray spectrum, it is hard to set a unique peak-to-background factor for the peak choise. In order to avoid the misjudgement in the using of the data comparision method, more conditions have to be considered for the peak searching procedure. At first, for each peak, there are at least three nearest points which are sucessively arrising, i.e.

$$N_{(i-1)} < N_i < N_{(i+1)} \qquad (3)'$$

And

$$N_t/N_b \geq 1.05 \qquad (4)$$

$$N_t = N_b + 2\sqrt{N_b}. \qquad (5)$$

Where, N_t is the content of the peak top point and N_b is the content in the peak bottom. Actually, the condition (3)' is the extension of (3). Condition (4) and (5) defined a necessary conditions for the peak choise in the low energy part and in the high energy part of the gamma spectrum respectively. For example, in the low energy part, only the peak top with 500 counts or more can be recognized as a peak in comparision with the 10,000 counts backgound; while in the high energy part, a 17 net counts of the peak top content can be recognized as a peak in comparision with the 10 counts background. The relation of (5) is also satisfied the fact that the statistical error of N_i for N_i; the constant 2 put in (5) because there are assumed that at least three points successive arise is required in a peak.

In order to distinguish the peak is singlet or doublet, some known permanent singlet peaks can be found in the spectrum*. The values of the FWHM of those known peaks and their corresponding channel number can be used to fit a linear equation which represents the relationship between the approximate FWHM values of the peaks and the channel number in the spectrum,

* for example, 511 keV of m_oC^2, 5107-, 5618-and 6129 keV γ-peaks of $^{19}F(p, \alpha\gamma)$ in the (p, γ) reactions.

$$GMIN_k = SAG * 12_k + SAG1 \tag{6}$$

Where, SAG and SAG1 are the two fitted parameters which have to be input previously; $GMIN_k$ corresponds to the minimum value of the FWHM for the kth peak at the channel $I2_k$. The ratio of FWHM of the kth peak IG_k and its calculated minimum FWHM value $GMIN_k$ is the key to determine the multiplets of peaks. We define,

$$SM_k = \frac{IG_k}{GMIN_k} = \begin{cases} 1, & \text{if } SM_k < 1.5 \\ 2, & \text{if } SM_k \geq 1.5 \end{cases} \tag{7}$$

When SM_k=1, it indicates that the kth peak is singlet; SM_k=2 the kth peak is boublet. In the case of a singlet peak, the problem is quite simple. However, a doublet peak appears in the spectrum, it might be little complicate. A double peak (1) may be caused by two very close peaks overlaped together (see Fig. 2a); or (2) a peak group contained two narrow peaks but with a broad bottom. In the case (1), a new parameter I21 is defened to indicated the approximate position of second componsent peak in the broad peak. That is

$$I21_k = I2_k + GMIN_k \tag{8}$$

Another parameter SN_k=0 is also introduced as an index for the choise of a proper mathematical model.

In the peak group as mentioned above, two close narrow peaks with a broad bottom (Fig. 2b), will be indentified by the comparison of $IEND_k$ and $ISTA_{k+1}$. If $IEND_k > ISTA_{k+1}$ then, the kth and (k+1)th peak overlaped, and they will be treated as a doublet peak. A new set of boundary points formed, such as,

for kth peak (group)

$$ISTA_k = ISTA_k ,$$

$$IEND_k = ISND_{(k+1)} ,$$

$$I2_k = I2_k ,$$

$$I21_k = I2_{(k+1)} ,$$

and $$SN_k = 1 .$$

Of cause, a peak group might consist of more than two peaks, however, in the spectrum measured by a high resolution Ge(Li) detector, two-peak group is the most possible case. Fig. 3 shows the flows chart of the subroutine KLOCP which represents the realization of the described peak searching method.

II-2 Fitting Functions and Parameter Estimations

The functions of the subboutine KLOCP are automatic searching the peaks, locating the positions of peaks and the multiplications of the peaks. Once the peaks and their corresponding regions of the data have been specified for a fit, the analysis of that region of the spectrum in perfacmed for fitting. Generally, the peaks in a real spectrum are assumed to be Gaussian[1], or Gaussian with a quadratic background[6],

$$y(x) = \sum_{i=1,2} G_i(x) + f(x) \tag{9}$$

where $$G_i(x) = A_i \exp\left[-\tfrac{1}{2} \left(\frac{x-b_i}{C_i} \right)^2 \right] \tag{10}$$

$$f(x) = s + tx + ux^2 \tag{11}$$

$i = 1$ for singlet peak

$i = 2$ for doublet peak

In the function (9) or (10), (11), the independent variable x represents the channel number in the Spectrum. s, t, u, are constants which are characteristized by the background. Due to the fact that the good resolution for a Ge(Li) detector, all the peaks are assumed not so wide, and the background of each peak is very close to be a linear. The value of u could be very small, and the value of t is the approximate slop of the background f(x). The initial values for those parameter could be assumed as,

$$u = 0.0001,$$

$$t = (N_{IEND_k} - N_{ISTA_k}) / (N+1), \qquad (12)$$

$$s = N_{ISTA_k} - t.$$

According to the characteristics of the Gaussian distribution; parameter a_i represent the ampitude of the peaks observed; b_1 represent the position of the peaks and c_i is the standard deviation of the peak. The initial values of the parameters could be estimated as[7]

$$C_i = GMIN_k / 2.354; \qquad i = 1,2. \qquad (13)$$

In case of a singlet peak the initial values of b_1 and a_1 could be estimated simply as

$$b_1 = I2_k, \qquad (14)$$

$$a_1 = N_{I2_k} - (N_{ISTA_k} + N_{IEND_k}) / 2. \qquad (15)$$

For the doublet peak, either in the case of a two-peak group, or a broad one, the peaks position have already been located by KLOCP,

$$b_1 = I2_k , \qquad b_2 = I21_k .$$

The other paramenters canbe defined by set $x=I2_k$ and $x=I21_k$, and subsitute in (9), then, we have

$$a_1 = (N_{I2_k} - N_{I21_k} * A) / (1-A^2) - s/(1+A) \qquad (16)$$

$$t(I2_k - I21_k * A) / (1-A^2)$$

$$a_2 = N_{I21_k} - a_1 * A - S - I21_k * t$$

$$\text{where } A = \text{Exp}\ [-\tfrac{1}{2} (\frac{b_1 - b_2}{c_1})^2] \qquad (17)$$

The initial value of these parameters will be estimated in the main program according to the characteristics of each peaks.

III. Program Description and Results

Concering to the requirements metioned above in Sec. 1, and for the purpose of treatment of the whole spectrum once a time by IBM 1130 computer. The program SPAN is designed in consists of eight subroutines, KSMOD, SUBGD, KLOCP, KURFT, DERF, KMATV, KENGY, and KAREA as will as four functions PUNAT, FUNCT, FUNKT and FCHIQ. The analysis procedure of this program are: (1) substracting the cosmic ray background from the laboratary spectrum, (2) smothing the data array, (3) locating the position of each peak and setting the peak region from the spectrum (4) fitting the found peak with the proper function by least square method (5) computing the area under each peak and the quadratic background for each peak as well as the gamma ray energy (6) calculating the best

fitting or Chi-square for each fit.

After reading into all the necessary input data, such as the spectral data array (x_i, y_i), the total number of data points, NX, the running time of the spectrum obtained (TT), the first and last channel that to be analyzed (INIT and IEND) etc., then the excution goes to call the subroutine SUBGD. In the subroutine SUBGD, a cosmic ray spectrum, which was obtained by a long period (10 hr.) measurement, is normalized by the running time ratio of the cosmic and laboratory spectra, and then substracted from the laboratary spectrum channal by channal. Then the subroutine KSMOD is called for smoothing the spectral data array. Based on the averaging over three adjacent channals with a binomial destribution[8], KSMOD averages the data y_i as

$$y_i' = (y_{(i-1)} + 2y_i + y_{(i+1)})/4, \tag{18}$$

which will provides a new data array (x_i, y_i') with reduced fluctuation for better fitting[9]. It is now the subroutine KLOCP starting to work. KLOCP, which has already been dailed described in Sec II, searched the total number of peaks, NP, in the spectrum, located the position of each peak, $I2_k$, and definded each peak region (from $ISTA_k$ to $IEND_k$), as well as the number of channals in each peak ($N=IEND_k-ISTA_k+1$). The KLOCP also identified that whether the peak is singlet (SM=1) or doublet (SM=2).

After all the peaks in the spectrum have been searched out by the subroutine KLOCP. The excution returned back to the main program; a "DO LOOP" then excuted DO j=1, NP. For each loop, following the evaluation of the initial values of the parameters of a_i, $b_i, c_i, s, t,$ and u according to characterestics of each peak, the computation transfered to the subroutine KURFT. KURFT is a least square fit subroutine which was modified from Bivington's CURFT (10). Combining a gradient search with the method of linearizing the

fitting function, KURFT fit the peak with function (9).

When SM=1, it indictaes that the peak is singlet, then $C_i(x) + f(x)$ is used for fitting. When SM=2, SN=0 which means that the peak is somewhat broad it may be composed of two peaks; one peak locating at $I2_k$ and the other assumed located at $I2_k$+$GMIN_k$. And in case of SM=1, SN=1 which means that the peak is a peak group with two narrow and sharp peaks; $I2_k$ and I21I will be the position of the two narrow peaks' position. Both is the two cases of SM=2, SN=0 and SM=2, SN=1 the function $G_1(x)+G_2(x)+f(x)$ are called to fit. In the fitting procedure, the fitting Chesquare is computed in order to check the goodness of fit. Subroutines KAREA and KENGY are also called to calculate the γ-ray energy and the area under the peak as well as the background which is the area under the curve f(x).

Th The flow chart of the main program SPAN can be seen in fig. 4

The application of the program used to analysis one gamma-ray spectrum from $^{63}Cu(p',\gamma)^{64}Zn$ reaction at Ep=1744.8 Kev on IBM 1130 Computer is partly given in Fig. 5. The peaks labelled with 1 and 1', 8 and 8' 10 and 10'...etc are identified as doublet peaks or two-peak group. Table 1, shows the anlaysis results. Since the high background in the low energy part of a gamma-ray spectrum, the fitting is much more difficult than the fitting in the high energy pant. From Table 1, it will be observed that the singlet peaks fitted much better than the doublet peaks. However, in the high energy part of the spectrum the results are better than what in the low energy part.

Fig. 6 shows the original data and the fitted results; the shadowed area shows the background.

IV. Conclussion

This program has been sucessfully used to analysis data obtained from our lab.[11,12] with very good result. A complex spectrum

with up to 400 peaks could be analyzed once a time on IBM 1130 computer.

The peak searching subroutine KLOCP also can be applied to any spectra with peaks.

The lists of SPAN-3 and KLOCP are shown in the appendex.

TABLE 1

The main characteristics of the peaks partly in the γ-spectrum obtained from the $^{63}Cu(p,\gamma)^{64}Zn$ reaction at E_p=1744.8 keV

Peak No.	Position Channel	E(KeV)	ISTA	IEND	reduced X^2	
1	125	436	119	135	5.10	DOUBLET
1'	128	445.1				
2	139.2	478.9	135	143	2.55	
3	150.3	511.8	145	155	2.8	
4	174.1	583.1	170	178	2.6	
5	183.1	611.4	179	185	2.9	
6	202.8	669.8	197	207	0.12	
7	220.7	724.9	216	226	0.51	
8	235	770	223	252	78.9	DOUBLET
8'	247	804				
9	261.2	874.2	256	268	3.5	
10	282 8	912.2	279	295	6.2	DOUBLET
10'	290.9	936.5				
11	301.1	967.5	297	305	0.16	
12	209	991	303	315	0.50	
13	338.9	1082	335	343	0.48	
14	350.6	1117.2	345	357	0.19	
15	371.8	1180	367	377	0.46	

16	380.5	1206.5	374	388	0.37	
17	390.8	1237.6	387	395	0.8	
18	404.7	1279	400	410	0.4	
19	416.7	1315.2	412	422	0.9	
20	434	1367.8	430	440	3.4	
21	440	1386.1	438	444	1.5	
22	447	1406.7	443	451	1.19	
23	465.4	1460.8	461	469	9.0	
24	477.1	1495.9	474	480	0.8	
25	497	1555.4	492	506	16.7	DOUBLET
25'	500	1564				
26	509.0	1591	504	514	0.63	
27	516.9	1615	512	527	79.6	DOUBLET
27'	523.7	1635				
28	537	7676.6	534	549	1.8	
28'	545	1701				
29	560.8	1746	556	566	3.8	
30	567	1765	563	571	2.7	
31	578.6	1799	572	586	2.2	
32	593	1845	587	603	0.4	

References

1. L.A. Slevic and S.P. Bingulac, Nucl. Instr. and Meth. 84 (1970) 261-268.
2. D.C. Robinson, Nucl. Instr. and Meth. 78 (1970) 120-124.
3. A.L. Connelly and W.W. Black, Nucl. Instr. and Meth. 82 (1970) 141-148.
4. Jorme T. Routti, Lewrance Radiation Lab. Report, UNCL-19452 1969.
5. W.W. Black, Nucl. Instr. and Meth. 71 (1969) 317-328.
6. Philip R. Bevington, Data Reduction and Error Analysis for the Physical Science, p. 214, Taiwan Reprint.
7. ibid., p. 45
8. ibid., p. 259
9. ibid., p. 260
10. ibid., p. 237
11. C.W. Wang, Y.C. Liu, E.K. Lin, C.C. Hsu, and G.C. Kiang, Phys. Rev. C. 9, 4 (1974) 1396.
12. C.C. Hsu, E.K. Lin, C.W. Wang, G.C. Kiang, Y.C. Liu and M.C. Wang, The level Structure of ^{64}Zn through the ^{63}Cu(P,γ) ^{64}Zn reaction (to be published).

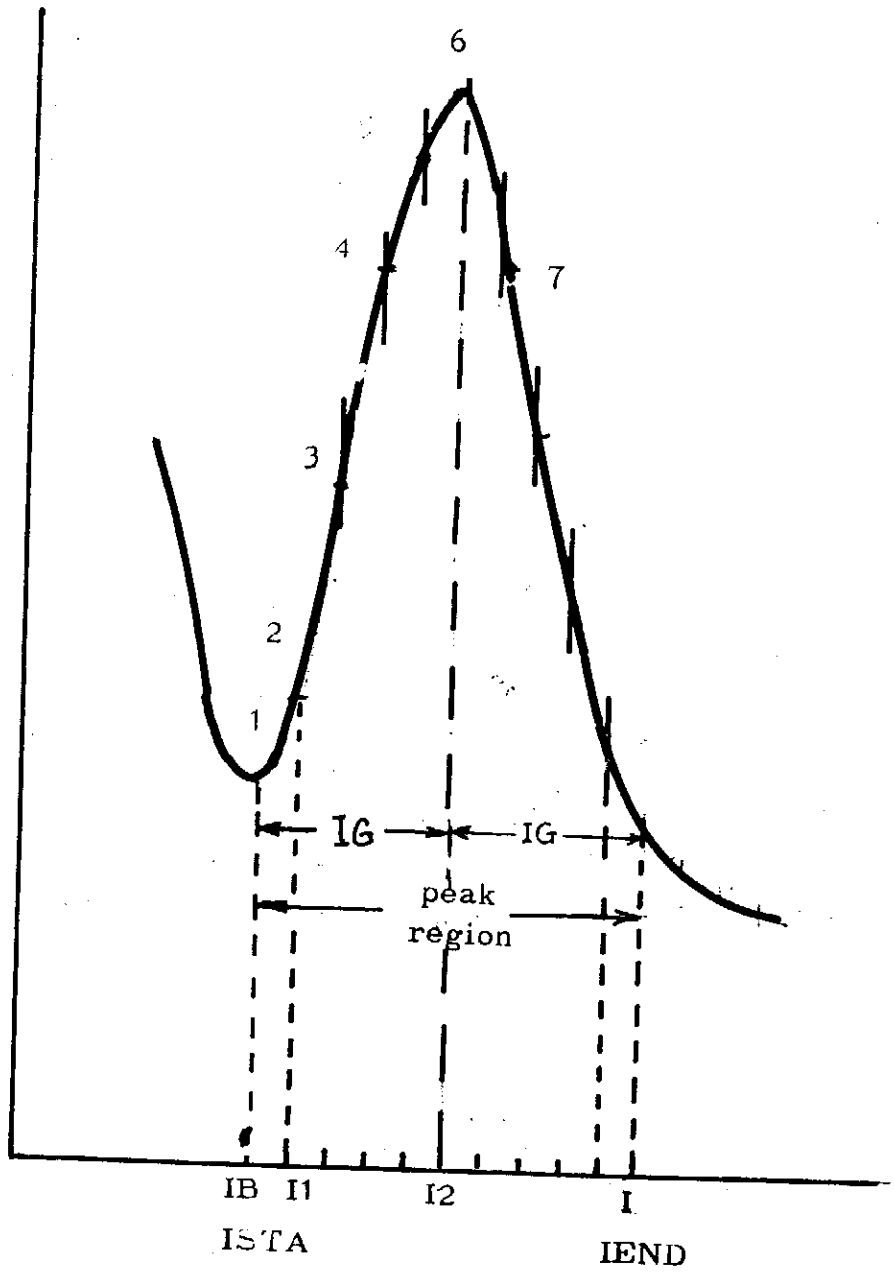

Fig. 1 The peak search procedure by the method of data comparsion

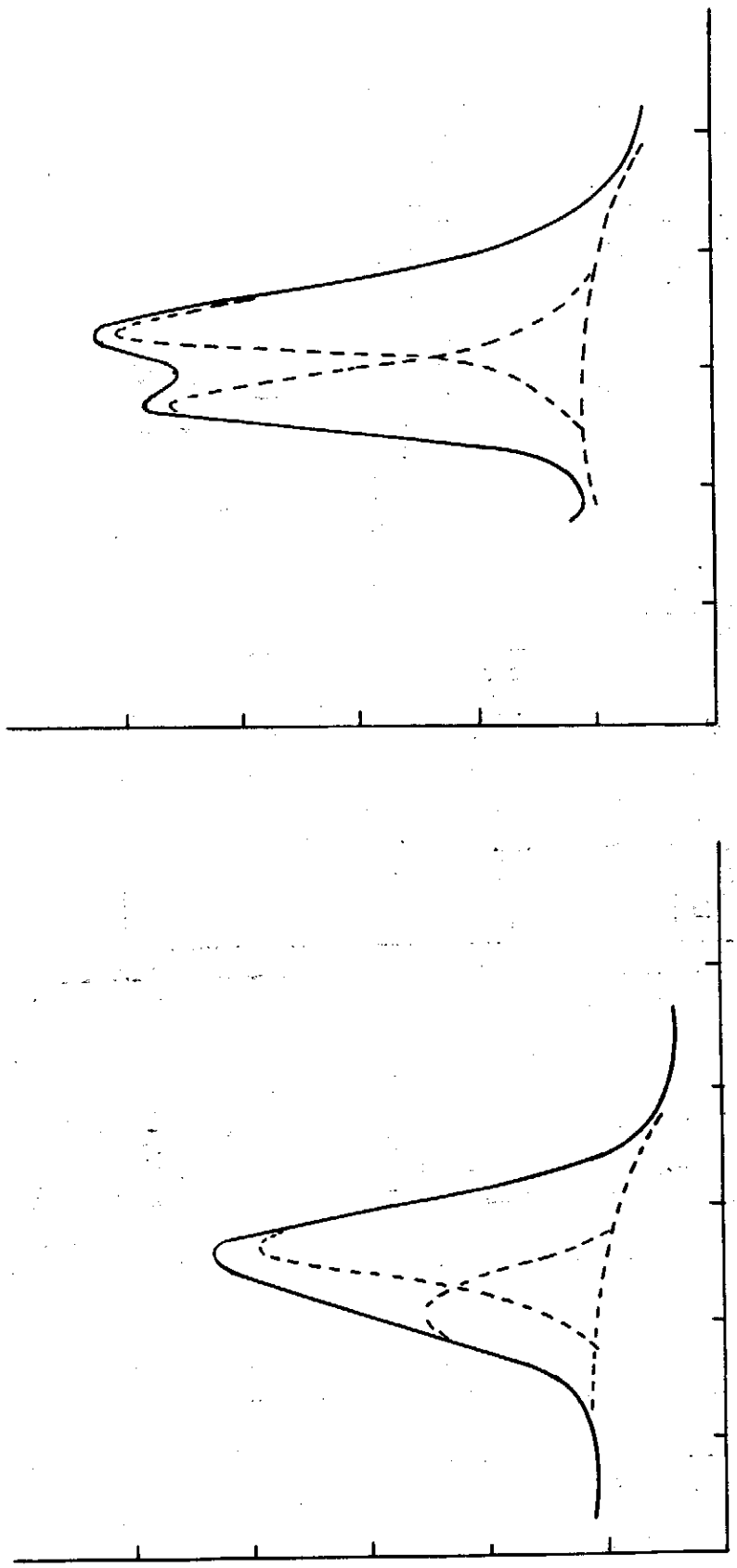

Fig. 2 A doublet peak formed by two narrow peaks overlap together (a) with a broad bottom; (b) a two-peak group.

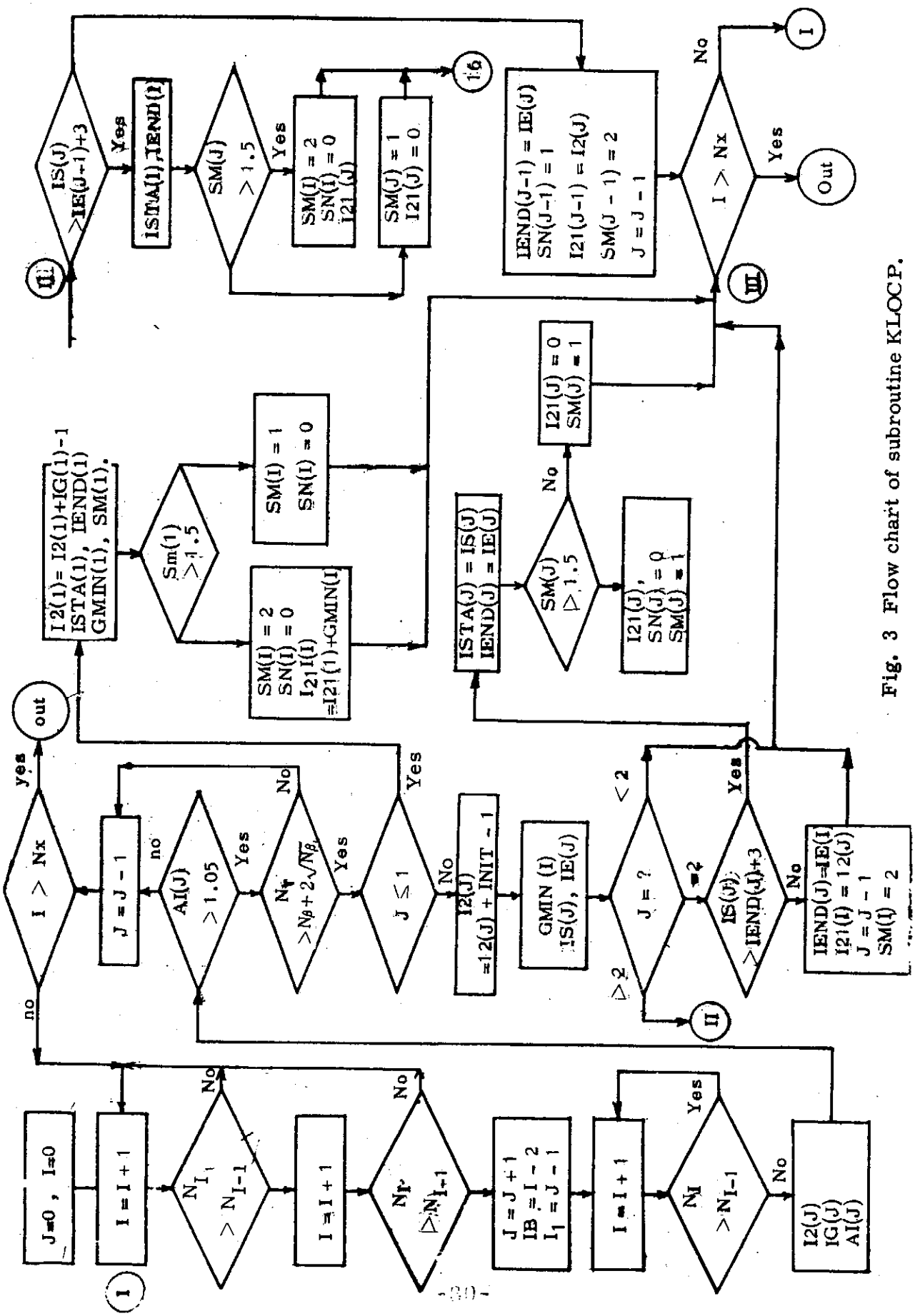

Fig. 3 Flow chart of subroutine KLOCP.

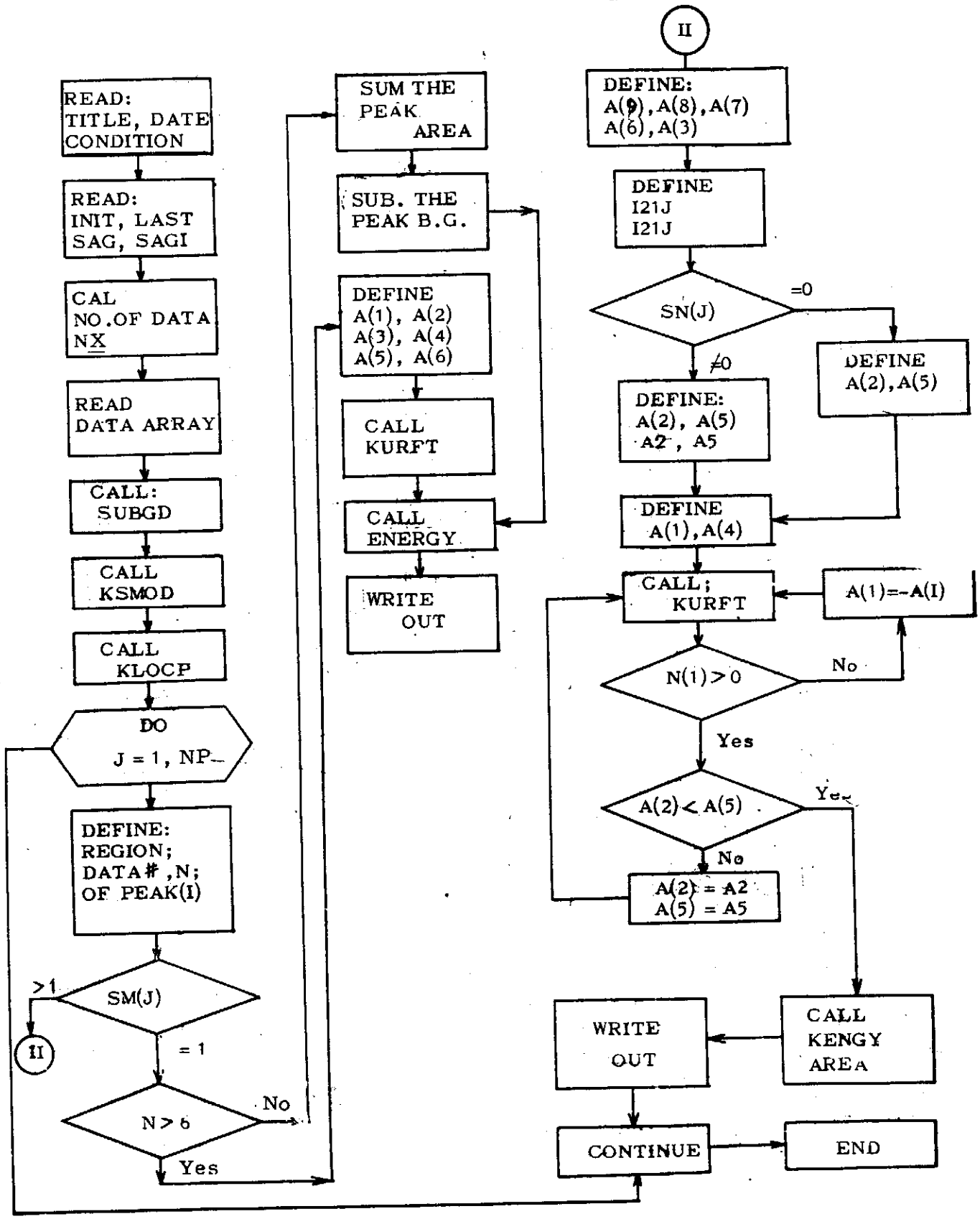

Fig. 4 Flow chart of the main program SPAN-3.

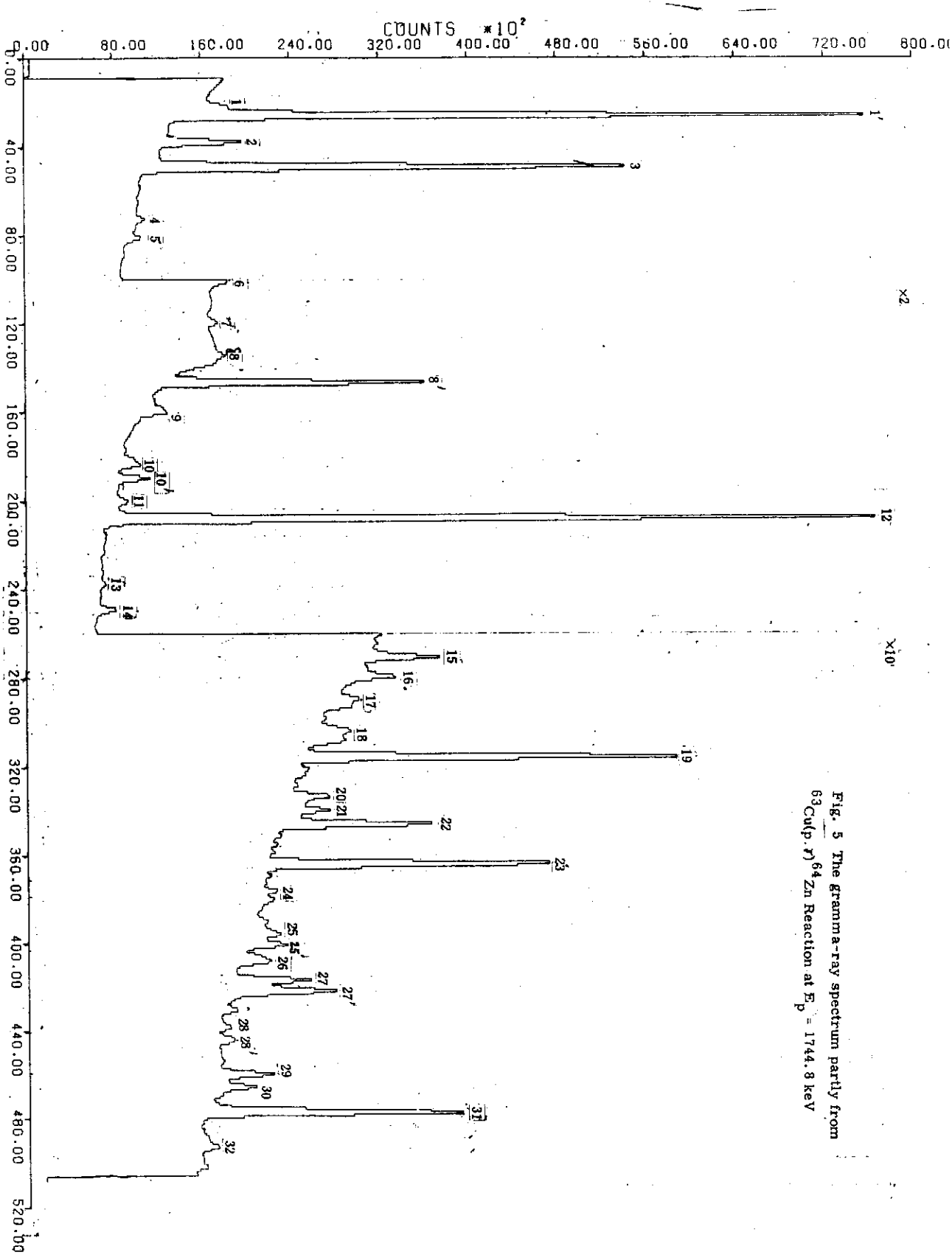

Fig. 5 The gramma-ray spectrum partly from $^{63}Cu(p,\gamma)^{64}Zn$ Reaction at E_p = 1744.8 keV

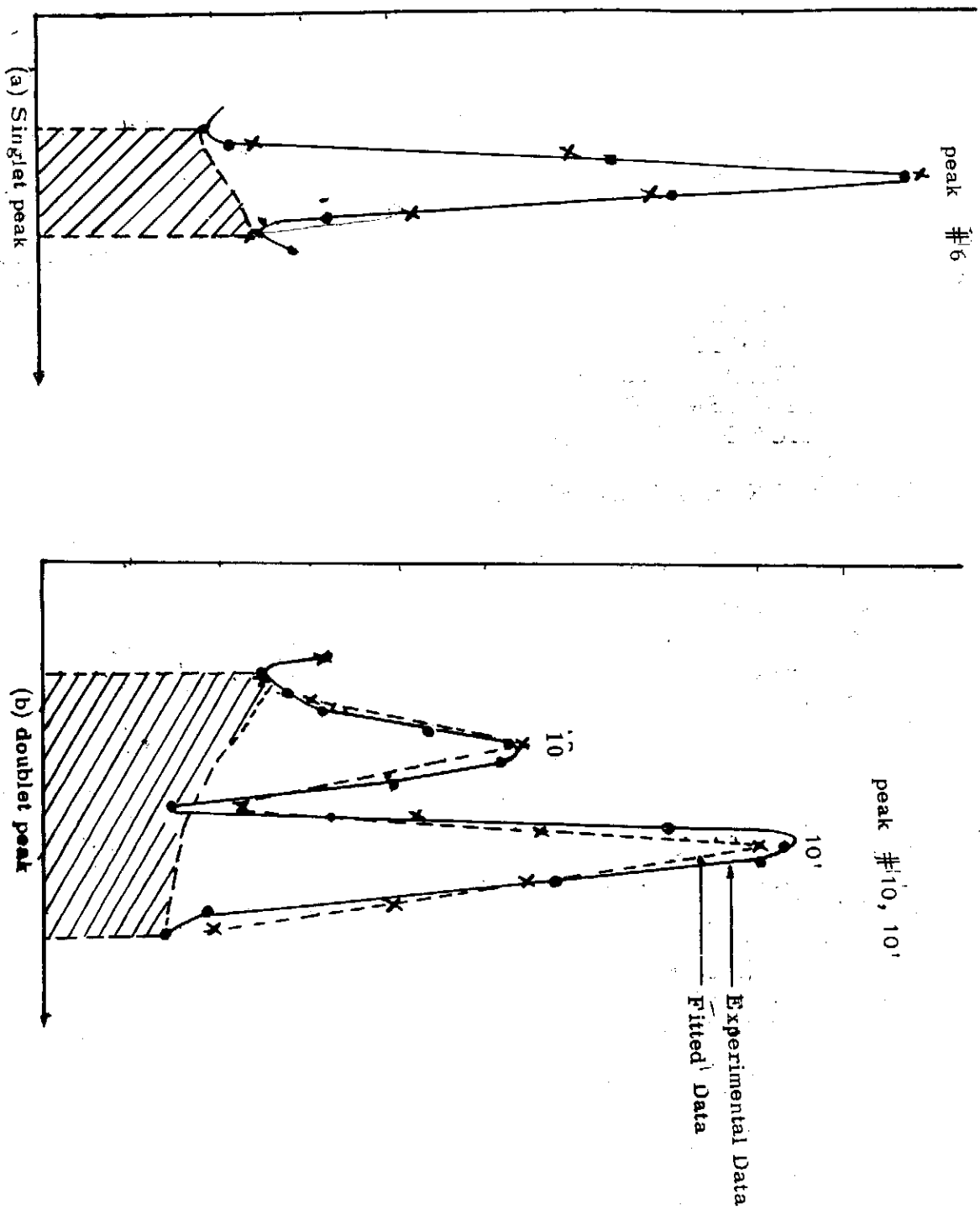

Fig. 6 An example of the analyzed peak by the program.

APPENDIX I
SOBROUTINE KLOCP

```
PAGE  1
// JOB T 0001
LOG DRIVE   CART SPEC   CART AVAIL   PHY DRIVE
    0000        0001        0001        0000
V2 M10   ACTUAL  32K  CONFIG  32K
// FOR
*ONE WORD INTEGERS
*LIST SOURCE PROGRAM
      SUBROUTINE KLOCP(FO,INIT,NX,SAG,SAG1,I2,IG,GMIN,
     1 ISTA, IEND,SM,NP,I21,SN)
      DIMENSION FO(1),I2(1),IG(1),GMIN(1),ISTA(1),IEND(1),SM(1),
      AI(300)
      DIMENSION IS(300),IE(300),I21(1),SN(1)
      NP=0
      I=1
    1 I=I+1
      IF(FO(I)-FO(I-1) ) 1,1,2
    2 I=I+1
      IF(FO(I)-FO(I-1) ) 1,1,2
    3 NP=NP+1
      IB=I-2
      I1=I-1
    4 I=I+1
      IF(FO(I)-FO(I-1) ) 5,5,4
    5 I2(NP)=I-1
      IG(NP)=I-I1
      M=I2(NP)
      AI(NP)=FO(M)/FO(IB)
      FOB=SQRT(FO(IB) )
      IF(AI(NP)-1.05) 7,6,6,
    6 IF(FO(M)-(FO(IB)+2*FOB) ) 7,7,8
    7 NP=NP-1
      IF(I-NX)1,17,17
    8 IF(NP-1)81,81,11
   81 I2(1)=I2(1)+INIT-1
      ISTA(1)=I2(1)-IG(1)-1
      IEND(1)=I2(1)+IG(1)+1
      GMIN(1)=I2(1)*SAG+SAG1
      SM(1)=IG(1)/GMIN(1)
      IF(SM(1)-1.5)9,9,10
    9 SM(1)=1.
```

```
      I21(1)=0
      GO TO 16
   10 SM(1)=2.
      SN(1)=0
      I21(1)=I2(1)+GMIN(1)
      GO TO 16
   11 I2(NP)=I2(NP)+INIT-1
      GMIN(NP)=I2(NP)*SAG+SAG1
      IS(NP)=I2(NP)-IG(NP)-1
      IE(NP)=I2(NP)+IG(NP)+1
      SM(NP)=IG(NP)/GMIN(NP)
      IF(NP-2)16,111,114
  111 IF(IS(NP)-(IEND(1)-3) ) 112,113,113
  112 IEND(1)=IE(NP)
      I21(1)=I2(NP)
      SN(1)=1

      NP=NP-1
      SM(1)=2
      GO TO 16
  113 ISTA(NP)=IS(NP)
      IEND(NP)=IE(NP)
      IF(SM(NP)-1.5)1131,1131,1132
 1131 I21(NP)=0
      SM(NP)=1.
      GO TO 16
 1132 I21(NP)=I2(NP)+GMIN(NP)
      SN(NP)=0
      SM(NP)=2.
      GO TO 16
  114 IF(IS(NP)-(IE(NP-1)-3) ) 15,12,12
   12 ISTA(NP)=IS(NP)
      IEND(NP)=IEN(P)
      IF(SM(NP)-1.5) 13,13,14
   13 SM(NP)=1.
      I21(NP)=0
      GO TO 16
   14 SM(NP)=2.
      I21(NP)=I2(NP+GMIN(NP)
      SN(NP)=0
      GO TO 16
   15 IEND(NP-1)=IE(NP)
      SN(NP-1)=1
      I21(NP-1)=I2(NP)
      SM(NP-1)=2.
      NP=NP-1
   16 IF(I-NX)1,17,17
   17 RETURN
      END
```

```
FEATURES SUPPORTED
  ONE WORD INTEGERS

CORE REQUIREMENTS FOR KLOCP
  COMMON         0     VARIABLES   1212   PROGRAM   848

RELATIVE ENTRY POINT ADDRESS IS 04C8 (HEX)

END OF COMPILATION

// DUP

*DELETE                KLOCP
D 18 INVALID FUNCTION DURING TEMPORARY JOB


*STORE          WS US KLOCP
D 06 ENTRY POINT NAME ALREADY IN LET/FLET
```

APPENDIX II
PROGRAM SPAN - 3

PAGE 1

```
// JOB T 0001
LOG DRIVE   CART SPEC   CART AVAIL   PHY DRIVE
    0000        0001         0001        0000
V2 M10  CATUAL 32K CONFIG 32K
// FOR
*ONE WORD INTEGERS
*LIST SOURCE PROGRAM
*IOCS(CARD,1132 PRINTER,DISK)
C       PROGRAM SPAN3
C       THIS IS A PROGRAM USED FOR ANALYSIS THE PHOTOPEAKS
C       IN THE (P,GAMMA) REACTION OR OTHER GAMMA SPECTRA
C       THIS PROGRAM IS A FULL AUTOMATIC GAMMA-RAY SPECTRA
C       ANALYSIS PROGRAM MODIFIED FROM SPAN2 (MAY 2., JULY
C       19,1973).
C       CODED BY G.C. HIANG OF INSTTITUTE OF PHYSICS,
C       ACADEMIA SINICA, OCT. 15,1973
C
C       THIS PROGRAM WAS ASSUMED TO BE USED FOR ANALYSIE
C       THE SPECTRUM WITH 400 PEAKS OR LESS. IF THE NUMBER
C       OF THE GAMMA RAYS IN THE SPECTRUM IS MORE THAN
C       THAT, THE DIMENSION SIZE OF ISTA, IEND, GMIN, I2, SM,
C       MAY NEED BE CHANGED.
C
C       INIT...THE FIRST CHANNEL WHICH BEING PUNCHED
C       TITLE...THE TITLE OF THE DATA WHICH BEING ANALYZED
C       LAST...THE LAST CHANNEL WHICH BEING PUNCHED
C       COND...THE CONDITIONS OF THE DATA
C       TT...THE TRUE TIME THAT NEED FOR THE SPECTRUM
C       ID...AN INTEGER
C              ID=1...ONE SET OF DATA
C              ID=2...MORE THAN ONE SET OF DATA
C       IC...AN INTEGER
C              IC=1...PRINT OUT THE LAB SPECTRUM, THE SMOOTHED
C                     SPECTRUM, AND THE SMOOTHED SPECTRUM
C                     WITHOUT COSMIC BACKGROUND
C              IC=2...NO PRINT OUT.
C       SAG, SAG1 ARE TWO PARAMETERS FOR DEFINE THE MIN.
C       FWHM,ACCORDING TO THE EQUATION GMIN(K)=SAG*K+SAG1
C       ISEC1,ISEC2,ISEC3 ARE THE PARAMETERS TO DIVID THE
C       WHOLE SPECTRUM
C       IN 3 SECTIONS FOR ENERGY CALIBRATION
```

```
C       FO...THE DATA OR THE COUNTING RATE OF EACH CHANNEL
C
        DIMENSION FO(3600),ISTA(300),IEND(300),X(40),Y(40),YFIT(40)
        DIMENSION SIGMY(40),SIGMA(40),A(12),PA(3),PB(3)
        DIMENSION I2(300),IG(300),GMIN(300),SM(300),I21(300)
        DIMENSION TITLE(15),COND(15),DATE(4),APK(2),SN(300)
      1 CONTINUE
        READ(2,10)TITLE
     10 FORMAT(15A4)
        READ(2,10)COND
        READ(2,11)DATE
     11 FORMAT(4A4)
        WRITE(3,12)TITLE,COND,DATE
     12 FORMAT(////1X,15A4//1X,15A4//1X,4A4)
        READ(2,15)TT
     15 FORMAT(F16.8)
        READ(2,16)ID,IC
     16 FORMAT(2I4)
        READ(2,17)INIT,LAST
     17 FORMAT(2I8)
        READ(2,18)(PA(I),I=1,3)
        READ(2,18) (PB(I),I=1,3)
     18 FORMAT(3F18.10)
        READ(2,19)SAG,SAG1
     19 FORMAT(2E17.9)
        READ(2,20)ISEC1,ISEC2,ISEC3
     20 FORMAT(3I10)
        NX=LAST-INIT+1
        READ(2,21) (FO(I),I=1,NX)
     21 FORMAT(4(10X,F10.0))
        GO TO (22,32),IC
     22 WRITE(3,23)
     23 FORMAT(///1X,'THE LAB. SPECTRUM'/)
        LX=NX/10
        DO 25 K2=1,LX
        CALL KRANG(K2,INIT,K,KK,KKK)
        WRITE(3,24)K,(FO(IX),IX=KKK,KK)
     24 FORMAT(2X,I5,10F10.0)
     25 CONTINUE
        WRITE(3,26)
     26 FORMAT(///1X,'THE SMOOTHED LAB. SPECTRUM'/)
        CALL KSMOD (FO,NX)
        DO 28 K2=1,LX
        CALL KRANG(K2,INIT,K,KK,KKK)
        WRITE(3,24)K,(FO(IX),IX=KKK,KK)
     28 CONTINUE
        WRITE(3,29)
     29 FORMAT(///1X,'THE SMOOTHED LAB. SPECTRUM WITHOUT
      1 COSMIC BACKGROUND '/)
```

```
      CALL SUBGD(FO,INIT,LAST,ISEC1,ISEC2,ISEC3,1440,o,TT,
     1 14164.0,  0,0000041,0.00012,PA,PB)
      DO  31  K2=1,LX
      CALL KRANG(K2,INIT,KX2,KX1,KXO)
      WRITE (3,24)KX2,(FO(IX),IX=KXO,KX1)
   31 CONTINUE
      GO TO 33
   32 CALL KSMOD (FO,NX)
      CALL SUBGD(FO,INIT,LAST,ISEC1,ISEC2,ISEC3,1440,0,TT,
     1 14164.0,  0.0000041,0.00012,PA,PB)
C
   33 CALL KLOCP(FO,INIT,NX,SAG,SAG1,I2,IG,GMIN,ISTA,IEND,
     1 SM,NP,I21,  SN)
      WRITE(3,34)NP
C     LOCATING THE PEAK POSITION AND E5FINE THE MULTIPLETY
      OF PEAKS.
   34 FORMAT(//1X,'THE TOTAL NUMBER OF PEAKS IN THE
     1 SPECTRUM IS',I5/)
      WRITE(3,341)
  341 FORMAT(//1X,5('NO.',1X,'POSITION',1X,'CLASS',4X))
      WRITE(3,342) (I,I2(I),SM(I),I=1,NP)
  342 FORMAT(/5 (1X,I3,3X,I4,5X,F2.0,4X))
      DO 1000 J=1,NP
      WRITE(3,35)J
   35 FORMAT(//1X,'PEAK NUMBER',I4/)
      LS=ISTA(J)
      LE=IEND(J)
      KL=I2(J)
      KLP=KL-LS
      N=LE-LS+1
      WRITE(3,36)LS,LE
   36 FORMAT(1X,'PEAK STARTED AT CHANNEL'1X,I4,/1X,'PEAK
      ENDED AT CHANNEL',1X,I4/)
      LSI=LS-INIT+1
      LEI=LE=INIT+1
      KLI=KL-INIT+1
      DO  37  K=1,N
      IS=K+LSI-1
      Y(K)=FO(IS)
      X(K)=K
      SIGMY(K)=SQRT(Y(K))
   37 CONTINUE
      WRITE(3,38)
   38 FORMAT(/1X,'THE ORIGINAL DATA',/)
      WRITE(3,39) (X(K),Y(K),K=1,N)
   39 FORMAT(6(1X,F5.0,1X,F10.3,1X),
      WRITE(3,40) (SIGMY(K),K=1,N)
   40 FORMAT(//1X,'THE UNCERTAINTIES OF THE DATA ARE',
```

```
    1 //10(1X,F10.4))
      IF(SM(J)-1)41,41,60
   41 WRITE(3,42)
   42 FORMAT(//1X,'THIS PEAK IS SINGLET')
      IF(N-6) 43,43,46
   43 SUM=0.
      DO  44 M=1,N
      MS=(M-1)+LSI
   44 SUM=SUM+FO(MS)
      BA=N*(FO(LSI)+FO(LEI))/2.
      APK(1)=SUM-BA
      WRITE(3,45)
   45 FORMAT(//1X,'THE NUMBER OF DEGREE OF FREEDOM IS
     1LESS THAN 6, THE PE  AK COULD NOT BE FITTED,'/1X,
     2'THE AREA AND THE BACKGOUND WAS CALCUL ATED
      DIRECTLY, '/)
      GO  TO  48
   46 A(6)=0.0001
      A(2)=KL-LS+1.
      A(3)=GMIN(J)/3.5
      W1=((1-A(2))/A(3))**2.
      W1=EXP(-W1/2.)
      W2=((n-A(2))/A(3))**2.
      W2=EXP(-W2/2.)
      A(1)=(N*FO(LSI)-FO(LEI)*(2.-N)+2.*(1.-N)*FO(KLI))/(W1-W2
     1+2.*(1.-N)*(1.-W2))
      A(5)=(A(1)*(1. -W2)-FO(KLI)+FO(LEI))*2./N
      A(4)=FO(KLI)-A(1)-N*A(5)/2.
      CALL KURFT (X,Y,SIGMY,N,0,0   ,6,-1,A,0,SIGMA,0.001,
     1YFIT,CHISQ)
      WRITE(3,47) (A(L),L=1,6)
   47 FORMAT(///1X,'THE COEFFICIENT,',//1X,6(2X,E16.8)
      WRITE(3,471) (X(K),YFIT(K),K=1,N)
  471 FORMAT(//1X,'THE FITTED DATA',//6(2X,F6.0,2X,F10.2))
   48 PE=A(2)+LS-1
      CALL KEN GY(PE,ISEC1, ISEC2,PA,PB,E)
      WRITE(3,54)PE,E
   54 FORMAT(//1X,'THE PEAK AT CHANNEL',1X,F10.3/,1X,
     1'ENERGY IS',F10.3, 'KEV'/)
      IF(N-6)67,57,55
   55 WRITE(3,56)CHISQ
   56 FORMAT(1X,'CHI SQURE',2X,E16.8)
      CALL KAREA(A,6,N,APK,BA)
   57 WRITE(3,58)BA
   58 FORMAT(/1X,'BACKGROUND OF THE PEAK',1X,E16.8)
      WRITE(3,59)APK(1)
   59 FORMAT(/1X,'INTENSITY OF THE PEAK',1X,E16.8)
      GO  TO  1000
C
```

```
C       FITTING THE DOUBLE PEAK
   60 WRITE (3,61)
   61 FORMAT(//1X,'THIS PEAK IS DOUBLET')
      A(9)=0.0001
      A(8)=(FO(LEI)-FO(LSI))/(N-1)
      A(7)=FO(LSI)-A(8)
      A(6)=GMIN(J)/3.5
      A(3)=A(6)
      I21J=I21(J)-LS
      I21I=I21(J)-INIT+1
      IF(SN(J) ) 611,611,612
  611 A(2)=KL-LS-1
      A(5)=I21I-LS I-1
      A2=A(2)
      A5=A(5)
      GO  TO  613
  612 A(2)=KL-LS+1
      A(5)=I21I-LSI-1
      A2=A(2)
      A5=A(5)
  613 AX=((A(2)-A(5))/(6) )**2
      AY=EXP(-AX/2)
      AY1=1+AY
      AY2=1-AY**2
      A(4)=(FO(KLI)*AY-FO(I21I)-A(7)*(AY-1.)-A(8)*(A(2)*AY-A(5)))/
     1(-Ay2)
      A(1)=FO(KLI)-A(4)*AY-A(7)-A(8)*A(2)
  614 CALL KURFT (X,Y,SIGMY,N,A2,A5,9,-1,A,0,SIGMA,0.001,
     1YFIT,CHISQ)
      U1=ABS(A5-A(5))
      IF(A(5)-A(2) ) 615,615,616
  615 A(2)=A2
      A(5)=A(2)+1
      GO  TO  614
  616 IF(A(1))617,617,618
  617 A(1)=-A(1)
      GO  TO  614
  618 IF(A(4) ) 619,619,620
  619 A(4)=-A(4)
      GO  TO  614
  620 IF(U1-3)624,624,622
  622 A(7)=0.0001
      A(6)=(FO(LEI)-FO(LSI))/(N-1)
      A(5)=(N*FO(LEI)-FO(LSI))/(N-1)
      A(4)=GMIN(J)/4.
      A(3)=(FO(I21I)-AY*FO(KLI)-A(5)*(1-AY)-A(6)*(A5-A2*AY))/
     1(1-AY**2)
      A(2)=GMIN(J)/4.
      A(1)=FO(KLI)-A(3)*AY-A(5)-A(6)*A2
```

```
      CALL KURFT(X,Y,SIGMY,N,A2,A5,7,-1,A,0,SIGMA,0.001,
     1YFIT,CHISQ)
      A(9)=A(7)
      A(8)=A(6)
      A(7)=A(5)
      A(6)=A(4)
      A(5)=A5
      A(4)=A(3)
      A(3)=A(2)
      A(2)=A2
  624 WRITE(3,47) (A(L),L=1,9)
      WRITE(3,471) (X(K),YFIT(K),K=1,N)
      PEI=A(2)+LS-1
      CALL KENGY(PE1,ISEC1,ISEC2,PA,PB,E1)
   63 FORMAT(/1X,'THE FIRST PEAK')
      WRITE(3,63)
      WRITE(3,69)PE1,E1
   69 FORMAT(//1X,'THE 1 ST. PEAK AT CHANNEL',1X,F10.3/1X,
     1'ENERGY IS',F10.3,'KEV'/)
      PE2=A(5)+LS-1
      CALL KENGY(PE2,ISEC1,ISEC2,PA,PB,E2)
      WRITE(3,75) PE2,E2
   75 FORMAT(/1X,'THE 2 ND, PEAK AT CHANNEL',1X,F10.3/1X,
     1'ENERGY IS',F10.3, 'KEV'/)
      WRITE(3,56) CHISQ
      CALL KAREA(A,9,N,APK,BA)
      WRITE(3,77) APK(1),APK(2)
   77 FORMAT (/1X,'THE INTENSITY OF THE 1 ST. PEAK IS',1X,
     1E16.8/1X,  'THE INTENSITY OF THE 2ND PEAK IS', 1X,
     2E16.8/)
      WRITE(3,78)BA
   78 FORMAT (/1X, 'THE BACKGROUND OF THE BOUBLE PEAK
     1IS', 1X, E16.8//)
 1000 CONTINUE
      IF(ID-1)79,1,1
   78 CALL EXIT
      END
```

ANNUAL REPORT OF THE INSTITUTE OF PHYSICS,
ACADEMIA SINICA, 1974

Even-Parity Energy Levels of Singly Ionized Magnesium Donor Impurities in Silicon*

L. T. Ho (何 恫 民)

Institute of Physics, Academia Sinica
Taipei, Taiwan

Three excited energy levels of singly ionized magnesium donor impurities in silicon are identified to be the $3s(A_1)$, $3s(E)$ and $3d_o$, respectively. Observed photoexcitation to these even-parity levels in violation of electric-dipole transition selection rule is attributed to effects of polarization of the donor by other defects and to breakdown of the effective-mass approximation.

I. Introduction

The group-II element magnesium, when diffused into silicon, has been shown to behave like a double donor rather than a double acceptor[1]. This behavior can be understood only if magnesium occupies an interstitial rather than a substitutional site. The Lyman spectra associated with both neutral and singly ionized magnesium donors in silicon have been obtained and studied[2]. In some of the samples examined, three extra excitation lines in the absorption spectrum of singly ionized magnesium donors in silicon were observed at 238.66, 239.60 and 241.26 meV, respectively. After calculating the binding energies of these levels and comparing with corresponding binding energies calculated in the effective-mass approximation, these lines should belong to the 3s and $3d_o$ levels, both

* Work supported in part by the National Science Council, Republic of China.

of which are even-parity energy levels. In the effective-mass approximation, however, no even-parity levels of an isolated silicon donor should be observable in photoexcitation spectra since electric-dipole transitions from a 1s ground level to an even-parity level are parity forbidden. The purpose of this paper is to report the identification of these levels and discuss why they can be observed in violation of electric-dipole transition selection rules.

II. Experimental Procedure

Sample preparation was begun by sandwiching vapor deposited magnesium between high purity floating-zone silicon wafers. Diffusion was accomplished at a temperature of about 1200°C in a continuously purged helium atmosphere for a period of about one hour. The silicon sample characteristics were changed from p-type conductivity and high-resistivity to n-type and low-resistivity. The specimens prepared in this way were adequate for observing the excitation spectra of neutral magnesium donors at low temperatures. By thermally ionizing neutral magnesium, the excitation spectra of singly ionized magnesium donors could be observed. The intensity of the excitation lines reached maximum at about 135°K[1].

Another method to produce singly ionized magnesium donors was to diffuse magnesium into silicon containing acceptors. Same diffusion technique as described above was used except starting with low-resistivity boron-doped or aluminum-doped floating-zone silicon instead of pure silicon and increasing diffusion time to about ten hours instead of only one hour. After magnesium was diffused into silicon, singly ionized magnesium donors were produced by compensating with acceptors. The specimens prepared in this way showed only the excitation spectrum of singly ionized magnesium donors and no trace of the excitation spectrum of neutral magnesium donors. These specimens were thus adequate to be measured at low temperatures. In this regard, the compensation method is much

better than the thermal ionization method since the lower the temperature of the specimen the sharper the excitation lines will be.

A double-pass Perkin-Elmer spectrometer, equipped with Bausch and Lomb plane reflection gratings and appropriate filters, was used for the measurements. Typical resolution in the measurements is about 0.5 cm^{-1}. The source of the radiation was a heated globar whose power was furnished by a regulated power supply. A vacuum thermocouple with a cesium-iodide window was used as the detector. In order to eliminate the atmospheric water vapor spectrum, the spectrometer was flushed continuously during the measurement with air dried by passing it through columns of molecular sieves.

An optical cryostat with cesium iodide windows was used for low temperature measurements. Sample was fastened directly to the tailpiece and its temperature was estimated to be about $12^{o}K$ using liquid helium as coolant.

III. Experimental Results and Discussion

The excitation spectrum for singly ionized magnesium donors in silicon measured with liquid helium as coolant is shown in Fig. 1. The energies of the excitation lines corresponding to the transitions from the $1s(A_1)$ ground state have the following positions in milli-electron volts: 208.63($2p_o$), 230.22($2p^{a}_{\pm}$), 230.42($2p^{b}_{\pm}$), 233.87($3p_o$), 238.66(a), 239.60(b), 241.26(c), 243.00($4p_o$), 243.99($3p_{\pm}$) and 247.92($4p_{\pm}$, $5p_o$). Except the a, b and c lines, which will be discussed later, the energy separations between other lines are approximately 4 times the corresponding spacings of those of group-V and neutral magnesium donors in silicon as well as calculated[3] in the effective-mass approximation. This can be seen from Table I where the spacings are compared. The reason for this can be easily explained as follows.

As an interstitial impurity the donor electrons of magnesium are

expected to be the two 3s valence electrons thus constituting neutral helium-like centers. When one of the two valence electrons is ionized, the singly ionized magnesium can be considered as the analog of singly ionized helium. In these manner, then, the Lyman spectrum associated with the singly ionized magnesium donors is expected to be like those of group-V and neutral magnesium donors in silicon except that the binding energy for each energy state is increased by a factor of "four" since now the effective nuclear charge is "two" instead of "one".

In order to identify the a, b and c lines, the binding energies for these lines have to be calculated first as in the following. The ionization energy for singly ionized magnesium donors can be estimated by adding four times the theoretical value of the binding energy of the $3p_{\pm}$ state calculated in the effective-mass approximation for group-V donors to the experimental energy of the transition labeled $3p_{\pm}$, which turns out to be 256.47 meV. Deducting 238.66, 239.60 and 241.26 meV from this ionization energy, the binding energies for a, b and c energy levels are thus 17.81, 16.87 and 15.21 meV, respectively. Presented in Table II are the effective-mass and some observed binding energies of 3s and $3d_o$ donor energy levels in silicon. It is quite clear that the a, b and c levels should be the 3s(E), $3s(A_1)$ and $3d_o$ levels, respectively. The identification and the observation of these energy levels can be justified by the following considerations.

In the effective-mass approximation, silicon donor levels with the magnetic quantum number m = 0 (such as s, p_o, d_o, etc.) are six-fold degenerate[9] if spin is neglected. There is one eigenstate for each of the six valleys of the silicon conduction-band edge. In the case of a donor impurity with tetrahedral T_d site symmetry (such as P, As, Bi, Mg, etc.), an m = 0 level splits into a nondegenerate A_1, a doubly degenerate E and a triply degenerate T_2 when central-cell corrections[10] to the effective-mass approximation are taken

into consideration. Electric-dipole transitions from the ground level $1s(A_1)$ are allowed only to T_2 levels.

From the above consideration, in the effective-mass approximation no even-parity levels of an isolated silicon donor should be observable in photoexcitation spectra since electric-dipole transitions from a 1s ground level to an even-parity level such as 3s and $3d_o$ are parity forbidden. The observation of even-parity levels, however, can be accounted for as a result of two effects: due to other crystal defects and/or due to breakdown of the effective-mass approximation. So far no even-parity peaks of a relatively isolated shallow donor have been reported indicating that breakdown of the effective-mass approximation is not significant for shallow donor impurities. However, the $3d_o$ is evident for phosphorus donors[4,6,11] and arsenic donors[6,11] in more heavily doped silicon samples. The presence of these $3d_o$ peaks can be attributed to perturbing effects of other defects, possibly ionized impurities. This could also be the case of singly ionized magnesium donors. After compensation, the ionized group-III acceptors presented in the silicon sample polarize the donor states, mix in components of opposite parity and destroy the parity selection rule.

As the donor binding energy increases, the breakdown of the effective-mass approximation becomes more important. Singly ionized magnesium donor is a much deeper donor compared with group-V and neutral magnesium donors in silicon. Therefore, the breakdown of the effective-mass approximation could also be one of the reasons why the even-parity energy levels 3s and $3d_o$ are observable in the excitation spectrum of singly ionized magnesium donors in silicon. For neutral magnesium donors, on the contrary, both the ionized-impurity effects and the breakdown of the effective-mass approximation should be less serious. This could explain why no even-parity energy levels are observed in the photoexcitation spectrum of neutral magnesium donors in silicon. This is also con-

sistent with the observation that the neutral magnesium donor peaks are generally narrower than those of the singly ionized magnesium donors.

Table I. Comparison of energy spacings for excited states of donors in silicon (in meV).

States	Theory[3]	P[4]	As[5]	Bi[5]	Mg[2]	$Mg^+/4$
$3p_\pm - 2p_o$	8.39	8.34	8.38	8.34	8.58	8.84
$3p_\pm - 2p_\pm$	3.28	3.28	3.27	3.26	3.26	(a) 3.44 (b) 3.39
$3p_\pm - 3p_o$	2.36	2.35	2.38	2.36	2.43	2.53
$3p_\pm - 4p_o$	0.21	0.19	0.18	0.22	0.21	0.25
$5p_o - 3p_\pm$	0.89	0.93	0.93	0.94	0.95	0.98
$4p_\pm - 3p_\pm$	0.93	0.93	0.93	0.94	0.95	0.98

Table II. Effective-mass and observed binding energies (in meV) of 3s and $3d_o$ donor levels in silicon.

State	Theory[3]	P[6]	As[6]	Bi[7]	S[8]	$Mg^+/4$
3s	4.75	----	-----	4.72	4.56(A_1) 4.80(E)	4.22(b) 4.45(a)
$3d_o$	3.75	4.10	3.80	3.79	3.90	3.80(c)

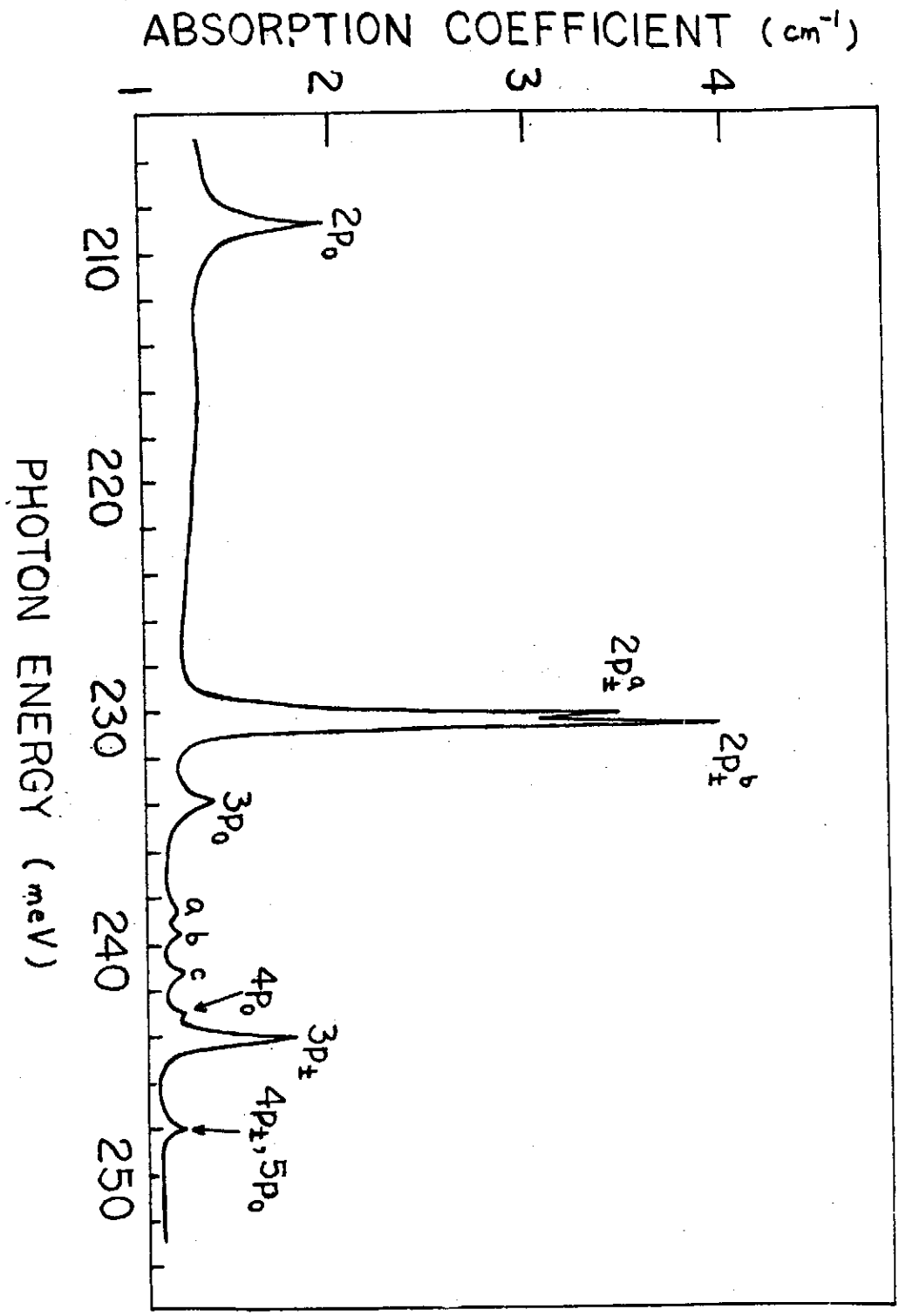

Fig. 1. Excitation spectrum of singly ionized magnesium donors in silicon. Liquid helium was used as coolant. Singly ionized magnesium donors were produced by compensating neutral magnesium donors with boron acceptors.

References

(1) R.K. Franks and J.B. Robertson, Solid State Commun. 5, 479 (1967).

(2) L.T. Ho and A.K. Ramdas, Phys. Rev. B5, 462 (1972).

(3) R.A. Faulkner, Phys. Rev. 184, 713 (1969).

(4) R.L. Aggarwal and A.K. Ramdas, Phys. Rev. 137, A602 (1965).

(5) P. Fisher and A.K. Ramdas, Physics of the Solid State (Academic Press, New York, 1969), p. 149.

(6) J.W. Bichard and J.C. Giles, Can. J. Phys. 40, 1480 (1962).

(7) S. Zwerdling, K. J. Button and B. Lax, Phys. Rev. 118,975 (1960).

(8) W. H. Kleiner and W. E. Krag, Phys, Rev. Letters 25, 1490 (1970).

(9) W. Kohn, Solid State Physics, Vol. 5 (Academic Press, New York, 1957), p. 257.

(10) W. Kohn and J.M. Luttinger, Phys, Rev. 98, 915 (1955).

(11) In Ref. 6 the $3d_o$ was identified as the $4p_o$.

Time Dependence of the Excitation Spectrum of Neutral Magnesium Donors in Silicon*

By

L.T. HO

Time-dependent effects on donor excitation spectra in silicon have been noticed in the spectra associated with lithium-oxygen complexes (1) and in EPR studies of sulfur-doped silicon (2). Recently, we have observed a similar effect on the excitation spectrum of neutral magnesium donors in silicon. The purpose of this paper is to report our observations.

Magnesium was introduced into silicon by the diffusion technique as follows. Pure magnesium was deposited by evaporation on the surfaces of the silicon sample. The sample was then heated at 1200 ^{o}C for one hour in a helium atmosphere. During diffusion, since the boiling point of magnesium is lower than the diffusion temperature, the sample has to be sandwiched between two other specimens, all three having magnesium deposited on the surfaces. In this manner, the sample and its two covers weld together to prevent magnesium from escaping into the ambient. After the heat treatment, the sample, together with the covers, was quenched in liquid nitrogen. The covers were then ground off. By following this procedure an undoped floating-zone silicon, initially high resistivity and p-type, was converted to a low resistivity n-type specimen with a room temperature carrier concentration of the order of 10^{15} cm^{-3}.

The excitation spectrum for neutral magnesium in silicon measured with liquid helium as coolant is shown in Fig. 1a. The excitation lines have the following positions in meV: 95.80($2p_0$), 101.12($2p_+$), 101.95($3p_0$), 104.17($4p_0$), 104.38($3p_+$), 105.33($4p_+$,$5p_0$), and 106.05($5p_+$). The energy separations between these lines and their relative intensities are in excellent agreement with those of the corresponding lines of group V donors in silicon (3). The labeling of the excitation lines for neutral magnesium donors is based on this similarity. Magnesium impurity behaves like a donor in silicon instead of an acceptor presumably due to its being interstitial rather than substitutional.

* This paper has been published in Phys. Stat. Sol. (a) 28, K73 (1975)

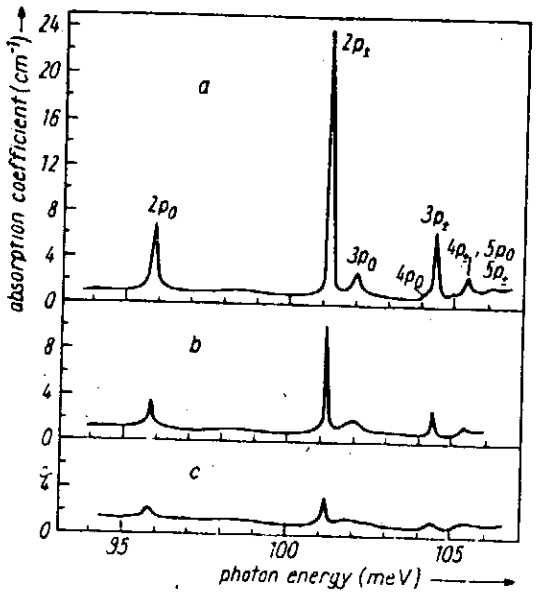

Fig. 1. Time-dependent effect on the excitation spectrum of neutral magnesium donors in silicon; a) see text, b) and c) show the decrease of intensity for the same sample remeasured after 19 and 49 months, respectively. Liquid helium was used as coolant in each measurement

The decrease in the intensity of the magnesium excitation lines is observed when the same spectrum is remeasured after a considerable lapse of time. Fig. 1 presents a typical example of such a spectrum. Shown in Fig. 1a is the spectrum measured within a few days after addition of the magnesium impurity. Fig. 1b shows the same spectrum remeasured after 19 months. The intensity of the excitation lines has clearly decreased. 30 months later the same spectrum was remeasured again and shown in Fig. 1c. Except a few lines such as $2p_0$, $2p_+$, and $3p_+$, others have become too weak to be observed. It is quite obvious that there is a time-dependent effect on the excitation spectrum of magnesium donors in silicon. The positions of the excitation lines, however, remain to be the same indicating that the time has no effect on the ground state.

The intensity decrease of the excitation lines may be a consequence of precipitation with great rapidity and lithium precipitates rather slowly in silicon under conditions of cooling from higher temperatures to room temperature (4, 5). In our case, the cooling of the sample from the diffusion temperature after the heat treatment should also result in the precipitation of magnesium. Furthermore, the precipitation process would continue when the sample was maintained at room temperature, though the rate might be very slow. In this regard, spontaneous changes in germanium containing lithium were early connected with its precipication at room temperature (6).

The behavior of magnesium in silicon is very similar to that of lithium. Both impurities can be diffused into silicon, enter the silicon lattice interstitially and

behave like donors. In (1) the study of lithium donors in silicon has shown a time dependence of the absorption spectrum resulting from the lithium-oxygen interaction if the silicon crystal contains rather large amounts of oxygen. In order to reduce this effect, the oxygen concentration should be much less than the donor concentration. Since the magnesium donor concentration in our sample is only of the order of 10^{15} cm^{-3}, the decrease in the intensity of the absorption lines with time can be at least partially accounted for by precipitation of the magnesium and a possible magnesium-oxygen interaction.

The author wishes to thank Prof. A.K. Ramdas for his encouragement and many helpful discussions.

References

(1) T.E. GILMER, Jr., R.K. FRANKS, and R.J. BELL, J. Phys. Chem. Solids 26, 1195 (1965).

(2) G.W. LUDWIG, Phys. Rev. 137, A1520 (1965).

(3) P. FISHER and A.K. RAMDAS, in: Physics of the Solid State, Ed. S. BALAKRISHNA, M. KRISHNAMURTHI, and B. RAMACHANDRA RAO, Academic Press, New York 1969 (p. 149).

(4) C.S. FULLER and J.A. DITZENBERGER, Phys. Rev. 91, 193 (1953).

(5) R.N. HALL, J. Phys. Chem. Solids 3, 63 (1957).

(6) C.S. FULLER and J.C. SEVERIENS, Phys. Rev. 96, 21 (1954).

(Received December 30, 1974)

A PHYSICAL THEORY OF ACUPUNCTURE ANESTHESIA *

CHUN CHIANG
Biophysics Laboratory, Institute of Physics, Academia Sinica, NanKang, Taipei, Taiwan, Republic of China

(Received December 18, 1973; Revised February 5, 1974)

That acupuncture can be used as a means for anesthesia is a very interesting fact; however, the mechanism for achieving this purpose is not clear.

Various authors[1-3] have suggested that the relief of pain is due to the inhibition of pain signals in the brain or due to the closure of the gate in the substantia gelatinosa. However, their theories cannot explain the following experimental facts: (1) Time lag and persistence effect: Anesthesia cannot be achieved instantaneously and, once the effect is achieved, it can last for some time. (2) The nerve conduction velocity is changed. (3) To achieve the anesthesia effect, the stimulation of the needle should create a feeling of soreness, swelling, heaviness and numbness to the patient. These feelings do not necessarily transmit along the route of the nearby nerves.

This paper proposes that the anesthesia effect of acupuncture is produced by blocking the pain signals from transmitting along the nerves. The blocking being due to the pressure effect, the electrostatic effect and the piezoelectric effect. When these effects influence the nearby nerves, the membrane potentials may be changed and the pain signals may be modified or blocked. To further elucidate the effects: *(a) Pressure Effect*: To achieve the acupuncture anesthesia, the patient has to obtain the feeling of swelling and heaviness. This is strong indication that pressure has been exerted locally in the area. The pulling and twirling of the needles in the body could set out a series of pressure waves. These pressure waves then propagate and transport the interstitial fluid along the route which is best suited for propagation. This route does not necessarily follow the nerve distribution. If there is nerve passing near this propagation route, the nerve will be pressured locally. Thus, the nerve conduction velocity may be changed and the pain signals may be modified or blocked, and, consequently, the pain cannot transmit from its origin to the pain perception center in the cortex. Also, many authors[4-6] have reported that, *in vitro*, the hydrostatic pressure can decrease the conduction velocity and the amplitude of the action current of the nerves. Schaffeniels[7] has shown that the hydrostatic pressure can modify the skin membrane potential and Chiang[8] has interpreted this as due to the pressure effect on the biochemical reactions involved in the active transport. All these evidences,

* This paper has been published in Physiol. Chem. & Physics, 6 (1974)

in vivo and *in vitro*, show indeed that the pressure can modify the membrane potential and thus interfere with the transmission of the pain signals along the nerves. Application of heat, instead ot an acupuncture needle, would expand the interstitial fluid and also set in motion the heat and pressure waves; thus, cauterization can achieve the same clinical purpose. *(b) Electrostatic Effect*: The interstitial fluid may contain highly ionizable materials such as water, CO_2 and organic acids. It also contains hormones and endocrine secretion. Depending on their distribution, the skin resistance may vary. Clinically, we do find that the distribution of skin resistance follows certain specific patterns on the human body. When these materials in the interstitial fluid are transported to the area near the nerve by the stimulation of the needle, they may diffuse across the nerve membrane and short circuit or modify the membrane potential; thus, the signal transmission along the nerve may be blocked. It has been well demonstrated, *in vitro*, that hormones and enzymes or electric current can modify the membrane potential.[9,10] Clinically, we find that anesthesia can also be achieved by electric current stimulation or by injecting certain chemicals. *(c) Piezoelectric Effect*: Shamos and Lavine[11] have shown that skin, callus, cartilage, bone and tendon can exhibit piezoelectricity. The twirling and pulling of the needle during acupuncture may produce electrical potential due to the piezoelectric property of tissues. The produced electrical potential may propagate along a route which is the easiest for it to pass through. Fisch[12] has shown that one can pick up electrical signals when a remote point on the skin is stimulated. This electrical signal can interfere with the nerve membrane nearby and the pain signals may be blocked.

The above three processes need time to develop; it takes time to propagate and transport the interstitial fluid from the stimulation point to the point where it interacts with the nerve. Once the interstitial fluid is built up at the point of interaction, it takes time for the diffusion process to restore the tissues and nerve membranes to normal conditions. This explains the time lag and persistence effect. This theory seems to be able to explain all the existing experimental facts.

REFERENCES

1. A. E. Smith and D. H. Kenyon, *Amer. J. Chinese Med., 1*, 91 (1973).
2. H. C. Tien, *Amer. J. Chinese Med., 1*, 105 (1973).
3. P. L. Man, *Int. Symp. Acupuncture*, Monarch Services, St. Petersburg, Florida, (1973), p. 48.
4. C. S. Spyropoulos, *Amer. J. Physiol., 189*, 214 (1957).
5. G. Grundfest and M. Cattell, *Amer. J. Physiol., 113*, 56 (1935).
6. V. Ebbecke and H. Schaefer, *Pfluger's Arch. Ges. Physiol., 236*, 678 (1935).
7. E. Schaffeniels, *Cellular Aspects of Membrane Permeability*, Pergamon Press, Oxford, (1967), p. 223.
8. C. Chiang, "Properties and responses of frog skin membranes," *Ann. Rep. Inst. Phys. Acad. Sinica, Taipei*, pp. 143-154 (1971-1972).
9. K. H. Johnston and T. Hoshiko, *Amer. J. Physiol., 220*, 792 (1971).
10. E. Katchalski, I. Silman and R. Goldman, in *Advances in Enzymology*, Vol. 34, F. F. Nord, Ed., Interscience, New York, (1971), p. 445.
11. M. H. Shamos and L. S. Lavine, *Nature (London), 213*, 267 (1967).
12. G. Fisch, *Int. Symp. Acupuncture*, Monarch Services, St. Petersburg, Florida, (1973), p. 112.

NERVE EXCITATIONS BY THE COUPLING OF THE DIPOLES AND THE MEMBRANE MATRIX *

■ CHYUAN-YIH LEE†
Department of Physics,
Tamkang College of Arts and Sciences,
Tamsuei, Taiwan, R.O.C.

CHUN CHIANG
Institute of Physics,
Academia Sinica,
Nankang, Taiwan, R.O.C.

Based on Wei's dipole flip-flop model and with the assumption that the dipole is coupled to the membrane matrix, the cathode-make-excitation, the anode-break-excitation and the cathode-gap-excitation can be explained in a systematic way. The strength–duration relations for these three processes are derived.

Introduction. Though many observations on nerve excitation have been made, the molecular mechanism is still not very clear. Recently, Wei (1969a, b, 1971a) proposed a dipole flip-flop model to explain the initiation of nerve impulses. While there is evidence for the existence of negative surface charges at the surface of nerve fibers (Tasaki *et al.*, 1961; Ling, 1962; Segal, 1968), we shall however make use of the recent work of Wei, who proposed that two dipole layers exist at the membrane surface, and the negative end of the dipole layer at outer surface faces outward, thus forms a barrier field F_b preventing the inward flow of sodium ions (or other cations). A cation with charge q will be subject to a force qF_b under this barrier. Since experiments (Hodgkin and Huxley, 1952) have demonstrated that a nerve impulse is initiated by the

* This paper has been published in Bull. of Math. Biology, Vol. 37, 1975

† Present address: Department of Physics, University of Delaware, Newark, DE 19711, U.S.A.

inward flow of cations, a method to excite a membrane is to reduce this barrier field F_b. Wei (1969a) assumed that the membrane dipole has two quantum states with energy E_1 and E_2 respectively ($E_2 > E_1$). If N_1 and N_2 are the numbers of the dipoles corresponding to quantum states E_1 and E_2, the barrier field will be proportional to $\Delta N = N_1 - N_2$. When the membrane is at rest, the population ratio obeys Boltzmann distribution, $N_1/N_2 = \exp(E_2 - E_1)/kT$. Upon cathodic stimulation with field strength F, some of the dipoles in state I will flip to state II and a new equilibrium will be reached, the population distribution will be $N_1/N_2 = \exp(E_2 - E_1 - 2pF)/kT$, where p denotes the dipole moment. During the process of transition, if ΔN is reduced to a critical value such that the barrier is sufficiently small, then the cation would flow inward and the nerve impulse is initiated. Thus, the mechanism of cathode-make-excitation can be explained based on this model. As for the mechanism for anode-break- and cathode-gap-excitation, Wei (1973) explained that, "During anodic stimulation, the upper state dipoles are de-excited at an enhanced rate, resulting in a lower energy of the dipole system. The energy is stored in the membrane. At the instant of anode break, the stored energy is quickly released in the form of a cathodic stimulus, which, if reaching the threshold, will excite the nerve." In this paper we shall extend Wei's idea and explain the anode-break process in detail; furthermore, we are able to treat all three processes of excitation (cathodic, anode-break and cathode-gap) systematically with the assumption that there is interaction between the dipoles and membrane matrix.

Postulates. (1) We use Wei's assumption that a membrane dipole can be in either of the two states with energy E_1 and E_2 ($E_2 > E_1$). When ΔN, the difference of dipole population between two states, is below a threshold value ΔN_t, ions can move inward and the impulse is initiated.

(2) A photon of frequency $\nu = (E_2 - E_1)/h$ will be emitted when a dipole transits from the higher state to the lower state (Wei, 1969a, 1972). This assumption has been supported by the experiment of Fraser and Frey (1968).

(3) We shall further assume that the membrane can absorb photons emitted from the dipole transition and the absorbed photons in the membrane matrix may decay exponentially and could be fed into the dipole system again. This assumption is supported by the data of Howarth *et al.* (1968) that heat is produced in the early stage of nerve impulse and reabsorbed during a later stage. If, during the early stage of nerve impulse, the photons are emitted from the dipole system and create phonons in the membrane, this may produce the heat; when the phonons in the membrane matrix are reabsorbed by the dipole system, the heat will disappear.

With these three assumptions, we shall proceed to explain the excitation processes.

Cathode-Make-Excitation. During cathode-make stimulation (Figure 1a), some of the dipoles in the lower energy states will flip to higher energy states. The population in the two energy states can be described by the following rate equations:

$$\begin{aligned} dN_1^c/dt &= -w_{12}^c N_1^c + w_{21}^c N_2^c \\ dN_2^c/dt &= w_{12}^c N_1^c - w_{21}^c N_2^c \end{aligned} \tag{1}$$

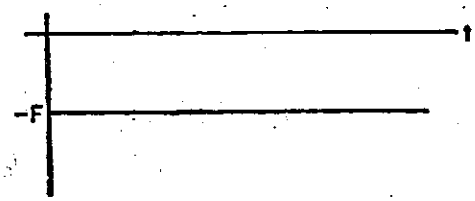

(a)

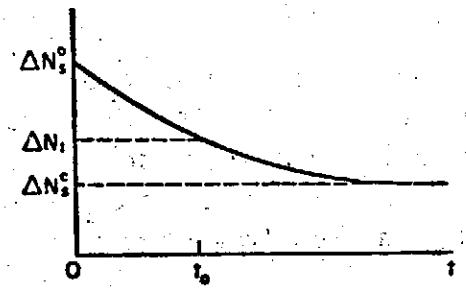

(b)

Figure 1. (a) The stimulus for cathode-make-excitation. (b) The change of dipoles during the period of stimulus used

where w_{12}^c is the probability per unit time for a dipole to jump from state I to state II, and w_{21}^c is the probability per unit time for the reverse process. The superscript "c" stands for cathodic stimulation. Equation (1) may be transformed to

$$d\Delta N^c/dt = -(w_{21}^c + w_{12}^c)\Delta N^c + (w_{21}^c - w_{12}^c)N \tag{2}$$

where

$$\Delta N^c \equiv N_1^c - N_2^c; \qquad N \equiv N_1^c + N_2^c$$

The solution of (2) is

$$\Delta N^c = \left(\Delta N_s^0 - N\frac{w_{21}^c - w_{12}^c}{w_{21}^c + w_{12}^c}\right)\exp\left[-(w_{21}^c + w_{12}^c)t\right] + N\frac{w_{21}^c - w_{12}^c}{w_{21}^c + w_{12}^c} \tag{3}$$

where the superscript "0" in ΔN_s^0 stands for the membrane with no external stimulus and subscript "s" stands for the steady state. Since for the membrane in rest, $(N_1^0)_s/(N_2^0)_s = \exp(E_2 - E_1)/kT$, we have

$$\Delta N_s^0 \equiv (N_1^0)_s - (N_2^0)_s = N\tanh(E_2 - E_1)/2kT. \tag{4}$$

When the system is in equilibrium under an electric field F, then $\mathrm{d}(N_1^c)_s\mathrm{d}t = \mathrm{d}(N_2^c)_s/\mathrm{d}t = 0$. Thus (1) becomes

$$w_{21}^c/w_{12}^c = (N_1^c)_s/(N_2^c)_s = \exp(E_2 - E_1 - 2pF)/kT \tag{5}$$

and we have

$$\Delta N_s^c \equiv (N_1^c)_s - (N_2^c)_s = N\tanh\left[(E_2 - E_1 - 2pF)/2kT\right] \tag{6}$$

From (6) and (3), we have

$$\Delta N^c = (\Delta N_s^0 - \Delta N_s^c)\exp\left[-(w_{21}^c + w_{12}^c)t\right] + \Delta N_s^c \tag{7}$$

Equation (7) shows that ΔN reduces exponentially to a steady state value ΔN_s^c upon cathodic stimulation (see Figure 1b). If a threshold value, say ΔN_t, is reached such that the barrier is small enough for the sodium ions to move inward, then the nerve will be excited. The strength–duration relation for constant cathodic stimulation can be obtained by substituting $\Delta N^c = \Delta N_t$ in (7), and we can obtain

$$t_0 = \frac{1}{w_{21}^c + w_{12}^c}\log\frac{\Delta N_s^0 - \Delta N_s^c}{\Delta N_t - \Delta N_s^c} \tag{8}$$

where t_0 is the minimum duration of applied stimulus for nerve excitation.

Equation (8) is similar to the strength–duration–frequency relation obtained by Spiegel and Joines (1973) if we neglect the dipole–dipole interaction in their equation. However, our derivation is simpler and can be extended to other excitation processes as will be shown later.

In order to express (8) in terms of applied field F, we first rewrite (5) as

$$w_{12}^c = A\exp\left[-(E_2 - E_1 - 2pF)/2kT\right];$$

$$w_{21}^c = A\exp\left[E_2 - E_1 - 2pF)/2kT\right] \tag{9}$$

where A is a ratio constant, and can be interpreted as rotation frequency of the dipoles. For convenience, we shall define

$$\tau \equiv \tfrac{1}{2}A; \quad U \equiv (E_2 - E_1)/2 \tag{10}$$

where τ can be interpreted as the average time required for the dipole to jump from one state to the other.

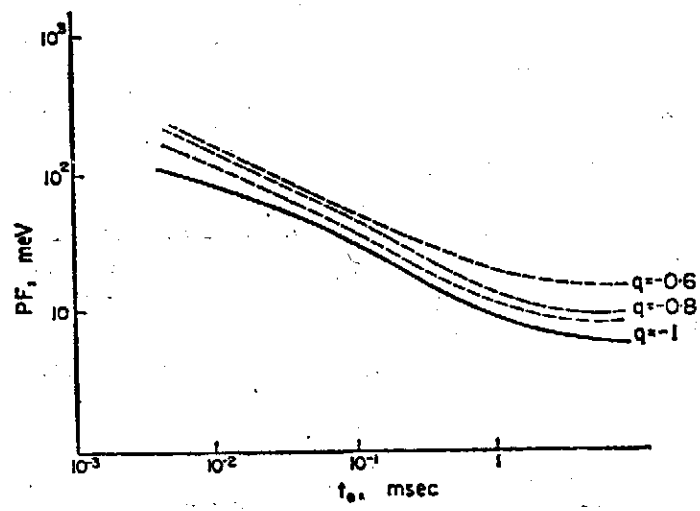

Figure 2. The strength duration relation. The thick line is calculated according to equation (13) for cathode make excitation, and the dashed lines are calculated according to (29) for anode break excitation

Thus, (9) becomes

$$w_{12}^c = \frac{1}{2\tau}\exp\left[-(U-pF)/kT\right]; \quad w_{21}^c = \frac{1}{2\tau}\exp\left[(U-pF)/kT\right]. \tag{11}$$

Let

$$r \equiv \Delta N_t/\Delta N_s^0 \tag{12}$$

and substituting (4), (6), (11) and (12) into (8), the duration t_0 can be expressed explicitly as a function of field F,

$$t_0 = \frac{\tau}{\cosh\,(U-pF)/kT}\log\frac{\tanh\,(U-pF)/kT - \tanh\,U/kT}{\tanh\,(U-pF)/kT - r\tanh\,U/kT}. \tag{13}$$

The parameters τ and U can be estimated to be 1 msec and 20 mv respectively (Wei, 1969b, 1971b, 1972) and r to be 0.8 (Lee and Chiang, 1973). The curve of (13) is shown in Figure 2.

Anode-Break-Excitation. During anodic stimulation (Figure 3a), some dipoles in the higher energy state will flip to the lower state, the photons thus emitted will be transmitted to the membrane matrix. We can write:

$$\begin{aligned} dN_1^a/dt &= -w_{12}^a N_1^a + w_{21}^a N_2^a \\ dN_2^a/dt &= w_{12}^a N_1^a - w_{21}^a N_2^a \\ dP &= dN_1^a = -dN_2^a \end{aligned} \tag{14}$$

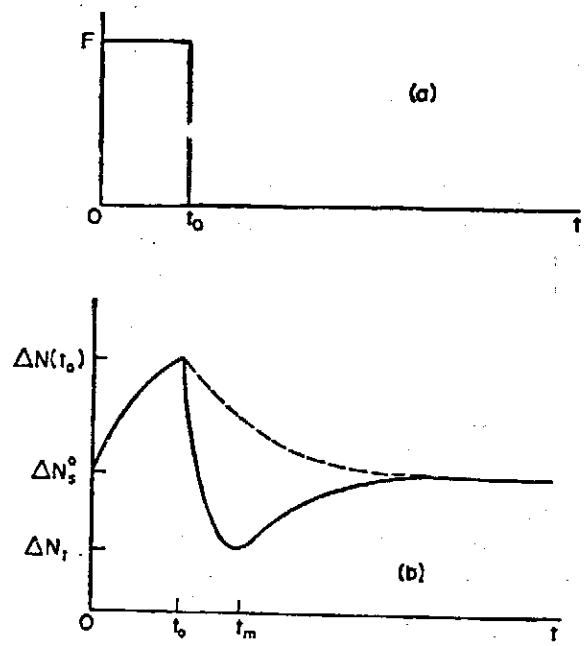

Figure 3. (a) The stimulus for anode break excitation. (b) The change of dipoles during the stimulus used. If there is no coupling between the dipoles and the membrane matrix, the change of dipoles will follow the dashed line

where P represents the photons, the superscript "a" stands for anode-break process, w_{12}^a and w_{21}^a have the same meaning as above. For simplicity, we have assumed that all the photons emitted are stored in the membrane matrix. The transition probability during anodic stimulation can similarly be expressed as

$$w_{12}^a = \frac{1}{2\tau} \exp\left[-(U+pF)/kT\right]; \quad w_{21}^a = \frac{1}{2\tau} \exp\left(U+pF\right)/kT. \tag{15}$$

The solution of (14) is

$$\Delta N^a = (\Delta N_s^0 - \Delta N_s^a) \exp\left[-(w_{12}^a + w_{21}^a)t\right] + \Delta N_s^a, \qquad t < t_0, \tag{16}$$

$$P = \tfrac{1}{2}(\Delta N^a - \Delta N_s^0) = \tfrac{1}{2}(\Delta N_s^a - \Delta N_s^0)\{1 - \exp\left[-(w_{12}^a + w_{21}^a)t\right]\}, \qquad t < t_0, \tag{17}$$

where t_0 is the duration of anodic stimulus. Similar to (6), ΔN_s^a is

$$\Delta N_s^a = N \tanh (U + pF)/kT. \tag{18}$$

Since $\Delta N_s^0 < \Delta N_s^a$, (17) shows that ΔN "increase" exponentially from ΔN_s^0 to ΔN_s^a (Figure 3b). Because the barrier field F_b is proportional to ΔN, F_b also increase exponentially, thus the nerve cannot be excited during anodic stimulation.

At the end of anodic stimulus (at $t = t_0$), the number of stored photons $P(t_0)$ in the membrane and the population difference $\Delta N^a(t_0)$ are respectively

$$P(t_0) = \tfrac{1}{2}(\Delta N_s^a - \Delta N_s^0)\{1 - \exp[-(w_{12}^a + w_{21}^a)t_0]\} \tag{19}$$

and

$$\Delta N^a(t_0) = (\Delta N_s^0 - \Delta N_s^a)\exp[-(w_{12}^a + w_{21}^a)t_0] + \Delta N_s^a . \tag{20}$$

When the anodic stimulus is released, P in the membrane matrix will decay and will be reabsorbed by the dipole system, the equations describing this process are:

$$\left.\begin{aligned} dN_1^a/dt &= -w_{12}^0 N_1^a + w_{21}^0 N_2^a + dP/dt \\ dN_2^a/dt &= w_{12}^0 N_1^a - w_{21}^0 N_2^a - dP/dt \end{aligned}\right\} \tag{21}$$

$$dP/dt = -bP. \tag{22}$$

Here, we have assumed that decay rate of the photons is proportional to the stored photons in the membrane matrix, b is the proportional constant, w_{12}^0 and w_{21}^0 are the transition probability without any applied field, namely,

$$w_{12}^0 = \frac{1}{2\tau}\exp(-U/kT); \quad w_{21}^0 = \frac{1}{2\tau}\exp(U/kT). \tag{23}$$

With the initial condition of stored photons in membrane matrix as specified by (19), (22) can be solved to be

$$P = \tfrac{1}{2}(\Delta N_s^0 - \Delta N_s^a)\{\exp[-(w_{12}^a + w_{21}^a - b)t_0] - \exp(bt_0)\}\exp(-bt), \quad t \geqslant t_0. \tag{24}$$

Note that P should satisfy (17) for $t < t_0$. Equation (21) can transform to be

$$d\Delta N^a/dt = -(w_{21}^0 + w_{12}^0)\Delta N^a + (w_{21}^0 - w_{12}^0)N + 2\,dP/dt \tag{25}$$

Substituting (24) into (25) with the initial condition $\Delta N^a = \Delta N^a(t_0)$ at $t = t_0$, we obtain

$$\Delta N^a = \Delta N_s^0 + [\Delta N^a(t_0) - \Delta N_s^0]\left\{\frac{w_{21}^0 + w_{12}^0}{w_{21}^0 + w_{12}^0 - b}\exp[-(w_{21}^0 + w_{12}^0)(t - t_0)]\right.$$

$$\left. - \frac{b}{w_{21}^0 + w_{12}^0 - b}\exp[-b(t - t_0)]\right\}, \qquad t \geqslant t_0. \tag{26}$$

This equation has the characteristics as shown in Figure 3b. We see that ΔN^a can be smaller than ΔN_s^0 after the anodic stimulus is taken away. If ΔN^a decreases to the threshold ΔN_t, then the nerve will excite. The dashed line in Figure 3b shows the change of ΔN^a, should there be no coupling between the dipole system and the membrane matrix.

To calculate the strength–duration curve for anode-break-excitation, we note that the minimum value of ΔN^a, namely, ΔN_m^a, should be equal to ΔN_t, thus

$$\Delta N_t = \Delta N_m^a = \Delta N_s^0 + [\Delta N^a(t_0) - \Delta N_s^0]\left\{\frac{w_{21}^0 + w_{12}^0}{w_{21}^0 + w_{12}^0 - b}\right.$$

$$\left. \times \exp[-(w_{21}^0 + w_{12}^0)(t_m - t_0)] - \frac{b}{w_{21}^0 + w_{12}^0 - b}\exp[-b(t_m - t_0)]\right\}, \tag{27}$$

where t_m is the time at which ΔN^a decrease to ΔN_m^a. t_m can also be obtained by differentiating (26) to be

$$t_m = \frac{2}{w_{21}^0 + w_{12}^0 - b}\log\frac{(w_{21}^0 + w_{12}^0)}{b} + t_0. \tag{28}$$

Combining (27) and (28), and using (4), (15), (18), (20), and (23), we obtain the strength–duration relation for constant anodic stimulation as

$$t_0 = \frac{\tau}{\cosh(U + pF)/kT}\log\frac{\tanh(U + pF)/kT - \tanh U/kT}{\tanh(U + pF)/kT - [(r + q - 1)/q]\tanh U/kT} \tag{29}$$

where

$$q \equiv \frac{\cosh(U/kT)}{\cosh(U/kT) - b\tau}\exp\left[\frac{2\cosh(U/kT)}{\cosh(U/kT) - b\tau}\log\frac{\cosh(U/kT)}{b\tau}\right]$$

$$- \frac{b\tau}{\cosh(U/kT) - b\tau}\exp\left[\frac{-2b\tau}{\cosh(U/kT) - b\tau}\log\frac{\cosh(U/kT)}{b\tau}\right].$$

Equation (29) is plotted in Figure 2 with q equal to be -0.6, -0.8 and -1. It can be seen that for larger F, t_0 becomes smaller. This is consistent with Solandt's observation (1936).

Cathode-Gap-Excitation. If a cathodic field F below the rheobasic field is applied to the membrane, the nerve would not be able to excite regardless of the duration of the applied stimulus. However, if the stimulation stops for a period of t_0 and resumes again at the same strength as before then the nerve can be excited (Solandt, 1936: see Figure 4). This kind of method for excitation is

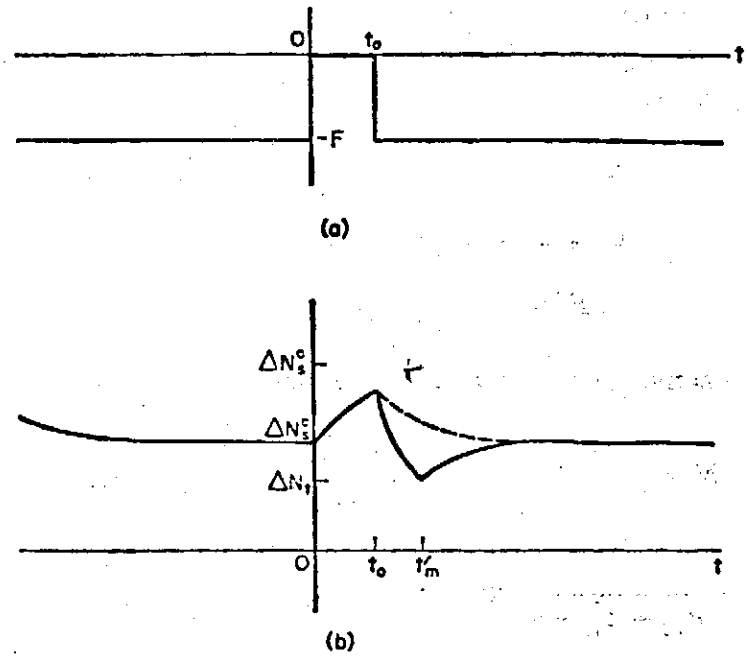

Figure 4. (a) The stimulus for cathode gap excitation. (b) The change of dipoles during the stimulus used

called cathode-gap-excitation. This process can similarly be explained as follows: During the initial cathodic stimulation, the variation of ΔN is the same as that in cathode make excitation (Figure 4b), namely, ΔN will reduce exponentially to the steady state $N \tanh (U - pF)/kT$ with a sufficiently long duration of applied stimulus. However, due to insufficient strength of F, ΔN will not reduce to ΔN_t and the nerve cannot be excited. When the stimulation stops, some dipoles in higher state will transit to lower state, and photons thus released will be delivered to the membrane matrix. The population change is governed by the following equatons:

$$\begin{aligned} dN_1^g/dt &= -w_{12}^0 N_1^g + w_{21}^0 N_2^g \\ dN_2^g/dt &= w_{12}^0 N_1^g - w_{21}^0 N_2^g \\ dP &= dN_1^g = -dN_2^g \end{aligned} \tag{30}$$

where g stands for the cathode-gap excitation. The solutions of (30) can similarly be obtained as:

$$\Delta N^g = (\Delta N_s^c - \Delta N_s^0)\exp[-(w_{12}^0 + w_{21}^0)t] + \Delta N_s^0, \qquad 0 < t < t_0 \tag{31}$$

$$P = [\Delta N_s^c - \Delta N^g]/2, \qquad 0 < t < t_0. \tag{32}$$

Where t_0 is the duration of the stimulus gap. During second cathodic stimulation, the stored photons will interact with the dipole system, and the population change equations are:

$$\begin{aligned} \mathrm{d}N_1/\mathrm{d}t &= -w_{12}^c N_1 + w_{21}^c N_2 + \mathrm{d}P/\mathrm{d}t \\ \mathrm{d}N_2/\mathrm{d}t &= w_{12}^c N_1 - w_{21}^c N_2 - \mathrm{d}P/\mathrm{d}t \\ \mathrm{d}P/\mathrm{d}t &= -bP. \end{aligned} \tag{33}$$

Following the same procedure as in the anode-break-excitation, we obtain

$$\Delta N^g = \Delta N_s^c + [\Delta N^g(t_0) - \Delta N_s^c]\left\{\frac{w_{21}^c + w_{12}^c}{w_{21}^c + w_{12}^c - b}\exp[-(w_{21}^c + w_{12}^c)(t - t_0)]\right.$$

$$\left. - \frac{b}{w_{21}^c + w_{12}^c - b}\exp[-b(t - t_0)]\right\}, \qquad t > t_0. \tag{34}$$

Equation (34) also shows a minimum at t'_m, namely,

$$\Delta N_m^g = \Delta N_s^c + [\Delta N^g(t_0) - \Delta N_s^c]\left\{\frac{w_{21}^c + w_{12}^c}{w_{21}^c + w_{12}^c - b}\exp[-(w_{21}^c + w_{12}^c)(t'_m - t_0)]\right.$$

$$\left. - \frac{b}{w_{21}^c + w_{12}^c - b}\exp[-b(t'_m - t_0)]\right\}. \tag{35}$$

t'_m can also be obtained by differentiation of (34) to be

$$t'_m = \frac{2}{w_{21}^c + w_{12}^c - b}\log\frac{w_{21}^c + w_{12}^c}{b} + t_0 \tag{36}$$

with the help of (4), (6), (11), (23) and (31), the strength–duration relation can be obtained by substituting (36) into (35) and letting ΔN_m^g equal to ΔN_t. Thus

$$t_0 = \frac{\tau}{\cosh U/kT}\log\frac{q'[\tanh(U - pF)/kT - \tanh U/kT]}{(q' - 1)\tanh(U - pF)/kT - (q' - r)\tanh U/kT} \tag{37}$$

where q' is

$$q' \equiv \frac{\cosh (U-pF)/kT}{\cosh (U-pF)/kT - b\tau} \exp\left[\frac{2\cosh (U-pF)/kT}{\cosh (U-pi\ )/kT - b\tau} \log \frac{\cosh (U-pF)/kT}{b\tau}\right]$$

$$- \frac{b\tau}{\cosh (U-pF)/kT - b\tau} \exp\left[\frac{-2b\tau}{\cosh (U-pF)/kT - b\tau}\right.$$

$$\left.\times \log \frac{\cosh (U-pF)/kT}{b\tau}\right].$$

In conclusion, we have shown the dynamic transient process of dipoles for the cathodic, anode-break, and cathode-gap excitation. With the assumption of coupling between the dipoles and the membrane matrix, we are able to explain the three excitation processes systematically. The strength–duration relations for these three processes are also derived. Assuming the relaxation time to be 1 msec, the strength–duration relation for constant field stimulation is plotted in Figure 2, and the minimum pF is estimated to be 5 meV. The minimum F can be estimated from the threshold voltage (17 mV) deduced by the constant current stimulation experiment (Guttman, 1966) and from the membrane thickness (70 Å) to be 17 meV/70A $= 2.5 \times 10^4$ V/cm, thus p is about 20 e-A. This seems to be a quite reasonable value. Thus, even though no data in constant field stimulation are available, indirect comparison indicates that this theory is consistent with those experiments carried out using constant current pulses and the estimated parameters are quite reasonable.

LITERATURE

Fraser, A. and A. H. Frey. 1968. "Electromagnetic Emission at Micron Wavelengths from Active Nerves." *Biophys. J.*, **8**, 731–734.

Guttman, R. 1966. "Temperature Characteristics of Excitation in Space-Clamped Squid Axons." *J. Gen. Physiol.*, **49**, 1007–1018.

Hodgkin, A. L. and A. F. Huxley. 1952. "A Quantitative Description of Membrane Current and Its Application to Conduction and Excitation in Nerve." *J. Physiol.*, **117**, 500–544.

Howarth, J. V., R. D. Keynes and J. M. Ritchie. 1968. "The Origin of the Initial Heat Associated with a Single Impulse in Mammalian Non-Myelinated Nerve Fibres." *J. Physiol. (Lond.)*, **194**, 745–793.

Lee, C. Y. and C. Chiang. 1973. "On the Dipole Model for the Initiation of Nerve Impulse." *Ann. Rep., Inst. Phys., Acad. Sin. (Taipei)*, **94–104**.

Ling, G. N. 1962. *A Physical Theory of the Living State: The Association-Induction Hypothesis*. New York: Blaisdell.

Segal, J. R. 1968. "Surface Charge of Giant Axons of Squid and Lobster." *Biophys. J.*, 8, 470–489.

Solandt, D. Y. 1936. "A Comparison of Various Methods of Measuring the Time Constant of Accommodation of Nerve." *Proc. R. Soc. (Lond.)*, **B120**, 389–408.

Spiegel, R. J. and W. T. Joines. 1973. "A Semiclassical Theory for Nerve Excitation by Low Intensity Electromagnetic Field." *Bull. Math. Biol.*, **35**, 591–605.

Tasaki, I., T. Teorell and C. S. Spyropoulos. 1961. "Movement of Radioactive Tracers Across Squid Axon Membrane." *Am. J. Physiol.*, **200**, 11–20.

Wei, L. Y. 1969a. "Role of surface Dipoles on Axon Membrane." *Science*, **163**, 280–282.

———. 1969b. "Molecular Mechanisms of Nerve Excitation and Conduction." *Bull. Math. Biophys.*, **31**, 39–58.

———. 1971a. "Quantum Theory of Nerve Excitation." *Ibid.*, **33**, 187–194.

———. 1971b. "Possible Origin of Action Potential and Birefringence Change in Nerve Axon." *Ibid.*, **33**, 521–537.

———. 1972. "Dipole Theory of Heat Production and Absorption in Nerve Axon." *Biophys. J.*, **12**, 1159–1170.

———. 1973. "Quantum Theory of Time-Varying Stimulation in Nerve." *Bull. Math. Biophys.*, **35**, 359–374.

Moiré Topography

Chun Chiang

Using geometrical optics, an oblique-shadow method is shown to generate moiré patterns, which under specific conditions can be interpreted as contour lines of the surface. The oblique-shadow method consists of illuminating a viewing grid with equal spaced parallel lines. The light can be either a point source or parallel light, the observation point can be either at finite distance or at infinity. Conditions for which moiré patterns become contour lines of the surface are given.

I. Introduction

Recently, several papers[1-3] have appeared in this journal discussing the measurement of surface topography with the moiré technique. The communication theory has been used to show that a periodic grating together with its shadow on a surface can form moiré patterns; these patterns may be interpreted as contour lines of the surface. However, the exact conditions for obtaining the moiré contour lines have not been discussed in detail. Earlier, the oblique-shadow method[4-6] has been shown to form the moiré patterns using geometrical optics; the conditions under which the moiré patterns may represent the contour lines of the surface has been given. Furthermore, if the surface is shining and can be served as a mirror, then the grating together with its mirror image can also form moiré contour lines.[6] The purposes of this paper are: (1) to give a systematic and mathematical treatment of the moiré patterns for various experimental conditions in the oblique-shadow method and to point out the conditions for interpreting the moiré patterns as contour lines of the surface, so that the experimenters can choose the best experimental setup for their measurement; (2) to clarify some previous derivation of moiré contour lines, which may be misleading.

II. General Equation for Moiré Patterns

Suppose the x-coordinate spacing of the parallel lines on the viewing grid and on the surface is a and b, respectively; thus, the lines can be represented as

$$x = ma + c_1, \tag{1}$$

$$x = nb + c_2, \tag{2}$$

where m and n are integers, 0, ±1, ±2, ..., c_1 and c_2 are the phase constants. Using the method similar to that of Chiang[6,7] and Meadows *et al.*,[3] the projection of the lines from the surface to the viewing grid with the viewing point at $O(x_0, 0, z_0)$ is

$$x = x_0 \frac{d(x_1, y_1)}{z_0 + d(x_1, y_1)} + (nb + c_2)\frac{z_0}{z_0 + d(x_1, y_1)}, \tag{3}$$

where d is the distance between the surface and the viewing grid, with the coordinate on the surface represented by x_1 and y_1. With the index equation

$$m - n = k, \tag{4}$$

the moiré patterns can be obtained by combining Eqs. (1), (3), and (4) to be

$$x = \frac{d(x_1, y_1)x_0}{z_0 + d(x_1, y_1)} + [(x - c_1)b/a - kb + c_2]\frac{z_0}{z_0 + d(x_1, y_1)}, \tag{5}$$

where k is also an integer. Equation (5) can be simplified to

$$d(x_1, y_1) = \frac{(a - b)x - ac_2 + bc_1 + abk}{a(x_0 - x)} z_0. \tag{6}$$

Since the point $(x_1, y_1, -d)$ on the surface, the point $(x, y, 0)$ of the moiré patterns on the viewing grid, and the observation point $O(x_0, 0, z_0)$ have to be on the same line, thus

$$\frac{x_0 - x_1}{x_0 - x} = \frac{y_1}{y} = \frac{z_0 + d(x_1, y_1)}{z_0} \tag{7}$$

Introducing Eq. (6) into Eq. (7), we have

$$x_1 = (bx + ac_2 - bc_1 - abk)/a, \tag{8}$$

$$y_1 = y(ax_0 - bx - ac_2 + bc_1 + abk)/a(x_0 - x). \tag{9}$$

Introducing Eqs (8) and (9) into Eq. (6), we have

The author is with the Institute of Physics, Academia Sinica, NanKang, Taipei, Taiwan, Republic of China.

Received 31 July 1973.

* This paper has been published in Applied Optics, Jan. 1975/Nov. 14, No. 1, p. 177 – 179.

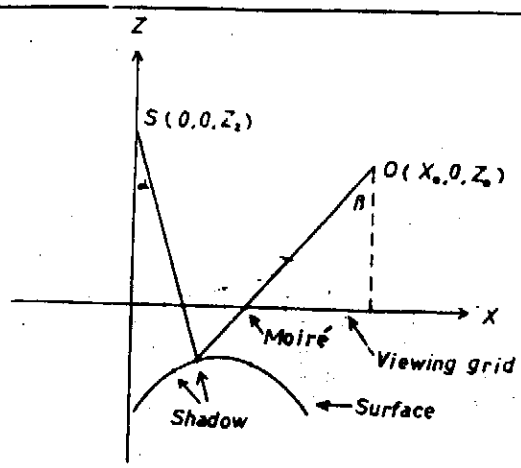

Fig. 1. A diagram showing the parallel lines on the viewing grid and their shadow on the surface which interfere to form the moiré patterns. S is the illumination point and O is the observation point.

$$d\left[\frac{bx + ac_2 - bc - abk}{a}, \frac{(ax_0 - bx - ac_2 + bc_1 + abk)y}{a(x_0 - x)}\right] = \frac{(a - b)x - ac_2 + bc_1 + abk}{a(x_0 - x)} z_0. \quad (10)$$

This is the general equation of the moiré patterns produced by a flat viewing grid and any surface, for which both are ruled with parallel lines.

III. Point Illumination and Point Observation at Finite Distance

If the lines on the viewing grid are

$$x = na + c_1, \quad (11)$$

with the illumination of a point source at $S(0, 0, z_2)$ as shown in Fig. 1, the projection of the shadow of the lines from the viewing grid to the surface is

$$x = (na + c_1)\frac{z_2 + d(x_1, y_1)}{z_2}. \quad (12)$$

Comparing with Eq. (2), we have

$$b = \frac{z_2 + d(x_1, y_1)}{z_2} a, \quad (13)$$

$$c_2 = \frac{z_2 + d(x_1, y_1)}{z_2} c_1. \quad (14)$$

From Eqs. (10), (13), and (14), we have

$$d\left\{(1 + d/z_2)(x - ak), \left[1 + \frac{ak(1 + d/z_2) - dx/z_2}{x_0 - x}\right]y\right\} = \frac{akz_0z_2}{x_0z_2 - akz_0 + x(z_0 - z_2)}. \quad (15)$$

Note that this equation has no phase constants c_1 or c_2; thus, the moiré patterns will be stationary against parallel movement of the grating. This has been previously pointed out by Takasaki.[1] Equation (15) shows that the moiré pattern is a very complicated pattern; however, under certain specific conditions, the moiré pattern may be simplified to contour lines of the surface and may be used to measure the topography of the surface.

(a) If $z_0 = z_2$, Eq. (15) can be simplified to

$$d\left\{(1 + d/z_2)(x - ak), \left[1 + \frac{ak(1 + d/z_2) - dx/z_2}{x_0 - x}\right]y\right\} = akz_2/(x_0 - ak). \quad (16)$$

(b) If $z_0 = z_2$ and $x_0 >> ak$, then Eq. (16) becomes

$$d\left\{(1 + d/z_2)(x - ak), \left[1 + \frac{ak(1 + d/z_2) - xd/z_2}{x_0 - x}\right]y\right\} = akz_0/x_0. \quad (17)$$

This equation indicates that the moiré patterns are contour lines of the surface under the condition that the viewing grid is illuminated at point S and observed at point O; furthermore, the conditions that $z_0 = z_2$ and $x_0 >> ak$ have to be fulfilled. Equation (17) is similar to Eq. (14) in the paper of Meadows *et al.*[3]; however, they derive the equation with the conditions that z_0 and z_2 are equal and very large. While this derivation may be valid, nevertheless, it may be misleading. As we can see from Eq. (16), if $x_0 >> ak$, then Eq. (17) is valid. $x_0 >> ak$ can be fulfilled if either x_0 is very large or ak is very small. Meadows *et al.*'s condition that z_2 is very large requires that ak be very small, as can be seen from Eq. (16). Since ak is very small, then k is small; thus, there are only a few contour lines that appear. This is a serious limitation in measuring the contour surface. Furthermore, if x_0 is also very small, then even if ak is very small, the condition that $x_0 >> ak$ is not fulfilled; thus, the moiré patterns which appear are not the contour lines as can be demonstrated in the diagram in Chiang's paper.[6] Thus, the conditions that z_0 and z_2 are equal and large may be valid for Eq. (17), but are not the sufficient nor the necessary conditions. However, the conditions that $z_0 = z_2$ and $x_0 >> ak$ are the necessary and sufficient conditions for Eq. (17) to be true.

Furthermore, Eq. (17) indicates that the moiré contour lines are not the true contour lines and have to be corrected with the amount as follows:

$$x_1 = (1 + d/z_2)(x - ak), \quad (18)$$

$$y_1 = \left[1 + \frac{ak(1 + d/z_2) - dx/z_2}{x_0 - x}\right]y. \quad (19)$$

Under various experimental conditions, the amount of correction may be varied. A formula has been proposed by Takasaki[2] to account for this kind of errors; the procedures presented here seem to be the most exact and direct derivation.

(c) If $z_2 >> z_0$, $z_2 >> d$, and $x_0 >> x$, conditions which can easily be fulfilled experimentally, then Eq. (15) becomes

$$d(x - ak, y) = akz_0/x_0. \quad (20)$$

This equation indicates that the moiré patterns under the above conditions are the contour lines of the surface with only a small amount of correction ak for x coordinate. This will relax the condition that z_0 and z_2 have to be equal and may give some flexibility in setting up the experimental device.

IV. Illumination by Point Source and Observation at Infinity

(a) If we observe the surface at infinity with an angle β, or observe with a collimating lens, then

$$(x_0 - x)/z_0 = \tan\beta. \quad (21)$$

Introducing Eq. (21) into Eq. (15), we obtain

$$d\left\{(1 + d/z_2)(x - ak), \left[1 + \frac{ak(1 + d/z_2) - dx/z_2}{x_0 - x}\right]y\right\} = \frac{akz_2}{z_2\tan\beta + x_0 - ak}. \quad (22)$$

This experimental setup is not very useful in measuring topography since the moiré patterns observed are not the contour lines.

(b) If $z_2 >> d$, $x_0 >> ak$, and $x_0 >> x$, then Eq. (22) becomes

$$d(x - ak, y) = \frac{akz_2}{z_2\tan\beta + x_0} \quad (23)$$

Thus, the moiré patterns under these conditions are the contour lines of the surface. The experimental setup for these conditions can be easily fulfilled.

V. Parallel Illumination and Point Observation

(a) If the viewing grid is illuminated with parallel light at an angle α, then $b = a$ and $c_2 = c_1 + d\tan\alpha$. Thus, Eq. (10) becomes

$$d\left(x - ak + d\tan\alpha, \frac{x_0 - x + ak - d\tan\alpha}{x_0 - x}y\right) = \frac{akz_0}{z_0\tan\alpha + x_0 - x}. \quad (24)$$

(b) If x_0 is much larger than x, ak, and $d\tan\alpha$, then Eq. (24) becomes

$$d(x - ak + d\tan\alpha, y) = \frac{az_0k}{z_0\tan\alpha + x_0} \quad (25)$$

Thus, the moiré patterns under these conditions are the contour lines of the surface with a small correction in x coordinate.

VI. Parallel Illumination and Observation at Infinity

(a) Under this condition, Eq. (21) can be applied. Substituting Eq. (21) into Eq. (24), we obtain

$$d\left(x - ak + d\tan\alpha, \frac{x_0 - x + ak - d\tan\alpha}{x_0 - x}y\right) = \frac{ak}{(\tan\alpha + \tan\beta)}. \quad (26)$$

(b) If $x_0 >> x$, $x >> ak$, and $x >> d\tan\alpha$, Eq. (26) becomes

$$d(x, y) = ak/(\tan\alpha + \tan\beta). \quad (27)$$

This equation is the same as Eq. (6) in the paper by Meadows *et al.*[3] and indicates that the moiré patterns are the contour lines of the surface under the experimental conditions given above. These conditions do not seem to have been pointed out previously.

VIII. Conclusions

The moiré patterns can be produced when a viewing grid with parallel lines is illuminated with light so that a shadow is cast on a surface. The illumination can be either parallel light or point source. The observation point can be either at finite distance or at infinity. Under these experimental situations, the moiré patterns produced are the contour lines of the surface if proper conditions are met. A systematic derivation of moiré patterns for various experimental conditions are given so that the experimenters can choose the best conditions for their measurements. Furthermore, a correction has to be made if exact locations of the contour lines are required. Some previous discussion which may be misleading is pointed out.

References

1. H. Takasaki, Appl. Opt. 9, 1467 (1970).
2. H. Takasaki, Appl. Opt. 12, 845 (1973).
3. D. M. Meadows, W. O. Johnson, and J. B. Allen, Appl. Opt. 9, 942 (1970).
4. P. S. Theocaris, J. Sci. Instrum. 41, 133 (1964).
5. P. S. Theocarus, Exp. Mech. 5, 153 (1964).
6. C. Chiang, Brit. J. App. Phys. (J. Phys. D), Ser. 2, 2, 287 (1969).
7. C. Chiang, J. Opt. Soc. Am. 57, 1088 (1967).

ANNUAL REPORT OF THE INSTITUTE OF PHYSICS,
ACADEMIA SINICA, 1974

Perception of pain and acupunctural analgesia

Chun Chiang (蔣炯)
Biophysics Laboratory
Institute of Physics, Academia Sinica
Nankang, Taipei, Taiwan, Republic of China

The question of physiological pain and psychological pain has been a quarrel for a long time, recently it draws attention especially regarding to the cause of acupunctural analgesia. Many people suspect that acupuncture effect is purely a suggestive effect, Clerk and Yang[1] have presented some interesting data on pain relief during the process of acupuncture; they use sensory decision theory[2] to evaluate data, and explain that "sensory decision theory yields two measures of the subject's performance. The sensory or physiological parameter, d', provides the measure of sensory sensitivity or discriminability. The attitudinal or psychological index, L_x, indicates the subject's response criterion, that is, his willingness or reluctance to report the presence of pain". Their data show that acupuncture increases both L_x and d', indicating that the subject's sensory system has not become insensitive--as, for example, after administration of an analgesic[3]. With this result, they suggest that acupunctural analgesia has not been produced by the stimulus they used; and conclude that the reduced report of pain had its sole origin in a raised criterion for reporting pain. This conclusion may not be true due to the fact that there is no direct correlation between discriminability d' and pain. Here, I will present the mechanism of perception of pain and give some evidence that "suggestion" alone could not be responsible for the reduced report of pain, and suggest a physiological mechanism at the chemical level to explain the acupunctural analgesia.

Figure 1 outlines a perception process of pain in a block di-

agram. The pain signals from the source of pain (such as tissue burn), are transmitted along the nerves to the brain; these signals can be modulated by either inhibition or amplification. The modulated signals are then relayed through a attention-mediated switch to the perception center. The switch normally is closed; in that case, the pain signals can reach the perception center. However, when attention is attracted away, the switch is open and pain cannot reach the perception center. For example, a person in an emergency sometimes is not aware of pain (the switch is open) until the emergency is over. The modulator is the place where the pain signals can be amplified or inhibited. If they are amplifed, then minor physiological pain can be perceived to be extremely painful; if the pain signals are inhibited, then the person can tolerate severe physiological pain. This idea conforms to the gate theory of Melzack and Wall[4] with a second gate at the thalamus, only this gate is now controlled psychologically; this kind of psychological control is conceptually similar to the illusory process[5]. This model is also consistent with Clark's notion of pain, analysed by signal detection theory[2]. The psychological factors such as expectation, attitude, and suggestion would selectively modulate the physiological pain signals as indicated by the modulator, thus one would feel different extent of pain, but this process will not influence the discriminability of the system. If the nervous system becomes insensitive because of administration of a drug such as 33 percent nitrous oxide[3], then not only the modulator, but also nerve transmission of pain signals will be affected. Also, since the nerve becomes insensitive, one may feel drowsy and less pain is perceived in the brain. These two processes would not only raise the psychological index L_x, but also decrease the discriminability d'.

Now suppose the membrane pain recepter at the source of the stimulus (burn, pressure, etc.) receives less pain signals, then less pain signals will be transmitted along the nerves and less pain will

be perceived in the brain, thus the pain threshold is increased, but the sensory discreminability d' may not be effected. With this reasoning, the experimental result of Clark and Yang[1] that acupuncture increases both L_x and d' leads to the conclusion that

(a) acupuncture may have effect at the membrane pain recepter at the source of the pain stimulus.

(b) acupuncture may increase the discrimibility.

We can further cite following facts to show that "suggestion effect" could not be respinsible for the pain relief:

(a) pain relief can not be produced by puncturing needles randomly in the body, only "specific" acupuncture points can relive "certain" pains at "certain" locations.

(b) acupuncture is effective for children and animals, which are not normally suggestive with acupuncture.

These facts could not be explained by the suggestion effect, and show that acupuncture effect is definitely in working. A physical theory regarding acupuncture anesthesia has been proposed[6], briefly it says that, during acupuncture, the pressure exerted by the needle, the piezo-electric property of the tissure and the electrostatic force of the body fluid could influence the nearby nerve and change the membrane potential, thus block the pain signals' transmission. At the chemical level, these physical processes can initiate a series of biochemical reactions either directly through tissues' piezoelectric properties or indirectly through the autonomic nervous system influenced by these physical processes. These biochemical reactions may either release substances to supress the pain substances such as histamine and bradykinin produced in burn or to increase the local metabolism and to digest the pain substance more quickly and effectively. In this way, after acupuncture, the actual physiological pain received at membrane receptor at source of pain stimulus is less and transmitted pain along the nerve is less and less pain is perceived in the brain. We have evidences that acupuncture produces appreciable changes in blood such as increasing the number of red

blood cells, white blood cells, and blood sugar. Brown et al[7] also find that white blood cells may be changed by acupuncture. Thus it is conceivable that metabolism rate can be increased and the pain substances can be digested more effectively, thus a "normal" and healthy condition can be restored more quickly and thus pain is relieved. Also, we observed that the patient after acupuncture generally feels more energetic and alert, this would increase the sensory discriminability d', as shown by Clark and Yang[1].

References

1. W.C. Clark and J. C. Yang, Science (Washington) "Acupuncture analgesia? Evaluation by signal detection theory.", 184, 1096 (1974).
2. W. C. Clark, "Pain sensitivity and the report of pain." Anesthesiology 40, 272 (1974).
3. C. R. Chapman, T. M. Murphy and S. H. Butler, "Analgesia strength of 33 percent nitrous oxide: A signal detection theory evaluation." Science 179, 1246 (1973).
4. R. Melzach and P. D. Wall, "Pain mechanisms: A new theory." Science, 150, 971 (1965).
5. C. Chiang, "Illusion and perceptual process." Ann. Rept., Inst. Phys., Acad. Sin. (Taipei) pg. 123 (1972-1973).
6. C. Chiang, "A physical theory of acupuncture anesthesia." Physiol. Chem. Phys. 6, 85 (1974).
7. M. L. Borwn, G. A. Ulett and J. A. Stern, "The effect of acupuncture on white cell counts." Am. J. Chinese Med. 2, 383 (1974).

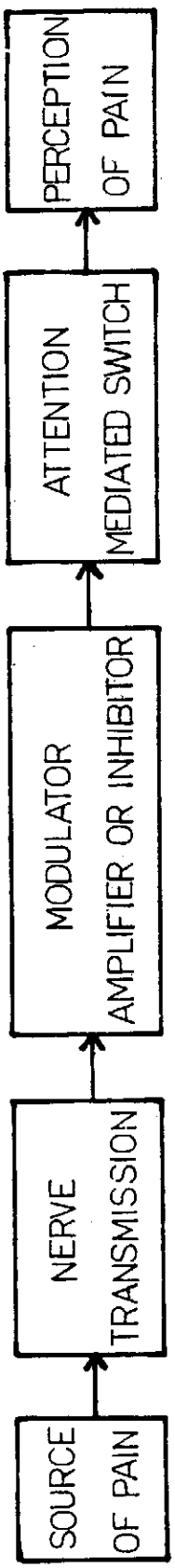

Fig. 1. A block diagram showing the pain transmission processes.

EARLY RECEPTOR POTENTIAL GENERATING MECHANISM IN VERTEBRATE RETINA*

WEI-KUNG WANG

Biophysics Laboratory Institute of Physics Academia Sinica
Nankang Taipei Taiwan Rep. of China

Received for publication, April 4, 1975

ABSTRACT

W. K. Wang (1975). *Early receptor potential generating mechanism in vertebrate retina.* Bull. Inst. Zool., Academia Sinica, 14(1): 19–26. A charge separation and subsequent charge spreading model is used to explain the generating mechanism of early receptor potential in the vertebrate retina. The R1 is from direct charge separation. The R2 is from ion absorption and subsequent ion migration, and this produce a diffused electrical double layer. Special attention is paid to the rod envelope which is a good capacitor. Because of this capacitor, the electric field due to charges separation needs only to extend to the rod envelope to charge up the capacitor, the induced charges outside the envelope will produce a transient potential which can be measured a long distance away. The absorbed ions are hydrogen ions, the OH ion to be the transmitter for the late receptor potential is also proposed.

The early receptor potential (E.R.P.) was first described by Brown and Murakami[1] in 1964. In the same year Cone[2] had shown that its magnitude is proportional to the number of the rhodopsins bleached. Its relation to temperature, pH and different ions has been shown by Brindley *et al.*[3] and Pak *et al.*[4]. Goldstein[5] found that most of the extracellular response originated from the cones. Toyoda *et al.*[6] proved that E.R.P. is not the cause for the late receptor potential (L.R.P.). Murakami and Pak[7] investigated the relationship between the extracellular recording and the intracellular recording and concluded that the rod outer segment envelope acts like a capacitor. Recently Rüppel and Hagins[8] measured the E.R.P. spatial distribution from a rod.

The two responses of E.R.P. which appear between the photon absorption and the appearance of the L.R.P. are called R1 and R2. They do not depend on the living cell; even after the treatment by formaldehyde the respose still can be measured[3]. The origin of this response was first suggested to be a result of some charge movement through some asymmetric structure in the rod or cone outer segment[9]. Brindley *et al.*[3] proposed independently an equivalent circuit which is based on the structure of the cone outer segment and a similar asymmetric concept.

To explain the spatial distribution of E.R.P. along the rod outer segment, Rüppel and Hagins[8] have suggested that the charge displacement is on the rod envelope. This model will explain some of the R1 results. For R2, the pH and the temperature dependence are two important requirements that any good model must meet.

In the present paper, a new mechanism

* This paper has been published in Bull. Inst. Zool., Academia Sinica 14(1):19–26 (1975)

which can explain all the available data will be presented. Some experiments are also suggested which distinguish this model from other models.

SOME GENERAL CONSIDERATION

Let us start with some simple examples. For a dipole, the potential will be positive near the positive charge and be negative near the negative charge. The concept of a dipole as consisting of two point charges is theoretical. In reality, a dipole usually has a volume which is positively charged and a volume which is negatively charged. The size of the positively charged volume does not have to be of the same magnitude as the negatively charged one. For example, in the water molecule, both hydrogen atoms are situated at the positive pole and the oxygen atom is at the negative pole. For large molecules, the charged volume may be very large, therefore there exists a situation in which the negative charge is confined to a very small volume, surrounded by a spreaded positive charge.

When we think of separation of opposite charges, what comes to mind is a dipole, a point charge dipole, and should there be a current, it must be from the positive charges toward the negative charges. However, a transient current may also be produced by spreading out of these poles. A common example is the electroscopic measurement of the charge built up in a plexiglas after it is rubbed with wool; the current flows from the plexiglas toward the electroscope which has no contact with the wool.

Here I shall present a special situation which will spread a transient potential into a large volume (Fig. 1). After the separation of charge, the positive pole will not be confined to the small volume A, but it will spread along the conductor toward the capacitor. The fraction of the original charge $+q$ that will stay in volume A is a funtion of r/d, where d is the distance between the two poles and r is the distance between the volume A and the capacitor. If $r \gg d$, most of the charge will stay on the volume A. If $d \gg r$, most of the charge will spread toward the capacitor. The charge $+q'$ on the right side of the capacitor will induce $-q'$ on the left side of the capacitor; the final situation is as shown in Fig. 1C. Because of this separation of charge, another separation of charge is induced at the left side of the cap-

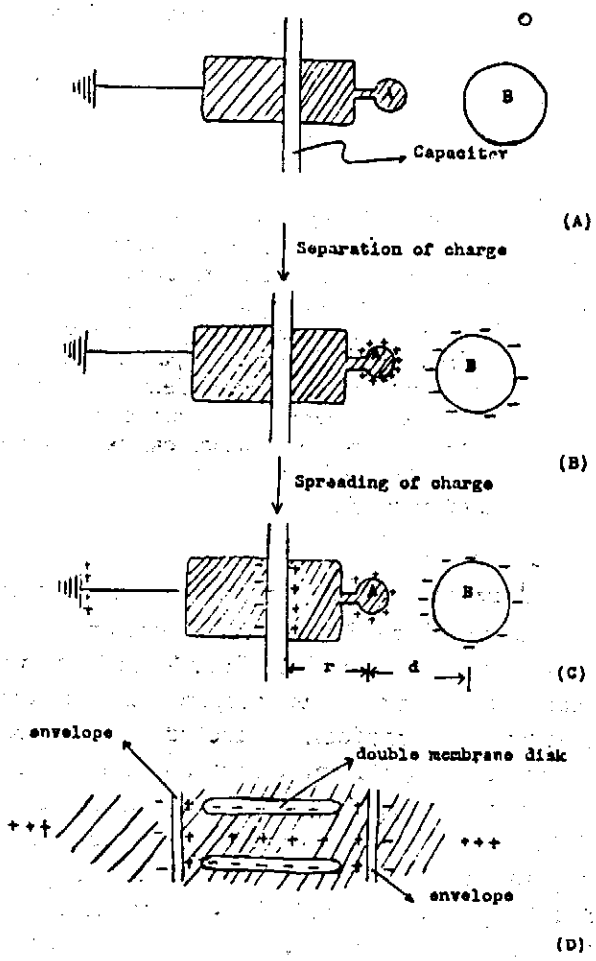

Fig. 1. The shaded areas are conductors. (A) is the situation before the charge separation. (B) is the situation right after the charge separation. (C) is the final situation after the charge spreading. (D) is a schematic drawing of a short segment of rod outer segment. The cytoplasm is the positive pole and the conductor, the double membrane disks are the negative pole, and the envelope is the capacitor.

EARLY RECEPTOR POTENTIAL GENERATING MECHANISM IN VERTEBRATE RETINA*

acitor. Therefore if we measure the potential at the left side of the capacitor immediately after the original separation of charges at A and B, a transient positive potential can be measured. The magnitude of the potential will depend on the conductance and the r/d.

The ultrastructure of the outer segment of rod and cone have been resolved by electron microscopy[10,11]. The outer segment consists of an envelope and a pile of double membrane disks which are photo-sensitive. For a cone the double membrane is actually a folding of the envelope. For a rod the double membrane disks are pinched off the envelope and there is about 100 Å space between the rod double membrane disks and the envelope[10].

R1 GENERATING MECHANISM

After a photon is absorbed by the rhodopsin, the 11-cis retinal isomerize to all-trans retinal. There is probably a charge separation process, and if some positive charge suddenly appear in the highly conducting cytoplasm, the negative charges remain on the dielectric double membrane disks (see Fig. 1). A dipole is produced, in which the interdisk cytoplasm is the positive pole and the double membrane disk is the negative pole. Because the cytoplasm has a high conductance, the positive charges tend to spread along the cytoplasm toward the envelope. The envelope behaves as a good capacitor[7] and we have the scheme in Fig. 1 D. The cytoplasm is the positive pole and conductor, the double membrane disks is the negative pole, the envelope is the capacitor and the outside ionic solution is the ground conductor. We may approach this mechanism more analytically by the method of image[12]. The positive charge is in the cytoplasm with distance r fom the double membrane disk surfaces and the negative charge are right on the double membrane disks.

For any charge q in the cytoplasm with distance γ from the membrane with high dielectric constant the image charge is at distance $\gamma=-\gamma$ with magnitude $q'=-q\ (\epsilon_2-\epsilon)/(\epsilon_2+\epsilon)$; ϵ is the the dielectric constant of cytoplasm. ϵ_2 is the dielectric constant of the membrane, and for $\epsilon_2 \gg \epsilon$, we have $q' \simeq -q$ $\gamma'=-\gamma$. For the negative charge, because $\gamma'=-\gamma=0$, q and its image $-q$ coincide and cancel with each other. For the positive charge q, we have $q'=-q$, $\gamma'=-\gamma$. Thus we may calculate the voltage and electric field at the rod envelope, contributed from the positive charge and its image. (Fig. 2A).

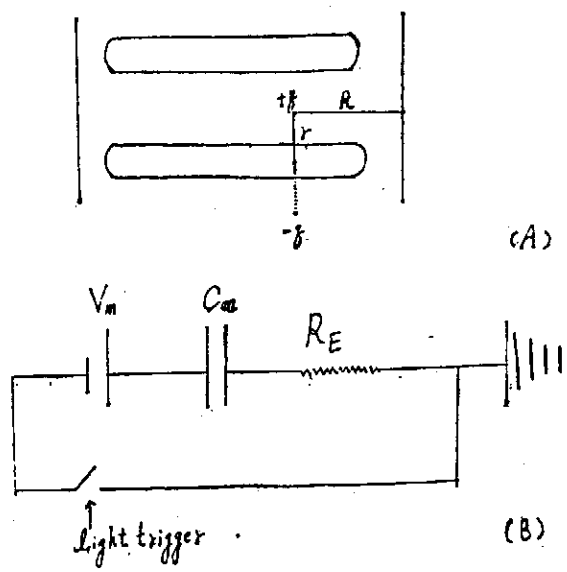

Fig. 2. (A). A diagramatic drawing of a short piece of outer segment. A charge separation will produce a potential at the envelope. (B). A simplified equivalent circuit of the E. R. P. C_m is the envelope capacitor and R_E is the external resistor. V_m is the potential produced by the charge separation as shown in Fig. 2A.

$$V(x)=\frac{q}{4\pi\epsilon R}-\frac{q}{4\pi\epsilon(R^2+4\gamma^2)^{1/2}}$$

The electric field

$$E=\frac{q}{4\pi\epsilon R^2}-\frac{qR}{4\pi\epsilon(R^2+4\gamma^2)^{3/2}}$$

This is the voltage and field from one charge displacement. This charge displacement alone will not produce a voltage at a long distance away, when R becomes large, both V and E will become zero.

The most important of this model is that

the rod envelope is a good capacitor. Outside the envelope we may consider it as a resistor. What the E_{intra} needs to do is to drive some charge toward and deposite on the envelope, the capacitor. Thus will induce charge from the other side of the envelope. This induced charge may be drawn from anywhere in the world. Therefore we may measure a transient voltage during the movement of these induced charge.

The equivalent circuit may be drawn as Fig. 2B. During the charge separation, the V_m at the envelope is $\sum_i \left(\frac{q_i}{4\pi\epsilon R_i} - \frac{q_i}{4\pi\epsilon(R_i^2+4\gamma^2)^{1/2}} \right)$, i is summed over all the charges each with charge q_i and at distance R_i from the rod envelope.

For one charge $q_i \simeq e$ substitutes $\epsilon \simeq \epsilon_o$. When $R_i \simeq 100$Å, and $\gamma = 20$Å we have $V_m \simeq 10$ mV. This is approximate the voltage that can be measured intracellularly and it is also the largest voltage can possibly be measured extracellularly. (Fig. 2B). As long as the charge separation occurs, the change of ionic condition or chemical composition will only change the speed of the appearance of the response as described by Brindley *et al.*[4].

R2 GENERATING MECHANISM

The response of R2 cannot be detected as the temperature approaches 0°C or at pH below 4[3,4]. This response can not be explained by the Meta I to Meta II transition, because at lower pH, the transition should be more complete and should not be terminated. R2 is the dominant component at physiological conditions and it appears immediately prior to the L.R.P. —the neural response indicating that it may be the most important signal for transduction.

This response may be generated by a similar mechanism: separation of charges followed by the spreading of one pole of the dipole as described for R1. However, the mechanism by which the charges are separated and spreading are probably different. Let us examine another example.

If some groups, for example the S^- on the solid surface absorbs some positive charges H^+. The negative charge will remain in the cytoplasm in the form of negative ions. These negative ions will not all pile up parallel to the positive charges. Because of thermal motion, all ions in the electrolyte tend to equalize their concentration. This will produce diffused electrical double layers[11]. This is another type of dipole. The positive pole is on the double membrane disks which carries the sulfhydryl groups while the negative pole is the cytoplasm. After the charge separation, the ions will have a distribution according to Boltzmann *Eq.*

$$\rho_i = \rho_{oi} \exp(-e_i\phi/kT) \qquad (1)$$

where ϕ is the potential due to the presence of the positive charges on the membrane. This potential extends into the interior of the electrolyte (cytoplasm). ρ_{oi} is the concentration of the ion of type i with charge e_i at $\phi = 0$, and e_i can be either positive or negative, k is the Botzmann constant and T is the absolute temperature. The charge density is:

$$\rho = \sum_i \rho_i e_i \qquad (1')$$

From one dimentional Poisson's *Eq.*

$$\frac{\partial^2\phi}{\partial x^2} = -(4\pi/\epsilon)\rho \qquad (2)$$

where ϵ is the dielectric constant of the cytoplasm and x is the distance from the membrane.

Substituting (1′) into (2) we have

$$\frac{\partial^2\phi}{\partial x^2} = -(4\pi/\epsilon)\sum_i \rho_{oi} \exp(-e_i\phi/kT)e_i \qquad (3)$$

For $e_i\phi \ll kT$, the Debye and Hückel's approximation gives

$$\frac{\partial^2\phi}{\partial x^2} = -(4\pi/\epsilon)\sum_i (\rho_{oi} - \rho_{oi}e_i\phi/kT)e_i \qquad (4)$$

For electroneutrality,

$$\sum_i \rho_{oi}e_i = 0 \qquad (5)$$

but if the electroneutrality does not hold in

the outer segment, $\sum \rho_{oi} e_i = C$. This contant C will give a constant potential shift which may be defined as the baseline. This constant potential shift will not influence the result just as the dark current which is defined as baseline does not have any effect on the measurement of E.R.P.

$$\frac{\partial^2 \phi}{\partial x^2} = \sum_i (4\pi \rho_{oi} e_i^2 / \varepsilon kT)\phi \qquad (6)$$

Let

$$K^2 = (4\pi e^2/\varepsilon kT)\sum \rho_{oi} Z_i^2; \quad e_i = eZ_i$$

We get

$$\phi = V \exp(-Kx) \qquad (7)$$

From the potential at $x=0$, we have

$$V = -(4\pi/\varepsilon K)Q_m \qquad (8)$$

Q_m is the charge absorbed by a unit area of membrane. ϕ is proportional to Q_m which in turn is proportional to the number of rhodpsins bleached. This will explain the linear relationship between the E.R.P. and the number of rhodopsins bleached[2]. When the number of bleached rhodopsin is very large, Q_m will become very large. According to *Eq.* 8, V also seems to become very large. But when $eV \simeq kT$, the electrostatic force will overcome the thermal motion and attract more negative ions to membrane. This will reduce the net Q_m on the members and in turn the V. Therefore there is a saturation value for V; $V < kT/e$. The magnitude of V at saturation is about 25 mV. For intracellular recording, the microelectrode is so large that it can not reach the membrane to measure the V, thus the measurable V_{max} will be a fraction of the V_{max}. For extracellular recording, the saturation value depends on the detailed structure of the outer segment and the place where the measurement is made. (Fig. 2B).

Suppose some charge Q is suddenly absorbed by the membrane, then the ions remaining in the cytoplasm will redistribute themselves to the final state as described by equations (1) and (7). For the transient movement, we will start with Nernst *Eq.* of ionic mobility. $N_i(t, x)$ is the number of mobile ion for type i at the time t and position x. D_i and ρ_i are the diffusion coefficient and density of this ion. Total mobile ions are given by the following:

$$N(t, x) = \sum_i N_i(t, x)$$

$$= \sum_i -D_i\left[\frac{\partial \rho_i}{\partial x} + \frac{e_i \rho_i}{kT}\left(\frac{\partial \phi}{\partial x}\right)\right] \qquad (9)$$

From the equation of continuity

$$\frac{\partial \rho}{\partial t} = -\nabla \vec{J} \qquad (10)$$

$\vec{J} = N_i e_i / A$ for a one dimensional uniform flow, where A is the area of the flow. Thus

$$\frac{\partial \rho}{\partial t} = -(1/A)\left(\frac{\partial \sum_i N_i e_i}{\partial x}\right) \qquad (11)$$

Substituting (9) into (11)

$$\frac{\partial \rho}{\partial t} = \sum_i \frac{D_i}{A}\left[\frac{\partial^2 \rho_i}{\partial x^2} + \frac{e_i \rho_i}{kT}\cdot\frac{\partial^2 \phi}{\partial x^2}\right]e_i \qquad (12)$$

From Poisson's equation

$$\frac{\partial^2 \phi}{\partial x^2} = -\frac{4\pi}{\varepsilon}\rho$$

We have

$$\frac{\partial \rho}{\partial t} = \sum_i \frac{D_i}{A}\left[\frac{\partial^2 \rho_i}{\partial x^2} - \frac{e_i \rho_i}{kT}\cdot\frac{4\pi\rho}{\varepsilon}\right]e_i \qquad (13)$$

The movement of ions depends on the diffusion term $\frac{\partial^2 \rho_i}{\partial x^2}$ and the electrostatic force term $\frac{e_i \rho_i}{kT}\cdot\frac{4\pi\rho}{\varepsilon}$. When positive charges are suddenly absorbed by the membrane, there is a small volume adjacent to the membrane with thickness δ where negative ions are concentrated. Because of thermal motion and electrostatic force, these negative ions will move away and some positive ions will move into this small volume. After the absorption of ion the diffusion term will only allow the hydrogen ions to enter, because in our case, the trapped ions are the hydrogen ions and only the hydrogen ions has a concentration gradient. The electrostatic force favor any positive ions to enter and any negative ions to exit. Since $\rho = \sum_i \rho_i e_i$, any ion with

larger mobility will flux in or out and change the value of ρ, and this will impede the motion of slow moving ions. The mobility of hydrogen ions is five to ten times that of other ions. Therefore with reference to the diffusion term or to the electrostatic force term, the moving ions are dominated by hydrogen ions. The change of ρ is also dominated by the change of hydrogen ion concentration as described by $\rho \simeq (\rho_h - \rho_{oh})e$, where ρ_h: hydrogen ion concentration and ρ_{oh}: hydrogen ion concentration before photo-excitation. Substitute $\rho \simeq (\rho_h - \rho_{oh})e$ into *Eq.* (13), we have

$$\frac{\partial \rho_h}{\partial t} = \frac{D_h}{A}\left[\frac{\partial^2 \rho_h}{\partial x^2} - \frac{e^2 \rho_h}{kT}\frac{4\pi}{\varepsilon}(\rho_h - \rho_{oh})\right] \quad (14)$$

The boundary conditions are $\rho_h(o, x) = 0$ at $x < \delta$, $\rho_h(o, x) = \rho_{oh}$ at $x > \delta$, where δ is the initial thickness of the double layers, and

$$\rho_h(\infty, x) = \rho_{oh} \exp\left[eV \exp\left(-Kx\right)/kT\right] \quad (15)$$

The double layers extends slowly from a very small thickness according to *Eq.* (14). This electrical double layers cannot extend a great distance from the membrane. The final situation is shown in *Eq.* (15) and the equilibrium potential is

$$\phi = V \exp\left(-K x\right) \quad (7)$$

This potential extends into the cytoplasm, but the magnitude decreases to $1/e$ at $x = 1/K$. At pH=7, with $[H^+] = 6.02 \times 10^{13}/cm^3$ we have $1/K \simeq 10^4$Å, thus the diffused double layers will extend about 10^4Å. At pH=3, with $[H^+] = 6 \times 10^{17}/cm^3$, we have $1/K \simeq 10^3$Å, the diffused double layers can only be extended to about 100Å. Therefore at pH=3, it would be difficult for the diffused double layers to extend from the double membrane disks to the envelope and thus can not be measured extracellulary.

Similarly, the cone envelope is directly connected to the double membrane disks while the rod envelope is separated a few hundred Å from the double membrane disks. Therefore the spreading of charges will reach the cone envelope more easily and deposit more charge on it, resulting in E. R. P_{extra} to be much larger in cone than in rod.

Origin of the R1 and R2

R1 is probably a result of a direct charge separation. The separation should be of considerable distance. One of the possible candidates is the 11-cis to all-trans isomerization, because it occurrs early in the photo-excitation and possibly represents the largest movement in all of the photo-excitation processes. It can not be stopped by freezing to 0°C, however it can be slowed down by freezing to -30°C. Only when the solution reachs -140°C this isomerization can be stopped[13]. It would be interesting to study the temperature effect on the R1 and compare it with the temperature effect on the 11-cis to all-trans isomerization.

The origin of R2 is probably due to the absorption of ions and then movement of ions. The ion absorption and movement are stopped at temperature near 0°C. This will explain the temperature effect on R2[3,4]. The pH dependence strongly suggests that the charges absorbed are H^+. The sulfhydryl groups are the most probable sites on the membrane to absorb the hydrogen ions[14]. Direct evidence has been obtained by Brindley *et al*,[4] They treated the retina with N-ethyl maleimide, a thiol blocking agent, and observed that the magnitude of R2 has been greatly reduced at neutral pH and room temperature.

Relationship between E. R. P. and L. R. P.

Toyoda *et al.*[6] demonstrated that E.R.P. is not the direct cause for L.R.P. However, this does not rule out the possibility that the charged particles that cause the E.R.P. are the transmitters for the L.R.P.. Although Toyoda[6] *et al.* proved that the coupling is not a electrical one, it does not rule out the possibility that the coupling is a chemical one comparable to other neurotransmitter mechanisms. In addition to Ca^{++}, another candidate worthy of investigation is the OH^- ion which remains in the cytoplasm and migrates toward the envelope

after photo-excitation.

Discussion

It is clear that the model of charge separation and subsequent charge spreading is sufficient to explain the temperature dependence and the conductance dependence of R1, as well as the pH and temperature dependence of R2 and the linear relationship to the amount of bleached rhodopsins. Both R1 and R2 should be much easier to detect extracellularly for cones because the charges need to extend a shorter distance to reach the envelope than for the rods. This model also makes use of the finding of Murakami *et al.*[7] that the envelope is a capacitor good enough to allow for a long distance travel of the response extracellularly. As to the spatial distribution of the potential and current, the proposed modal is compatible with the model proposed by Rüppel and Hagins[8]. There is a simple way to test the two models. The experiment of Rüppel and Hagins must be repeated by measuring the spatial distribution in a three dimensional way instead of along the rod outer segment, and the spatial distribution should be measured at different distance from the rod envelope as well as along the rod to determine whether current distribution is more like a "source" with a "sink" in the rod, as Rüppel and Hagins suggested, or like a single "source" for R1 and like a single "sink" for R2 at the outer segment. According to Rüppel and Hagins, intracellular recording of E.R.P. should detect the potential change polarity with respect to E.R.P. extracellular. However, this had not been observed by Murakami *et al.*[7] Because the "sink" and "source" in the model of Rüppel and Hagins are both inside the rod, the E.R.P. will probably be difficult to measure at a far distance from the retina, for example in the cornea of the eye[2].

REFERENCE

1. Brown, K.T. and M. Murakami (1964). A new receptor potential of the monkey retina with no detectable latency. Nature 201: 626–628.
2. Cone, R.A. (1964). Early receptor potential of vertebrate retina. Nature 204: 626–628.
3. Brindley, G.S. and A.R. Gardner-Medwin (1966). The origin of the early receptor potential of the retina. J. Physiol. 182: 185–194.
4. Pak, W.L., V.P. Rozzi and T.G. Ebrey (1967). Effect of change in chemical enviroment of the two components of the early receptor potential. Nature 214: 109–110.
5. Glodstein, E.B. (1968). Visual pigment and the early receptor potential of the isolated frog. retina. Vision Research. 8: 953–964.
6. Toyoda, J., H. Nosaki and T. Tomita (1969) Light induced resistance changes in single photoreceptor of necturns and gekko. Vision Research 9: 453–463.
7. Murakami, M. and W.L. Pak (1970). Intracellularly recorded early receptor potential of the vertebrate photoreceptors. Vision Research 10: 965–975.
8. Rüppel, H. and W.A. Hagins (1972). Spatial orgin of the fast photovoltage in retina rods. Symposium on vision mechanism, Bochum.
9. Lettvis, J.Y. (1965). General discussion: early receptor potential. Cold Spr. Harb. Symp. 30: 501.
10. Nilsson, E.G. (1965). The ultrasturcture of the receptor outer segment in the retina of the leopord frog. J. Ultrastructure Res. 12: 207–231.
11. Cohen, A.I. (1968). New evidence supporting the linkage to extracellular space of outer segment saccules of cones but not rods. J. Cell Biol. 37: 424–444.
12. Panofsky, W.K.H. and H. Philip (1962). Classical Electricity and Magnetism. Addison-Wesley Inc.
13. Grahame, D.C. (1947). Theory of electrocapillarity. Chemical Review 41: 441–501.
14. Radding, G.M. and G. Wald (1956). Acid-base properties of rhodopsin and opsin. J. Gen. Physiol. 39: 909–992.
15. Wald, G. and P.K. Brown (1965). Cold Spr. Harb. Symb. Quant. 30: 345.

脊椎動物視網膜接受體早期電位產生之動作原理

王　唯　工

一個正負電分離後，一電極擴散開的模型，可以解釋視網膜接受體之早期電位。R1 信號係由正負電直接分離產生。R2 信號是由離子的吸附及後隨之離子移動而產生，由此產生一擴散的雙電層。桿細胞之細胞封套是一個高電容器，因爲這一良好電容性質，由正負電分離所產生之電場，只須將電充於電容器上，而封套外邊所引起之感應電就能產生一瞬息電位，此電位可在遠處量得。所吸附之離子可能爲氫離子，氫氧離子亦推斷，可能爲接受體後期電位的信號物質。

THE LIMITATION OF HUMAN KNOWLEDGE *

Wei Kung Wang
Biophysics Lab Institute of Physics, Academia Sinica, Nankang
Taipei, Taiwan, Rep. of China

* This paper has been published in ICUS IV (commentary)

From a neurophysiological point of view, our understanding of the world is all obtained through various sensory input, such as vision, hearing, touch, smell and taste. Physiologically for each sense the body is equipped with a specific receptor. We have photo-receptors, sensory receptors, taste buds, etc. We also have receptors for hydrogen ion, temperature, water molecule, glucose molecule, etc. That will tell us the conditions of the surroundings and of our body. All these mechanisms are possibly interpreted by physical or chemical processes. From these basic sensory inputs, we may develop feelings and memories, even dreams and thoughts, surely, human feelings and thoughts. I think, so I exist. I feel, so I exist. Then there comes the question, what is "I", "the ego"? This problem has been thoroughly discussed by Sir J.C. Eccles at the 2nd I.C.U.S.[1]

We will be able to explain many of our knowing processes by physical and chemical processes, then what remains to be understood may be defined as "I", the ego. In other words, it is possible to build a computer which can sense, symbolize (while the intuition may just be a subconscious memory which probably does not exist in the computer) and think. The computer can use a sensor, similar to our sensory organs, to know the outside world; it may even have some safety device which protects itself by some feed-back system, then the computer is equipped with both the outer sense and inner sense similar to what has been mentioned by Sir J.C. Eccles. The computer has senses, it can symbolize patterns, and it may also have a superior logic system, however the computer is not yet a human being.

It was agreed by classical physicists, a particle can be described by its equation of motion, such as the Lagrange's equation. To describe the later movement of any object completely, all that is needed are the present state of the

particle (position and momentum) and the interaction with others (potential). In other words, principly, the movement of everything in the future is determined by the present situation.

Our knowledge is limited by our sensory input; we can't see x-rays or neutrons with our eyes, we have to use indirect methods by converting x-rays or neutrons into visible light or electric current to detect them. In Quantum Mechanics terminology our sensory organ (the tool we used can be looked at as part of the sensory organ too) is doing measurement, it can only measure what interacts with the instrument. A demon or a ghost could be a being that lives in a five dimensional space, it may hide in the 4th and 5th dimensions and we do not have the ability to detect them. From a neurophysiological point of view, it is correct to conclude that "It would appear that man's perspectives of reality are necessarily encapsulated for it is impossible to completely transcend the limitations of epistemic norms on the one hand and man's cognitive capabilities on the other hand".[2]

However, this conclusion is similar to the conclusion in classical physics that the future of the world is determined. Both conclusions are from a similar point of view that the world is a mechanical one. According to classical physics, there is no freedom in any form, once it is described as the motion of particles. There is no creativity at all. In modern physics, Quantum Mechanics brings in new aspects for single participles. The uncertainty principle guarantees the minimum freedom for every particle. The behavior of a particle cannot be described precisely. When the number of particles increases, the discription becomes less and less precise. The mechanics of a single particle is simple; we can describe it as precisely as the uncertainty principle allows. The mechanics of two particles become much more complicated. When we talk about the behavior of a group of

atoms-- the molecule-- the description cannot be as precise as that of physics which are usually dealing with only one or two particles. The behavior of a cell or an organ belongs to biological and physiological phenomena, these phenomena involve millions and millions of molecules; no wonder we cannot describe it precisely any more.

In social science and history, we deal with millions and millions of human beings, each of them is composed of millions and millions of cells which are composed of millions and millions of macromolecules. And those macromolecules are composed of millions and millions of atoms. It is natural that we cannot describe it analytically. Therefore we have to use a less precise way to search for the truth.

To depend on senses is not a very reliable way of knowing. We love different colors, maybe just because we see color differently. Besides, the environment may modify our sensory process.[3] It is no wonder the process of education may change our epistemic style. It is amazing that we do communicate idea and thought with each other. I believe that this is the basic assumption for all social science, that we communicate with others, search for their thinking, try to get a statistical significant statement which becomes the principle or law in social science. When we are summarizing the data and analyzing it, we use symbols, logic, etc. However the most important part of this process is "I"know how the others think, I understand others through some magic process in my own brain. Here we still come back to the same question, the most crucial question is what is "I", the "ego". This question is certainly going to become the most interesting part of epistemology. We will find out more and more about our epistemological process, we will understand our sensory process, our sensory organ, our memory process, our recalling process, even our logic and dreaming process. Then

what is left is still the unattainable limitation, that is "what is I". This is the "uncertainty principle" in epistemology. We will certainly get closer and closer to knowing almost everything in our knowing process, however, we will never be able to get into this limit. It is rather sad even to think that there is a limitation on the understanding of our epistemological process. Actually, it is not so. The uncertainty principle puts a limit on the physical measurement, at the same time it gives certain degree of freedom for a particle, then, the mechanical world is no longer a determined one, while the "uncertainty principle" in epistemology "what is I" will give us the freedom for our mind. It is the hope of human knowledge. Let us recall the conclusion by Royce. "It would appear that man's perspective of reality is necessarily encapsulated for it is impossible to completely transcend the limitation of epistemic norms on the one hand and man's finite cognitive capabilities on the other hand". Man's perspective of reality is encapsulated in the limit, if we do not consider the "I". We may be free through this "uncertainty principle" of epistemology, the "I". This will not only give us the freedom of will, it may also be the connection to tunnel through the barrier between us and the ultimate reality.

REFERENCES

[1]John C. Eccles: Culture : The creation of Man and the creator of man. p. 23-35. Cerebral activity and the Freedom of the will p. 35-53, In: Modern Science and Moral Values, 1973, International Cultural Foundation.

[2]Joseph R. Royce: Three ways of knowing and the scientific world view. This volume.

[3]Gina B. Kolata: Behavior Development: Effects of Environments, Science (AAAS), Vol. 189, p. 207-209, 1975.

ANNUAL REPORT OF THE INSTITUTE OF PHYSICS,
ACADEMIA SINICA, 1974

On Vortex Structure in the Wake of a Sphere

by

Hsien-Ping Pao and Timothy W. Kao
The Catholic University of America, Washington, D.C. 20064

Abstract

This paper presents results showing the three-dimensional vortex shedding structure when a sphere is towed at a constant velocity through a stratified fluid. It is found that for small Richardson numbers (weak stratification) and Reynolds numbers in the range from 4×10^3 to 2×10^4 the vortex is shed three-dimensionally. The stratification however quickly and effectively inhibits the vertical motion and the initially turbulent wake collapses and reveals the vertically oriented portion of the vortex structure, reminiscent of two-dimensional vortex street behind a circular cylinder when viewed from above. The structure is however distinctly three-dimensional. It is also found that the estimated vortex shedding frequency is in reasonable agreement with previously published results for a sphere in a homogeneous fluid. It is suggested that a weak stratification is an excellent means for revealing the vortex structure of a three-dimensional body in a homogeneous fluid and that the vortex tube in the wake of a sphere in a homogeneous fluid has a close-ended double helical structure. Two branches of the double helix are continuously unwinding in an opposite sense from the formation region. Moreover, the present double helical model satisfies Thompson's circulation theorem in contrast to previously proposed helical models.

The experiments were performed in a long channel made of clear acrylic sheet 14 in. wide, 24 in. deep and 30.5 ft. long. The sphere was attached to a towing carriage by means of a slender steel rod 3/16 inch in diameter. Two spheres were used. The diameter of the spheres D were $2\frac{1}{4}$ in. and 5 in. The carriage was carefully designed to minimize mechanical vibrations when towed. The motion was initially accelerated gradually to avoid impulsive transients and the sphere travelled several feet before the final steady towing speed was reached and maintained. The channel was filled with 18 one-inch layers of salt solutions of decreasing density by means of a floater. The procedure was the same as that described in Kao, Pao and Wei (1974). The experiments were performed 20 hours after the filling process and the fluid was then linearly stratified. For flow visualiaztion the sphere was coated with nigrosine crystals around the forward stagnation point. When moving the dye marked out the wake region very effectively.

The pictures shown in Fig. (1) are from a representative experiment for the $2\frac{1}{4}$ in. sphere. The sphere was towed at the mid-depth of the fluid at a steady speed U of 2.75 in/sec. This speed was maintained for 1 min. and 30 sec. Pictures were taken from an overhead camera and a side-view camera simultaneously by means of a synchronous device. Both cameras were at a fixed location, so that the scenes were flow patterns at the same fixed location, looking from above and from the side, at various stages of development of the wake.

The stratification was characterized by the Vaisala frequency N defined as

$$N^2 = -\frac{g}{\rho_o}\frac{d\overline{\rho}}{dz}$$

where $\overline{\rho}(z)$ was the ambient density stratification and $\rho_o = \overline{\rho}(0)$ and z = 0 corresponds to the level of the sphere center. In the experiment, $N = 0.567\ \text{sec}^{-1}$, U = 2.75 in./sec., D = 2.25 in. so that the Reynolds

number is Re $= UD/\nu = 4,300$ and the Richardson number is Ri $= N^2D^2/U^2 = 0.215$.

The Richardson number is a measure of the effect of stratification. Indeed it is the ratio of the potential energy needed to raise a fluid particle vertically through a distance equal to the radius of the sphere to the available-kinetic energy of the particle.

Figure (1) shows the time development of the wake. In all the pictures the grid in the background is 1 in. x 1 in. and the shining dots are neutrally buoyant oil droplets used as velocity tracers.

In 1(a) we see the initial moment of the wake with the sphere in view. Simultaneous pictures of the top and side views are shown. The wake is seen to be fully turbulent and resembles that of the wake in a homogeneous fluid. This picture was taken 25 secs. after the commencement of the experiment.

In 1(b) the scenes are at 23 secs. afterwards. Again simultaneous pictures of the top and side views are shown. The top view reveals in the horizontally spreading turbulent wake the first hints of organized vortex structure whereas the side view shows the collapse of the wake vertically into a more confined vertical extent.

1(c) are top and side view scenes at 56 seconds after the sphere has passed the location. (At that time the sphere was still travelling at the same speed at 154 inches upstream). A definite vortex shedding structure is now revealed in the top picture. The side-view indicates a double sheeted dye structure.

1(d) are the top and side views at 119 secs. afterwards. A beautiful double row vortex very similar to the vortex arrangement behind a circular cylinder is seen. The spacing between the vortices is about 14 inches when corrected for parallax. The side view now shows clearly the double sheeted structure of the dye. (incidentally the spacing of Strouhal shedding for the 3/16 inch supporting rod

would be less than 2 inches at the rod Reynolds number of 400 and was definitely nonrelated with the present results.)

Several experiments were conducted similar to the above. The experimental range in Reynolds numbers was from 4.3×10^3 to 1.74×10^4 and the Richardson number range was from 0.065 to 0.643. The vortex pattern in all experiments were of similar nature to the pictures shown but with different spacings. The results of these experiments were analyzed to estimate the frequency of vortex shedding. This is done by measuring the vortex spacing, the towing speed and the average speed of the flow in the wake as indicated by the neutrally buoyant tracers. Thus if the period of vortex shedding is T, the sphere would have moved a distance UT in time T. If αU is the average velocity of the wake flow then the spacing of one complete vortex loop is $\lambda = UT - \alpha UT = (1-\alpha) UT$. The frequency f is then, $f = 1/T = (1-\alpha) U/\lambda$ and the Strouhal number is given by $S = fD/U = (1-\alpha) D/\lambda$. The results of three experiments are shown in Table 1. The wake velocity was estimated by measuring the movement of neutrally buoyant droplets in the wake. The wave-length was measured directly from the photographs and corrected for parallax due to non-coincidence of the grid plane and the level of the vortex system. Errors in the frequency or Strouhal number come mainly from the wake velocity and the lack of precision in the wave length. The Strouhal numbers S found here are comparable with the values obtained by Winny (1932) in the wake from hot-wire measurements in the range of Reynolds numbers from 2000 to 8000 and with the values given by Achenbach(1974). The agreement is seen to be reasonably good and it therefore indicates that the vortex shedding frequency is indeed governed by the initial shedding for the range of Richardson numbers explored.

Observations during the experiments revealed that the dye streams delineating the streamlines around the nose was symmetrical and therefore definitely three-dimensional. This is shown in

Fig. (2). The question then arises whether the present results together with the previous results of other workers on the wake of a sphere in a homogeneous fluid could reveal a more comprehensive picture of the vortex structure in the wake of a sphere. Winny (1932) proposed a helical vortex system. Levy and Forsdyke (1927) showed theoretically that evenly spaced vortex rings were unstable and Rosenhead (1931) suggested that a stable wake configuration would involve vortex loops. Magarvey and MacLatchy (1964) demonstrated the roll-up process of the detached vortex sheet into vortex loops. Foch and Chartier (1935) proposed an open - ended double helical vortex system for high Reynolds numbers. Achenbach (1974) in a detailed and exhaustive study discovered the important fact that the vortex separation point rotates around the sphere for Reynolds numbers above 6×10^3. Although this fact suggests a helical vortex system, Achenbach (1974) points out that the open-ended double helix of Foch and Chartier (1935) or a single vortex system has to be rejected since the circulation across a plane perpendicular to the wake axis is non-zero in violation of Thompson's circulation theorem.

From the above discussion and from our own observations, we propose a double helical vortex loop. The term "double - helical" vortex loop is used loosely in the present paper and does not demand a regular double helix of constant pitch. It provides for the vortex tube to interact as the two branches cross each other. Such an interaction would lead to a nodal element where the strength of the circulation is double that of the individual branch of the vortex tube. It is important to emphasize that the double helix must form a close-ended loop in the fluid at the initiation of the process of vortex tube formation. The two branches of the double helix are then continuously unwinding in an opposite sense from the cylindrical vortex sheet in the formation region as the process continues. The realization of the close-ended loop demands that the vorticity vector is continuous along the helical loop and therefore the vorticity vectors in the two

branches at any cross-section perpendicular to the wake axis must be in opposite sense. The net flux of the vorticity across planes perpendicular to the wake axis is then always zero in agreement with Thompson's circulation theorem. The present close-ended double helix model therefore does not have the objectionable feature of the open-ended double helix of Foch and Chartier (1935). The helical nature of the vortex tube is clearly seen in Figure (2). A picture of the model with circulations as indicated is shown in Figure (3). This model is also consistent with Achenbach's (1974) sketch of the vortex loops at $Re = 10^3$ in one view and suggests that Achenbach's loops should be crossed over in the other view as shown in Figure (4).

At the points where the double helix crosses itself the strength of the ciruclation is doubled. These are nodal elements corresponding to the initial roll-up of the vortex sheet in the formation region of the vortex loop. At lower Reynolds numbers the formation region extends over 1 to 3 diameters downstream from the sphere according to Achenbach (1974). For the higher Reynolds number range Achenbach reported an abrupt drop-off of signals at $Re = 6 \times 10^3$ from his sensors located at the surface of the sphere. This appears to suggest that below $Re = 6 \times 10^3$ the roll-up process has moved away from the sphere. The two branches of the double helical loop presumably unwind in an opposite sense from the sphere at higher Reynolds numbers so that the point of separation appears to rotate around the sphere as observed by Achenbach (1974).

As mentioned above the nodal elements are elements around which the strength of the circulation is doubled. These elements of reinforced circulation were subsequently revealed by the stratification during the wake collapse process while the remaining portions of the helical system were dispersed. An examination of the model in Figure (3) indicates that these points of enhanced ciruclation would be arranged in precisely the manner shown in Figure 1 (d) when viewed from above if the nodal elements were oriented approximately

in a vertical direction. The double sheeted structure of the dye layers is perhaps due to the finite extent and slightly non-vertical orientation of the nodal elements. The stratification appears to play a role in restraining the orientation of the nodal elements to be nearly vertical but this remains to be confirmed through more careful experiments. What is indicated is the use of stratification to reveal the regularity of the spacing which would not be possible otherwise.

It is also interesting to note that the vortex structure in the wake of a spanwise elongated body would have an appearance as shown in Figure (5) which in the limit of infinite-span body would approach the well-known two-dimensional case of Karman vortex street.

Flow visualization experiments were also conducted in a homogeneous fluid. The results for Re = 4,300 is shown in Figure (6). The dye structure was repeatable and again indicated the helical nature of the wake. More detailed experiments over a larger range of Reynolds numbers with the sphere held at a stationary position are being conducted. Dye study and hot-film probing are now in progress.

The authors wish to acknowledge the support of the Fluid Dynamics Program of the Office of Naval Research under contract No. N00014-67-A-0377-0027. One of the authors (HPP) would also like to acknowledge the support in part by the National Science Foundation under Grant GA-41513.

References

Achenbach. E. (1974), "Vortex shedding from spheres", J. Fluid Mech. 62, 209-221.

Foch, A. and Chartier, C. (1935), Sur l'ecoulement d'un fluide a l'aval d'une sphere. Comptes Rendus, 200, 1178-1181.

Kao, T.W., Pao. H.P., Wei. S.N. (1974), "Dynamics of establishment of selective withdrawal of a stratified fluid from a line sink. Part 2. Experiment", J. Fluid Mech. 65, 689-710.

Levy, H. and Forsdyke, A.G. (1927), "The stability of an infinite system of circular vortices", Proc. Roy. Soc. (London), Ser. A., 114, 594-604.

Magarvey, R.H. and MacLatchy, C.S. (1965), "Vortices in sphere wakes", Can. J. Phys. 43, 1649-1656.

Rosenhead, L. (1941), "The formation of vortices from a surface of discontinuity", Proc. Roy. Soc. (London) Ser. A, 134, 170-192.

Winny, H.F. (1932), "The Vortex system generated behind a sphere moving through a viscous fluid", A.R.C. Rep. No. 1531.

Expr. No.	Diameter D (in.)	Velocity U (in./sec.)	Vaisala freq. $N(sec^{-1})$	Wake Velocity factor, α	Wave length λ(in.)	Frequency $f(sec^{-1})$	$Ri=N^2D^2/U^2$	$Re=\frac{UD}{(x10^{-3})}$	$S=\frac{fD}{U}$
E-12	2.25	2.75	0.567	0.1	14	0.17	0.215	4.3	0.14
E-10	2.25	5	0.567	0.1	11	0.40	0.065	7.82	0.18
E-14A	5	5	0.802	0.18*	18	0.24	0.643	17.4	0.22

* adjusted for blockage

TABLE 1.

Figure 1. Formation of turbulent wake and its gradual transformation to an organized quasi-two dimensional vortex structure during wake collapse. (a) Time = 25 sec. (b) Time = 48 sec. (c) Time = 81 sec. (d) Time = 144 sec. Experimental conditions: Towing speed U = 2.75 in/sec; sphere diameter D = 2.25 in; Brunt-Vaisala frequency 0.567 sec^{-1}; Reynolds No. $Re = UD/\nu$ = 4,300; Richardson No. $Ri = N^2D^2/U^2$ = 0.215.

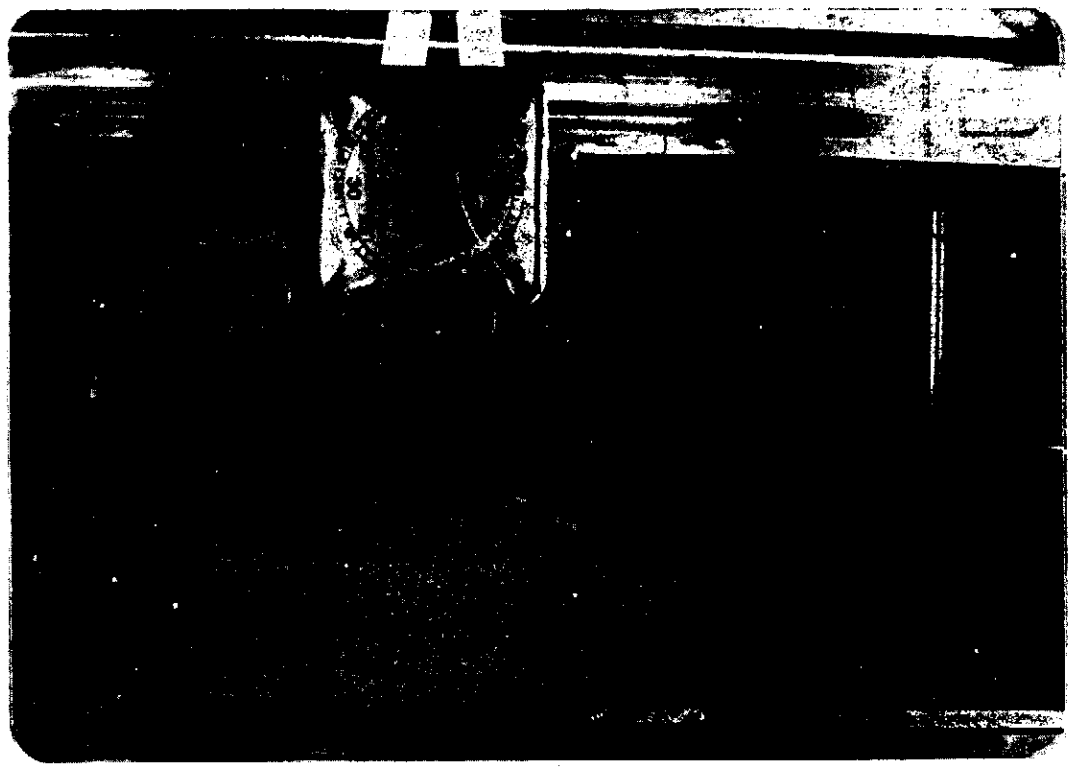

Top view

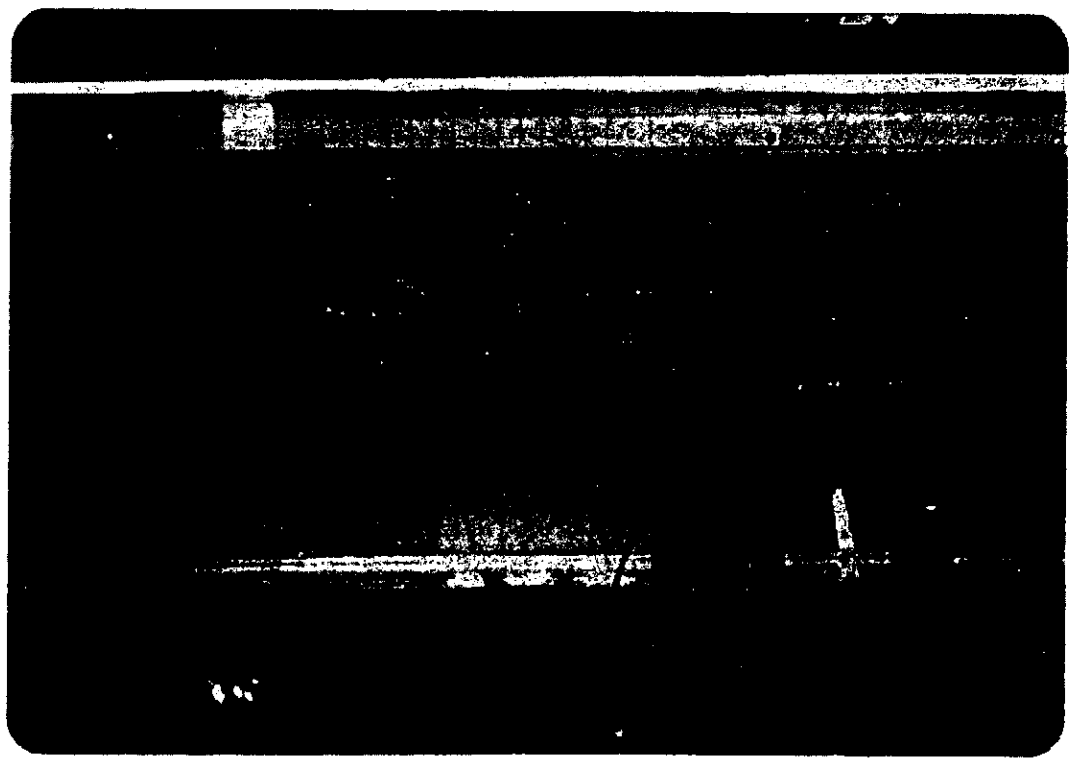

Side View

(a) Time = 25 sec.

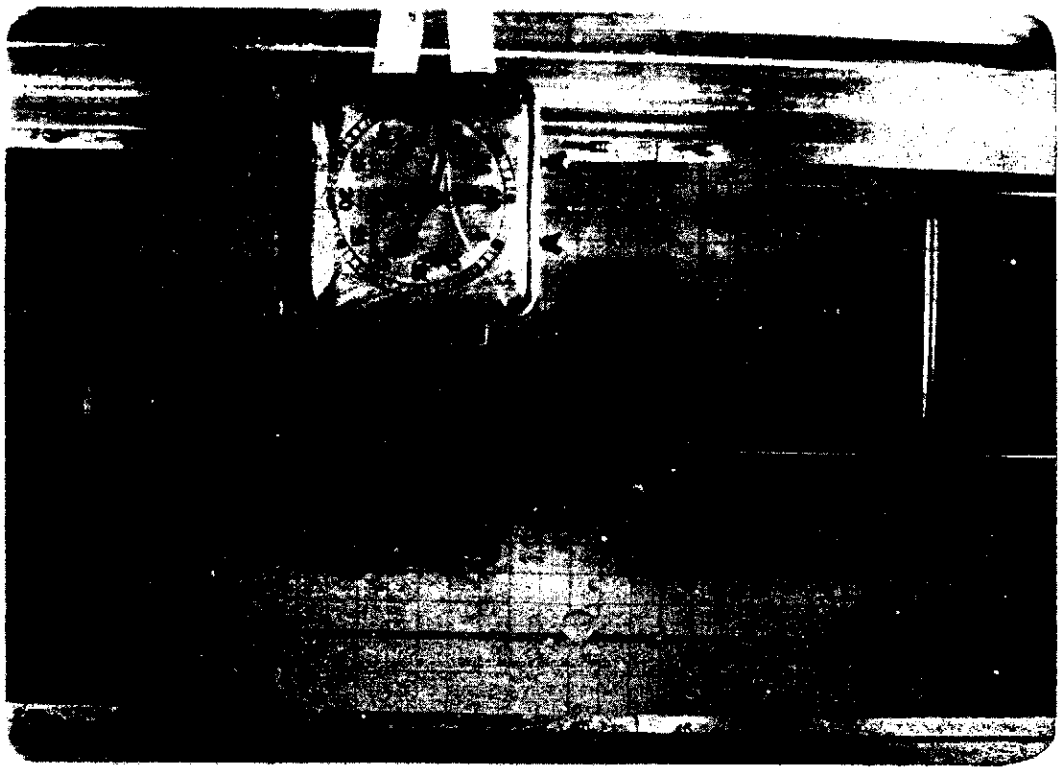

Top View

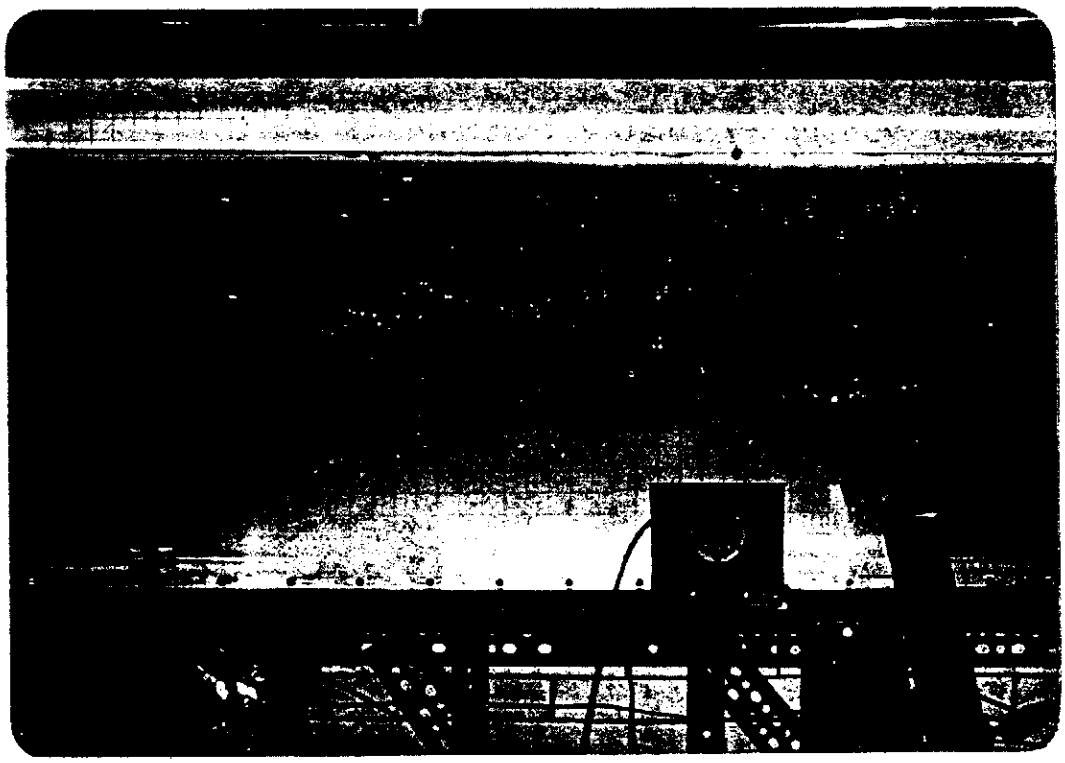

Side View

(b) Time = 48 sec.

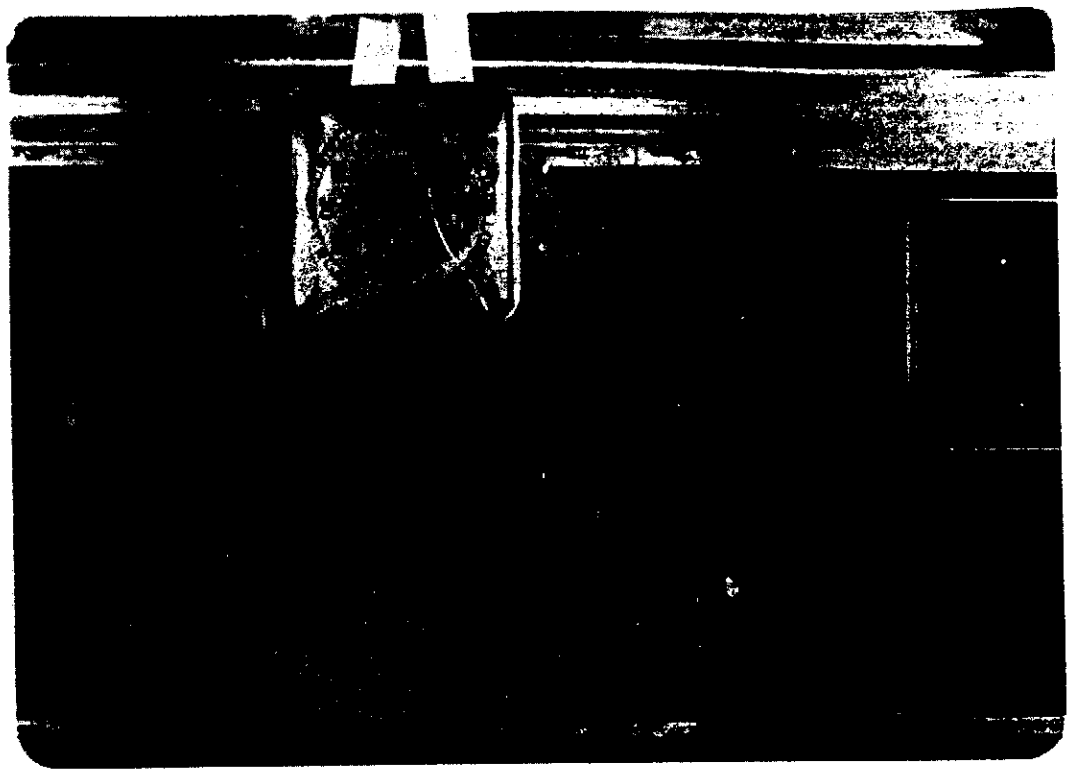

Top View

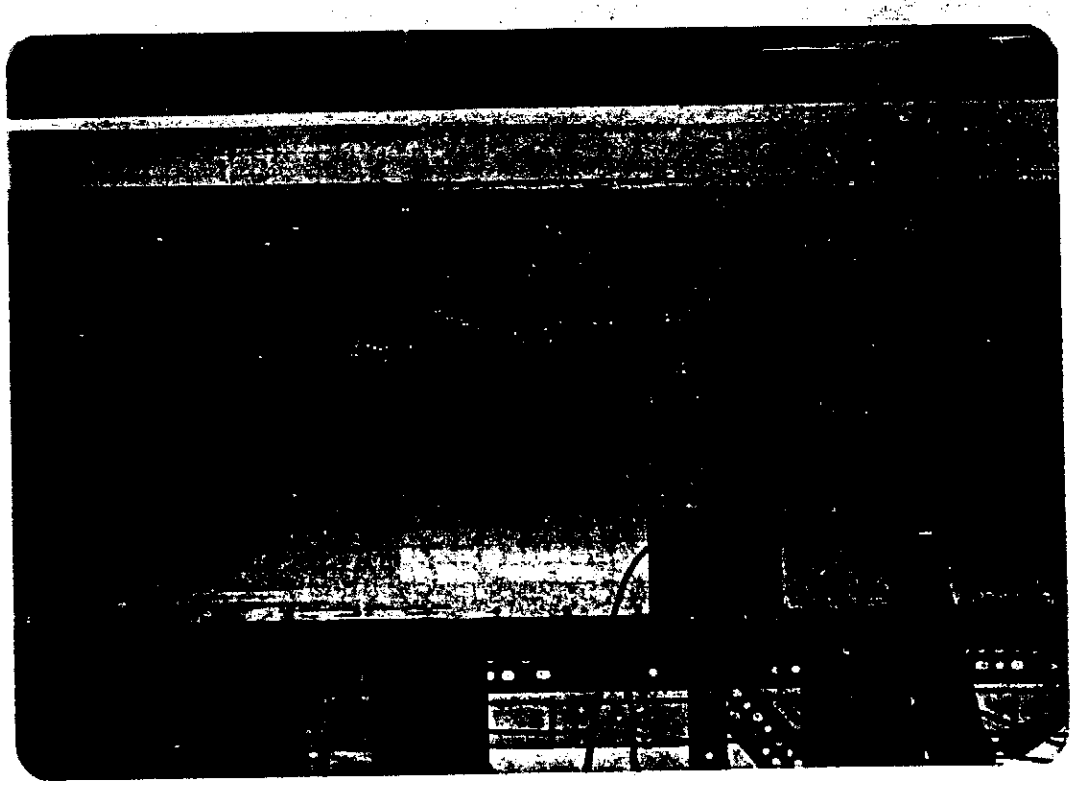

Side View

(c) Time = 81 sec.

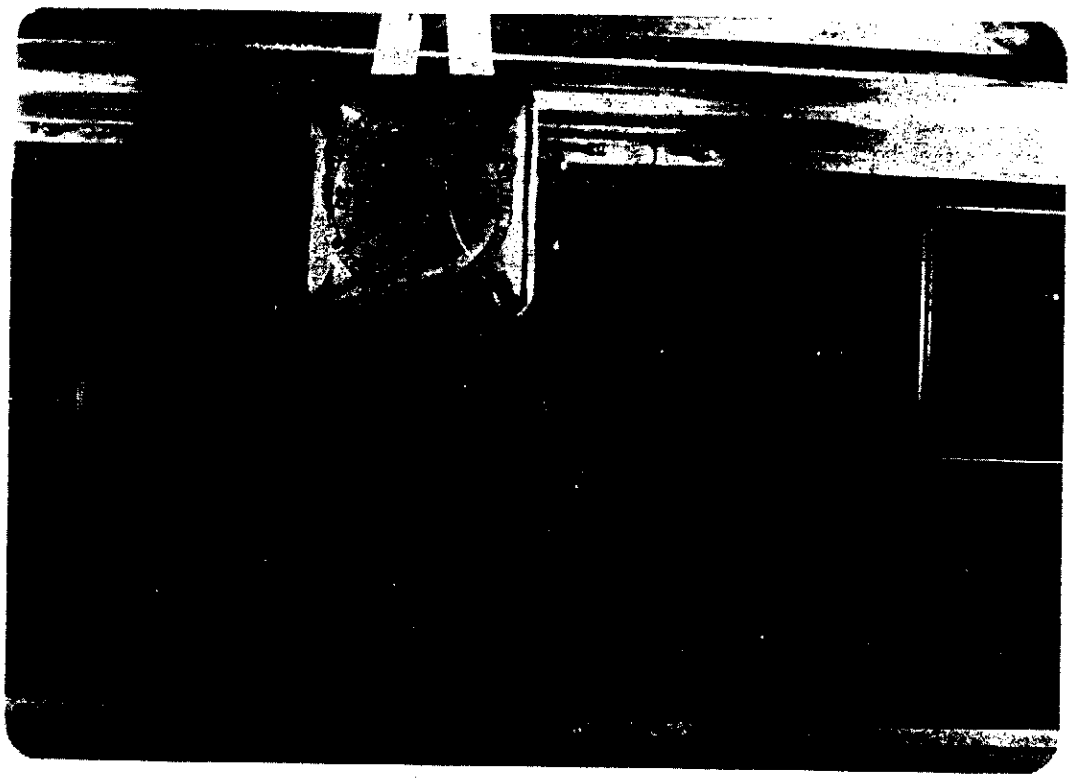

Top View

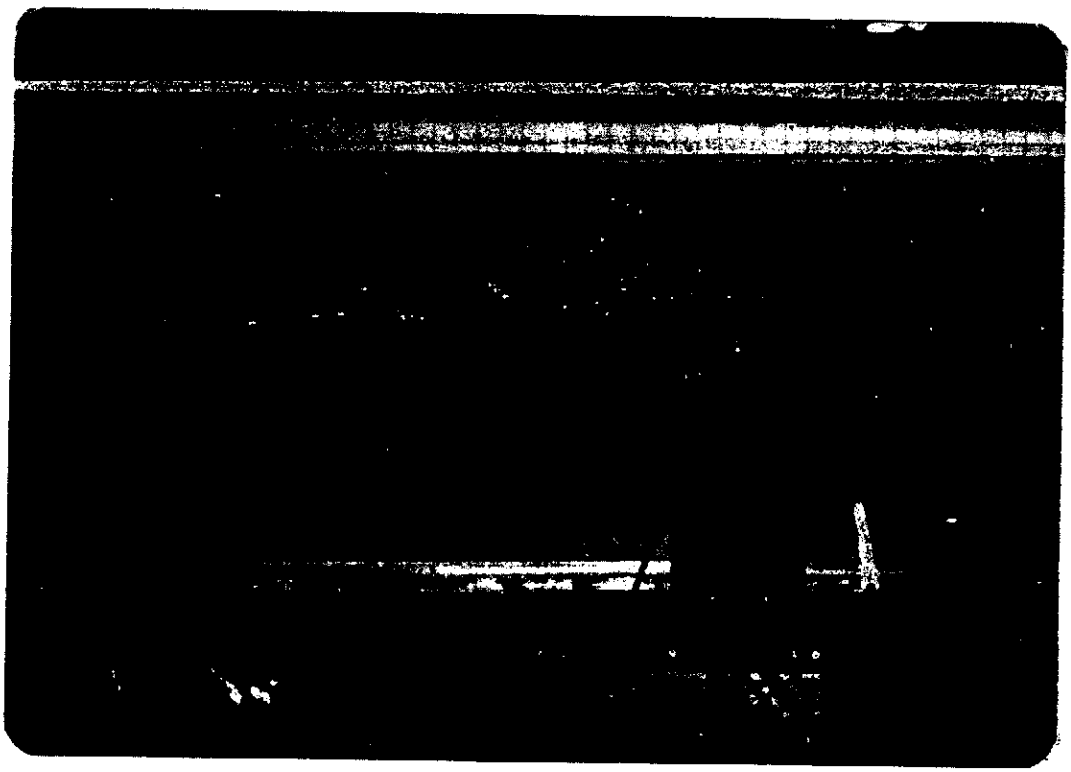

Side View

(d) Time = 144 sec.

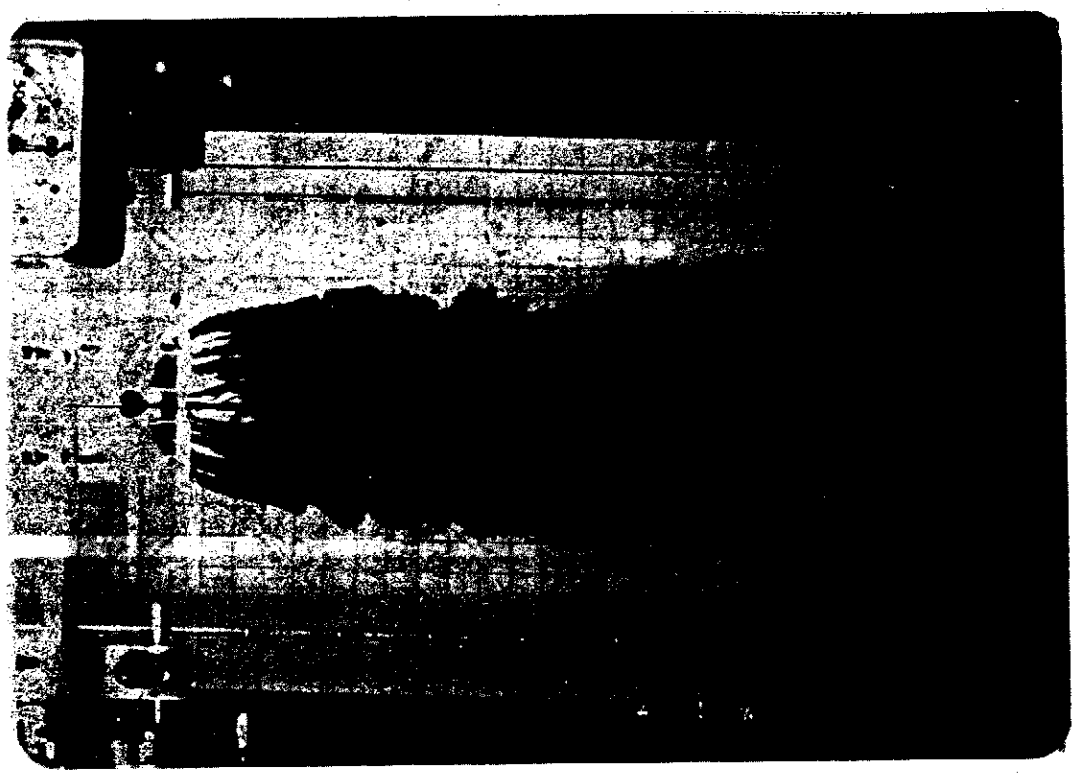

Figure 2. A top view of the helical nature of the vortex tube in the wake of a sphere. The vortex shedding is clearly seed to be three-dimensional. Experimental conditions: U = 5.0 in/sec; D = 5.0 in; N = 0.802; Re = 17.4 × 10^3; Ri = 0.643. The picture was taken 22 sec. after the commencement of the towing.

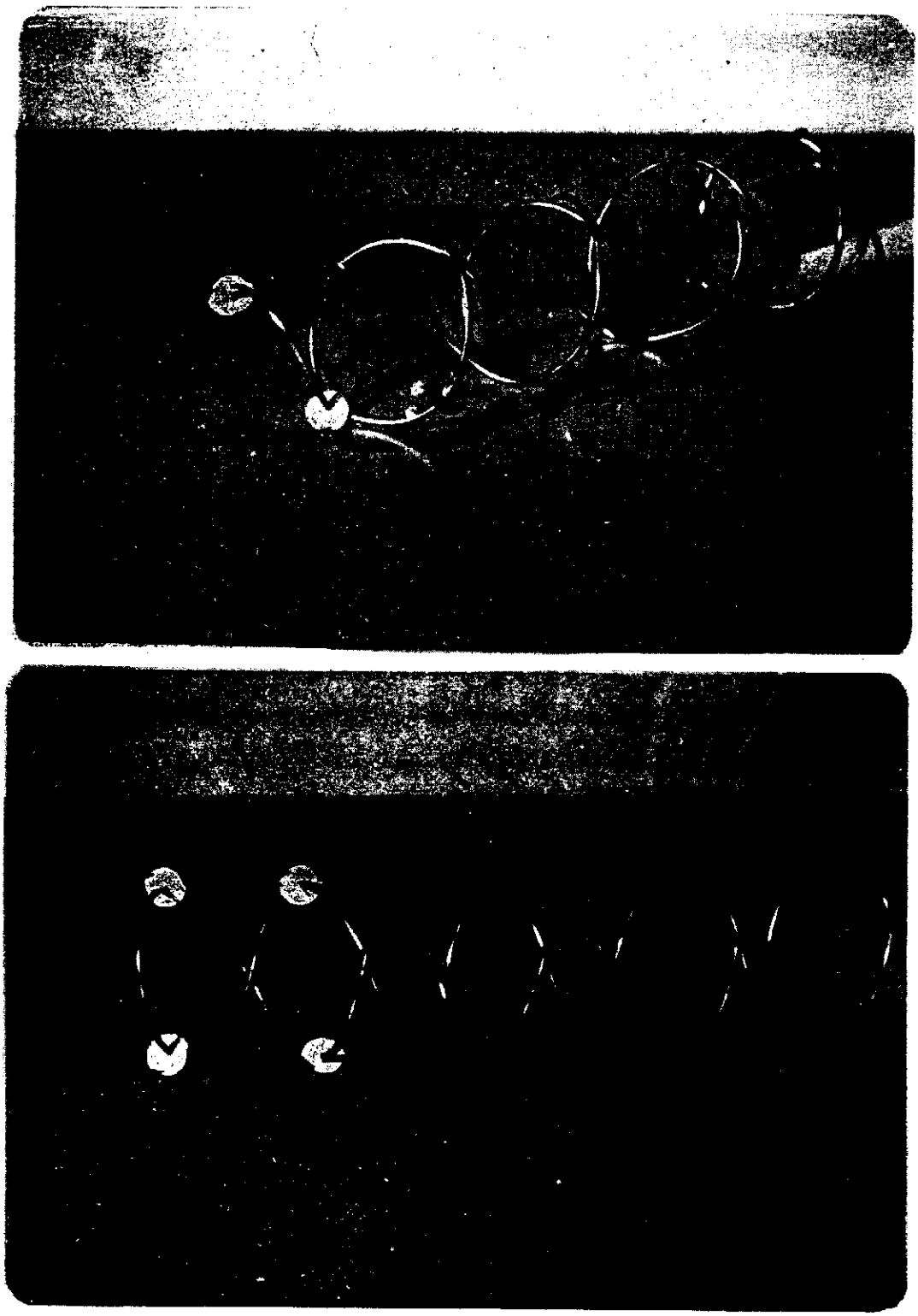

Figure 3. Pictures of the closed-ended double helix model for the vortes structure in the wake of a sphere. The circular arrows around the vortex tube indicate the circulations while the arrows along the tube represent the vorticity vectors.

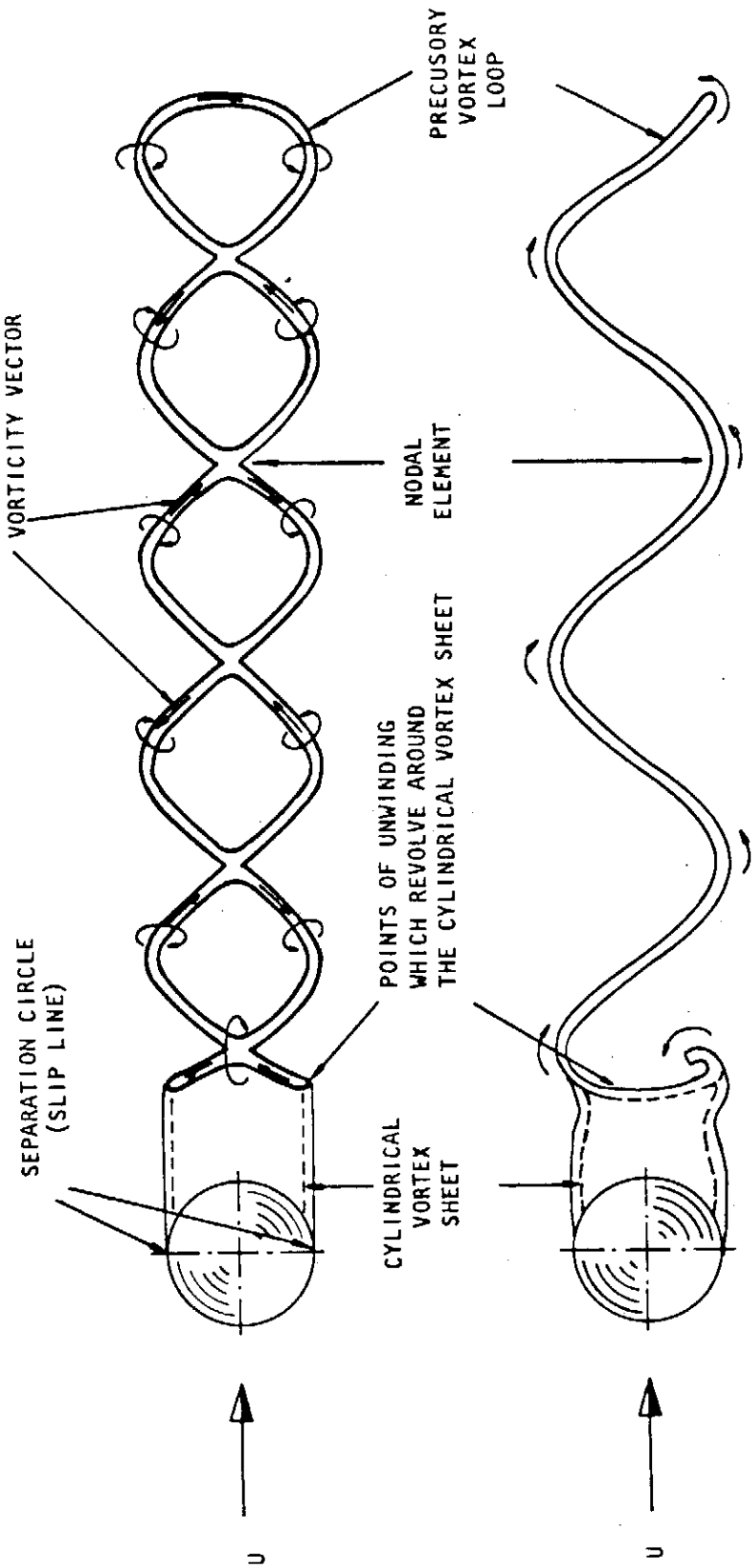

Figure 4. Schematic representation of the vortex configuration in the wake of spheres at Re = 10^3. The two branches of the double-helix vortex tube are continuously unwinding in an opposite sence from the cylindrical vortex sheet in the formation region. The arrows along the vortes tube represent the vorticity vectors.

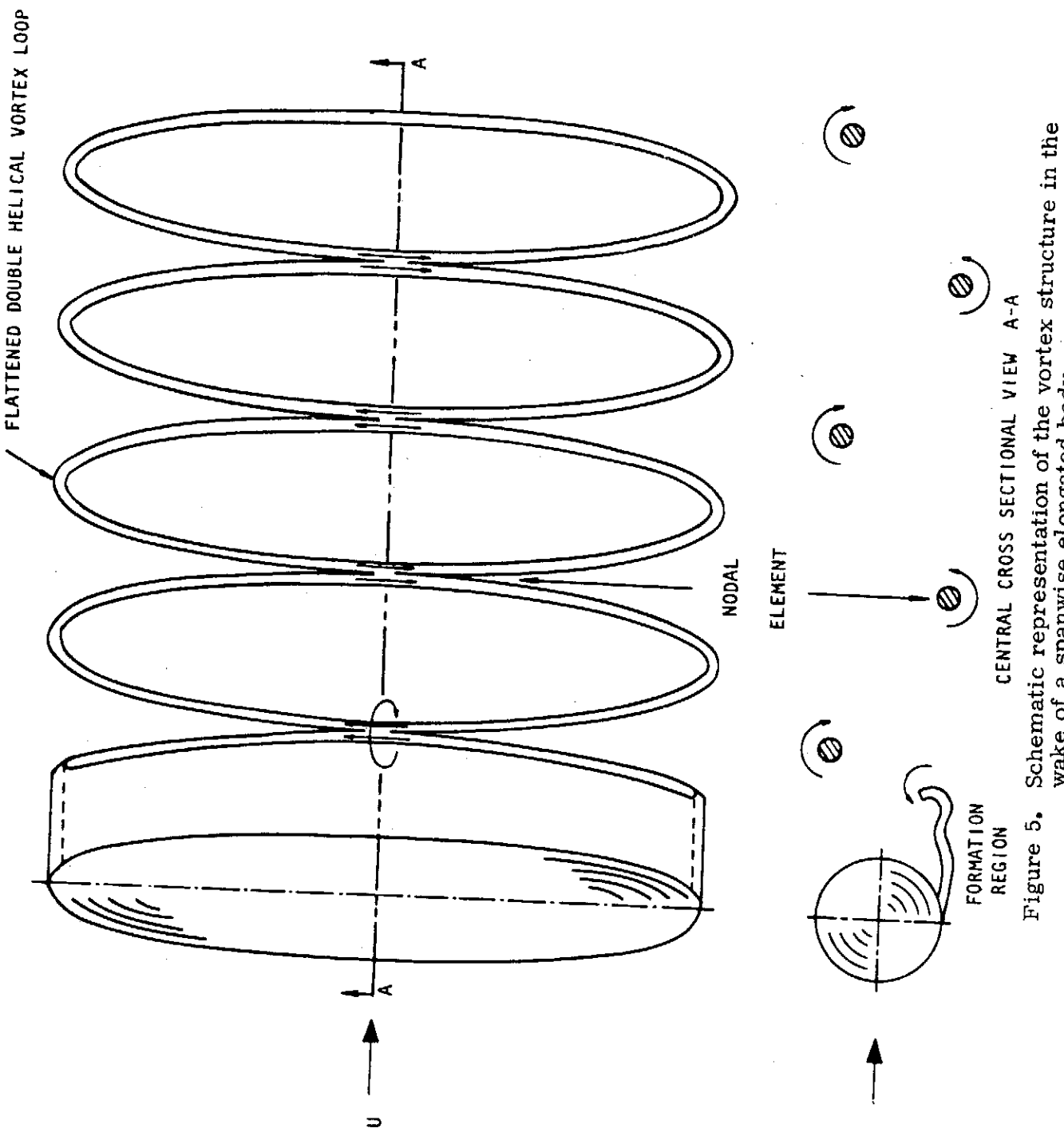

Figure 5. Schematic representation of the vortex structure in the wake of a spanwise elongated body.

Figure 6. Flow visualization experiment in a homogeneous fluid. The dye structure showing the helical nature of the wake. (a) Side view; Time = $27\frac{1}{2}$ sec. (b) Top view; Time = $27\frac{1}{2}$ sec. (c) Top view; Time = 36 sec. Experimental conditions: U= 2.75 in/sec; D = 2.25 in; Re = 4,300.

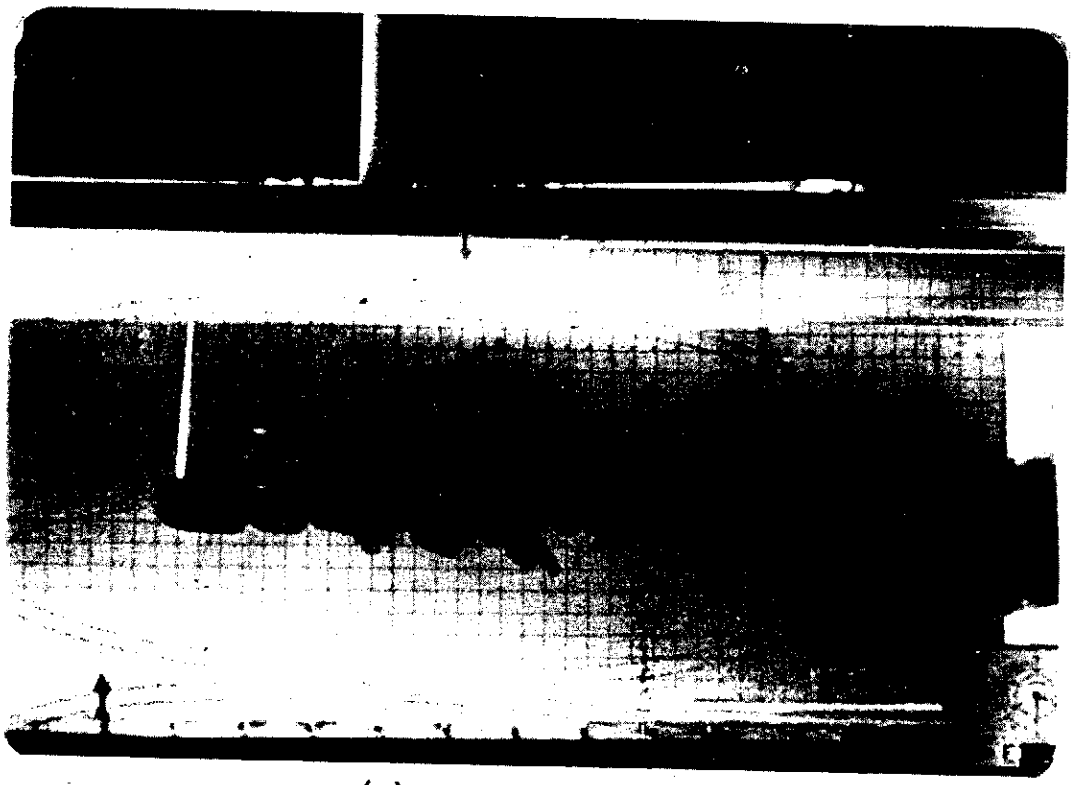

(a) Side view

Time = 27½ sec.

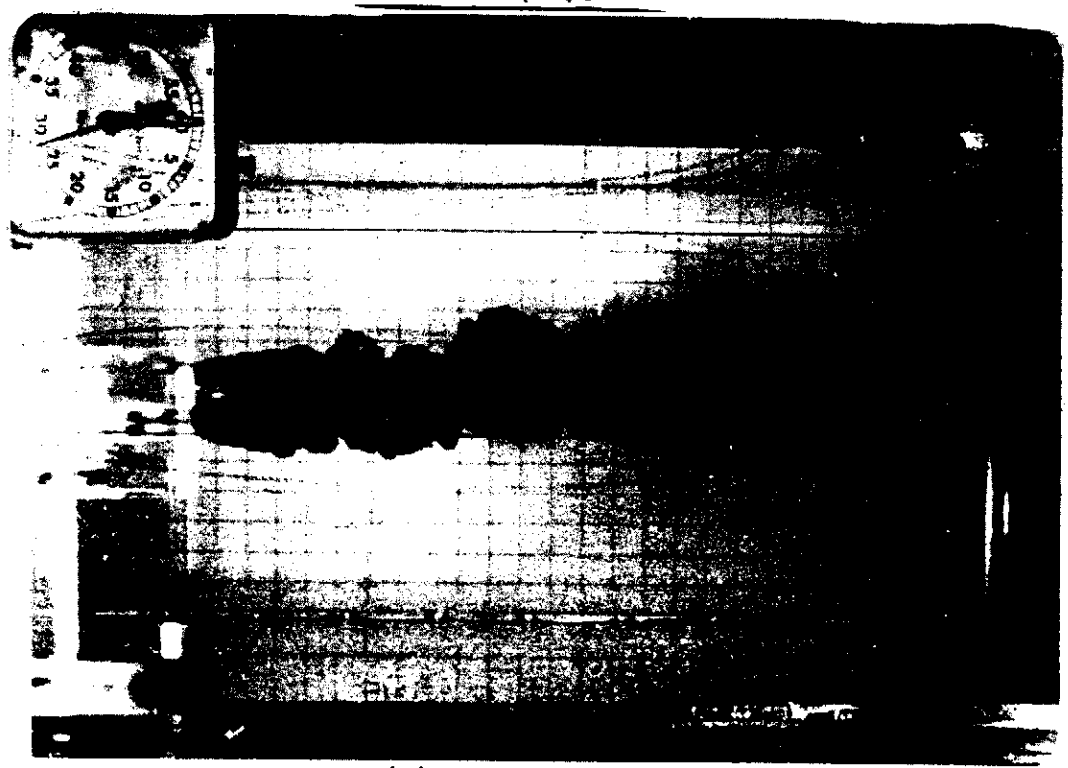

(b) Top view

Time = 27½ sec.

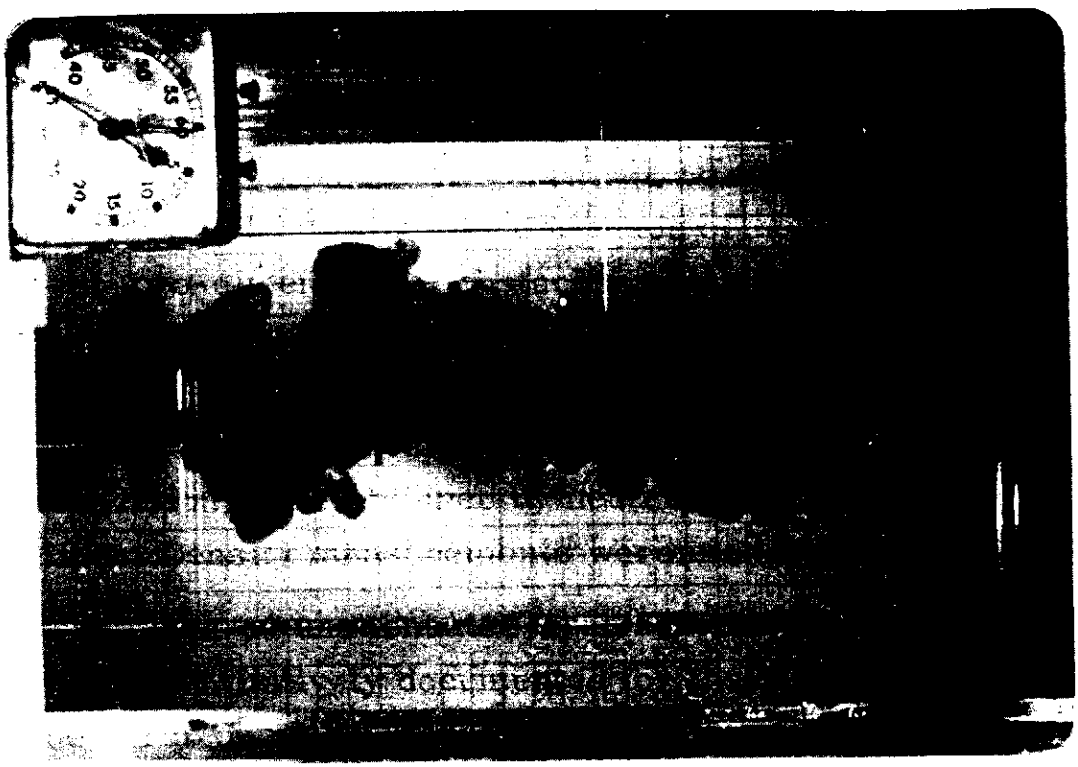

(c) Top view

Time = 36 sec.

ANNUAL REPORT OF THE INSTITUTE OF PHYSICS,
ACADEMIA SINICA, 1974

Experimental Study of Upstream Influence in the Two-dimensional Flow of a Stratified Fluid Over an Obstacle+

Shuang N. Wei, Timothy W. Kao, and Hsien-Ping Pao*

Department of Aerospace and Atmospheric Sciences
The Cathblic University of America
Washington, D.C. 20017

(Received May 14 1974)

An experimental investigation was made of the upstream influence in front of two-dimensional obstacles when they were towed in a linearly stratified fluid. The experiments were performed in a plexiglas channel 30.5 feet long, 2 feet high and 14 inches wide filled with a linearly stratified salt solution. Velocity measurements and flow visualization were obtained by neutrally buoyant liquid droplets and dye lines. Density measurements were made by a salinity probe.

The existence of unattenuated upstream influence in front of an obstacle was quantitatively documented for the first time. It occurred in the form of multiple unattenuated horizontal jets when there was a separated open wake behind the obstacle. These jets were identified to be the super-position of "columnar disturbance modes". The total number of columnar modes was determined solely by the Froude number of the flow and was equal to the number of lee-wave modes excited. The drag due to upstream columnar modes was estimated and found to be lower than the drag due to the lee wave modes.

+ This paper will be published in Geophysical Fluid Dynamics 1975.

* On sabbatical leave 1975-76 at Institute of Physics, Academia Sinica.

Introduction

The flow over a two-dimensional obstacle of an incompressible Boussinesq fluid, whose mean density stratification $\rho(Z)$ varies linearly with height, has been studied extensively (see the review articles by Miles, 1968 and Yih, 1969). When the flow is bounded between two parallel horizontal planes at $Z = 0$ and $Z = d$, it is characterized by a densimetric Froude number F defined by

$$F = \frac{U}{\overline{N}d}$$

where U is the undisturbed uniform flow and N is the Väisälä frequency given by

$$N = \left(\frac{-g}{\rho_o}\frac{d\overline{\rho}}{dZ}\right)^{1/2}$$

with $\rho_o = \overline{\rho}(0)$. On the hypothesis of no upstream influence, Long (1958) obtained exact solutions exhibiting large amplitude lee waves behind the obstacles for $F < 1/\pi$. This hypothesis is often referred to as Long's hypothesis (LH). The truth of (LH) is subject to much controversy in view of the experimental observation (Long, 1958 and Yih, 1959) of a stagnant blocked region or a partially blocked region in front of the obstacle when $F \ll 1/\pi$. Moreover, from an examination of the dispersion relationship for infinitesimal waves, it may be easily seen that x-independent columnar modes that penetrate to far-upstream are allowed whenever lee waves are present (where x is the dimension less horizontal distance measured from the obstacle, normalized by d). Subsequent investigation in the linearized framework has shown that for a source-like forcing effect, steady columnar modes are indeed excited to the first order in the ratio of obstacle height to channel depth, ε (Trustrum, 1964, 1971, Wong and Kao, 1970) and (LH) is invalidated for such flows. However, for a dipole-like or slender obstacle of finite length, linearized theory predicts zero excitation of columnar modes. Nevertheless, solutions based on (LH) become unrealistic with many closed eddies

appearing in the lee when the obstacle is high and when F is sufficiently low (Drazin and Moore, 1967). This led Miles (1968) to classify the flow into a blocked régime ($F \to 0$) and a lee-wave régime ($F_c < F < 1/\pi$) where F_c is the Froude number that marks the appearance of closed eddies which make the flow statically unstable. (LH) was considered to be valid for dipole-like bodies in the lee-wave régime. Recently McIntyre (1972) has shown that even for these bodies, in the lee-wave regime upstream influence in the form of steady columnar disturbances is still present. The induced flows, however, are only of second order in ε and can have a speed-up instead of a blocking effect. McIntyre's analysis supported an earlier qualitative study by Benjamin (1970) based on an impulse principle. The intervening régime of flow $0 < F < F_c$ has not been subject to rational analysis. It thus appears that, from the theoretical viewpoint, (LH) remains essentially valid in the lee-wave régime for a sufficiently small obstacle of finite length with no open separated wake in the lee. The effect of an open separated wake is to cause the obstacle to behave like a source-like disturbance. Separation and vortex shedding depend on viscous effects and obstacle shape. These have not been investigated theoretically.

Experimentally, unattenuated columnar disturbances have never been quantitatively demonstrated in the lee-wave régime and some conflicting results have been reported. (For the purpose of this paper, we will use the term "lee-wave régime" in a looser sense than Miles (1968), and allow F to have values between $1/\pi$ and $1/5\pi$ for which Long (1955) found good qualitative agreement between his theoretical and experimental lee-wave fields.) Davis (1969), for example, reported no upstream influence in the range of Froude numbers for which upstream influence is present in Long's experiments. Most of the other experimental study in stratified flow either concentrated on observing the lee waves (Carpenter and Keulegan, 1960, Droughton and Chen, 1971) or on the very small Froude number ré-

gime ($F < 0.01$) where viscous influences are strong (Browant and Winant, 1972, Debler, 1971). In Debler's study, a criterion for downstream vortex shedding is also included. In addition Pao et al. (1969) examined vortex street separation and gave a criterion for the occurrence of vortex street in stratified flow over circular cylinders.

Thus the main question of the existence and extent of upstream influence in the lee-wave régime in an essentially inviscid fluid remains unanswered experimentally. In this study we performed experiments by towing circular cylinders and a vertical plate in a slightly stratified fluid at Froude numbers between $1/\pi$ and $1/4\pi$ and Reynolds numbers between 400 and 2,260. (The Reynolds number is defined by $Re=Ua/\nu$ where a is the diameter or height of the obstacle and ν is the kinematic viscosity of water). The results provide for the first time quantitative demonstration of first order unattenuated upstream columnar modes for flows with a separated open downstream wake, and upstream influence that decays like x^{-1} for flows over a cylinder without separation.

Experimental Results and Discussion

(i) Theoretical Preliminary

Before presenting the experimental results it seems appropriate to summarize briefly some fundamental features of infinitesimal 2-dimensional waves in a linearly stratified Boussinesq fluid at rest and confined between parallel horizontal planes at a distance d apart.

The dispersion relationship for these waves is given by

$$\omega^2 \left(k^2 + \frac{n^2\pi^2}{d^2} \right) - N^2 k^2 = 0 \qquad (1)$$

where, $k = 2\pi/\lambda$ is the horizontal wave number and ω is the circular frequency. It is seen that waves with $k = 0$ have $\omega = 0$ but have group velocity $C_n = Nd/n\pi$. These are called "columnar disturbances

modes" since they propagate in the form of horizontal jet-like columns. These disturbances will propagate upstream of the obstacle which travels with constant speed U if $C_n > U$ or $Nd/n\pi > U$ or $F < 1/n\pi$. Thus for $1/\pi > F > 1/2\pi$, only the lowest mode n = 1 can propagate upstream, for $1/2\pi > F > 1/3\pi$, modes n=1,2 can propagate upstream and so on. Now the phase veloicty for waves with $k \neq 0$ is

$$C^2 = \frac{N^2 d^2}{k^2 d^2 + n^2 \pi^2}$$

Stationary waves are present only if U = Cor

$$F^2 = \frac{1}{k^2 d^2 + n^2 \pi^2} \qquad (2)$$

or

$$F < \frac{1}{n\pi}$$

These waves have group velocity less than U and therefore appear only in the lee. Thus columnar disturbances are possible whenever lee waves are present. For any given F the wave lengths of the stationary lee waves are found from Eq. (2).

A total of 9 experiments were undertaken using three different obstacles; namely a 1 inch cylinder, a 1 inch flat plate and a 2 inch cylinder. The summary of the experimental data is listed in Table 1. The emphasis of the towing experiments was focused on upstream influences and the field downstream was examined only briefly.

(ii) Upstream Influence

The purpose of the towing experiments is to study in detail the establishment of the flow field especially upstream of the obstacle and to determine quantitatively the extent and strength of the upstream influences in relation to obstacle shape and towing speed.

TABLE I

Summary of towing experimental data

Run No.	Obstacle	Wake	U(in/sec)	N(sec^{-1})	F=J/Nd	Re=Ua/ν	Ri=$(Na/U)^2$	Temp(^oF)
0-1	2" cyl	Vortex St.	1.754	0.819	0.238	2,260	0.872	67
0-2	2" cyl	Vortex St.	0.900	0.819	0.122	1,160	3.318	69
0-3	2" cyl	Border Ln.	0.640	0.819	0.0868	825	6.554	74
0-4	1" Plate	Vortex St.	1.705	0.819	0.231	1,100	0.231	64
0-5	1" Plate	Border Ln.	0.972	0.819	0.1317	627	0.712	71
0-6	1" Plate	Border Ln.	0.665	0.819	0.0902	428	1.517	74
0-7	1" cyl	Vortex St.	1.748	0.819	0.237	1,128	0.220	66
0-8	1" cyl	Border Ln.	1.028	0.819	0.1394	663	0.635	69
0-9	1" cyl	Vortex Pair	0.617	0.819	0.0836	398	1.767	75

The carrier travelling speeds were so determined that only a desired number of modes was excited. It was decided to run the experiments for Froude numbers lying between $1/\pi$ to $1/2\pi$, $1/2\pi$ to $1/3\pi$ and $1/3\pi$ to $1/4\pi$ so that 1 mode, 2 modes and 3 modes would be excited.

For each experiment, the maximum forward velocity which occurred along the center line of the obstacle was obtained from x = 1 to 3. It should be pointed out that x = 3 corresponded to 27 and 13.5 obstacle diameters for the 1 inch and 2 inch diameter respectively. The time interval that elapsed between the start of the carrier and the time at which the first picture was taken corresponded to the time interval for the obstacle to travel 100 diameters. In order to examine whether steady-state had been achieved in the region under consideration, pictures taken at earlier and later times were both analyzed. Figures 4 to 6 show the maximum center line velocity U_m at various distances in front of the three obstacles for two different times for each of the three values of F. The dimensionless times in this paper are normalized by N^{-1}. It is seen steady-state has indeed been achieved for all cases with the exception of the case for t = 133, F = 0.0868 in Figure 4. In that case steady-state has not been achieved for $2 < x < 3$. This is indeed to be expected since for F = 0.868 and $2 < x < 3$ in front of the obstacle, the third mode has not yet reached its full strength. Indeed, the third mode would arrive at x = 3 at t = 155 for F = 0.0868. This may be seen by dividing the dimensionless distance in front of the obstacle by the speed of the disturbance relative to the obstacle velocity, non-dimensionalized by Nd; or $x/(C_n-F)$. Thus for F = 0.122 steady-state would be achieved up to x = 3 in $t > 81$ and for F = 0.238 in $t > 37.5$.

Figures 4 to 6 also show the attenuation, if any, of steady upstream flow with distance. It is seen that for F = 0.238, the disturbance is unattenuated for all three of the obstacles. For F = 0.13 -0.14, there is strong attenuation for the 1 inch cylinder, weak attenuation for the 1 inch vertical plate but no attenuation for the 2 inch

cylinder. Similarly for $F \sim 0.09$. This attenuation for 1 inch obstacles cannot be explained from the view point of columnar disturbance modes obtained from theoretical consideration outlined in (i). They do not attenuate once they are excited. Neither can this attenuation be attributed to viscosity because of the rather high Reynolds number $Re = Ua/\nu$ of the experiments. This can best be seen from an estimation of viscous damping on columnar modes on assuming the diffusion of vorticity by viscosity. It can then be readily shown that the viscous damping factor for the nth mode disturbance is $\exp[-(\nu/Nd^2)n^3\pi^3 x]$ for $x > 0$, where ν is the kinematic viscosity of the fluid. Thus for $\nu = 10^{-5}$ feet^2/sec, d = 9 inches, the damping factor of even the third mode (n = 3) is still very small and is approximately equal to $\exp[-0.018x]$. Indeed, viscous damping is negligible in so far as the contribution to the attenuation is concerned.

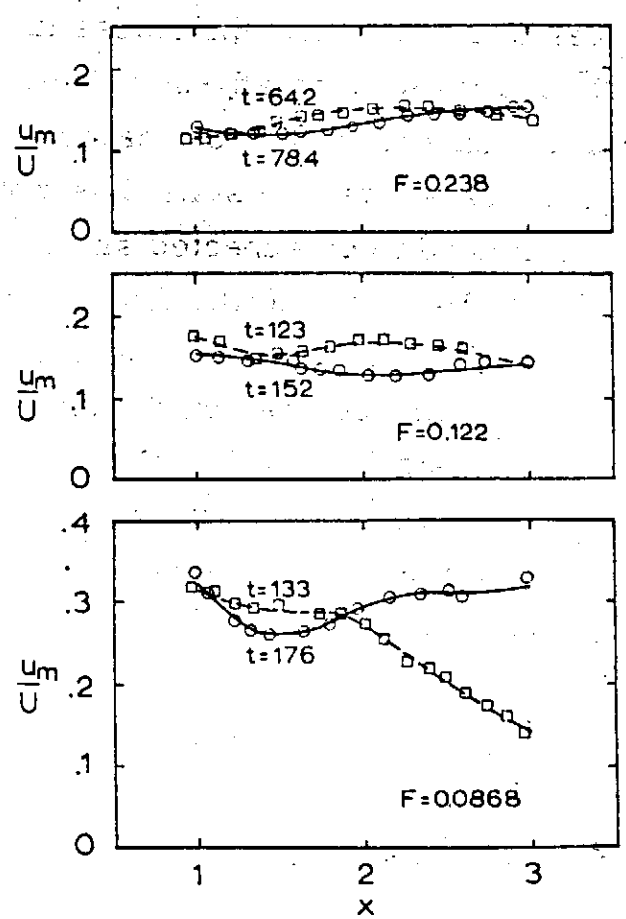

FIGURE 4 Center-line velocity in front of a 2" cylinder obstacle at various x and two different times.

The question is then: In these cases were the columnar modes really excited? and if they were not, why not? It is well known that in unstratified flow over obstacles, separation occurs downstream of the obstacles. For a circular cylinder, downstream attached eddies are formed for $3 < Re < 40$. For $Re > 40$, Karman street appears. For $Re > 300$, a turbulent Karman street is present. In the presence of a turbulent Karman street, the wake is generally considered as an open wake and the obstacle has a source-like behavior. With stratification, downstream separation is inhibited to a certain extent. For a fixed Reynolds number, the effect of stratification or separation is measured through a ratio of buoyancy to viscous forces or the product of the Reynolds number and the Richardson number, where the Richardson number is defined as $Ri = (Na/U)^2$. A Richardson number of 0(1) or less

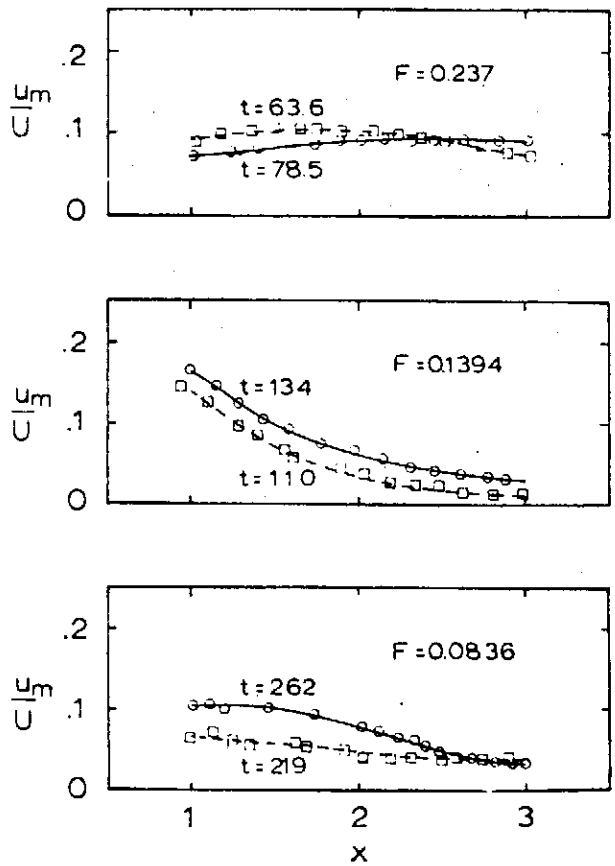

FIGURE 5 Center-line velocity in front of a 1" cylinder obstacle at various x and two different times.

indicates weak stratification effect. In our experiments, Re was between 400 and 2,260, Ri was between 0.22 and 6.55 and Re Ri was between 250 and 5,400. A detailed study of the wake region for stratified fluid has been undertaken by Pao et al., (1969) and Debler (1971). In both these studies regions in the Re Ri vs Re plane have been identified where the downstream flow exhibits a Karman street. It has been shown by Wong and Kao (1970) that first order unattenuated columnar disturbances are excited by source-like obstacles and if the obstacle is closed or dipole-like, it has been shown by Trustrum (1964) that no such disturbances are excited and upstream influence is a weak second order effect according to McIntyre (1972). An explanation about the presence or absence of unattenuated upstream disturbance may now be given. Based upon Pao's and Debler's criterion,

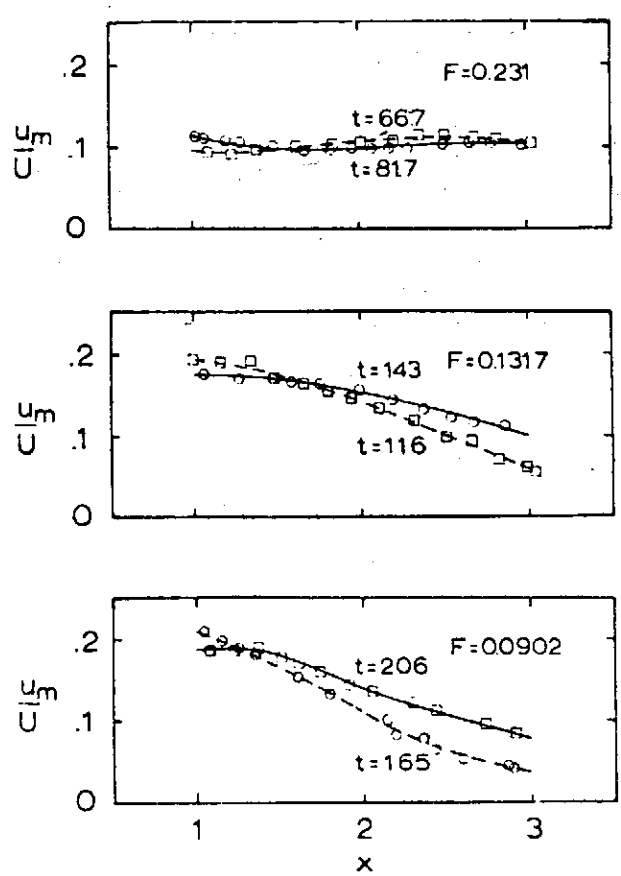

FIGURE 6 Center-line velocity in front of a 1" flat plate obstacle at various x and two different times.

complete flow separation is denfinite for all the experimental case with unattenuated upstream influence (2 inch cylinder at F = 0.238, 0.122 and 0.0868, and 1 inch cylinder and 1 inch plate at F ~ 0.23). While for the case of 1 inch cylinder at F = 0.1394 and 0.0836, the flow is not separated. i.e. the data fall either in the stable region with attached vortex pair or near the borderline dividing the regions of open wake and stable vortex pair. (It should be noted that the division is not sharp as may be seen by comparing Debler's and Pao's results). Thus, the upstream influence, according to McIntyre (1972), is second order effect and should attenuate rapidly away from the obstacle. Indeed the data show that the disturbance attenuates like x^{-1}. For the 1 inch plate at F = 0.1317 and 0.0902, even though the experimental conditions are nearly the same as that of the corresponding cases for 1 inch cylinder, the upstream influence shows only weak attenuation (Figure 6). This may be due to the "uneasy-shape"+ or sharp edge of the flat plate which would certainly cause more separation that the 1 inch cylinder would under the same experimental conditions.

Among the 9 experiments, 5 were analyzed in detail for velocity profiles of the upstream influence. The vertical profile of the up-

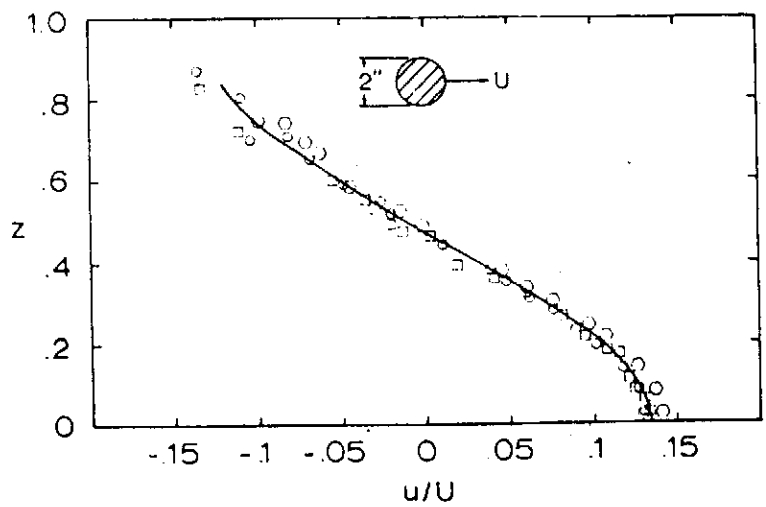

FIGURE 7. Steady-state velocity profile at x = 1, 2, and 3 in front of a 2" cylinder; F = 0.238: ■ (x = 1), □ (x = 2), and ○ (x = 3).

+The use of this terminology finds precedence in Long (1955)

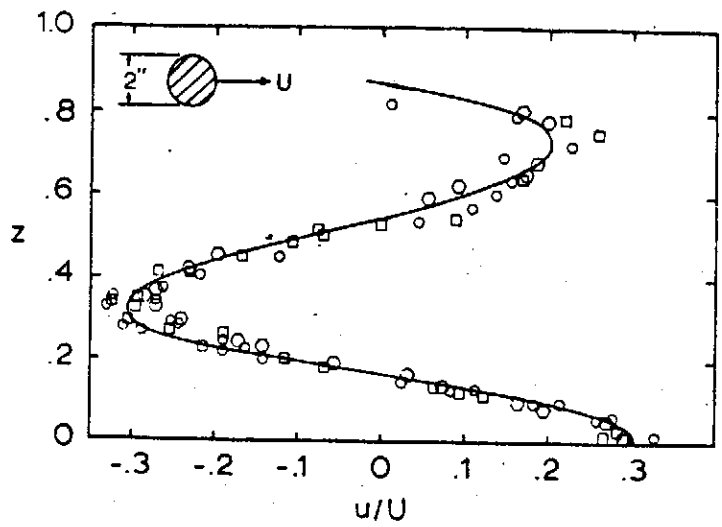

FIGURE 8 Steady-state velocity profile at $x = 1, 2$, and 3 in front of a 2" cylinder; $F = 0.122$: ■ ($x = 1$), □ ($x = 2$), and ○ ($x = 3$).

stream flow were obtained at x = 1, 2 and 3, and they are shown in Figures 7-11.‡ The symmetry of the profile was verified quantitatively and therefore no distinction was made for data obtained above and below the line of symmetry. Figures 7, 8 and 9 show the vertical distribution of the unattenuated upstream jets for the 2 inch cylinder obstacle at F = 0.238, F = 0.122, and F = 0.0868. The multiple-jets profiles was the prominant feature of the upstream field regardless the shape and the size of the obstacle and the total number of jets

‡ z denotes the dimensionless vertical distance measured from the centerline of the obstacle and normalized by d, and u denotes the disturbance horizontal velocity.

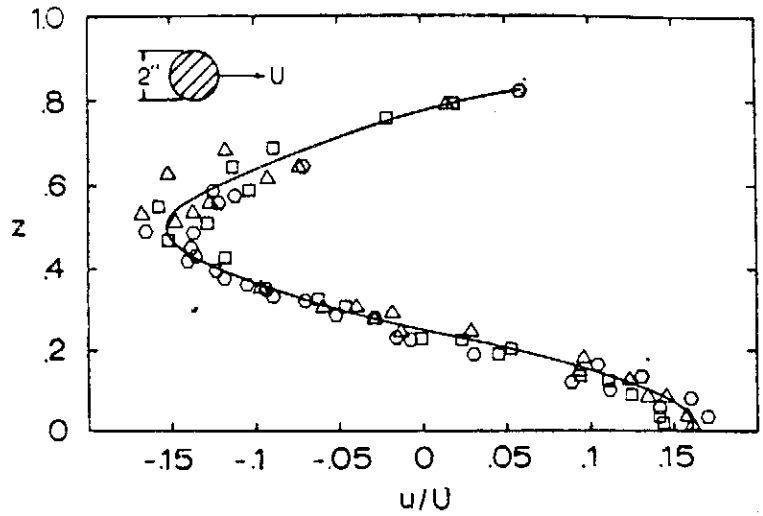

FIGURE 9 Steady-state velocity profile at $x = 1, 2$, and 3 in front of a 2" cylinder; $F = 0.0868$: ■ ($x = 1$), □ ($x = 2$), and ○ ($x = 3$).

in the upstream field was determined only by the total number of modes excited.

This experimental result of the existence of unattenuated upstream jets contradicted Davis' result (1969). The possible explanations for his failure to detect any upstream jets are as follows: in his experiment, the tank was too short (only 2 meters), the towed obstacle has to be stopped long before the establishment of the upstream field, especially for experiments run at high Froude number close to $1/\pi$. In addition, the reflection from the end wall will cancel out some of the already established influences in the upstream field.

The shape of horizontal velocity distribution of the upstream jets, according to the interpretation given in terms of infinitesimal waves, should be proportional to the sum of cos $n\pi z$ regardless of the sources of disturbances (i.e. the geometry of the obstacle.) This was verified by Figures 7, 8 and 9 and was most clearly illustrated by Figure 7 which is indeed a half cycle cosine curve with a period of 2d. For various Froude numbers, the general shape of the up-

stream velocity profile (i.e. the number of upstream jets) agreed qualitatively with theoretical solution given by Wong and Kao (1970) and Trustrum (1971). No quantitative comparison was made since Trustrum's result is for a vertical plate whose vertical height is much larger than that in the present experiments and Wong and Kao's result is for a source with a resulting half body of small height.

(iii) Downstream Field

To study the detailed downstream field, cameras stationary to the obstacle or probes positioned in the obstacle wake were necessary and this required considerable modifications of the existing laboratory set-ups. Hence the downstream field was obtained by employing a flow visualization technique of dropping nigrosine particles on top of the obstacle prior to each experiment run. As the obstacle was towed, they were washed away by the surrounding fluid and left dark streaks behind the obstacle, thus enabling the flow field immediately behind the obstacle to be examined. By observing the streamlines close to the obstacle, the effects of boundary layer separation and the formation of weak turbulent wake were observed. When flow separation occurred at the back side of the obstacle, the dyed streamlines broke up in the lee of the obstacle. The dye clouds were the result of turbulent mixing and indicated roughly the region of turbulent wake. The turbulence in the wake, however, was short lived and suppressed by the density stratification. This was demonstrated by the disappearance of small scale variations in light intensity caused by the large gradients of refraction index associated with turbulent mixing. Because of the complexity of the velocity field and the difficulty in identifying and tracing the same oil droplet on the next negative, the nature and extent of the wake structure was not determined. Whether it was completely separated with the presence of Karman vortex street associated with vortex shedding or it was partially separated with a pair of stable vortices attached to

the obstacle was indistinguishable. Consequently, Pao's (1969) and Debler's (1970) criterion was employed and their results concerning the wake structure were listed in Table I.

As to the downstream lee waves, due to the same difficulties mentioned above, only one quantitative result was obtained for the case of a 2 cylinder at $F = 0.238$ (i.e. a single mode of lee wave was excited). The amplitude of the lee waves for this case was presented in Figure 12. The lee-waves are symmetric with increasing wave length. The wave length measured from the first two wave crests is about 20 inches which agrees with the value predicated by Long (1955) or by Eq. (2). The wave amplitude first increases slightly and then decreases and is roughly equal to the radius of the 2 inch cylinder. The wave lengths of the lee waves calculated from Eq. (2) are approximately 19 inches for $F = 0.23$, 8.43, and 14.4. inches for $F = 0.135$ and 5.32, 6.17 and 9.6 inches for $F = 0.09$. For the experiments at lower Froude numbers the Strouhal vortex shedding happened to have a wave length of the same order as that of some of the lee waves, which further complicated the downstream field. The wave length of Strouhal vortex shedding according to the formula from Goldstein (1938) is

$$\lambda_s = \frac{\alpha}{0.21(1-20/Re)}$$

Therefore the values are $\lambda_s = 9.7$ inches for a 2 inch cylinder at Re = 825 - 2,260 and $\lambda_s = 4.9$ inches for 1 inch obstacle at Re=413 - 1, 110.

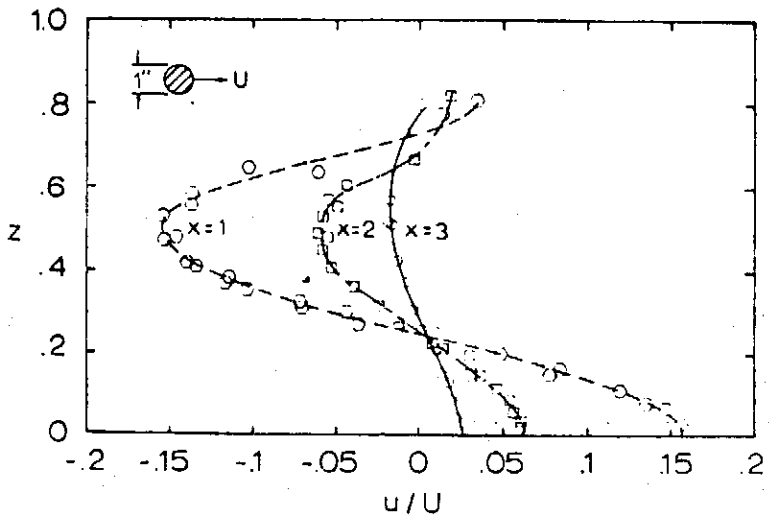

FIGURE 10 Steady-state velocity profile at $x = 1, 2$, and 3 in front of a 1" cylinder; $F = 0.1394$: ■ ($x = 1$), □ ($x = 2$), and ○ ($x = 3$).

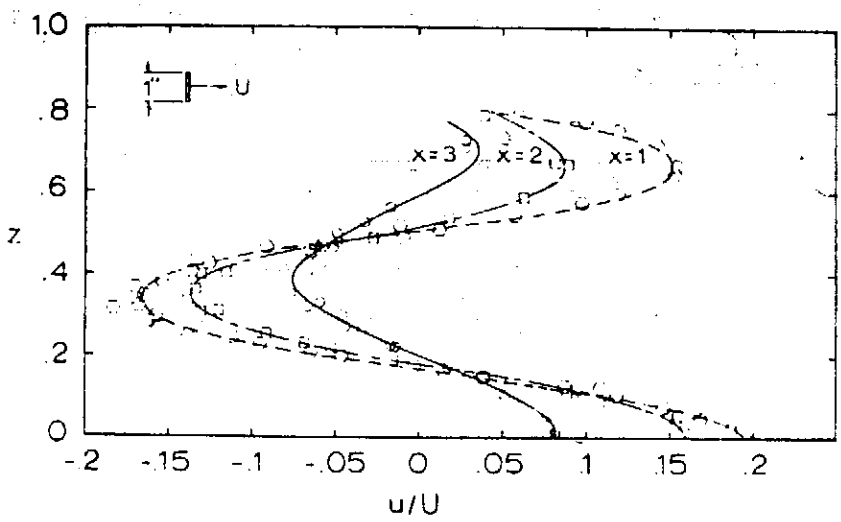

FIGURE 11 Steady-state velocity profile at $X = 1, 2$, and 3 in front of a 1" vertical Plate: $F = 0.0902$: ■ ($x = 1$), □ ($x = 2$), and ○ ($x = 3$).

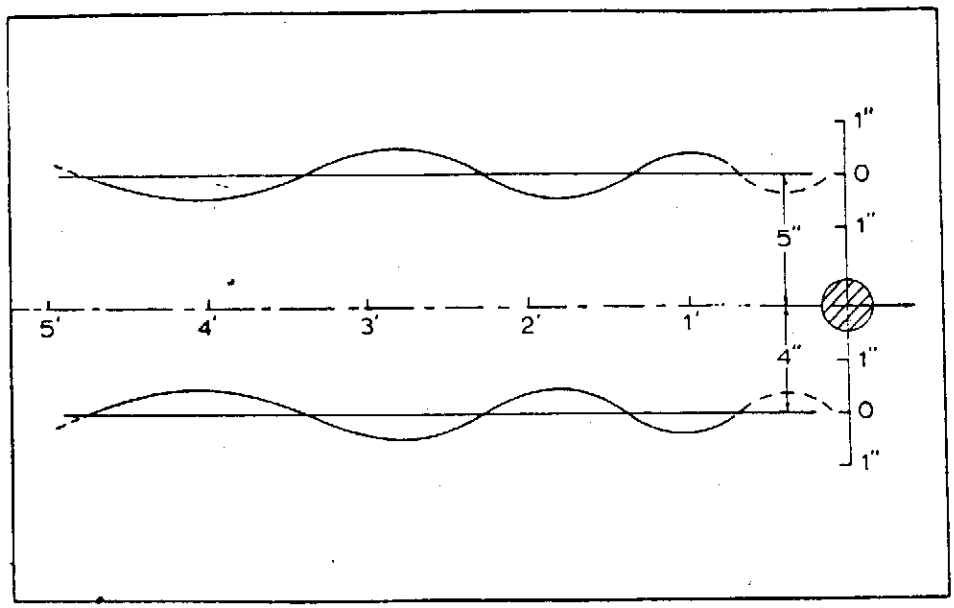

FIGURE 12 Downstream lee-waves pattern behind a 2" cylinder obstacle; $F = 0.238$.

(iv) Wave Drag Estimation

We now estimate the drag on the obstacle due to the lee-wave modes and the upstream columnar modes. The interest here is to compare the relative magnitudes of these two sources of drag. The calculation is done only for the 2 inch cylinder running at F = 0.238 for which good lee-wave data were obtained.

According to Miles (1968) the lee-wave drag coefficient is

$$C_{DW} = \frac{4\pi^2 d^2}{a^2} \sum_{n=1}^{N} A_n^2[(\pi F)^{-2} - n^2]$$

where a is the diameter of the cylinder and A_n is the dimensionless amplitude of the nth mode. For F = 0.238, N = 1

$$C_{DW} = \frac{4\pi^2 d^2}{a^2} A_1^2[(\pi F)^{-2} - 1]$$

For the present case shown in Figure 12, $C_{DW} = 0.438$.

The drag due to the upstream columnar disturbance may be claculated by assuming that the rate of increase of perturbation energy upstream is equal to the rate of work done by the obstacle to

create this upstream energy.

For the nth columnar mode we assume

$$u = U(1- \delta_n \cos n\pi z \; H(t-X/c_n))$$

where u is the pertubation velocity, δ_n is its amplitude and H is the Heaviside step function. The energy per unit length in this disturbance is

$$\frac{\rho U^2 d}{2} \int_0^1 \{(1- \delta_n \cos n\pi z)^2 - 1\} \, dz$$

$$= \frac{\rho U^2 d}{4} \delta_n^2$$

The rate of increase of upstream energy is

$$C_n \frac{\rho U^2 d}{4} \delta_n^2 ,$$

or

$$\frac{Nd}{n\pi} \frac{\rho U^2 d}{4} \delta_n^2 .$$

Denoting the drag coefficient for N upstream modes by C_{DU} we have

$$C_{DU} = \sum_{n=1}^{N} \frac{\delta_n 2}{n\pi F} \left(\frac{d}{a}\right)$$

For the case under consideration N = 1 and

$$C_{DU} = 0.1.$$

Thus, the drag due to upstream mode is 1/4 of the drag due to the lee-wave mode.

The authors are indebted to the Atmospheric Sciences Section, National Science Foundation for their support under Grant GA-23784.

References

Benjamin, T.B. (1970). "Upstream influence," J. Fluid Mech., 40, 49-79.

Browand, F. K. and Winant, C. D. (1972). "Blocking ahead of a cylinder moving in a stratified fluid," Geophys. Fluid Dynamics, 4, 29-53.

Carpenter, L.H. and Keulegan, G.H. (1960). "Disturbances due to

motinn of cylinders in a liquid with linear density gradient," US Nat. Bureau of Standards Rep. No. 7007.

Davis, R.E., (1969). "The two-dimensional flow of a stratified fluid over an obstacle," J. Fluid Mech., 36, 127-143.

Debelr, W. R. (1971). "The towing of bodies in a stratified fluid," Tech. Rep. EM-71-1, Ann Arbor, Mich.

Drazin, P. G. and Moore, D. W. (1967). "Steady two- dimensional flow of fluid of variable density over an obstacle," J. Fluid Mech., 28, 353-370.

Droughton, J.V. and Chen, C.F., (1971). "The channel flow of a density stratified fluid about immersed bodies," J. Basic Eng., Trans. ASME, Paper No. 71FE23.

Goldstein, S., (1938). "Modern developments in fluid dyhamics" Dover.

Long, R.R. (1955). "Some aspects of the flow of stratified flûids, III. Continuous density gradients," Tellus, 7,342-357.

McIntyre, M.E., (1972). "On Long's hypothesis of no upstream influence in uniformly stratified or rotating flow," Dept. of Applied Mech. and Theoretical Phys., Univ. of Cambridge.

Miles, J.W., (1968a). "Lee waves in a stratified flow. Part 1. Thin barrier," J. Fluid Mech., 32, 549-567.

Miles, J.W. (1968). "Waves and wave drag in stratified flows," 12th Int. Congress of Applied Mech., Stanford, Calif.

Pao, Y.H., Callaham, M.E. and Timm, G.K., (1969), "Vortex streets in stably stratified fluid," Boeing Scientific Research Lab. Document D1-82-0736.

Trustrum, K., (1964). "Rotating and stratified fluid flow," J. Fluid Mech., 19,415-432.

Trustrum, K., (1971). "An Oseen model of the two-dimensional flow of a stratified fluid over an obstacle," J. Fluid Mech., 50,177-188.

Wong, K.K. and Kao, T.W., (1970). "Stratified flow over extended obstacles and its application to topographical effect on vertical

wind shear," J. Atmospheric Sci., 27, 884-889.

Yih, C.S., (1959). "Effect of density variation on fluid flow," J. Geophys. Res., 64, 2219-2223.

Yih, C.S., (1969), "Stratified flow," Annual Review of F. Mech., 1, 73-110.

Experimental Observation of Internal Solitary Waves in a Stratified Fluid*

David A. Hurdis

University of Maryland, College Park, Maryland 20742

Hsien-Ping Pao

The Catholic University of America, Washington, D.C. 20017. Now at Institute Physics, Academic Sinica

Propagation of internal solitary waves has been experimentally observed within a region of sudden vertical density variation. The propagation speeds compare well with the theoretical predictions of Benjamin and Davis.

An experimental study has been conducted of disturbances caused by the motion of a vertical flat plate through a region of sudden vertical density variation. The study was focused primarily on the phenomenon of upstraem influence, [1,2] but it was noticed that internal solitary waves of the type considered by Benjamin[3] and Davis[4,5] were also generated. The amplitudes and speeds of propagation of the waves were measured. It is the purpose of this note to present these data together with comparisons with the theoretical predictions of Benjamin and Davis.

The experiments were carried out in a Plexiglas channel 10 m long, 0.60m deep, and 0.36m wide. The laboratory two-dimensional-flow model consisted of a layer of fresh water on top of a layer of salt water with a thin transition region at the interface. A vertical flat plate 2.54 cm in height was towed through the interfacial layer at various speeds and for various denisty profiels. Flow visualization was accomplished with the aid of droplets of a mixture of carbon tetrachloride, mineral oil, and oil red dye. These were injected into the upper layer with a syringe and hypodermic needle,

*This paper has been published in The Physics of Fluids, Vol. 18, No. 3, March 1975.

and settled to levels of neutral buoyancy within the density gradient region. Flow visualization was further aided by the use of vertical dye lines which were created by dropping nigrosine dye crystals upstream of the approaching vertical flat plate. Flow velocities were determined from displacements of the particles and dye lines as recorded on photographs taken in rapid sucession at accurately measured time intervals. Density profiles were measured before and after each run with a conductivity probe. These profiles were fitted to Benjamin's expression,[3] $\rho = \overline{\rho}(1 - \overline{\omega} \tanh \alpha z)$, where $\overline{\rho} = \frac{1}{2}$

TABLE 1. Comparison of Benjamin's predictions for internal solitary-wave speed with experimental measurements.

$\overline{\omega}$	α (cm^{-1})	$C_{sw}^{o} = (\frac{g\overline{\omega}}{2\alpha})^{\frac{1}{2}}$ (cm/sec)	Measured amplitude a (cm)	Measured wave speed C_{sw} (cm/sec)	calculated wave speed C_{sw} [Eq. (1)] (cm/sec)
0.00771	0.50	2.75	2.5	3.73	3.64
0.00771	0.48	2.81	0.6	2.95	3.04
0.01417	2.44	1.69	1.5	3.18	3.02
0.01417	1.09	2.52	2.8	4.75	4.24
0.01417	0.73	3.08	1.8	4.11	4.12
0.01417	0.65	3.27	1.3	4.06	4.01
0.01408	0.32	4.64	0.0	4.62	4.64
0.01408	0.31	4.72	0.0	4.65	4.72
0.01408	0.30	4.80	0.6	5.02	5.50
0.01408	0.29	4.88	0.6	5.05	5.13

$(\rho_u + \rho_l)$ is the average density of the upper and lower layers; $\overline{\omega} = (\rho_l - \rho_u)/(\rho_l + \rho_u)$; α is a number determined by a least-squares fit whose reciprocal is a measure of the gradient-layer thickness, and z is the height above the level at which $\rho = \overline{\rho}$.

The flow field upstream of the vertical flat plate exhibited two separate phenomena. At the front of the upstream disturbance an internal solitary wave of the type predicted by Benjamin and observed by Davis was always present. Behind the solitary wave was a region of upstream influence. The solitary wave, which was generated by the impulsive start of place motion was a distinct phenomenon from the upstream influence and did not appear to interact with it.

Benjamin[3] predicted that for a region whose density profile is described by $\rho = \overline{\rho}(1 - \overline{\omega} \tanh \alpha z)$, an infinitesimal solitary wave of the first mode would propagate with the speed $C^0_{sw} = (g\overline{\omega}/2\alpha)^{1/2}$. A wave with finite amplitude a is predicted to propagate with speed.

$$C_{sw} = C^0_{sw} (1 + \frac{3}{5} \alpha a)^{\frac{1}{2}}. \qquad (1)$$

In the present study, the speed C_{sw} could be obtained accurately from the slope of a straight line determined by a least-squares fit of photographicly recorded wave positions and elapsed times. Thus, it was possible to compare Benjamin's theory with experimental results by measuring the observed solitary wave amplitudes, using Eq. (1) to predict wave speeds, and comparing these predictions with experiment. For the purpose of these measurements, the amplitude was defined as the maximum vertical displacement of the streamline at $z = \alpha^{-1}$. The results of the compariosn are presented in Table 1. Considering the crudeness of the experimental amplitude measurements, the agreement between the last two columns of Table 1 is quite good.

A correlation between the dimensionless amplitude αa and the dimensionless group $\lambda = (g/2\alpha c^2_{sw}) \ell n(\rho_i/\rho_u)$ is predicted by Davis' theory.[4,5] Moreover, for small values of αa, the relation $\lambda = 2.0 - 1.2 \alpha a$ is predicted to be a good approximation to this correlation. Figure 1 is a plot of λ vs αa for the solitary waves observed in the present study. The theoretical predictions of both Davis and Benjamin are plotted in the same figure. The agreement between

these theories and the results of the present experiment is good. Since the theories have nothing to do with upstream in luence, this agreement indicates that the observed solitary waves were generated by the impulsive start of plate motion and were independent of the existence of upstream influence.

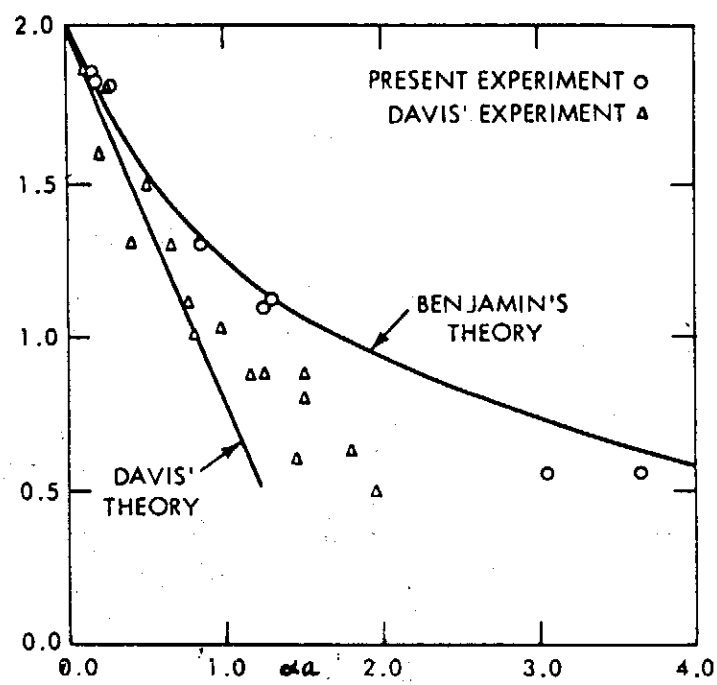

FIG. 1. Correlation of the parameter λ with the dimensionless amplitude αa for observed solitary waves and theoretical predictions of Benjamin and Davis.

In conclusion, the behavior of the internal solitary waves observed in this study was found to be in good agreement with the theories of Benjamin and Davis. For larger amplitudes the experimental results appear to agree more closely with the predictions of Benjamin's theory than with those of Davis' theory.

This research was conducted at the Catholic University of America in partial fulfillment of the requirements for the Ph. D of one of the authors (D. A. H.).

The authors acknowledge with gratitude the support of this research by the National Science Foundation under Grant GA-23784 and the Office of Naval Research under Contract N00014-67-A-0377-0027.

[1]T. B. Benjamin, J. Fluid Mech. 40, 49 (1970)

[2]D. A. Hurdia, Ph. D. thesis, The Catholic University of America (1973).

[3]T. B. Benjamin, J. Fluid, Mech. 29, 559 (1967).

[4]R. E. Davis, Ph. D. thesis, Stanford University (1967).

[5]R. E. Davis and A. Acrivos, J. Fluid, Mech. 29, 593 (1967).

ANNAUL REPORT OF THE INSTITUTE OF PHYSICS,
ACADEMIA SINICA, 1974

Dynamics of Establishment of Selective Withdrawal of A Stratified Fluid From a Line Sink. Part 1. Theory

*

By Hsien-Ping Pao and Timothy W. Kao

Department of Aerospace and Atmospheric Sciences,
The Catholic University of America, Washington, D.C. 20017

(Received 30 August 1973 and in revised form 4 R arch 1974)

An investigation is made of selective withdrawal of a linear stratified fluid from a line sink in a channel of depth d. The flow is characterized by a densimetric Froude number $F = Q/Nd^2$, where Q is the discharge per unit width and N is the Väisälä frequency. The dynamics of establishment of flow are investigated theoretically. Analytic results are obtained from a linearized theory based on a systematic perturbation scheme for small values of F. These results lead to a proper identification of the successive arrival of 'columnar distrubance modes' as the mechanism responsible for the development of flow concentration in the withdrawal region. Viscous and diffusive effects are also examined. For larger times and higher discharges (higher values of F), nonlinear effects become important, and the full Navier-Stokes equations are now solved numerically by a finite-difference procedure in a 'stretched' co-ordinate system. The solutions indicate that the establishment of the steady flow field is due to the successive arrival and interaction of 'columnar disturbance modes'. Steady-state solution are also presented, and a similarity profile is obtained. Comparison of the theoretical findings with experimental results are presented in part 2. Agreement with experimental measurements is found to be excellent.

1. Introduction

The main characteristic that distinguishes a stratified medium in

a gravitational field from a homogeneous medium is its ability to sustain internal gravity waves and flow concentrations. This has been observed in nature, it has wide-spread geophysical implications, and it is of fundamental importance for fluid mechanics. That this is so for water quality management is shown by the 'selective withdrawal' of water in a reservoir (Wunderlich & Elder 1971; Wunderlich 1971). In deep lakes or reservoirs, seasonal change in solar radiation is the cause of density stratification from spring to late autumn. Solar heating, aided by mixing due to surface winds, penetrates downward, to establish a warm upper layer (the epilimnion), followed by a transition layer (the metalimnion or thermocline), which leads to the lower dense cold region (the hypolimnion). In north temperate lakes (such as Cayuga lake in upper New York state), the hypolimnion is thick, whereas, in more southern lakes or reserviors (such as those in the Tennessee Valley Authority (TVA) river basin system), the metalimnion is thick and shows an almost linear increase in density with depth. When outflow is withdrawn from density-stratified reserviors, the water comes mainly from zones at elevations corresponding approximately, in hydroelectric dams, to the level of the intake openings leading to the turbine penstocks. This is selective withdrawal. The various water quality parameters (such as temperature, dissolved oxygen (DO), foreign mineral contents, etc.) are interrelated with the density and advected by the withdrawal current. Thus, selective withdrawal has a long-range effect on the environment, especially on the quality of drinking water and on aquatic life, in both the reservoir and its downstream river (Wunderlich & Elder 1968). It has been reported (Sport Fishing U.S.A., 1971, Government Printing Press) that the population of some warm-water species declines drastically after a dam begins to release cold water from the lower layers of its reservoir. Further-more, when a hydroelectric power plant operates

as a peaking plant, the quality and quantity of discharge in the downstream river also undergo periodic variation.

In the present study, selective withdrawal from a line sink is investigated in terms of the dynamics of establishment. In part 1 we present analytic results from a linearized theory, and numerical solutions of the full nonlinear governing equations. In part 2 (Kao, Pao & Wei 1974) we make comparisons between experimental data and the relevant theoretical, numerical and field results. The emphasis is on the nature of the propagation of disturbances, the development of the flow field, and the final steady-state velocity field.

The analysis of the flow of a linearly stratified fluid into a horizontal line sink was first made by Yih (1958), who obtained the exact steady-state solution, valid for $\pi^{-1} < F < \infty$, where F is the densimetric Froude number Q/Nd^2 (Q is the discharge rate per unit width, d is the depth of the channel, the Väisälä frequency $N = (\kappa g)^{\frac{1}{2}}$, and $\kappa = -(1/\rho_0)\, d\bar{\rho}/dZ$ is the slope of the density variation far upstream, (a constant). Yih assumed the velocity and density to be undisturbed far upstream, so that no solution was obtained for $F < \pi^{-1}$. Debler (1959) then showed by experiment that $F \sim \pi^{-1}$ is indeed a critical Froude number, above which Yih's solution is valid, and below which the flow separates into a flowing region near the level of the sink, the fluid remaining essentially stagnant elsewhere (i.e. selective withdrawal occurs). *Debler also found that the densimetric Froude number F_1, based upon the depth of the flowing zone, remained essentially constant, having a value of 0.28 for various discharges. By introducing a free stream-line which separates the flowing zone from the completely stagnant regime, Kao (1965, 1970) obtained a family of solutions corresponding to $\pi - 1 < F_1$

*The analogous phenomenon of selective withdrawal in rotating fluids was studied by Pao & Kao (1969), Shih & Pao (1971) and Pao & Shih (1973).

$< \infty$ for any given discharge rate. Kao (1970) gave $F_1 = 0.33$ as the unique Froude number for all separated flows. In his solution, the thickness of the flow zone remains constant with distance upstream, as a consequence of the invisicd assumption. Koh (1966a) obtained a steady-state solution for an infinite medium, incorporating viscous and diffusive effects and neglecting the nonlinear terms. His solution predicts that the growth rate of the thickness of the flowing zone is proportional to $X^{\frac{1}{3}}$, where X is distance from the sink. By partitioning the flow into inner and outer regimes, and using the outer flow as the upstream boundary condition for his inner flow equations, Imberger (1972) obtained a steady-state solution, which improved Koh's prediction about the thickness of the flowing zone, by requiring that the flowing zone be thick enough to achieve Kao's value near to the sink. These studies were all concerned with the steady-state problem, so that the dynamics of establishment were not investigated. Trustrum (1964) solved a linearized initial-value problem based on the Boussinesq and Oseen approximations, and obtained an asymptotic solution for large times, valid for $F > \pi^{-1}$. The approximations involved, however, invalidated her solutions for $F < \pi^{-1}$. Koh (1966b) also solved a linearized initial-value problem for a skin in an infinite medium. His solution predicted an increase in the horizontal velocity towards the sink with time along the horizontal plane containing the line sink. But this increase is felt instantaneously at all distances away from the sink, by an amount inversely proportional to the radial distance from the sink, which is physically unrealistic. The time-dependent behaviour of stratified flow into a line sink is therefore largely unexplored. To trace the actual history of flow establishment, an initial-value problem is solved, and solutions obtained for various times. For low values of F, a linearized invisicd problem, obtained by a systematic perturbation scheme, is solved analytically. Viscous and diffusive effects are also examined. For larger F, nonlinear interactions become important, and the full Navier-Stokes equations are solved numerically. The solutions in-

dicate that the establishment of the steady flow field is due to the successive arrival and interaction of columnar disturbance modes. Steady-state numerical solutions are also found. A similarity velocity profile is obtained.

References

Debler, W. E. 1959 Stratified flow into a line sink. J. Eng. Mech. Div., Proc. A.S.C.E. 85, 51-65.

Imberger, J. 1972 Two-dimensional sink flow of a stratified fluid contained in a duct. J. Fluid Mech. 53, 329-349.

Kao, T. W. 1965A free-streamline solution for stratified flow into a line sink. J. Fluid Mech. 21, 535-543.

Kao, T.W. 1970 Free-streamline theory for inviscid stratified flow into a line sink. Phys. Fluids, 13, 558-564.

Kao, T.W., Pao, H.-P. & Wei, S.N. 1972 Time dependent behaviour of stratified flow in a channel towards a line sink. Int. Symp. Stratified Flow, IAHR, Novosibirsk.

Kao, T.W., Pao, H.-P. & Wei, S.N. 1974 Dynamics of establishment of selective with-drawal from a line sink. Part 2. Experiment. J. Fluid Mech. 65, 689.

Koh, R.C.Y. 1966a Viscous stratified flow towards a sink. J. Fluid Mech. 24, 555-575.

Koh, R.C.Y. 1966b Unsteady stratified flow into a sink. J. Hydraulic Res. 4, 21-35.

Pao, H.-P. & Kao, T.W. 1969 Sources and sinks at the axis of a viscous rotating fluid, Phys. Fluids, 12, 1536-1546.

Pao, H.-P. & Shih, H.H. 1973 Selective withdrawal and blocking wave in rotating fluids. J. Fluid Mech. 54, 459-480.

Shih, H.H. & Pao, H.-P. 1971 Selective withdrawal in rotating fluids, J. Fluid Mech, 49, 409-527.

Torrance, K.E., & Rockett, J.A. 1969 Numerical study of natural

convection in an enclousre with localized heating from below: creeping flow to the onset of laminar instability. J. Fluid Mech. 36, 33-54.

Trustrum, K. 1964 Rotating and stratified fulic flow. J. Fluid Mech. 19, 415-432.

Wunderlich, W. O. 1971 The dynamics of density-stratified reservoirs. American Fisheries Soc. Special Publication on Reservoirs.

Wunderlich, W.O. & Elder, R.A. 1968 Evaluation of Fontana Reservoir field measurements, A.S.C.E. Speciality Conf. Current Res. into Effects of Reservoirs on Water Quality, Portland, Oregon.

Wunderlich, W.O. & Elder, R.A. 1971 Mechanics of flow through man-made lakes. Symp. on Man-made Lakes, their Problems and Environmental Effects, Knoxville, Tennessee.

Yih, C.-S. 1958 On the flow of a stratified fluid. Proc. 3rd U.S. Nat. Cong. Appl. Mech., pp. 857-861.

Yih, C.-S. 1965 Dynamics of Nonhomogeneous Fluids. Macmillan.

Dynamics of Establishment of Selective Withdrawal of a Stratified Fluid from a Line Sink. Part 2. Experiment*

By Timothy W. Kao, Hsien-Ping Pao
and
Shuang N. Wei

The Department of Aerospace and Atmospheric Science,
The Catholic University of America, Washington, D.C. 20017

* This paper has been published in J. Fluid Mech. (1974), Vol. 65, part 4, pp. 689-710.

Experiments were conducted to examine the development and establishment of the withdrawal current in the selective withdrawal of a stratified fluid from a line sink. The experiments were performed in a Plexiglas channel 30.5 ft long 14 in. wide, and filled with a linearly stratified salt solution to a depth of 18 in. The line sink was located at mid-depth. The flow was symmetric about the mid-depth. Velocity measurements and flow visualization were obtained by neutrally buoyant liquid droplets and vertical dye lines. Density measurements were made by a salinity probe. The development of the upstream velocity field was found by measurement to be brought about by the successive arrival of 'columnar disturbance modes', discussed in part 1. Agreement with the theroetical predictions is excellent. A similarity profile of the steady-state horizontal velocity is obtained, and the Froude number based on the thickness of the flowing zone is found to approach a constant value in the essentially inviscid reginn. The results are compared with field data from the Tennessee Valley Authority (TVA) reservoirs.

1. Introduction

In part 1 (Pao & Kao 1974), a theory was presented which identifies the successive arrival and nonlinear interactions of columnar

disturbance modes as the mechanism for the development and establishment of the withdrawal layer in the selective withdrawal of a stratified fluid from a line sink in a channel of finite depth 2d. The mean density $\bar{\rho}(Z)$ varies linearly with height. In this paper, careful experiments to verify quantitatively the theoretical findings, and to complete the full understanding of the dynamics of establishment of the flow are reported. As mentioned in part 1, the governing parameter of the problem is the Froude number F, defined as Q/Nd^2, where 2Q is the discharge per unit width, and the Väisälä frequency

$$N = \left(-\frac{g}{\rho_o}\frac{d\bar{\rho}}{dZ}\right)^{1/2}, \quad \rho_o = \bar{\rho}(0), \quad z = Z/d.$$

The experiments were performed in a Plexiglas channel 30.5 ft long, 2ft high and 14 in. wide, filled with a linearly stratified salt solution to a depth of 18 in. The line sink was located at mid-depth. The fluid was initially at rest, and the discharge was started suddenly. The flow field at any subsequent time was perfectly symmetric about the mid-depth centre-line. Thus, the half-depth of the fluid was taken as d. Velocity measurements were obtained by neutrally buoyant liquid droplets, and density measurements were made by a salinity probe. Flow visualization was also obtained by vertical dye lines.

The results show clearly the following sequence of events after the initiation of the discharge: instantaneous establishment of potential flow in the whole flow field, arrival of jet-like columnar disturbance at upstream stations, development and intensification of the withdrawal layer, establishment of steady-state velocity profile with fully stagnant fluid outside the withdrawal layer. Quantitative measurements are obtained at each stage of the development and show excellent agreement with the theoretical findings of part 1.

In the steady state, a similarity profile of the horizontal velocity is obtained, and the Froude number based on the thickness of the

flowing zone is found to approach a constant value in the essentially inviscid region. The results are compared with the steady-state results of part 1, with the steady-state theories of Kao (1965, 1970), Kao (1966) and Imberger (1972), as well as with the experiment of Debler (1959). Applications of the results to selective withdrawal from density-stratified reservoirs are also indicated.

References

Debler, W.R. 1959 Stratified flow into a line sink. J. Eng. Mech. Div., Proc. A.S.C.E., 84,51-65.

Imberger, J. 1972 Two-dimensional sink flow of a stratified fluid contained in a duct. J. Fluid Mech. 53, 329-349.

Kao, T.W. 1965 A free-streamline solution for stratified flow into a line sink. J. Fluid Mech. 21, 535-543.

Kao, T.W. 1970 Free-streamline theory for inviscid stratified flow into a line sink. Phys. Fluids, 13, 558-564.

Koh, R.C.Y. 1966 Viscous stratified flow towards a sink, J. Fluid Mech. 24, 555-575.

Pao, H.-P. & Kao, T.W. 1974 Dynamics of establishment of selective withdrawal of a stratified fluid from a line sink. Part 1. J. Fluid Mech. 65, 657.

Wunderlich, W.O. & Elder, R.A. 1968 Evaluatino of Fontana Reservoir field measurements. A.S.C.E. Specialty Conf. on Current Research into Effects of Reservoirs on Water Quality, Portland, Oregon.

ANNUAL REPORT OF THE INSTITUTE OF PHYSICS,
ACADEMIA SINICA, 1974

旋流與層流動力學

鮑咸平　主講　　王時鼎　記述

Dynamics of Rotating and Stratified Fluids

Lectured by H. P. PAO
Noted by S. T. WANG

ABSTRACT

This paper deals with some special aspects of the dynamics of rotating and stratified fluids. Emphasis is on the selective withdrawal of stratified fluids. Both the theorectical and experimental studies are worked out with the results showing that the successive arrival of "columnar disturbance modes" are the mechanism responsible for the developmen of flow concentration in the withdrawal region (selective withdrawal.) In addition, some common features of rotating and stratified fluidis are also discussed.

大氣與海洋均係密度隨高度變化，$\rho(Z)$，即：屬於密度成層流體（Stratified fluid）。至於此處何以將旋流（Rotating fluid）與層流作爲共同討論對象，乃因兩者 —重力場中密度分層（Stratified）流體與加速或稱旋轉流體 —之動力學有甚多類似性質，若干現象且爲一一對應。且兩種流體中，某一方面的發展，常可應用於另一方面。其類似性質，如：

(1)兩種流體均可維持（Sustain）波動

(A)在層流中，因密度分層而造成重力波（gravity waves）（註一）（參見圖一）。

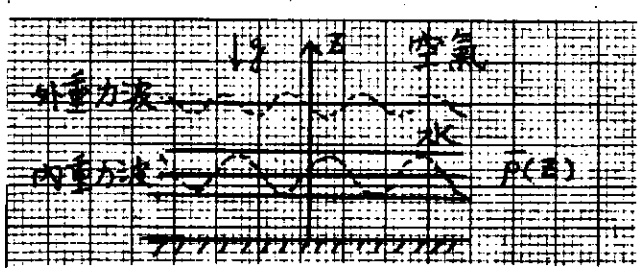

圖一、在層流中，因密度分層而造成之重力波

* 鮑咸平博士爲 The Catholic University of America, Washington, D.C. 太空與大氣科學系教授。本文係民國 62 年 8 月返國參加經建會議期間，應氣象學會之請於 8 月 22 日發表之講詞。

本文曾發表於「氣象預報與分析」（六十三年五月出版，第五十九期）

(B)在旋流中，因離心力作用可造成離心波或稱慣性波（Centrifugal waves or Inertial waves）（註二）。（參見圖二）。

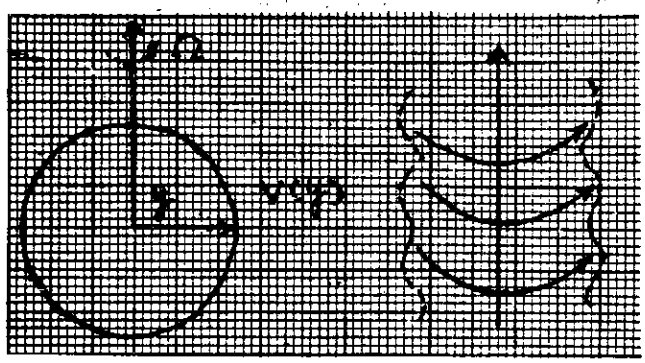

圖二、在旋流中因離心力作用造成之離心波或稱慣性波

(2)當佛路德數（Froude number）甚小之時，兩種流體均可造成流速集中呈激流狀態（Velocity concentration in the form of jet），或稱選擇流出（Selective withdrawal）（參見圖三）。而本文主要即係討論層流及旋流中選擇流出之動力學。

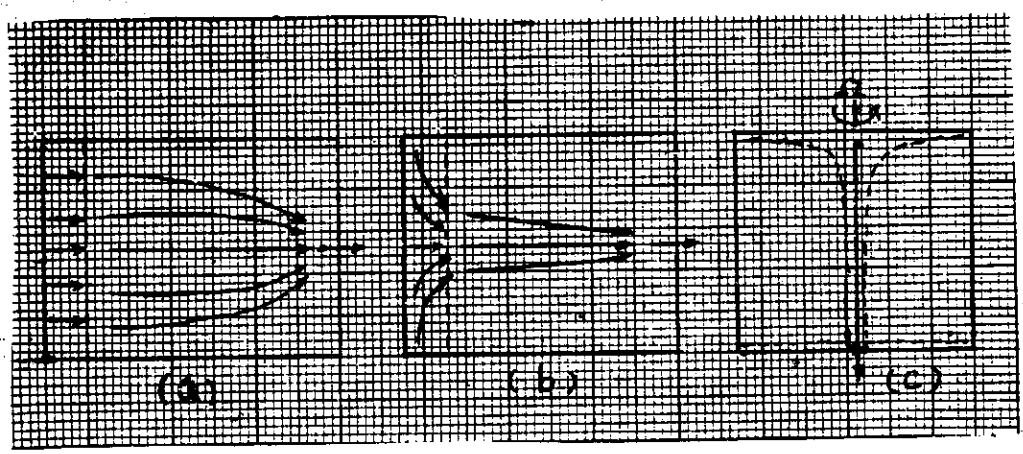

圖三、層流與旋流內速度集中所造成之選擇流出（Selective withdrawal）
(a),(b)層流中情形(c)施號中情形

有關「選擇流出」現象，近年來極引人注意，特以蓄水庫或水壩爲尤然。因當水之流出（Sink）不大時，常可形成速度集中而選擇排出。至其他部份即呈滯留或阻滯現象（Stagnation or blocking），造成水污染，直接或間接影響魚殖或危害人類。注意上述現象並非一般流動均有，乃係僅出現於密度分層之流體中。而實際上如水壩蓄水因日射引起之上下溫差每可造成垂直密度差異而成層流（Stratified fluid）形式。有關類此「選擇流出」現象與佛路德數（Froude number F）有關，其條件爲：

$$F = \frac{U}{Nd} > \frac{1}{\pi} \simeq 0.318$$

此處：U與d如圖四中所示，U爲上游未經擾動之均勻流動，d爲流體厚度，N爲Brunt Väisälä 週率。

$$\left(N = \sqrt{\frac{-\frac{d\rho}{dz} g}{\rho_o}}, \ (sec^{-1}) \right)$$

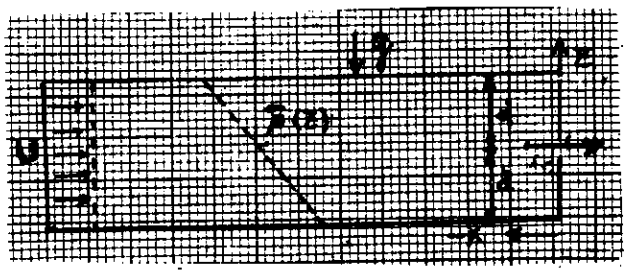

圖四、層流佛路德數（Froude number）中各參數值之決定

如爲均勻流體，ρ不變，N = 0。特以F小時，N值特爲重要。如當層流中，$F > \frac{1}{\pi}$，或旋流中，Ro > 0.261（Ro = Rossby number），即無「速度集中」或「選擇流出」發生。此處：

$$Ro = \frac{U}{2\Omega b} > 0.261$$

式中U爲未經擾動之均勻速度，b爲半徑，Ω爲旋流之轉動角速度（參見圖五）。

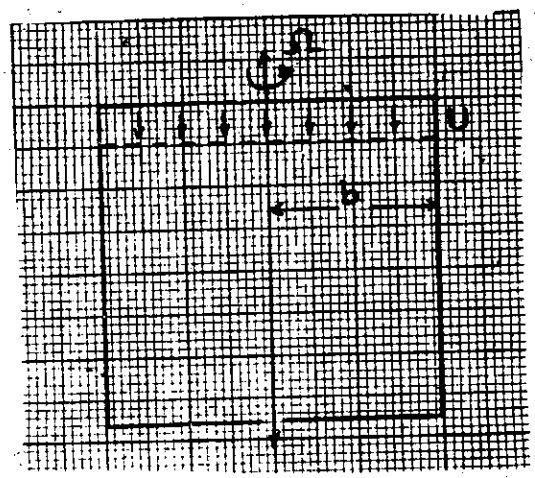

圖五、旋流洛士貝數（Rossby number）中各參數值之決定

圖五旋流中之Ω，即相當於層流中之N。實際N相當於2Ω（註三）。N及Ω愈大，速度之集中亦愈大。又U小時爲線性問題（Linear Problem），U大時爲非線性問題（Non-linear Problem）。

當層流中 $F > \frac{1}{\pi}$，及旋流中 Ro > 0.261 時，將無「速度集中」現象發生。前者業經C.S. Yih（易家訓，國人），及後者業經R. Long 於理論與實驗中證實（另有關層流研究與旋流研究，可參看所列參考文獻(1)(2)(3)）。而於：

$$F < \frac{1}{\pi} \simeq 0.318$$

$$Ro < 0.261$$

情形下出現「速度集中」或稱「選擇流出」乃係講者等(1)(2)(3)(4)(5)(6)(7)(8) 研究求得。其實驗結果與理論推釋；甚爲一致。因Ro = 0.261，或F < 0.318時，流動速度小，黏性效應變爲甚相重要。而Yih及Long所建立之控制方程系，未考慮黏性作用（Viscous effects），故不能應用於上述兩臨界條件內流體之運動。

以下所述爲有漏（Sink）時，層流中擾動（Disturbances）發生之情形。

開始時流體爲靜止，而後在「漏」（Sink）處突然開始流出（Discharge），致在「漏」處造成擾動（Disturbances）。其在擾動係向上游傳播，即：與基本流動之流向相反。擾動之模（Modes），略如圖六所示。

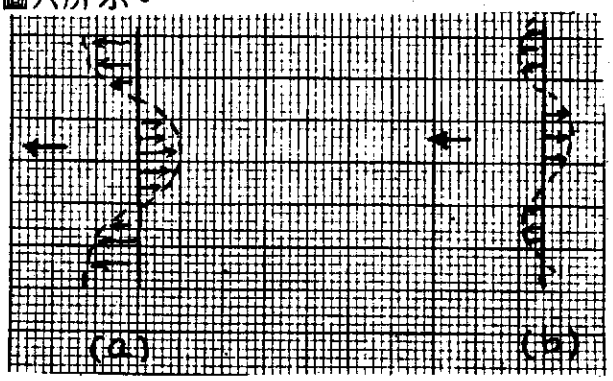

圖六、層流有漏（Sink）情形下，各擾動之模（Modes）型式及運動舉例。(a)第一模，(b)第二模。

各不相同之模式均以不同速度向上游傳播，惟波動模式愈高，其波速愈小，各模之速度如下：

$$\text{第一模者爲 } C_0 = \frac{Nd}{n\pi} = \frac{Nd}{\pi} \quad (n = 1)$$

$$\text{第二模者爲 } C_1 = \frac{Nd}{n2\pi} = \frac{1}{2} Co \quad (n = 2)$$

$$\text{第三模者爲 } C_2 = \frac{Nd}{n3\pi} = \frac{1}{3} Co \quad (n = 3)$$

$$\vdots$$

故較高之擾動模式，因其移速將較流體流動速度爲小，致無法越過而向上游傳播（註五），其擾動發生及造成選擇流出（Selective withdrawal）之程序略如下述：

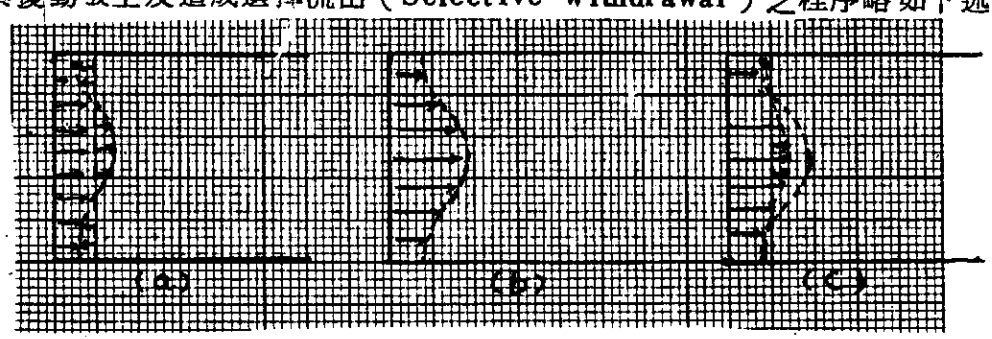

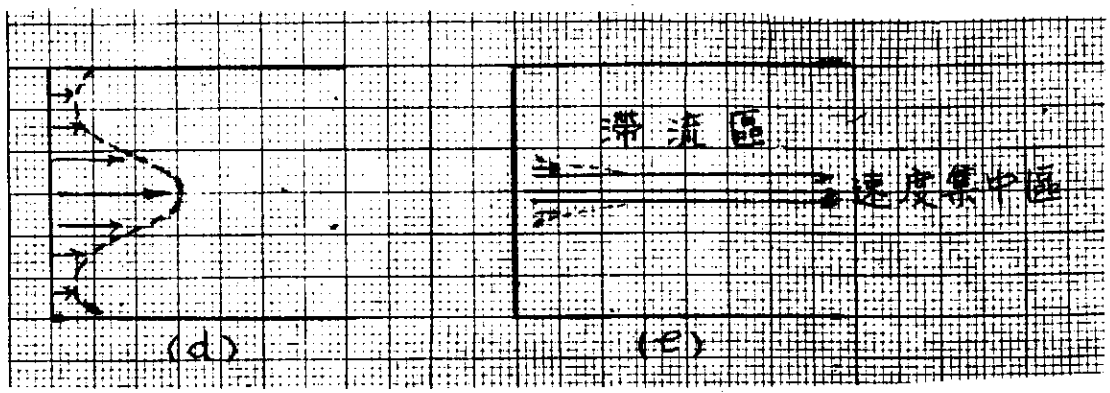

圖七、層流有漏（Sink）情形下，各擾動向上游傳播之情形。(a)受第一模影響時；(b)受第一模影響後之流速剖面；(c)受稍後移至第二模影響時，(d)受第二模影響後之流速剖面；(e)受向上游傳播各模次第影響下，最後在穩定狀態時之流速剖面。沿流軸之處造成速度之集中，兩側則爲滯流區(Stagnant Zone)

第一階段：流體排出（Discharge）開始。此瞬時之所有流場爲非旋轉流動或稱位流（Irrotational or potential flow），流動均勻一致，見圖七a。

第二階段：因「漏」處擾動各「模」，連續向上游傳播，及各「模」間非線性之交互作用，漸造成如激流形式（Jet-like）之擾動，見如圖七b，c，d。圖七b爲第一模（參見圖六a）到達時之流場剖面。圖七c爲第二模隨後到達時之流場剖面。圖七d爲第一及第二模到達並交互作用後之合成剖面圖。藉圖七d可見，激流式之擾動更見增強。

第三階段：由於各連續擾動之模次第向上游傳播及匯聚而造成沿「漏」軸上之顯著速度集中帶，亦即選擇流出層（Selective withdrawal layer）。

第四階段：穩定狀態（Steady-state）速度剖面之建立。在選擇流出層兩側造成完全之滯流區。佛略德數，F，愈小，滯留區範圍愈大。

於旋流情形下，「選擇流出」現象與層流情形相若。其出現係在洛士貝數（Rossby number）甚小之時，（$Ro < 0.261$）。此時流出流量大於上游流心（flowing cone）中之流量。故實際在艾克曼邊界層中亦同時有流體排出。（參見圖三c）。

以下爲鮑咸平博士對本問題藉幻燈片所作之部份介紹：

(1)層流中「選擇流出」動力學

對二維不可壓縮，無黏性及無擴散流體，控制方程式包括X、Z軸之兩運動方程，連續方程，及不可壓縮方程，並經Boussinesq近似化之形式，因變數爲u^*，w^*，P，ρ'。分別爲

$$\rho_0 \left(\frac{\partial u^*}{\partial t} + u^* \frac{\partial u^*}{\partial x} + w^* \frac{\partial u^*}{\partial z} \right) = - \frac{\partial P}{\partial x} \qquad (1)$$

$$\rho_0 \left(\frac{\partial w^*}{\partial t} + u^* \frac{\partial w^*}{\partial x} + w^* \frac{\partial w^*}{\partial z} \right) = - \rho' g \frac{\partial P}{\partial Z} \tag{2}$$

$$\frac{\partial w^*}{\partial x} + \frac{\partial w^*}{\partial z} = 0 \tag{3}$$

$$\frac{\partial \rho'}{\partial t} + u^* \frac{\partial \rho'}{\partial x} + w^* \frac{\partial \rho'}{\partial z} = 0 \tag{4}$$

式中 $\rho' = \overline{\rho}(Z) + \rho^*(x, z, t)$ (5)

$$\overline{\rho} = - \frac{\rho_0 - \rho_s}{d} (Z - d) + \rho_s \tag{6}$$

藉上各式消去氣壓並代入氣流函數 $u^* = \frac{\partial \Psi^*}{\partial z}$ ，$w^* = - \frac{\partial \Psi^*}{\partial x}$ 後得控制方程式：

$$\frac{\partial}{\partial t} \Delta^* \Psi^* + \frac{\partial \Psi^*}{\partial z} \frac{\partial}{\partial x} \Delta^* \Psi^* - \frac{\partial \Psi^*}{\partial x} \frac{\partial}{\partial z} \Delta^* \Psi^* = \frac{g}{\rho_0} \frac{\partial \rho^*}{\partial x} \tag{7}$$

$$\frac{\partial \rho^*}{\partial t} + \frac{\partial \Psi^*}{\partial Z} \frac{\partial \rho^*}{\partial x} - \frac{\partial \Psi^*}{\partial x} \frac{\partial \rho^*}{\partial Z} = - \frac{\rho_0 - \rho_s}{d} \frac{\partial \Psi^*}{\partial x} \tag{8}$$

將(7)(8)兩式標準化，並以 Ψ ，$NQ\rho_0/gd$ ，d ，$1/N$ 及 $U = Q/d$ 爲相應特性氣流線函數，密度，長度，時間與速度標尺（非一般性符號已各見文中所述）。經標準化後，上述(7)、(8)可寫爲：

$$\frac{\partial \Delta \Psi}{\partial t} + F \left(\frac{\partial \Psi}{\partial Z} \frac{\partial}{\partial x} \Delta \Psi - \frac{\partial \Psi}{\partial x} \frac{\partial}{\partial Z} \Delta \Psi \right) = \frac{\partial \rho}{\partial x} \tag{9}$$

$$\frac{\partial \rho}{\partial t} + F \left(\frac{\partial \Psi}{\partial Z} \frac{\partial \rho}{\partial x} - \frac{\partial \Psi}{\partial x} \frac{\partial \rho}{\partial Z} \right) = - \frac{\partial \Psi}{\partial x} \tag{10}$$

(9)(10)爲因變數與之完全方程式。

經線性化（引入 F 之微擾級數）得 0 次（Zeroth order）Ψ^0 與 ρ^0 之控制方程式爲：

$$\frac{\partial^2}{\partial t^2} \Delta \Psi^0 + \frac{\partial^2 \Psi^0}{\partial x^2} = 0 \tag{11}$$

$$\frac{\partial^2}{\partial t^2} \Delta \rho + \frac{\partial^2 \rho^0}{\partial x^2} = 0 \tag{12}$$

引入邊界及起始條件，並藉以下表明式代入 $\Psi = \Psi^0 - ZH(t)$ (12)

（H(t)爲Heaviside unit step function）並經較複雜數學處理而求得(11)式之解爲：

$$\Psi^0(x, y, z) = Z + \sum_{n=1}^{\infty} \frac{2}{n\pi} \sin n\pi \, ZH(n\pi x + t) \tag{13}$$

此結果明顯指示擾動各不同之「模」（Modes），一如波動係以速度 $Cn = \frac{1}{n\pi}$ 移行。改爲有因次形式爲：$Cn = \frac{Nd}{n\pi}$ (14)

（n = 1，2，3 n=1 表第一模）

⋮

此如波動狀之擾動模式被稱爲圓柱擾動（Columnar disturbances）或稱頻率爲零之圓柱狀波動（Columnar waves of zero frequency），因其係以呈水平狀激流柱（Horizontal jet-like Columns）之形式。有關層流中「選擇流出」理論僅簡介至此爲止。

以下爲藉上述理論及實際試驗所得某些結果之介紹（講演時係用幻燈片）。

圖八所示爲在不同時間 t ，在 x=-0.4 處（此處 $x=\frac{X}{a}$，t 係實際時間除以 N^{-1}，均爲無因次者。負號表上游方向，d 表流體厚度）之水平速度之垂直剖面。各曲線爲藉理論得出者。至各時間之實驗所得數值各以中空之圓形，三角形及正方形表示。圖中縱標爲 $Z=\frac{Z}{d}$，橫標爲 $\frac{u}{U}$（其中 $U=\frac{Q}{d}$，u 爲各點之實際水平流速）。藉圖可見在「漏」處，亦即 Z=0 處，流速係隨時間而急劇增加；至其側，流速則隨時間而減小至 0 值或至負值，而呈明顯之激流（jet-like）形式。另外，可見理論所得與實驗結果，甚爲一致。

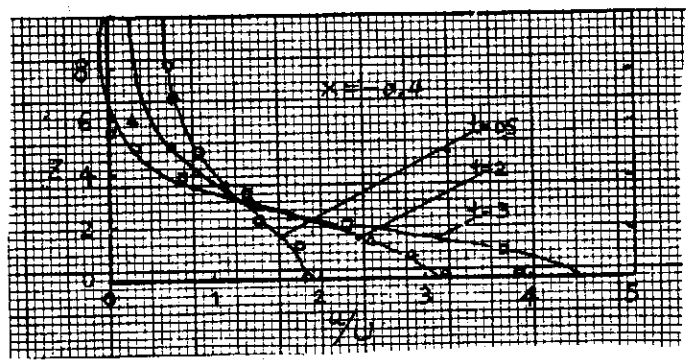

圖八、在不同 t 時，在 x=-0.4 處水平速度之垂直剖面。「——」表理論所得結果，於 F=0.0143 時之實驗結果各如下述符號所示：Δ（t=2.04），□（t=3.15），及 F=0.062時：○（t=0.5）。

Figure 8. Horizontal velocity profile at x =.-0.4 for various t; —analytic theory; experiment for F=0.0143 : Δ(t=2.04),□(t=3.15) and F=0.062 :○(t=0.5)

圖九爲在沿「漏」處中心軸上不同距離之水平速度 Um 隨時間分佈，示各波動之「模」（Modes）連續匯合之情形。圖中實線之曲線爲根據 Navier Stokes 運動方程之數值解答，另各種符號（如圓形，三角形等）代表實驗所得結果。本例係代表 F=0.0143，及雷諾數（Reynolds number），Re=625 時之情形。在此甚低之佛路德數下，吾人可清晰見出各波動之「模」，次第到達上游，彼此聚合，並加強水平速度。例如在 x=−3 處，吾人可見五個波「模」，並造成五相對之最高 Um 值。各較高之「模」，由於黏性及非線性交互作用影響，並未到達其應有最強之值。例如，當運動黏性 $\nu=10^{-8}ft^2/sec$，1/N=1.75 sec 時，第五模之波幅被減少一 e^{-1} 之比例值，較高之模削減更甚，故對速度場之進一步發展

甚少助力。

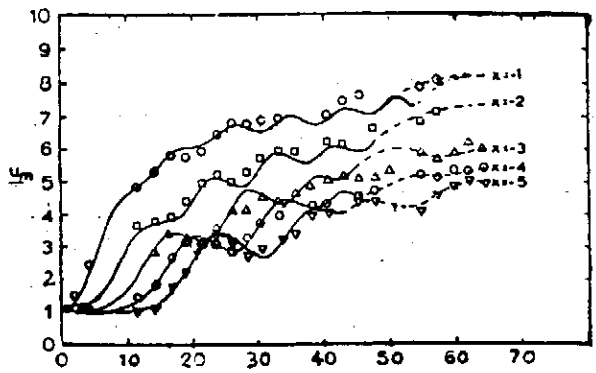

圖九、在不同 x 處，中心線上速度（Um）隨時間增大增形，「——」表數值解答，「……」實驗所得各點之連線；F = 0.0143 Re = 625，○（x = −1），□（x = −2），Δ（x = −3），⬡（x = −4），▽（x = −5）。

Figure 9. Growth of center-line velocity with time at avrious x; —— numerical solution, ---- connection of experimental points; F=0.0143, Re=625 ○ (x = −1), □ (x = −2), Δ (x = −3), ⬡ (x = −4), ▽ (x = −5),

圖十爲 F = 0.106，Re = 3440 時之情形。佛路德數愈大，非線性作用（Non- linear effects）愈見重要，故到達穩定之狀態愈早。在圖九之高佛路德數下，僅兩波「模」能向上游傳播，非線性作用至強，第一模之強度仍與解係之解答相若。非線性作用顯似已壓制其他各「模」。

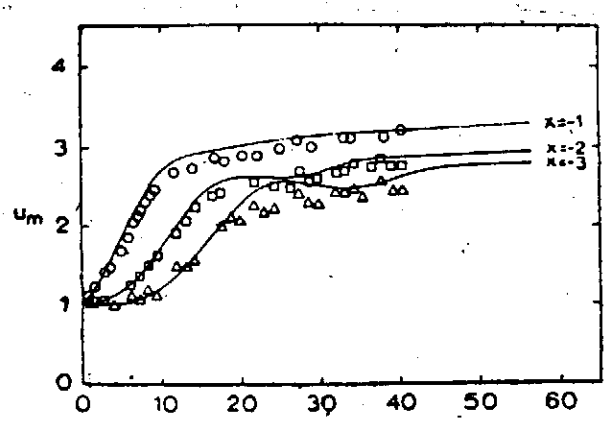

圖十、在不同 x 處，中心線上速度（Um）隨時間增大情形，F = 0.106，Re = 3440：○（x = −1），□（x = −2）Δ = （x = −3）。

Figure 10. Growth of center-line velocity with time

various x; ——numerical solution, F=0.106;
○(x=−1), □(x=−2) and Δ(x=−3)

圖十一所示爲F=0.0143時，在x=−1，−2及−3處，於穩定狀態（Steady-state）情形下水平速度（u／U）之垂直剖面。另F=0.032，F=0.07125及F=0.106之圖亦經作出（此處略去）。在所有情形，穩定狀態水平速度剖面均明顯顯示一完全靜止區（Stagnant zone，即u／U爲0值時）及一流動或排出層（A flowing or withdrawal layer）之存在。且均未見可量度之迴流（Reverse flow）。當佛路德數愈小時，排出層，或選擇流出層將愈見集中，此與理論上之解釋，流暢係由於擾動自「漏」（Sink）處向上游傳播所造成，完全一致。

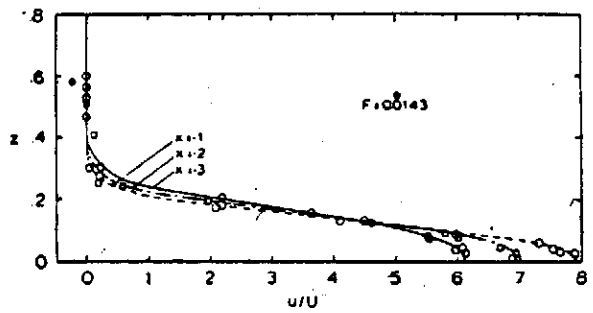

圖十一、在x=−1，−2及−3處，穩定狀態下之水平速度之垂直剖面；F=0.0143；○(x=−1)，□(x=−3) 及⬡(x=−3)。

Figure 11. Steady-state horizontal velocity Profile at x=-1, -2 and -3; F=0.0143: ○(x=−1), □(x=−2) and (x=−3)

× ×　　× ×　　× ×　　× ×

以上爲筆記者業師鮑咸平教授返國參加民國六十二年八月間經建會議，應氣象學會亢理事長玉瑾之邀在氣象學會舉辦學術研討會中之講詞。內容均爲鮑教授等近年來有關層流及旋流動力學上最新研究。筆者應邀整理此項講演紀錄。必需說明者，上整理之講演稿，因鮑師遠在美國，故並未經其過目。文中如有失誤之處，概由筆記者負責。

註一：因在重力場中密度分層流體當受到一輕微擾動而驅離其平衡位置時，因浮力及重力影響而造成重力波。當密度均勻時

$$N = \sqrt{-\frac{d\rho}{dz} g / \rho_0} = 0 \quad (N = \text{Brunt} - \text{Väisälä Frequency})$$

，無波動，此時流體爲中性，可隨遇平衡。

註二：在旋轉流體中，由於邊界層摩擦影響，流體亦將作Solid rotation。如流體質點受

輕微擾動向外移動，如周圍流體之離心力大於該流體質點之離心力時，以離心力不足，該質點將返回其原位置。但當返回時，質點獲得動能，並向內移過其平衡位置。以動能增加，因之離心力又增大，如此往復波動，即所謂離心波（Centrifugel wave, or inertia wave）。

註三：按 Stratified fluid 中小振幅波動之管制方程式爲：

$$\frac{\partial^2}{\partial t^2}(\nabla^2 w) + N^2\left(\frac{\partial^2 w}{\partial x^2} + \frac{\partial^2 w}{\partial \eta^2}\right) = 0 \qquad (1)$$

而 Rotating fluid 管制方程式爲：

$$\frac{\partial^2}{\partial t^2}\nabla^2\vec{u}4 + \Omega^2\frac{\partial \vec{u}}{\partial y^2} = 0 \qquad (2)$$

(1)式中 w 爲擾動速度在 Z 方向之分力，(2)中之 u 爲流體速度向量。由上兩式可見兩方程式甚爲類似，並可知：N 相當於 2Ω。

註四：按 Stratified fluid 中大振幅（Frinite Ampll tude）波動管制方程式爲：

$$\left(\frac{\partial^2}{\partial \xi^2} + \frac{\partial^2}{\partial \eta^2}\right)\Psi - F^{-2}\eta = -F^{-2}\Psi$$，ξ，η，Ψ，F 此處均爲無因次者，$\xi = \frac{x}{d}$，$\eta = \frac{Z}{d}$，$\Psi = \frac{\Psi}{Ud}$ 在於有 Sink（漏）情形之解爲：

$$\Psi = \eta + \frac{2}{\pi}\sum_{n=1}^{\infty}\frac{1}{n}\exp\left[\left(n^2\pi^2 - F^{-2}\right)^{1/2}\xi\right]\sin n\pi\eta$$

其解僅於 $F > \frac{1}{\pi}$ 時才有效。於此情形下，無 Velocity concentration 出現。（見參考書目 3 中，Stratified flow into a sink 一節之討論）。

註五：在此線性化理論（Linearized theorey）有效之流暢中，各擾動之模（Modes）係次第抵達，且其解僅爲各模之疊加。但流動開始後，整個流場，係流向漏（Sink）處，故僅各擾動傳播速度大於均勻速度（$U = Q/d$，Q 爲流量，d 見圖四）者才能到達上游較遠之處。例如，於 $F = 0.014$，僅共 22 模可向上游傳播。當在漏處「排出」之量，Q 愈大，能向上游傳播之模亦愈少。如流量之值使 $F \geq 1/\pi = 0.328$ 時，均勻流速已高過最快之模，即：$n = 1$，（第一模），則各模對上游將均無影響。註四中之解，即爲適用於此情形之下者。

References

1. Greenspan, H. P., "The theorey of rotating fluids" Combridge Uni. Press, 1968.
2. Phillips, O. M., "The dynamics of upper ocean", Combridge Uni. Press, 1966.
3. Yih, C.S., "Dynamics of non-homogenous fluids", New York, Mac-Millan Company, 1965.
4. Pao, H. P. & T.W., Soruces and sinks at the axis of a viscous rotating fluid," The physics of fluids, Vol. 12, No. 8, 1969.
5. Pao, H.P., "A numerical computation of a confined rotating flow," Journal of applied mechanics, June, 1970.
6. Shih, H.H. & Pao, H. P., "Selective withdrawal in rotating fluids," Journal of fluid Mechanics, Vol. 49, 1971.
7. Pao, H. P., "Numerical solution of the Navier-Stokes equations for flow in the disk-cylinder system," The physics of fluids, Vol. 15, No. 1, 1972.
8. Pao, H. P. & Shih, H. H., "Selective withdrawal and blocking wave in rotating fluids," Journal of fluid mechanics, Vol. 57, 1973.
9. Pao, H. P. & Kao, T. W., "The dynamics of establishment of selective withdrawal of a stratified fluid from a line sink. Part 1. Theorey," 1973.
10. Kao, T.W., Pao, H. P. & Wei, S.N., "Dynamics of establishment of a stratified fluid from a line sink 2 Experiment," 1973.
11. Wei, S.N., Kao, T.W. & Pao, H. P., "Experimental study of usptream influence in the two-dimensional flow of a stratfied fluid over an obstacle," 1973 (to be published in J. geophysical fluid dynamics.)

ANNUAL REPORT OF THE INSTITUTE OF PHYSICS,
ACADEMIA SINICA, 1974

300 G.T.級拖網漁船之簡易直板船型設計研究

戴堯天（Yau-Tien Dai）廖清照、高雅平

摘　要

本文係以台灣大學造船研究所改良之300 G.T. 拖網漁船爲母船，作直板船型設計研究，主要的目的在於探討方塊係數較小之該種船型改作直板船型之可能性及直板和稜線不同安排時對阻力及馬力的影響，以尋求一種直板及稜線安排的正確途徑。本文首先以攝影方法取得母船的流線，再以此流線作直板及稜線安排之基準，以設計船型。最後藉阻力及推進試驗比較直板船型之各種變化與母船間之性能，以尋求適當之方法，供做設計直板船型之參考。

一、前　言

簡易船型係由直板或簡單之可展開曲面連接而成之船之外形，根據以往資料顯示，簡易船型在某一情況下之阻力可能接近一般船型，甚至低於一般船型，而其效率又可能比一般船型爲高，此一論述雖尚爲人所懷疑，但吾人若能藉諸理論與試驗求得配合本省漁船船型特性之某種較佳直板船型，並由此尋求出一種設計直板船型之方法，則對本省漁船及軍用船隻之建造必有所助益。

簡易船型的存在爲時已久，但是眞正有系統的研究還是到二十世紀初才開始，而且結論均各有不同，1914年David W. Tayler，1917年William McEntee，1918年Sadler〔1〕先後均曾對簡易船型作研究，結果認爲簡易船的阻力可能與普通船型相似；同時英國方面的研究也都支持他們所作結論。1964年Johnson〔2〕曾作系列試驗，研究簡易船在靜水中的阻力與推進，從他的系列試驗結果可知在適當設計下簡易船型可以代替一般船型。1965年德國Blohm& Voss船廠設計了一個眞正完全直板的船型（球形艏艉除外），由試驗結果顯示其效果亦相當良好，然而Ronal K. Kiss 於1972年在他的研究中所作結論〔1〕說明直板船型在其所研究之船型上應用前途似乎是暗淡的，因此簡易船型，尤其對某種特殊船舶來說，其可行性至今尚無一定論。

目前台灣大學造船研究所正從事300 G.T.級拖網漁船之改良研究，且有相當成果，根據初步實驗資料顯示改良船的阻力及推進性能均較原船爲佳，由於該船型船艉甚爲方整極有利於更改爲直板船型，復因該船C_B值較“Johnson 71”系列爲低，爲探討此型船直板化之可能性，並尋求一種直板及稜線安排之正確途徑以作今後類似船型直板化之設計參考，故本文藉300 G.T.改良船型來作直板船型之研究。

二、直板船阻力之探討

直板船型主要的目的在於簡化船殼建造之方式及便於大量生產，但是若忽略其對阻力及推進之影響，則因燃油之持續性消耗，可能反而得不償失，爲了直板船型在阻力上之增加達到最小，理論上乃使船殼上之稜線（Knuckle Line）與水流流線（Streamline)不產生交角，其主要作用在避免分離（Seperation）及渦流（Eddy）現象之產生〔3〕，一般言之船在水面航行，其阻力可分爲興波阻力與摩擦阻力兩大部份，摩擦阻力在任何速度時均存在，興波阻力在高速時尤爲重要，所以在設計時對興波阻力的改善實不可忽視。摩擦阻力是由於流體具有黏性，與物體有相對運動時產生，摩擦力大小與水流之速度梯度有關，由於一般船隻均有相當長度，且表面有些部位曲率甚大，水流往往無法跟上，於是在此部位發生分離，造成渦流，消耗能量而增加阻力，同時由於渦流造成低壓，形成船體前後壓差，也增加阻力，因此由摩擦阻力觀點，欲減少船之阻力，一則在減少浸水面積，尤其在水流集中之部位如舭部等位置儘量減少水流流過之距離以減少接觸面積，二則在減少造成水流分離以及渦流，以免消耗能量。直板船在先天上由於表面之不連續最易引起分離現象，所以在設計時必須克服此一困難，其最簡單而易於了解的原則爲使直板船表面不連續部位儘量與水流平行。至於興波阻力因受水面形狀影響很大，故只有在安排水面形狀時避免斜率變化太大，並儘量使直板船之水面形狀及面積與一般船型之母船接近。影響興波阻力的另一因素爲入水角，雖然入水角對波阻的影響很難單獨加以討論，但一般言之，入水角愈小對阻力愈有利，不過也不能過份減小，否則肩部突出反而對興波阻力有不良影響。

三、直板船型設計之探討

3.1. 簡易直板船型設計之原則

在設計之初，吾人應先求得母船之流線以作爲割切直板之基準，流線之求法有兩種，一爲以理論計算，假設船體表面流過之水流爲勢流〔4〕，藉數學上之轉換求船體表面各點之速度向量即可求得流線，但此種方法僅適用於由已知之速度算出一船型及其流線，而欲從一已知之船型算出其流線則極爲複雜費時，另一種方法是以實驗直接測出，一般可將塗料塗在船表面或將毛線貼於其上，置風洞或水渠（Water Channel）或水槽中與水產生相對運動，經攝影分析而得。

改變某船爲直板船型時應注意以下幾點：㈠排水量應儘量保持和母船一樣大小㈡主要尺寸及線型係數之改變儘量減小㈢浮力中心應保持不變。

直板船之割切，最基本的原則當然是配合母船的流線，其稜線及稜角點（ Knuckle Point）應沿著流線，以避免分離現象。從船體幾何及流體之基本原則綜合得出改變某船爲直板船型時割切之九點原則，詳閱台大造船研究所報告NTU－ INA －37 。

3.2. 母船之決定

本文中直板船之設計係以造船所設計之300 G.T. 拖網漁船改良船型爲母船，而該改良船原先所依據之母船爲本省現有之300 G.T. 艉拖網漁船。改良船之剖面圖如圖1 所示

，其與本省現有之300 G.T. 艉拖漁船最大差別爲船長增加，同時船型較爲瘦脊，C_B 及 C_P 減少許多，但甲板面積及載重容積變化不多，經阻力試驗結果顯示該改良船在阻力上比原有之300 G.T. 艉拖網漁船爲佳，因此以之作爲母船較有意義。

3.3. 線圖設計及稜線位置安排之探討

本文係利用毛線之方法攝取母船（改良船）在設計速度時之流線照片（如圖2所示），圖1爲其流線圖，然後配合此一流線圖及前述之設計原則而繪製300G.T. 拖網漁船直板船型之線圖（圖3）。（本省現有300G.T. 艉拖網漁船、本文母船及設計之直板船型的主要尺寸請參閱NTU－INA－37）。

本文直板船之設計由艏部開始，以母船之剖面圖爲基準，經過多次改變與嚐試，發現欲全部以直板代替原來的曲面而且想保持原來的體積，另一方面又希望稜線與流線完全配合，實際上由於幾何之限制，必須把直板分得很細，稜線的數目必有很多條方可，如此將失簡化之本意，且稜線太多會影響水流。再者艏部水線下之流線很明顯地是向下方流（圖2），如安排稜線由艏部起即沿著流線，最後將導致艏部下方之排水體積完全被削去（此爲幾何上之困難，蓋難以直板完全替代曲面），此時流線將完全改變，前面所說與流線配合也就無意義了。同時由流線圖可看出水流大部分都是在第2及第3座標（Station）以後才流到船底及舭部，所以與其令稜線順著流線倒不如以一水平之稜線取代，既簡單又能使底下之排水量保留，準此得出第一條直板船型稱爲直板一號，（圖3），另外將直板一號修改得直板二號及三號，二號是將一號第一條稜線（水平者）在第1½座標以前下半部尖削的直板補成與母船相似之形狀，以探討這一部分對阻力是否一如構想中的影響不大（試驗結果見4.1），三號則將船舯舭部之突出部分削去（如圖3虛線所示），以了解稜線之不同安排對阻力的影響。

四、試驗結果分析與討論

4.1. 阻力試驗

母船與直板一號之阻力試驗在相同之情況下在台灣大學造船所船模試驗槽（$74.5^m \times 4^m \times 2.2^m$）進行，根據文獻〔5〕三米以下之船模在該船槽中進行試驗時槽壁效應（Wall Effect）不大，本文船模長爲2.6m，故未考慮槽壁效應，船模與實船比例 $\alpha = 15$，試驗時在½座標處加1.00mm直徑之尼龍線作爲激紊裝置，由阻力試驗結果（圖5）可看出兩船阻力互有高低，相差最大者係在低速約爲8%，在7～8節之間直板一號低於母船，10節以後又略高出母船，兩船在9至11節阻力差異不多，若與試驗誤差比較幾乎無法分辨何者爲大，至此獲得一結論即此型直板船之阻力在適當情況下可能低於一般船型。在直板船舯部及艏部之變化方面，舯部的改變係指舭部之稜線變化亦即直板三號，其流線圖〔5〕與稜線較接近，艏部變化係指修改直板一號第1條水平稜線以下部分，使之與母船之形狀接近亦即直板二號，其阻力試驗結果如圖4，由圖可看出直板一號之EHP在低速時略高於直板二號，但是在速度大於6節以上時幾乎沒有差別，由此說明艏部底下之形狀略爲改變時對阻力影響不大。直板三號之EHP在整個速度範圍都比直板一號略低，在高速時相

差2%～3%，低速時約5%，此乃因直板一號之舯舷部突出所致，在修改後一則由於突出部分削去，再則其稜線與流線更形接近，所以摩擦阻力較小。由此說明兩直板相交時，若兩板交角太小，可能使阻力增加。

4.2. 推進試驗

原設計之改良船型在推進方面係採用寇特噴嘴螺槳，本文直板船也利用改良船型之噴嘴螺槳作爲推進設施。推進試驗所用之方法係在每一速度時附加其相對之R_a值，求出其轉矩Q_m及推力T_m，此一方法所得並非船模在該速度下之阻力R_{Tm}所對應之T及Q，而是$R_{Tm}-R_a$所對應之T及Q，試驗之數據請參考NTU－INA－37。圖5係船模之EHP與DHP換算成實船之EHP與DHP，排水量之差異已經過修正。由圖可看出速度在9.8節以下時直板船之推進效率比較高，所需DHP較小，當$V_s>9.8$節，直板一號馬力上升較速，到11節時高出6.2%，而在10.8節（設計速度）比母船略高3.6%，顯然在此範圍直板一號之性能略遜於母船。但綜合以上結果可以看出直板船型無論在阻力及推進方面皆有可能達到或近於一般船型的程度。

由於漁船之載重情況，從出航以至回航，其水線變化大致都維持在滿載水線附近，因此本文所作實驗只在設計吃水進行。

五、結　論

(1)本文直板船之設計是依據3.1所述之九點原則，配合母船流線而進行，由阻力及推進試驗及照相結果顯示該等原則可適於設計時之用。

(2)由試驗結果得知本文直板船型阻力及推進兩方面皆與母船相差不多，推進方面直板一號之DHP在設計速度時高出母船3.6%，由此可知本文所設計之直板船型在阻力及推進兩方面皆可以達到或接近一般船型之程度。

(3)本文中直板船型係依流線設計，其困難不大，但在艄部爲簡化及保持排水量，及由於實際上幾何限制，常不能使稜線依流線設計，惟由流線圖得知艄部之水雖然從F.P.即有往船底之趨勢，但大部分水流都是在第2至第3個座標以後才流至船底及舭部，故由實驗結果可證明船艄稜線在與流線交角不太大的情況下，其方向對水流及阻力影響不大。

(4)由直板一號及二號的阻力試驗可看出艄部形狀在低速略有影響，在稍高速時其影響即減小。因此證實本文中另一假設，即艄部稜線變化對阻力的影響不大。由直板三號與二號之比較可看出，船舯突出部分對阻力略有影響，其影響主要是由於突出部分兩直板交角較小，而在此一部分水流甚速，有分離現象產生，故而使阻力增加。

(5)雖然直板船型在某些船型不太適用，如Ronald K. Kiss在他的研究〔1〕中所作結論，說明直板船型在其所作研究之船型上應用前途似乎是暗淡的，但由本文試驗結果顯示直板船型應用到本省300C.T.漁船及相類似船型，其前途大有可爲，尤其對於具有方型艉者因直板船型艉部易與母船配合，更適於使用直板船型。

參 考 資 料

(1) Ronald K. Kiss., "Aspects of Simplified Hull Forms - Past, Present, and Future." Marine Technology October, 1972. P. 377-392.

(2) Johnson, N. V., "Experiments with Straight Framed Ship." Trans. RINA, Vol. 118, 1965, P. 108.

(3) Harold, E, Sounders, "Hydrodynamics in ship Design", Vol. 2, Chapter 27, page 403.

(4) Tatsuo Jinaka, Member., "On the Streamlines Around a ship Hull." The society of Naval Architects of Japan. Vol. 118, 1965. P. 108

(5) "國立台灣大學船模試驗室比較試驗之研究"台灣大學造船研究所研究報告，NTU－SHL－17民國六十二年六月。

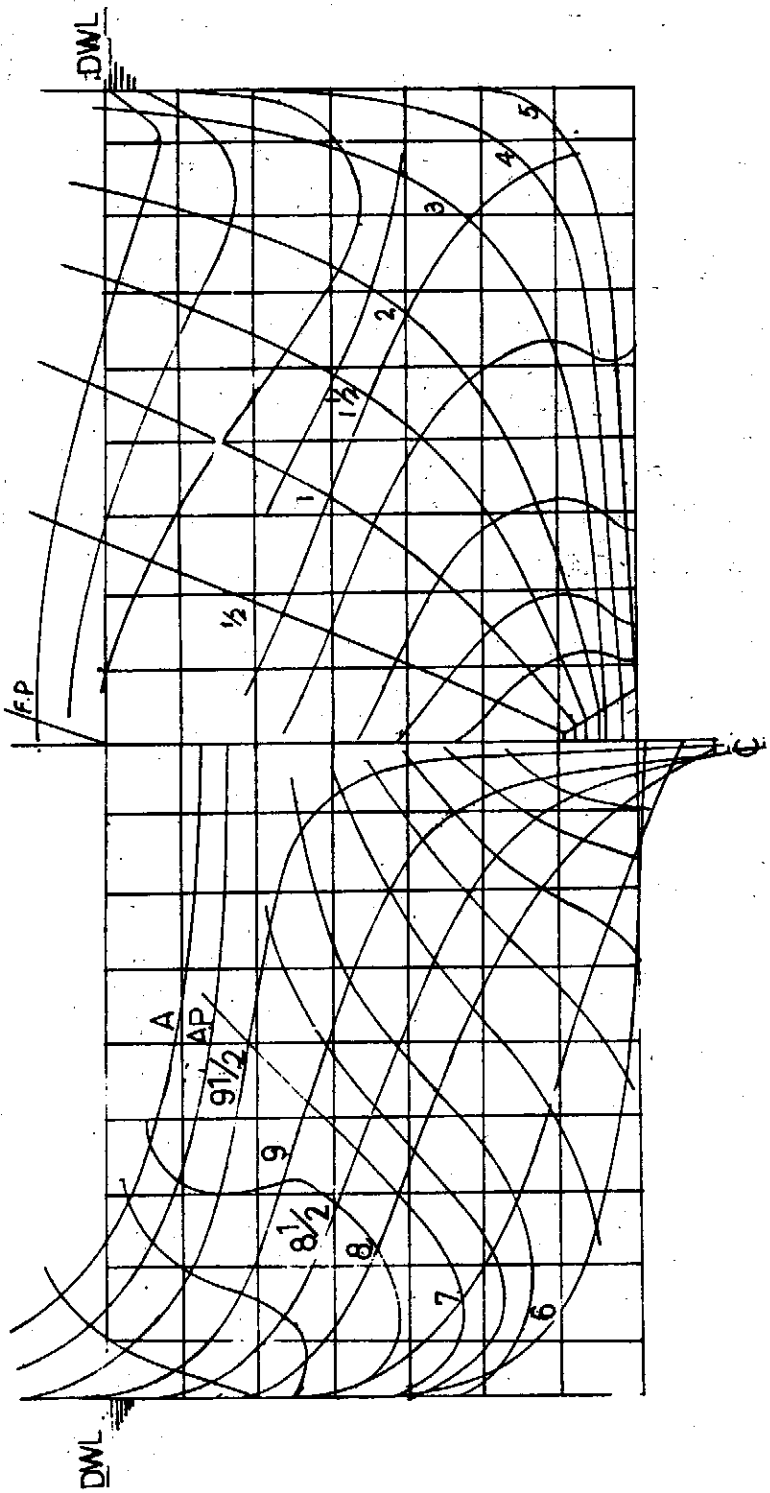

圖 1　母船（改良船）之線圖及流線圖

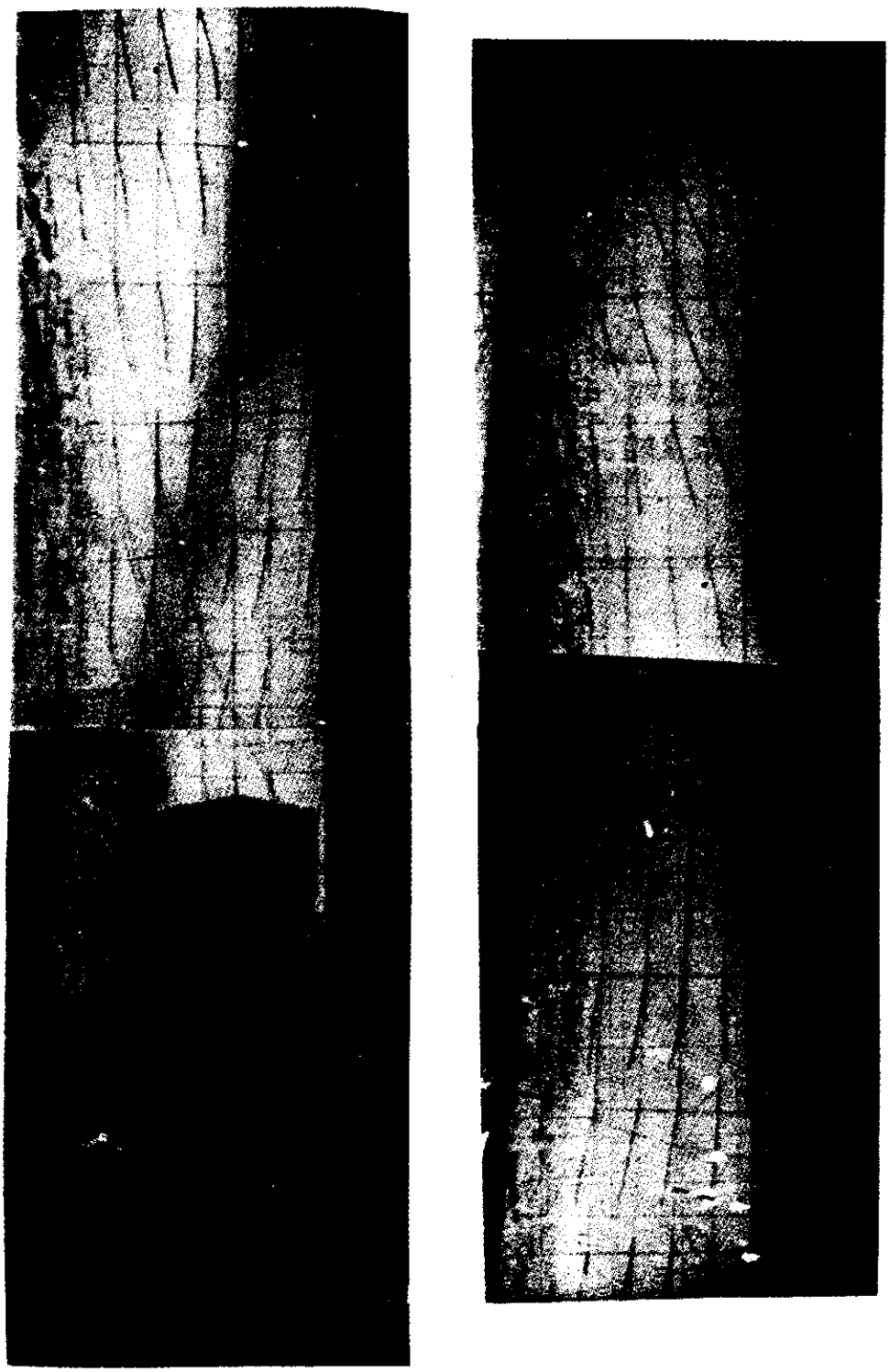

圖 2 母船流線

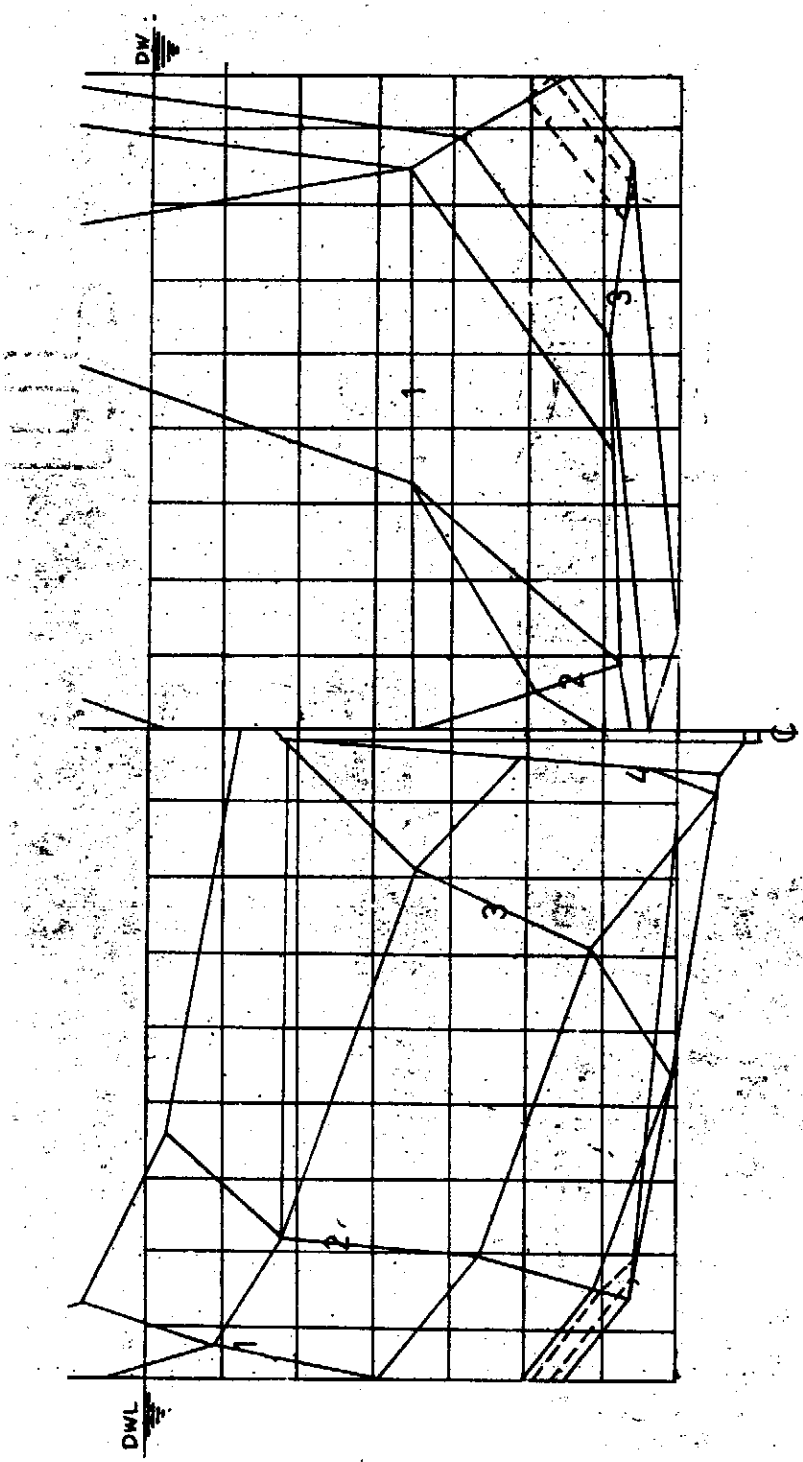

圖 3　直板一號線圖（作虛線改變後者爲直板三號線圖）

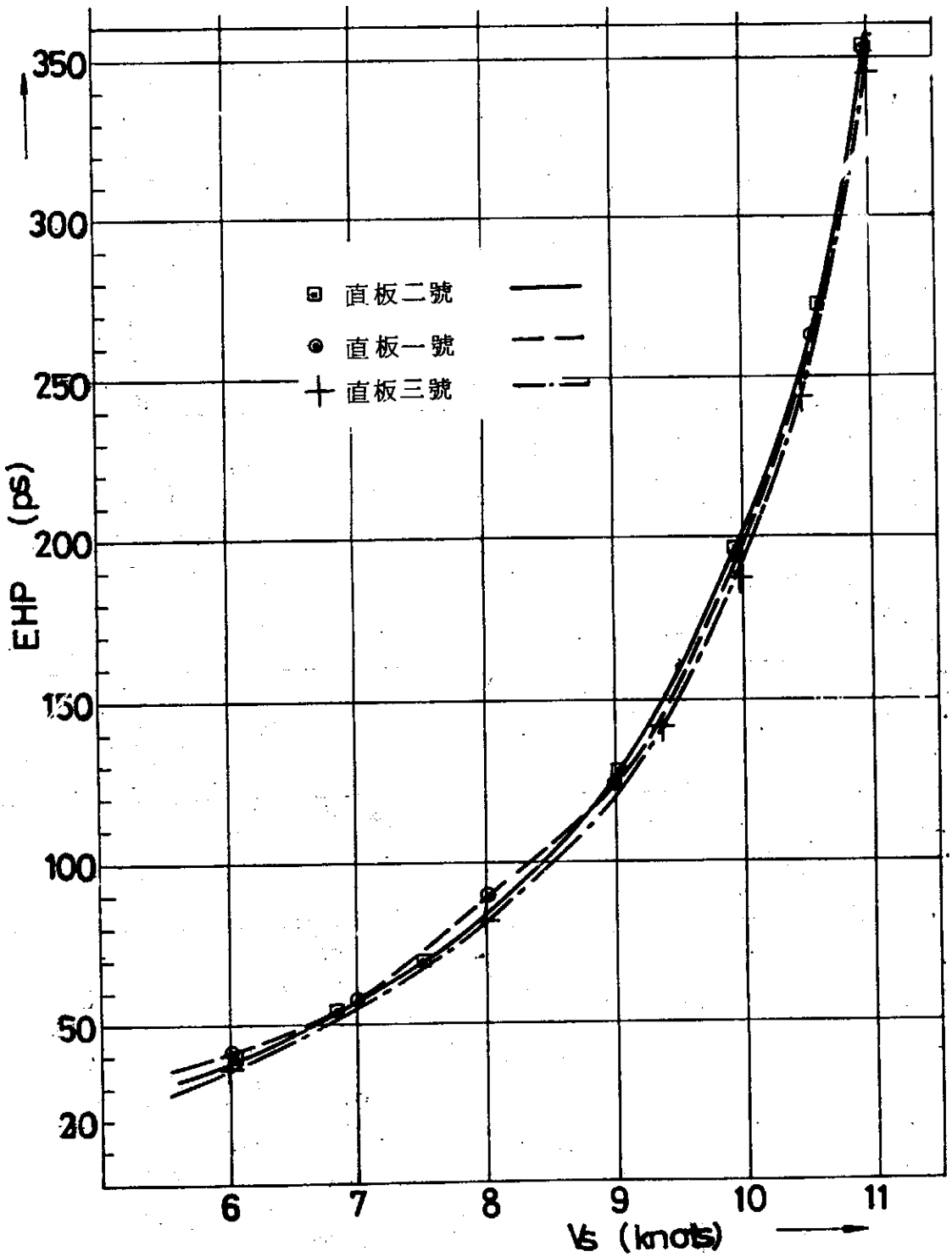

圖 4　直板一號，二號及三號 EHP 比較曲線

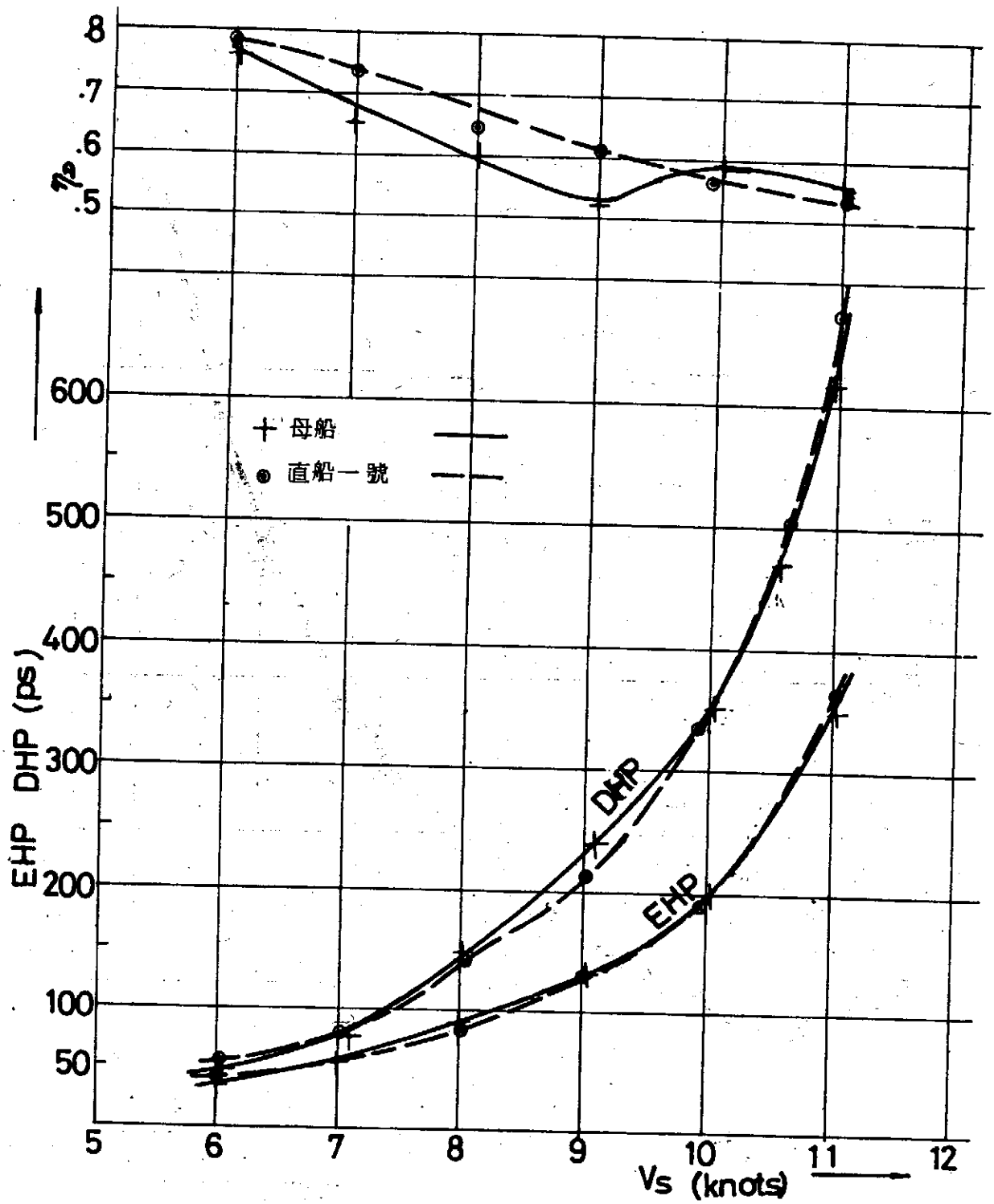

圖 5　直板一號與母船 EHP，DHP 及 η_D 比較

ANNUAL REPORT OF THE INSTITUTE OF PHYSICS,
ACADEMIA SINICA, 1974

BAROTROPIC INSTABILITY IN RELATION TO THE GENERATION OF SYNOPTIC-SCALE ATMOSPHERIC VORTICES

Chung Yi Tseng (曾忠一)

ABSTRACT

It is generally known that barotropic instability cannot account for the development and intensification of a cyclone by means of conversions between available potential energy and kinetic energy. That is a baroclinic process. However, after the cyclone has initially developed due to baroclinic instability, the barotropic process may explain the subsequent development of synoptic-scale disturbances. This study will explore the relation between barotropic instability and the generation of synoptic-scale disturbances during the extreme tornadic outbreak of April 3-4, 1974 in the U.S. continent.

The stability characteristics (unstable waves, growth rates, most preferred wavelength, momentum transport, etc.) of each wind profile at four mandatory levels during the April 3-4, 1974 tornado outbreak are investigated. It is found that the atmosphere over the area of maximum tornadic activity was barotropically most unstable on 0000Z April,4, i.e., shortly before the tornado outbreak. This result indicates the possibility that barotropic instability may be synoptically associated with the tornado outbreak.

1. INTRODUCTION. The study of hydrodynamic instability of parallel flow U(y) has been a classical problem in hydrodynamics, but its application to geophysical problems is relatively modern. Rayleigh (1880, 1913) has shwon that parallel flow of an inviscid nonrotating fluid is stable if the velocity profile U(y) has no inflection point, and for instability to occur, the absolute value of the vorticity of the basic current must have a maximum in the field of flow.

Tollmien (1935) has shown that, for symmetric velocity profiles in a channel, and for the boundary-layer velocity profiles, the condition $\frac{d^2U}{dy^2} = 0$ at some point in the basic current is a sufficient condition for instability. The earlier works on hydrodynamic instability of parallel flow have been surveyed by Lin (1955) and Yih (1969). Recent developments have been treated by Drazin and Howard (1966). The viscous theory of parallel-flow instability has been summarized by Reid (1965).

Kuo (1949) and Foote and Lin (1950) extended the nonrotating instability theory of Rayleigh for geophysical applications to a rotating earth by the addition of the β term. They showed that the absolute vorticity must be a maximum or minimum at some point(s) in the basic current. It was also found that the β-effect, in general, reduces the instability of westerly jets and increases the instability of easterly jets (see also Kuo, 1973). Kuo (1951) considered the energetics of barotropic instability and showed that when amplified waves exist, kinetic energy is fed from the basic current into the disturbances, while the effect of damped disturbances is to feed the energy into the basic current. Lipps (1962) considered the barotropic instability of a nondivergent Bickley jet. Lipps (1963) examined the instability of a Bickley jet in a divergent, barotropic fluid and applied the theory to the Gulf Stream. Howard and Drazin (1964) investigated the stability characteristics of various basic velocity profiles. Lipps (1965) discussed the stability properties of hyperbolic-tangent shear flow. Jacobs and Wiin-Nielsen (1966) extended the instability theory of homogeneous fluids to a stratified atmosphere. Lorenz (1972) considered the barotropic instability of the Rossby wave motion and suggested that barotropic instability is largely responsible for the unpredictability of the real atmosphere.

In the tropics, where the baroclinicity is weak, barotropic instability has naturally drawn the attention of many authors who have attempted to correlate it to tropical phenomena. Indeed many studies

have recently been published on barotropic instability in the tropics as an energy source of easterly flow. Nitta and Yanai (1969) studied the instability of an easterly current with a symmetric sine-curve profile. Lipps (1970) examined the stability characteristics of a hyperbolic tangent wind profile in the tropics. Yamasaki and Wada (1972a) extended Nitta and Yanai's research and showed that the stability properties of the easterly current are different from those of the westerly current in several respects. Yamasaki and Wada (1972b) investigated the vertical structure of the barotropic unstable waves in tropical easterlies. Despite many investigations of various authors, barotropic instability associated with the horizontal shear of the easterlies has not yet been fully explored.

Since the barotropic instability equation is a nonlinear one, and mathematical treatment is very difficult except for limited cases of special velocity profiles, such as sine-curve velocity profiles, the Bickley jet and the hyperbolic tangent shear layer. One must resort to numerical methods to determine the stability characteristics of basic currents with various profiles. Various authors (Wiin-Nielsen, 1961; Haltiner and Song, 1962) have investigated the instability problem by finite difference methods or finite Fourier series. Yanai and Nitta (1968) investigated the accuracy of the finite difference approximation in solving the stability problem of a nondivergent barotripic current. It was shown that for a sufficiently accurate description of the instability, a large number of subdivisions, at least 20, are required for a symmetric sine-curve basic current. Applications of the finite difference method proposed by them are found in Nitta and Yanai (1969) and Yamasaki and Wada (1972a,b). Dickinson and Clare (1973) used the shooting method and a fourth-order matrix approximation to solve the instability problem of a hyperbolic tangent barotropic shear flow. The barotropic stability equation can be formulated as a variational problem. This allows us to use the finite-element method to solve the instability problem numerically.

In middle latitudes, barotropic instability has been investigated in conjunction with variations of the westerly jet. It is generally accepted that barotropic instability is not as important as baroclinic instability in middle latitudes where baroclinicity dominates. Barotropic models rarely predict occurrences of strong intensification of weather systems, and do not account for the formation of extratropical cyclones. However, after large-scale disturbances develop due to baroclinic instability, further development may be produced by barotropic instability. The purpose of the present work is to attempt to relate barotropic instability to the generation of synoptic-scale atmospheric vortices. The data for the present analysis are taken from the synoptic data of the tornado outbreak during April 3-4, 1974. This tornado outbreak was the greatest in recorded history in terms of number of tornadoes, track lengths, area affected and damage. One hundred and fifteen tornadoes occurred within the area generally encompassed by a line from Chicago southward to the Gulf of Mexico and eastward to the Atlantic coast. The hardest hit area consisted of Indiana, Ohio, Kentucky, Tennesse and Alabama. The barotropic instability analysis of the wind profiles over this area is performed for sixteen wind profiles, i.e., wind profiles for four mandatory levels: 850 MB, 700 MB, 500 MB and 300 MB and for four time steps: 0000Z April 3, 1200Z April 3, 0000Z April 4 and 1200Z April 4. The domain considered is chosen so that the atmospheric flow is quasi-parallel and the disturbances are small, as shown in Figures 8, 9, 10 and 11. The atmosphere over the central and east-central United States is very baroclinic during this period of intensification and, following the thermal wind constraint, the quasi-parallel jet stream is predominantly due to this baroclinicity. Shortly after 0000Z April 4 a tornado outbreak took place in this quasi-parallel flow area. It is easily conjectured that the tornado outbreak might be associated with the parallel-flow instability, although other instabilities of more complicated processes may also be possible. It would be interesting and rewarding to examine a

simple physical mechanism such as barotropic instability in the synoptic environment which supported a severe tornado outbreak.

2. BASIC EQUATIONS. In this study the atmospheric motion is assumed to be horizontal, nondivergent and barotropic. The equations of motion, continuity equation, vorticity equation and energy equation take the form

$$\frac{\partial u}{\partial t} + u\frac{\partial u}{\partial x} + v\frac{\partial u}{\partial y} - fv = -\frac{\partial \Phi}{\partial x} \tag{1}$$

$$\frac{\partial v}{\partial t} + u\frac{\partial v}{\partial x} + v\frac{\partial v}{\partial y} + fu = -\frac{\partial \Phi}{\partial y} \tag{2}$$

$$\frac{\partial u}{\partial x} + \frac{\partial v}{\partial y} = 0 \tag{3}$$

$$\frac{\partial \zeta}{\partial t} + u\frac{\partial \zeta}{\partial x} + v\frac{\partial \zeta}{\partial y} + v\beta = 0 \tag{4}$$

$$\frac{\partial E}{\partial t} = \frac{\partial}{\partial t}\tfrac{1}{2}\iint (u^2 + v^2)\, dxdy = 0 \tag{5}$$

where u and v are the x-andy-component of velocity, f is the Coriolis parameter, $\Phi = gz$ the geopotential, g the acceleration of gravity, z the pressure height, ζ the relative rovticity, $\beta = \frac{df}{dy}$ the Rossby parameter and E the kinetic energy. Eq. (4) expresses the conservation of absolute vorticity and Eq. (5) the conservation of kinetic energy. Since the effect of the variation of the density ρ is assumed to be small, ρ will be taken as constant and will not enter into the equations defining physical quantities.

We define

$$\begin{aligned} u &= \bar{u}(y, t) + u'(x, y, t) \\ v &= v'(x, y, t) \\ \zeta &= \bar{\zeta}(y, t) + \zeta'(x, y, t), \quad \bar{\zeta} = -\frac{\partial \bar{u}}{\partial y} \end{aligned} \tag{6}$$

$$\Phi = \overline{\Phi}(y, t) + \Phi'(x, y, t)$$

Here the barred quantities denote average values in x-direction, which are zeroth order functions. The primed quantities denote the departures from the average values, which can also be taken as representing first order perturbations. The $\overline{u}(y, t)$ is assumed to be parallel to the x-axis and $\overline{v}$ is assumed to be zero. From Eq. (6) it is obvious that the average values of the departures are zero, i.e. $\overline{u'} = \overline{v'} = \overline{\zeta'} = \overline{\Phi'} = 0$. On substituting (6) into (1), (2) and (4), we obtain

$$\frac{\partial \overline{u}}{\partial t} + \overline{u' \frac{\partial u'}{\partial x}} + \overline{v' \frac{\partial u'}{\partial y}} = 0 \tag{7}$$

$$\overline{u' \frac{\partial v'}{\partial x}} + \overline{v' \frac{\partial v'}{\partial y}} + f\overline{u} = -\frac{\partial \overline{\Phi}}{\partial y} \tag{8}$$

$$\frac{\partial \overline{\zeta}}{\partial t} + \overline{u' \frac{\partial \zeta'}{\partial x}} + \overline{v' \frac{\partial \zeta'}{\partial y}} = 0 \tag{9}$$

The continuity equation is automatically satisfied.

If we define the mean-flow kinetic energy $\overline{E}$ as

$$\overline{E} = \tfrac{1}{2} \int \overline{u}^2 \, dy$$

and the perturbation kinetic energy E' as

$$E' = \tfrac{1}{2} \int \overline{(u')^2 + (v')^2} \, dy$$

Then from Eq. (5) we obtain

$$\frac{\partial \overline{E}}{\partial t} = -\frac{\partial E'}{\partial t} \equiv -\frac{\partial}{\partial t} \tfrac{1}{2} \int \overline{(u')^2 + (v')^2} \, dy \tag{10}$$

Substituting (6) into (1), (2), (3) and (4) and using the relations (7), (8) and (9) we get, to lowest order, the following equations for the perturbations:

$$\frac{\partial u'}{\partial t} + \overline{u} \frac{\partial u'}{\partial x} + v' \frac{\partial \overline{u}}{\partial y} - f v' = -\frac{\partial \Phi'}{\partial x} \tag{11}$$

$$\frac{\partial v'}{\partial t} + \bar{u}\frac{\partial v'}{\partial x} + fu' = -\frac{\partial \Phi'}{\partial y} \tag{12}$$

$$\frac{\partial u'}{\partial x} + \frac{\partial v'}{\partial y} = 0 \tag{13}$$

$$\frac{\partial \zeta'}{\partial t} + \bar{u}\frac{\partial \zeta'}{\partial x} + v'\frac{d\bar{\zeta}}{dy} + v'\beta = 0 \tag{14}$$

This kind of formulation is characteristic of the regular perturbation theory. When we want to formulate the prognostic equation for the perturbations, we ignore the time rate of change of the mean flow, since the latter is of second order, as can be seen from (7), (9) and (10). After the quantities of the perturbation have been calculated, we can find the time rate of change of the mean flow. However, these second order variations are essential in determining the stability of the mean flow.

From equations (11) and (12) one finds the time rate of change of the perturbation kinetic energy

$$\frac{\partial E'}{\partial t} = \tfrac{1}{2}\frac{\partial}{\partial t}\int \overline{(u')^2 + (v')^2}\, dy$$

$$= -\int \overline{u'v'}\frac{\partial u}{\partial y}\, dy = \int \tau \frac{\partial \bar{u}}{\partial y}\, dy \tag{15a}$$

$$= -\int \bar{u}\frac{\partial \tau}{\partial y}\, dy \tag{15b}$$

where $\overline{u'v'}$ is the y-direction momentum transport and $\tau = \overline{-u'v'}$ is the Reynolds' stress. For the inviscid theory, the momentum transport and the Reynolds' stress should vanish at solid boundaries. From Eq. (10) the time rate of change of the mean-flow kinetic energy becomes

$$\frac{\partial \bar{E}}{\partial t} = -\int \tau \frac{\partial \bar{u}}{\partial y}\, dy \tag{16a}$$

$$= \int \bar{u}\frac{\partial \tau}{\partial y}\, dy \tag{16b}$$

The integrand $\bar{u}$ —— in (16b) represents the rate of work done by the Reynolds' stress and therefore the rate of increase in mean-flow

kinetic energy. The integrand $\tau \frac{\partial \bar{u}}{\partial y}$ in (15a) correspondingly represents the rate at which the Reynolds' stress increases the kinetic energy of perturbations.

If the perturbations are assumed to be cyclic in x, from (7) and (9) we obtain the time rata of change of the momentum of the relative vorticity of the mean flow in the form

$$\frac{\partial \bar{u}}{\partial t} = \frac{\partial \tau}{\partial y} = -\frac{\partial}{\partial y} \overline{u'v'} \tag{17}$$

$$\frac{\partial \bar{\zeta}}{\partial t} = -\frac{\partial}{\partial y} \overline{v'\zeta'}$$

where the term $\overline{v' \zeta'}$ is vorticity transport.

Normal Mode Solution of Perturbatinn Equations. The continuity equation for perturabtion flow (13) allows us to define a stream function for the perturbation flow

$$u' = -\frac{\partial \psi'}{\partial y} \qquad v' = \frac{\partial \psi'}{\partial x} \tag{19}$$

and it follows that

$$\zeta' = \frac{\partial^2 \psi'}{\partial x^2} + \frac{\partial^2 \psi'}{\partial y^2}$$

If we now set

$$\psi' = \varphi(y)\, e^{i\alpha (x-ct)} \tag{20}$$

i.e., proceed with the normal mode solution, the vorticity equation for a two-dimensional disturbance (14) becomes (Kuo, 1949)

$$(U - c)(\varphi'' - \alpha^2 \varphi) + (\beta - U'')\varphi = 0$$

Here we use a prime to denote a differentiation with respect to y and use $U = \bar{u}(y)$ for convenience in the following discussion. α is the

real wavenumber in x-direction, c the complex phase velocity. We now define the dimensionless variables as follows

$$y^* = \frac{y}{b}, \quad U^* = \frac{U-U_{min}}{U_{max}-U_{min}}, \quad \varphi^* = \frac{\varphi}{b(U_{max}-U_{min})},$$

$$\alpha^* = \alpha b, \quad B^* = \frac{\beta b^2}{U_{max}-U_{min}},$$

$$c^* = c_r^* + ic_i^* = \frac{c-U_{min}}{U_{max}-U_{min}},$$

$$c_r^* = \frac{c_r-U_{min}}{U_{max}-U_{min}}, \quad c_i^* = \frac{c_i}{U_{max}-U_{min}}$$

where b is a characteristic length for a specified problem (here defined as half the width of the channel or the shear zone). U_{max} and U_{min} are the maximum and minimum value of the basic current U(y) in the field of flow. The nondimensional parameter β^* measures the ratio of planetary vorticity to the scale of the shear vorticity. The nondimensionalized equation without the asterisks assumes the form

$$(U-c)\,(\varphi'' - \alpha^2\varphi) + (\beta - U'')\,\varphi = 0 \tag{21}$$

Note that when $\beta = 0$ Eq. (21) becomes the Rayleigh stability equation, i.e., inviscid form of the Orr - Sommerfeld equation. It is easily seen that with proper nondimensionalization, all the equations from (1) to (20) are also valid in dimensionless form.

Boundary Conditions. At a rigid wall, such as shown in Figure 1, the normal veloscity v' of the disturbances vanishes. This can be shown to imply that

$$\varphi = 0 \qquad \text{at} \qquad y = 0, 2 \tag{22}$$

if we take the position of rigid walls at dimen-

sional y = 0, 2b. If the flow extends to infinity, then, by physical requirements φ must be bounded there. Thus boundedness of φ at infinity in general implies that φ must tend to there, and we may use boundary condition (22) at an infinite as well as at a finite boundary (Drazin and Howard, 1966).

Eq. (21) is an eigenvalue problem under appropriate boundary conditions for a given profile U of the basic current. We can find c as an eigenvalue by solving (21) with the wavenumber α specified. The phase speed c may in general be complex. When its imaginary part c_i is equal to zero, the disturbance is neutral, and when $c_i = 0$, the disturbance is amplified or damped.

Momentum Transport. The physical mechanism of momentum and vorticity transport associated with the stability of mean flow has been discussed by Kuo (1951). Here we briefly review the momentum and vorticity transport equations. From equations (19), (20), and (21) we obtain the y-direction momentum transport equation

$$\overline{u'v'} = -\tau = -\frac{\alpha}{2\pi}\int_0^{2\pi/\alpha} u'v'\,dx$$

$$= -\tfrac{1}{4}\,i\alpha\left(\varphi\frac{d\varphi^*}{dy} - \varphi^*\frac{d\varphi}{dy}\right)e^{2\alpha c_i t}$$

$$= -\tfrac{1}{2}\alpha\left(\varphi_r\frac{d\varphi_i}{dy} - \varphi_i\frac{d\varphi_r}{dy}\right)e^{2\alpha c_i t} \qquad (23a)$$

$$= \frac{\alpha c_i}{2}\int_0^y \frac{(\beta - U'')|\varphi|^2}{|U-c|^2}\,dy\,e^{2\alpha c_i t},\quad 0<y<2 \qquad (23b)$$

or

$$\frac{\partial\tau}{\partial y} = -\frac{\alpha c_i}{2}\frac{(\beta - U'')|\varphi|^2}{|u-c|^2}\,e^{2\alpha c_i t} \qquad (23c)$$

It whould be remembered that the physical quantities u', v', φ', ζ', etc. are understood to be the real part of their representation. The term $|\varphi|^2$ in Eq. (23b) and 23c) is proportional to $(v')^2$. The momemtum transport can also be expressed in terms of the tilting of the troughs and ridges, defined as the curves along which v' is zero.

Thus, the location of trough and ridge curves is determined by (Kuo, 1951)

$$\tan \alpha \ (x - c_r t) = - \frac{\varphi_i}{\varphi_r}$$

and therefore the tangent of the angle of tilt θ, measured from positive y direction, is (Kuo, 1951)

$$\tan \theta = \frac{dx}{dy} = - \frac{1}{\alpha} \frac{\varphi_r \varphi_i' - \varphi_i \varphi_r'}{|\varphi|^2} \tag{24a}$$

$$= \frac{2}{\alpha^2} \frac{\overline{u' v'}}{|\varphi|^2} e^{-2 \alpha c_i t} \tag{24b}$$

From the above equation we see that the momentum transport is proportional to the tilting of the troughs and ridges,

Vorticity Transport. The vorticity transport can either be obtained in the same way, or simply by differentiating (23) with respect to y. Thus, we have the vorticity transport equation (Kuo, 1951)

$$\overline{v'\zeta'} = \frac{\alpha}{2} (\varphi_r \varphi_i'' - \varphi_i \varphi_r'') e^{2\alpha c_i t}$$

$$= - \frac{\alpha c_i}{2} \frac{(\beta - U'') |\varphi|^2}{|U - c|} e^{2\alpha c_i t}$$

This equation shows that the vorticity transport produced by the amplifying disturbance is in the direction of decreasing absolute vorticity of mean flow.

Time Rate of Change of Momentum of Mean Flow. Substituting Eq. (23) into (17) we get the time rate of change of momentum mean flow

$$\frac{\partial U}{\partial t} = \frac{1}{2} \alpha (\varphi_r \varphi_i'' - \varphi_i \varphi_r'') e^{2 \alpha c_i t} \tag{26a}$$

$$= -\frac{\alpha c_i}{2} \frac{(\beta - U'')\,|\varphi|^2}{|U-c|^2} e^{2\alpha c_i t} \tag{26b}$$

$$= \frac{}{v'\ \zeta'} \tag{26c}$$

It follows that the effect of the damped disturbance ($c_i < 0$)is to produce an increase of U in the region where B-U" is positive and a decresae where β -U" is negative, thus their effect is to sharpen the mean velocity profile. The effect of the amplifying disturbances ($c_i > 0$) is in the oppositive direction, that is to flatten the mean velocity profile.

Time Rate of Change of Kinetic Energy of Mean Flow. Substituting the expression for $\frac{\partial \tau}{\partial y}$(24c) into the energy equation of mean flow (16b), we obtain

$$\frac{\partial \bar{E}}{\partial t} = -\frac{\alpha c_i}{2} \int_0^2 \frac{U(\beta - U'')\,|\varphi|^2}{|U-c|} dy$$

$$= -\frac{\partial \bar{E}'}{\partial t}$$

Since the only energy which the disturbances can withdraw for the growth is the mean-flow kinetic energy, the expression at the righthand side should be negative. Thus, if the perturbation kinetic energy is to increase ($c_i > 0$), then, we must also have positive β-U" associate with higher values of U and negative β-U" with lower values of U. This result is essentially due to Fjortoft (1950).

3. GENERAL STABILITY CHARACTERISTICS. In this chapter we shall discuss some features of the determination of critical wavelengths and phase speeds for barotropic instability.

Lower Critical Wavelength of an Unstable Wave. According to

Kuo (1949), the lower critical wavelength L_κ can be found by solving (21) after setting $c = U_\kappa$, i.e., by solving the eigenvalue problem

$$\varphi'' + \frac{\beta - U''}{U - U_\kappa}\varphi - \alpha^2\varphi = 0, \quad \alpha = \frac{2\pi}{L_\kappa} \tag{28}$$

$$\varphi = 0, \text{ at } y = 0, 2$$

For a velocity profile expressible in mathematical functions, the L_κ's can be determined quite accurately by solving (28). However, for actual atmospheric wind profiles we had better solve (21) and determine c as an eigenvalue by specifying α and locate the wavelength L_κ at which the phase speed of an unstable wave first becomes complex.

Upper Critical Wavelength of an Unstable Wave. For a westerly basic current, the upper critical wavelength L_o of an unstable wave can be found by solving (21) after setting $c = 0.$, i.e., by solving the eigenvalue problem (Kuo, 1949).

$$\varphi'' + \frac{\beta - U''}{U}\varphi - \alpha^2\varphi = 0, \quad \alpha = \frac{2\pi}{L_o} \tag{29}$$

$$\varphi = 0 \text{ at } y = 0, 2$$

In general L_o can be determined quite accurately.

(c_r, c_i) - L Diagrams. If we want to know the general feature of stability characteristics, the best method is to solve (21) and find c and φ as functions of α or L. Figure 1, called a (c_r, c_i)-L diagram in this study, shows an example of the relationship between phase velocity c and the wavelength L for the symmetric sine-curve profile $U(y) = \frac{1}{2}(1 - \cos \pi y)$, $0 < y < 2$ when the dimensionless $\beta = 0.375$ and the number of subdivisions $N = 20$. We obtain nineteen series of phase velocities c, among which a pair become complex

for intermediate wavelengths as denoted by the thick line in the figure. The other seventeen series correspond to "singular" solutions having phase speeds equal to the velocities of the basic current somewhere in the field of flow. For a more detailed description of this figure, see Yanai and Nitta (1968).

Figure 2 shows the (c_r, c_i)-L diagram for the atmospheric profile at 500 MB, 0000Z April 3, 1974, The number of subdivisions is 20. The values of the dimensional and dimensionless velocity profile, dimensionless absolute vorticity gradients, and the lower and upper critical wavelengths for the unstable waves found from (28) and (29) are shown in Table 1. For this wind profile, there are four critical points and five unstable waves. The real parts of the phase speeds of these unstable waves are denoted by thick lines and the imaginary part by dotted lines. It is difficult from Figure 2 to tell the "true" unstable waves from "spurious" unstable waves due to trucnation errors or errors inherent in the finite difference approximation. A closer examination of the value of $\beta - U''$ at each point in Table 1 shows that the critical points at $y = 1.64$ and $y = 1.79$ are very close to each other. These two critical points can be easily smeared out by smoothing the basic current. Hence it is possible that four of the unstable waves are actually the same unstable wave, which will be contiguous to a Rossby-Haurwitz wave. It is also found that the L_κ's calculated from Eq.(28), shown in Table 1 are in general different from those shown in Figure 2. The L_κ for one of the unstable waves is especially difficult to find accurantely since the real part of the phase speed c_r for this unstable wave changes little as L increases. A little inaccuracy in interpolating y_κ and U_κ will change L_κ significantly. On the other hand, the unstable wave associated with the Rossby-Haurwitz wave has its $\frac{dc_r}{dL}$ quite large and therefore it is easier to find its L_κ more accurately. This type of unstable wave in general contributes to larger growth rate. It is intereating to note that for all the atmospheric wind profiles considered in this

study, the eigenfunctions φ for the singular waves which become this type of unstable wave at L_k are of first mode. The unstable waves of this type are in general the "true" unstable waves for an atmospheric wind profile and are in general of practical importance, since they contribute larger growth rate.

There are other unstable waves which change into singular waves or exist even at infinite L. Their c_r's in general change little as L increases and thus it is more difficult to determine their L_k's accurately. They contribute in general less growth rates as compared to the unstable waves contiguous to a Rossby-Haurwitz wave.

Since it is not economical or feasible to increase the number of subdivisions N for the actual atmospheric wind profiles, the best method to determined whether an unstable wave is spurious is to use the technique of smoothing. For a velocity profile expressible in mathematical functions, true unstable waves can be identified by their insensitivity to variations of number of subdivisions N.

Unstable Waves. In Figure 3 and Figure 4 the eignefunctions for some unstable waves are shown in terms of their amplitude $|\varphi|$ and phase angle arg φ. Also plotted is $\frac{d\varphi}{dy}$ expressed in terms of the component in phase and the component out of phase with φ.

For small c_i, it can be found that the in-phase and out-of-phase component of $\frac{d\varphi}{dy}$ has a distinct singular behavior at the points where c_r is equal to the velocity of the basic current. For c_i equal to zero, i.e., for a singular wave, this singularity is more profound and will be discussed later.

The disturbance stream function of an unstable wave can be calculated from (20). In Figure 5 is shown the disturbance stream function of the most unstable wave for 500 MB 0000Z April 3 wind profile, which has a wavelength of 2.6 (2476) km and amplifies by a factor of e in 3.44 days. The maximum amplitude of the disturbance

occurs at y = 1.0, just at the middle of the channel. The letter C and A represent the primary centers of cyclonic and anticyclonic vorticity. The dashed lines show the trough and ridge line, where v' vanishes. The location of trough and ridge line is determined by

$$\tan\alpha\,(x - c_r) = -\frac{\varphi_i}{\varphi_r}$$

and the tangent of the angle of tile θ measured from positive y direction is given by (24a) and (24b), which is proportional to the momentum transport.

The momentum transport $\overline{u'v'}$ is given by Eq. (23a,b) and is represented by a curve in Figure 8b. It goes from zero to a minimum at the first critical point, then increases from here to a maximum positive value at the second critical point. From this critical point it decreases to zero at the upper boundary except at the two critical points close to each other, where it is negative. It is seen from Figure 6b that $\overline{u'v'}\frac{dU}{dy}$ is mainly negative so that the time rate of change of mean-flow kinetic energy, given by (16) and (27) is negative, i.e., the perturbation is withdrawing the kinetic energy from the basic current.

The time rate of change of the basic current is given by (26) at every point of y. From Figure 6, in which are poltted the basic current U and its time rate of change $\frac{\partial U}{\partial t}$, it is readily seen that the momentum transfer reducs the maximum shear in the mean flow and hence intensifies the disturbances.

It is found thatthe $\frac{\partial U}{\partial t}$ calculated by (26a) and (26b) can be used as a measure of the accuracy of the finite difference approximations. The maximum root mean square difference between these two calculations for the wind profiles considered in this study is 0.7935×10^{-3}. The maximum percentage error is less than 0.01%. Therefore, the accuracy of the finite difference approximation of Eq. (21) is satisfactory.

The vorticity transport $\overline{v'\zeta'}$, which is numerically equal to the time rate of change of the basic current $\frac{\partial U}{\partial t}$ for a plane parallel flow, is given by (25). It is found from Figure 6c that the vorticity transport is in the direction of negative y at the center part of the channel and in the direction of positive y near the boundaries.

Rossby Waves. In Figure 1 and 2 it is seen that Rossby-Haurwitz waves appear at a certain wavelength L_o. They are Rossby-Haurwitz waves of the first mode. Rossby-Haurwitz waves appear in the order of the number of modes, as can be seen from the classical frequency relation of Rossby-Haurwitz waves. Let U(y) = $U_{max} = 1$, $U_{min} = 0$, then the frequency relation reads

$$\frac{n^2 \pi^2}{4} + \frac{4\pi^2}{L^2} = \frac{\beta}{1-c}$$

Keeping the right-hand side constant, we can see that the number of modes n increases if the wavelength L increases. That is, the Rossby-Haurwitz waves of higher modes will apepar first at larger wavelengths.

Singular Waves. In addition to the regular solutions (unstable waves and Rossby-Haurwitz waves) mentioned above, there are "singular" or "continuum" solutions, which are denoted by thin solid lines in Figures 1 and 2. These solutions correspond to continuous eigenvalues of c which are equal to the basic current U somewhere in the field of flow. It is clear from Eq. (21) that these singular solutions possess discontinuous $\frac{d\varphi}{dy}$. The eigenvalues φ at L = 1.0 for 500 MB 0000Z April 3 wind profile are shown in Figure 7 in order of numerical values of the phase speed c. The singular waves possess real phase velocity which are equal to the velocities of the basic current shown by dots. These waves have discontinuous first derivatives of φ at the points, although a small discrepancy due to the coarse finite difference is observed.

4. BAROTROPIC INSTABILITY IN RELATION TO THE GENERATION OF TORNADOES AND SEVERE ATMOSPHERIC VORTICES. In this study the value of β for calculating the stability characteristics of actual atmospheric wind profiles is assumed constant, though our results have simple extensions for the more general function $\beta(y)$. The dimensional β is taken at latitude 36^{o}. The domain of the atmosphere considered in this study is shown in Figure 8, 9, 10, and 11, We chose 23 x 35 grid points in this domain and on the boundaries. Only 21 x 33 values of u were obtained. Thus, we had 21 values of U(y). Most of our calculations were based on a bounded profile, i.e., we assumed the atmospheric motions occurred in a channel bounded by two rigid walls. This will in general underestimate the growth rates. The gridlength is 95.2 km. Thus it is not feasible to refine the mesh and use a larger value of N.

On 0000Z April 3, 1974, a remarkable cyclone development took place over western Kansas. This cyclone moved toward the northeast through Iowa and Wisconsin and reached its maximum intensity on 0000Z April 4 over eastern Wisconsin. During this period, a quasi-permanent anticyclone was located over Cuba and its intensity did not change. As the cyclons moved toward the northeast, the flow field between the cyclone and anticyclone was intensified and a jet developed over the region between the Mississippi and the Atlantic coast. Shortly after 0000Z April 4 a tornado outbreak took place over this area. In the early stage of cyclone development and the intensification of the flow field the underlying physical process was primarily the baroclinic instability. However, baroclinic instability along could not account for the variations of the jet which played a significant role in the tornado outbreak in that area. Now let us consider the effect of barotropic instability, which in general rarely occurs in the middle latitudes. After the cyclone has developed due to baroclinicity, the barotropic process may account for the subsequent intensification of the flow field.

Table 2 shows the e-folding time of the most unstable wave, and the most preferred wavelength for each profile. Most of the most preferred wavelengths of the unstable waves are comparable to actual wavelengths in the pressure system shown in Figures 8-11, except the wind profiles at 850 MB 1200Z April 4, 700 MB 0000Z April 3 and 300 MB 1200Z April 3, which are significantly less than the dominant wavelength of the pressure system. This means that the actual growth rate for these profiles could be smaller.

In the linear theory assumed in this study, the growth rates represent only the initial growth. After the disturbances have grown to some extent the linear theory is no longer valid.

As already noted, the calculated growth rates may underestimate the actual growth rates of the disturbances. The artificial boundaries prevent the momentum transports necessary to maintain unstable disturbances. Furthermore, with artificial boundaries, the dimensional U_{min} may have been oversetimated, which will reduce the value of growth rate. Thus, the actual e-folding times may be smaller than those shown in Table 2.

Thus, it is found that the atmosphere at all levels over the domain chosen is barotropically most unstable during 0000Z April 4, i.e., shortly before and at the time of the tornado outbreak, except at 850 MB, where its degree of instability was decreasing from 0000Z April 3. It is also found that the atmosphere at the upper level is barotropically more unstable than the lower level, which is generally accepted to be true.

In Figures 8-11 the dotted line in the domain chosen is the line where $\beta - \frac{\partial U}{\partial y} = 0$. At the center part of the domain $\beta - \frac{\partial U}{\partial y}$ is positive, while near the northwestern and southeastern boundaries it is negative. It is interesting to note that the hardest hit area (Indiana, Ohio, Kentucky, Tennesee and Alabama), which may be identified in the figures) was located just at the region in which the

distance between the critical points is shortest. If we take the local u(x,y) as mean flow instead of the averaged U(y), it is found that this region is most unstable. Hence, the five states were confined to this most unstable area and were hardest hit by tornadoes.

The equation for the time rate of change of mean-flow kinetic energy.

$$\frac{\partial E}{\partial t} = \int \overline{u'v'} \frac{\partial U}{\partial y} \, dy \qquad (16a)$$

still holds approximately. The momentum transport is proportional to the tilting of troughs and ridges, as already noted. It is found from Figures 8 -11 that the tilting of troughs and ridges was in a direction such that the mean-flow kinetic energy would decrease with respect to time. This means that the tilting of troughs and ridges, in relation to the position of the mean jet, was favorable for instability to occur.

From the above results it is concluded that barotropic instability may be synoptically associated with the generation of tornadoes and severe atmospheric vortices.

5. CONCLUDING REMARKS. In middle latitudes, where baroclinicity predominates, the importance of barotropic instability, despite its simpler physical mechanism, is always overshadowed by the importance of baroclinic instability. Most studies have not associated barotropic instability with geophysical phenomena, possibly due to the fact that the geophysical applications of barotropic instability are now in their exploratory stage. The present work performed a barotropic instability analysis of wind profiles over the area hardest hit by the April 3-4 tornado outbreak. It was found that the atmosphere over this area was barotropically most unstable during this tornado outbreak. This result indicates the possibility that

barotropic instability may have been synoptically associated with that outbreak. Additional case studies should be done to confirm the above results. Also, the relative importance of baroclinic and barotropic instability should be evaluated. Another promising area for future research would be to investigate whether the atmosphere over areas where tornadoes occur most often is barotropically unstable.

6. ACKNOWLEDGEMENTS. This study was supported by the National Science Foundation under Contract GA 30976, and also for several months by the National Aeronautics and Space Administration under Contract NAS 9-13360, and was conducted under the direction of Dr. Yoshi Kazu Sasaki, to whom I wish to express my hearty thanks for his guidance, assistance and encouragement. Support was also received from the Graduate College Research Development Fund, University of Oklahoma and the National Science Council, Taiwan, Republic of China. I am particularly indebted to Dr. Jay S. Fein for his valuable discussions and suggestions on the manuscript of this research. A very special thanks is extended to Ms. Anita Cameron for typing the manuscript.

REFERENCES

Drazin, P.G., and L.N. Howard, 1966: Hydrodynamic Stability of Parallel Flow of Inviscid Fluid. Adv. Appl. Mech., 9, 1-89.

Fjortoft, R., 1950: Application of Integral Theorems in Deriving Criteria of Stability for Laminar Flows and for the Baroclinic Circular Vortex. Geofys. Publ., 17, No. 6, 1-52.

Foote, J.R., and C.C. Lin, 1950: Some Recent Investigations in the Theory of Hydrodynamic Stability. Quart. Appl. Math., 8, 265-280.

Haltiner, G.J., 1971: Numerical Weather Prediction. John Wiley & Sons, New York, 317 pp.

_____, and R.T. Song, 1962: Dynmaic Instability in Barotropic Flow. Tellus, 14, 383-393.

Howard, L.N., 1961: Note on a Paper of John M. Miles. J. Fluid Mech., 10, 509-512.

_____, and P.G. Drazin, 1964: On Instability of Parallel Flow of Inviscid Fluid in a Rotating System with Variable Coriolis Parameter. J. Math Phys., 43, 83-99.

Jacobs, S.J., and A. Wiin-Nielsen, 1966: On the Stability of a Barotropic Basic Flow in a Stratified Atmosphere. J. Atmos. Sci., 23, 682-687.

Kuo, H.L., 1949: Dynamic Instability of Two-Dimensional Nondivergent Flow in a Barotropic Atmosphere. J. Meteor., 6, 105-122.

_____, 1951: Dynamical Aspects of the General Circulation and the Stability of Zonal Flow. Tellus, 3, 268-284.

_____, 1973: Dynamics of Quasigeostrophic Flows and Instability Theory. Adv. Appl. Mech., 13, 247-330.

Lin, C.C. 1955: The Theory of Hydrodynamic Stability. Cambridge University Press, 155 pp.

Lipps. F.B., 1962: The Barotropic Stability of the Mean Wind in the Atmosphere. J. Fluid Mech., 12, 397-407.

_____, 1963: Stability of Jets in a Divergent Barotropic Fluid. J. Atmos. Sci., 20, 120-129.

_____, 1965: The Stability of an Asymmetric Zonal Current in the Atmosphere. J. Fluid Mech., 21, 225-239.

_____, 1970: Barotropic Stability and Tropical Disturbances. Mon. Wea, Rev., 98, 122-131.

Lorenz, E.N., 1972: Barotropic Instability of Rossby Wave Motion. J. Atmos, Sci., 29, 258-264.

Nitta, T., and M. Yanai, 1969: A Note on the Barotropic Instability of the Tropical Easterly Current. J. Meteor, Soc. Japan, 47, 127-130.

Rayleigh, Lord, 1880: On the Stability or Instability of Certain Fluid Motions. Scientific Papers, 1, 474-487, Cambridge University Press.

_____, 1913: On the Stability of the Laminar Motion of an Inviscid Fluid. Scientific Papers, 6, 197-204, Cambridge University Press.

Reid, W.H., 1965: The Stability of Parallel Flows. Basic Development in Fluid Dynamics, Maurice Holt, Editor, Vol. I, 249-307.

Tollmien, W., 1935: Ein Allgemeines Kriterium der Instabilitat Laminarer Geschwindigkeitsverteilungen. Nachr. Ges. Wiss. Gottingen, Math-Phys. Klasse, 50, 79-114.

Wiin-Nielsen, A., 1961: On the Short and Long-Term Variations in Quasi-Barotropic Flow. Mon. Wea. Rev., 89, 461-476.

Yamasaki, M., and M. Wada, 1972a: Barotropic Instability of an Easterly Zonal Current. J. Meteor, Soc. Japan, 50, 110-120.

_____, 1972b: Vertical Structure of the Barotropic Unstable Wave in a Tropical Easterly Current. J. Meteor. Soc. Japan, 50, 271-284.

Yanai, M., and T. Nitta, 1968: Finite Difference Approximation for the Barotropic Instability Problem. J. Meteor. Soc. Japan, 46, 389-403.

Yih, C.S., 1969: Fluid Mechanics. McGraw-Hill, New York, 622 pp.

y(95.2km)	U(y) (m/sec)	U(y)	$\beta - U''(10^{-11}/\text{sec-m})$
0	18.205	0.048	
0.1	18.759	0.079	-1.267
0.2	19.596	0.125	-3.229
0.3	20.894	0.198	-3.141
0.4	22.645	0.296	-3.604
0.5	24.891	0.421	-4.354
0.6	27.700	0.578	-2.777
0.7	30.929	0.758	8.166
0.8	33.585	0.907	15.200
0.9	35.030	0.987	15.266
1.0	35.258	1.000	16.258
1.1	34.179	0.940	14.924
1.2	31.914	0.813	7.132
1.3	29.170	0.660	-0.849
1.4	26.671	0.520	-1.289
1.5	24.457	0.397	-2.392
1.6	22.628	0.295	-0.716
1.7	21.032	0.205	0.805
1.8	19.531	0.122	-0.055
1.9	18.203	0.047	-3.417
2.0	16.353	0	-

$y_k = 0.63$	$U_k = 0.624$	$L_k = 1.570$
$y_k = 1.29$	$U_k = 0.676$	$L_k = 1.308$
$y_k = 1.29$	$U_k = 0.676$	$L_k = 3.501$
$y_k = 1.64$	$U_k = 0.253$	$L_k = 3.877$
$y_k = 1.79$	$U_k = 0.127$	$L_k = 4.452$

$L_o = 5.497$

Table 1. Dimensional and dimensionless U(y) and $\beta - U''$ at each grid point, and low critical wavelength L_k and upper critical wavelength L_o calculated from (34) and (35), for the 500 MB 0000Z April 3 wind profile.
The corresponding (c_r, c_i)-L diagram is shown in Figure 2.

		850 MB	700MB	500 MB	300MB
	(a)	(5.68, 3619)	(85.38, 1524)	(3.44, 2476)	(18.97, 4191)
0000Z April 3	(b)	-	stable	(3.70, 2286	-
	(c)	(6.35, 3619)	-	(3.20, 2286)	-
1200Z April 3	(a)	(12.85, 2857)	(32.96, 3429)	(6.91, 3619)	(6.71, 1905)
	(a)	(15.20, 4572)	(7.98, 2857)	(3.77, 4752)	(3.60, 3619)
0000Z Apirl 4	(b)	-	(117, 4572)	-	-
	(c)	-	-	(3.76, 4572)	(2.74, 4000)
	(a)	(33.50, 1524)	(18.11; 4572)	(4.27, 4000)	(2.93, 3810)
1200Z April 4	(b)	stable	-	-	-
	(c)	(29.49, 1524)	-	-	-

(a) for a bounded nonsmoothed profile

(b) for a bounded profile smoothed once $S_1 = 0.25$

(c) for a semiinfinite profile

(d) for a semiinifinite profile smoothed once $S_1 = 0.25$

Table 2. The e-folding time of the most unstable wave, and the most preferred wavelength, for each wind profile considered in this study. The first value in the pa anthesis is the e-folding time in days, the second value is the most preferred wavelength in km.

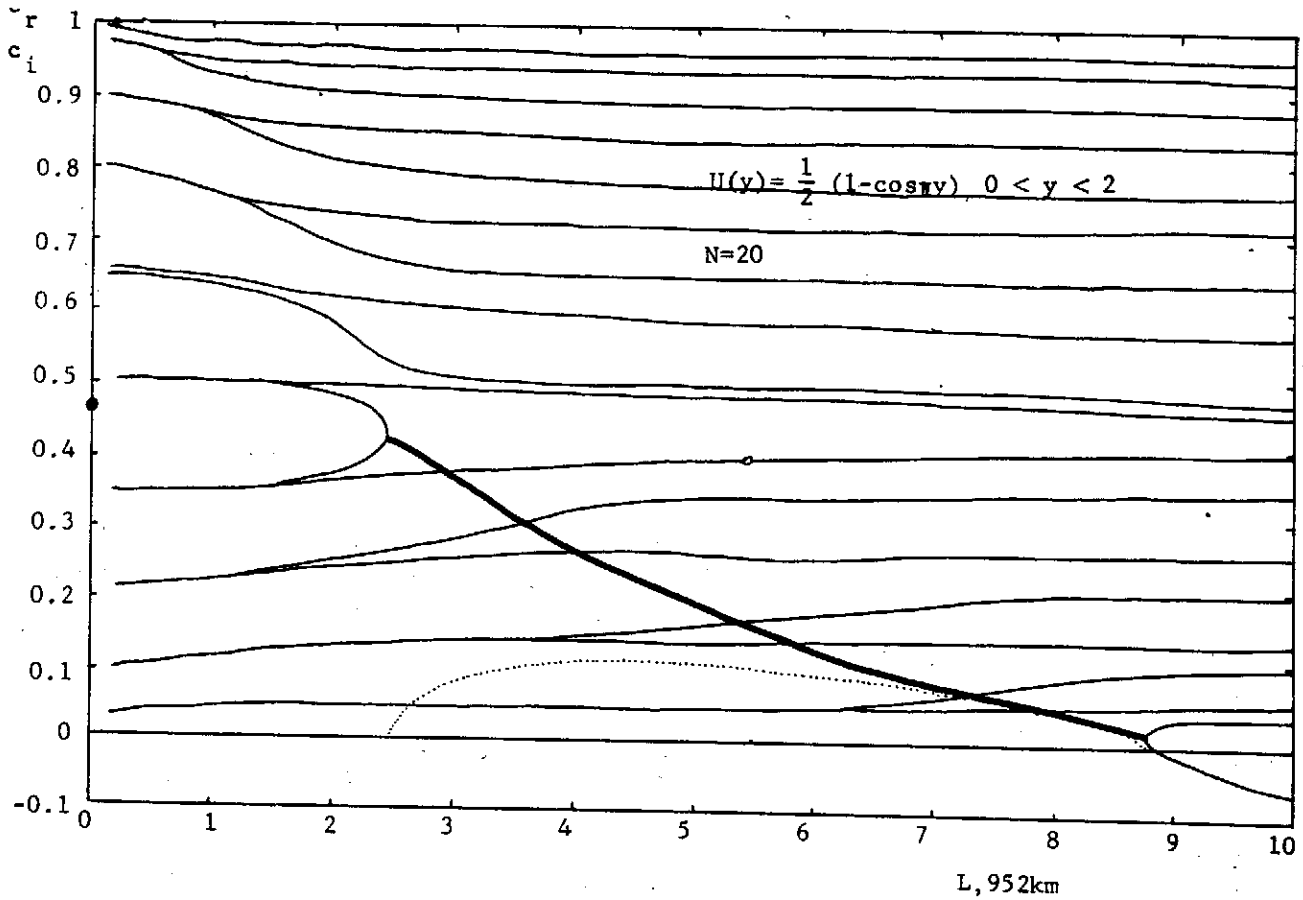

Figure 1. A (c_r, c_i)-L diagram for symmetric sine-curve velocity profile $U(y) = \frac{1}{2}(1-\cos \pi y)$ when $\beta = 0.375$ and $N = 20$. The thick solid line and the dotted line correspond to c_r and c_i of the unstable wave respectively. Black dot on the ordinate represents U_κ.

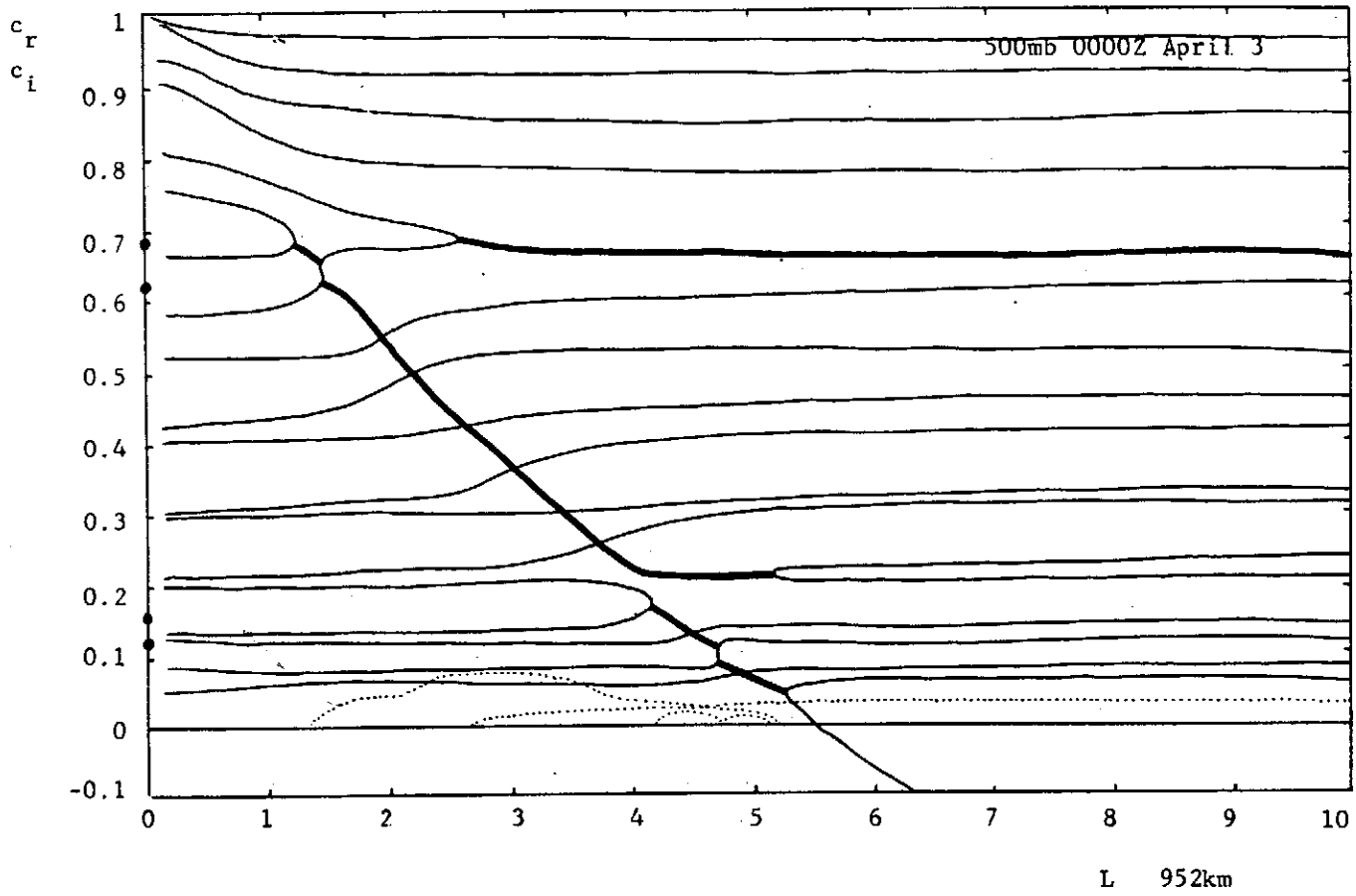

Figure 2. A (c_r, c_i)-L diagram for 500 MB 0000Z April 3 wind profile. The thick solid lines and the dotted lines correspond to c_r and c_i of unstable waves reapectively. Black dots on the ordinate represent U_K's.

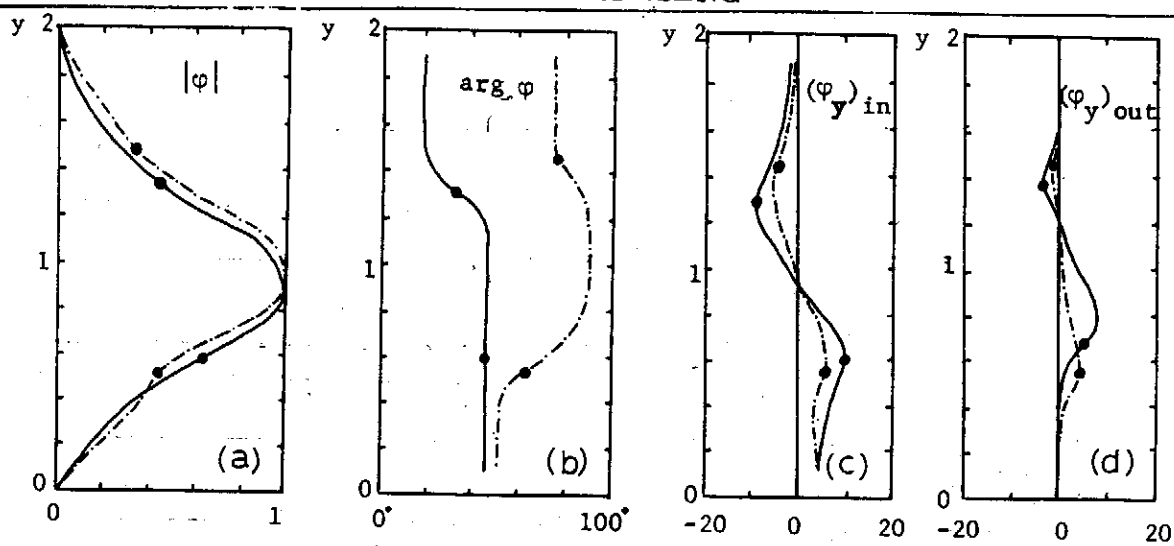

Figure 3. Unstable solutions for 500 MB 00000Z April 3 wind profild; (a) Absolute value of eigenfunction φ. (b) Phase of φ in degrees. (c) Derivatives of φ in phase with φ. (d) Derivatives of φ out of phase with φ. Note the singular behavior at the points, denoted by black dots, where c_r is equal to the velocity of the basic current.

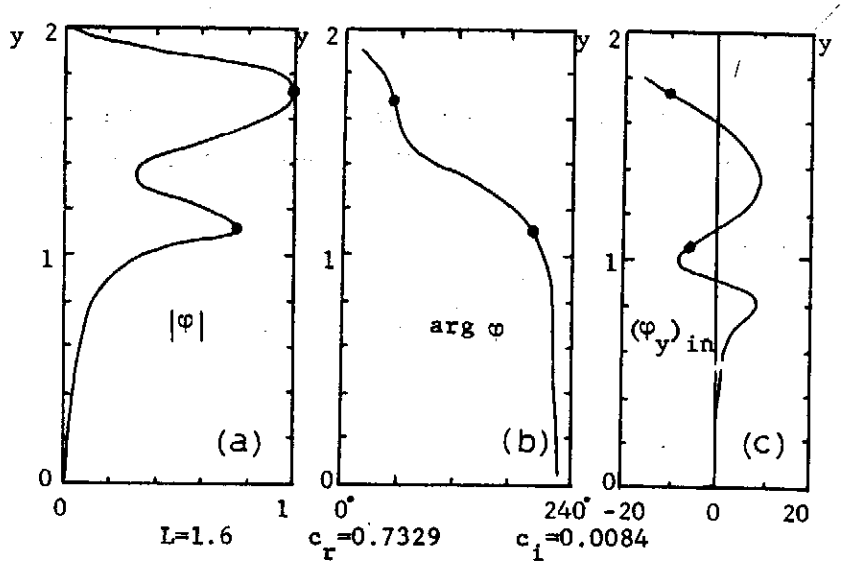

Figure 4. Unstable solution for 700 MB 0000Z April 3 wind profile. (a) Absolute valre of eigenfunction φ. (b) Phase of φ in degrees. (c) Derivative of φ in phase with φ. Note the singular behavior at the points, denoted by black dots, where c_r is equal to the velocity of the basic current.

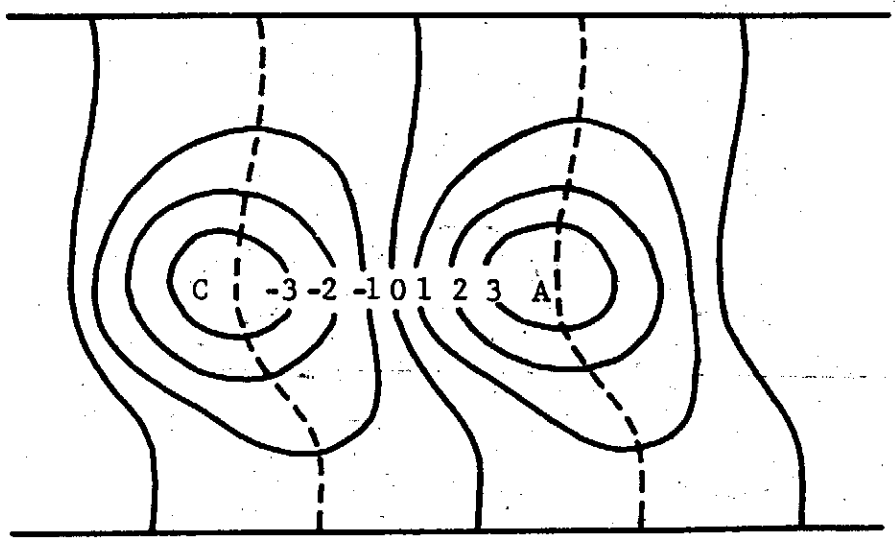

Figure 5. Disturbance stream function of mosttunstable wave at L =2.6 for 500 MB 0000Z April 3 wind profile. The primary centers of cyclonic and anticyclonic vorticity are marked by C and A. The dashed line shows where v' vanishes, i.e., trough and ridge lines.

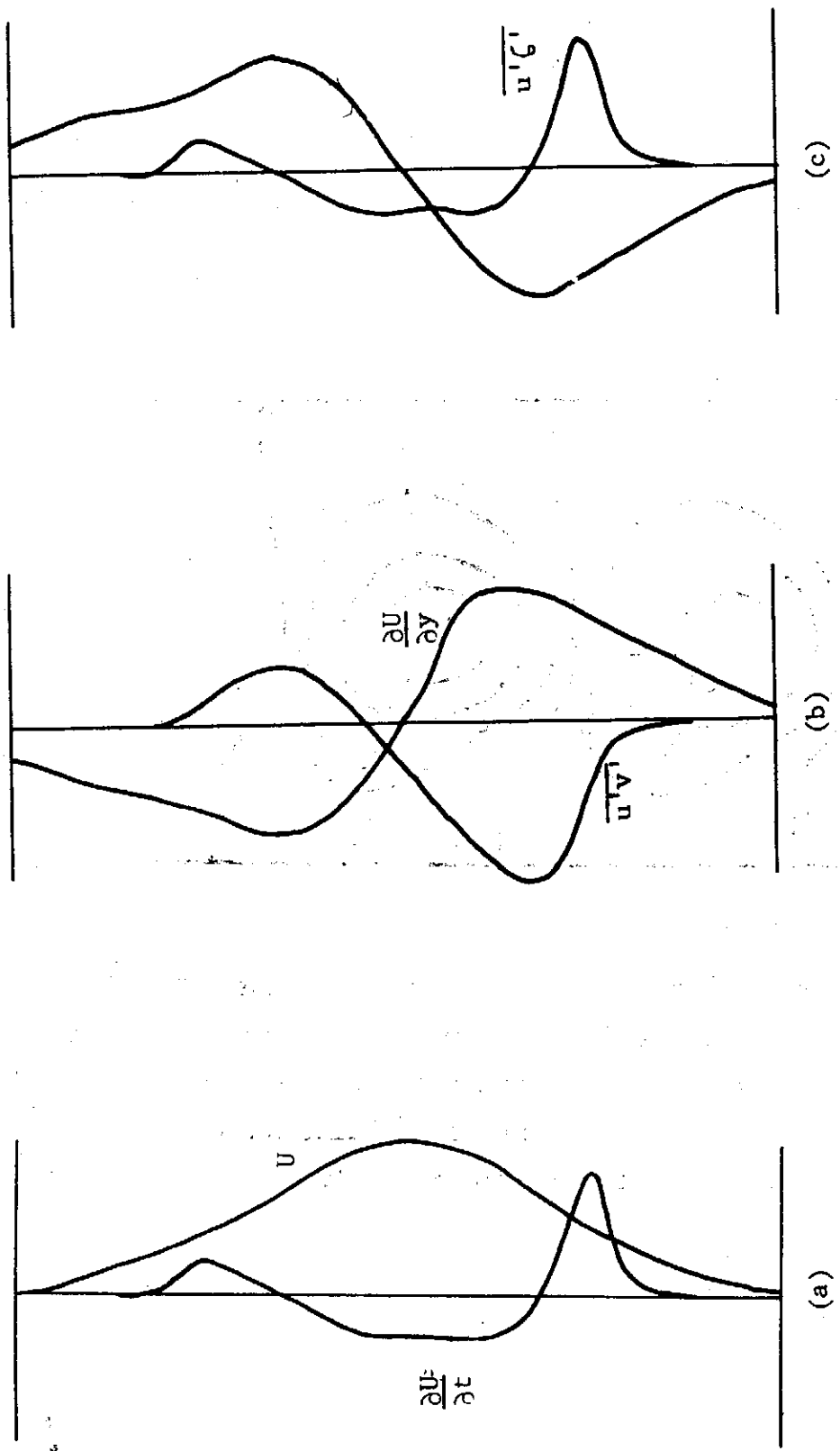

Figure 6. $u, \frac{\partial U}{\partial t}, \overline{u'v'}, \frac{\partial U}{\partial y}, \overline{\zeta}$ and $\overline{v'\zeta'}$ for 500MB 0000Z April 3 wind profile.

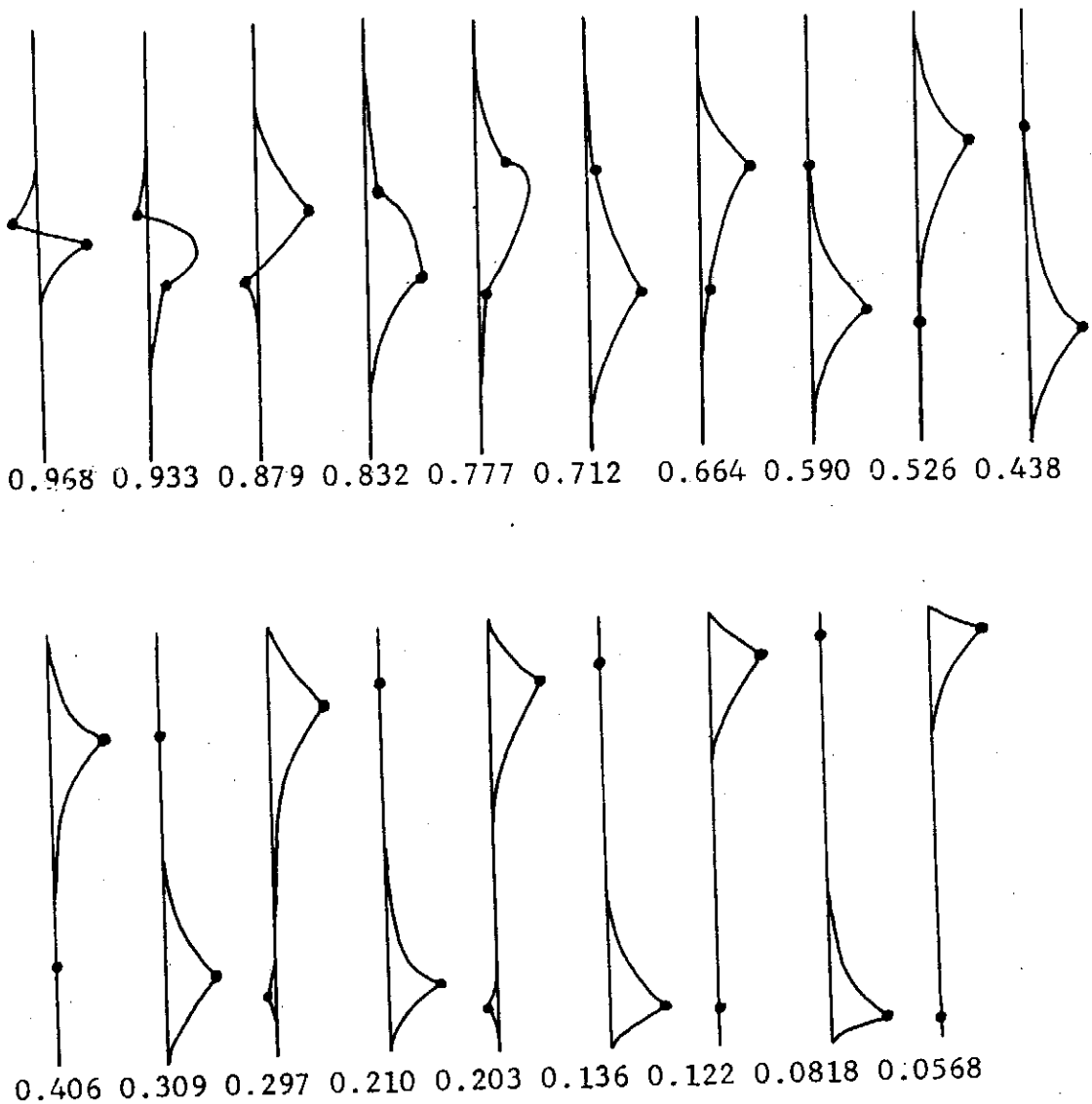

Figure 7. Eigenfunction φ of singular waves at L=1.0 for 500 MB 0000Z April 3 wind profile. Nondimen sionalized phase velocities are shown below. The singular waves possess phase velocities equal to the basic current velocity at the points indicated by black dots.

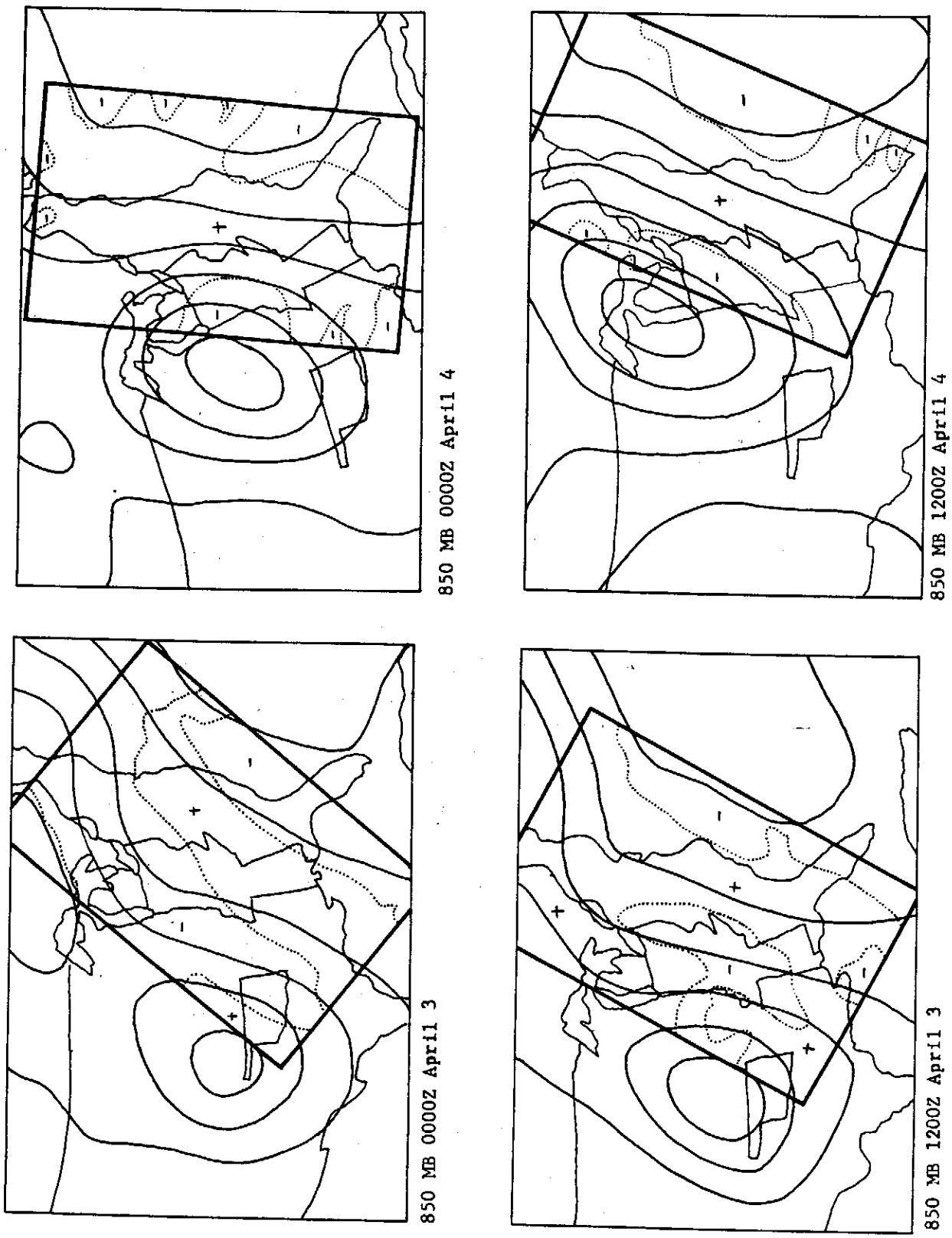

Figure 8. Weather maps at 850 MB for four time steps and the domains considered in this study.

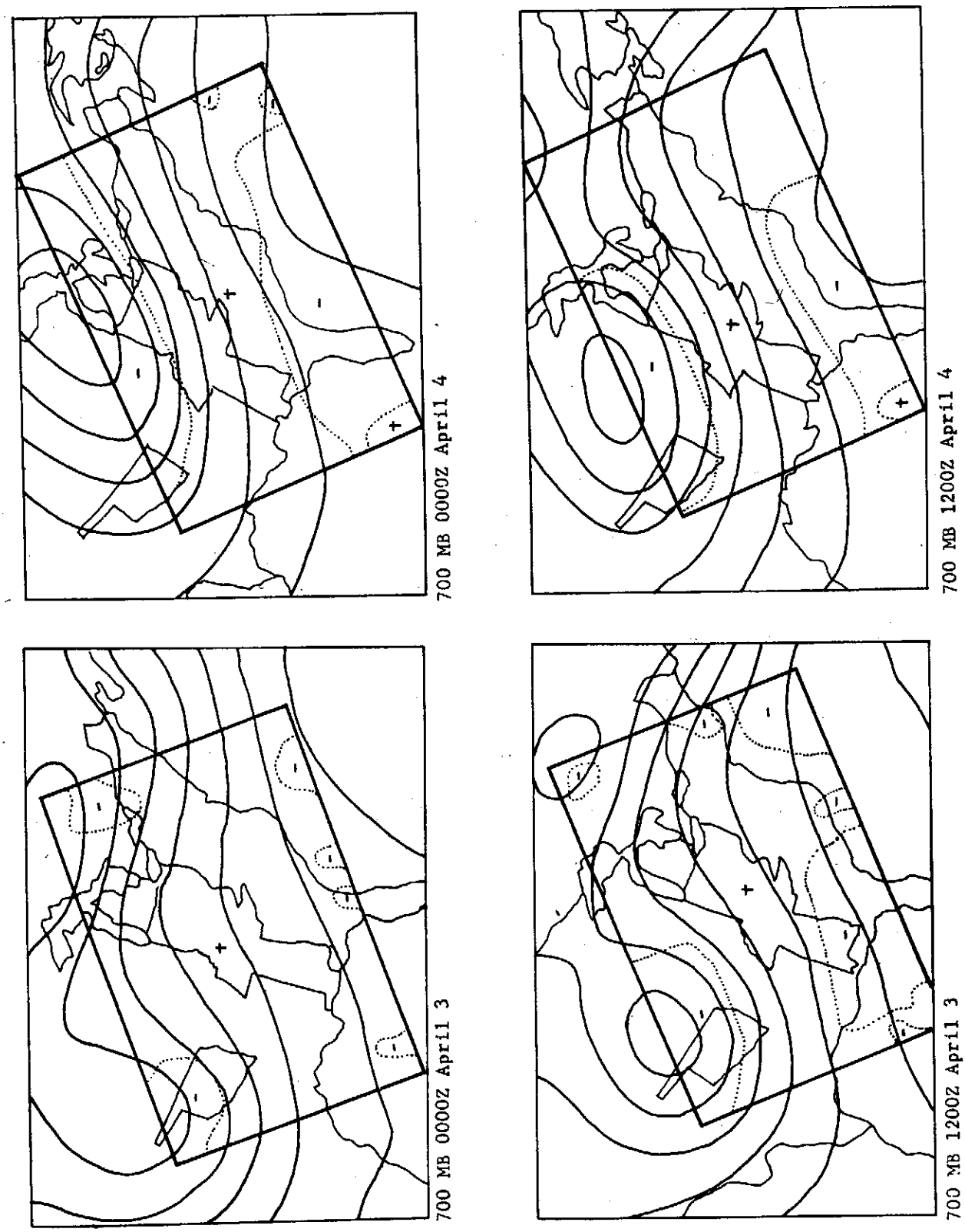

Figure 9. Weather map at 700 MB for four time steps and the domains considered in this study.

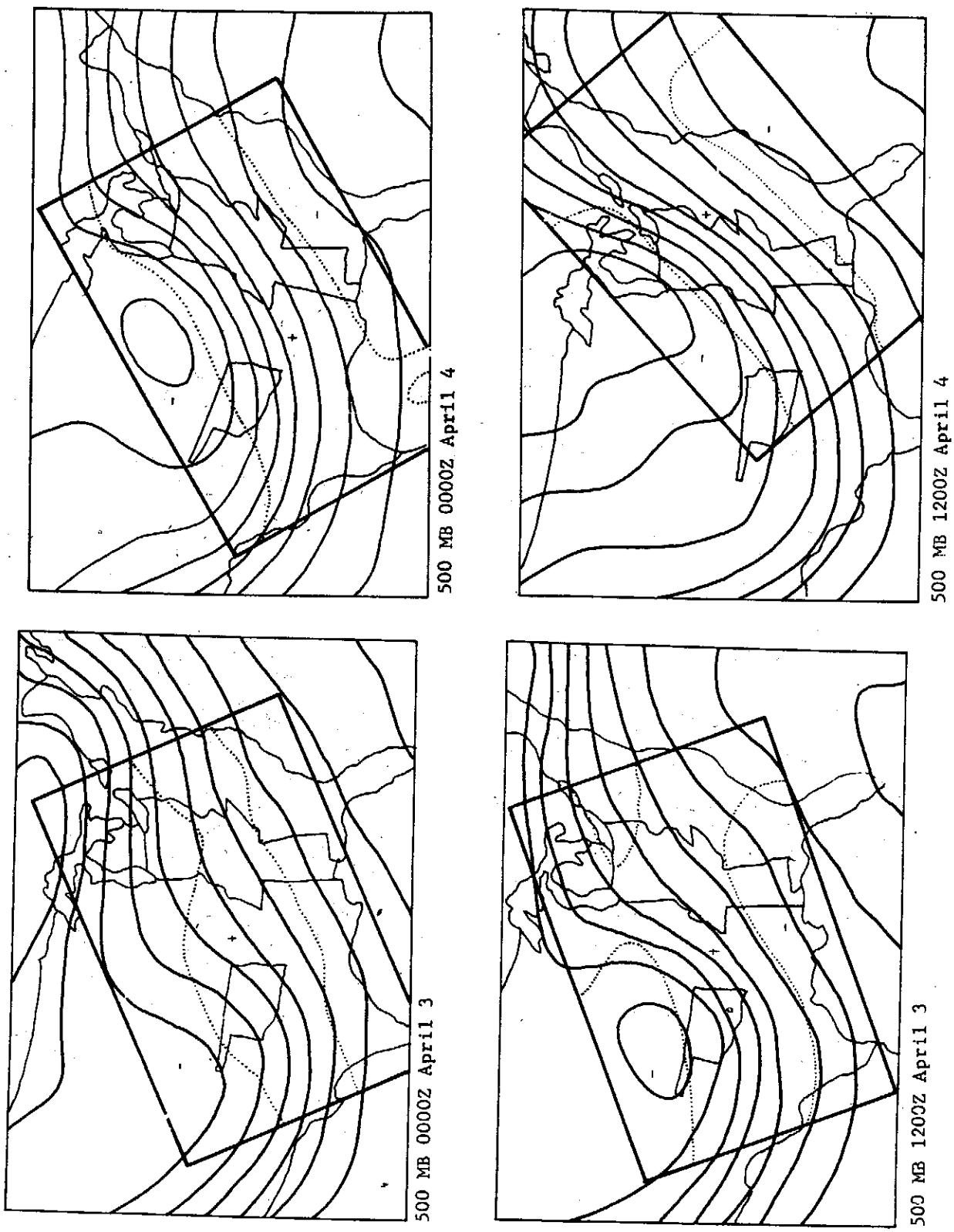

Figure 10. Weather map at 500 MB for four time steps and the domains considered in this study.

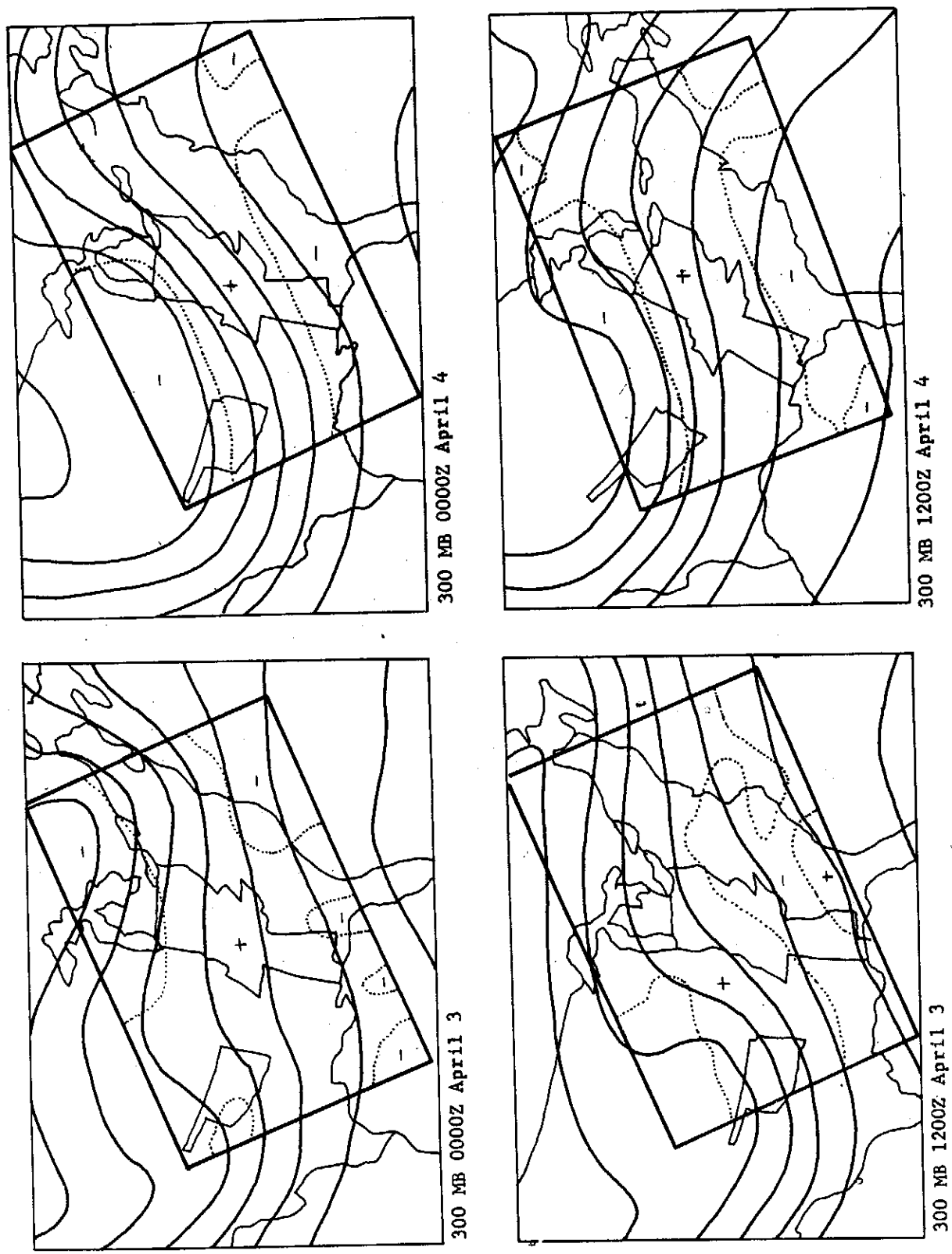

Figure 11. Weather map at 300 MB for four time steps and the domaims considered in this study.

ANNUAL REPORT OF THE INSTITUTE OF PHYSICS,
ACADEMIA SINICS, 1974

Particle distribution for dilute suspension in flow

Robert R. Hwang (黃榮鑑) and Chun Chiang (蔣炯)

Institute of Physics

Academia Sinica

Nankang, Taipei, Taiwan

ABSTRACT

Analytic expression for particle distribution of a dilute suspension in the flowing blood was investigated as functions of radial distance at any distance from the inlet where the velocity and concentration profiles are fully developed. Theoretical analysis was concerned in solving the equation of convection-diffusion of mass subjected under two boundary cases while a parabolic valocity profile which is obtained for Hagen-Poiseuille flow was used for convection velocity in the mass equation.

I. Introduction

Particle distribution in a flowing fluid is of interest not only in the field of engineering and physical science, but in biomedical field as well, the distribution of materials in the flowing blood is of keen interest.

Recently, Tesfagaber and Lin have used the method of variational calculus under the minimum energy dissipation hypothesis to show that the particle distributes uniformly in a flowing fluid in contrast to their initial expectation; in their calculations, the assumptions are:

(1) The system has attained steady state.
(2) There is no radial or rotational flow.
(3) No body force is acting on the system, i. e., the tube is horizonal.

(4) Pressure is constant across section.

(5) There is no slipping on the tube wall.

(6) The fluid is incompressible.

(7) The tube has a constant cross section.

(8) Fluid is a continuum.

Furthermore, the quantity of fluid passing through the tube and the particle delivered are constant, namely:

$$Q = 2\pi \int V\, r\, dr = \text{const} \tag{1}$$

$$H = 2\pi \int V\, r\, dr = \text{const} \tag{2}$$

where h is the concentration and V , r have the usual meaning in the cylindrical coordinates.

However, we are able to show simply that the concentration is uniform under the above conditions without much mathematical manupilation as follows:

For steady-state and constant density and diffusivity, the equation for convection-diffusion of mass in a tube is

$$V_z \frac{\partial h}{\partial z} + V_r \frac{\partial h}{\partial r} = D\left[\frac{1}{r}\frac{\partial}{\partial r}\left(r\frac{\partial h}{\partial r}\right) + \frac{\partial^2 h}{\partial z^2}\right] \tag{3}$$

in the fully developed region, $v_r = 0$; in addition, from eq. (2) we can get

$$\frac{\partial h}{\partial z} = 0 \quad \text{thus, eq. (3) simplifies to} \tag{4}$$

$$D\left[\frac{1}{r}\frac{\partial}{\partial r}\left(r\frac{\partial h}{\partial r}\right)\right] = 0 \tag{5}$$

The solution of eq. (5) is

$$h(r) = A \ln r + B \tag{6}$$

where A and B are constant. Since $\frac{\partial h}{\partial r} = 0$ at $r = 0$ (This is so if eq. (5) exists at $r = 0$), thus we obtain $A = 0$ and $h = B$.

Intuitively, we can also understand that the concentration is uni-

form under the above assumption.

Since there is no rotational and rodial flow, and since there is no pressure gradient along tube cross section, there is no source-sink along the tube cross section. Thus if there exists any concentration gradient, the concentration gradient will eventually disappear due to the diffusion process, thus the particle distribution must be uniform.

The above discussion deals with the situation that there is no exchange of mass at the wall, in real case such as blood vessels, nutrients must be transported by the blood to the tissue and the waste in the tissue must be transported away by the blood, thus the blood wall functions as a filter. Under this situtation, the particle distribution will be nonuniform. We can classify two boundary cases:

(1) Uniform mass flux along the wall, that is the wall can actively digest a fixed amount of material, thus the material exchanged per unit of time is the same.

(2) Uniform concentraction at the wall, that is the wall may actively keep the concentration for a fixed value. Any concentration higher than this threshold value can quickly be filtered by the wall.

The present paper attempts to investigate the particle distribution in a flowing fluid subjected under these two boundary cases. Theoretical analysis will be concerned in solving the equation of convection-diffusion of mass.

II. Formulation and Analysis of Problems

The problems as mentioned above for the flow in the blood vessels, the blocd wall may be functioned as a filter in which nutrients and wastes in the tissue can be transported through it. Let us assume the blood entering the vessel has an initial particle distribution of component A, and the concentration or the mass flux at the wall is maintaned constant. If the concentration of component A is sufficiently dilute then the total density is approximately constant.

We wish to find the concentration profile within the tube at some distance from the inlet where the velocity and concentration profiles are fully developed.

Mass balance applied to component A in an annular control volume in the flowing region for the steady-state and constant density and diffusivity yields the equation for convection-diffusion of mass in a tube as eq. (3) . For fully developed region, $V_r=0$. In addition, diffusion in the axial direction is small in comparing with the radial direction and hence, can be neglected. Thus Eq. (3) simplifies to

$$V_z \frac{\partial h}{\partial z} = D\left[\frac{1}{r}\frac{\partial}{\partial r}\left(r \frac{\partial h}{\partial r}\right)\right] \tag{7}$$

For any set of boundary conditions, we define a fully developed concentration profile to be existed when $(h-h_o)/(h_m/h_o)$ is a unique function of r/r_o independent of z, then

$$\frac{h - h_o}{h_m - h_o} = f\left(\frac{r}{r_o}\right) \tag{8}$$

where h_o is particle concentration at the wall and h_m is maximum particle concentration at center. Since $\frac{\partial}{\partial z}\left(\frac{h - h_o}{h_m - h_o}\right) = 0$, we have

$$\frac{\partial h}{\partial z} - \frac{\partial h_o}{\partial z} - \frac{h - h_o}{h_m - h_o}\left(\frac{\partial h_m}{\partial z} - \frac{\partial h_o}{\partial z}\right) = 0 \tag{9}$$

The axial velocity V_z may be obtained from the equations of continuity and motion for laminar pipeline flow. For fully developed flow, the velocity distribution is obtained as

$$V_z = 2\bar{V}\left[1 - \left(\frac{r}{r_0}\right)^2\right] \tag{10}$$

where $\bar{V} = -\frac{r_0^2}{8\mu}\frac{dp}{ax}$

(i) For the case of Uniform concentration at the wall:

Since h_o = constant, from eq. (9), we can have the relation

$$\frac{\partial h}{\partial z} = \left(\frac{h - h_0}{h_m - h_0}\right) \frac{\partial h_m}{\partial z} = f\left(\frac{r}{r_0}\right) \frac{\partial h_m}{\partial z} \tag{11}$$

Two boundary conditions in this case can be specified to obtain the particle distribution. They are:

$$\frac{\partial h}{\partial r} = 0 \qquad \text{at} \quad r = 0 \tag{12}$$

$$h = h_0 = \text{Const.} \quad \text{at} \quad r = r_0$$

Substitution of the velocity distribution of eq. (10) and $\partial h / \partial z$ in eq. (11) into the mass balance equation of eq. (7), a differential equation concerning the f function in eq. (8) can be obtained as

$$f'' + \frac{1}{R} f' + K(R^2 - 1) f = 0 \tag{13}$$

where prime indicates the derivative with respect to R and $R = \frac{r}{r_0}$, $K = \frac{2 r_0^2 \overline{V}}{D}$

Eq. (13) has a regular singlur point at R = 0. By the method of Frobenius, the differential equation can have a solution in series form as

$$f(R) = R^s \sum_{m=0}^{\infty} A_m R^m \tag{14}$$

in which $A_o \neq 0$.

In the substitute of eq. (14) into (13), coefficients s and A_m's can be obtained. Solution of eq. (13) is then

$$f(R) = \sum_{m=0}^{\infty} A_{2m} R^{2m} + \sum_{m=1}^{\infty} A_{2m+1} R^{2m+1} \tag{15}$$

where

$$A_2 = \frac{K}{4} A_0 \ , \ A_4 = \frac{K}{4^2}(A_2 - A_0) \ , \ \cdots\cdots$$

$$\cdots\cdots\cdots, \ A_{2m} = \frac{K}{(2m)^2}\left[A_{2(m-1)} - A_{2(m-2)}\right]$$

and

$$A_3 = \frac{K}{9} A_1 \ , \ A_5 = \frac{K}{5^2}(A_3 - A_1) \ , \ \cdots\cdots$$

$$\cdots\cdots\cdots, \ A_{2m+1} = \frac{K}{(2m+1)^2}\left[A_{2m-1} - A_{2m-3}\right]$$

the series solution of f(R) is converge for m increasing. Coefficients of A_o and A_1 are determined from the substitute of f(R) into the boundary conditions of eq.(12). The particle distribution is then obtained from eq.(11)

$$h(r,z) = f\left(\frac{r}{r_0}\right)\int z\,\frac{dh_m}{dz} \tag{16}$$

(ii) For the case of uniform mass flux along the wall:

We can define the radial mass flux $\left(\omega_a / A\right)_r = H_D\,(h_m - h_o)$, H_D is mass transform coefficient, Since $\left(\omega_a / A\right)_r = -D\,\frac{\partial h}{\partial r}$ then

$$H_D = \frac{(\omega_a/A)_r}{h_m - h_o} = -\frac{D}{r_0}\;\frac{\partial}{\partial(r/r_0)}\left(\frac{h - h_o}{h_m - h_o}\right) \tag{17}$$

From eq.(8), it can be known that the term of $\frac{h - h_o}{h_m - h_o}$ is independent of z and functions only of r. Therefore, H_D is constant along the tube. The constant of mass flux along the wall states the relation of $\frac{dh_o}{dz} = \frac{dh_m}{dz}$. With the relation of eq.(9), we have

$$\frac{\partial h_o}{\partial z} = \frac{\partial h_m}{\partial z} = \frac{\partial h}{\partial z} = \text{Constant} \tag{18}$$

To obtain the particle distribution in the case of uniform mass flux along the wall, it can be done by substituting eq.(18) and the axial velocity distribution of eq.(10) into the mass equation of eq.(7) for fully developed flow with the following two boundary conditions specified in this case.

$$\begin{aligned} &\partial h / \partial r = o \qquad \text{at} \quad r = 0 \\ &h = h_o(z) \qquad \text{at} \quad r = r_0 \end{aligned} \tag{19}$$

The particle distribution is obtained as

$$h(r,z) = h_o + \frac{V}{8 r_0^2 D}\left(\frac{dh_m}{dz}\right)\left(3 r_0^4 - 4 r_0^2 r^2 + r^4\right) \tag{20}$$

Reference

1. Bird, R. B., W. E. Stewart and E. N. Lightfoot. 1960. Transport Phenomena, New York: Wiley.
2. Eckert R.E.G. and Drake, R.M. 1972. Analysis of Heat and Mass Transfer, McGraw-Hill.
3. Mathews J. and Walker R. L. 1964. Mathematical Methods of Physics, Benjamin.
4. Tesfagaber A. and Lih M. M. 1973. "Particle Distribution for Dilute Suspension in Flow". Bulletin of Mathematical Biology, Vol. 35.

ANNUAL REPORT OF THE INSTITUTE OF PHYSICS,
ACADEMIA SINICA, 1974.

THE MIXING CHARACTERISTICS OF TURBULENT BUOYANT JETS IN AMBIENT RECEIVING ENVIRONMENTS

Robert R. Hwang (黃榮鑑)
Institute of Physics
Academia Sinica
Nankang, Taipei, Taiwan

Abstract

The behavior of a set of heated water jets discharging into a shallow flowing environment was considered in a laboratory study. The relative effects of jet interaction and surface distortion were considered and three aspects of this problem singled out for particular attention: firstly, some means whereby stratified flow might be distinguished from mixed flow; secondly, the manner in which mixing varies with distance downstream from the discharge ports; thirdly, the flow regimes arising from combined mixing and buoyancy effects which can be expected in this type of flow system.

I. Introduction

The ever increasing emission of pollutants such as heat and chemical substances into ocean, lakes, rivers, and the atmosphere has become a threat to our enviornment. In order to reduce the detrimental effects of such emissions, it is important to understand the mechanism and to predict the dispersion of pollutants for any given discharge configurations.

Disposals of sewage and heated water into the ocean and esturies have been practiced by many coastal cities around the world. Inadequate dispersal of the pollutants has often resulted in serious contamination of the coastal areas. Controlling of such pollution problems relies on a clear understanding of the basic flow phenomena involved. Submerged diffuser is the recent practice of marine dis-

posal. The discharge of sewage or heated water from a submerged source into a body of water results in mixing which may dilute the original discharge so that its concentration or temperature is greatly reduced. The predominate mechanism for the reduction of concentration or temperature is physical mixing. As the density of the effluent is different from the density of the ambient fluid (e.g., sewage has nearly the same density as fresh water, it is about 2.6% lighter than sea water; heated water under different temperature is lighter than fresh water or sea water, etc.), the buoyancy effect on the the jet behavior will be important. Therefore, the physical mixing may contain three phases in the usual processes. Near the source, differences in velocity and volume flux between the effluent and the ambient flow can produce mixing due to the instability of the interface and due to the turbulent energy contained in the jet. The second is the byoyance effect. Buoyancy causes rise of a submerged jet and horizontal spreading of a surface jet. The third phase of physical mixing is which mixing is caused by ambient turbulence. To the problem of mixing in a shallow flowing environment, the attension is also being focussed on the effect of free surface distortion. These multiply effects on the mixing processes cause the study of mixing problem complicatelly and difficulty both in the theoratical analysis and in the experimental study.

The usual purpose in near-field mixing due to a submerged discharge is to achieve the maximum amount of mixing or dilution. Upon the processes of physical mixing mentioned above mixing due to the buoyancy effect and momentum flux of turbulent jets can be controlled to obtain a reasonable degree of mixing or dilution in the near-field stage. The present study is concerned with the case that buoyant fluid was jetted submergibly into a shollow flow environment to study the interaction of the three phases of effect on jet mixing processes mentioned above. Three areas will be observed and investigated in this study:

(1) the inter-relationship of degree of mixing.

(2) classification of mixing and stratified flow systems.

(3) the qualitative observation of upstream wedge forms.

II. Review of Previous Works:

There are two basic methods of discharging waste water and buoyancy fluid into the receiving water environment (e.g., Ocean, lake or river etc.). The water-borne waste matter can be discharged as surface discharged or submerged discharge. The former is the simplest and the most economic of the commonly used disposal techniques; the passing of sewage through an ocean outfall, the discharge of heated water from a canal into a cooling pond or river, are applications of this technique. That cannot have a good mixing situation at the near-field stage from disposal is the charactor of this disposal technique. Mechanism and theory of the surface disposal have been studied theoretically and experimentally by many investigators. In the extension of the work of Morton (1961), Fan (1967), and Zellen (1967), Motz (1972a,b) developed a particular stream model and studied the spreading behavior of a heated surface jet discharging into the ambient flow stream at a specified angle. By setting a new expression for surface heat loss from an artificially heated water surface from testing in the field and the laboratory, Ryan and Harleman (1972, 1973), Stolzenbach and Harleman (1971) carried out a series of analytical and experimental studies of transient cooling pond behavior. Applying the expression for surface heat loss exchange, Hwang et al (1793) investigated the flow behavior and predicted the expected value of the ratio of the excess tamperature of the station intake to the excess temperature at station outlet of the disposal cooling water into a cooling lake from a nuclear power station for different discharge configurations and geometric conditions. Other investigations about this topics have been summaried in papers by Harleman and Stolzenach (1972), and Fan and

Brook (1975).

The recent practice of submerge disposal is to discharge the waste matter of water-borne in jets. The initial mixing of the effluent with the ambient water is induced by the turbulent jet motion. One of the early attempts to understand the influence of density variation in plumes was the work of Rouse, Yih and Humphrey (1952) who studied experimentally both plane and round vertical plumes in uniform surroundings. Morton, Taylor and Tumer (1956) analyzed the plume flow in stratified surrounding using integral forms of the equations governing the mean quantities and, to close the problem, they introduced a coefficient for the entrainment of fluid into the plume, which it was assumed a universal constant. Many subsequent studies were carried out recently in studying the behavior of buoyant jets. Anwar (1969) dealed with the case of a quiescent ambient fluid in which the buoyancy force dominates the rising plume. Fan and Brook (1969) obtained the dilution ratio in functions of longitudinal distance and vertical depth analytically from solving the momentum flux equations of jets in which the ambient fluid is at rest. Putting the concept of entrainment on a rational basis, List and imberger (1973) shew that the behavior of turbulent jets in uniform density environments is governed by an entrainment function and buoyancy function, both of which are functions of the local jet densimetric Froude number and the local jet angle. Excluding the effect of jet excess momentum on buoyant jets, Weil and Fischer (1974) studied the properties of mixing and spreading of heated water plumes experimentally and obtained the behavior of jet temperature variation describing in forms of four independent dimensionless variables: x/D, d/D, U_*/U_n and F_j which are distance ratio, depth ratio, friction factor, and deusimetric Froude number bassed on channel velocity and jet diameter.

Most of investigators studied the behavior of turbulent jets based on their assumptions to describe the flow configurations of problem.

None of them gave a simple way and result to describe the characteristics of mixing fully at the near-field stage as turbulent jet submerging into the ambient environment.

III. Analysis of the Mixing Problem

The mixing of heated water jets in flowing environments is only part of the much broader proolem of mixing within density differentiated environments. Viewed in this light, the role of temperature in the present enquiry is seen as providing simply the means by which density differences are produced. As mention previous, the disposal of heated effluent through submarine jets subjects the mechanic effects of the jet momentum, buoyancy, and turbulence of the flow. For the near-field model, the mixing is concerned with interaction of the first and second mixing effects, in which only the jet momentum and buoyancy are important. In order to achieve a great rate of dilution or temperature reduction, discharge is often from a multiport diffuser from which many small single jets are discharged. This study is intended to investigate the mixing characteristics of submerged multipleport diffusers for heated effluents in a receiving water of uniform current flow and hopefully to provide information on mixing of heated water effluent for the design of new power plants.

Dimensional Analysis. -- Considering the flow system shown in figure 1, the functional relationship which exists between the degree of mixing at a section, distance x downstream from a line of jets, and the other variables involved, may be written in the form

$$M_X = \phi_1(H, U_a, \rho_a, \nu_a, D, \theta, U_j, \triangle\rho, \nu_j, x, L, g) \qquad (1)$$

in which, H = depth of flow; U_a, ρ_a, ν_a, = velocity, density and viscosity of current flow respectively; D, U_j, ν_j, = dismeter, velicity and viscosity of heated water jet respectively; $\bigtriangledown\rho$ = density deficiency of source heated water; L= port spacing of diffusers; θ = angle between port centerline and bed. By dimensional analysis,

M_x can be written as

$$M_X = \phi_2 \left[\frac{U_i}{U_j}, \left(\frac{U_a^3}{\frac{\Delta\rho}{\rho} gqi} \right)^{1/2}, \frac{UaH}{\nu a}, \frac{U_j D}{\nu_j}, \frac{x}{H}, \frac{L}{H}, \frac{D}{H}, \left(\frac{U_a^2}{gH} \right)^{1/2}, \theta \right] \qquad (2)$$

The first term of eq.(2) is the velocity ratio of jet and ambient flow. Combing with the dependences of $\frac{D}{H}$ and $\frac{L}{H}$, the dimensionless term is substitute with the kinematic momentum ratio $M_r = \frac{q_a U_a}{q_j U_j}$ the second term is now defined as a densimetric Froude number, Fd, where the denominator is the buoyancy flux and is similar as Cederwall's (1971) source Froude number or Weil's (1974) densimetric Froude number. The terms of $R_a = \frac{U_a H}{a}$ and $R_j = \frac{UjD}{j}$ are Reynolds numbers of ambient and jet flows. By observing certain well established experimental procedures, Ackers (1969) suggested that it is possible to yield turbulent conditions by ensuring that $R_a > 600$ and $R_j > 2500$. The term of $F = (U_a\ gH)^{\frac{1}{2}}$, the ambient Fround number, may be eliminated on the ground that the gravity dependence on the flow is weak. For fixing the jet angle ($\theta = 15$ in this study), the experimental program of the study was therefore designed to determine the relationship of the mixing factor in a simplified form as

$$M_x = \phi \left[M_x, F_d, \frac{X}{H} \right] \qquad (3)$$

Investigation of mixing factor. --There are two extreme flows may be formed as heated water effluents submarinely flowing into a receiving evnironment: well mixed and stratified flow. Any attempt to distinguish between "well mixed" flow and "stratified" flow must confront the basic fact that such flow descriptions are entively qualitative. For this reason, a quantitative descriptor of "mixed flow" is required to enable "grades" of mixing to be distinguished.

Two criteria are adopted as the quantitative descriptor to grade the degree of mixing in this study. These two criteria are described as follow.

Criterion 1: $M_x = [\ \frac{1}{N-1} \sum_{i=1}^{N} (T_i - \overline{T})^2\ ]^{\frac{1}{2}} / (\overline{T} - T_a)$, the coefficient of temperature variation measured at distance x-downstream from the ports, is used as the quantitative descriptor to study the degree of mixing, where N = number of temperature readings, T_i, taken at section x; $\overline{T}$ = mean of the N temperature readings; T_a = temperature of ambient flow.

From statistical point of view, the small value of deviation will have a small range temperature distribution at a section. Therefore, it shows a better degree of mixing. Otherwise, a larger value of M_x will show a worse degree of mixing. Two sets of experimental result are plotted and shown in fig. 2 for the comparison.

Criterion 2: A stratified slow exists when the flow near the bed is at ambient density. Test for identifying stratification will involve the measurement of temperatures near the surface and near the bed of the flow. For the classification of a flow system by comparing only surface and bed temperature to be meaningful, the measurements are taken at a point downstream where the flow system is typical of its form. (The distance downstream, x/D = 15, was adopted in the present study). A typical set of results (surface level and bed level temperatures averaged across the width for wide range of jet ambient temperature differences) is shown in fig. 3.

On the basic of these two criteria mentioned above, the classification of flow systems into the three categories -- well-mixed, intermediate mixed and stratified will be investigated in the connection with parameters discussed before.

IV. Experimental Program

Apparatus. -- Experiments were performed in a glass-walled, tilting, recirculating channel. Channel dimensions were 61 cm in width, 10.6 m in length between entrance and exit chambers, and a

30 cm maximum flow depth. The flume was supplied with water by a pumping set through recirculating pipe system in the connection between two chambers, flow depth being controlled with the aid of an adjustable tail-gate. Heated water from a set of heat generator was discharge into this flowing environment through a set of discharge ports fitted into the floor of the flume. Each port was made of copper pipe of internal diameter 13 mm, the axis of each port where it discharged into the flow, being set at 15° to horizontal. In order to ensure that the flow from each port was similar, both as regards flow rate and temperature, the heated water was first fed into a manifold from which issued 3 pipes, each pipe being available for the supply of heated water to the diffuser ports.

Instrumentation. -- The discharge of ambient flow in the flume was measured from an orifice of internal diameter 64.5mm mounted in the recirculating pipe system. From the reading of pressure difference between static and dynamic heads in the manometer, the discharge can be computed from the formula, $Q = C_a A(2\Delta P/\rho)^{\frac{1}{2}}$, where C_a is the contraction coefficient; A, the area of orifice; the pressure difference across the orifice; is the density of fluid. The discharge of heated water was measured directively from a rotometer which was mounted in the supplied system of heated water. Temperatures were measured with a set of TSI Hot-film Anemometer system, and were read in a 20-sec timing cycle for each measurement. The minimum temperature can be read from this set of Hot-film anemometer system is $0.01^{\circ}C$.

Procedure. -- Each run began with the establishment of uniform flow for the selected channel variables. The criterion 1 test required temperature data to be collected at a number of sections in the field downstream from the discharge ports. The region of greatest interest for taking these cross-section was down to the point where mixing appeared to cease. Eleven sets of data covered a wide range of flow system were obtained at a number of sections selected

in the field as mentioned above. Each was taken with a 6x3 grid pattern at a section. Three or four sections downstream from the discharge ports were taken for the measurement of each set of data collection.

In the criterion 2 test, a set of flow cinditions was selected which corresponded to a certain value of Mr. The jet temperature was set at a value approximately $3^{o}C$ above ambient temperature and temperature was changed (increased) by approximately $3^{o}C$ in each subsequent investigation. This temperature increment specified a particulare value of F_d in the combination of flow conditions. A temperature survey was then conducted at two levels only (surface and bed) at a flow cross section approximately 15 times flow depth downstream from the discharge ports where mixing appeared to cease. As shown in fig. 3, the set of point: A, a, b, ..., B indicates the mean surface temperatures recorded for the various temperature condition tested, while the points A', a', b', ... B' give the corresponding mean temperatures measured at bed level. Twenty-eight sets of data for both surface and bed temperature measurements covered a wide range of flow system were obtained in this criterion test.

V. Results of the Investigation

In accordance with criterion 1, the quantitative test, 11 flow systems were tested and analysed. The inter-relationship of degree of mixing along the distance downstream from discharge ports were obtained. For any flow systems, the coefficient of temperature variance in a section is decreased along the downstream direction due to the mixing between heated water and ambient fluid, and the value of the coefficient to decrease to a constant value at where mixing appeared to ceases. Differential flow cinditions had varied critical values of coefficient of variance. The small value of M_{xc} indicated the high degree of mixing of flow system. Varied nambers

of discharge ports, (i.e. varied port-spacing) were also studied. The results shew that the section for mixing appeared to cease at a distance downstream of x = 9H for 3-port (port spacing 20 cm), while x = 12H and x = 17H for port spacing 30 cm and 60 cm respectively. Small port-spacing of heated water discharge had faster degree of mixing than large port-spacing case. Comparing with the comprehensive test of criterion 2 test, it states that for the cases of $M_{xc} < 0.035$, the flow systems have well mixed flow.

In accordance with criterim 2, the comprehensive test, 28 flow systems were tested and analyzed based on the temperature measurement at two level (surface and bed). For a chosen momentum ratio M_r of flow condition, the temperature rising at surface level and bed level due to the temperature increasement of jet was investigated. Fig. 3. shew the case for $M_r = 1.0$. Where differences of the ambient and jet temperatures are small (i.e. small values of $\triangle\rho/\rho$) the two sets of temperature readings are almost indistinguishable and beyond a certain point (e.g. the pair of points (A, A') in fig. 3.) they begin to diverge. The bed temperstures eventually become constant (point B in fig. 3.) while surface tamperatures continue to rise steeply as the jet temperature (and hence the ratio $\triangle\rho/\rho$) increases. Therefore, for flow cases before A may be classified as well-mixed flows, while flow cases beyond B to be stratified flows and intermediate-mixed flows between these two cases. Points A, B obtained from such investigation relate directly to two points on the F_d — M_r plane. By varying the momentum ratio, it can then have various sets of points on the F_d — M_r plane as shown in fig. 4. Results are summarized, in fig. 5. Three types of mixing situtation can be distingushed for any given flow and temperature conditions of both ambient and jet configurations.

VI. Summary and Conclusion

The major objective of the present work was to investigation the

mixing characteristics of submerged multi-port diffusers for heated water discharge into shallow receiving water. Experimental study based on dimensional analysis of flow configurations was proposed and investigated. From the results, it may be concluded that:

(1) The mixing of heated water with ambient flow in the near field increases with increasing discharge momentum (i.e. decreasing values of M_r) and decreases with increasing density difference between the discharged and ambient water (i.e. decreasing values of F_d).

(2) The near-field region is characterized by the heated water being convected relative to the ambient water and the turbulent mixing is due principally to turbulence generated by the velocity difference between the ambient and heated water discharge.

(3) Flow mixing varies with distance downstream from the discharge ports. The mixing characteristics of flow can be investigated by coefficient of temperature variation. For $M_{xc} < 0.035$, flow is well-mixed.

(4) The investigation of mixing based on criterion 2 test (the comprehensive test) obtained a relationship for mixing being characterized by momentum ratio and densimetric Froude number of flow system.

For flow systems on the $M_r - F_d$ plans at region

$$M_r - 1.25F_d + 1.13 < 0$$

are well-mixed flows, while flow systems at the region

$$M_r - 3.06F_d + 1.55 > 0$$

are stratified flows.

References

1. Anwar H.O., "Behavior of Buoyant Jet in Calm Fluid", ASCE, 95, HY 4, p. 1289-1303. (1969).
2. Brook N.H. and C.Y. Koh, "Fluid Mechanics of Waste-water Disposal in the Ocean", Annual Review of Fluid Mechanics, Vol. 7, 1975.
3. Cederwall, K., "Buoyant Slot Jets into Stagnant or Flowing Environments", W.M. Kech Laboratory, CIT, KH-R-25, 1971.
4. Parker F.L. and Krenkel P.A., Engineering Aspects of Thermal Pollution, Vanderbilt Univ., 1969.
5. Hwang R.J., Sayve W.W. and Kennedy J.F., "Model Study of lasalle Cooling Lake", IHR Report, Univ. of Iowa, 1973.
6. List E.J. and Imberger J., "Turbulent Entrainment of Buoyant Jets", ASCE, Vol. 99, HY 9, 1973, pp. 1461-1473.
7. Harleman, D.R.F. et al, Engineering Aspects of Heat Disposal, Summer Symposium Notes, MIT, 1972.
8. Morton B.R. et al, "Turbulent Gravitational Convection from Maintained and Instantaneous Sources", Proceedings, Royal Society, A 234, 1956.
9. Rouse, H., Yih C.S. and Humphrey, H.W., "Gravitational Convection from a Boundary Source", Tellus, 4, 1952, pp. 201-210.
10. Ryan, P.J. and Harleman D.R.F., "An Analytical and Experimental Study of Turbulent Cooling Pond Behavior", Tech Report No. 161, R.M. Parsons Lab for Water Resources and Hydrodynamics, MIT, 1973.
11. Turner, J.S., Buoyancy Effect in Fluids, Cambridge Univ. Press, 1973.
12. Weil, J. and Fischer, H.B., "Effect of Stream Turbulence on Heated Water Plumes", ASCE, HY 7, Vol. 100, 1974, pp. 951-970.

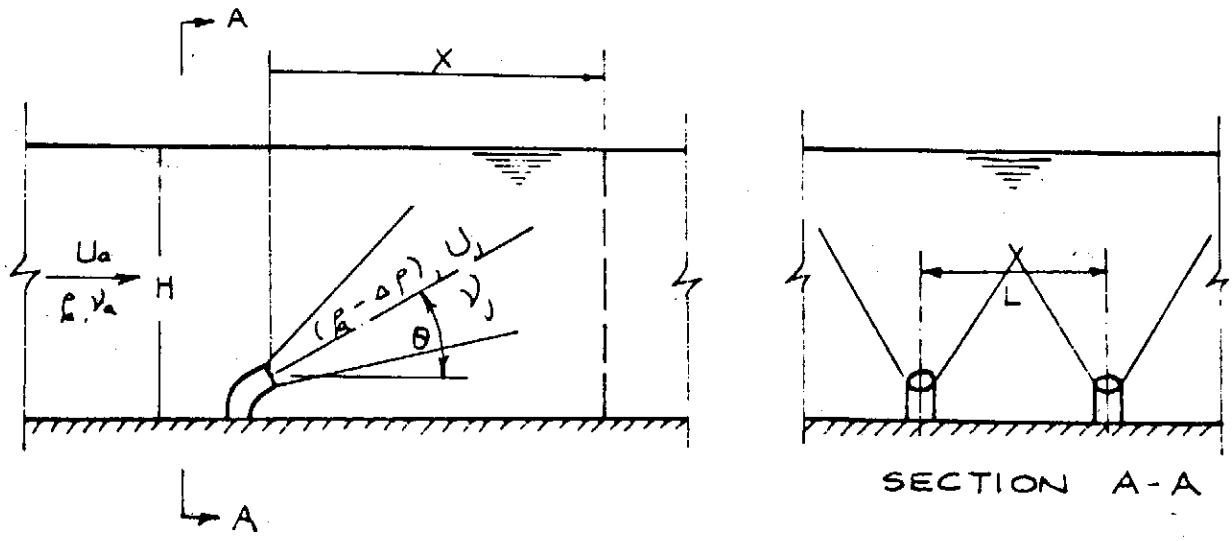

(1 a)

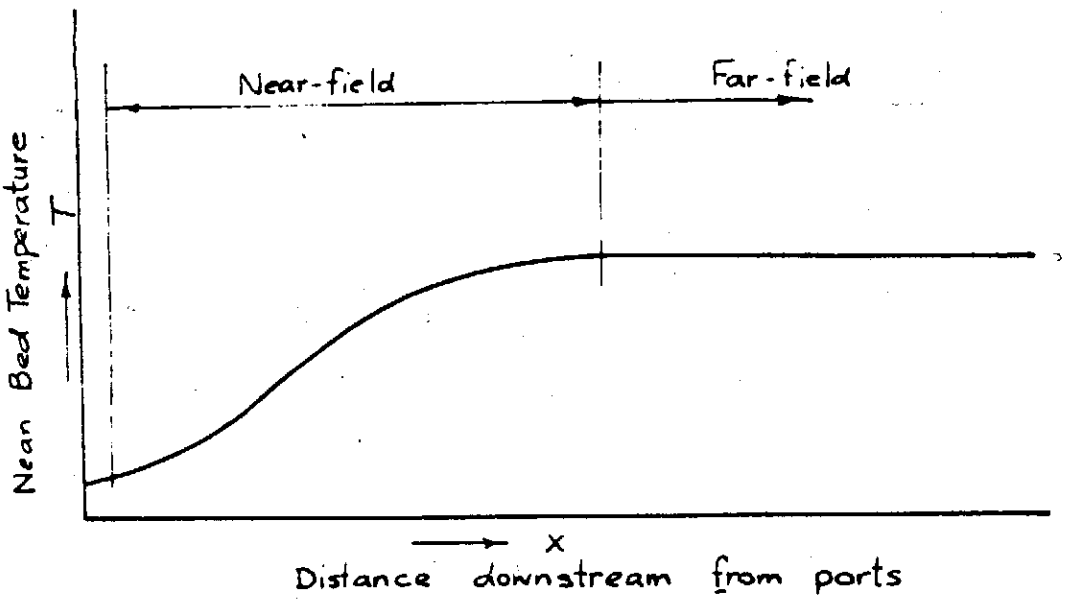

(1 b)

Figure 1. Flow Configuration

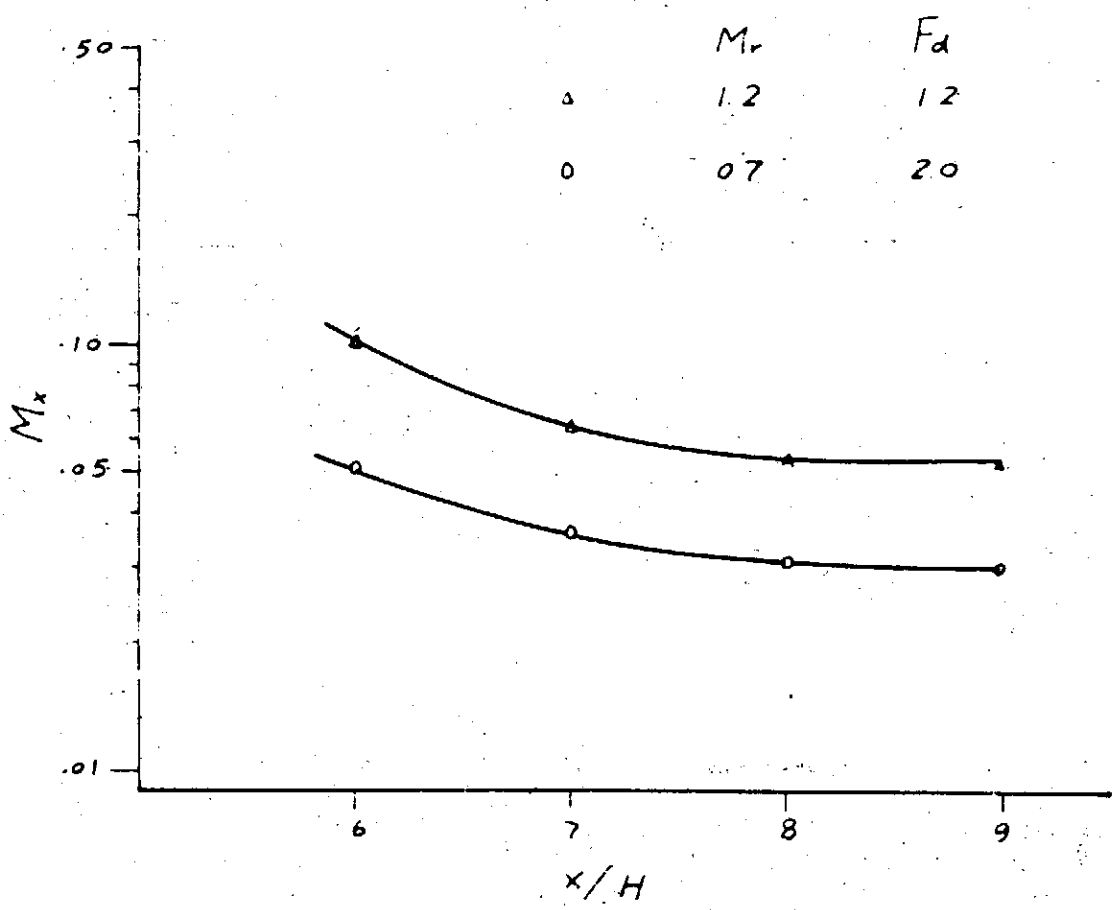

Figure 2. Typical Results of Criterion 1

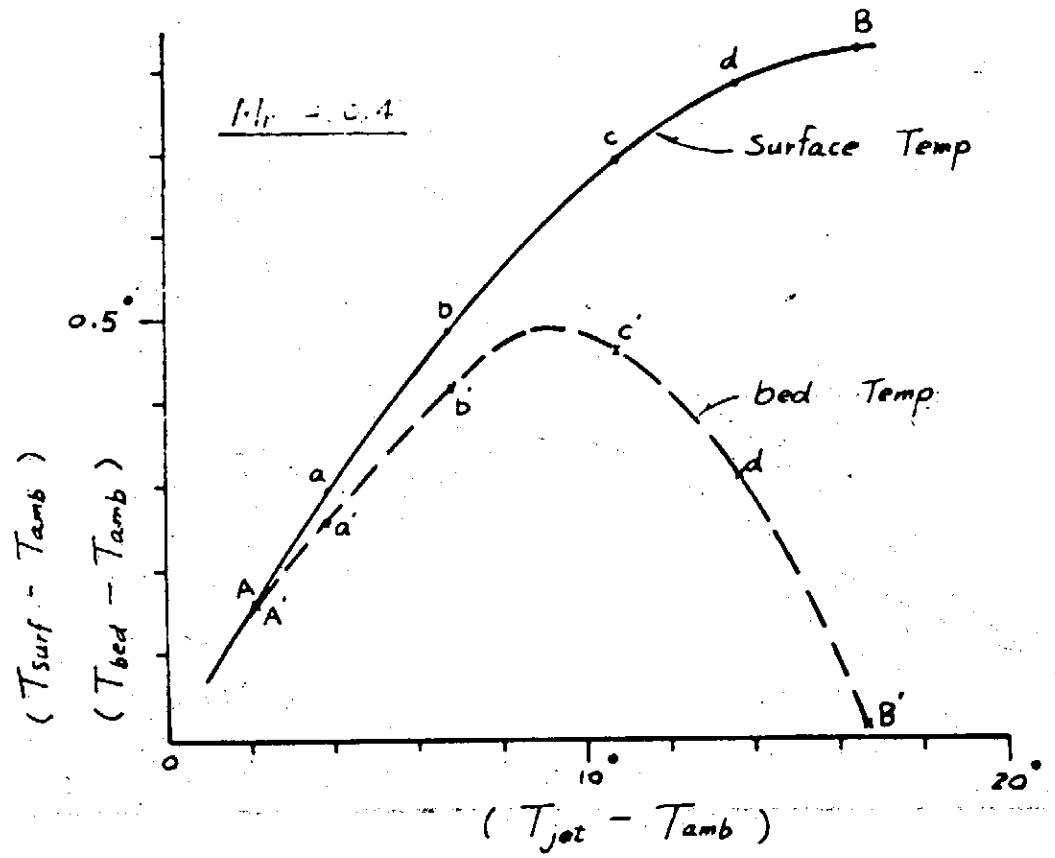

Figure 3. Typical Result of Criterion 2 for $M_r = 0.4$

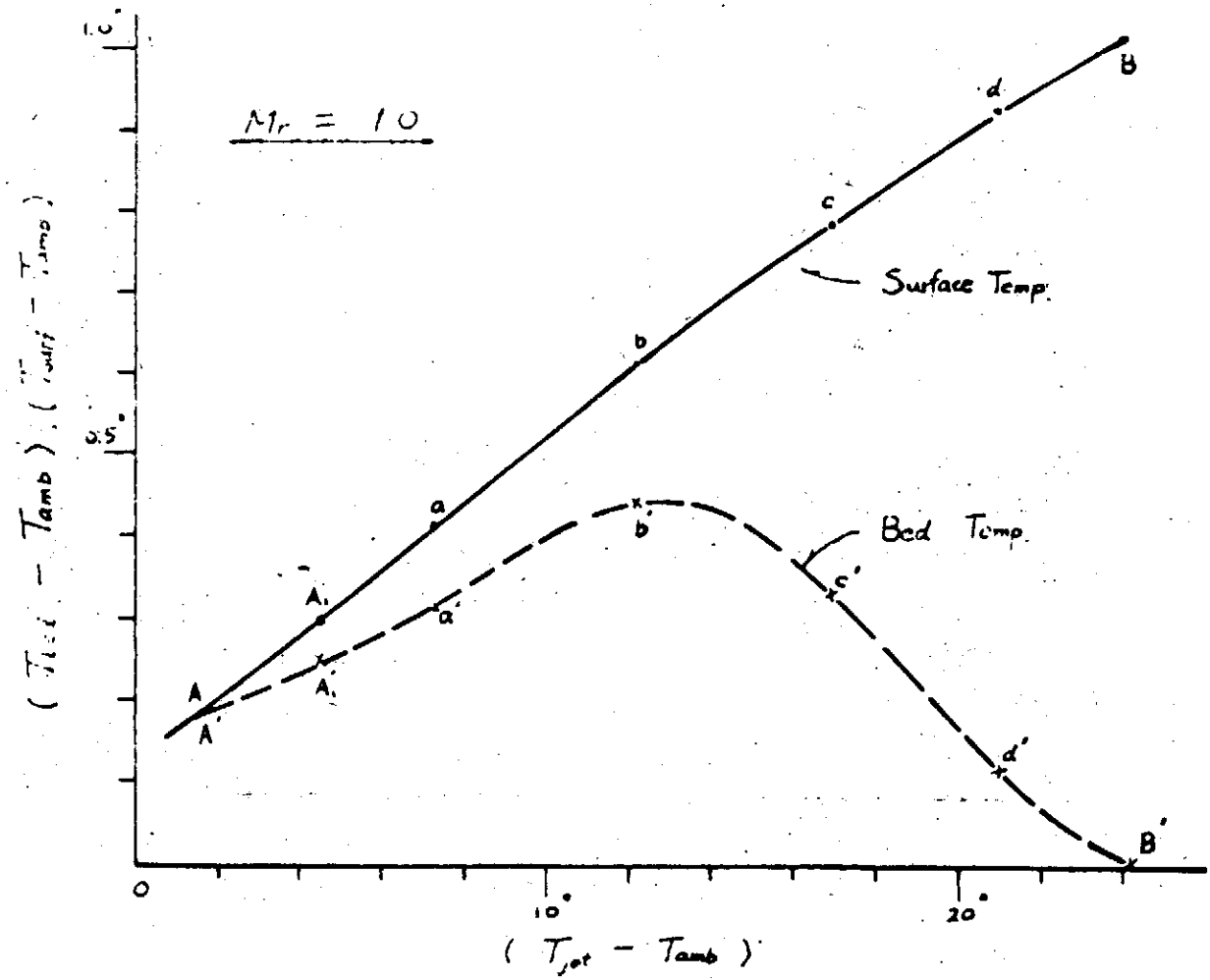

Figure 4. Typical Result of Criterion 2 for M for $M_r = 1.0$

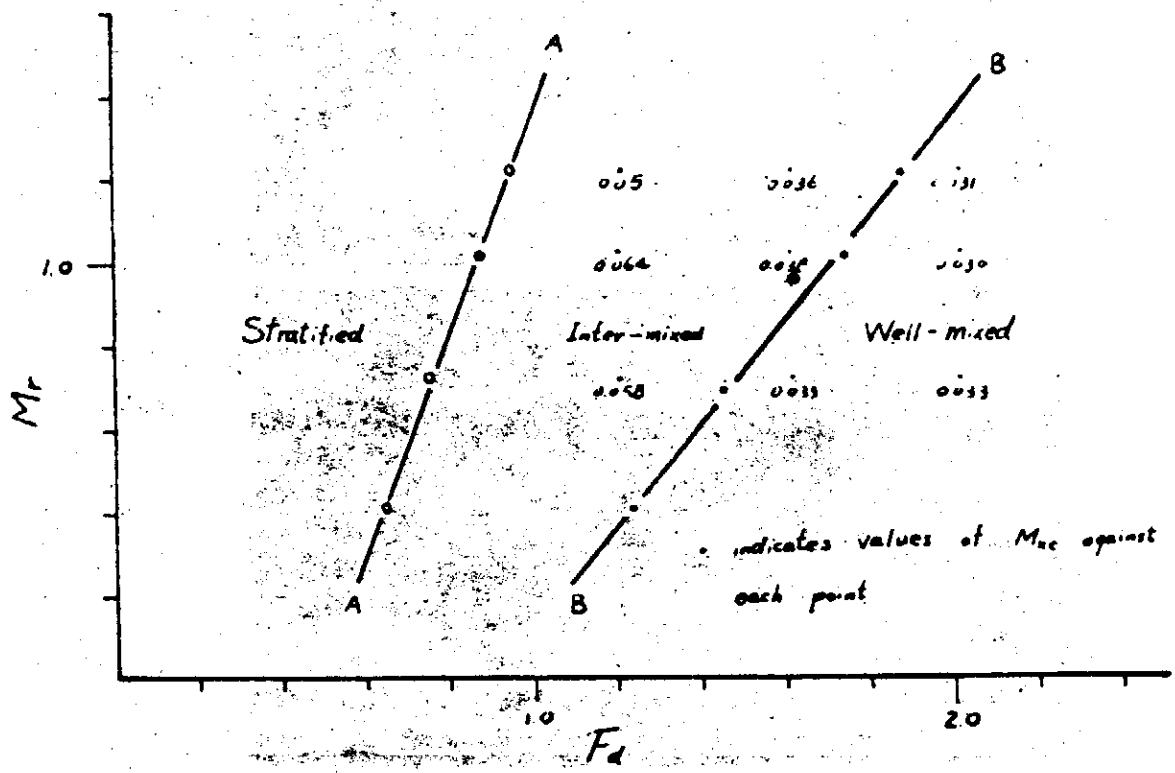

Figure 5. Classification of Mixed and Stratified Flows

(A)

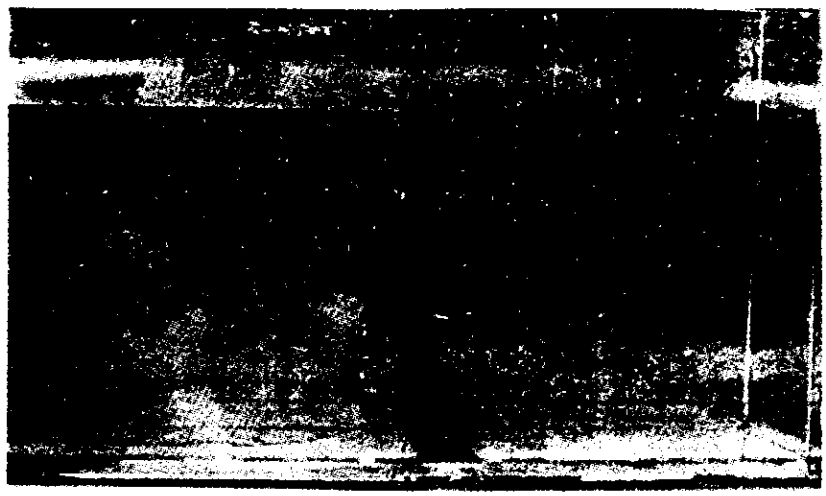

(B)

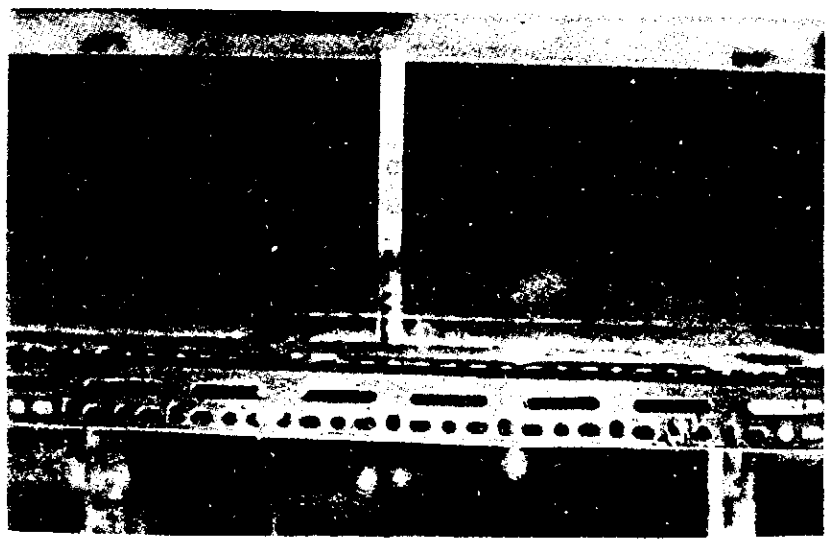

(C)

Well-mixed Flow

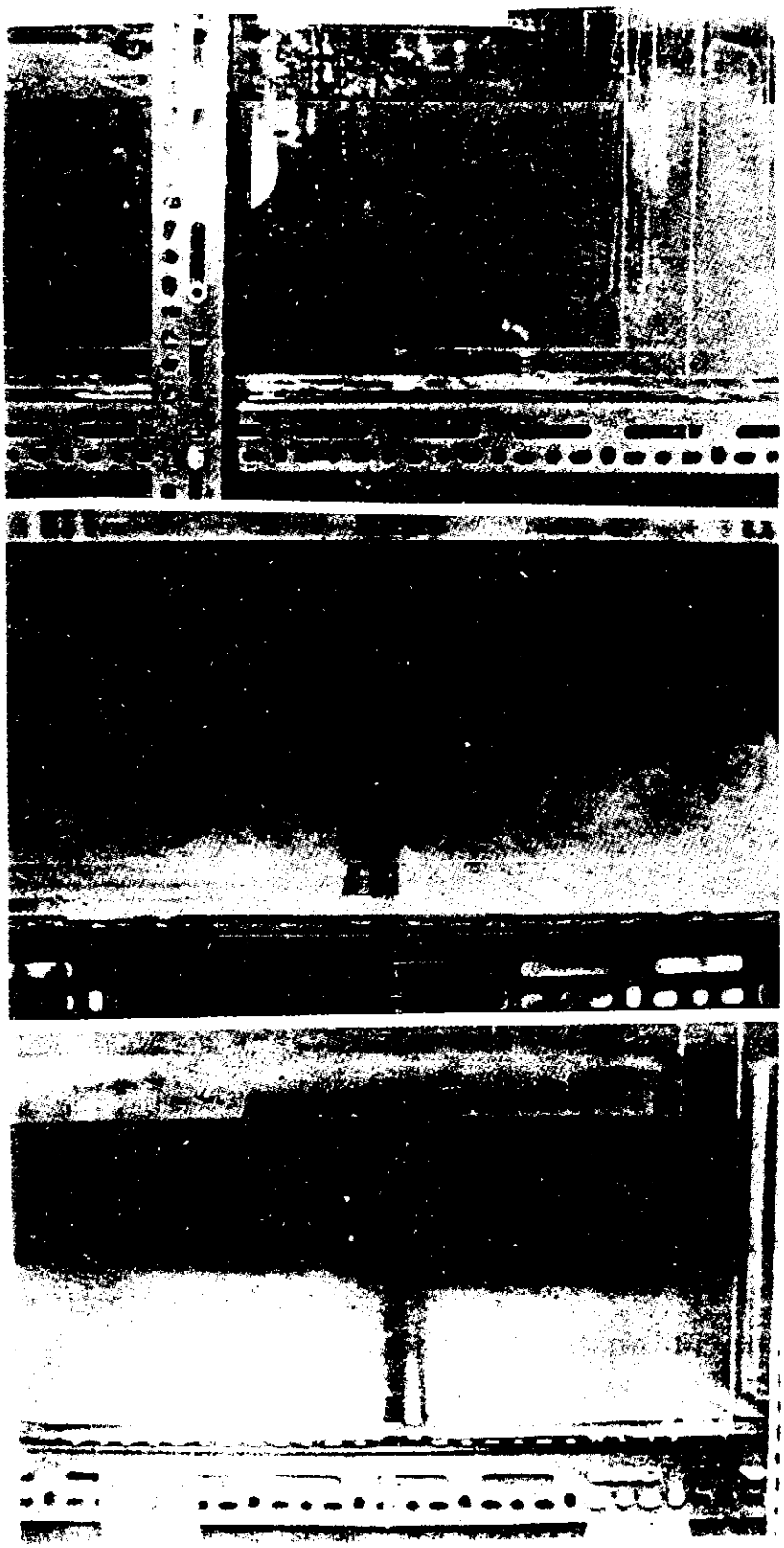

(A)

(B)

(C)

Stratified Flow

ANNUAL REPORT OF THE INSTITUTE OF PHYSICS,
ACADEMIA SINICA, 1974

Finite Element Method For Convection-Diffusion Problems

Robert R. Hwang (黃榮鑑)
Institute of Physics
Academia Sinica

Abstract

Finite element method based on Galerkin's approach was applied to study two dimensional convection-diffusion problems. A numerical solution scheme has been proposed. This solution scheme is based on the use of Galerkin's method within a finite element context in using triangular elements. The governing matrix equations were derived in cartesian coorinate system. By the approach of a qusi-steadiness, the time derivative is fixed at a certain instant in time. Implicit method of Crank-Nicolson method was used to yield a recurrence relation in time dependence of matrix form.

I. Introduction

Finite element method has been used extensively in the realm of solid mechanics [1a,b] in the last decade. Recently, it has been applied to simple heat and fluid flow problems [2,3,4]. The fundamental idea in the finite element method is to subdivide the continuum into a number of finite-sized elements, each with a discrete number of nodal points (or lines) by which the various elements are connected, and to approximate in a piecewise fashion within each element some appropriate functional for the problem at hand. By the appropriate interconnection of the elements across their interfaces, the nodal values of the variables can be determined from the solution to a set of algebraic equations.

In the present study, the finite element method is combined with

a subclass of the method of weighted residuals [5,6], Galerkin's method, to derive an approximate solution scheme for two-dimensional flows of time dependent convection-diffusion problems.

II. Finite Element Method--Galarkin Approach

The method of weighted residuals [6] consists of assuming a trial solution to the governing equations in the form of a finite series of known functions of position multiplied by undetermined parameters, and requiring that these parameters be such that the field equations and boundary conditions be satisfied in some approximate sense. The subclass chosen for the work described herein is Galerkin's method which consists of using the approximating functions as the weighting functions.

Consider the problem of solving the differential equation

$$Aw = f \tag{1}$$

in some domain D, in which A is some differential operator which acts upon unknown function w to given known function f. On boundary S of D, w will be required to satisfy certain boundary conditions.

A large class of approximate solution techniques is based upon the concept of assuming that the solution of Eq. 1 may be expressed as the form

$$\omega^M(x_i, t) = \sum_{k=1}^{M} a_k(t)\phi_k^M(x_i)$$

where ω^M is the M-term approximate solution to the true solution w, the ϕ_k^M are known linearly independent mode shapes or coordinate functions of x_i defined over D and the unknown parameters a_k are here functions of time. By successively increasing M, a succession or suquence of trial solutions are obtained that are required to converge to the correct answer.

Consider the approximation that domain D is divided into a number, e.g., 1, of subdomains D_e, or elements. In each of these elements it is assumed that the approximate solution may be expressed as

$$\omega^e = \sum_{k=1}^{N} a_k^e \phi_k^e(x_i);$$

The ϕ_k^e are defined only in D_e and the a_k^e are generally chosen to be the value of w^o at certain nodal points of D_e. Thus, letting

$$\phi_k^e = \psi_k^e(x_i) \qquad \text{for} \quad x_i \in (D_e + S_e)$$

$$\phi_k^e = 0$$

in which, S_e denotes the boundary of element e. For the number of terms M being chosen as equal to N, an expression for the assumed solution may then be written as

$$\omega = \sum_{e=1}^{\ell} \sum_{k=1}^{M} a_k^e(t)\phi_k^e(x_i)$$

Imposing compatibility relations on the a_k^e between neighboring elements allows the form of Eq. 2, in which M is the total number of nodal degrees of freedom in $D_e + S_e$. The essential feature of the finite element method lies in formulating an approximate expression for the required function defined over the whole domain in terms of an approximation defined to be nonzero only over subdomains.

If the form of the approximate solution is chosen as Eq. (5), substituting the assumed solution into Eq. (1), then the residual, or error, in the differential equation in D and on S can be constructed as

$$R = A\hat{w} - f \tag{6}$$

If $\hat{w}$ had been the true solution, the residual, R, would be identically zero. The best choice of the a_k^e for a given set of shape function $\phi_k^e(x_i)$ in Eq. (5) in the domain D is that which makes R minimum. Galerkin's method considers of making the residual orthogonal to

each of the shape functions ϕ_k^e in each element, i.e., let

$$\int_V \phi_k \, R \, dV = 0$$

$$\sum_e \int_{De} \phi_k \, R \, dV_e = 0 \tag{7}$$

which leads to a set of algebraic equations for $\hat{\omega}$.

III. Formulation of Problem

Diffusion-Convection is one of important phenomena in problems of applied physics, e.g., the dispersal of pollutants in the sea and estuaries; the heat transfer problems etc.. Its general form of partial differential equation can be obtained as:

$$L[\phi] = \frac{\partial \phi}{\partial t} + \sum_{x_i = x}^{z} \frac{\partial}{\partial x_i} \left(U_i \phi - K_{ij} \frac{\partial \phi}{\partial x_j} \right) + Q = 0 \tag{8}$$

in which ϕ is variable such as, pollutant concentration, temperature etc.; K_{ij}, diffusion coefficient tensor; U_i, convective velocities; Q is source or sink term such as dissipation etc.; L is differential operator. If the priciple axes of the diffusion tensor are aligned with the axes of the coordinate system, a two-dimensional convection -diffusion problem has equation in the form of

$$L[\phi] = \frac{\partial \phi}{\partial t} + \frac{\partial}{\partial x} \left(U_x \phi - K_{xx} \frac{\partial \phi}{\partial x} \right) + \frac{\partial}{\partial y} \left(U_y \phi - K_{yy} \frac{\partial \phi}{\partial y} \right) + Q = 0 \tag{9}$$

Eq.(9) to be solved, it must be adjoined one initial condition for function ϕ at t = 0 and two boundary condition prescrbing values of ϕ or $\partial\phi/\partial n$ on boundary.

To obtain the approximate solution of eq.(9) by finite element analogue, the domain D is subdivided into a finite number of elements, e.g. triangular shape for the present study. The subdivision of a two-dimensional region into triangular elements with nodes at the vertices is illustrated in fig. 1. It will be assumed that the solution

ϕ is prescribed in functional form, element by element, across the region, i.e., can be defined piecewise over the region. Within an element, it is supposed that

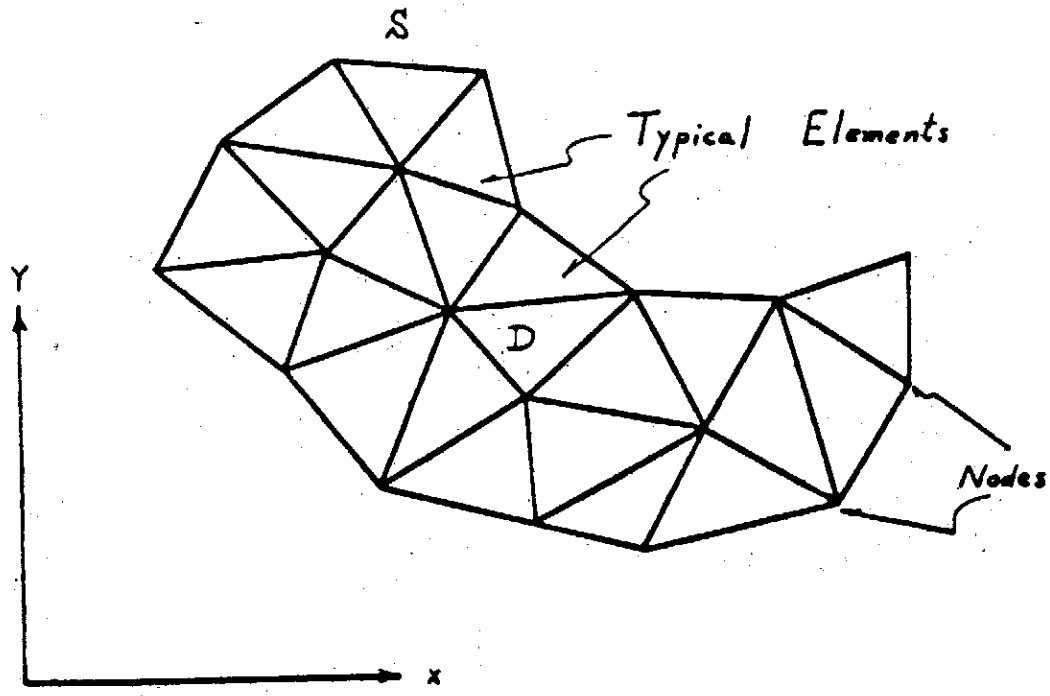

Figure 1. Subdivision of the region into finite elements.

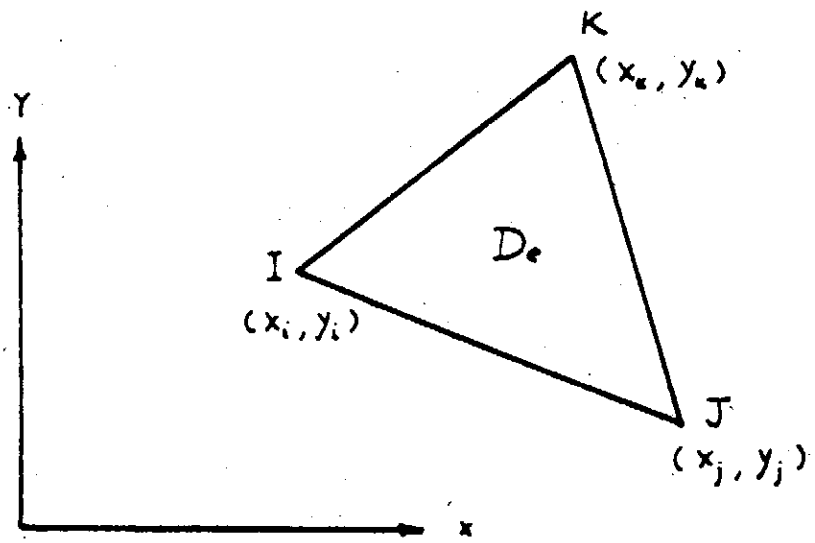

Figure 2. Typical triangular elements.

can be described by a linear combination of functions N_1^e, N_2^e, ..., N_s^e and nodal values ϕ_1^e , ϕ_2^e , ..., i.e.

$$\phi^e = (N_1^e , N_2^e , \cdots\cdots , N_3^e) \{\bar{\phi}^e\}$$

$$\phi^e = [N^e] \{\bar{\phi}^e\} \tag{10}$$

the shape functions N_1^e, N_2^e,....,N_s^e are restricted to being functions of position.

For a triangular element of fig. 2, it is assumed ϕ to be a linear function of x and y, namely

$$\phi^e = \alpha_1 + \alpha_2 x + \alpha_3 y \tag{11}$$

where α_1 , α_2 and α_3 are constants, values of which are determined in terms of ϕ at the three vertices as follows

$$\left.\begin{aligned} \phi_i^e &= \alpha_1 + \alpha_2 x_i + \alpha_3 y_i \\ \phi_j^e &= \alpha_1 + \alpha_2 x_j + \alpha_3 y_j \\ \phi_i^e &= \alpha_1 + \alpha_2 x_k + \alpha_3 y_k \end{aligned}\right\} \tag{12}$$

By solving eq.(12), eq.(11) can be obtained a form in eq.(10) as,

Fig. 2. A triangular element e

$$\phi^e = [N^e] \{\bar{\phi}^e\} = [N_i^e , N_j^e , N_k^e] \{\bar{\phi}^e\} \tag{13}$$

where, $N_i^e = \frac{1}{2\Delta} (a_i + b_i s + c_i y)$ etc.,

$$\Delta = \frac{1}{2} \begin{bmatrix} 1 & x_i & x_i \\ 1 & x_j & x_j \\ 1 & x_k & x_k \end{bmatrix}$$

$\{\bar{\phi}^e\}^T = [\bar{\phi}_i^e , \varphi_j^e , \bar{\phi}_k^e]$

and, $a_i = x_i y_k - x_k y_i$; $b_i = y_j - y_k$, $c_i = x_k - x_j$ etc.

By the use of equations (11) and (12), can also have

$$\frac{\partial \phi^e}{\partial x} = [A^T] \{\bar{\phi}^e\} \tag{14a}$$

$$\frac{\partial \phi^e}{\partial y} = [\, B^T \,] \{ \bar{\phi}^e \}$$

where

$$A^T = \frac{1}{2\Delta} [\, b_i , b_j , b_k \,] = \frac{1}{2\Delta} [\, y_j - y_k , y_k - y_i , y_i - y_j \,]$$

$$B^T = \frac{1}{2\Delta} [\, c_i , c_j , c_k \,] = \frac{1}{2\Delta} [\, x_k - x_j , x_i - x_k , x_j - x_i \,]$$

Substitution of eq.(9) into eq.(7) and integration by parts, the Galerkin's criterion ($D = \sum_e De$) is in the form of

$$\sum_e \int_{De} N_i^e \left[Q + \frac{\partial \phi}{\partial t} + U_x \frac{\partial \phi}{\partial x} + K_{xx} \frac{\partial N_i^e}{\partial x} \frac{\partial \phi}{\partial x} + K_{yy} \frac{\partial \phi^e}{\partial y} \frac{\partial \phi^e}{\partial y} \right] dA_e -$$

$$K_{xx} \phi_c N_i^e \frac{\partial \phi}{\partial x} \ell_s \, d_s - K_{yy} \phi_c N_i \frac{\partial \phi}{\partial y} m_s \, d_s = 0$$

After substituting equatinos (10) and (14) into eq.(15), the finite element analogue to eq.(9) for two dimensional convection-diffusion problem is

$$\frac{\partial \{\phi\}}{\partial t} \sum_{e=1}^{\ell} \int_{De} N_i [N] \, dA_e + \{\phi\} \sum_{e=1}^{\ell} \int_{De} \left[U_x N_i A^T + U_y N_i B^T + K_{xx} \frac{\partial N_i}{\partial x} A^T \right.$$

$$\left. + K_{yy} \frac{\partial N_i}{\partial y} B^T \right] dA_e = \left\{ K_{xx} \sum_{e=1}^{\ell} \phi_{c_e} N_i A^T \ell_s d_s + K_{yy} \sum_{e=1}^{\ell} \phi_{c_e} N_i B^T m_s d_s \right\}$$

or in matrix form

$$\{\phi\} - \sum_{e=1}^{\ell} \int_{De} N_i Q \, dA_e$$

$$[C] \frac{\partial \{\phi\}}{\partial t} + [H] \{\phi\} = [F]$$

where matrix [C] is built up from elemental matrices

$$[CE] = \int_{De} N_m [N] \, dA_e = \int_{De} \begin{bmatrix} N N & N N & N N \\ N N & N N & N N \\ N N & N N & N N \end{bmatrix} dA_e = \Delta \begin{bmatrix} \frac{1}{6} & \frac{1}{12} & \frac{1}{12} \\ \frac{1}{12} & \frac{1}{12} & \frac{1}{6} \\ \frac{1}{12} & \frac{1}{12} & \frac{1}{6} \end{bmatrix}$$

and [H] is constructed from elemental matrices of [He], such as

$$H = \sum_e \int_{De} \left[U_x N_m A^T + U_y N_m B^T + K_{xx} \frac{\partial N_m}{\partial x} A^T + K_{yy} \frac{\partial N_m}{\partial y} B^T \right] dA_c$$

$$= \sum_e [\, He \,] = \sum_e \{ [\, He_1 \,] + [\, He_2 \,] + [\, He_3 \,] + [\, He_4 \,] \}$$

$$[H_{e_1}] = \int_{De} UxNmA^T \alpha Ae = \int Ux \frac{1}{2\Delta} \begin{pmatrix} Ni\frac{\partial Ni}{\partial x}, & Ni\frac{\partial Nj}{\partial x}, & Ni\frac{\partial Nk}{\partial x} \\ Nj\frac{\partial Ni}{\partial x}, & Nj\frac{\partial Nj}{\partial x}, & Nj\frac{\partial Nk}{\partial x} \\ Nk\frac{\partial Ni}{\partial x}, & Nk\frac{\partial Nj}{\partial x}, & Nk\frac{\partial Nk}{\partial x} \end{pmatrix} dAe$$

$$= \frac{U_x}{6} \begin{pmatrix} b_i, & b_j, & b_k \\ b_i, & b_j, & b_k \\ b_i, & b_j, & b_k \end{pmatrix}$$

$$[He_2] = \int_{De} U_y N_m B^T dAe = \frac{Uy}{6} \begin{pmatrix} c_i, & c^j, & c_k \\ c_i, & c_j, & c_k \\ c_i, & c_j, & c_k \end{pmatrix}$$

$$[He_3] = \int_{De} K_{xx} \frac{\partial Nm}{\partial x} A^T \, dAe = \frac{Kxx}{4\Delta} \begin{pmatrix} b_ib_i & b_ib_j & b_ib_k \\ b_jb_i & b_jb_j & b_jb_k \\ b_kb_i & b_kb_j & b_kb_k \end{pmatrix}$$

$$[H_{e_3}] = \int_{De} Kyy \frac{\partial Nm}{\partial y} B^T dAe = \frac{Kyy}{4\Delta} \begin{pmatrix} c_ic_i & c_ic_j & c_ic_k \\ c_jc_i & c_jc_j & c_jc_k \\ c_kc_i & c_kc_j & c_kc_k \end{pmatrix}$$

$$[He] = [He_1] + [He_2] + [He_3] + [He_4]$$

$$[F] = \{Kxx \oint_S N_i \frac{\partial \phi}{\partial x} dy + Kyy \oint_S N_i \frac{\partial \phi}{\partial y} dx\} - \sum_{e=1}^{\ell} \int_{De} N_i \, SdAe$$

The time dependent nature of Eq. (17) is introducted in an approximate manner by assuming that the time darivative is fixed at a certain instant in time. At t = 0, $\{\phi_o\}$ is some known starting condi-

tion. The solution $\{\phi_1\}$ at time Δt can be obtained from implicit mathods of Crank-Nicolson method [7]. Eq.(17) yields a recurrence relation as

$$\left\{[H] + \frac{1}{\Delta t}[C]\right\} \{\phi\}_{i+1} = \frac{1}{\Delta t}[C]\{\phi\}_i - [F] \tag{18}$$

IV. Numerical Example

For a rectangular flow domain of (X x Y) as shown in fig. 3, the convective velocities are u in x direction and zero in y direction. Considering laminar flow problem, diffusion coefficients are assumed the same in both x and y directions, i.e., $K_{xx} = K_{yy} = K$. No dissipation for pollutants was occurred in the flow system or Q=0 in Eq. (9). The convection-diffusion of concentration of pollutants at any time t subjected some initial and boundary conditions as shown in fig. 4 is solved by the use of finite element method which was analyzed and discussed in the previous sections. In order to arrange the numerical scheme, the governing equation of Eq.(9) is non-dimensionlized by letting

$$x' = \frac{x}{X}, \quad y' = \frac{y}{X}$$
$$\text{and} \quad t' = \frac{kt}{X}, \quad U = \frac{uX}{K} \tag{19}$$

Substituting dimensionless variables of eq.(19) into eq.(7), the governing differential equation with initial and boundary conditions in dimensionless form become

$$\frac{\partial \phi}{\partial t'} + U\frac{\partial \phi}{\partial x'} = \frac{\partial^2 \phi}{\partial x'^2} + \frac{\partial^2 \phi}{\partial y'^2} \tag{20}$$

Initial condition (as shown in fig. 4)

$$\phi = \phi_o (x', y') \qquad \text{at } t = 0 \tag{20a}$$

Boundary conditions

$$\frac{2\phi}{\partial y'} = 0 \qquad \text{at } y' = 0 \text{ and } y' = Y/X \tag{20b}$$

$$\phi = 0 \text{ or } \frac{\partial \phi}{\partial x'} = 0 \text{ at } x' = 0 \text{ and } x' = 1 \tag{20c}$$

Ey the techniques of finite element scheme and computer programming, Eq.(20) was solved. Fig. 5 shew the result of pollutant distribution at t = 2000 sec for the case of u = 0. 25 m/sec and k = 1. 5 m sec subjected initial and boundary conditions as shown in Fig. 4.

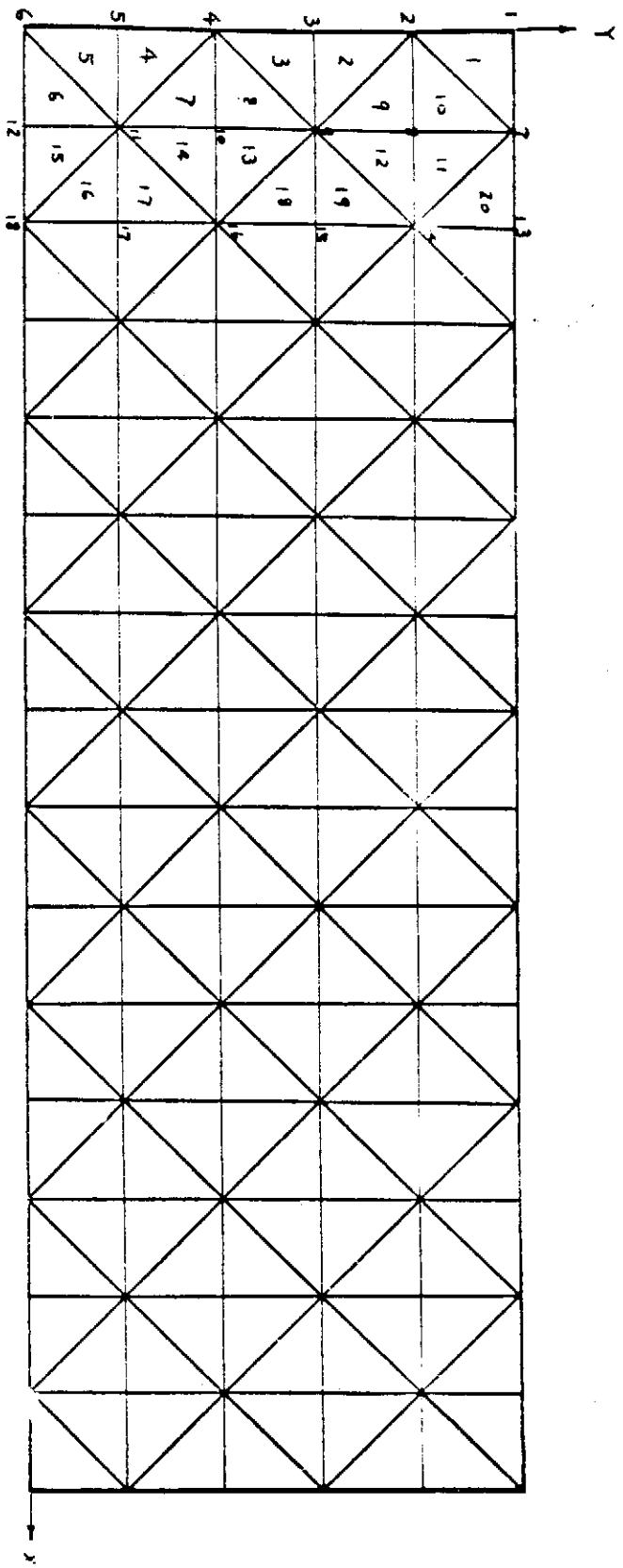

Figure 3. Domain and its subdivision regions proposed for numerical example.

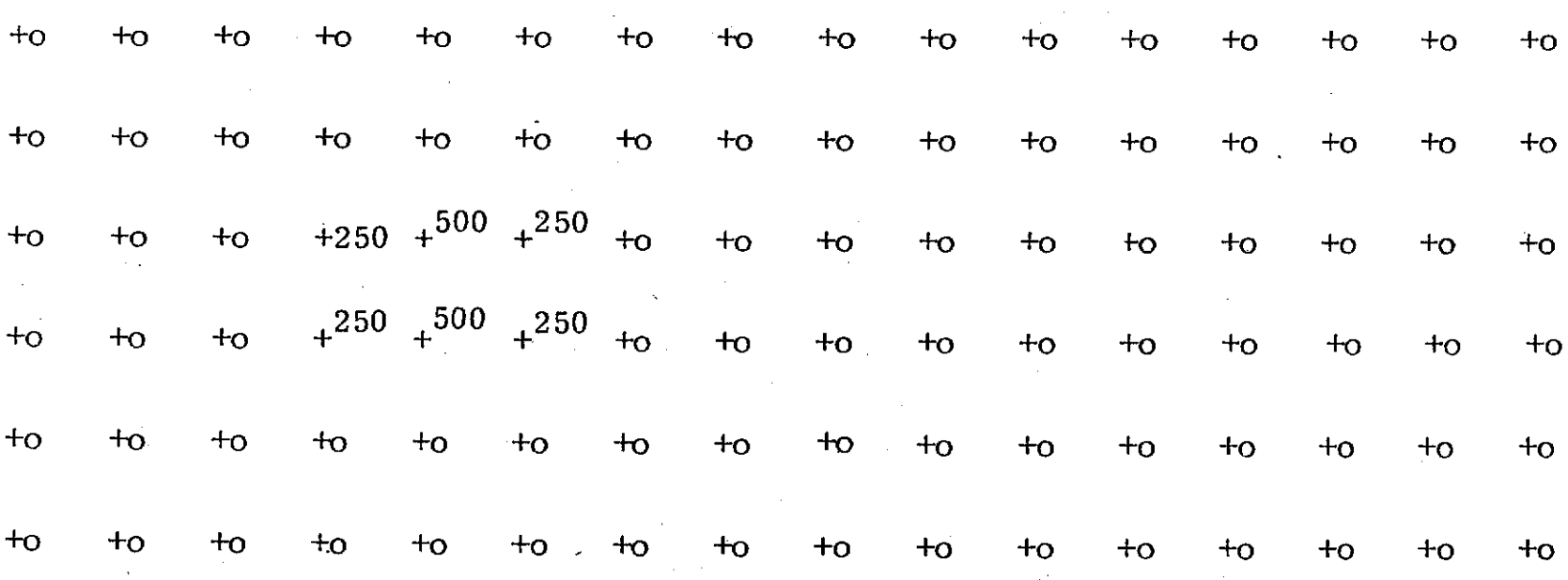

Figure 4. Initial pollutant distribution proposed for numeriacl example.

+0	$+_{-1.0}$	$+_{-1.5}$	+0	+6	+8	+12	+26	+311	+14	+8	+0	+0	+0	+0	+0
+0	+0	+0.5	+2	+21	+28	+32	+68	+102	+31	+10	+2	+1.5	+1.0	+0	+0
+0	+0.5	+2	+8	+29	+181	+403	+442	+315	+86	+32	+6	+3	$+_{-1.0}$	+0	+0
+0	+0.5	+2	+8	+29	+181	+403	+442	+315	+86	+32	+6	+3	$+_{-1.0}$	+0	+0
+0	+0	+0.5	+2	+21	+28	+32	+68	+102	+31	+10	+2	$+_{-1.5}$	+1.0	+0	+0
+0	$+_{-1.0}$	$+_{-1.5}$	+2	+6	+8	+12	+26	+31	+14	+8	+0	+0	+0	+0	+0

$\triangle X = \triangle Y = 200$ m

Figure 5. Concentration distribution in domain at t=2000 sec for u=0.25 m/sec and k=1.5 m/sec.

V. Conslusions

A numerical solution scheme has been proposed for a two-dimensional convection-diffusion problems. This solution scheme is based on the use of Galerkin's method within a finite element context. A numerical example for two-dimensional time dependent convection-diffusion problem has been presented.

Several important points were underscored concerning the proper use of Galerkin's method in a finite element context. For example, all possible integrations by parts must be carried out in order to properly satisfy the boundary conditions on all portions of the boundary.

The governing matrix equations can be derived independently of the number of space dimensions and coordinated system used. For illustrative purposes, the special case of two-dimensional diffusion-convection problems in cartesian coordinates was considered in detail using triangular elements and linear approximating functions.

References

1. a. Zienkiewicz, O.C., The Finite Element Method in Structural and Continuum Mechanics, 1967.
   b. Zienkiewicz, O.C., The Finite Element Method in Engineering Science, 1971.
2. Norrie, D.H. and Gerard de Vries, The Finite Element Method, 1973, Academic Press.
3. Hutton, S.G. and Anderson, D.L., "Finite Element Method: A Galerkin Approach", Journal of Mech. Eng., ASCE, EM 5, 1971, pp. 1503-1519.
4. Ikegawa, M and Washizu, K, "Finite Element Method Applied to Analysis of Flow Over a Spillway Crest", International J. for Numerical Methods in Eng., Vol. 6, 1973, pp. 179-189.
5. Mikhlin, S.G., Variation Method in Mathematical Physics, McGraw-Hill, 1968.
6. Finlayson, B.A., The Method of Weighted Residuals and Variational Principles, Academic Press, 1972.
7. Mitchell A.R., Computational Methods in Partial Differential Equations, John Wiley, 1969.

ANNUAL REPORT OF THE INSTITUTE OF PHYSICS,
ACADEMIA SINICA, 1974

Surface Wind Field and Precipitation Activity over Taiwan in Meiyu Season *

Shun-Der Ko (柯順德)**

Abstract

Surface wind field and precipitation intensity over Taiwan in Meiyu season during 1961-1965 are studied by the frequency distribution and spectral methods. During the Meiyu season the wind speed and precipitation intensity are almost less than 8 m/sec and 2 mm/hr respectively. The wind speed is small even when heavy rainfalls take place and the so-called "low-level jet" does not appear at the surface level.

It rains most frequently in northern region but the heavy rainfalls visit the central region most. The cores of heavy precipitation are located on the central mountain ranges and around the southern cape of Taiwan. As a whole, during the Meiyu season, rainfall in northern and central regions is more active and evident than that in southern and eastern regions.

Spectral analysis of precipitation intensity and wind speed shows that they fluctuate conspicuously at intervals of 20-24 and 24 hours respectively in northern and central regions. High correlation coefficient between them is also obtained.

*Work supported by the National Science Council of Republic of China

**Associate Prof., Taipei Inst. Tech., and Visitor, Inst. Phys., Academia Sinica.

1. Introduction

The onset of summer monsoon is responsible for the pre-summer rainy season, which usually extends approximately from the middle of June or sometimes the end of May to the middle of July, in the Far East. The rain in this season is called "Meiyu" (plum rain) in China and "Baiu" in Japan. During this season, rainy weather continues day after day and a belt-shaped heavy precipitation zone extends from the southern China continent to the northern Pacific.

Many meteorologists, such as Akiyama (1973a,b), Matsumoto et al. (1969; 1970a, b; 1971; 1972; 1973) and Ninomiya et al. (1971, 1972, 1973), have studied the characteristics of the meteorological elements in relation to the rainfall along the so-called "Baiu Front", a stationary frontal zone between the tropical monsoon and the middle latitude continental air mass. They pointed out a ageostrophic low-level jet develops in the vicinity of the heavy rainfall area and concluded that the jet is deeply related with the precipitation and, therefore probably, with the convective activity. Matsumoto (1973) also indicated that at 850-, 700-, 500-, and 300-mb levels, in case of heavy precipitation, unbalanced low-level jets are most likely to appear and the wind speed of maximum frequency is observed around 18 m/sec throughout the troposphere.

The Meiyu season in Taiwan often comes and ends earlier than the above one. It usually begins at the end of May and end in the middle of June. Although several authors, such as Chi (1964), Wang (1970), C.H. Hsu (1971) and M.T. Hsu et al. (1974, 1975), have made study on the rainy phenomena in Taiwan by means of synoptic charts, 5-day mean meteorological elements, etc., many features, especially in small scale, in relation to the precipitation activity are not yet clear. Therefore, it is necessary and important to study them in more detail from the point of view of forecasting and of natural water resources.

The principal cause of precipitation is ascribed to the vertical motion of air, which in turn develops the convergence of wind field. Thus, in this paper, the author will devote to study the frequency distribution of the wind field and the precipitation in Meiyu season and reveal their correlation by means of spectral analysis.

2. Data and Observation Network

Three-hourly observations of precipitation, surface wind speed and precipitation time from 1961 to 1965 are used in this study. The duration of Meiyu season for each year is mostly referred to the results obtained by C. H. Hsu (1971) and is listed in Table 1.

Table 1. Date of Meiyu season during 1961–1965.

Year	Date	Total days
1961	May 29 - June 11	14
1962	June 5 - June 16	12
1963	June 31 - June 7	8
1964	May 28 - June 17	21
1965	June 4 - June 23	20

The including 20 weather stations (black circles) is shown in Fig. 1. We divide them into four regions (northern, central, southern and eastern regions) according to their latitudes and topographic features. The northern region contains Pengchiayu, Anpu, Tanshui, Keelung, Taipei, Hsinchu and Yilan stations; the central region Taichung, Jihyuehtan, Penghu, Alishan and Yushan; the southern region Tainan, Kaohsiung, Lanyu and Hengchun; the eastern region Hwalien, Hsinkang, Taitung and Tawu.

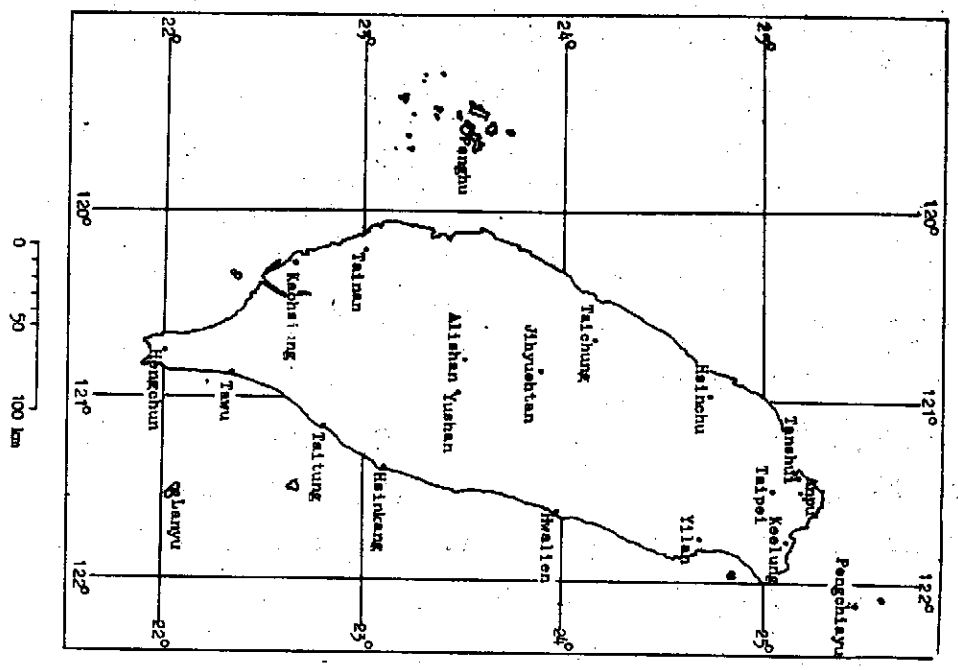

Fig. 1. Location of weather stations.

3. Frequency Distribution of Precipitation and Wind Field

In order to calculate the frequency distribution, the precipitation intensity is classified into eight categories, i.e., pp=0, $0<pp<1$, $1\leq pp<2$, $2\leq pp<3$, $3\leq pp<4$, $4\leq pp<5$, $5\leq pp<6$, $pp\geq 6$ mm/hr and the wind field into eight classes at intervals of 4 m/sec; i.e., $v\leq 4$, $4<v\leq 8$, $8<v\leq 12$, $12<v\leq 16$, $16<v\leq 20$, $20<v\leq 24$, $24<v\leq 28$, $28<v\leq 32$ m/sec respectively.

Fig. 2 shows the percentage frequency of wind speed for classified precipitation intensity in different year. It is evident that the percentage in each year has the same tendency for every precipitation intensity. That is, independent of precipitation intensity, it always decreases with increasing magnitude of wind speed. The wind speed of maximum frequency is less than 4 m/sec. This fact suggests that during Meiyu season the wind speed is small even when heavier rainfalls ($pp\geq 6$ mm/hr) take place and, therefore, that low-level jet does not occur at the surface level.

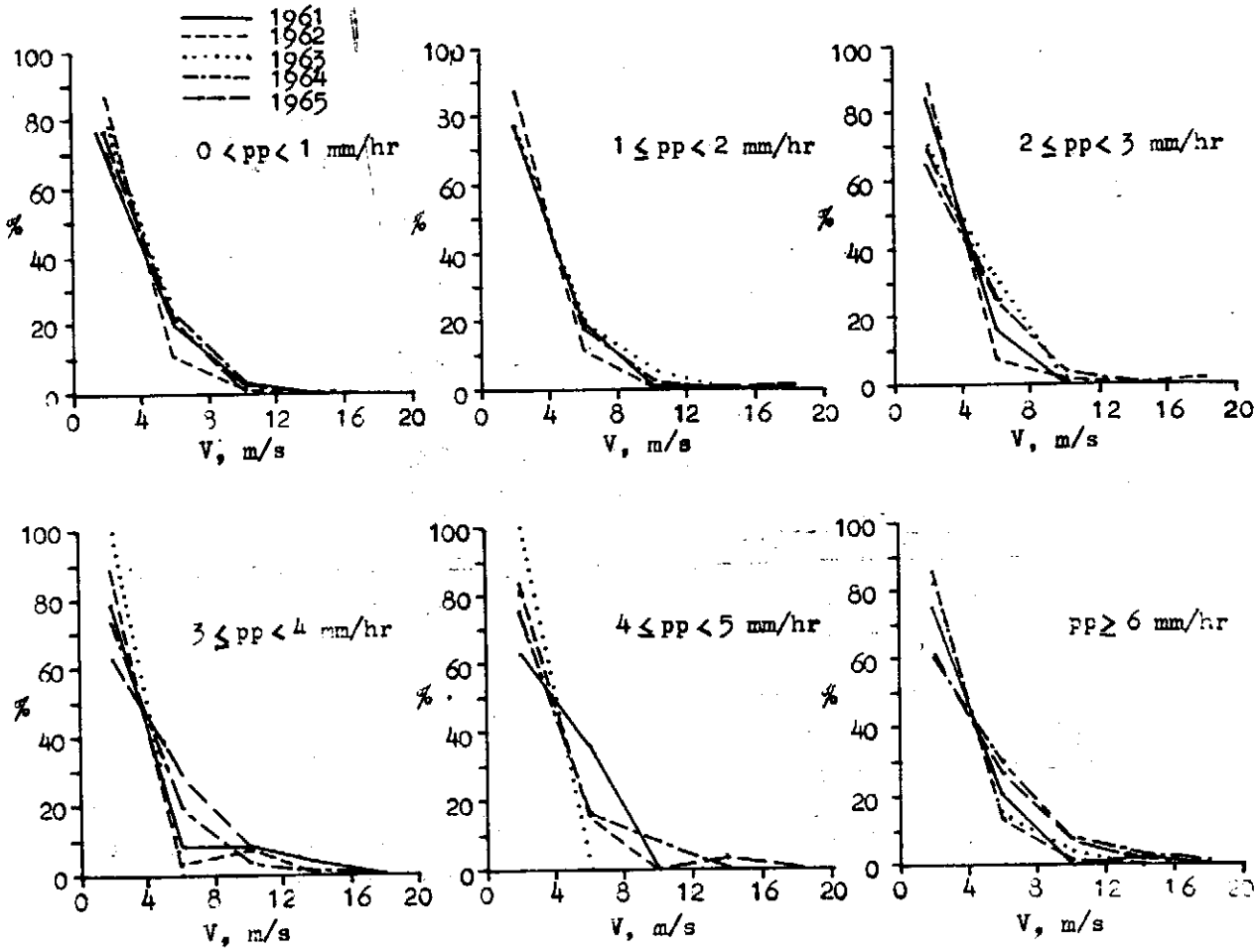

Fig. 2. Percentage frequency of wind speed for categorized precipitation intensity.

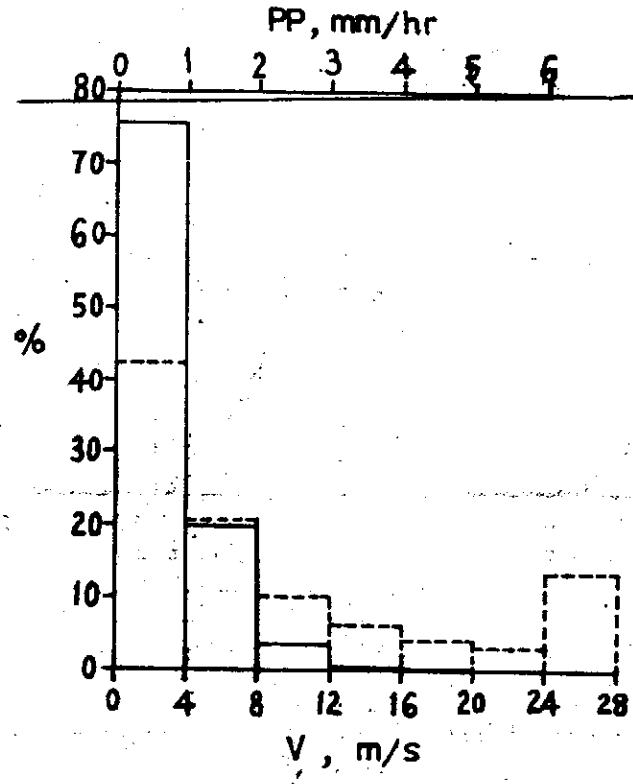

Fig. 3. Percentage frequency of classified precipitation intensity (dashed line) and of classified wind speed (full line).

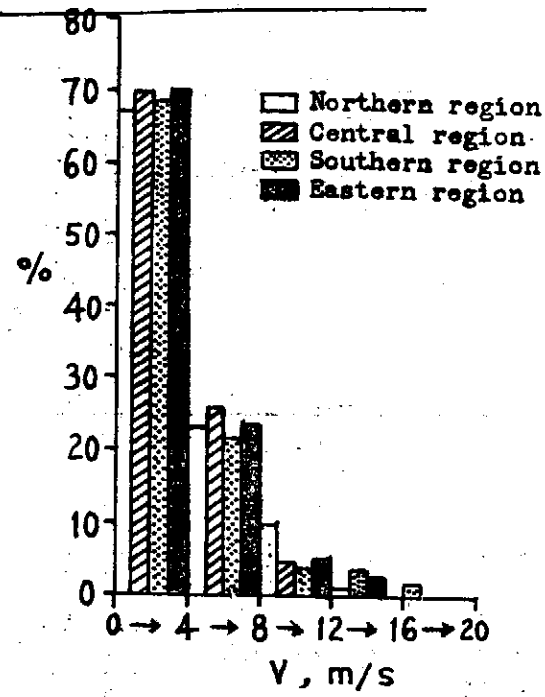

Fig. 4. Percentage frequency of various wind speed during heavy precipitation (pp $\geq$ 6 mm/hr) in northern, central, southern and eastern regions respectively.

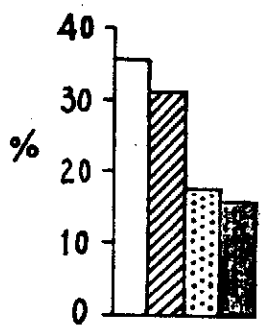

Fig. 5. Probability of precipitation among the four regions.

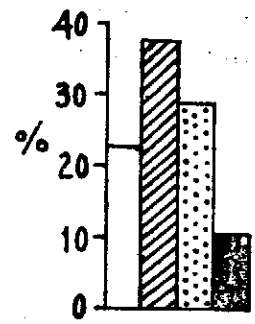

Fig. 6. Probability of heavy precipitation among the four regions.

The total percentage frequency of wind speed when rainfall occurs (full line) and of various precipitation intensity (dashed line) are illustrated in Fig. 3. It is seen clearly that the wind speed in Meiyu season when rainfall happens is almost (96%) not larger than 8 m/sec. From Fig. 3, we also note that the precipitation intensity of less than 2mm/hr occurs often with percentage about 64% and that the percentage frequency of heavy precipitation ($pp \geq 6$mm/hr) is only about 13%. The average wind speed, in case of this heavy rainfall, is 3.68 m/sec. From these results, we conclude that, during Meiyu season in Taiwan, heavy rainfall does not occur often and its correspondent wind speed is not large. This is one distinct feature during Meiyu season in Taiwan and does not agree well with that in Japan and Yangtze river areas.

In consideration of the effect of regional topographic features on the wind field and the precipitation activity, frequency of wind speed during heavy rainfalls, probability of precipitation and of heavy precipitation among the four regions are calculated. The results are illustrated in Figs. 4-6 respectively. As shown in Fig. 4, in case of heavy precipitation, the percentage frequency of wind speed less than 8 m/sec is about 90% in each region. In central region the wind speed is not greater than 12 m/sec. Only in southern region is the wind speed greater than 16 m/sec observed when heavy rainfalls occur. In Fig 5, the probability of rainfall in both northern and central regions are nearly the same and twice as much as those in southern and eastern regions. This implies that during Meiyu season the rainy weather almost arises in the former two regions. Although in northern region the rainfall occurs most frequently, the probability of heavy precipitation (Fig.6) is smaller than those in central and southern regions. The probability of heavy precipitation in eastern region is the least and only about 10%. This is of course due to the shadow effect of the central mountain ranges. Most of the moisture deposits on the western slopes of the ranges.

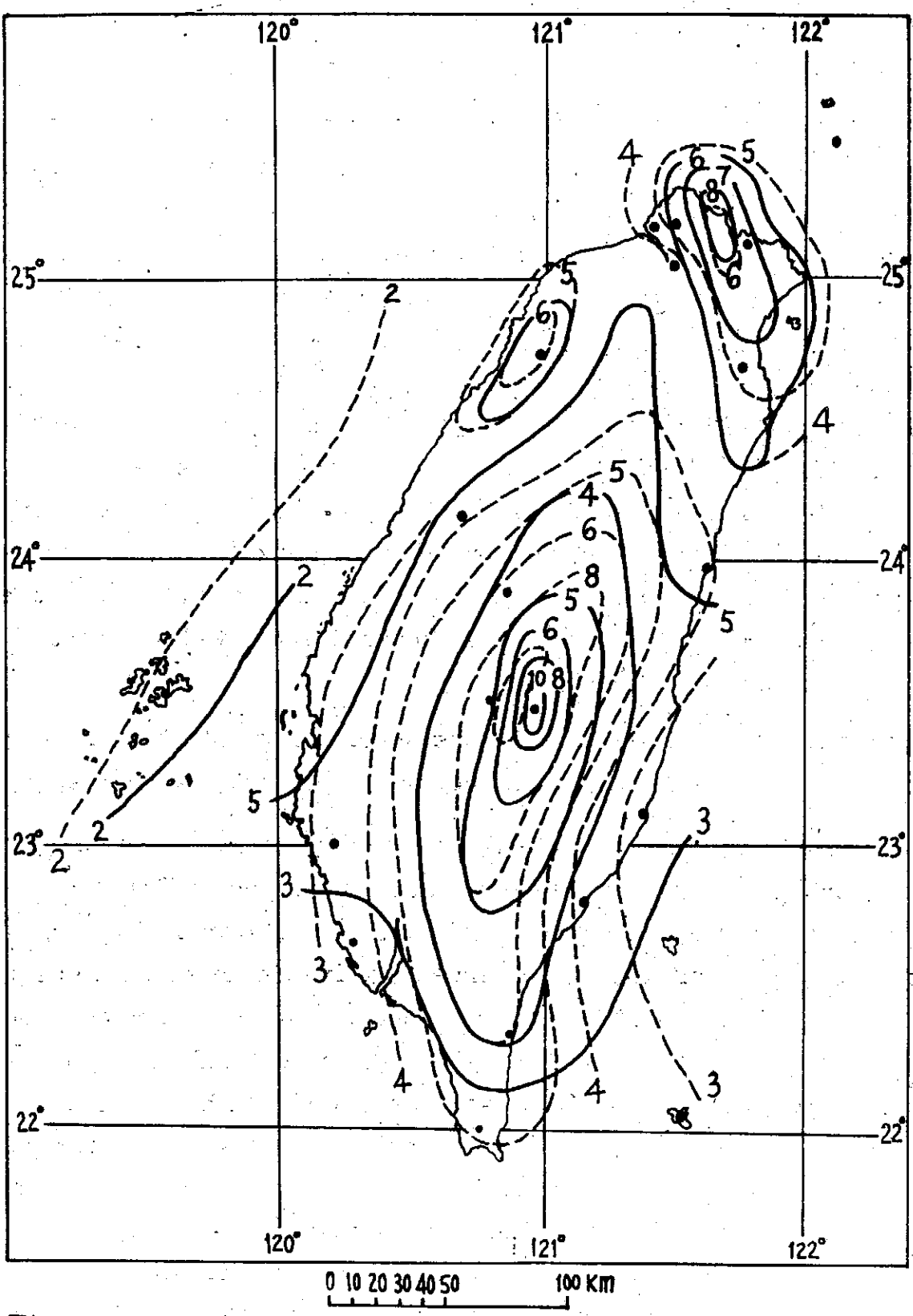

Fig. 7. Spatial distribution of percentage frequency for precipitation intensity of $0 < pp < 1$ mm/hr and of $1 \leq pp < 2$ mm /hr over Taiwan.

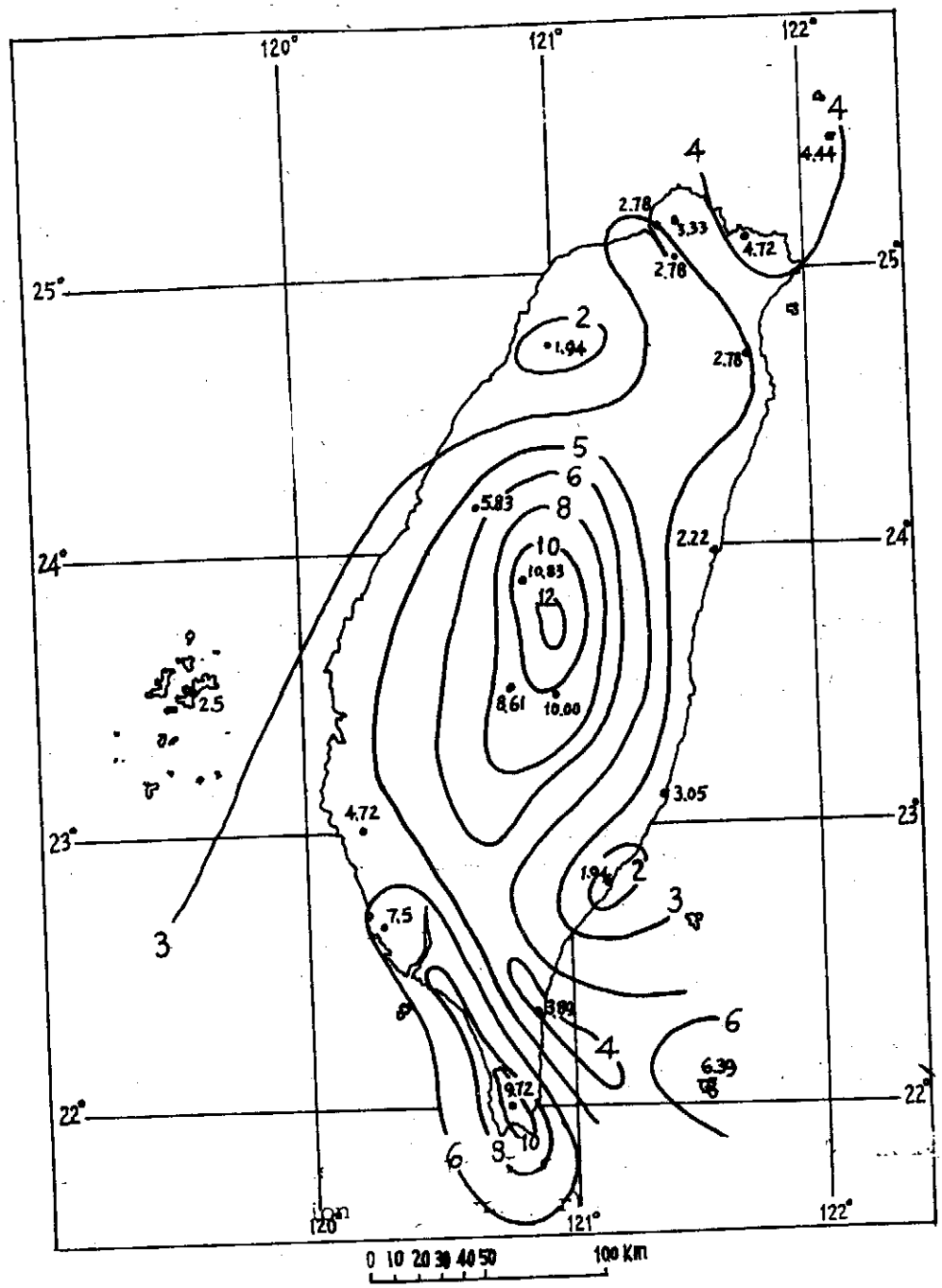

Fig. 8. Spatial distribution of percentage frequency for heavy precipitation (pp $\geqslant$ 6 mm/hr) over Taiwan.

In order to investigate further the spatial distribution of precipitation intensity over Taiwan area, the percentage frequency among the 20 observation stations is computed. We only pay attention to the result of intensity less than 2 mm/hr and of the heavy one, since the former occurs mostly in Meiyu season and the latter may bring tremendous damages. As seen in Fig. 7, Hsinchu area, northeastern area and the central mountain ranges abound with rain but over the sea rain is scarce. Along the western and eastern coastal regions rain is not plentiful. These facts correspond to the influence of topographic features. The rainfall increases gradually on the windward side of the central mountain ranges and decreases on the lee side. Fig. 8 shows the spatial distributinn of frequency for heavy rains. It is obvious that the cores of heavy rainfall are located on the central mountain ranges and around the southern cape of the island.

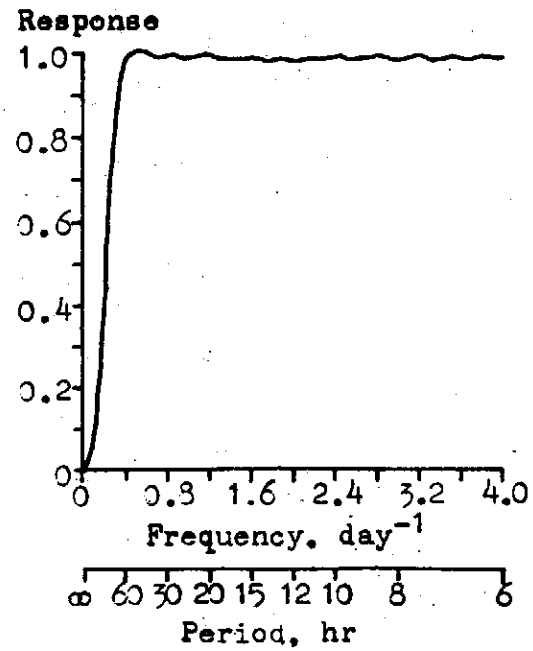

Fig. 9. Respone of filter used in this study.

4. Periodicity of Precipitation and Wind Field

In this study we only pay attention to the analysis of short period perturbation. Therefore, priod to the analysis, we design a filter (Ko, 1974b) to remove the longer period than about 2.5 days or 60 hours. The filtering weights are computed by

$$W_k = \frac{1}{\sigma\sqrt{2\pi}} \exp\left[-(k\Delta t)^2 / 2\sigma^2 \right] \cdot \Delta t \qquad (1)$$

with $\Delta t = 0.125$ day or 3 hr, $\sigma = 1$, $k = 0, 1, \ldots, 11$. The response of this filter is given in Fig. 9 and is almost kept equal to unity shorter than 60 hours. After filtering the original data, we calculate the power spectrum of precipitation intensity and of wind speed according to the following expression,

$$P_k(X) = \sum_{L=0}^{M} C_L(X, X) \cdot \cos(KL\pi/M) \cdot D_L \cdot \delta_L \qquad (2)$$

with

$$D_L = 1 + \cos(\pi L / M) \qquad (3)$$

and

$$\delta_L = \begin{cases} 1/2, & L = 0 \text{ or } M \\ 1, & \text{otherwise,} \end{cases}$$

where L is the lag number, M is the maximum lag number, X represents precipitation intensity or wind speed, and C(X,X) is the autocovariance of precipitation intensity or of wind speed (Ko, 1974a), In this paper we obtain 21 spectral estimates with maximum lag number equal to 20 and frequency interval 0.2 day^{-1}.

Figs. 10-13 show the power spectra of precipitation intensity (left coordinate) and of wind speed (right coordinate) during 1961-1965 in northern, central, southern and eastern regions respectively.

It is worth mentioning that the spectra of rainfall intensity over

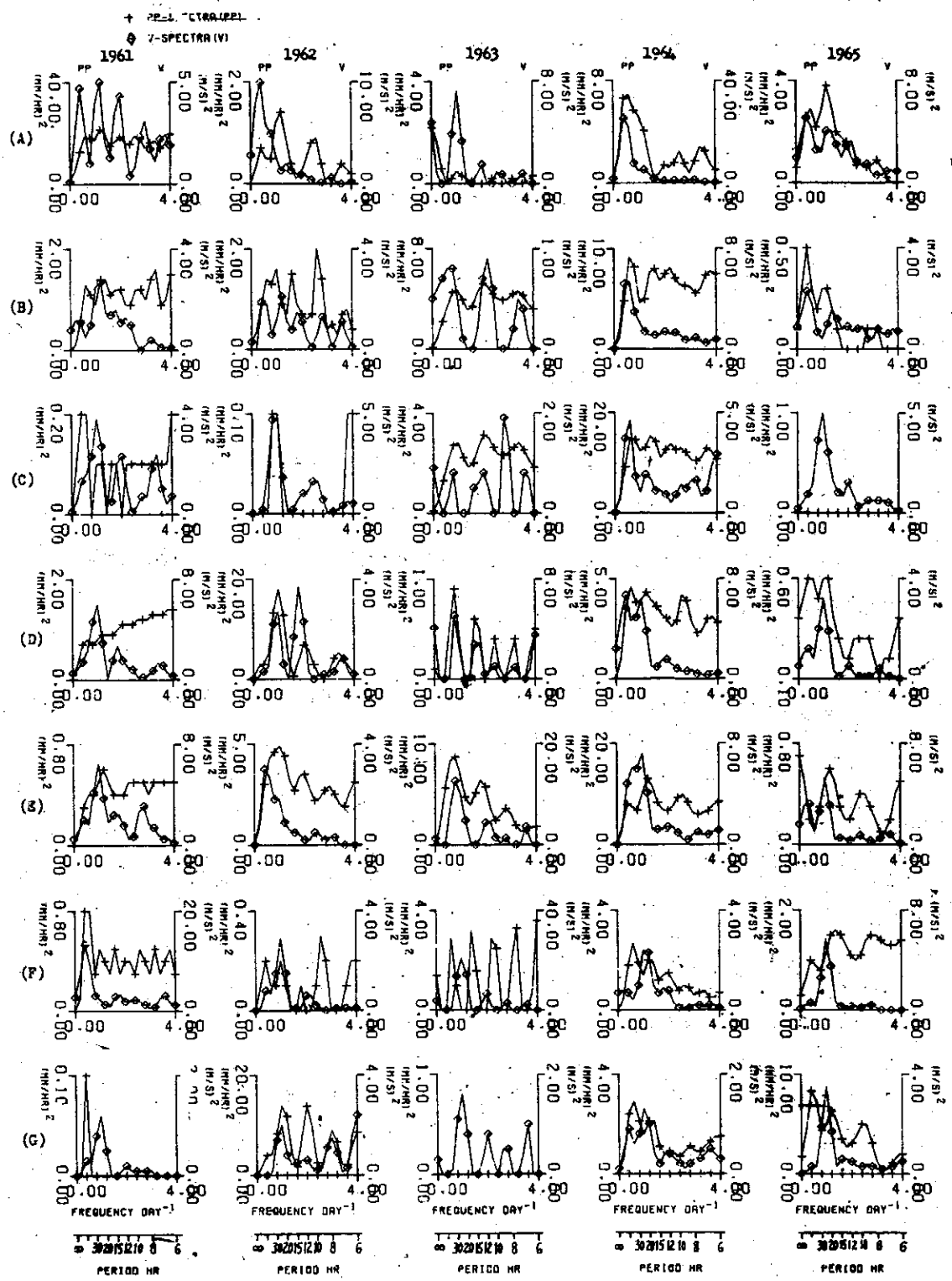

Fig. 10. Power spectra of precipitation intensity and of wind speed over (A) Pengchiayu, (B) Anpu, (C) Tanshui, (D) Keelung, (E) Taipei, (F) Hsinchu, and(G) Yilan in northern region during 1961-1965.

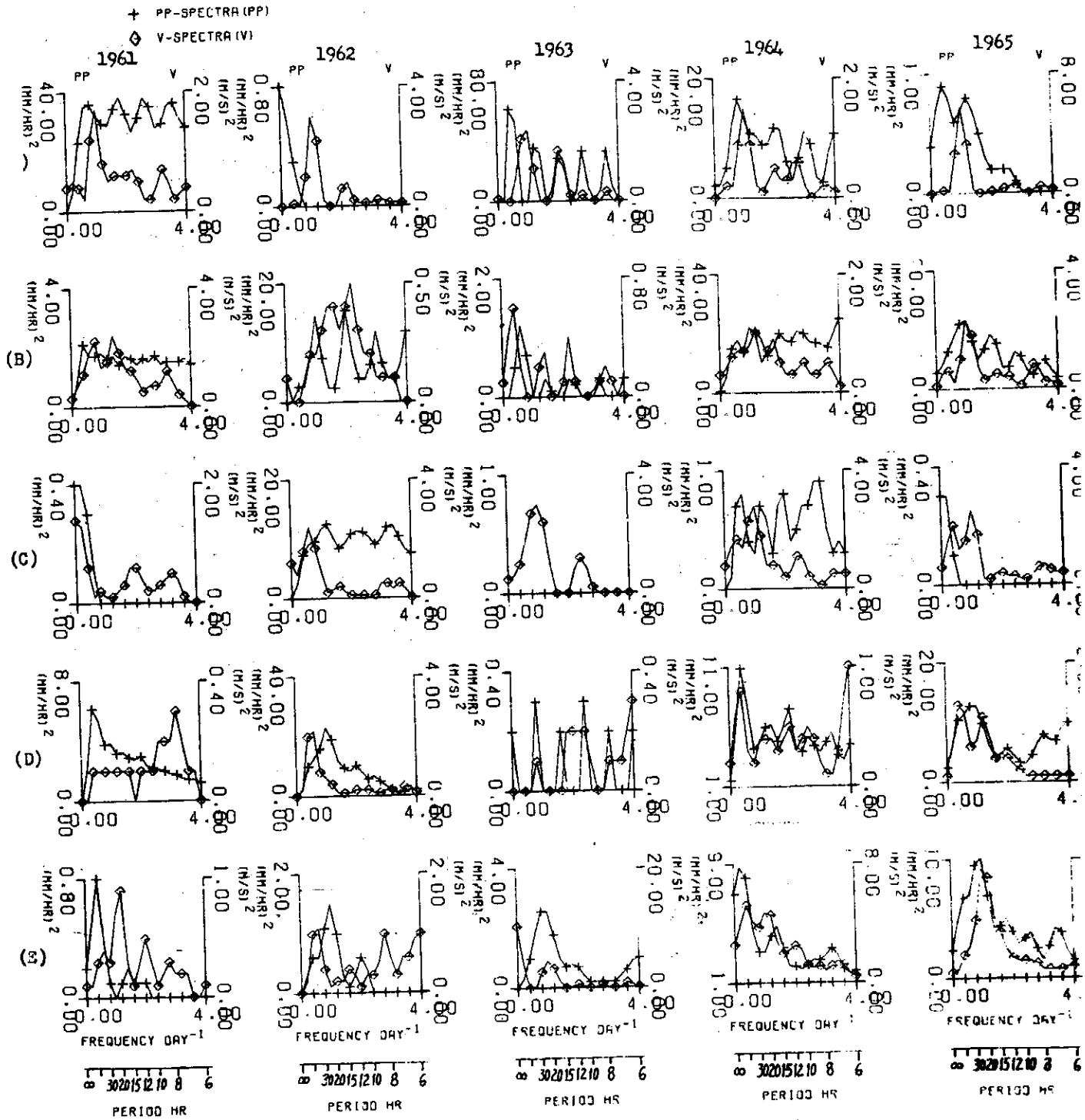

Fig. 11. The same as Fig. 10 except for (A) Taichung, (B) Jihyuehtan, (C) Penghu, (D) Alishan, and (E) Yushan in central region.

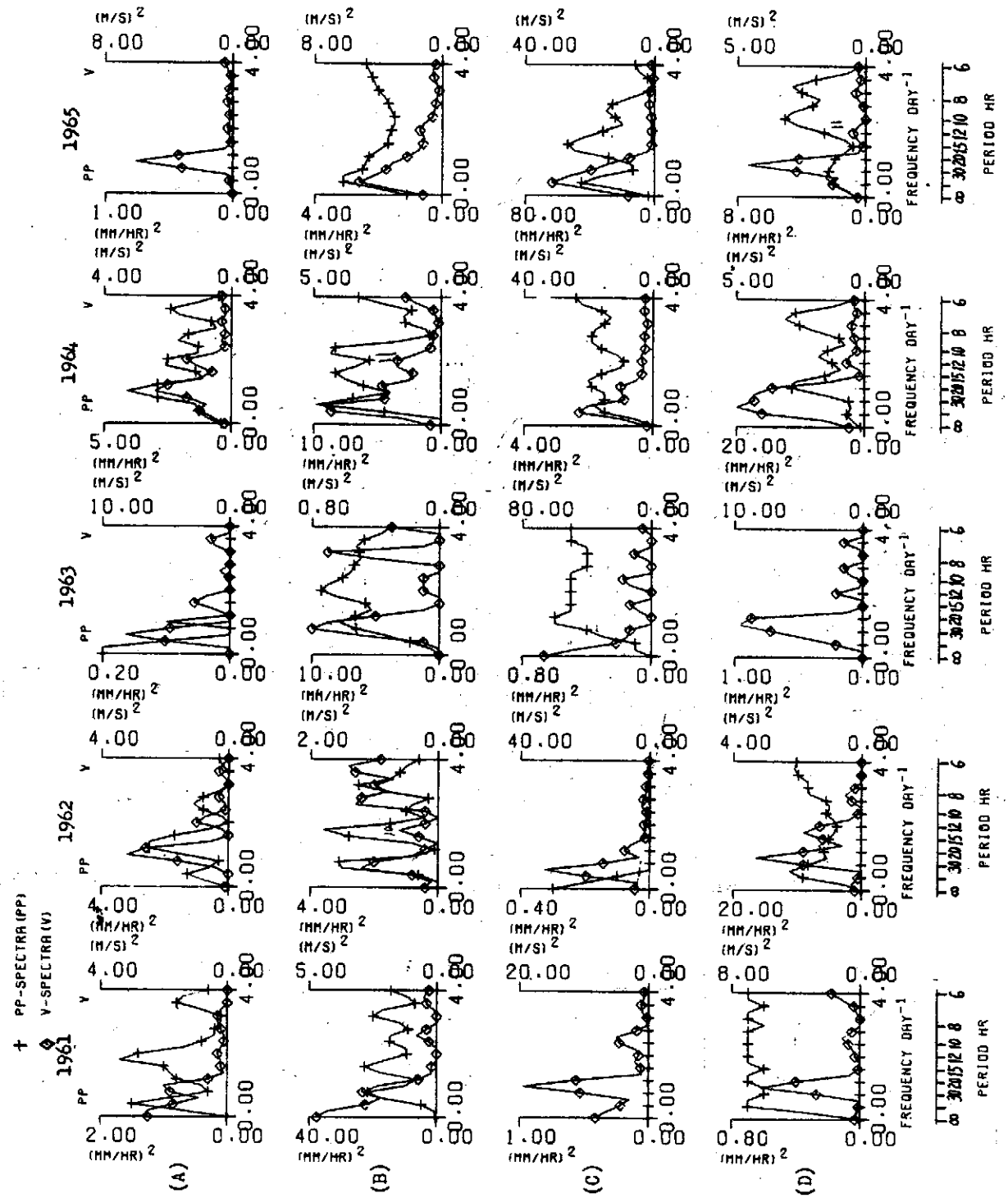

Fig. 12. The same as Fig. 10 except for (A) Tainan, (B) Kaohsiung, (C) Lanyu, and (D) Hengchun in southern region.

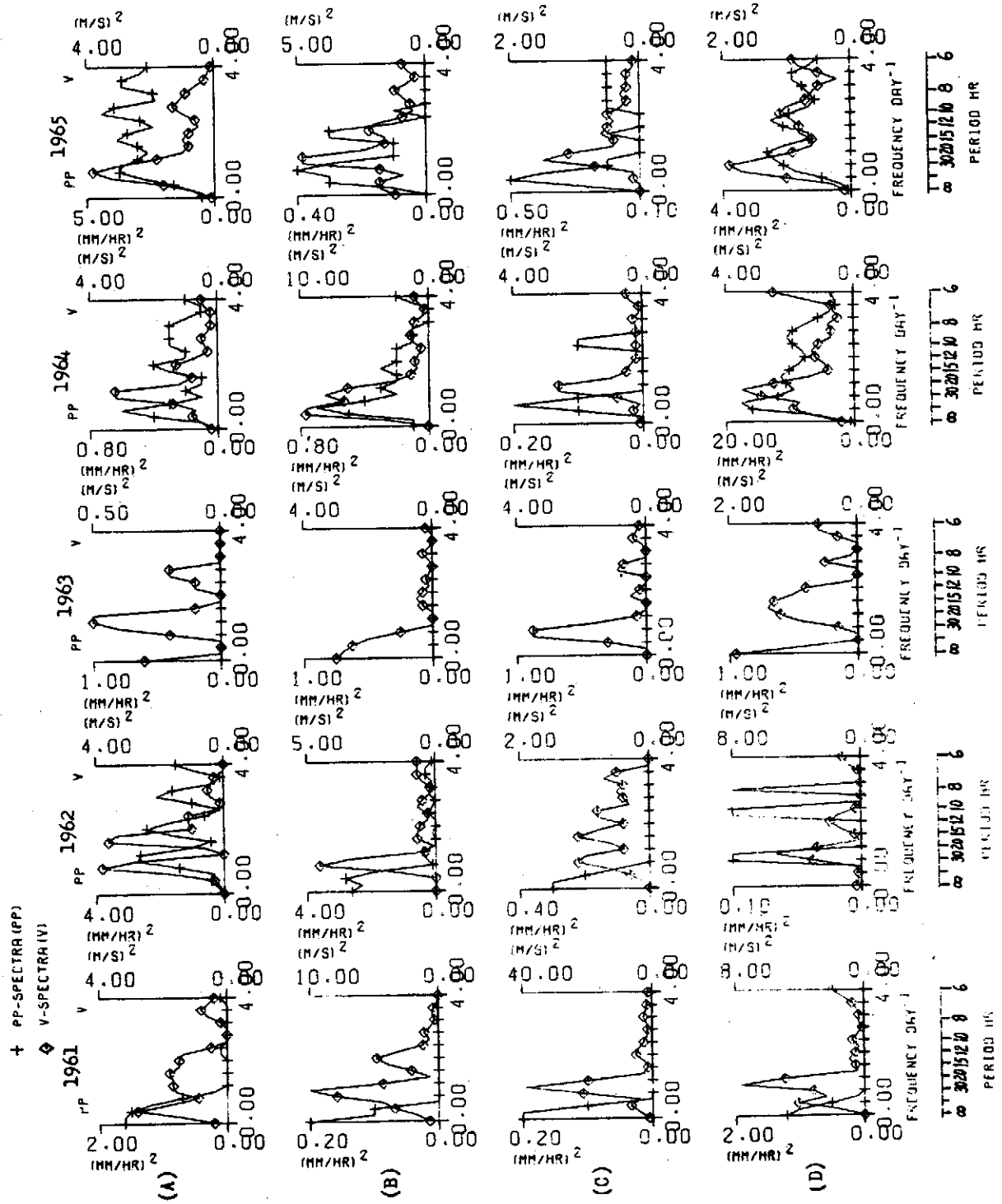

Fig. 13. The same as Fig. 10 except for (A) Hwalien, (B) Hsinkang, (C) Taitung, and (D) Tawu in eastern region.

northern stations have remarkable peaks in the period ranges of 20-24 hours. This suggests that during Meiyu season the rainfall intensity in northern region varies periodically at an interval of 20-24 hours. In addition, at Pengchiayu, Anpu, Tanshui and Keelung the variation of the intensity has period around 7 hours. It is also worthy of note that the periodicity of wind speed in northern region is the same as or slightly longer than that of the rainfall intensity. That is, the wind speed has diurnal variation with period about 24 hours. It seems that the precipitation intensity has intimate relation to the wind speed. Their relationship is discussed in the next section.

In central region, there are five stations including Taichung, Penghu, Jihyuehtan, Alishan and Yushan. The latter three are located on the mountain area and their elevations are higher than 1000 m but the second one is in the sea. Consequently, the features of rainfall and wind field over these stations are expect to differ from each other. In general, the variation of precipitation intensity are almost unanimous among the mountain stations but nearly no regular variation can be found in the sea area. The period of variation found in the mountain area are generally around 24 hours and sometimes about 12 or 7 hours in addition. It should be pointed out that at Taichung both the precipitation and the wind speed vary distinctly in the same manner with periods at 24 and 11-12 hours. As a whole, the spetra of wind speed in Fig. 12 show evident peaks mostly at the periods of 24 hours and around 12 hours.

In southern region, the behavior of precipitation intensity is complex. No identical periodicity is observed for each station and for all region during the five years. However, the wind speed exists similar periodicity especially at Tainan and Hengchun. At these two stations the wind field changes periodically at the interval of 24 hours. At Kaohsiung it shows longer period variation.

Among eastern stations, no regular variation of precipitation intensity can be found during 1961-1965. But somewnat regular

variation is observed in the spectra of wind speed. Most of them have definite period of 24 hours and some have longer period.

From the above analysis, we obtain that the precipitation intensity reveals identical periodic variation in northern and central regions. The period lies in the range of 20 to 24 hours in both regions. In central region additional period of variation is observed at about 12 hours. The wind field in these two regions reveals similiar periodicity too. It seems interest and necessary to investigate the relationship between the precipitation activity and the wind field especially in the above period ranges.

5. Relationship between Precipitation and Wind Field

To examine the relation between precipitation intensity and wind field, we calculate their cospectrum (CS) quadrature-spectrum(Q), coherence (H) and phase difference (θ), respectivelу, according to the equations below:

$$CS_k(pp,v) = \sum_{L=0}^{20} EC_L(pp,v) \cdot \cos\frac{kL\pi}{20} \cdot D_L \cdot \delta_L \tag{4}$$

$$Q_k(pp,v) = \sum_{L=0}^{20} OC_L(pp,v) \cdot \sin\frac{kL\pi}{20} \cdot D_L \cdot \delta_L \tag{5}$$

$$H_k(pp,v) = \left\{\left[CS_k^2(pp,v) + Q_k^2(pp,v)\right] / \left[P_k(pp) \cdot P_k(v)\right]\right\}^{1/2} \tag{6}$$

$$\theta_k(pp,v) = \tan^{-1}\left[Q_k(pp,v) / CS_k(pp,v)\right], \tag{7}$$

where $k=0,1,\ldots,20$, $EC_L(pp,v)$ and $OC_L(pp,v)$ are respectively the even and odd parts of covariance between precipitation intensity and wind speed.

In this section we shall examine the relation between the precipitation and wind field in the period ranges of 20-24 hours. For this period range, the average coherence and phase difference at northern

and central stations are respectively listed in Tables 2 and 3.

At both northern and central weather stations, the coherences between precipitation intensity and wind speed are all larger than 0.5 and the phase differences are all negative at the mountain stations (Anpu, Jihyuehtan, Alishan, Yushan) and small in the sea area (Pengchiayu, Penghu). From these results we may perhaps judge that the disturbance of precipitation intensity and of wind field are closely related in the period range of 20-24 hours and that on mountain area the former lags behind the latter by about 1.5 hours. But they are nearly identical and simultaneous in the sea area. In the plains, the disturbance of precipitation intensity generally leads that of wind speed except at Tanshui and Hsinchu.

Table 2. Average coherence (H) and phase difference (θ) between precipitation intensity and wind speed at northern stations in the period range of 20–24 hours.

Northern stations	Pengchiagu	Anpu	Tanshui	Keelung	Taipei	Hsinchu	Yilan
H	0.74	0.61	0.56	0.52	0.62	0.65	0.71
θ	3.70	-25.39	-11.63	34.61	40.23	-17.61	64.02

Table 3. The same as Table 2 except for central stations

Central stations	Tacihung	Jihyuehtan	Penghu	Alishan	Yushan
H	0.64	0.73	0.58	0.54	0.65
θ	31.93	-25.6	5.95	-18.05	-30.74

6. Conclusions and Remarks

Surface wind field and precipitation activity over Taiwan in Meiyu season during 1961-1965 are studied by methods of frequency distribution and spectral analysis. The remarkable results are summarized as follows:

(1) The wind speed during the whole Meiyu season when rainfalls take place is almost (96%) not larger than 8m/sec.

(2) In Meiyu season the precipitation intensity is usually less than 2mm/hr and heavy rainfalls do not occur often.

(3) The average wind speed in case of heavy precipitation is not large (about 3.7m/sec) and low-level jet does not appear at the surface level.

(4) The probability of precipitation in both northern and central regions are nearly the same and twice as much as those in southern and eastern regions.

(5) It rains most frequently in northern area but in which the probability of heavy precipitation is smaller than those in central and southern regions.

(6) Areas with plentiful rain are located in Hsinchu, northeastern areas and the central mountain ranges; cores of heavy rainfall are on the central mountain ranges and around the southern cape of Taiwan.

(7) In both northern and central regions, the precipitation intensity varies periodically at an interval of 20-24 hours and the wind speed shows distinctly diuranl variation with period about 24 hours. The correlation between precipitation intensity and wind field is high in the above period ranges.

(8) Generally speaking, the disturbance of precipitation intensity and of wind speed are nearly identical and simultaneous in the sea area, the former leads the latter on the mountaneous regions and reverse in the plains.

From results (1), (2) and (3), we find that, during the presummer

rainy season in Taiwan, heavy rainfalls do not occur often and its correspondent wind speed is not large, which do not agree with what obtained in Yangtze river and Japan areas. This discrepancy may be due to that the so-called "Baiu front" is prevailing usually far to the north or northwest of Taiwan. Results (4), (5) and (6) suggest the effect of the central mountain ranges on the precipitation activity is strong. It rains often and heavily on the windward side but scarcely and light on the lee side. Result(7) agrees well with what obtained by Matsumoto (1970, 1973). This probably implies that the mechanism governing the variation of precipitation in Taiwan area is correlated with that in Japan area. Further study on the dew point, humitity, and divergence and vorticity of surface wind field seems necessary for making definite conclusions.

7. Acknowledgements

Thanks are due to Dr. C. T. Wang, Research Fellow of Institute of Physics, Academia Sinica, for his suggestions and financial support, and to Mr. P. I. Wang for his help in revising the original data. Computations and plotting are executed at the Computer Center of Taipei Institute of Technology and of National Science Council at National Tsing Hua University.

References

Akiyama, T., 1973a: The large-scale aspects of the characteristic features of the Baiu front. Pap. Meteor. Geophy., 24, 157–188.

Akiyama, T., 1973b: Ageostrophic low-level jet st am in the Baiu season associated with heavy rainfalls over the sea area. J. Meteor. Soc. Japan, 51, 205-208.

Chi, K. h., 1964: Plum rains in Taiwan. Meteor. Bull., 10, 2, 1-12.

Hsu, C.H., 1971: A study of heavy rain in the Taipei area. Meteor. Bull., 17, 3, 49-71.

Hsu, M.T. and S.S. Chi, 1974a: On the analysis of "Mei-yu" in Taiwan. Meteor. Bull., 20, 4, 25-44.

Hsu, M.T., and S.S. Chi, 1974b: On the forecasting of the Mei-Yu in Taiwan. Quart. J. Meteor., 63, 242, 5-11.

Ko, S.D., et al., 1973: Power spectra of upper wind over Taiwan in Summer. Ann. Rept. Inst. Phys. Acad. Sini., 3, 239-255.

Ko, S.D., 1974a: Spectrum analysis of wave disturbances over northern Taiwan in winter. Atmos. Sci. Meteor. Soc. ROC, 1, 19-34.

Ko, S.D., 1974b: Normalized weights of Gaussian filtering function. J. Tai. Inst. Tech., 7, 83-97.

Ko. S.D., 1974c: Wave disturbances in winter over the coastal area of southern China continent. Ann. Rept. Inst. Phys. Acad. Sini., 4, 197-213

Matsumoto, S., and T. Akiyama, 1970a: Mesoscale disturbances and related rainfall cells embedded in the "Baiu front" with a proposal on the role of convective momentum transfer. J. Meteor. Soc. Japan, 48, 91-102.

Matsumoto, S., S. Yoshizumi, and M. Takeuchi, 1970b: On the structure of the "Baiu Front" and the associated intermediate-scale disturbances in the lower atmosphere. J. Meteor. Soc. Japan, 48, 479-491.

Matsumoto, S., K. Ninomiya and S. Yoshizumi, 1971: Characteristic features of "Baiu front" associated with heavy rainfall. J. Meteor. Soc. Japan, 49, 267-281.

Matsumoto, 1973: Lower tropospheric wind speed and precipitation activity. J. Meteor. Soc. Japan, 51, 101-107.

Ninomiya, K., and T. Akiyama, 1971: The development of the medium-scale disturbances in the Baiu front. J. Meteor. Soc. Japan, 49, 663-677.

Ninomiya, K., and T. Akiyama, 1972, 1973: Medium-scale echo

clusters in Baiu front as revealed by muti-radar composite echo maps (parts I and II). J. Meteor. Soc. Japan, 50 & 51, 558-569 & 108-118.

Wexler, H., 1961: A boundary layer interpretation of the low-level jet. Tellus, 13, 368-378.

Annual Report of the Institute of Physics, Academia Sinica, 1974

A Typhoon Movement Study by Balance Barotropic Model

C. J. Shiau

Abstract

Using data from typhoon Elsie 11 Oct. 1975 and June 21 Nov. 1975, the numerical forecasting experiments by using a linear balance barotropic model have been carried 24 hours.

Near the tropical region, the use of stream function field for weather prediction is better than that of using height field. Thus stream function field obtained from the balance equation is adopted in the divergence barotropic model. For comparing with the real weather data, the height field is presented at 12 and 24 hours. The obtained results of computation are well in agreement with the real weather situation.

1. Introduction

Since 1950, a number of forecasts for 24, 48, 72 hours with barotropic model are taken under the assumption of geostrophic approximation. But it is mentioned by Bolin (1956) that this assumption is deficient, for it is not satisfied at low latitude zone and, when replacing the geostrophic relation by a more general balance equation, the barotropic forecasts might be improved better, especially in areas with large cyclonic or anticyclonic vorticity or in that with a strong deformation field.

In this work, we therefore attempted to eliminate the geostrophic approximation to get a more general balance equation between the mass and wind fields. Moreover because the non-linear balance equation is very complex and time consuming, we adopted the linear balance equation as the diagnostic equation. For avoiding the problem of spurious retrogression of very long wave, the divergent barotropic equation is chosen to be the prognostic equation (Cressman, 1958).

2. Basic Equations

a) The diagnostic numerical equation that we chose for this study is commonly called the linear balance equation, while the prognostic numerical model selected is called the divergent barotropic model. The equation pertaining to this system are (Haltiner, 1971)

$$\frac{\partial \zeta}{\partial t} + \vec{V} \cdot \nabla (f + \zeta) = \bar{f} \frac{\partial \omega}{\partial p}$$

$$\text{or} \quad (\nabla^2 - M) \frac{\partial \psi}{\partial t} = -\vec{V} \cdot \nabla (f + \nabla^2 \psi) = -J(f + \nabla^2 \psi, \psi) \tag{2.1}$$

where $\zeta = \nabla^2 \psi$, $\vec{V} = \vec{k} \times \nabla \psi$, $M = f^2 \frac{A_0}{RT_0}$ ($A_0 = 1$, in the barotropic atm.). The term $M \frac{\partial \psi}{\partial t}$ is the so-called Helmholtz term and the addition of this term leads to better control of the ultralong or planetary waves, (P.M. Wolff 1958). The coefficient M is normally treated as a constant and is taken to be 0.13×10^{-12} m^{-2} here. J is the Jacobican operator. The balance equation is

$$f \nabla^2 \psi + \nabla f \cdot \nabla \psi + 2J(\psi_x, \psi_y) = \nabla^2 \psi \tag{2.2}$$

In order to permit the solution of equation (2.2) as that of an elliptic equation by relaxation techniques, usually a slight modification of the initial geopotential height field with restrictions on subsequent approximations of ψ i.e.

$$\nabla^2 \psi + \frac{1}{2} f^2 - \nabla f \cdot \nabla \psi > 0 \tag{2.3}$$

must be satisfied. It requires that the absolute vorticity be positive and exceeds a prescribed minimum value i.e.

$$\nabla^2 \psi^{(n)} + f > \varepsilon \tag{2.4}$$

with (n) denotes the nth guess and ε an arbitrary small positive value. For conveniencing, the linear balance equation

$$f \nabla^2 \psi + \nabla f \cdot \nabla \psi = \nabla^2 \psi \tag{2.5}$$

is furthermore adopted. Since it satisfies the condition (2.3), only the constraint of the positive absolute vorticity is required.

In this work, we tried to check the initial geopotential field. If at point (i, j), the left side of equation (2.3) is not greater than zero, we modify the geopotential field $\phi_{i,j}$ by adding $\frac{1}{8}(\nabla^2\phi+\frac{1}{2}f^2-\nabla f\cdot\nabla\psi)$ to the initial value, i.e.

$$\phi^*\leftarrow\phi+\frac{1}{8}(\nabla^2\phi+\frac{1}{2}f^2-\nabla f\cdot\nabla\psi)$$

where ϕ^* is the modified value.

The procedure is done cycle by cycle until all points of the ϕ-field satisfy the above condition. We call the modified geopotential field the balanced geopotential field. From this balanced geopotential field and linear balance equation, we obtain the so-called balanced stream function field. Using these balanced streamfunction field and eq. (2.1), we thus can predict ψ for every time step. Moreover we convert ψ into ϕ by eq. (2.5), so to obtain the ϕ-field at every 12 hrs.

b) The operators

(i) Arakawa's finite difference method is used to calculate the various differentials in the equation of model.

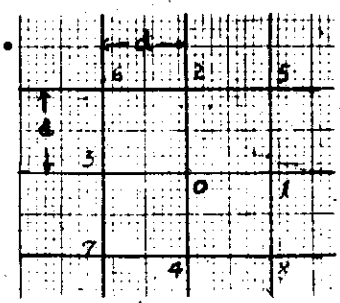

$$\left(\frac{\partial A}{\partial x}\right)_0=\frac{1}{8d}[A_5+2A_1+A_8-(A_6+2A_3+A_7)]$$

$$\left(\frac{\partial A}{\partial y}\right)_0=\frac{1}{8d}[A_5+2A_2+A_6-(A_8+2A_4+A_7)]$$

$$\nabla A\cdot\nabla B=\frac{1}{2d^2}[(A_1-A_0)(B_1-B_0)+(A_0-A_3)(B_0-B_3)+(A_2-A_0)(B_2-B_0)+(A_0-A_4)(B_0-B_4)]$$

$$J(A,B)=\frac{1}{12d^2}[B_3(A_4+A_7-A_2-A_6)-B_1(A_8+A_4-A_2-A_5)+B_4(A_1+A_8-A_3-A_7)-B_2(A_1+A_5-A_3-A_6)+B_8(A_1-A_4)+B_5(A_2-A_1)+B_6(A_3-A_2)+B_7(A_4-A_3)]$$

(ii) The smoothing operation is five-point and two-dimensional. It can be expressed as follows:

$$\bar{A} = A + K \nabla^2 A \quad , \quad K = 0.17,$$

where A denotes the original field and $\bar{A}$ denotes the smoothed field.

(iii) The relaxation method we used is the over-relaxation method. For a Helmholtz type equation

$$\nabla^2 T_{i,j} - \mu^2_{i,j} T_{i,j} = F_{i,j} ,$$

After assuming the mth guess value of $T_{i,j}$ is $T^m_{i,j}$, the equation

$$\nabla^2 T^m_{i,j} - \mu^2_{i,j} T^m_{i,j} - F_{i,j} = R^m_{i,j}$$

is obtained, with $R^m_{i,j}$ as the residual. The (m+1)th guess value of $T_{i,j}$ is

$$T^{m+1}_{i,j} = T^m_{i,j} + \frac{\alpha R^m_{i,j}}{4+\mu^2_{i,j}}$$

and α is an over-relaxation factor, adopted to be 1.65, 1.82 in equations (2.5), (2.1) respectively.

3. Domain of integration and grid structure

The horizontal domain is a rectangular one covering the large part of East Asia in Lambert conformal conic projection with standard parallels 30^oN and 60^oN. The Coriolis parameter $f_{i,j}$ and mapping factor $m_{i,g}$ are calculated from the latitude of each grid points (See Fig. 2)

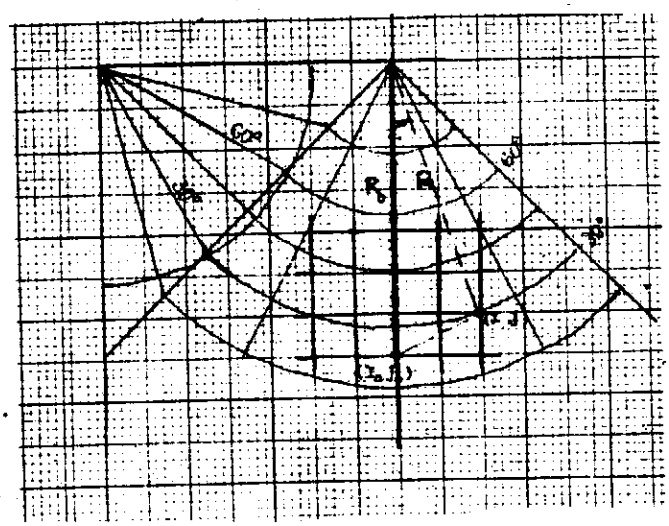

Fig. 2. Lambert Conical Projection True At 30° and 60° Latitude.

$$f_{i,j} = 2\omega \sin\varphi_{i,j}\ ,\quad \omega = 0.7292 \times 10^{-4}\ \text{sec}^{-1} \tag{3.1}$$

$$m_{i,j} = (0.866/\sin\varphi_{i,j})\left[1.732 \times \tan\left(\frac{\varphi_{i,j}}{2}\right)\right]^{n} \tag{3.2}$$

where

$$\lambda_{i,j} = \lambda_0 + \frac{1}{n}\sin^{-1}\left[(I - I_0)/R_{i,j}\right] \tag{3.3}$$

$$\varphi_{i,j} = 2\tan^{-1}\left[\left(\frac{R_{i,j}\ nd}{a\ \sin 60^{\circ}}\right)\tan\frac{60^{\circ}}{2}\right] \tag{3.4}$$

$a = 6367$ km , $\lambda_0 = 120^{\circ}$, $d = 240$ km

$n = 0.716$, $\varphi_0 = 30^{\circ}$

$$R_0 = \frac{a}{nd}\sin 60^{\circ}\left[\frac{\tan\varphi_0/2}{\tan 60^{\circ}/2}\right]^{n}$$

$$R_{i,j}^2 = (I - I_0)^2 + R_0^2 - (J - J_0)^2$$

and I, J, I_o, J_o are the grid point (i,j) and the reference grid point (i_o, j_o).

The grid is a 240 km square mesh consisting of 38 x 28 points (See Fig. 1). In the vertical, only one level is investigated, i.e., the 500 mb-level. The model utilizes the (x,y,p) coordinate system. The distance x and y are measured toward east and south respectively. The dependent variables are placed on a coordinate mesh as illustrated in Fig. 3.

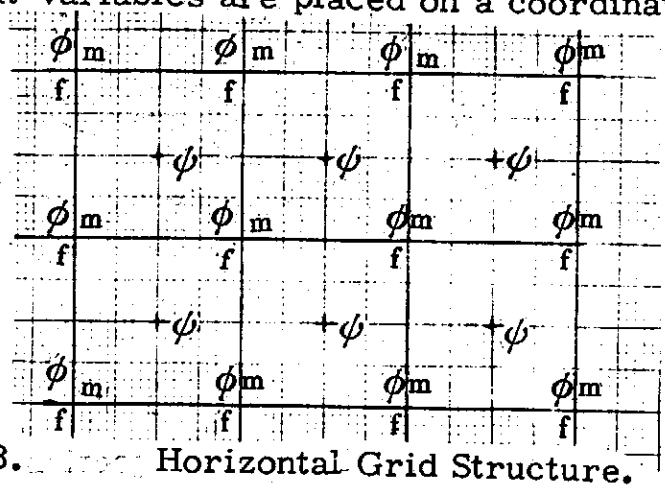

Fig. 3. Horizontal Grid Structure.

They are staggered in space but not in time.

4. Initial data and boundary condition

a) The initial data for the model are derived from the balance eq. on a square grid consisting of 38 x 28 grid points. Basic input data are the geopotential heights of two typhoons, Elsie (Oct. 11, 1975) and June (Nov. 21, 1975) at 500mb level.

In order to obtain the balance field (balance between the mass field and the wind field), we put the original raw data into the balance equation, then the balanced geopotential and stream function field can be obtained. We believe it is more suitable for the tropical area study, because we have not made the assumption of quasi-geostrophic wind which is not satisfied in that area.

The obtained stream function field is used as the initial field for the divergent barotropic model.

b) For this model, the fixed boundary conditions $\frac{\partial \phi}{\partial t} = 0$ and $\frac{\partial \psi}{\partial t} = 0$ are considered at the boundary.

c) Time integration

As a time increment, Δt=3600 sec. is adopted. At the initial time, $t = 0$, (the 1'st step), the forward time difference is used. Later, when $t > 0$, the centered time difference is used until the whole forecast period is covered.

5. Procedure for performing numerical time integration

a) From the initial ϕ-field, we can calculate the balanced and smoothed stream function ψ-field. By using this ψ-field and equation (2.1) and taking time extropoiation, we can obtain the ψ-field at the next time step. After each 12 hours, ϕ-field is calculated for presention via the linear balance equation.
The predictions have been made to 24 hours.

6. Case study results and conclusion

Using the procedure outlined above, two 24-hour forecasts have been made. They are based on 500 mb maps from 11 October, 1200Z, and 21 November, 1200Z, 1975.

For the first case (See Figure 4.1), the center of typhoon Elsie, 11 Oct. 1200Z is located at the grid point (22, 22) near (19.5^{o}N, 124.5^{o}E). The Paciffic high center is located at grid point (27, 19) near (24.2^{o}N, 136.5^{o}E) along the axis about 25^{o}N, extended westward to Indochina peninsula on which there is also a high center, is located at grid point (13, 21) near (20.2^{o}N, 104.5^{o}E). This high is blocked in the north of typhoon circulation.

In the east coast of mainland, the low center is located at grid point (25, 8) near (48.7^{o}N, 135.5^{o}E). Through this center, a trough extended SSW to Liaodong Peninsula (遼東半島). Near Sakhalin, another low center is located at grid point (29, 8) about (50.3^{o}N, 149^{o}E), and through this center, a trough extended to 30^{o}N. In the west of Baikal Lake, there is a ridge, parallel to 90^{o}E.

After balance (See Figure 4.2), except that the height of high center deepened little (about 20m), in the north of the typhoon circulation, the Paciffic high separated two, while the location and strength of each low center is still be maintained. Only the range of typhoon circulation expanded litt[illegible]

The weather pattern has no sign[illegible]nt change.

After 12 hours (See Figure [illegible]) as typhoon center moves a little northwest. The height field near [illegible] deepened, and the maximum is at grid (21, 21). By the calcu[illegible]n of relative vorticity the NW

deepened, and the maximum is at grid (21, 21). By the calculation of relative vorticity the NW of typhoon center has upward current, and the SE has down ward current. The axis of Paciffic high is about 25°N, extending to 130°E. In the east coast, the two low combined. Through its center, the trough extended to Japan Sea. In comparison with the original position, the trough moved eastward about 3.5° longitude. The ridge in the west of Baikal Lake moved eastward 2° longitude, parallel to 92°E.

After 24 hours (See Figure 4.4), typhoon moved NW to (121.5°E, 21.5°N). Comparing with the real situation, the location of the predicted center inclines northly about 20°, while its speed is identical to the real situation. The axis of the Paciffic high is about 25°N, extending westward to 126°E. The low center at the east of Sakhalin is located at the grid point (28, 6). The height is deepened when comparing to 12 hrs. Through this center, the trough extended SW to Japan Sea and moved eastward about 4° longitude (comparing with 12 hrs.).

The second case is typhoon June 21 Nov. 1975, 1200Z (See Figure 5.1), the center is located at grid point (28, 23), (19.8°N, 137°E). The axis of Paciffic high is about 20°N, with center locating at grid point (37, 20) and extending westward to 145°E. In the NW of Baikal Lake, a ridge parallel to 80°E. In the mainland a low center located at (120°E, 50°N). Through this center, the major trough extended SW to Yangtze River. In the east of Kamchatka Peninsula, there is another low. Through its center, the trough extended SW.

From the reading off map by subjective method at the grid point (13, 3) i.e. in the NE of the above ridge, the data value inclines so high that the contour line 5520m is not smooth at this point.

After balance (See Figure 5.2), this error is modified and smoothed to be reasonable. The remaining data of this field is the same as the original field.

After 12 hours (See Figure 5.3), the height of typhoon center fills and moves NW a little. The major trough tilts toward NE, and moves a little. In the east of Kamchatka P., the trough moves NE about 2 grid distance. The ridge moves eastward parallel to about 82°E.

After 24 hours (See Figure 5.4), the center of typhoon moves toward NNW about 1.5 grids distance, the central height fills and the major trough moves eastward about 1 grid distance. The ridge moves eastward parallel to about 85°E. Compare with the real weather map, the Siberia high, due to the setting up of a major trough in the east coast of mainland, steered the cold air to advect southly, so the path of typhoon loss its original way NW, and inclines to north.

The prediction fits well with the real situation, and the motions of the ridge and trough are completely agreed.

Generally speaking, the initial field data after blance is good. The results of case studies are close to the real field situation such as the speed of typhoon and the speed and direction of trough and ridge. But Because the model is barotropic one, the effects of heat, friction and orography are not considered, and the direction of motion of typhoon have some deviation in comparison to the real weather map. These shortcomings will be improved in the latter work.

7. Acknowledgment

The author is deeply grateful to Mr. C.Y. Hu for his many fruitful discussions and help, to Professor C.T. Wang for his suggestion and encouragement, and to Mr. Jin Jso, Mr. T.S. Tai and Mr. S.Y. Chen for their kind help.

Symbols list

f	Coriolis parameter
g	Acceleration of gravity
$\vec{k}$	Unit vector in the Z-direction
p	Atmosphere pressure
φ	Degree of latitude
λ	Degree of longitude
ζ	Vorticity
ω	P-velocity
ψ	Stream function
ϕ	Geopotential
∇	Gradicent operator
∇^2	Laplacian operator
J	Jacobian operator

References

1. Bolin B.: Numerical Forecasting with The Barotropic Model, Tellus, 7, 27-49, 1955
2. Bolin B.: An Improved Barotropic Model and Some Aspects of Using the Balance Equation For Three-Dimensional Flow, Tellus, 8, 61-75, 1956.
3. Baumhefner David P.: Application of A Diagnostic Numerical Model to The Tropical Atmosphere, M.W.R., 96, 218-221, 1968.
4. Cressman G. P. and W. E. Hubert, A study of Numerical Forecasting Errors, M.W.R., 85, 235-242, 1957.
5. Geirmundur Árnason: A Convergent Method for Solving the Balance Equation, Jour. of Met., 15, 220-225, 1958.
6. Haltiner G.J.: Numerical Weather Prediction, Wiley 1971.
7. Krishnamurti T.N.: A Diagnostic Balance Model for studies of Weather System of Low and High Latitudes Rossby number Less Than 1, M.W.R., 96, 197-207, 1968.

8. Shuman F.G.: Prodictire Consequences of Certain Physical Inconsistencies in the Geostrophic Barotropic Model, M. W. R., 85, 229-234, 1957.

9. Shuman F.G: Numerical Methods in Weather Prediction I. The Balance Equation, M. W. R., 85, 329-361, 1957.

10. Wolff P. M. The Error In Numerical Forecasts Due to Retrogression of Ultra-long Waves, M. W. R., 86, 245-250, 1958.

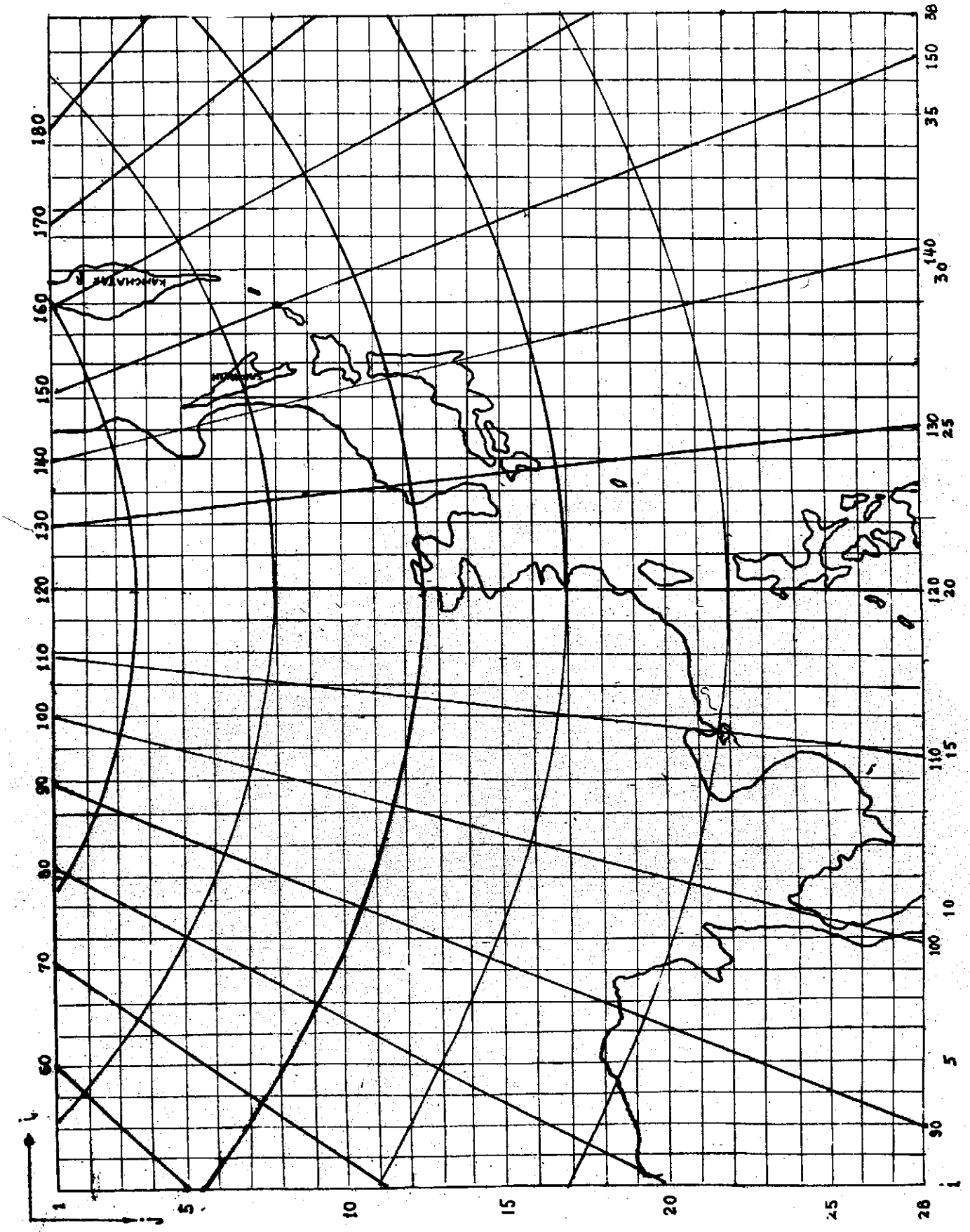
KAMCHATKA
180
170
160
150
140
130
120
110
100
90
80
70
60
i
j
1
5
10
15
20
25
28
38
150
35
140
30
130
25
120
20
110
15
100
10
90
5
1

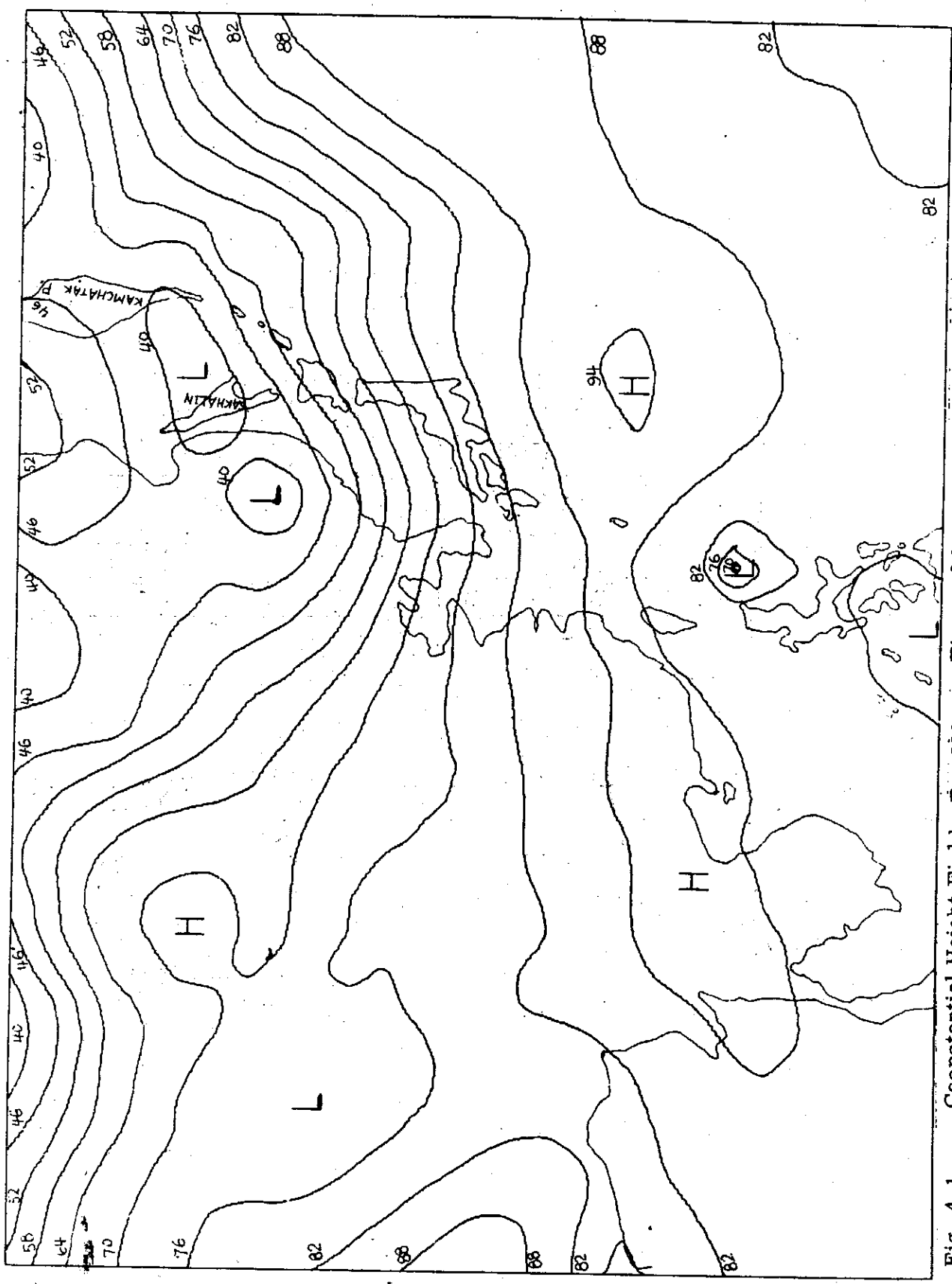

Fig. 4.1 Geopotential Height Field P = 500 mb Time = 0 hr. For 12Z, 11 Oct. 1975.

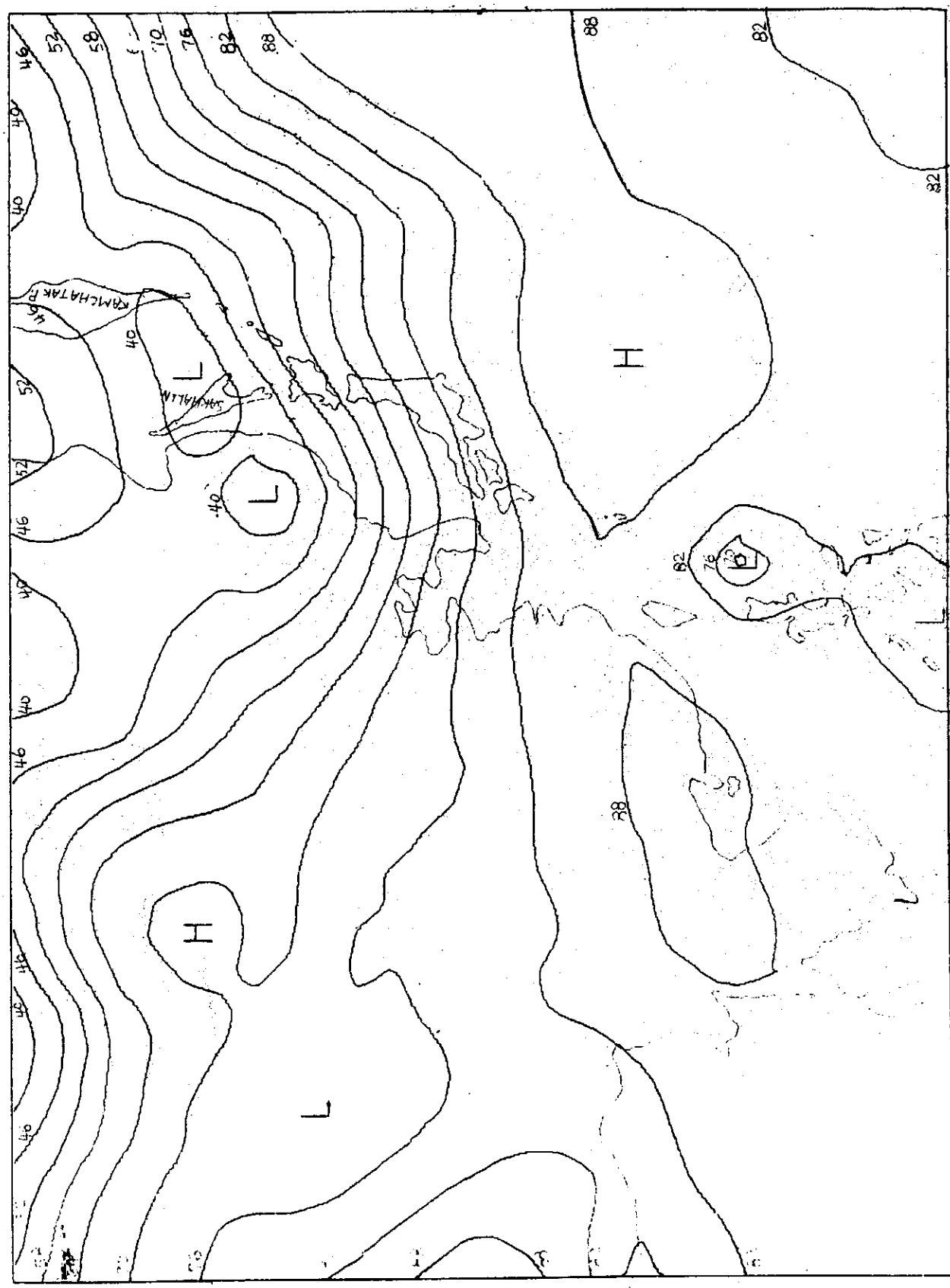

Fig. 4.2 Geopotential Height Field (Balanced) P = 500 mb Time = 0 hr. For 12Z, 11 Oct, 1975

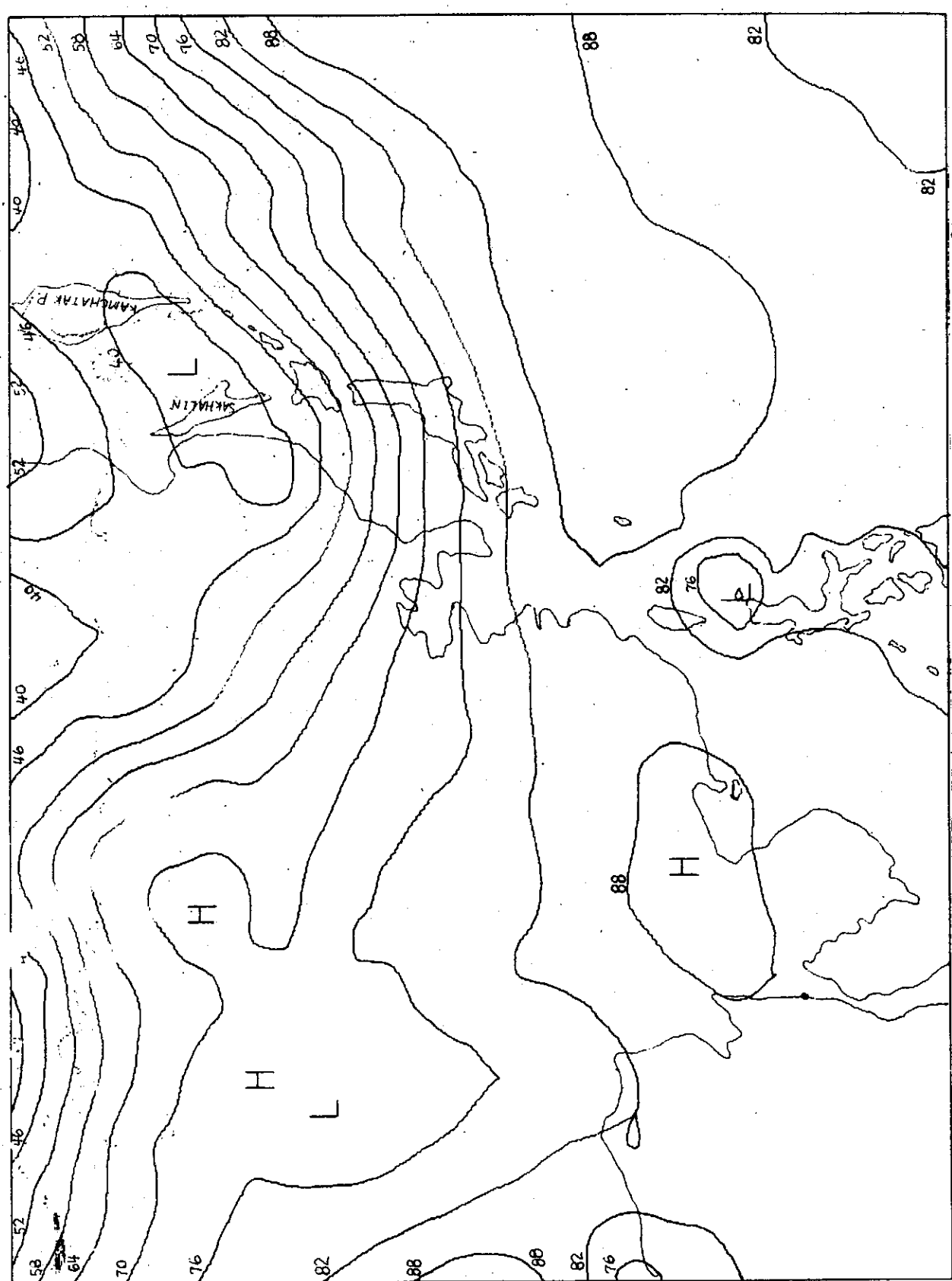

Fig. 4.3 Geopotential Height Field P = 500 mb Time = 12 hrs. For 12Z, 11 Oct. 1975

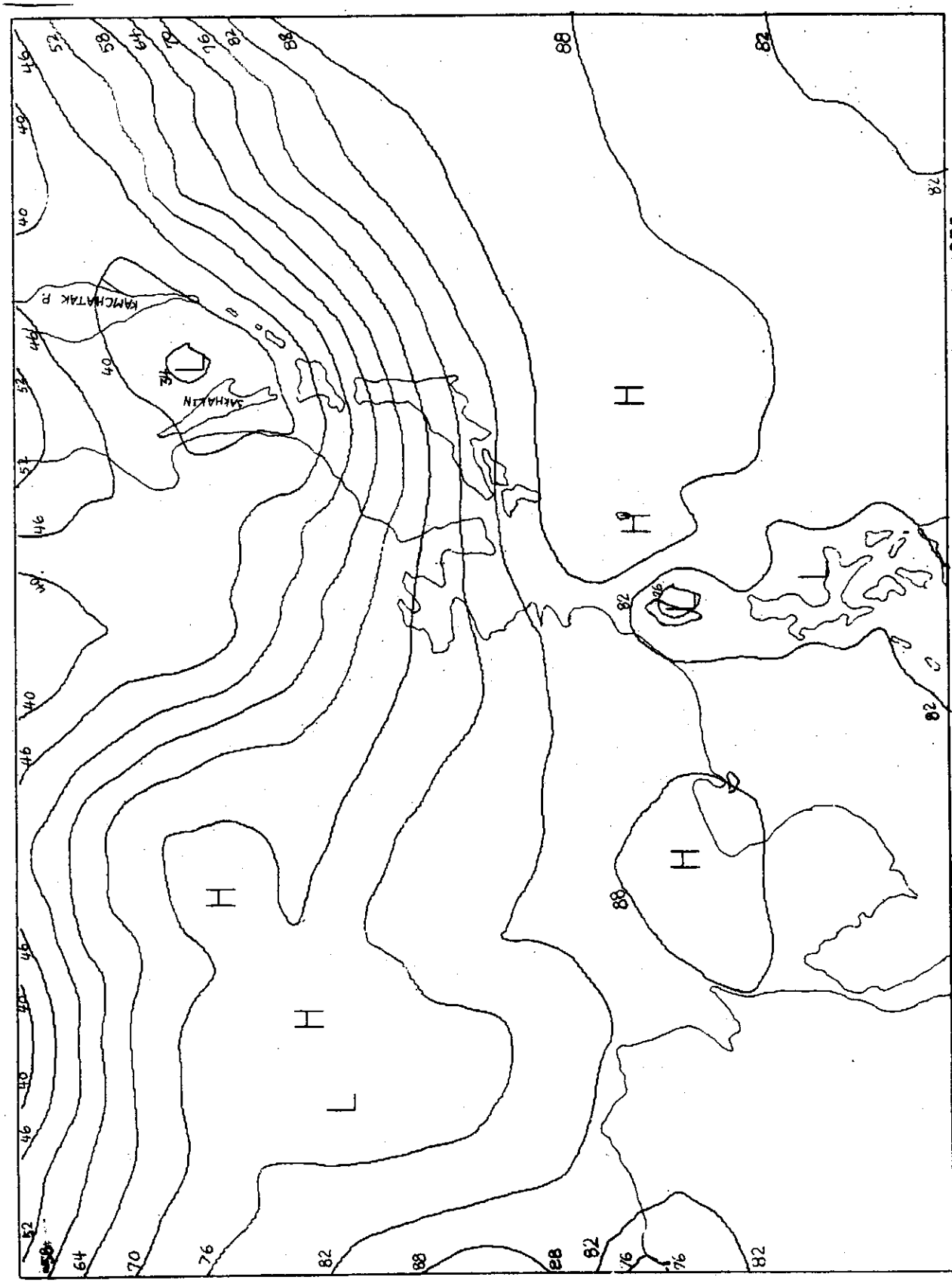

Fig. 4.4 Geopotential Height Field P = 500 mb. Time = 24 hrs. For 12Z. 11 Oct. 1975

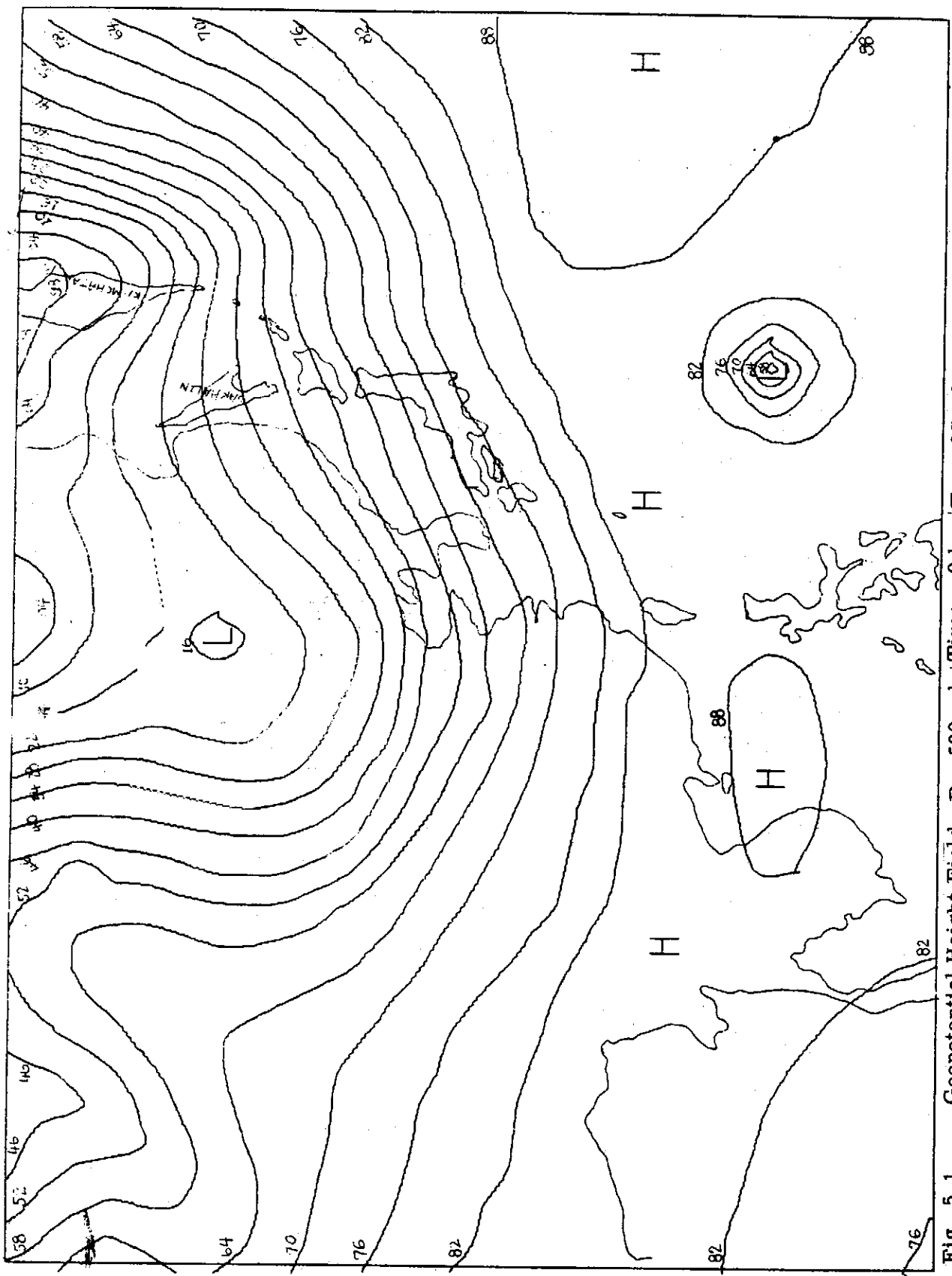

Fig. 5.1 Geopotential Height Field P = 500 mb Time = 0 hr. For 12Z, 21 Nov. 1975

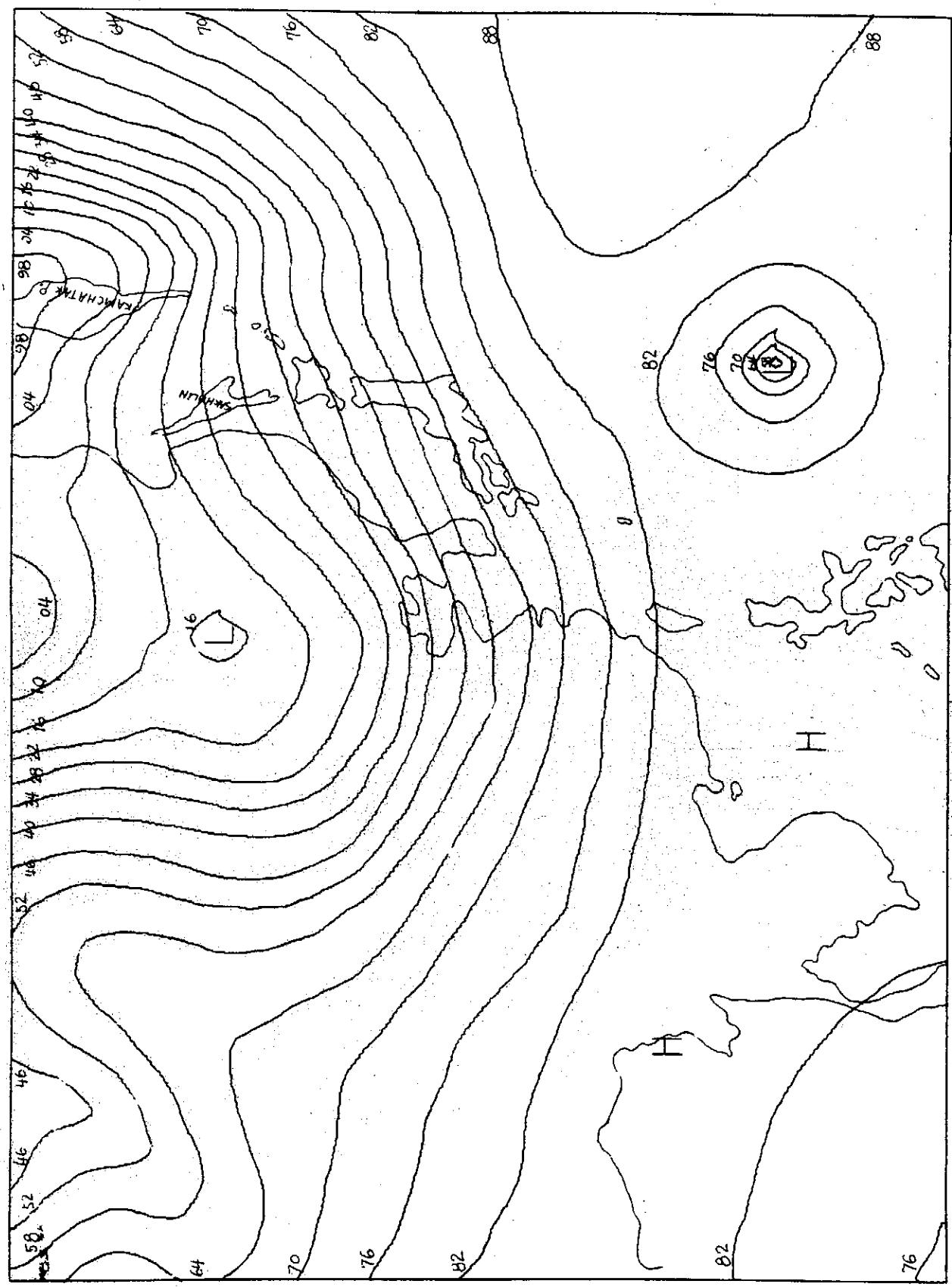

Fig. 5.2 Geopotential Height Field (Balanced) P = 500 mb Time = 0 hr. For 12Z, 21 Nov. 1975

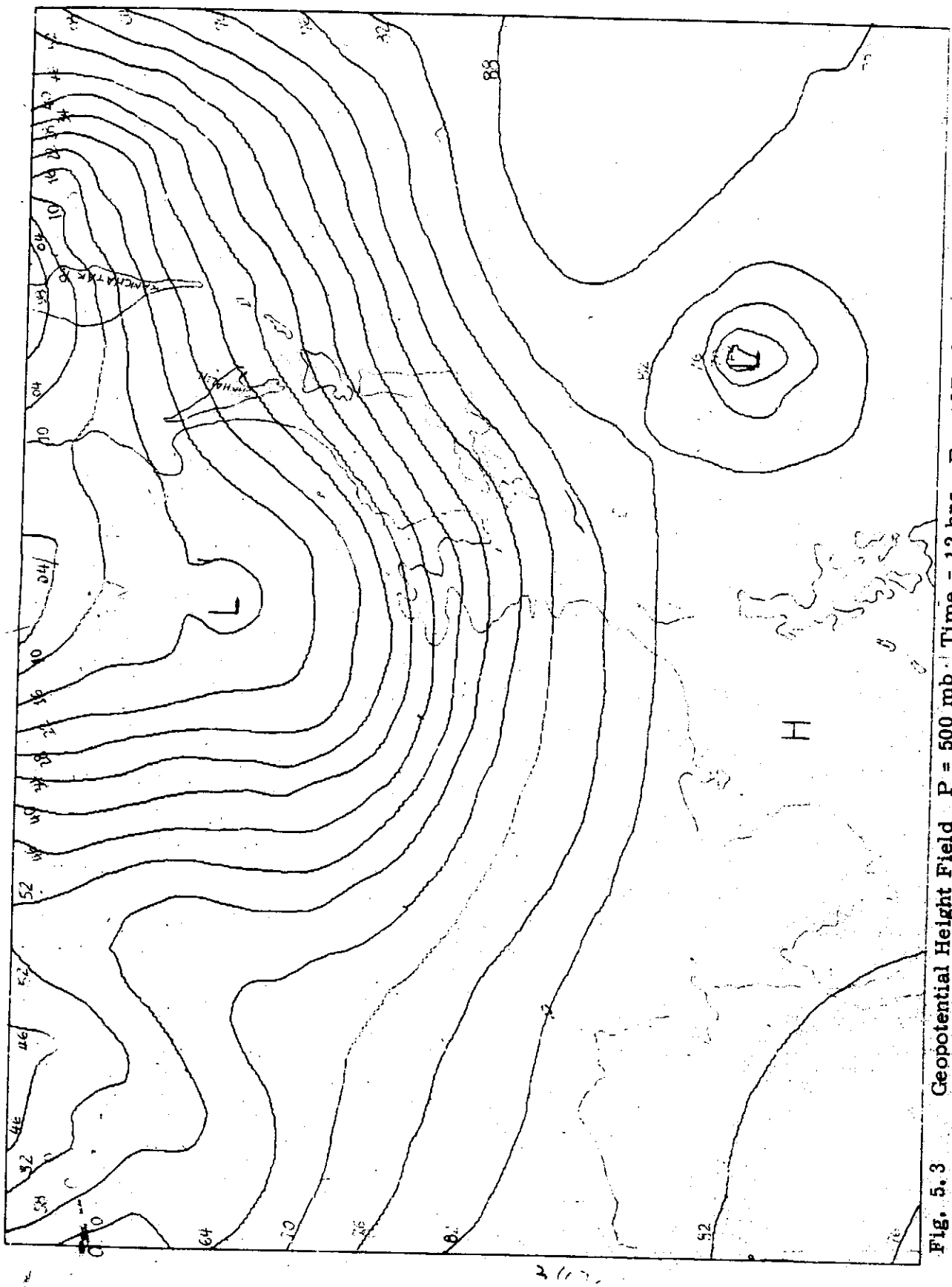

Fig. 5.3 Geopotential Height Field P = 500 mb, Time = 12 hrs. For 12Z, 21 Nov. 1975

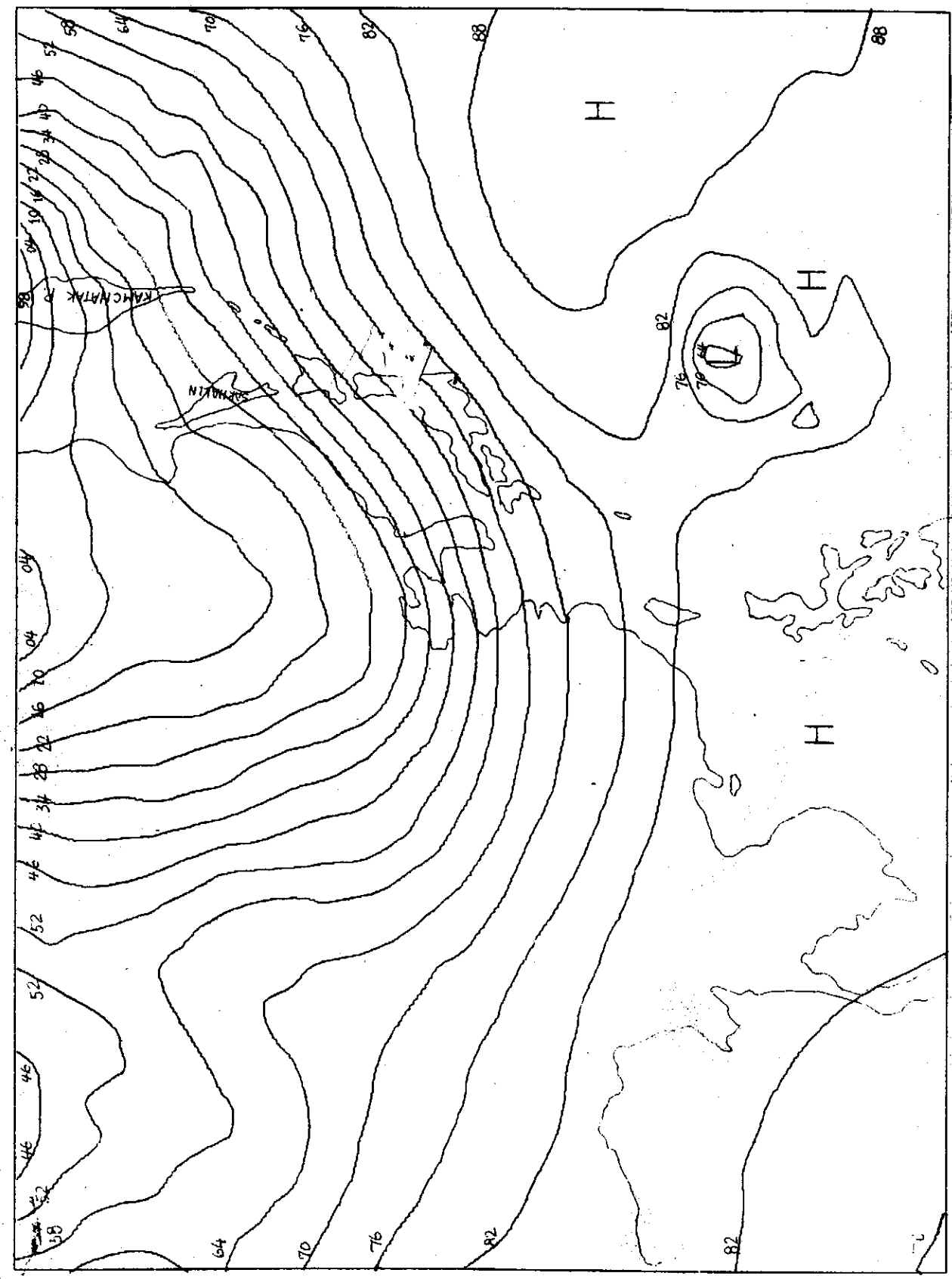

Fig. 5.4 Geopotential Height Field P = 500 mb Time = 24 hrs. For 12Z, 21 Nov. 1975

A Sublayer in the Density Interface

by Jin Jso

Institute of Physics, Academia Sinica, R.O.C.

Abstract

A sublayer, in which

$$U_1/\tau_{1/2} = (A_1 - A_2 P_{e_i}^{-1})^{-1/2}$$

U_1: ther.m.s velocity at the outer edge of the sublayer.

Pe: $U_1\delta/K$ the local Peclet number

holds, is assumed in the density interface of turbulent entrainment. It gives a reasonable interpretation to the difference between $Ue/U_* \sim Ri^{*-3/2}$ and $Ue/U_* \sim R_i^{*-1}$. As we will see, for cases $R_i^* > 1$, the influence of molecule diffusivity and shear are significant, while for cases $R_i^* < 1$, it is not. Besides, in both situations, the effect due to viscosity can be neglected.

Notation

Ue: the entrainment velocity.

U_*: the scale valocity in experiment.

Δb: small buoyancy difference across the homogeneous layer.

b_1: r.m.s. buoyancy fluctuation.

*When using with the order notation "$\sim$", U', W' and ρ' are taken to be the turbulent scale quantities, with signs the same as $\bar{U}z$, $\bar{U}z$, $\bar{\rho}_z$ respectively. This actually doesn't affect the general results.

$\overline{\Delta b}$: the buoyancy jump across the density interface.

D, δ : the thickness of the homogeneous layer and the sublayer.

U_1, ℓ_1: the r.m.s velocity and the integral length scale at the outer edge of the sublayer.

k, ν : molecule diffusivity and viscosity.

U', W' : horizontal and vertical velocity perturbation.

ρ': density perturbation.

$\overline{U}_z$, $\overline{\rho}_z$ mean horizontal velocity and density gradient.

τ , q: vertical flux of horizontal momentum and buoyancy.

T', V': available kinematical and potential energy.

Pe: $\frac{U_1\delta}{K}$ the local Peclet number.

R_i: $\frac{\ell_1 \Delta b}{U_1^2}$ the local Richardson number.

R_i^*: $\frac{D\Delta b}{U_*^2}$ etc. the overall Richardson number.

1. Introduction

The experiments on turbulent mixing across the density interface have been done by Rouse & Dodu (1955), Gromwell (1960), Turner (1968, 1973), Thompson (1969), Linden (1973) and others for cases of zero mean velocity shear, and by Kato and Phillips (1969), Moore and Long (1971) and others for the situations of non-zero mean velocity shear. The controvercy now happens in the dependence of the entrainment rate on K and ν, the molecule diffusivity and viscosity, and the energy balance in the homogeneous layer and near the interface.

Recently, Long (1975) extend the validity of $T' \sim V'$ to the case. $R_i^* > 1$, salt-stratified, without shear and $U_e/U_* \sim R_i^{*-3/2}$, that $U_e/U_1 \sim R_i^{-1}$ then holds for shearing experiments and experiments without shear we have had, that

$$Ue/U_* \sim Ri^{*-1/6}$$

and

$$\overline{\Delta b}/\Delta b \sim Ri^{*-4/3}$$

should be satisfied in the above case. The former, for the present, is not able to be checked with experimental data. The latter, however, do not fit Wolanskis data (1972) better than $\overline{\Delta b}/\Delta b \sim R_i^{*-3/2}$. As the extension is reasonable, some defect may happen in other part of our arguments. We accept this extension and develop furthermore a concept of "sublayer" in the density interface where

$$U_1/\tau^{1/2} = (A_1 - A_2 P_e^{-1})^{-1/2}$$

U_1: the r.m.s velocity at the outer edge of the sublayer.

Pe: $\frac{\mu_1 \delta}{K}$ the local Peclet number

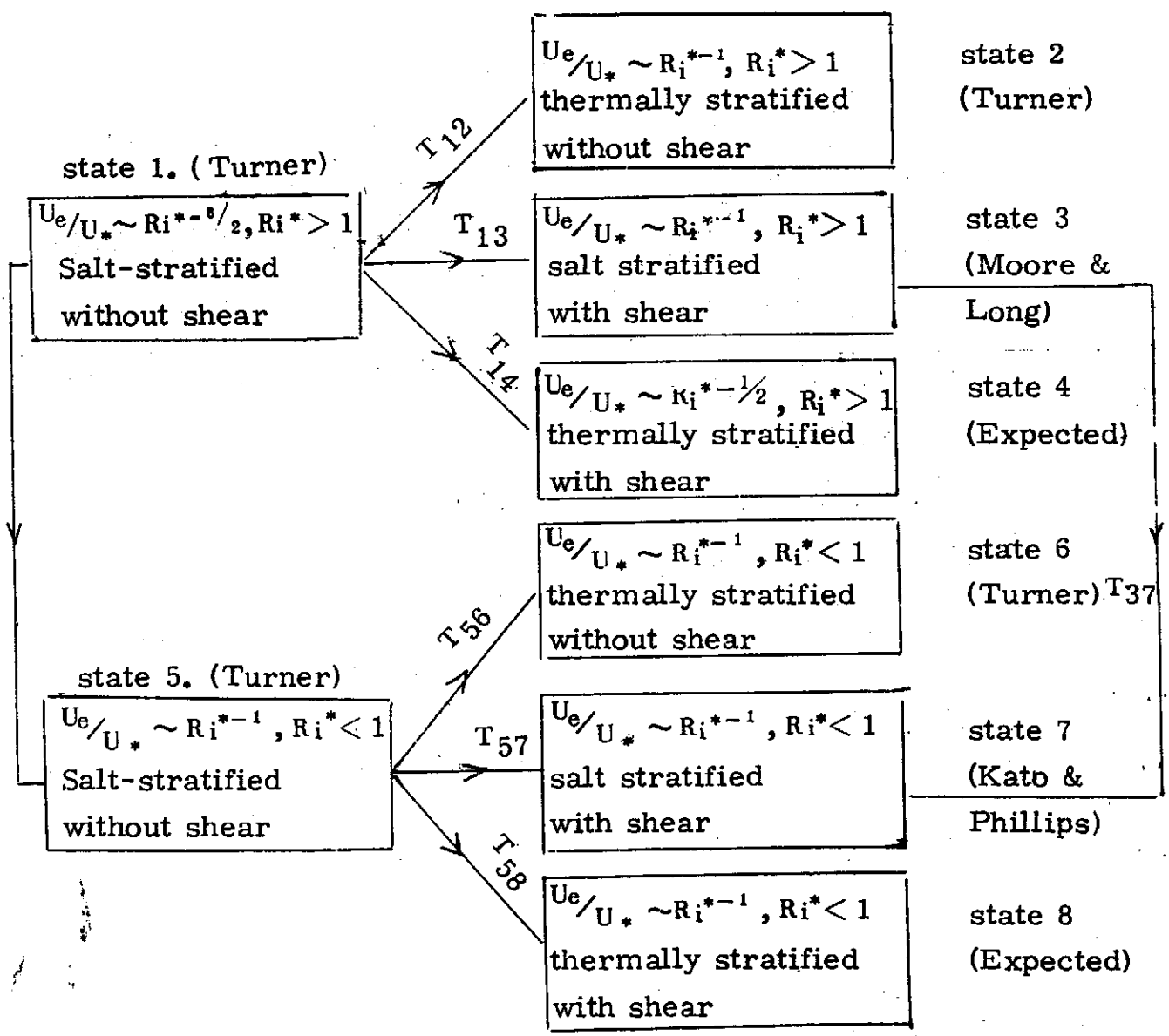

holds. This sublayer, in our viewpoint, plays an essential role in the interfacial mixing. It provides a consistent picture to the transitions T_{12}, T_{13}, T_{15} from $Ue/U_* \sim Ri^{*-3/2}$ to $Ue/U_* \sim Ri^{*-1}$ and to the invariance of $Ue/U_* \sim Ri^{*-1}$ in the transitions T_{56}, T_{57}. The transions arranged are arbitrary and only mean the variation in shear, stratification and Richardson number. Here Ri^* is the overall Richardson number properly defined in each state, or say experiment. We have for convenience chosen state 1 as the basic state.

Besides, Ue/U_* (Ri^*) will be expected along the arguments for

$$\text{state } 4 \left\{ R_i^* > 1, \begin{matrix}\text{thermally} \\ \text{stratified}\end{matrix}, \begin{matrix}\text{with} \\ \text{shear}\end{matrix} \right\}$$

and

$$\text{state } 8 \left\{ Ri^* < 1, \begin{matrix}\text{thermally} \\ \text{stratified}\end{matrix}, \begin{matrix}\text{with} \\ \text{shear}\end{matrix} \right\}$$

for which the experimental data are not available now.

As we will see, the effect of molecule diffusivity and shear is significant, while the molecule viscosity is not.

$$2.\ U_1 / \tau^{\frac{1}{2}} = (A_1 - A_2 Pe^{-1})^{-\frac{1}{2}}$$

By examining the relations*

$$\tau = \nu \bar{U}_z - \overline{U'W'}$$

$$q = K\bar{\rho}_z - \overline{W'\rho'}$$

τ, q: the vertical flux of horizontal momentum and buoyancy

we get

$$\frac{\tau - \nu \bar{U}_z}{q - K\bar{\rho}_z} \sim \frac{\bar{U}_z}{\bar{\rho}_z}$$

$U' \sim \bar{U}_z \delta$ and $\rho' \sim \bar{\rho}_z \delta$ are assumed. δ is the thickness of a sublayer in the density interface.

Since $\bar{U}_z \simeq U_1/\delta$, $\bar{\rho}_z \simeq \Delta\rho/\delta$ and $\delta U_1 \sim \nu$

*details of derivation in Appendix I.

ΔP: the density jump across the sublayer.

U_1: the r.m.s velocity at the outer edge of the sublayer.

$U_1/\tau^{1/2} = (A_1 - A_2 P_e^{-1})^{-1/2}$ $A_1 > 0$, $A_2 > 0$

$Pe = \frac{\delta U_1}{K}$ the local peclet number.

is thus obtained. δ is expected to be very small. $P_e^{-1} = \frac{K}{\delta U_1}$ is not always neglibible. When K or U_1 has some variation, $U_1/\tau^{1/2}$ should have too.

In the derivation of $U_1/\tau^{1/2} = (A_1 - A_2 Pe^{-1})^{-\frac{1}{2}}$, the assumptions

(a) $\overline{U}_z \simeq U_1/\delta$, $\overline{\rho}_z \simeq \Delta\rho/\delta$

(b) $U' \simeq \overline{U}_z \delta$, $\rho' \sim \overline{\rho}_z \delta$

(c) $\nu \sim \delta U_1$

are used. From (a) $\overline{U} \simeq U_1/\delta\, z$, $\overline{U}(0)$ taken to be zero. Then at the edge of the sublayer, $z = \delta$, $\overline{U}_{edge} \simeq U_1$. From (b), $U' \sim \overline{U} z\delta \sim U_1/\delta\, \delta = U_1$, then $\overline{U}_{edge} \simeq U' \sim U_1$ is obtained. Similarly we may get $\overline{\rho}_{edge} \simeq \overline{\rho}(0) + \Delta p$ and $\rho' \sim \Delta\rho$. Considering $\overline{U}_{edge} \sim U' \sim U_1$ and $\rho' \sim \Delta\rho$, the sublayer is supposed to be turbulent.

As to $\nu \sim \delta U_1$, we essentially means $\nu/U_1\delta = C_1 \leqslant$ a number of order 1. For state 6: $R_i^* < 1$, thermally stratified, with $K/U_1\delta$ probably very small than 1 due to the effect of "$R_i^* < 1$" and $\nu \sim K$, we may obtain $\nu/U_1\delta$ much less than one too. In this case the notation "$\sim$" better be carefully noticed for misleading.

Moreover since in Wolanski's data (1974) of different stratification, the molecule viscosity ν varies by 40% in the worse case from its fresh water value, while the molecule diffusivity K changes largely as shown in the table below, the molecule viscosity ν is taken to be constant in the derivation of $U_1/\tau^{\frac{1}{2}} = (A_1 - A_2 Pe^{-1})^{-\frac{1}{2}}$.

Coefficients of molecular diffusivity in water at 25°C (Wolanski, 1974). K(cm^2/sec)

Heat	1.4×10^{-3}
Sale	1.1×10^{-5}
Sugar	6.7×10^{-6}
Suspension of Silica (mean Diam. = 150A°)	2.0×10^{-7}
Clay (Kaolinite)	$\leqslant 10^{-9}$

Of course, the molecule diffusivity K is taken to be a variable in the present sense.

3. The transitions of Ue/U_1 (R_i*)

3.1 The Key Steps

The key steps in this comments are

(a) $U_1 \sim \tau^{1/2}$ is not assumed in the sublayer, but is replaced by

$$U_1/\tau^{\frac{1}{2}} = (A_1 - A_2 Pe^{-1})^{-\frac{1}{2}}$$

while $U^* \sim \tau^{\frac{1}{2}}$ is still assumed.

(b) T′~V′ or say $U_1^2 \sim b_1 D$, $\ell_1 \sim D$, and $q = Ue\ \Delta b \sim U_1 b_1$ are accepted in the sublayer such that

$$Ue/U_1 \sim R_i^{-1}, \quad Ri = \frac{\ell_1 \Delta b}{U_1^2}$$

U_1, ℓ_1: the r.m.s velocity and the integral length scale at the outer edge of the sublayer.

(c) The dependence of Ue/U_* on R_i* is determind by $Ue/U_1 \sim Ri^{-1}$ and U_1/U_* (Ri*) directly. $Ue/U_1 \sim Ri^{-1}$ is assumed for all states. Assuming $\tau^{\frac{1}{2}} \sim U_*$ in the sublayer, than

$$U_1/U_*\ (R_i^*) = U_1/\tau^{1/2}\ \tau^{1/2}/U_*$$

is decided by $\tau^{1/2}/U_* \sim 1$ and

$$U_1/\tau^{1/2} = (A_1 - A_2 P_e^{-1})^{-1/2}$$

If, due to the formulas, we can reasonably interpret the various dependence of U_1/U_* on R_i^*, we then understand the variation of $U_e/U_* \sim R_i^{*n}$ in different states. Here n is the exponent available in different states.

3.2 Transitions from $U_e/U_* \sim R_i^{*-3/2}$ to $U_e/U_* \sim R_i^{*-1}$

For state 1, $U_e/U_* \sim R_i^{*-3/2}$, and states 2, 3, 5, $U_e/U_* \sim R_i^{*-1}$, using assumptions in (b), we may get

$$U_1/U_* \sim R_i^{*-1/6}$$

and

$$U_1/U_* \sim 1$$

respectively. In the transition T_{12}, from salt-stratified state to thermally stratified state, K is increased by order $0(10^2)$, then $(A_1 - A_2 P_e^{-1})^{-\frac{1}{2}} = (A_1 - A_2 \frac{K}{U_1 \delta})^{-\frac{1}{2}}$ is increased. In transition T_{13}, we have

$$-\overline{U'W'} = \tau$$

and

$$-\overline{U'W'} = \tau - \nu \bar{U}_z$$

for state 1 without shear and state 3 with shear. Since $\tau^{1/2} \sim U_*$, for numerically equal U_*, $-\overline{U'W'}$ in state 1 is expected to be larger than that in state 3. $U_1^2 \sim -\overline{U'W'}$ in the sublayer, U_1 in state 3 is thus expected to be smaller than that in state 1. $(A_1 - A_2 P_e^{-1})^{-\frac{1}{2}}$ is increased in state 3. In transition T_{15}, as R_i^* is reduced to the range less than one, U_1 is generally increased, then $(A_1 - A_2 P_e^{-1})^{-\frac{1}{2}} = (A_1 - A_2 \frac{K}{U_1 \delta})^{-1/2}$ is decreased in state 5. Therefore, $(A_1 - A_2 P_e^{-1})^{-\frac{1}{2}}$ can be assumed to be varied by a factor $BR_i^{*1/6} V_6$ $(B \geq 1)$. In the transitions T_{12} and T_{13}, $R_i^* > 1$, $U_1/\tau^{\frac{1}{2}}$ is increased in state 2 and state 3. In the transition T_{15}, $R_i^* < 1$ in state 5, $U_1/\tau^{\frac{1}{2}}$ is decreased. These match

the above arguments. Now since $U_1/\tau^{1/2}$ is varied by a factor $\sim R_i^{*1/6}$, with $\tau^{1/2}/U_1 \sim 1$ and $U_1/U_* \sim R_i^{*-1/6}$ in state 1, the transitions to U_1/U_* in state 2, 3, 5 then do seem reasonable.

In the above arguments, for transition T_{13} from state 1 without shear to state 3 with shear,

$$-\overline{U'W'} = \tau$$

and

$$-\overline{U'W'} = \tau - \nu \overline{U}_z$$

are used in the sublayer. Strictly speaking, the neglecting of $\overline{U}z$ for state 1 is valid only when the local mean is relatively smaller than externally applied $\overline{U}z$ in the present comparison. Though the neglecting do not change the result of the arguments, it should be pointed out.

3.3 Invariance of $U_e/U_* \sim R_i^{*-1}$

In transitions T_{56} and T_{57}, however, R_i^* is less than one in state 5, 6, 7 that U_1 is relatively larger than that in states with $R_i^* > 1$. Though K and $\overline{U}z$ is increased respectively in state 6 and state 7, their effect is suppressed by the larger U_1. Thus $U_1/U_* \sim 1$ still holds, or equivalently $U_e/U_* \sim R_i^{*-1}$ still holds in states 6, 7.

As a conclusion, it is clearly seen that, for $R_i^* > 1$, the influence f molecule diffusivity and shear are significant, while, for $R_i^* < 1$, it is not. Besides, in both situations, the effect due to viscosity can be neglected.

4. Discussion

4.1 Expectation

Along with the above arguments, if we consider the transition T_{12} followed by T_{13}, the process is equivalent to the transition T_{14} from state 1 to state 4. Due to the double effect from molecule diffusivity and shear, we expect

$$U_1/U_* \sim R_i^{*1/6} \qquad (4.1)$$

and thus

$$Ue/U_* \sim R_i^{*-1/2} \qquad (4.2)$$

in state 4. However, in state 8, the role of "$R_i^* < 1$" is still predominant, that

$$U_1/U_* \sim 1 \qquad (4.3)$$

and

$$Ue/U_* \sim R_i^{*-1} \qquad (4.4)$$

still hold in state 8.

4.2 About Long's $\overline{\Delta b}/\Delta b \sim R_i^{*-1/6}$

In Long's paper (1975), $q = Ue\ \Delta b \sim U_1 b_1 \sim \tau^{\frac{1}{2}} \overline{\Delta b}$ is assumed. It is also accepted in this context. Since $U_1/\tau^{1/2} \sim R_i^{*-1/6}$ for state 1,

$$\overline{\Delta b}/b_1 \sim R_i^{*-1/6} \qquad (4.5)$$

is obtained. From $U_1^2 \sim b_1 D$, $(T' \sim V')$, and $U_1/U_* \sim R_i^{*-1/6}$, we get

$$b_1/\Delta b \sim R_i^{*-1/6} \qquad (4.6)$$

Hence

$$\overline{\Delta b}/\Delta b \sim R_i^{*-1/2} \qquad (4.7)$$

This result in fact fits Wolanski's data (1972) better than $\overline{\Delta b}/\Delta b \sim R_i^{*-1/6}$ We take it as a support to the existence of the "sublayer" in the interface.

4.3 Pe and R_i^*

For state 1, from $U_1/U_* \sim R_i^{*-1/6}$ and $U_* \sim \tau^{1/2}$

$$U_1/U_* \sim (A_1 - A_2 P_e^{-1})^{-1/2} \sim R_i^{*-1/6}$$

Hence

$$P_e \sim (B - R_i^{*1/6})^{-1} \qquad (4.8)$$

for states 2, 3, 4, 5, 6, 7, $U_1/U_* \sim 1$. With $U^* \sim \tau^{\frac{1}{2}}$, $P_e \sim 1$ is obtained. Moreover, for state 8, $U_1/U_* \sim R_i^{*1/6}$, we obtain

$$P_e \sim (B - R_i^{*-\frac{1}{6}})^{-1}$$

4.4 Linden's Arguments

It is interesting to notice that, using similar energy argument, a mechanism model prefering $U_e/U_* \sim R_i^{*-\frac{3}{2}}$ was suggested by Linden (1973). Since this model, neglecting K-effect and using supporting data of $\{R_i^* > 1$, salt-stratified, without shear$\}$ experiment, is also permissible in the above arguments, we don't think the controvercy exists. Besides, Kato & Phillips' data was suggested to be described by $U_e/U_* \sim R_i^{*-\frac{3}{2}}$. As shown above for state 7, which is equivalent to Kato & Phillip's experiment when R_i^* is defined as $\frac{H\Delta\rho}{(2\Delta U)^2}$ in Moore & Long's paper (1971), $U_e/U_* \sim R_i^{*-1}$ is prefered.

5. Summary

As a working hypothesis, the "equivalence" between R_i^*s' already chosen in each state, or say experiment, is assumed in the above comparing arguments. The transition from $U_e/U_* \sim R_i^{*-\frac{3}{2}}$ to $U_e/U_* \sim R_i^{*-1}$ in transitions T_{12}, T_{13}, T_{15}, or furthermore T_{16}, T_{17}, T_{37} etc. and the invariance of $U_e/U_* \sim R_i^{*-1}$ in transitions T_{56}, T_{57}, T_{58} etc. are reasonably interpreted. For cases $R_i^* > 1$, the in fluence of molecule diffusivity and shear are seen to be significant, while for cases $R_i^* < 1$, it is not. Besides, in both situations, the effect due to viscosity can be neglected. The experiments corresponding to states 4 and 7 are certainly expected to be held in the near furture.

Reference

Kato, H. & Phillips, O.M. 1969 On the penetration of a turbulent layer into a stratified fluid. J. Fluid Mech. 37, 643-655.

Linden, P.F. 1973 The interaction of a vortex ring with a sharp density interface: a model for turbulent entrainment J. Fluid Mech. 60, 467-480.

Long, R.R. 1970 A theory of turbulence in stratified fluids. J. Fluid Mech. 42, 349-365.

Long, R.R. 1972 Some aspects of turbulence in stratified fluids, Appl. Mech. Rev. pp. 1297-1301.

Moore, M.J. & Long, R.R. 1971 An experimental investigation of turbulent stratified shearing flow. J. Fluid Mech. 49, 635-655.

Long, R.R. 1975 Influence of shear on mixing across density interfaces. J. Fluid Mech. Vol. 70. Part 2, 305-320.

Turner, J.S. 1968 The influence of molecular-diffusivity on turbulent entrainment across a density interface. J. Fluid Mech. 33, 639-656

Appendix

$$\tau = \nu \overline{U}_z - \overline{U'W'}$$

$$q = K\overline{\rho}_z - \overline{W'\rho'}$$

τ . q. the vertical flux of horizontal momentum and buoyancy

$$\frac{\tau - \nu \overline{U}_z}{q - K\overline{\rho}_z} = \frac{\overline{U'W'}}{\overline{W'\rho'}} \sim \frac{U'}{\rho'} \sim \frac{\overline{U}_z}{\overline{\rho}_z}$$

$U' \sim \overline{U}_z \delta$, $\overline{\rho'} \sim \overline{\rho}_z \delta$, δ the thickness of the sublayer, is assumed. Here, when using with the order notation "$\sim$", U', W' and ρ' and taken as the turbulent scale quantities, with signs the same as $\overline{U}_z$, $\overline{U}_z$ and $\overline{\rho}_z$ respectively. This actually doesn't affect our general result.

Now

$$\frac{\tau}{\overline{U}_z} - \nu \sim \frac{q}{\overline{\rho}_z} - K$$

Assuming $\overline{U}_z \simeq U_1/\delta$, $\overline{\rho}_z \simeq \Delta\rho/\delta$, U_1 the r.m.s velocity at the outer edge of the layer, $\Delta\rho$ the density jump across the sublayer, we have

$$\frac{\delta\tau}{U_1} - \nu \sim \frac{\delta q}{\Delta\rho} - K$$

thus

$$\frac{\tau}{U_1^2} - \frac{\nu}{\delta U_1} \sim \frac{q}{U_1 \Delta\rho} - \frac{K}{\delta U_1}$$

Since $q \sim U_e \Delta\rho_L \sim U_1 \Delta\rho$, $\Delta\rho_L$ the density jump across the interface,

$$q/U_1\Delta\rho \sim 1$$

with $\nu \sim \delta U_1$ is furthermore assumed,

$$\frac{\tau}{U_1^2} - C_1 \sim C_2 - \frac{K}{\delta U_1}$$

After proper arangement, we may thus obtain

$$U_1/\tau^{1/2} = \left(A_1 - A_2 \frac{K}{\delta U_1} \right)^{-1/2} \qquad A_1 > 0 \quad A_2 > 0$$

Let $P_e = \frac{\delta U_1}{K}$

$$U_1/\tau^{1/2} = \left(A_1 - A_2 P_e^{-1} \right)^{-1/2}$$

ANNUAL REPORT OF THE INSTITUTE OF PHYSICS,
ACADEMIA SINICA, 1974

A MICROEARTHQUAKE STUDY OF TWO GEOTHERMAL AREAS IN TAIWAN

Y. B. TSAI, H. B. LIAW, C. C. FENG AND S. B. YU

CHINESE EARTHQUAKE RESEARCH CENTER
INSTITUTE OF PHYSICS
ACADEMIA SINICA

JULY 31, 1975

CONTENTS

A MICROEARTHQUAKE STUDY OF TWO GEOTHERMAL AREAS ON TAIWAN

ABSTRACT

Microearthquakes have been observed in two geothermal areas in Taiwan - Tatun volcanic region and Tuchang geothermal area. In the Tatun volcanic region, microearthquakes were found to be closely associated with local faults adjacent to the zones of hydrothermal alternation. Both thrust faulting and normal faulting mechanisms were observed from some of these earthquakes. In the Tuchang geothermal area, very few microearthquakes were observed in the area having thermal springs and successful exploratory drillholes. Instead, several tens of microearthquakes concentrated in a north-northwesterly trending zone of $5 \times 1.5\ km^2$ approximately 10 km west of Tuchang. A normal fautling mechanism was observed for this group of earthquakes. All micro-earthquakes in these geothermal areas took place at depths shallower than nine kilometers.

INTRODUCTION

Positive evidence for a genetic relationship between seismic activity and major hydrothermal activity has increasingly become available in recent years. At Wairakei, New Zealand, Grindley (1965) and others noted that the pattern of active faults is the controlling factor in the location of the upward flow of hydrothermal fluids. Westphal and Lange (1966) observed continuous microearthquake activity in the vicinity of hot spring areas in the Sawtooth Range, Idaho; Socorro Monutain, New Mexico; Bridgeport, California; and Dixie Valley, Nevada. In another study, these same authors (Lange and Westphal; 1969) located during a 120-hour recording period nineteen small earthquakes on the fault system associated with Geysers steam zone in Sonoma County, California. Brune and Allen (1967) noted that microseismicity at Obsidian Butte, in the Salton Sea geothermal area, California, exceeded that observed elsewhere

along the San Jacinto and San Andreas fault zones of southern California. Kasuga (1967) observed in a 13-month period a distinct relationship between the frequency of occurrence of earthquakes and changes in the temperature and discharge of hot springs in Japan. Ward and Björnsson (1971) noted that nine of the thirteen zones of microearthquakes in Iceland coincided spatially with geothermal areas and two other zones were in areas of submarine volcanism where geothermal activity might take place. Ward and Jacob (1971) found that microearthquakes occurred on a steeply dipping fault plane which allowed hot water to circulate to the surface in the Ahuachapan geothermal area in El Salvador. Existence of a genetic relationship between microearthquake activity and geothermal activity suggests that mapping of microearthquakes could be used in the exploration for geothermal power.

Taiwan is located at the junction of the Ryukyu and the Phillippine arcs. Microearthquake activity is high in many parts of Taiwan. And according to Yen (1955) there are more than 100 thermal springs known to exist throughout the entire island and some of its offshore islets. In order to see if these two phenomena are related in Taiwan like they have been observed in many other places in the world, we have studied since 1974 microearthquakes in two known geothermal areas which have been explored in details by the Mining Research and Service Organization (MRSO). These two geothermal areas are the Tatun volcanic region in northern Taiwan and the Tuchang geothermal region located about 40 kilometers southwest of Ilan in the northeastern part of Taiwan. Their locations are shown in Figure 1.

MICROEARTHQUAKES IN THE TATUN VOLCANIC REGION

The Tatun volcanic region in the northern tip of Taiwan comprises about 20 volcanoes and volcanic domes. It is divided by the Chinshan fault into a northern zone of very weak hydrothermal activities and a

southern zone with strong hydrothermal activities manifested on the surface by fumaroles and thermal springs. The volcanic rocks are composed mainly of various andesites of Pleistocence age and their pyroclastics. Underlying the volcanic formations with pronounced unconformity are formations of Miocene sandstones and shales. The sandstone formations generally strike northeasterly and dip to the southeast at angles for 10° to 20°. Sandstones are not exposed in the southern zone except at a few places. The Chinshan fault is an overthrust fault striking east-northeasterly and dipping toward the southeast. The southern boundary of the Tatun volcanic region is marked by the Kanchiao fault which is also an overthrust fault parallel to the Chinshan fault. Aparts from these two major faults there are numerous minor faults inside the Tatun volcanic region.

Observation of microearthquakes in the southern zone of Tatun volcanic region was made in separate recording periods. During the first recording period from 1 February to 6 March 1974, an array of nine temporary stations equipped with sensitive portable seismographs was deployed in the Tatun volcanic region and the Hsintien region, north and southeast of the capital city of Taipei, respectively. In addition, records from two permanent seismograph stations, TWA and TWS, of the Chinese Earthquake Research Center's (CERC) islandwide telemetered network located in the area were also used. The coordinates of these stations are given in Table 1 and their locations are shown by the open triangles in Figure 2.

Each portable seismograph consists of a short-period vertical seismometer, a smoked-paper drum recorder and a chronometer. The system is battery powered. Normally, the internal timing was checked with the standard time broadcasting both at the beginning and the end of each record.

The computer program HYP071 using the Geiger's method was used for determining the hypocenter and the origin time of earthquake. The program was originally developed by Eaton (1969) and

modified later by Lee and Lahr (1971) for studying earthquakes in California. Since at least three readings of P-wave arrival time and one reading of S-wave arrival are required to locate an earthquake, the number of locatable earthquakes is less than the number of events recorded at individual stations. In general, the P-wave arrival times can be read with the aid of microscope to within 0.05 second. The reading precision of the S-wave arrival times is poorer than P-wave readings.

Since the stations differed in elevation for as much as 790 meters, an elevation correction of arrival times was made approximately by the formula $\delta t = -\frac{H}{V}$ where H was station elevation in kilometers, V was seismic wave velocity of rocks above the mean sea level in kilometer per second. δt was added to the observed arrival times. According to measurements of the cored samples by MRSO, the P-wave velocity of the volcanic rocks in the southern zone of the Tatun volcanic region ranges from 2.8 km/sec to 4.3 km/sec. For the present purpose we adopted an intermediate value of 3.3 km/sec. The corresponding elevation correation of P-wave arrivals for all stations are also given in Table 1. The crustal model used for hypocentral location is given in Table 2. The precision of epicentral location is believed to be within one kilometer for earthquakes inside the recording network.

The earthquake magnitude M is determined by using the total signal duration τ according to the following formula:

$$M = -0.87 + 2.0 \log \tau + 0.0035\Delta$$

where Δ is the epicentral distance in kilometers.

In all, twelve earthquakes were located during the first recording period. Nine of these events were in the Tatun volcanic region and the remainin three in the Hsintien region. Pertinent data of these earthquakes are given in Table 3. Their epicenters are further

shown in Figure 2. It is evident from this figure that microearthquake activity in the Tatun volcanic region is confined in a small area centered at station 11 where several exploratory producing steam and hot water were drilled by the MRSO. All but one of these nine earthquakes were located in the upper six kilometers of the crust. The only exception was at a depth of 9.3 km. It is remarkable that none of the observed nine earthquakes took place either north-west of the Chinshan fault or southeast of the Kanchiao fault.

In order to examine more closely the relation between geothermal activity and microearthquake activity, epicenters of the nine events are superimposed on the geologic map of the southern zone of Tatun volcanic region. As shown by dots in Figure 3, all nine earthquakes were located adjacent to the hydrothermal alteration zones.

To follow up the first survey, a second field recording of microearthquakes was made for sixteen days starting on 25 April 1974. During this period five temporary stations were set up in a small area centered at station 11 with a radius of approximately five kilometers. The coordinates of these stations are given in Table 4. Their locations are also shown in Figure 2 by the open squares. Eleven events were located during this second recording period of sixteen days. Pertinent data of these earthquakes are given in Table 5. Their epicenters are shown by the crossed circles in Figure 3. It is again found that all microearthquakes were located adjacent to the hydrothermal alteration zones. Like earlier results the focal depths of all these eleven earthquakes were not larger than five kilometers.

The fact that microearthquakes took place in areas adjacent to hydrothermal alteration zones seems to suggest that hot water at depth may play an important role in causing them. The most widely accepted mechanism for this effect of fluids on earthquake occurrence involves pore pressure (Hubbert and Rubey, 1959). If T is the shear stress on a fault plane. To is the intrinsic shear strength,

Sn is the normal stress across the fault plane. P is the pore pressure, and μ is the friction coefficient, then

$$T = To + \mu(Sn-P)$$

The effect of increasing the pore pressure is thus to reduce the frictional resistance to slippage by decreasing the normal stress across the fault plane.

Two composite fault-plane solutions based on an equal-area projection of the lower hemisphere of the polarities of initial P-wave motion are obtained from records of four earthquakes located near station 11 during the first recording period. They represent two different types of earthquake mechanism. Figure 4 represents a normal faulting earthquake mechanism. One nodal plane strikes N37°E and dips N40°W. Another nodal plane strikes N45°W and dips S50°E. In contrast, Figure 5 shows an overthrust faulting earthquake mechanism. One of two nodal planes strikes N60°E and dips S50°E, the other nodal plane strikes N14°E and dips N30°W. These fault-plane solutions indicate that both normal and overthrust faultings were associated with earthquakes in the Tatun volcanic region near Matsao (Station 11).

MICROEARTHQUAKES IN THE TUCHANG GEOTHERMAL AREA

The Tuchang geothermal area is located about 40 kilometers southwest of Ilan which is the largest town in northeastern Taiwan. Numerous thermal springs are located along banks of the two north-running rivers, the Tienkuerh Hsi and the Towang Hsi which are separated by a low ridge. As shown in Figure 6, the area is covered by a monotonous sequence of slates with scarcely interbedded thin quartzitic sandstone. These rock formations strike north-northeast and dip 50°-60° toward the east. Four faults have been recognized in the area. Six exploratory wells producing hot waters were drilled by

the MRSO since September, 1973.

A microearthquake survey of the Tuchang geothermal area was conducted for eleven days from April 10 to April 20, 1975. An array of five temporary seismograph stations was deployed in the area. Each station was equipped with a vertical-component seismograph. In addition, three of the five stations were also occupied by a horizontal-component seismograph to facilitate better readings on S-wave arrival times. Pertinent data about these stations are given in Table 6. Their locations are shown in Figure 7. Essentially the same procedures for field operation and data processing were followed in the present case as described in the previous case of the Tatun volcanic area. To account for the local geologic condition, the top layer with a P-wave velocity of 4.0 km/sec was deleted from the crustal model for hypocentral location.

A total of seventy-six earthquakes with magnitude ranging from 0 to 2.8 were located during the eleven-day recording period. Pertinent data about these events are given in Table 7. The epicenters of these earthquakes are shown in Figure 7. According to this figure, only one earthquake with magnitude $M < 1.0$ took place within the Tuchang geothermal area near Station 3 during the present observation period. It is thus impossible to make direct correlation with the geologic faults or geothermal activity in the area. A large number of the observed events were concentrated in a small zone about ten kilometers to the west of the Tuchang geothermal area. The elongated zone extends north northwesterly for about 5 kilometers. It has a width of about 1.5 km. Results of projection of the hypocenters onto vertical planes AA' and BB' are shown in Figures 8 and 9 respectively. It is remarkable that all earthquakes were located at depths shallower than 9.0 km. In addition, the hypocenters of earthquakes in the concentrated zone appears to vaguely define a trend slightly toward the west as shown in Figure 9. A composite fault-plane solution based on P-wave initial motions of two larger events

in this zone are shown in Figure 10.

Data from some telemetered stations maintained by the Chinese Earthquake Research Center are included in the figure. This fault-plane solution represents a normal faulting. According to the trend of epicentral distribution and the vertical projection of hypocenters it is concluded that the nodal plane striking N24^{o}W and dipping 66^{o} toward west may represent a fault surface. Inspections of a 1/50,000 topographic map and an ERTS photo seem to show a north north-westerly trending feature in the area of concentrated microearthquakes observed in the present study. If the area is accessible, a field inspection would be desirable to accertain whether the intense microearthquake activity is related to geothermal activity in that area. In comparison with the Tatun volcanic region, the Tuchang area apparently has a much higher level of microearthquake activity.

CONCLUSION

Detailed surveys of microearthquake activity in two known geothermal areas in Taiwan have been carried out since 1974. The outcomes can be summarized as the following:

In the Tatun volcanic region in northern Taiwan, microearthquakes were found to be closely associated with local faults adjacent to the areas having various manifestations of geothermal activity on the surface. All microearthquakes took place at depths shallower than nine kilometers. Both thrust faulting and normal faulting mechanisms were observed from some of these earthquakes.

In the Tuchang geothermal area approximately 40 km southwest to Ilan in northeastern Taiwan, very few microearthquakes were located during an eleven-day recording period directly in the area having thermal springs and successful exploratory drillholes. Instead, several tens of microearthquakes were found to concentrate in

a north-northwesterly trending zone of 5 x 1.5 km^2 approximately 10 km west of the Tuchang geothermal area. Their focal depths were again found to be shallower than nine kilometers. A normal faulting mechanism was observed for this group of earthquakes. If the intense microearthquake activity in this area is confirmed by field evidence to be related to geothermal activity, the geologic condition will be favorable for extracting geothermal fluids in view of probable presence of normal fault.

ACKNOWLEDGEMENT

We are very grateful to Messrs. W. S. Liu, S. Y. Chen, C. C. Hsu, Y. C. Yang and J. S. Lin for their assistance in the field operations. Coopération with the Mining Research and Service Organization (MRSO) is also appreciated. This project was supported by MRSO, Taiwan Power Company and the National Science Council, Republic of China.

REFERENCES

1. Brune, James N., and Clarence R. Allen, A microearthquake survey of the San Andreas fault system in Southern California, Bull. Seismol. Soc. Am., 57, 277, 1967.
2. Eaton, J.P., HYPOLAYR - a computer program for determining hypocenters of local earthquakes in an earth consisting of uniform flat layers over a half space, U.S. Geological Survey, Open File Report, 155 p., 1969.
3. Grindley, C.W. The Geology, structure, and exploitation of the Wairakei geothermal field, Taupo, New Zealand, Bull. N. Z. Geol. Surv., New Ser., 75, 1965.
4. Hubbert, M.K., and W.W. Rubey, Role of fluid pressure in mechanics of overthrust faulting. I Mechanics of fluid filled

porous solids and its application to over thrust faulting, Bull. Geol. Soc. Amer. 70, 115 p., 1959.

5. Kasuga, Isao, Aspect on the relation of thermal water and Matsushiro earthquakes in Kagai hot spring area, Nagano Prefecture, J. Geography, Tokyo, 76, 76, 1967.
6. Lange, A.L., and W.H. Westphal, Microearthquakes near the Geysers, Sonoma County, California, J. Geophys. Res. 74, 4377, 1969.
7. Lee, W.H.K., and J.C. Lahr, HYPO71 - a computer program for determining hypocenter, magnitude and first motion pattern of local earthquakes, U.S. Geological Survey, Open File Report, 100 p., 1972.
8. Ward, P.L., and S. Bjornsson, Microearthquakes, swarms, and the geothermal areas of Iceland, J. Geophys. Res. 76, 3953, 1971.
9. Ward, P.L., and K.H. Jacob, Microearthquakes in the Ahuachapan geothermal field, El Salvador, Central America, Science, 173, 328-330, 1971.
10. Westphal, W.H., and A.L. Lange, Local seismic monitoring, Final Tech. Rept. SRI Project PHU-5043, Advanced Research Projects Agency, Washington, D.C., 242 pp., 1966.
11. Yen, T.P., Thermal springs in Taiwan, Quart. Jour. Bank of Taiwan, Vol. 7, No. 2, pp. 129-147, 1955.

Table 1 Seismic recording stations in the Tatun and Hsintien Regions between 1 February and 6 March 1974

Station No.	Lat. (N)	Long. (E)	Elevation (m)	Station correction (sec)
1	25° 10.32'	121° 33.17'	790	- 0.26
2	25° 14.46'	121° 36.66'	30	- 0.01
3	25° 11.90'	121° 33.47'	0	0.0
4	25° 06.46'	121° 40.15'	210	- 0.07
5	25° 06.36'	121° 35.15'	210	- 0.07
6	24° 51.74'	121° 32.85'	200	- 0.07
7	24° 59.04'	121° 29.04'	150	- 0.05
8	24° 55.76'	121° 25.21'	90	- 0.03
19	24° 57.55'	121° 37.50'	465	- 0.14
11	25° 10.14'	121° 33.54'	790	- 0.26
TWA	24° 58.82'	121° 35.02'	260	- 0.09
TWS	25° 07.70'	121° 24.87'	300	- 0.09

Table 2 Crustal Model for Locating Earthquakes Hypocenters

Depth (km)	P-Velocity (km/sec)	S-Velocity (km/sec)
0 - 4	4.0	2.2
4 - 15	6.0	3.4
15 - 35	6.8	3.8
Below 35	8.1	4.5

Table 3 Earthquakes located in the Tatun and Hsintien Areas between 1 February and 6 March 1974

No.	Month	Day	Hr.	Mn	Sec	Lat. (N)	Long. (E)	Depth (km)	Mag.
1	Feb.	06	04	23	00.5	25° 10.8'	121° 33.6'	2.6	1.6
2		07	19	11	56.8	25° 11.1'	121° 33.2'	0.7	1.1
3		08	19	32	55.3	24° 53.5'	121° 27.6'	4.4	1.8
4		09	14	27	53.4	24° 54.7'	121° 34.1'	5.6	0.9
5		09	18	11	41.4	24° 51.8'	121° 33.0'	5.3	1.7
6		14	23	09	26.3	25° 10.3'	121° 34.4'	3.0	1.5
7		20	01	17	26.7	25° 10.0'	121° 33.6'	6.2	1.9
8		21	15	25	30.6	25° 09.3'	121° 34.0'	1.0	0.8
9		21	20	35	33.5	25° 10.1'	121° 34.2'	3.3	2.1
10		23	04	03	55.7	25° 13.4'	121° 36.7'	9.3	0.8
11	Mar.	03	09	18	27.8	25° 08.9'	121° 33.3'	3.9	1.2
12		04	11	34	59.4	25° 09.5'	121° 34.2'	3.3	1.9

Table 4 Seismic recording stations in the Tatun Volcanic Region between 25 April and 10 May 1974

Station No.	Lat. (N)	Long. (E)	Elevation (m)	Station correction (sec)
1	25° 07.7'	121° 33.4'	836	- 0.25
11	25° 12.0'	121° 35.2'	257	- 0.11
3	25° 12.0'	121° 35.2'	244	- 0.07
4	25° 08.3'	121° 30.7'	758	- 0.23
5	25° 11.1'	121° 31.2'	180	- 0.06

Table 5 Earthquakes located in the Tatun Volcanic Region between 25 April and 10 May 1974

No.	Month	Day	Hr.	Mn.	Sec.	Lat. (N)	Long. (E)	Depth	Mag.
1	April	25	12	01	18.9	25° 09.5'	121° 34.6'	5.0	2.8
2		25	12	07	33.0	25° 10.2'	121° 34.0'	5.0	1.0
3		25	12	23	19.6	25° 09.2'	121° 35.3'	5.0	1.3
4		26	21	05	10.6	25° 10.6'	121° 33.5'	5.0	0.8
5.		28	10	50	02.0	25° 10.6'	121° 31.8'	2.6	0.5
6		28	15	14	43.7	25° 10.2'	121° 32.3'	5.0	0.8
7		30	13	56	12.9	25° 09.9'	121° 32.4'	0.8	0.4
8	May	04	16	17	00.0	25° 09.0'	121° 31.3'	4.8	0.2
9		06	12	18	23.0	25° 10.2'	121° 32.9'	4.0	0.8
10		07	06	53	56.0	25° 10.6'	121° 33.5'	5.0	0.9
11		09	18	07	50.2	25° 10.2'	121° 33.5'	5.0	1.2

Table 6. Temporary seismographic stations

STATION	CODE	POSITION LATITUDE	LONGITUDE
Nantai	TC01	24°32,32'N	121°31.06'E
Shaoshui	TC02	24°32.98'N	121°30.00'E
Tuchang	TC03	24°33.90'N	121°39.14'E
Yingshihchiao	TC04	24°36.85'N	121°30.91'E
Liumaoan	TC05	24°31.93'N	121°26.53'E

TABLE 7 LISTING OF TU-CHANG EARTHQUAKES (APR. 10 to 20, 1975)

1975	DAY	HR	MN	SEC	LAT-N	LONG-E	DEPTH	MAG	NO	DMIN	GAP	RMS	ERH	ERZ	Q
APR.	10	20	32	08.43	24-37.39	121-27.51	5.0	1.11	6	7.0	350	0.13	4.2	5.8	D
	11	01	01	42.38	24-32.42	121-31.16	5.9	0.62	6	0.2	273	0.04	0.6	0.1	C
	11	05	58	01.87	24-34.91	121-25.63	3.9	0.90	5	5.7	311	0.03	8.8	4.0	D
	11	07	31	21.24	24-32.42	121-31.16	4.3	0.44	5	0.2	273	0.05	4.3	0.8	D
	11	14	35	22.69	24-34.96	121-24.75	3.5	1.23	7	6.3	313	0.08	0.3	0.1	C
	11	14	51	51.37	24-34.37	121-22.65	2.9	0.86	8	7.9	327	0.10	1.0	0.4	C
	11	17	00	50.75	24-34.77	121-24.36	3.6	1.04	9	6.4	286	0.10	0.7	0.3	C
	11	17	06	36.98	24-35.03	121-24.19	3.2	1.04	8	7.0	288	0.12	0.9	0.4	C
	11	19	13	39.74	24-31.46	121-27.43	3.9	1.22	8	1.8	224	0.07	0.6	0.2	C
	11	21	06	40.99	24-35.27	121-26.11	8.8	0.78	6	5.7	307	0.02	0.6	0.6	C
	11	22	22	00.38	24-33.21	121-32.30	5.2	0.75	8	2.7	251	0.06	0.6	0.8	C
	14	05	37	53.50	24-32.91	121-27.84	8.0	1.52	7	2.9	165	0.16	2.3	1.4	C
	14	10	28	28.18	24-34.19	121-31.91	3.2	0.65	7	3.7	222	0.03	0.3	0.4	C
	14	10	56	37.87	24-30.51	121-26.31	8.0	1.17	8	2.6	301	0.10	1.9	0.8	C
	14	11	08	20.41	24-32.22	121-27.52	4.4	0.73	8	1.8	164	0.06	0.6	0.7	B
	14	14	22	15.72	24-34.79	121-24.48	3.7	1.36	9	6.3	284	0.08	0.6	0.2	C
	14	21	32	18.45	24-31.91	121-33.33	7.7	0.84	5	3.9	344	0.03	0.2	0.1	C
	15	04	15	35.87	24-35.11	121-24.18	3.3	1.81	7	7.1	288	0.07	0.6	0.3	C
	15	08	17	59.16	24-28.96	121-29.79	4.9	1.50	8	6.6	296	0.03	0.3	1.6	C
	15	12	32	06.07	24-30.93	121-30.33	6.3	1.50	9	2.9	260	0.13	1.2	1.1	C
	15	17	57	26.64	24-34.23	121-24.64	5.4	0.99	6	5.3	311	0.06	1.6	2.8	C
	16	01	16	13.49	24-34.74	121-24.20	4.3	1.36	10	6.5	288	0.12	1.3	1.1	C
	16	01	13	12.42	24-35.17	121-24.61	4.2	1.17	10	6.8	282	0.16	0.9	0.7	C
	16	04	32	55.63	24-34.04	121-24.93	3.8	2.80	8	4.7	278	0.12	1.1	0.4	C
	16	04	34	39.30	24-33.13	121-25.73	4.4	0.93	7	2.6	287	0.09	1.5	1.6	C
	16	04	36	45.35	24-34.49	121-24.68	3.2	1.42	8	4.7	281	0.14	1.3	0.8	C
	16	04	45	16.28	24-33.30	121-24.62	4.2	1.25	8	4.1	290	0.12	1.9	0.6	C
	16	04	52	11.84	24-34.12	121-24.79	3.8	1.74	9	5.0	280	0.13	0.9	0.3	C
	16	04	54	07.55	24-34.74	121-27.49	8.7	1.20	5	3.2	288	0.02	1.0	0.5	C
	16	05	06	20.32	24-33.96	121-24.62	4.0	0.94	9	4.9	284	0.13	2.0	0.7	C

LISTING OF TU-CHANG EARTHQUAKES (APR. 10 to 20, 1975)

975	DAY	HR	MN	SEC	LAT-N	LONG-E	DEPTH	MAG	NO	DMIN	GAP	RMS	ERH	ERZ	Q
PR.	16	05	11	29.24	24-32.03	121-26.00	5.9	0.74	6	0.9	315	0.09	2.3	0.9	C
	16	05	30	06.38	24-34.67	121-25.06	2.1	1.00	5	5.6	308	0.05	0.8	1.8	C
	16	05	41	50.30	24-32.03	121-26.63	5.0	0.82	7	0.2	189	0.17	1.6	0.9	C
	16	06	46	35.05	24-34.60	121-29.43	4.6	1.81	8	4.2	256	0.20	1.9	4.1	C
	16	06	49	53.95	24-33.78	121-25.51	4.0	1.34	7	3.8	295	0.06	0.7	0.2	C
	16	07	12	51.50	24-33.02	121-24.43	4.8	1.05	6	4.1	319	0.07	1.5	1.8	C
	16	07	36	40.82	24-34.89	121-24.66	2.2	1.54	9	6.3	281	0.17	1.6	4.1	C
	16	07	37	29.63	24-34.76	121-24.58	2.4	1.04	8	6.2	282	0.13	1.5	3.9	C
	16	07	38	28.22	24-33.76	121-25.16	4.0	1.06	7	4.1	302	0.06	0.6	0.2	C
	16	08	41	11.90	24-32.03	121-26.33	7.9	0.96	7	0.4	282	0.08	1.7	0.7	C
	16	08	54	20.79	24-34.62	121-24.64	3.8	1.03	9	5.9	281	0.12	0.8	0.3	C
	16	09	14	27.93	24-33.59	121-25.09	4.2	1.03	6	3.9	304	0.07	2.8	0.9	D
	16	09	26	04.59	24-33.93	121-24.82	4.1	1.07	7	4.7	280	0.07	1.4	0.5	C
	16	09	54	14.36	24-32.03	121-26.63	5.0	1.08	7	0.2	177	0.19	1.1	0.6	C
	16	10	02	32.60	24-35.07	121-24.63	3.3	1.63	9	6.6	282	0.16	1.1	0.4	C
	16	11	30	44.79	24-34.75	121-24.65	3.6	1.75	10	6.1	281	0.15	0.9	0.3	C
	16	11	31	46.13	24-33.44	121-24.89	4.3	1.06	7	3.9	308	0.09	2.1	0.7	C
	16	12	00	57.30	24-33.61	121-24.93	4.2	1.39	8	4.1	307	0.08	2.1	0.7	C
	16	13	54	31.65	24-34.00	121-29.23	4.4	0.14	6	0.2	273	0.09	0.8	0.1	C
	16	14	44	16.45	24-28.85	121-28.92	3.9	1.28	5	7.4	333	0.04	1.3	0.3	C
	16	16	03	44.57	24-32.83	121-24.79	3.3	1.48	10	3.4	295	0.32	2.3	0.7	D
	16	16	18	17.35	24-33.29	121-28.59	3.9	0.08	5	1.4	165	0.00	0.0	0.0	C
	16	22	58	20.08	24-33.68	121-25.04	5.7	0.90	5	6.9	321	0.02	0.8	1.5	C
	17	03	41	36.12	24-33.99	121-24.72	4.0	1.58	7	4.9	282	0.08	1.4	0.5	C
	17	03	43	02.54	24-34.05	121-24.51	3.9	1.89	7	5.2	286	0.10	1.8	0.7	C
	17	04	32	17.85	24-32.03	121-25.50	7.1	1.05	6	1.7	325	0.07	2.2	0.8	C
	17	04	56	00.92	24-34.87	121-23.27	3.1	1.31	6	7.7	300	0.11	1.6	0.9	C
	17	10	02	28.51	24-31.12	121-27.24	5.7	1.07	5	1.9	267	0.03	1.3	0.5	C
	17	12	39	10.37	24-28.65	121-42.50	10.6	1.55	9	20.5	335	0.06	1.9	3.6	C
	17	16	02	54.93	24-34.22	121-24.30	4.4	0.99	7	5.7	316	0.02	0.5	5.1	D

LISTING OF TU-CHANG EARTHQUAKES (APR. 10 to 20, 1975)

1975	DAY	HR	MN	SEC	LAT-N	LONG-E	DEPTH	MAG	NO	DMIN	GAP	RMS	ERH	ERZ	Q
APR.	18	00	17	22.44	24-33.18	121-27.02	6.2	1.07	6	2.5	230	0.08	1.8	1.2	C
	18	02	55	10.20	24-34.23	121-24.36	5.0	0.93	7	5.6	287	0.03	0.5	1.5	C
	18	05	35	09.90	24-33.51	121-27.91	1.9	0.18	5	2.2	212	0.01	0.1	0.2	C
	18	08	31	20.28	24-31.03	121-26.39	6.1	1.03	7	1.7	295	0.04	0.7	0.4	C
	18	08	40	12.93	24-34.22	121-24.37	4.1	1.19	8	5.6	287	0.16	2.7	1.0	D
	18	16	04	35.79	24-30.29	121-26.04	6.5	1.61	7	3.1	322	0.05	0.9	0.4	C
	18	21	42	33.60	24-30.90	121-19.01	6.5	1.17	6	12.8	340	0.02	1.0	2.0	C
	18	22	20	32.79	24-32.63	121-25.36	5.8	0.91	6	2.3	307	0.06	1.6	0.9	C
	19	01	39	01.12	24-33.83	121-25.17	4.0	0.75	6	4.2	302	0.03	0.4	0.1	C
	19	02	23	21.30	24-34.11	121-24.63	4.2	1.31	7	5.1	283	0.11	1.6	0.6	C
	19	10	59	58.12	24-28.78	121-26.27	5.4	0.66	6	5.8	325	0.06	1.1	1.9	C
	19	13	03	30.03	24-33.49	121-24.36	6.5	1.18	6	4.7	316	0.04	1.1	1.0	C
	19	15	52	39.03	24-33.15	121-25.75	4.2	0.58	5	2.6	287	0.02	1.3	0.5	C
	19	18	00	13.28	24-34.60	121-24.75	4.3	0.72	7	5.8	280	0.07	1.7	1.6	C
	20	11	44	09.02	24-33.98	121-24.33	5.4	1.71	6	5.3	289	0.01	0.2	0.4	C
	20	17	05	47.48	24-34.61	121-24.54	4.1	0.92	6	6.0	283	0.10	0.4	0.2	C

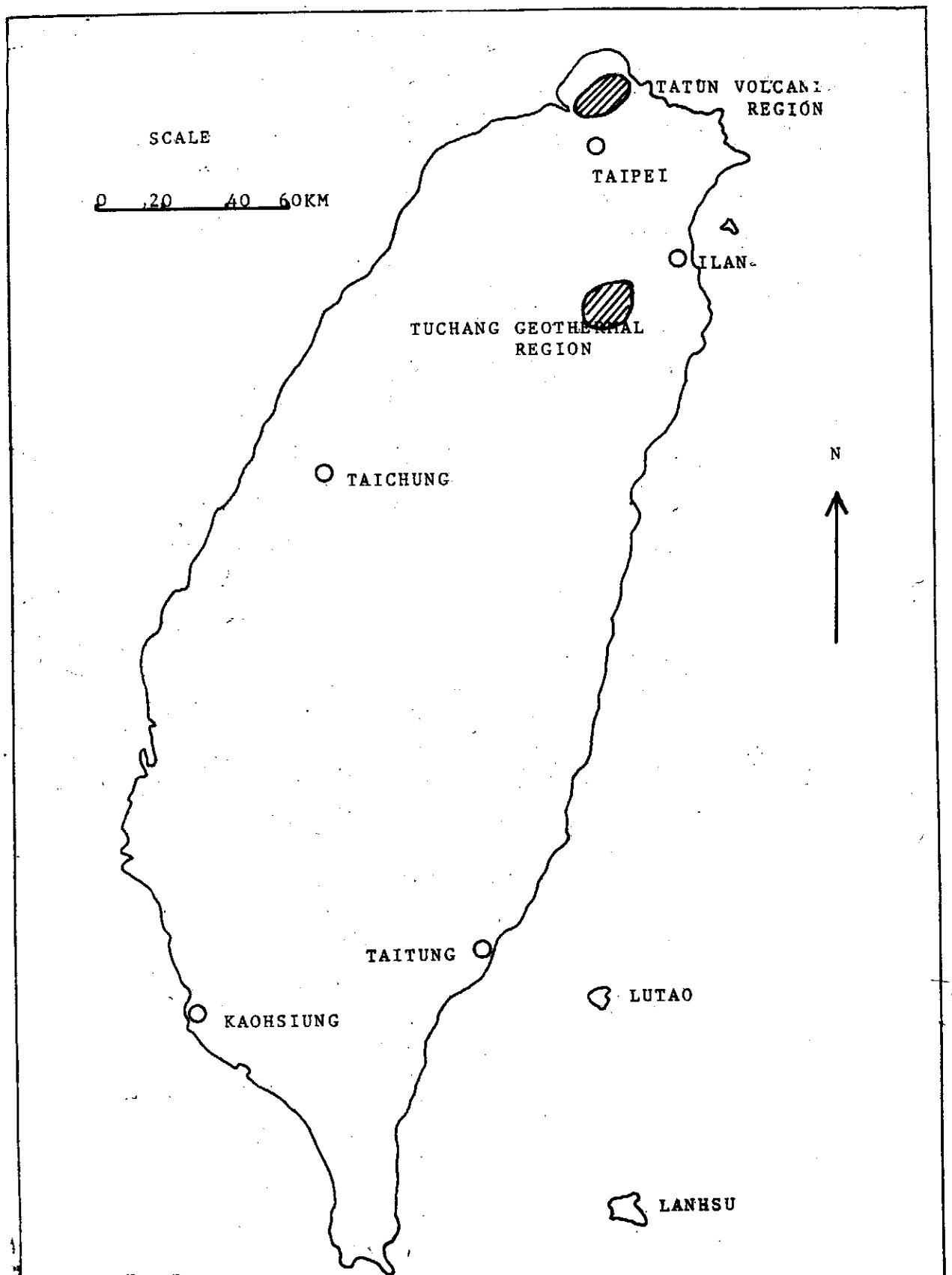

Figure 1. Locations of two geothermal areas in Taiwan - Tatun volcanic region and Tuchang geothermal region.

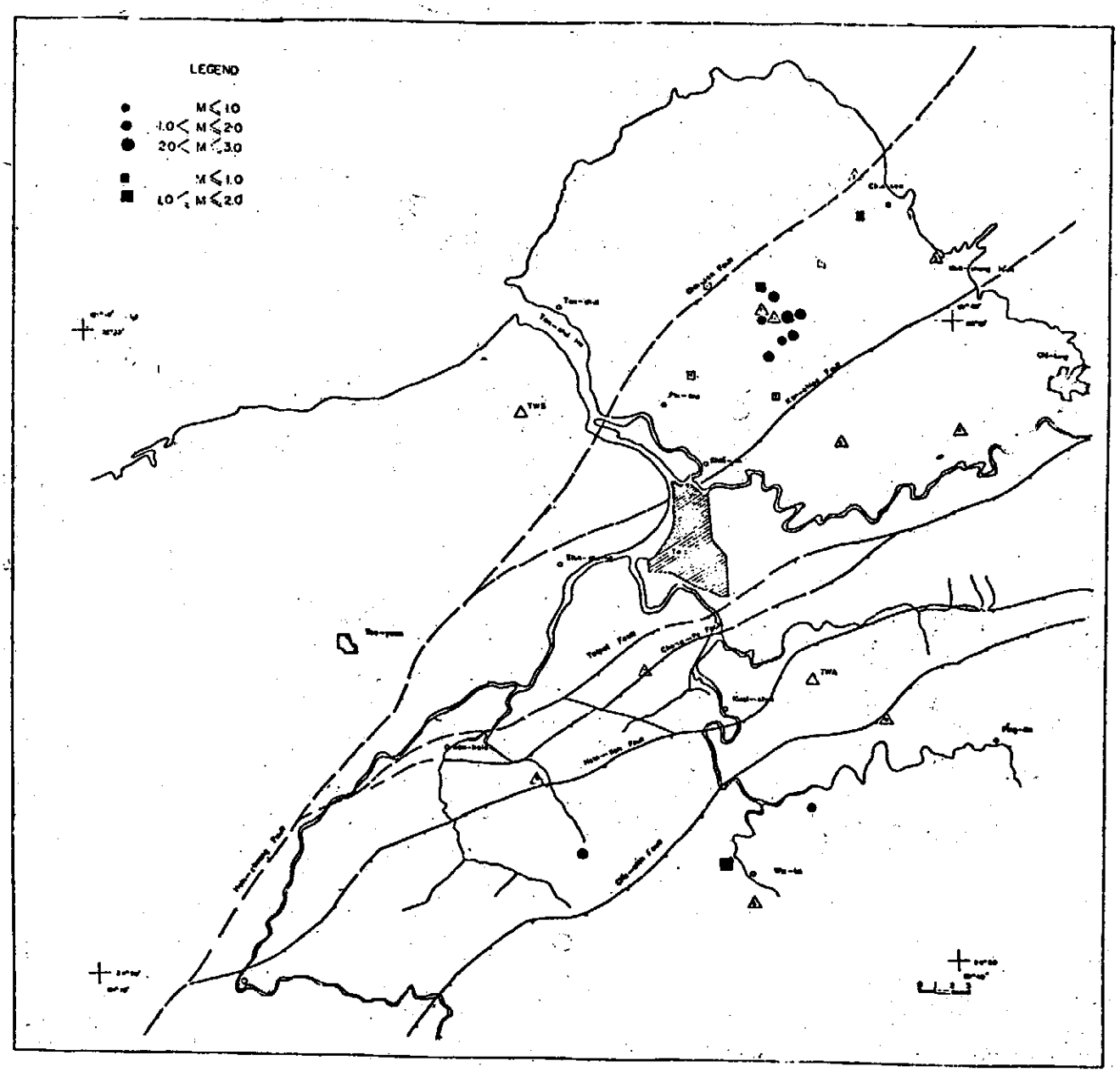

Figure 2. Locations of seismic stations, denoted by open triangles and squares, set up to observe microearthquakes in Tatun and Hsintien areas in northern Taiwan. Epicenters of microearthquakes located during Feburary - March 1974 are showed by the solid dots and squares. The fault structures are also presented in the figure.

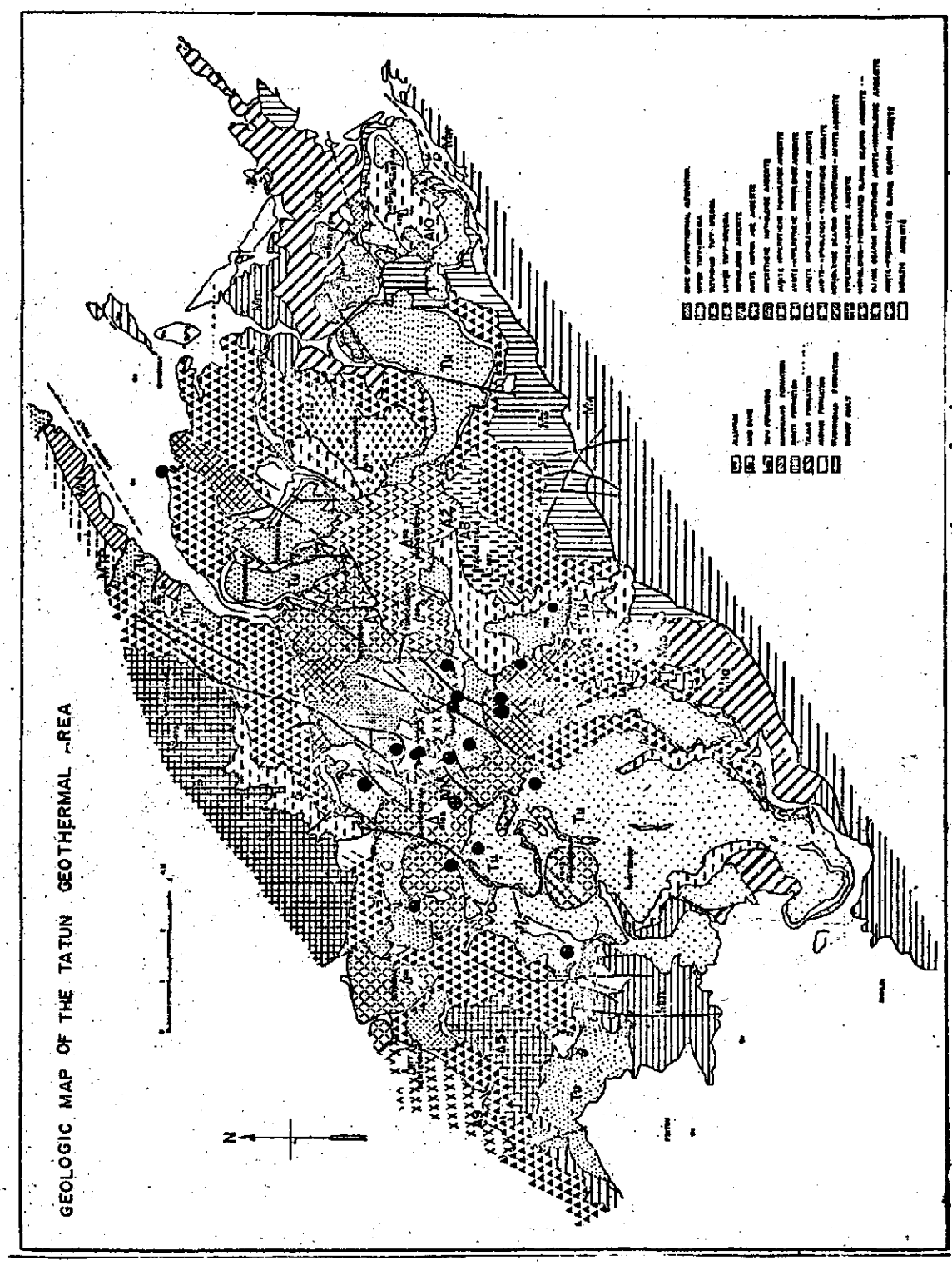

Figure 3. Epicenters of microearthquakes shown on the geologic map of the Tatun Volcanic Region.

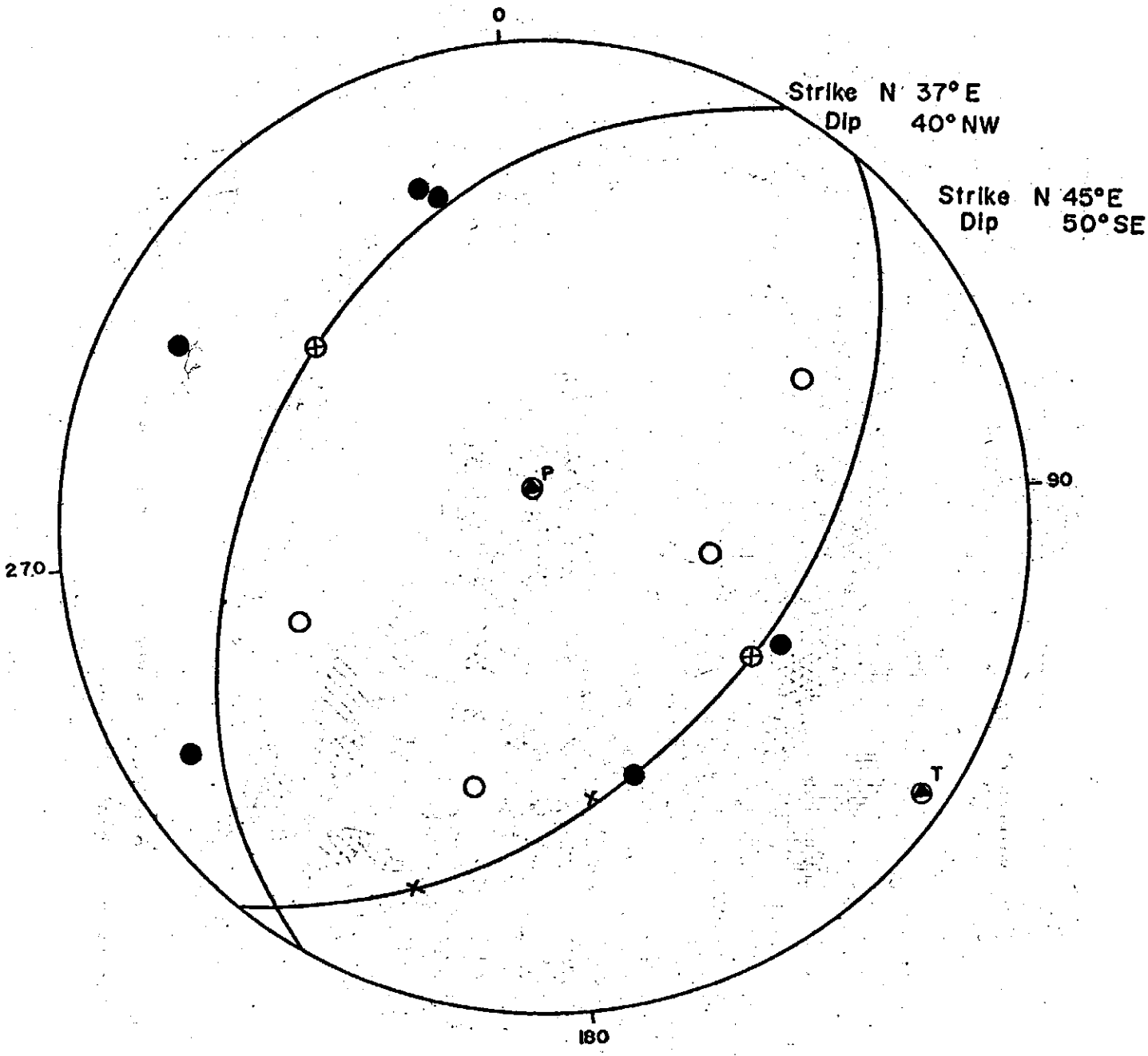

Figure 4. Fault plane solution representing normal faulting earthquake source mechenism in the Tatun Volcanic Region.

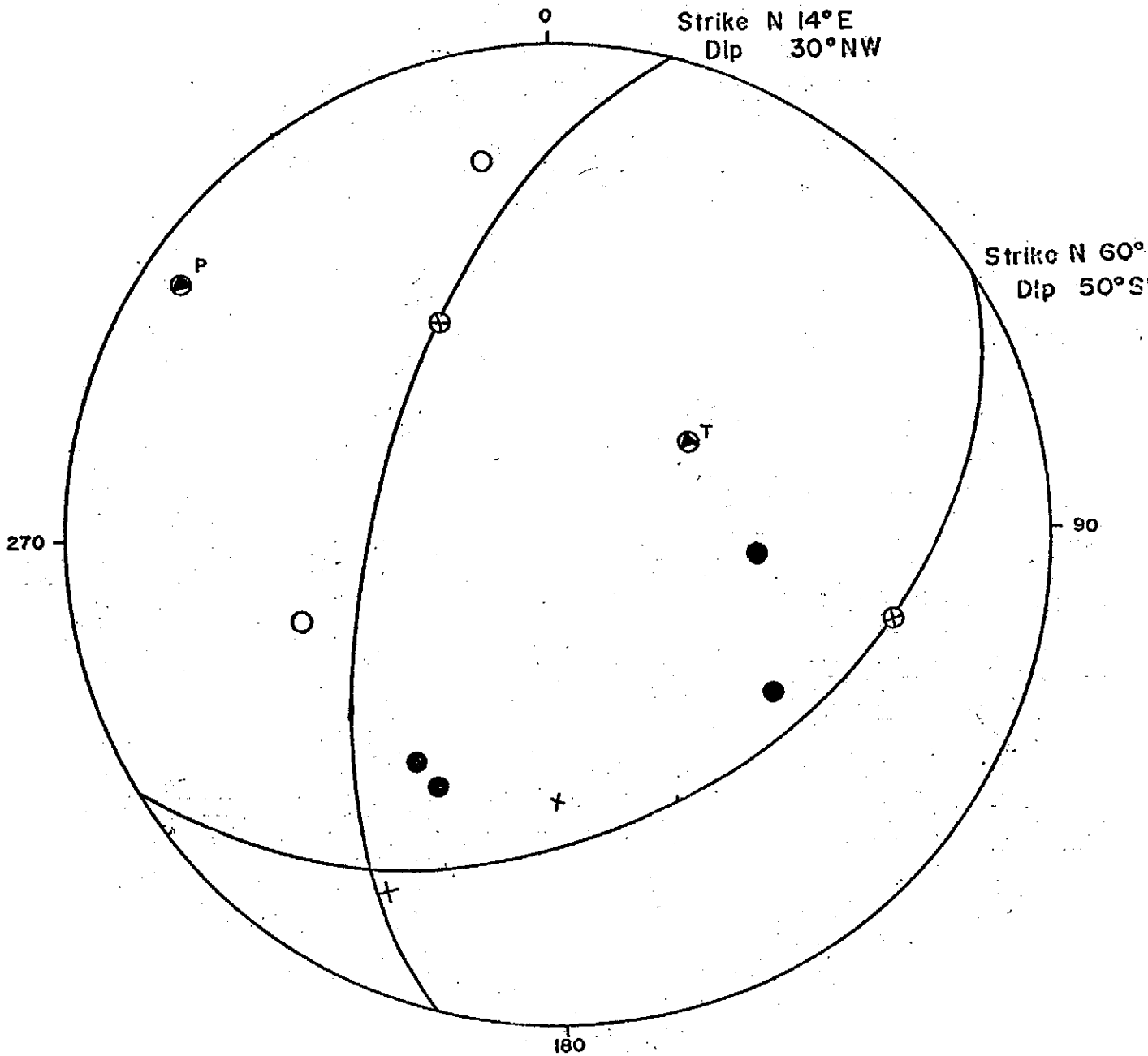

Figure 5. Fault plane solution representing overthrust faulting earthquake source mechenism in the Tatun Volcanic Region.

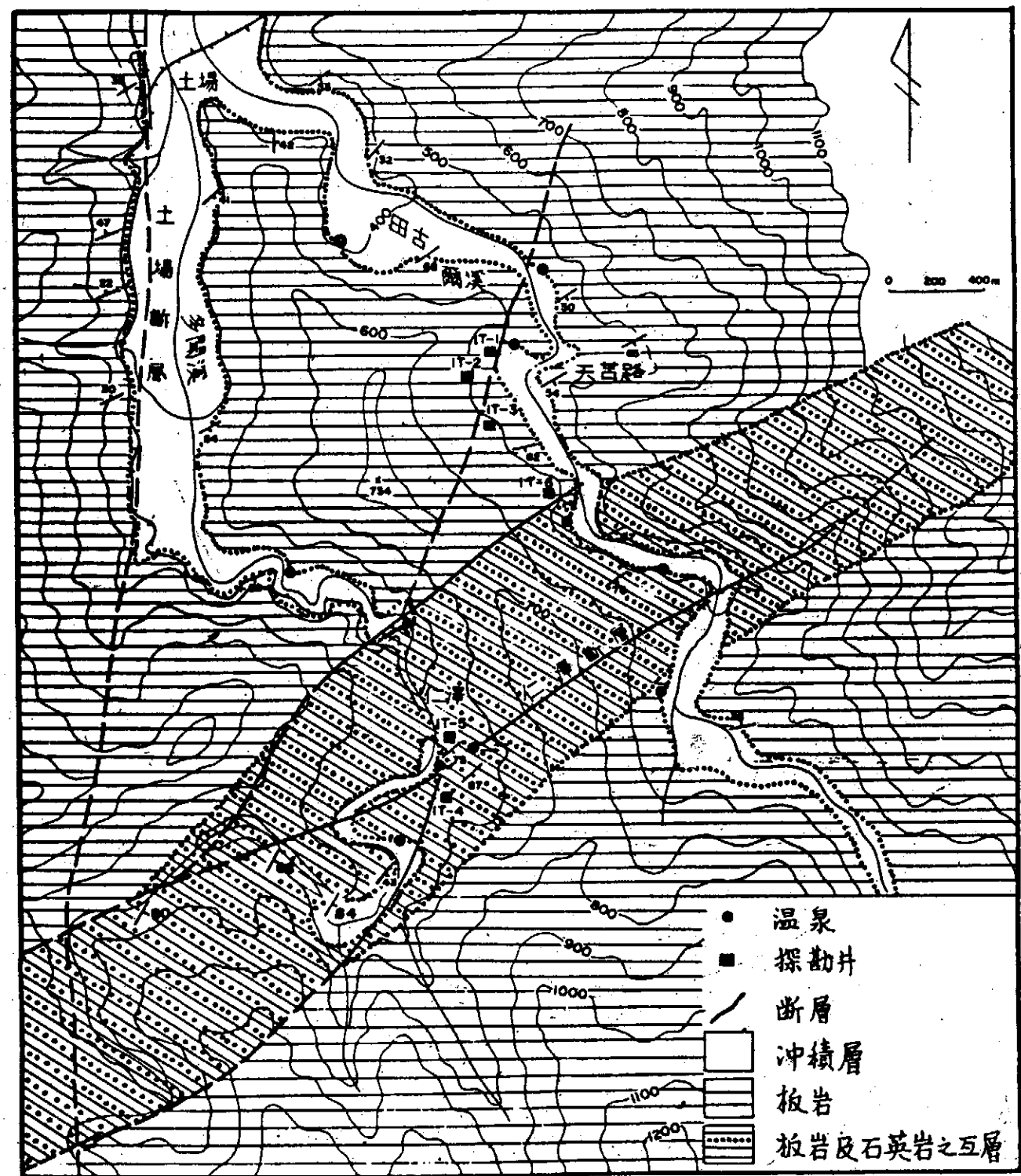

土場地熱區地質圖

Figure 6. Geologic map of the Tuchang geothermal region.

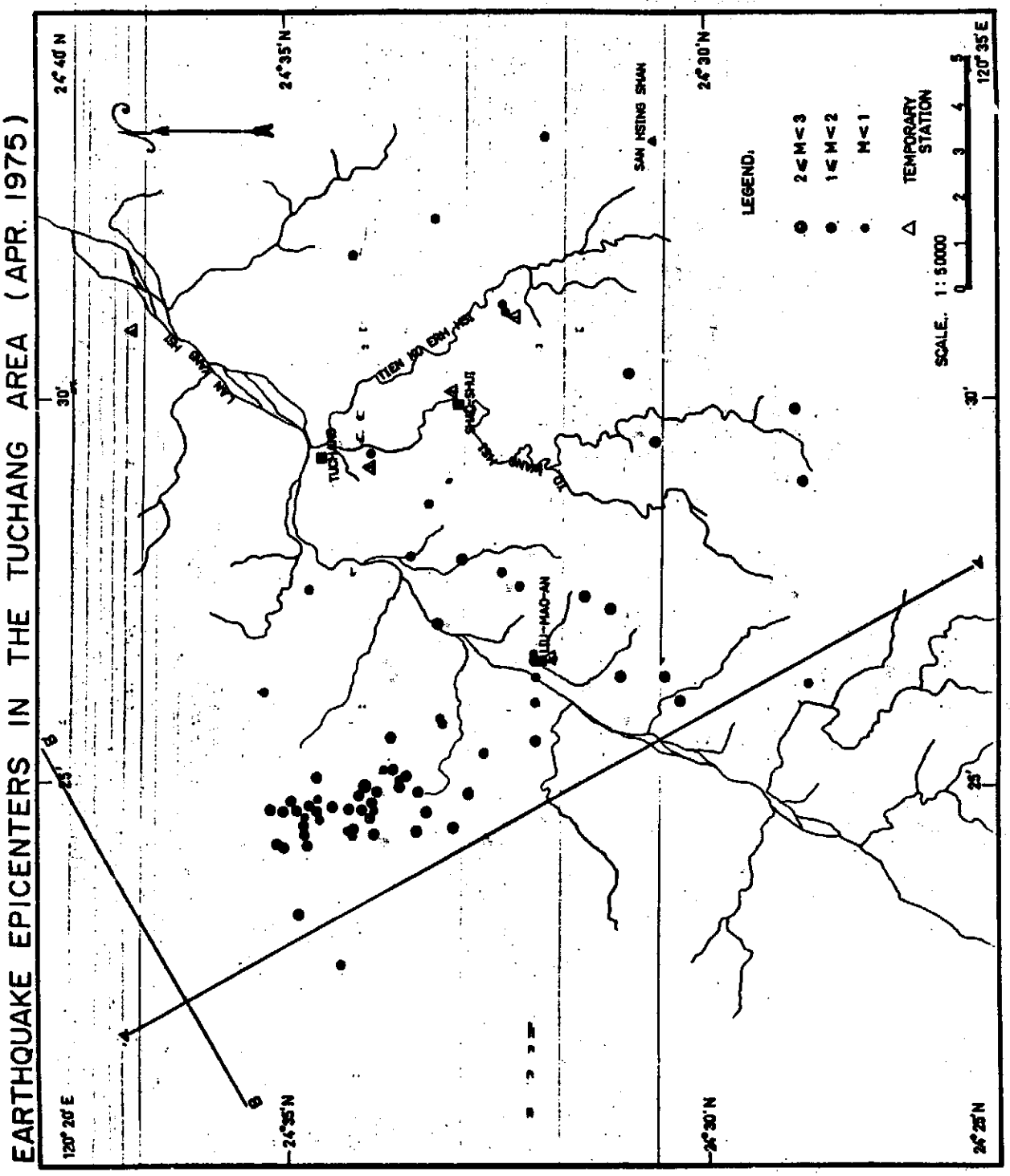

Figure 7. Locations of temporary stations and epicenters of microquakes in Tuchang area (April, 10-20, 1975).

-381-

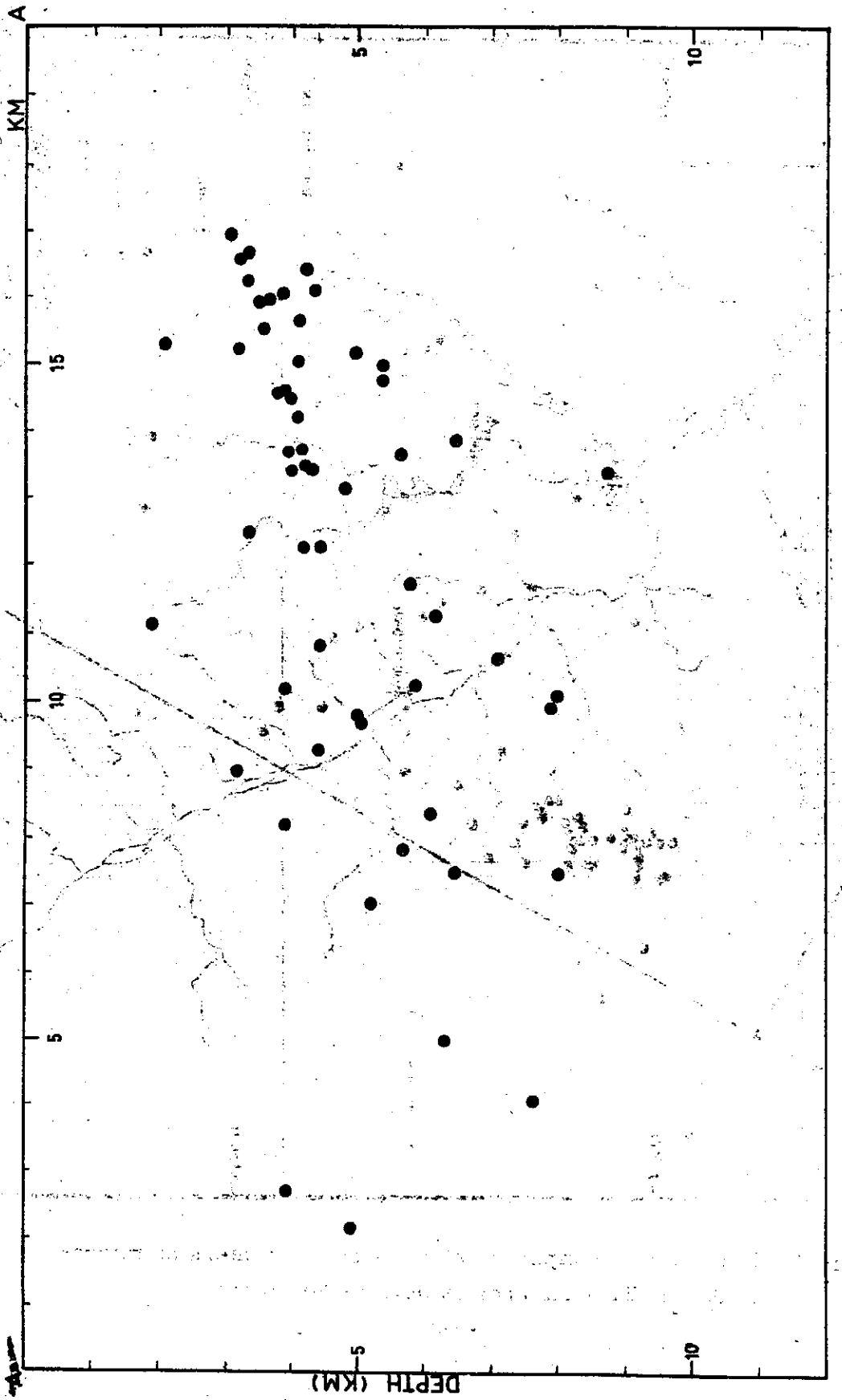

Figure 8. Projection of the hypocenters onto vertical plane AA'.

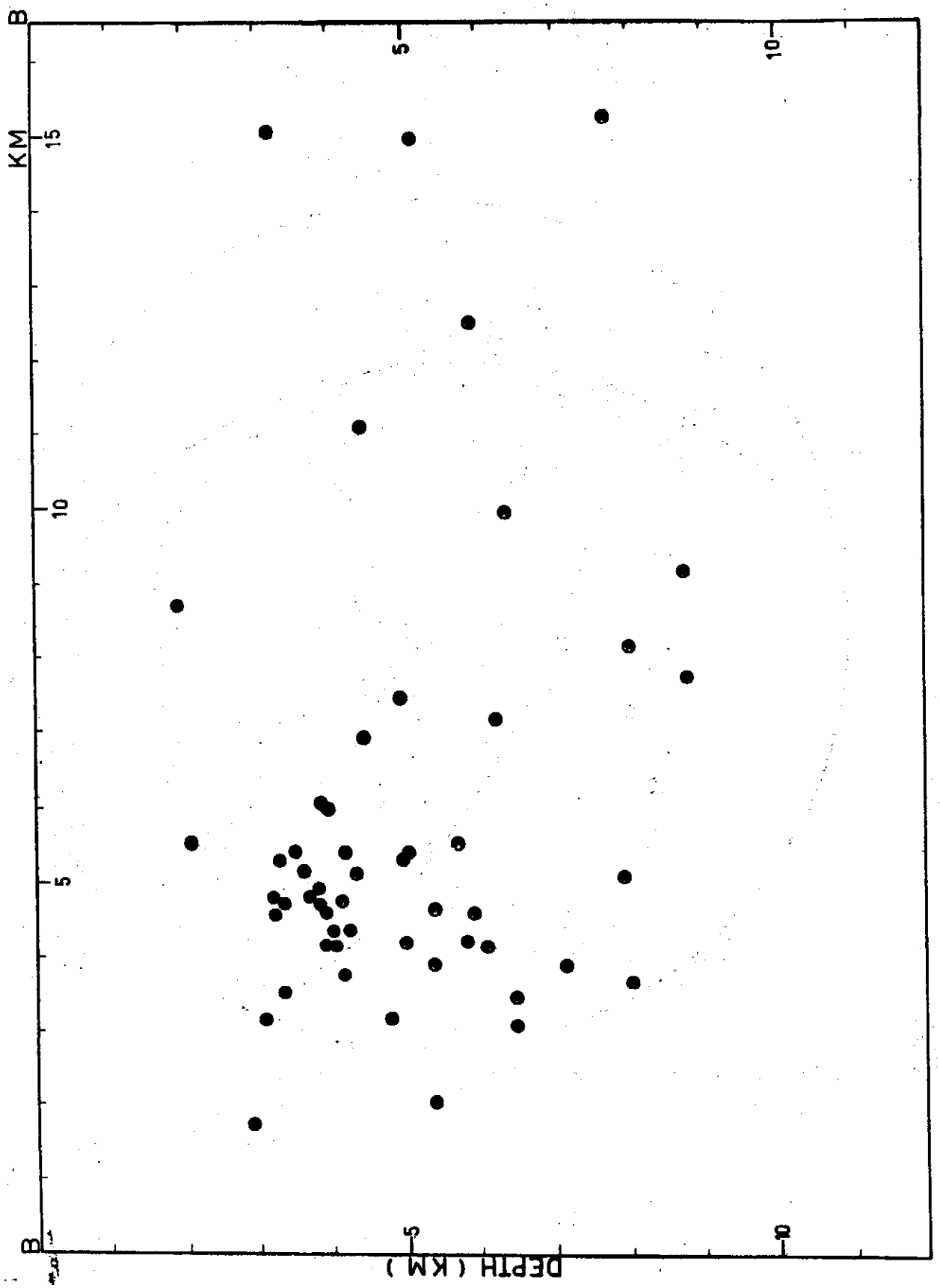

Figure 9. Projection of the hypocenters onto vertical plane BB'.

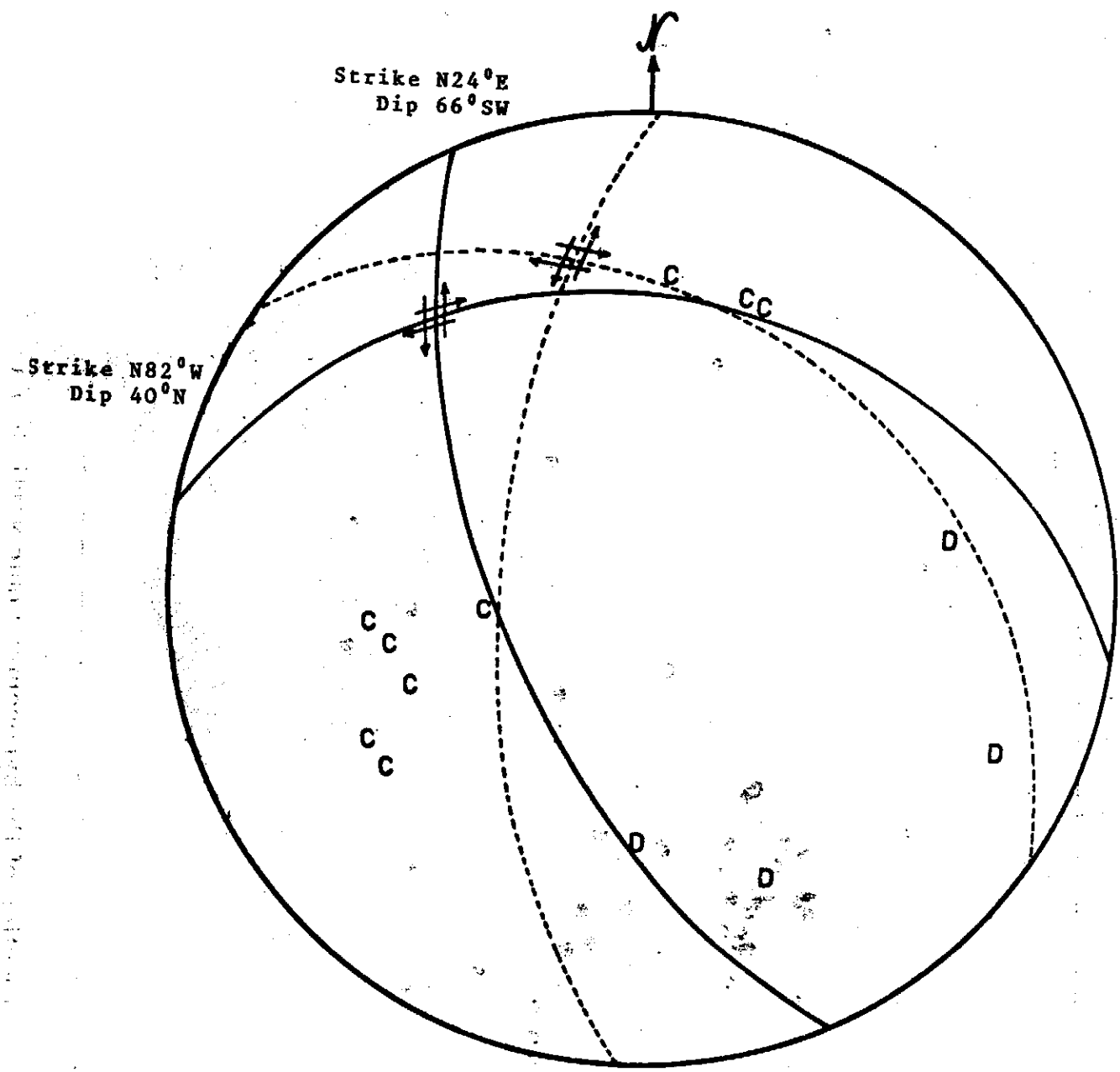

Figure 10. Composite fault-plane solution of two earthquakes in Tuchang area.

ANNUAL REPORT OF THE INSTITUTE OF PHYSICS,
ACADEMIA SINICA, 1974

TWO WELDED ELASTIC WEDGES SUBJECTED TO AN INTERNAL DISPLACEMENT DISCONTINUITY ALONG THE DIPPING BOUNDARY

Yu-Chiung Teng (鄧玉瓊)
Seismology Division, Institute of Physics
Academia Sinica
The Republic of China

Abstract

This paper investigates the case of two welded elastic wedges, with different elastic constants and arbitrary wedge angles, subjected to a concentrated displacement discontinuity along the dipping boundary. The formal solution of displacements and stresses are obtained.

The elastic theory of dislocation has been introduced to the field of seismology since the early fifties. Press [1]* has reviewed the practical applications of the dislocation theory to the study of static deformation in connection with faulting. He studies vertical dip-slip models and for the first time pointed out that the residual fields from major earthquakes are detactable by the modern instruments. Later, Savage and Hastie [2, 3] investigated inclined faults. Recently, Mansinha and Smylie [4] applied the dislocation theory to inclined, finite strike-slip and dip-slip faults. Ben-Menahemand Gillon [5], Sato]6], Sato and Matsu'ura [7], being more realistic in their investigations, have studied the static deformations in a horizontally

* Numbers in brackets designate References at end of paper.

layered medium. As for the elastostatic wedge problems, the author and Kuo [8,9] have studied, by starting with the Papkovitch functions, the following two-dimensional cases

(1) A single wedge subjected to

(i) an inclined concentrated line load

(ii) a concentrated N-th multipole line load (couple when N=1, double couples when N=2)

on one of the free surfaces of the wedge.

(2) A welded multiwedge, with arbitrary wedge angles and different elastic constants, subjected to a concentrated line load on one of the free surfaces.

(3) A single wedge subjected to a concentrated line load in the interior of the wedge.

In this paper, we consider two welded wedges (plain strain two-dimensional approximation), with different elastic constants, subjected to a concentrated displacement discontinuity D_o along the dipping boundary $\theta = \theta_o$ (Figure 1), since the displacement discontinuity problem is believed to be of more significance than the force discontinuity problem to seismology. It is noted from Figure 1 that when $\alpha = \pi/2$, the problem reduces to the more geophysically interesting case of a sloping interfaced half-space (Figure 2).

We shall summerize the mathematical techniques required as follows: The elastostatic equation of equilibrium is separated into two Poison's equations in two stress functions (one scalar and one vector). These two stress functions are called Papkovitch functions. The displacement and stress can be expressed in terms of the Papkovitch functions whose Laplacians are known if the body force is known. The concentrated displacement discontinuity, which is written in a form of Delta functions's Fourier transform, is treated as jump conditions along the dipping boundary. The geometry of the

problem in question suggests the use of cylindrical polar coordinates. Thus we find the general expressions of Papkovitch functions and in turn the graeral expressions of the displacements and stresses can be expressed as the source function in the integral form. After having satisfied the boundary conditions, the formal solutions of the stresses and displacements can be obtained in integral form. By evaluating the residues at the poles of the integrand, the solutions of displacements and stresses can be obtained in series form by Cauchy's Theorem.

Here we are considering the two-dimensional problem. In Figure 1, wedge I (λ_1, μ_1) is perfectly welded with wedge II (λ_2, μ_2). Both media are assumed to be homogeneous and isotropic. Wedge I is bounded by $\theta = \theta_o$ and $\theta = +\alpha$. Wedge II is bounded by $\theta = -\alpha$ and $\theta = \theta_o$, $\theta = +\alpha$ and $\theta = -\alpha$ being the free surface. A tangential displacement D_o takes place at the point (r_o, θ_o), $P(r, \theta)$ is the observation point.

The boundary conditions on the wedge surfaces are

$$\tau^{(1)}_{\theta\theta}\Big|_{\theta=\alpha} = \tau^{(2)}_{\theta\theta}\Big|_{\theta=-\alpha} = \tau^{(1)}_{\theta r}\Big|_{\theta=\alpha} = \tau^{(2)}_{\theta r}\Big|_{\theta=-\alpha} = 0 \qquad (1)$$

At the interface between two dissimilar media, there must be continuity of the traction and the vertical displacement. These conr ditions are

$$\tau^{(1)}_{\theta\theta}\Big|_{\theta=\theta_o} = \tau^{(2)}_{\theta\theta}\Big|_{\theta=\theta_o} \qquad (2)$$

$$\tau^{(1)}_{\theta r}\Big|_{\theta=\theta_o} = \tau^{(2)}_{\theta r}\Big|_{\theta=\theta_o} \qquad (3)$$

$$u_\theta^{(1)}\Big|_{\theta=\theta_o} = u_\theta^{(2)}\Big|_{\theta=\theta_o} \tag{4}$$

The tangential displacement must satisfy the jump condition, that is

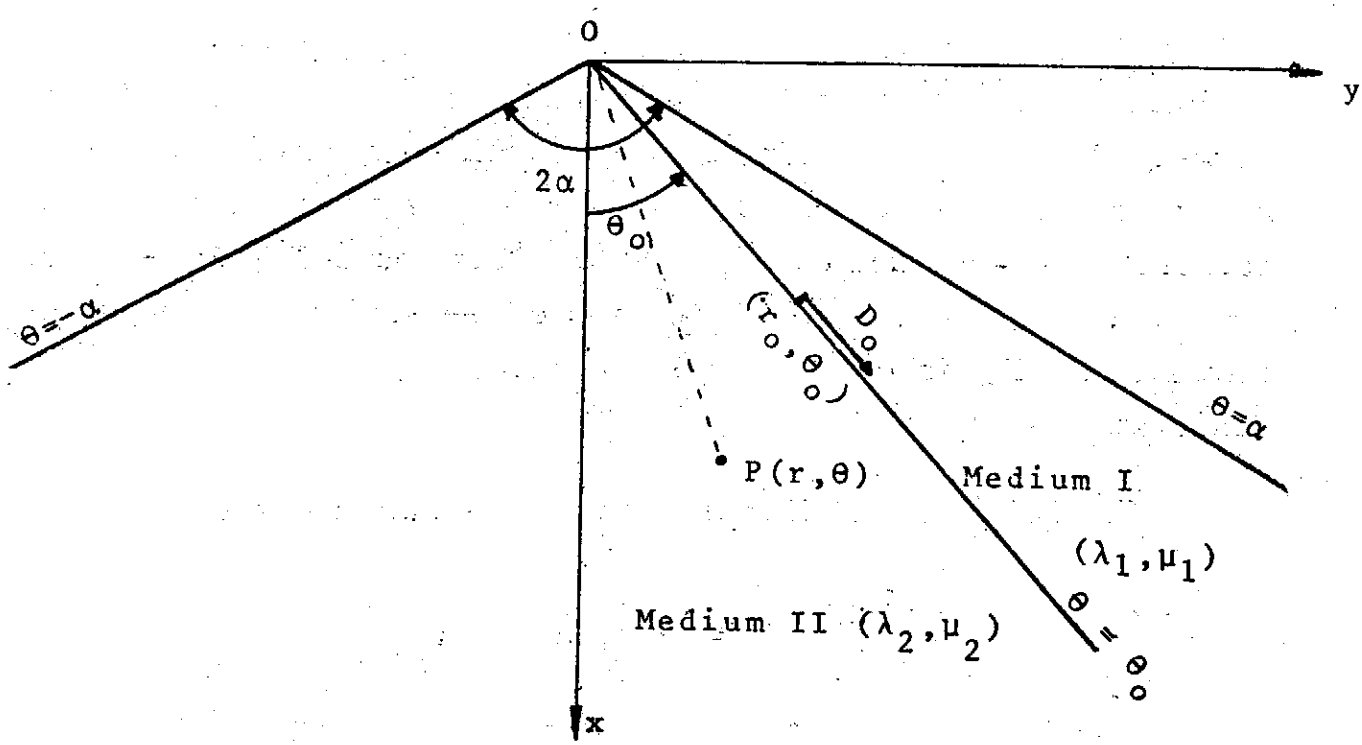

Figure 1. Two Welded Wedges Subjected to an Internal Concentrated Displacement Discontinuity.

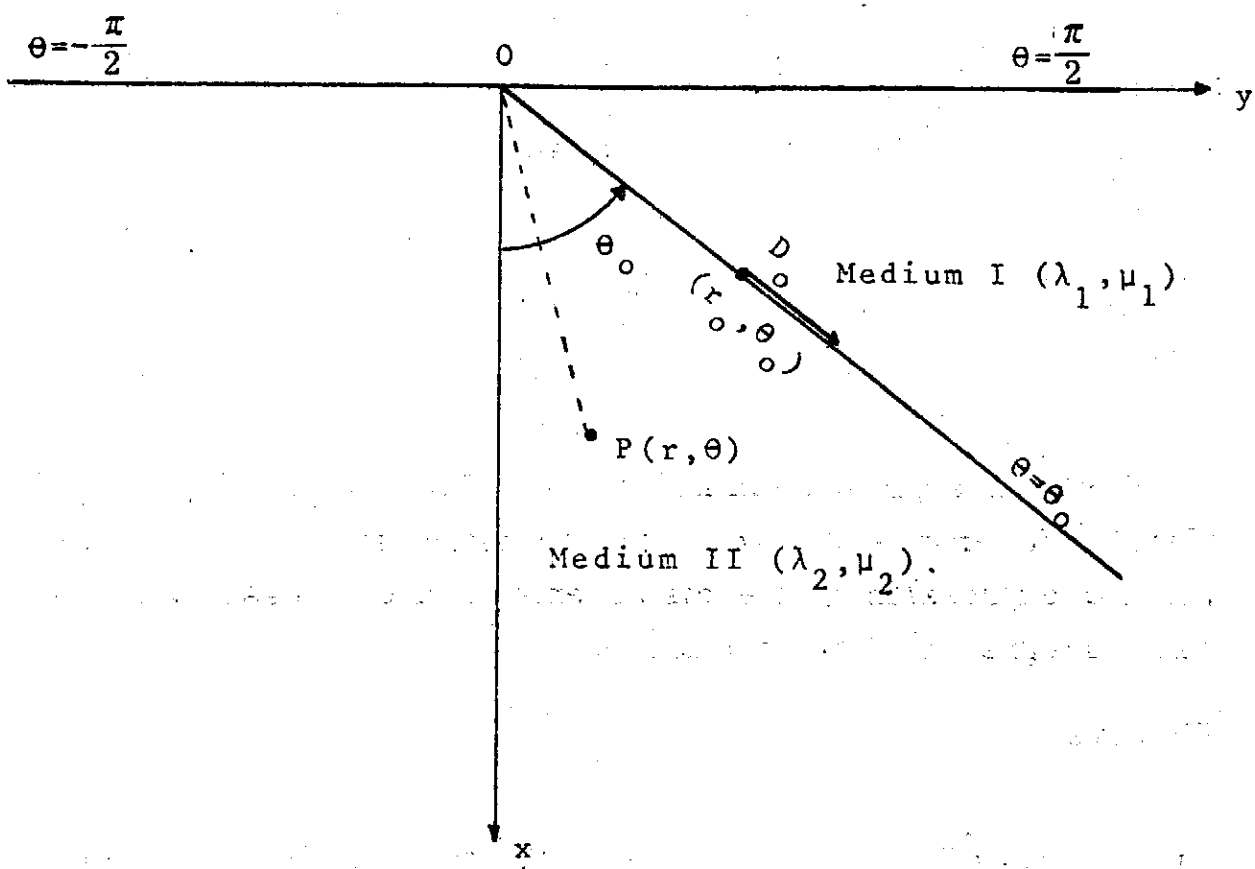

Figure 2. A Sloping Interfaced Half-Space Subjected to an Internal Concentrated Displacement Discontinuity.

$$u_r^{(2)}\Big|_{\theta=\theta_o} - u_r^{(1)}\Big|_{\theta=\theta_o} = D_o\ \delta(r-r_o) \tag{5}$$

Letting $r = r' e^{\rho}$, $r_o = r' e^{\rho_o}$, and taking $r' = 1$, and normalizing r_o to 1, we have

$$u_r^{(2)}\Big|_{\theta=\theta_o} - u_r^{(1)}\Big|_{\theta=\theta_o} = \frac{D_o e^{-\rho}}{2\pi} \int_{-\infty}^{\infty} e^{in\rho} dn \tag{6}$$

Using an approach similar to that of surface loading wedge problem in Reference [8], we make a transformation m=in-1 so that the general expression of the displacements and stresses will have the same integral form as equation (6).

We have

$$\tau_{rr}^{(j)} = -S_j^{-2\rho} \int_{-\infty}^{\infty} (in-1) \left\{ \begin{array}{l} (in-4)\ \left[B_n^{(j)} \cos(in-2)\theta + F_n^{(j)} \sin(in-\right. \\ \left. 2)\theta\right] + in\ \left[Y_n^{(j)} \cos in\theta + Z_n^{(j)} \sin in\theta\right] \end{array} \right\} e^{in\rho} dn \tag{7}$$

$$\tau_{\theta\theta}^{(j)} = S_j^{-2\rho} \int_{-\infty}^{\infty} (in-1)\, in \left\{ \begin{array}{l} B_n^{(j)} \cos(in-2)\theta + F_n^{(j)} \sin(in- \\ 2)\theta + Y_n^{(j)} \cos in\theta + Z_n^{(j)} \sin in\theta \end{array} \right\} e^{in\rho} dn \tag{8}$$

$$\tau_{\theta r}^{(j)} = S_j^{-2\rho} \int_{-\infty}^{\infty} (in-1) \left\{ \begin{array}{l} (in-2)\ \left[B_n^{(j)} \sin(in-2)\theta - F_n^{(j)} \cos(in-\right. \\ \left. 2)\theta\right] + in\ \left[Y_n^{(j)} \sin in\theta - Z_n^{(j)} \cos in\theta\right] \end{array} \right\} e^{in\rho} dn \tag{9}$$

$$\mu_\theta^{(j)} = -B_o^{(j)} \sin\theta - F_o^{(j)} \cos\theta + F_1^{(j)} r + \frac{e^{-\rho}}{2\mu_j} \int_0^\infty \left\{ \left[R_j + S_j (in-1) \right] \left[B_n^{(j)} \sin(in-2)\theta - F_n^{(j)} \cos(\right. \right. \left. \left. in-2)\theta \right] + in S_j \left[Y_n^{(j)} \sin in\theta - Z_n^{(j)} \cos in\theta \right] \right\} e^{in\rho} dn \quad (10)$$

$$\mu_r^{(j)} = B_o^{(j)} \cos\theta - F_o^{(j)} \sin\theta + \frac{e^{-\rho}}{2\mu_j} \int_0^\infty \left\{ \left[R_j - S_j (in-1) \right] \left[B_n^{(j)} \cos(in-2)\theta - F_n^{(j)} \sin(\right. \right. \left. \left. in-2)\theta \right] - in S_j \left[Y_n^{(j)} \cos in\theta - Z_n^{(j)} \sin in\theta \right] \right\} e^{in\rho} dn \quad (11)$$

$$S_j = \frac{\lambda_j + \mu_j}{2(\lambda_j + 2\mu_j)} \quad (12)$$

$$R_j = \frac{\lambda_j + 3\mu_j}{2(\lambda_j + 2\mu_j)} \quad (13)$$

where the superscripts j=1, 2 represent the first and second medium respectively. B_o, F_o, and F_1 are the rigid body motion constants.

Substituting equations (8) to (11) into equations (1) to (4) and (6), we have

$$B_o^{(j)} = F_o^{(j)} = F_1^{(j)} = 0 \tag{14}$$

$$B_n^{(1)} \operatorname{Cos}(in-2)\alpha + F_n^{(1)} \operatorname{Sin}(in-2)\alpha + Y_n^{(1)} \operatorname{Cos} in\alpha + Z_n^{(1)} \operatorname{Sin} in\alpha = 0 \tag{15}$$

$$B_n^{(2)} \operatorname{Cos}(in-2)\alpha - F_n^{(2)} \operatorname{Sin}(in-2)\alpha + Y_n^{(2)} \operatorname{Cos} in\alpha - Z_n^{(2)} \operatorname{Sin} in\alpha = 0 \tag{16}$$

$$(in-2)\left[B_n^{(1)} \operatorname{Sin}(in-2)\alpha - F_n^{(1)} \operatorname{Cos}(in-2)\alpha \right] + in\left[Y_n^{(1)} \operatorname{Sin} in\alpha - Z_n^{(1)} \operatorname{Cos} in\alpha \right] = 0 \tag{17}$$

$$(in-2)\left[B_n^{(2)} \operatorname{Sin}(in-2)\alpha + F_n^{(2)} \operatorname{Cos}(in-2)\alpha \right] + in\left[Y_n^{(2)} \operatorname{Sin} in\alpha + Z_n^{(2)} \operatorname{Cos} in\alpha \right] = 0 \tag{18}$$

$$\frac{S_1}{S_2}\left[B_n^{(1)} \operatorname{Cos}(in-2)\theta_o - F_n^{(2)} \operatorname{Sin}(in-2)\theta_o + Y_n^{(1)} \operatorname{Cos} in\theta_o - Z_n^{(1)} \operatorname{Sin} in\theta_o \right] = B_n^{(2)} \operatorname{Cos}(in-2)\theta_o - F_n^{(2)} \operatorname{Sin}(in-2)\theta_o + Y_n^{(2)} \operatorname{Cos} in\theta_o - Z_n^{(2)} \operatorname{Sin} in\theta_o \tag{19}$$

$$\frac{S_1}{S_2}\left\{(in-2)\,[B_n^{(1)}\,\mathrm{Sin}\,(in-2)\,\theta_o + F_n^{(1)}\,\mathrm{Cos}\,(in-2)\theta_o]\right.$$

$$\left. + in[Y_n^{(1)}\,\mathrm{Sin}\,in\,\theta_o + Z_n^{(1)}\,\mathrm{Cos}\,in\,\theta_o]\right\}$$

$$= (in-2)\,[B_n^{(2)}\,\mathrm{Sin}\,(in-2)\,\theta_o + F_n^{(2)}\,\mathrm{Cos}\,(in-2)\,\theta_o]$$

$$+ in\,[Y_n^{(2)}\,\mathrm{Sin}\,in\,\theta_o + Z_n^{(2)}\,\mathrm{Cos}\,in\,\theta_o] \qquad (20)$$

$$\frac{\mu_2}{\mu_1}\left\{[R_1+S_1(in-1)]\,[B_n^{(1)}\,\mathrm{Sin}(in-2)\theta_o - F_n^{(1)}\,\mathrm{Cos}(in-2)\theta_o]\right.$$

$$\left. + in\,S_1[Y_n^{(1)}\,\mathrm{Sin}\,in\,\theta_o - Z_n^{(1)}\,\mathrm{Cos}\,in\,\theta_o]\right\}$$

$$=[R_2+S_2(in-1)]\,[B_n^{(2)}\,\mathrm{Sin}(in-2)\theta_o - F_n^{(2)}\,\mathrm{Cos}(in-2)\theta_o]$$

$$+in\,S_2[Y_n^{(2)}\,\mathrm{Sin}\,in\theta_o - Z_n^{(2)}\,\mathrm{Cos}\,in\,\theta_o] \qquad (21)$$

$$\frac{\mu_2}{\mu_1}\left\{[R_1-S_1(in-1)]\,[B_n^{(1)}\,\mathrm{Cos}(in-2)\theta_o + F_n^{(1)}\,\mathrm{Sin}\,(in-2)\theta_o]\right.$$

$$\left. - in\,S_1\,[Y_n^{(1)}\,\mathrm{Cos}\,in\,\theta_o + Z_n^{(1)}\,\mathrm{Sin}\,in\,\theta_o]\right\}$$

$$- [R_2-S_2(in-1)]\,[B_n^{(2)}\,\mathrm{Cos}(in-2)\theta_o + F_n^{(2)}\,\mathrm{Sin}\,(in-2)\theta_o]$$

$$+ in\,S_2[Y_n^{(2)}\,\mathrm{Cos}\,in\theta_o + Z_n^{(2)}\,\mathrm{Sin}\,in\,\theta_o]$$

$$= \frac{-\mu_2 D_o}{\pi} \qquad (22)$$

From equations (15) to (22), we obtsain

$$B_n^{(1)} = \frac{\Delta_1}{\Delta} \qquad (23)$$

$$B_n^{(2)} = \frac{\Delta_2}{\Delta} \qquad (24)$$

$$F_n^{(1)} = \frac{\Delta_3}{\Delta} \tag{25}$$

$$F_n^{(2)} = \frac{\Delta_4}{\Delta} \tag{26}$$

$$\Delta = \begin{vmatrix} a_{11} & a_{12} & a_{13} & a_{14} \\ a_{21} & a_{22} & a_{23} & a_{24} \\ a_{31} & a_{32} & a_{33} & a_{34} \\ a_{41} & a_{42} & a_{43} & a_{44} \end{vmatrix} \tag{27}$$

$$\Delta_1 = \begin{vmatrix} 0 & a_{12} & a_{13} & a_{14} \\ 0 & a_{22} & a_{23} & a_{24} \\ 0 & a_{32} & a_{33} & a_{34} \\ \frac{-\mu_2 D_o}{\pi} & a_{42} & a_{43} & a_{44} \end{vmatrix} \tag{28}$$

$$\Delta_2 = \begin{vmatrix} a_{11} & 0 & a_{13} & a_{14} \\ a_{21} & 0 & a_{23} & a_{24} \\ a_{31} & 0 & a_{33} & a_{34} \\ a_{41} & \frac{-\mu_2 D_o}{\pi} & a_{43} & a_{44} \end{vmatrix} \tag{29}$$

$$\Delta_3 = \begin{vmatrix} a_{11} & a_{12} & 0 & a_{14} \\ a_{21} & a_{22} & 0 & a_{24} \\ a_{31} & a_{32} & 0 & a_{34} \\ a_{41} & a_{42} & \frac{-\mu_2 D_o}{\pi} & a_{44} \end{vmatrix} \tag{30}$$

$$\Delta_4 = \begin{vmatrix} a_{11} & a_{12} & a_{13} & 0 \\ a_{21} & a_{22} & a_{23} & 0 \\ a_{31} & a_{32} & a_{33} & 0 \\ a_{41} & a_{42} & a_{43} & \frac{-\mu_2 D_o}{\pi} \end{vmatrix} \tag{31}$$

where

$$a_{11} = [in\,Cos(in-2)\theta_o - b_3\,Cos\,in\theta_o + b_1\,Sin\,in\theta_o]\,\frac{S_1}{S_2} \tag{32}$$

$$a_{12} = -in\,Cos\,(in-2)\theta_o + b_3\,Cos\,in\theta_o + b_1\,Sin\,in\theta_o \tag{33}$$

$$a_{13} = [-in\,Sin(in-2)\theta_o + b_2\,Cos\,in\theta_o + b_4\,Sin\,in\theta_o]\,\frac{S_1}{S_2} \tag{34}$$

$$a_{14} = in\,Sin(in-2)\theta_o + b_2\,Cos\,in\theta_o - b_4\,Sin\,in\theta_o \tag{35}$$

$$a_{21} = [(in-2)\,Sin(in-2)\theta_o - b_3\,Sin\,in\theta_o - b_1\,Cos\,in\theta_o]\,\frac{S_1}{S_2} \tag{36}$$

$$a_{22} = -(in-2)Sin(in-2)\theta_o + b_3\,Sin\,in\theta_o - b_1\,Cos\,in\theta_o \tag{37}$$

$$a_{23} = [(in-2)\,Cos(in-2)\theta_o + b_2\,Sin\,in\theta_o - b_4\,Cos\,in\theta_o]\,\frac{S_1}{S_2} \tag{38}$$

$$a_{24} = -(in-2)\,Cos(in-2)\theta_o + b_2\,Sin\,in\theta_o + b_4\,Cos\,in\theta_o \tag{39}$$

$$a_{31}=\left\{[R_1+S_1(in-1)]\sin(in-2)\theta_o-S_1b_3\sin in\theta_o+S_1b_1\cos in\theta_o\right\}\frac{\mu_2}{\mu_1} \quad (40)$$

$$a_{32}=-[R_2+S_2(in-1)]\sin(in-2)\theta_o+S_2b_3\sin in\theta_o+S_2b_1\cos in\theta_o \quad (41)$$

$$a_{33}=\left\{-[R_1+S_1(in-1)]\cos(in-2)\theta_o+S_1b_2\sin in\theta_o+S_1b_4\cos in\theta_o\right\}\frac{\mu_2}{\mu_1} \quad (42)$$

$$a_{34}=[R_2+S_2(in-1)]\cos(in-2)\theta_o+S_2b_2\sin in\theta_o-S_2b_4\cos in\theta_o \quad (43)$$

$$a_{41}=\left\{[R_1-S_1(in-1)]\cos(in-2)\theta_o+S_1b_3\cos in\theta_o+S_1b_1\sin in\theta_o\right\}\frac{\mu_2}{\mu_1} \quad (44)$$

$$a_{42}=-[R_2-S_2(in-1)]\cos(in-2)\theta_o-S_2b_3\cos in\theta_o+S_2b_1\sin in\theta_o \quad (45)$$

$$a_{43}=\left\{[R_1-S_1(in-1)]\sin(in-2)\theta_o-S_1b_2\cos in\theta_o+S_1b_4\sin in\theta_o\right\}\frac{\mu_2}{\mu_1} \quad (46)$$

$$a_{44}=[R_2-S_2(in-1)]\sin(in-2)\theta_o-S_2b_2\cos in\theta_o-S_2b_4\sin in\theta_o \quad (47)$$

$$b_1=(in-1)\sin 2\alpha+\sin 2(in-1)\alpha \quad (48)$$

$$b_2=(in-1)\sin 2\alpha-\sin 2(in-1)\alpha \quad (49)$$

$$b_3=(in-1)\cos 2\alpha+\cos 2(in-1)\alpha \quad (50)$$

$$b_4=(in-1)\cos 2\alpha-\cos 2(in-1)\alpha \quad (51)$$

and

$$Z_n^{(1)}=-\frac{1}{in}\left(b_1B_n^{(1)}+b_4F_n^{(1)}\right) \quad (52)$$

$$Z_n^{(2)}=\frac{1}{in}\left(b_1B_n^{(2)}-b_4F_n^{(2)}\right) \quad (53)$$

$$Y_n^{(1)}=\frac{1}{in}\left(-b_3B_n^{(1)}+b_2F_n^{(1)}\right) \quad (54)$$

$$Y_n^{(2)} = - \frac{1}{in} (b_3 B_n^{(2)} + b_2 F_n^{(2)}) \qquad (55)$$

We have now obtained the formal solutions of the stresses and displacements in integral form. These stresses and displacements can be evaluated without any difficulty by means of the residue theorem as we have done in [8, 9] previously, though the process itself is very cumbersome. The evaluated stresses and displacements, as well as the numerical results will be given in the next paper.

References

1. Press, F., "Dsiplacements, Strains, and Tilts at Teleseismic Distances", Journal of Geophysical Research, Vol. 70, 1965, pp. 2395-2412.

2. Savage, J.C. and L.M. Hastie, "Surface Deformation Associated with Dip-Slip Faulting" Journal of Geophysical Research. Vol. 71, 1966, pp. 4897-4904.

3. Savage, J. C. and L. M. Hastie, "A Dislocation Model for the Fairview Peak, Nevada, Earthquake", Bulletin of the Seismological Society of America, Vol. 59, 1969, pp. 1937-1948.

4. Manshia, L. and D. E. Smylie, "The Displacement Fields of Inclined Faults", Bulletin of the Seismological Society of America, Vol. 61, 1971, pp. 1433-1440.

5. Ben-Menahem, A. and A. Gillon, "Crustal Deformation by Earthquakes and Explosions", Bulletin of the Seismological Society of America, Vol. 60, 1970, pp. 193-215.

6. Sato, R., "Crustal Deformation Due to Dislocation in a Multi-layered Medium", Journal of Physics of the Earth, Vol. 19, 1971, pp. 31-46.

7. Sato, R. and M. Matsu'ura, "Static Deformations Due to the Fault Spreading over Several Layers in a Multi-layered Medium, Part: Displacement", Journal of Physics of the Earth, Vol. 21, 1973, p. 227-249.

8. Teng, Y.C. and J. T. Kuo, "Displacements and Stresses in a Two-Dimensional Wedge Shaped Medium", Journal of Applied Mechanics, Vol. 41, No. 3, 1974, pp. 719-724.

9. Teng, Y.C., "A Concentrated Line Load Acting in the Interior of an Elastic Wedge Shaped Medium", Annual Report of the Institute of Physics, Academia Sinica, Taiwan, The Republic of China, Vol. 4, 1973, pp. 271-294.

ANNUAL REPORT OF THE INSTITUTE OF PHYSICS,
ACADEMIA SINICA, 1974

Correlation Between Microearthquakes and Geologic Faults in the Hsintien-Ilan Area *

Y. B. TSAI, C. C. FENG, J. M. CHIU and H. B. LIAW

Academia Sinica

ABSTRACT

This study uses the spatial distribution of microearthquakes to identify the potentially active faults in the Hsintien-Ilan area in Northeastern Taiwan. The data available for this study include: (1) 12 microearthquakes located in the Tatun Volcanic Region and the Hsintien area during 6 February to 4 March 1974 by means of nine portable seismographs; (2) 181 microearthquakes located in the Hsintien-Ilan area during 20 August to 14 October 1974 by means of nineteen portable seismographs; and (3) About 60 earthquakes located in the Hsintien-Ilan area during the first three months of 1975 by means of the islandwide telemetered seismograph network operated by the Chinese Earthquake Research Center. The findings of this study can be summarized as follows:

(1) Microearthquakes in the Tatun Volcanic Region cluster along faults in the vicinity around the area marked by geothermal activity.

(2) An 15-km segment of the northeasterly trending Hôushaochang fault southeast of Houshaochang can be classified as potentially active.

(3) An 30-km segment of the northeasterly trending Shihchao fault southeast of Shihchao can be classified as potentially active.

(4) A subsurface vertical fault no deeper than 20 km has been discovered to lie between Ilan and Lotung. It extends from the Ilan Plain northeasterly into the Pacific Ocean and passes by the Kueishan Island to join the northern boundary of the Ryukyu folded zone. It is apparently the extension of the Median fault which bisects longitudianlly the whole length of Taiwan into eastern and western halves and potentially the most active fault in the Hsintien-Ilan area. Appropriate measures should be taken to reduce potential hazards posed by future earthquakes along this fault when developments of the Ilan-Lotung area are planned.

(5) The epicenters of microearthquakes in the Tananao Schist Formation south of the Ilan Plain are much more diffused than elsewhere in the Hsintien-Ilan area. In the meantime, existing geologic information about the area is also very limited. Consequently, it is not possible to correlate microearthquakes with geologic faults in the area. Nevertheless, it should be pointed out that the microearthquake activity in the Tananao Schist Formation is not only high but also has a tendency to extend southeasterly into the Pacific Ocean to join the southern boundary of the Ryukyu folded zone.

(6) No microearthquakes were located during the three recording periods considered by the present study along several thrust faults lying northeasterly between Hsintien and Taipei. This appears to suggest that these faults are probably more stable than those in the Hsintien-Ilan area.

INTRODUCTION

According to new geologic map of Taiwan (Ho, 1975), the Hsintien[1]-Ilan[2] area is transected by numerous northeasterly trending thrust faults, as shown in Figure 1. At

1. 新店 2. 宜蘭

* This paper has been published in Petroleum Geology of Taiwan, No. 12, p. 149–167, 8. FIGS., June 1975.

least seven to eight major thrust faults have been recognized in the Hsintien area as members of the northeasterly trending imbricate fault system characteristic of the eastern or inner foothills zone of the western Neogene geosyncline of Taiwan. These faults all have their southeast blocks upthrown and probably belong to the same episode of thrust faulting. Most of these faults are low-angle thrusts. Some are bedding thrusts over some distances. They generally die out en echelon at varying lengths along the strike in northeast direction. Sometimes, one fault is intersected by another.

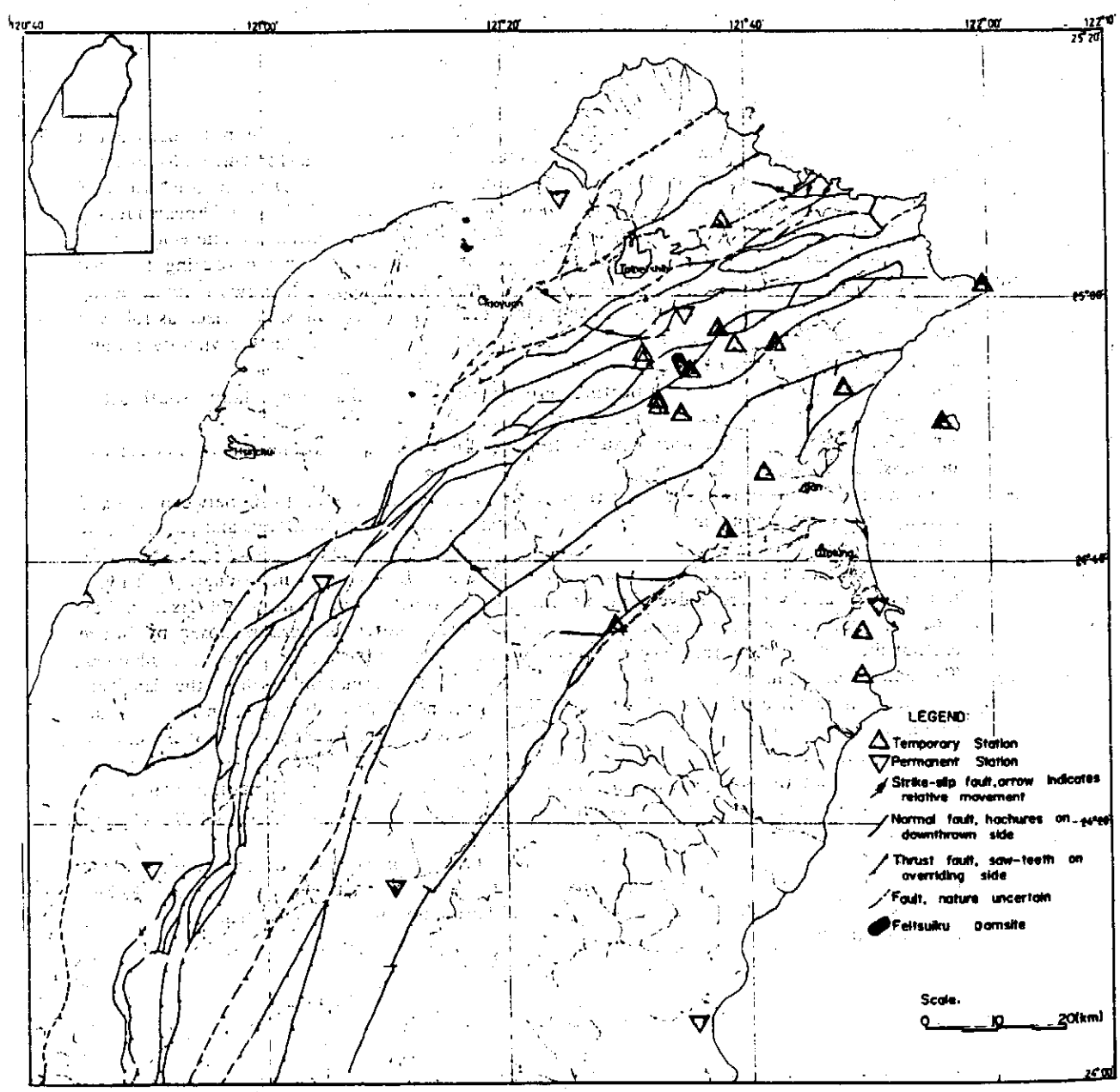

Figure 1. Locations of Seismograph stations and geologic faults in the Hsintien-Ilan area.

Southeast of this imbricate thrust fault system and about half way between Hsintien and Ilan there lies another parallel northeasterly trending thrust called the Shihchao[1] fault.

Unlike the Hsintien area, no fault trace has been observed in the Ilan Plain. The Median fault which marks the boundary between the Hsuehshan[2] Mountain Range and the Central Mountain Range disappears at the southwestern edge of the Ilan Plain. It is not known whether this major fault continues northeastward to pass through the Ilan Plain from underneath the alluvial deposits. North of the Ilan Plain there is a Y-shaped fault system. On the other hand, no clearcut fault traces have been mapped out in the Tananao[3] schist formation lying south of the Ilan Plain.

Existence of so many faults in the Hsintien-Ilan area clearly attests the intensity of tectonic movements in the area during the past. In view of the heavy investments in construction of transportation facilities in recent years, the study area is expected to become a major population center, especially in the Ilan Plain. It is thus of great importance to identify which of these faults are potentially active so that inadvertent placement of major development projects close to the potentially active faults can be avoided, or otherwise some effective seismicresistant precautions can be taken beforehand.

One approach to identify a potentially active fault is to correlate it with recent earthquake data. According to Hsu (1971), only five earthquakes during the 1900-1935 period and ten earthquakes during the 1936-1973 period were located in the Hsintien-Ilan area, as shown in Figure 2 and Figure 3, respectively. Unfortunately, these past earthquake data are inadequate both in quantity and in quality for meaningful correlation with the geologic faults in the area. In other words new data are indispensable for the present approach. To meet this need, three sets of high-quality microearthquake data have become available recently. The first and second sets of data were obtained by means of temporary local networks of portable seismographs deployed in the Hsintien-Ilan area during the time periods from 6 February to 4 March 1974 and from 19 August to 20 October 1974, respectively. The third set of data was obtained during the first three months of 1975 by means of the CERC's islandwide telemetered network of seismographs.

OBSERVATION OF MICROEARTHQUAKES

Two detailed surveys of microearthquakes in the Hsintien-Ilan area were carried out during 1974. The first survey was made for one month from 6 February to 4 March 1974. Nine temporary seismograph stations plus two permanent stations TWA and TWS of the CERC's telemetered seismograph network were deployed in the Tatun[4] Volcanic Region and in the Hsintien area. Relevant information concerning these stations is given in Table 1. Their locations are shown by the open triangles in Figure 4. The second survey was undertaken six months later for two months from 20 August to 14 October 1974. A total of nineteen temporary seismograph stations plus seven permanent stations in the northern part of the CERC's telemetered seismograph network formed a dense regional seismograph network over the Hsintien-Ilan area. Relevant information about these stations is given in Table 2. Their locations are shown

1.石槽 2.雪山 3.大南澳 4.大屯

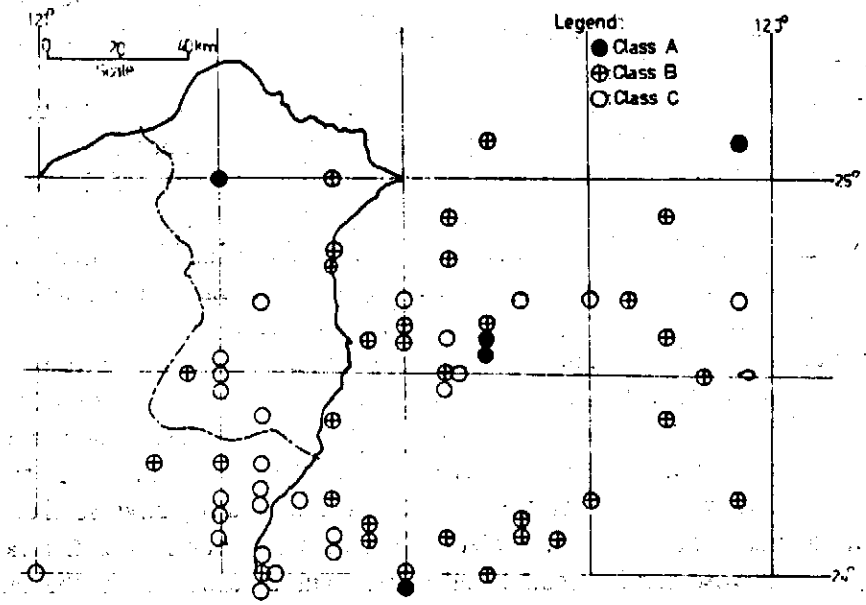

Figure 2. Distribution of earthquakes in the northern district (1900 - 1935).

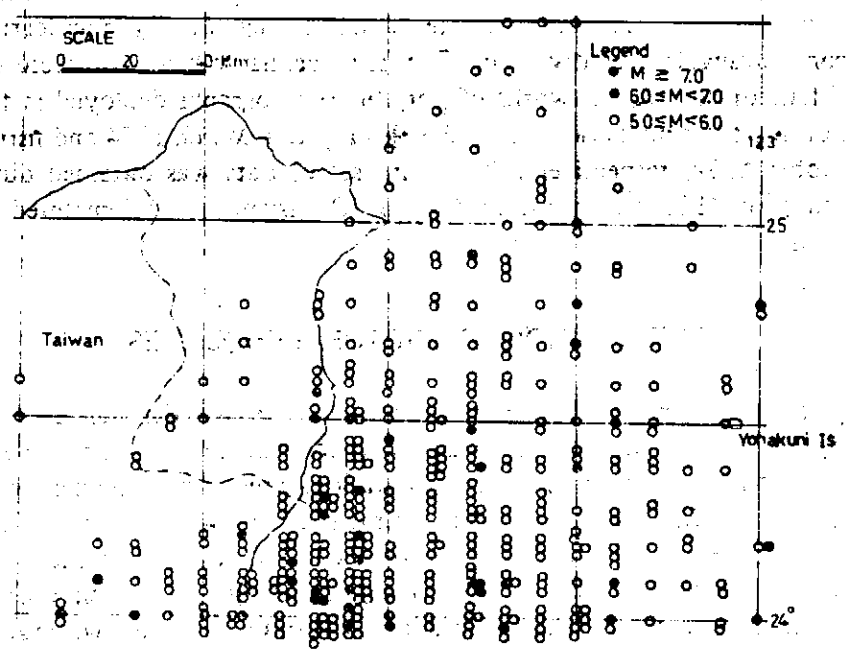

Figure 3. Distribution of earthquakes in the northern district (1936 - 1973).

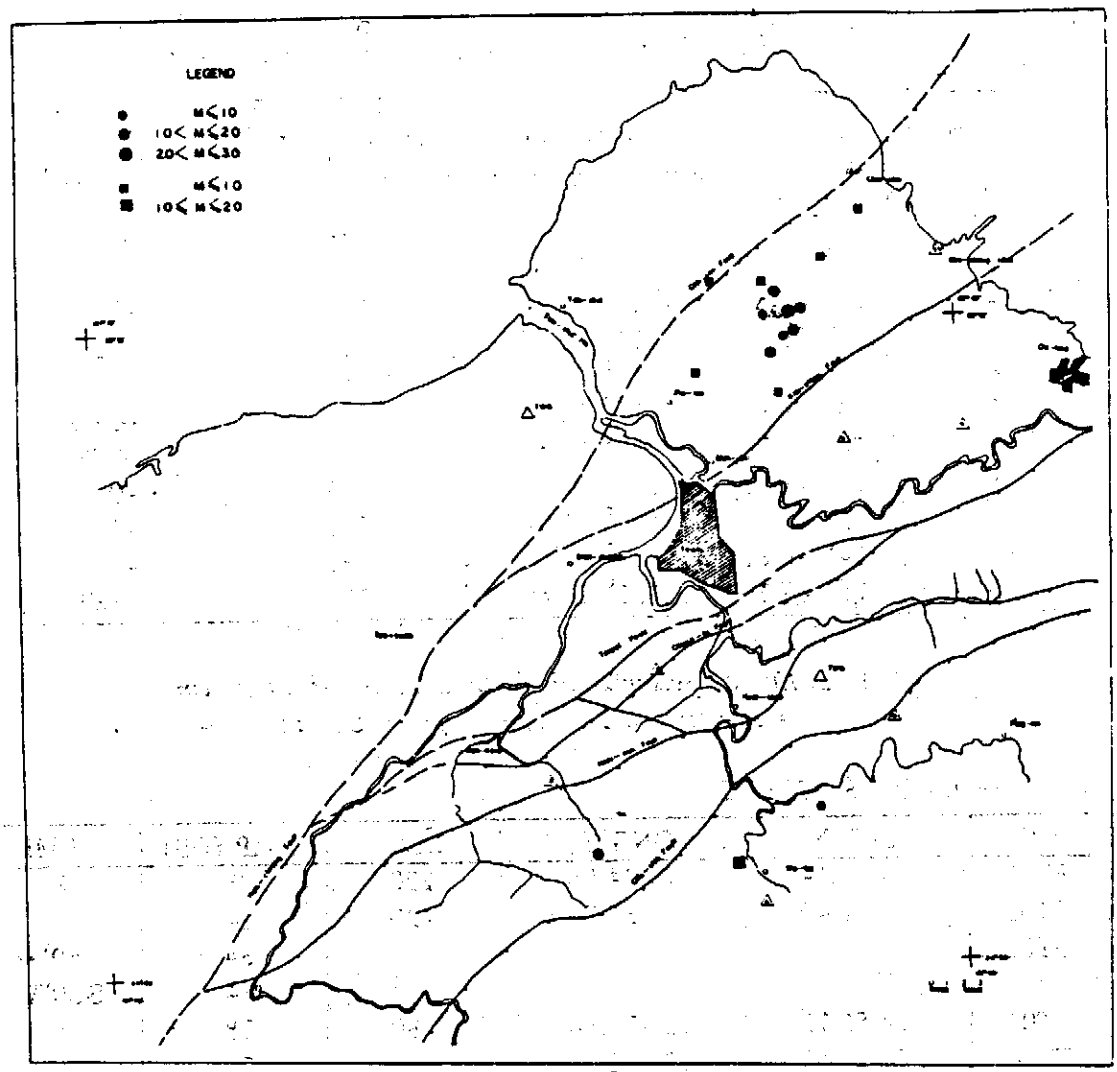

Figure 4. Locations of seismograph stations and microearthquake epicenters in the Tatun Volcanic Region and in the Hsintien area between 6 February and 4 March 1974.

by the shaded triangles in Figure 1.

Each temporary station was equipped with a short-period vertical seismometer, a smoke-paper drum recorder and a chronometer. The system is battery powered. In order to facilitate more reliable reading of S arrivals, short-period horizontal seismographs were deployed alongside with vertical seismographs at some stations. Instrumentation of the telemetered stations has been reported elsewhere by Tsai *et al*, (1974).

Normally, the internal timing of each temporary seismograph was checked with the standard time broadcasting both at the beginning and at the end of each record.

In order to determine the hypocentral location, origin time and magnitude of an earthquake, the arrival times of first P and S waves and the total signal durations at different stations were first read from the smoke-paper records by means of microscopes. Generally speaking, a high precision of 0.05 second was attainable in reading the arrival

TABLE 1. *Seismograph stations in the Tatun and Hsintien Regions between 1 February and 6 March 1974*

Station No.	Lat. (N)	Long. (E)	Elevation (m)	Station correction (sec)
1	25° 10.32′	121° 33.17′	790	-0.26
2	25° 14.46′	121° 36.60′	30	-0.01
3	25° 11.90′	121° 33.47′	0	0.0
4	25° 06.46′	121° 40.15′	210	-0.07
5	25° 06.36′	121° 35.15′	210	-0.07
6	24° 51.74′	121° 32.85′	200	-0.07
7	24° 59.04′	121° 29.04′	150	-0.05
8	24° 55.76′	121° 25.21′	90	-0.03
19	24° 57.55′	121° 37.50′	465	-0.14
11	25° 10.14′	121° 33.54′	790	-0.26
TWA	24° 58.82′	121° 35.02′	260	-0.09
TWS	25° 07.70′	121° 24.87′	300	-0.09

TABLE 2. *List of Seismograph Stations in the Hsintien-Ilan Area between 20 August and 14 October 1974*

A. TEMPORARY STATIONS

CODE	LAT N	LONG E	ELV	AMP (DB)	COMP
FT01	24-51.14	121-34.56	220	78	V
FT02	24-54.40	121-35.32	120	84	V
FT03				84	N60°W
				84	S 30°W
FT03	24-55.12	121-31.36	80	78	V
FT04	24-56.45	121-42.48	240	78	V
FT05	24-57.56	121-37.82	430	78	V
FT06	24-42.14	121-38.09	90	78	V
FT07	24-34.95	121-29.02	410	78	V
FT08	24-36.55	121-50.93	20	60	V
FT09	24-00.95	121-59.67	50	66	V
FT10	24-31.36	121-49.36	30	72	V
FT11	24-53.06	121-48.12	180	84	V
				84	N-S
FT12	24-56.39	121-39.06	280	78	V
FT13	24-50.72	121-56.19	60	78	V
FT14	25-05.76	121-38.05	90	66	V
FT16	24-34.66	121-49.49	50	78	V
FT21	24-51.74	121-32.76	200	72	V
FT22	24-46.66	121-41.38	110	78	V
FT31	24-52.02	121-32.67	185	84	V
FT32	24-55.66	121-31.50	50	60	V

B. PERMANENT STATIONS

CODE	LAT N	LONG E	ELV	AMP (DB)	COMP
TWA	24-58.82	121-35.02	260	72	V
TWC	24-36.55	121-50.93	20	60	V
TWD	24- 4.89	121-35.73	30	60	V
TWQ	24-16.48	121-50.15	443	60	V
TWR	24-38.41	121- 4.72	800	84	V
TWS	25- 7.70	121-24.87	300	78	V
TWT	24-15.20	121-10.55	1300	78	V

times of first P wave. On the other hand, readings of the S-wave first arrival times were significantly less precise than the readings for P-wave arrivals.

The observed data of arrival times for each earthquake were subsequently fed into the computer program HYPO71 to determine the hypocentral location and origin time of the earthquake by minimizing the residuals between the observed and the expected arrival times by means of the Geiger's method (Eaton, 1969; Lee and Lahr, 1972). The expected travel time and its partial derivatives as functions of epicentral distance were calculated by assuming a horizontally layered crustal model. The crustal model used in the present study was composed of the following layers:

Layer	Depth (km)	P-velocity (km/sec)	S-velocity (km/sec)
1	0 - 4	4.0	2.2
2	4 - 15	5.6	3.1
3	15 - 35	6.8	3.8
4	> 35	8.1	4.5

Finally, the earthquake magnitude M is determined according to the following formula:

$$M = -0.87 + 2.0 \log \tau + 0.0035 \Delta$$

where τ represents the total signal duration in seconds and Δ is the epicentral distance in kilometers.

Most microearthquakes located during these surveys had magnitudes M greater than 1.0. Since a minimum of four simultaneous readings of P- and S-wave arrival times are required to make the hypocenter and origin time determinable, the number of located earthquakes was somewhat less than the number of events actually recorded at individual stations.

The error in epicentral location was believed to be well within two kilometers for most earthquakes, especially for those located inside the recording network. The error in focal depth determination was usually greater than that in epicentral location.

An essentially similar procedure as the above one was followed for determination of microearthquake hypocenters and origin times using data from the telemetered seismograph network. Because of larger spacings between stations the lower limit of magnitudes of locatable earthquakes was about one magnitude unit higher than that achieved by the local microearthquake surveys. High precision in hypocenter location was attained in this case due to uniform timing of all redords provided at the recording center.

CORRELATION BETWEEN MICROEARTHQUAKES AND GEOLOGIC FAULTS IN THE HSINTIEN–ILAN AREA

Twelve microearthquakes with magnitudes ranging from 0.8 to 2.1 were located in the Tatun Volcanic Region and in the Hsintien area during one-month recording between 6 February to 4 March 1974. Pertinent data of these microearthquakes are given in Table 3. The table shows that all but one of these twelve microearthquakes were located at depths shallower than 6.2 km with the only exception being at a focal depth of 9.3 km. The epicenters of these earthquakes are shown in Figure 4. According to this figure, 9 microearthquakes were located in a small area in the Tatun Volcanic Region where geothermal activities are still taking place. The remaining three microearthquakes were located in the Hsintien area. One of these three events was located between the Hsintien and Chuchih[1] faults. The two others were located southeast of the Chuchih fault and fell on the Houshaochang[2] fault which is shown in Figure 1.

During the second field survey for two months between 20 August to 14 October 1974, a total of 181 microearthquakes with magnitudes M ranging from 0.3 to 3.0 were located in the Hsintien-Ilan area. Pertinent data of these events are given in Table 4. Their epicenters are plotted on the geologic map shown in Figure 5. This figure clearly shows that occurrence of microearthquakes in the Hsintien-Ilan area is by no means random in space. On the contrary, microearthquakes tend to cluster along certain fault segments. It is this positive spatial correlation that will enable us to identify which of the geologic faults are potentially active. In the case of Ilan Plain area where fault traces have not been observed on the ground, the present microearthquake data make it possible for us to delineate the potentially active fault zone underneath the superficial layer of alluvial deposits. Specifically, the following remarks can be made with regard to the distribution of microeatrthquake epicenters in Figure 5:

(1) Two microearthquakes having magnitudes between 1.0 and 2.0 were located in the same area of the Tatun Volcanic Region where nine events were located during the first survey of microearthquakes described earlier. These microearthquakes apparently were associated with the local geothermal activities.

(2) Six microearthquakes having magnitudes smaller than 2.0 were located along a segment of the Houshaochang fault. It is remarkable that two microearthquakes were already located on this same fault segment during the earlier survey. It is thus concluded that this segment of about 15 km of the Houshaochang fault is potentially active.

(3) Approximately 15 km southeast of the Houshaochang fault there lies the Shihchao fault which is also a northeasterly trending thrust fault. There were five microearthquakes having magnitudes smaller than 2.0 located along a 30 km segment of the Shihchao fault. Accordingly, this portion of the Shihchao fault may also be classified as potentially active.

(4) Approximately 30 km farther to the southeast an elongated zone of intense microearthquake activity was found to lie between Ilan and Lotung[3]. It extends northeasterly offshore and passes by the Kueishan[4] Island a few kilometers south of it. This zone appears to be the continuation of the Median fault which is concealed

1. 屈尺 2. 火燒掉 3. 羅東 4. 龜山

TABLE 3. *Earthquakes located in the Tatun and Hsintien Areas between 1 February and 6 March 1974*

No.	Month	Day	Hr.	Mn	Sec	Lat. (N)	Long. (E)	Depth (km)	Mag
1	Feb.	06	04	23	00.5	25° 10.8′	121° 33.6′	2.6	1.6
2		07	19	11	56.8	25° 11.1′	121° 33.2′	0.7	1.1
3		08	19	32	55.3	24° 53.5′	121° 27.0′	4.4	1.8
4		09	14	27	53.4	24° 54.7′	121° 34.1′	5.6	0.9
5		09	18	11	41.4	24° 51.8′	121° 33.0′	5.3	1.7
6		14	23	09	26.3	25° 10.3′	121° 34.4′	3.0	1.5
7		20	01	17	26.7	25° 10.0′	121° 33.6′	6.2	1.9
8		21	16	35	30.6	25° 09.3′	121° 34.0′	1.0	0.8
9		21	20	35	33.5	25° 10.1′	121° 34.2′	3.3	2.1
10		23	04	03	55.7	25° 13.4′	121° 36.7′	9.3	0.8
11	Mar.	03	09	18	27.8	25° 08.9′	121° 33.3′	3.9	1.2
12		04	11	34	59.4	25° 09.5′	121° 34.2′	3.3	1.9

TABLE 4. *Listing of Earthquakes in Hsintien-Ilan Area*
(Located During 20 August to 14 October 1974)

1974	HR	MN	SEC	LAT N	LONG E	DEPTH	MAG
AUG 20	10	1	19.8	24 45.1	121 50.0	5.0	1.0
20	12	14	16.4	24 43.0	121 25.4	31.8	1.3
20	12	22	21.6	24 54.5	121 35.4	6.6	1.0
20	13	34	20.7	24 33.2	121 48.1	5.0	1.9
20	16	31	42.4	24 50.8	122 1.3	0.1	1.3
20	16	45	50.6	24 48.1	121 55.7	14.5	1.4
20	17	4	37.4	25 7.8	121 32.1	10.8	1.8
21	3	36	21.0	24 48.4	121 54.0	4.1	1.2
21	8	43	31.4	24 56.0	121 15.0	3.4	1.1
23	14	11	36.9	24 47.7	121 53.9	5.0	1.6
24	12	33	5.4	24 38.3	121 38.2	5.0	1.0
24	13	50	55.5	24 25.4	121 49.4	4.6	2.5
25	1	11	20.2	24 30.8	121 43.9	4.0	2.3
25	2	9	40.8	24 48.5	121 53.3	9.4	1.0
25	12	29	41.8	24 26.7	121 27.5	9.3	1.6
25	13	16	29.4	24 35.1	121 24.0	8.3	1.1
25	13	46	6.2	24 26.5	121 33.9	4.1	1.1
25	19	20	8.7	24 21.5	121 51.0	5.0	2.2
26	7	47	7.1	24 27.5	121 52.6	14.8	2.1
26	16	38	4.1	24 42.2	121 41.9	16.7	1.8
26	22	25	17.2	24 20.7	121 55.1	9.7	2.1
26	23	43	51.3	24 44.6	121 45.6	5.0	1.2

TABLE 4. *(continued)*

1974	HR	MN	SEC	LAT N	LONG E	DEPTH	MAG
AUG 27	7	52	34.9	24 32.0	121 51.0	10.7	1.6
27	10	19	6.7	24 26.1	121 51.8	2.4	1.3
27	11	30	58.9	24 24.5	121 54.4	4.5	1.6
27	12	55	32.7	24 25.7	121 32.0	8.7	1.5
27	13	29	54.4	24 32.8	121 21.0	11.5	2.0
27	18	18	27.3	24 32.7	121 51.1	5.0	1.5
27	19	45	27.1	24 46.7	121 52.3	4.1	1.7
27	20	15	20.6	24 48.1	121 56.3	9.2	2.3
28	0	24	20.2	24 43.2	121 44.6	20.2	1.3
28	2	21	29.1	24 44.6	121 46.5	5.0	1.3
28	5	52	40.4	24 25.4	121 49.5	5.0	1.7
28	17	58	59.4	24 30.5	121 49.5	5.0	1.7
29	0	32	2.8	24 49.8	121 37.3	2.1	0.8
29	3	20	34.2	24 23.4	121 53.0	10.0	1.8
30	3	17	9.9	24 46.6	121 46.4	0.3	0.9
30	5	36	39.4	24 24.7	121 31.3	5.0	2.0
30	7	16	30.4	24 24.0	121 30.8	5.0	1.5
30	23	54	55.3	24 38.1	121 27.2	12.4	1.3
31	3	48	19.6	24 50.1	121 57.7	5.0	1.4
31	13	23	17.2	24 36.8	121 27.7	14.4	1.4
31	15	23	35.1	24 37.9	121 26.0	12.6	1.5
31	15	25	7.5	24 38.1	121 25.8	12.6	1.4
31	18	57	48.8	24 22.3	121 31.8	5.0	1.6
31	19	54	47.5	24 48.7	121 53.6	0.5	1.3
31	21	48	1.8	24 31.5	121 49.5	6.7	1.5
31	22	39	58.4	24 48.2	122 0.1	0.8	2.0
SEP 1	2	7	10.1	24 24.3	121 31.9	9.3	1.9
1	3	30	11.4	24 52.8	121 35.4	3.1	0.9
1	4	27	0.8	24 23.5	121 53.6	14.4	2.1
1	11	30	58.5	24 28.9	121 52.4	7.6	1.9
2	14	49	32.6	24 39.3	121 35.6	37.4	2.4
2	15	45	22.1	24 53.0	121 59.8	5.0	1.6
2	20	7	32.1	24 37.0	121 40.9	8.7	1.3
2	20	9	19.0	24 36.6	121 40.6	5.0	1.1
3	10	43	47.2	24 24.7	121 31.0	3.8	1.8
3	12	48	1.5	24 32.8	121 23.9	9.4	2.0
3	13	26	56.1	24 23.2	121 31.7	0.5	2.2
4	3	47	54.7	24 34.9	121 48.5	3.0	1.4
4	20	14	48.5	24 33.4	121 23.7	11.4	1.3
4	20	24	3.9	24 32.4	121 23.3	6.1	1.8
4	20	40	21.6	24 34.2	121 22.4	5.0	1.2

TABLE 4. *(continued)*

1974	HR	MN	SEC	LAT N	LONG E	DEPTH	MAG
SEP 5	6	50	38.9	24 25.5	121 48.6	8.8	2.2
5	14	19	29.1	25 5.7	121 32.2	13.6	0.3
6	14	21	42.4	24 50.3	121 27.6	7.0	1.7
6	14	31	11.9	24 48.9	121 57.2	9.4	1.4
6	16	7	18.3	24 31.0	121 52.9	7.7	1.7
6	20	4	59.5	24 33.1	121 50.3	5.0	1.7
8	5	34	6.9	24 43.9	121 46.3	9.1	3.0
8	5	44	9.5	24 44.0	121 47.6	5.0	1.4
8	5	48	53.8	24 44.2	121 47.3	5.0	1.4
8	5	55	10.0	24 44.2	121 47.0	9.3	2.1
8	6	17	11.4	24 44.8	121 47.9	1.4	1.2
8	6	26	8.9	24 43.9	121 46.7	5.0	1.5
8	6	30	40.5	24 41.3	121 41.9	10.7	1.0
8	6	34	17.3	24 43.0	121 46.8	10.0	1.9
8	6	46	49.6	24 44.5	121 47.6	4.0	1.9
8	7	19	27.6	24 44.5	121 47.3	8.9	1.9
8	7	37	19.4	24 45.3	121 49.0	14.2	1.3
8	8	3	3.5	24 44.5	121 47.6	1.1	0.5
8	8	20	46.6	24 44.5	121 48.2	5.0	0.4
8	9	12	12.8	24 44.1	121 47.1	8.3	1.1
8	9	50	3.9	24 44.7	121 47.8	5.0	1.5
8	9	54	0.1	24 44.6	121 47.8	5.0	1.6
8	10	17	52.9	24 44.3	121 48.5	5.0	1.2
8	11	11	30.0	24 44.4	121 47.8	5.0	1.2
8	11	40	53.0	24 44.6	121 47.8	9.6	0.3
8	11	45	30.7	24 27.1	121 35.6	3.7	2.1
8	12	2	30.4	24 44.6	121 47.8	5.0	0.4
8	12	5	59.7	24 44.7	121 47.9	5.0	0.4
8	19	15	7.1	24 44.8	121 48.1	5.0	1.4
8	20	6	2.1	24 44.1	121 46.4	0.6	1.0
8	22	26	31.1	24 44.4	121 47.5	0.4	1.0
8	23	24	56.2	24 27.6	121 55.2	17.8	1.6
9	0	25	55.0	24 44.5	121 47.9	5.0	1.8
9	1	28	57.3	24 44.5	121 48.5	13.6	0.8
9	4	7	13.6	24 44.4	121 48.1	5.0	1.0
9	6	20	14.3	24 43.4	121 46.6	5.0	1.8
9	7	59	31.1	24 44.7	121 48.0	9.5	0.7
10	2	26	42.5	24 44.2	121 47.3	5.0	0.7
10	15	39	55.6	24 30.7	121 44.8	32.9	1.9
10	22	58	29.0	24 27.1	121 35.8	5.0	2.1
10	23	27	31.6	24 43.1	121 45.6	11.2	1.5
10	23	56	19.5	24 43.9	121 47.1	11.4	1.7

TABLE 4. *(continued)*

1974	HR	MN	SEC	LAT N	LONG E	DEPTH	MAG
SEP 11	6	45	20.8	24 44.8	121 47.5	8.4	1.7
11	8	22	32.5	24 43.7	121 46.5	9.4	1.8
11	8	55	23.6	24 51.6	121 58.4	8.7	1.7
11	9	27	21.6	24 22.5	121 47.4	5.0	2.1
12	8	7	23.8	24 44.2	121 47.4	8.6	1.4
12	8	24	55.3	24 45.7	121 50.2	0.3	1.0
12	12	38	28.8	24 53.8	121 32.6	4.3	0.3
12	14	20	13.0	24 26.4	121 41.7	26.5	1.3
12	18	24	47.0	24 49.4	121 52.1	3.4	1.1
12	18	53	44.3	24 43.1	121 46.1	9.4	1.4
12	19	23	9.8	24 20.8	121 53.6	6.2	1.5
13	2	23	33.9	24 44.3	121 47.3	9.4	1.5
13	7	44	59.7	24 43.7	121 46.9	9.2	2.0
13	8	21	6.4	24 43.3	121 46.3	5.8	1.6
13	9	8	46.8	24 42.2	121 46.2	17.7	0.7
13	9	19	54.4	24 42.5	121 46.0	0.6	2.3
13	9	26	48.0	24 43.7	121 46.8	7.9	0.6
13	13	40	5.1	24 25.2	121 50.1	8.9	0.8
13	15	53	51.5	24 43.6	121 46.4	9.0	1.7
13	16	25	0.0	24 39.7	121 50.7	12.7	0.5
15	5	48	27.9	24 23.7	121 49.3	9.8	2.0
15	5	49	25.3	24 24.2	121 49.6	5.0	1.7
15	6	57	26.4	24 33.5	121 51.3	20.2	1.3
15	20	7	31.8	24 32.5	121 34.7	9.2	2.4
16	13	0	38.7	24 44.0	121 46.7	5.0	1.3
16	16	53	52.3	24 48.3	121 56.1	5.0	1.7
17	16	45	32.0	24 44.9	121 50.4	8.9	1.0
20	8	47	42.4	24 43.9	121 47.1	5.0	0.9
24	17	28	0.1	24 47.0	121 52.8	5.0	2.2
24	17	29	45.5	24 47.2	121 53.0	5.0	1.8
24	23	0	42.3	24 47.3	121 53.0	5.0	1.5
25	4	7	27.7	24 47.3	121 53.1	1.6	1.8
25	4	58	31.6	24 48.1	121 55.2	5.0	2.0
25	5	10	29.5	24 48.2	121 56.1	4.1	1.9
26	7	23	57.7	24 44.3	121 47.0	5.0	1.1
26	8	0	27.6	24 35.8	121 37.3	37.0	2.5
26	17	2	17.1	24 23.4	121 26.8	9.4	1.7
26	22	6	15.8	24 46.8	121 50.7	5.0	1.6
27	19	59	29.3	24 47.9	121 53.8	5.7	1.5
29	6	22	52.1	24 43.8	121 45.1	7.5	1.2
OCT 1	2	2	15.7	24 48.6	121 54.3	9.3	1.3
1	15	42	57.6	24 26.2	121 27.0	5.0	2.1

TABLE 4. *(continued)*

1974	HR	MN	SEC	LAT N	LONG E	DEPTH	MAG
OCT 2	5	16	38.0	24 23.8	121 53.2	13.6	2.1
2	5	30	51.6	24 24.4	121 49.4	10.0	1.6
2	6	2	52.6	24 24.5	121 52.2	13.7	1.6
2	11	53	34.9	24 46.5	121 52.6	3.0	1.7
2	23	19	32.9	24 30.5	121 45.4	35.8	1.8
3	17	49	22.5	24 34.8	121 46.7	2.3	1.4
4	16	35	3.8	24 46.0	121 50.0	5.0	1.1
4	18	4	0.0	24 23.8	121 50.5	12.2	1.6
4	18	37	28.7	24 44.3	121 46.3	0.4	1.5
5	1	25	29.5	24 45.5	121 47.3	1.0	1.0
5	1	38	40.1	24 45.7	121 46.4	2.2	1.0
5	2	6	21.8	24 45.6	121 46.4	2.2	1.0
5	12	25	25.7	24 49.5	122 1.2	5.0	1.6
5	21	29	7.5	24 36.4	121 51.0	5.0	1.4
6	16	7	4.6	24 47.9	121 35.1	36.5	1.8
6	19	52	53.8	25 8.5	121 31.1	9.9	1.3
7	14	2	20.8	24 25.3	121 20.3	0.6	1.9
7	14	3	59.2	24 24.4	121 21.4	5.0	2.0
7	20	56	37.1	24 43.1	121 46.2	9.5	0.6
9	0	10	13.5	24 46.3	121 33.0	4.9	1.3
9	1	59	52.6	24 51.6	121 31.3	5.0	0.7
9	3	36	9.0	24 51.3	121 31.7	4.3	1.3
9	5	34	18.7	24 29.9	121 43.9	11.3	2.3
10	20	27	38.6	24 43.9	121 45.6	8.4	1.6
10	20	29	34.7	24 43.6	121 45.3	8.0	2.0
13	15	58	26.7	24 48.1	121 58.5	5.0	2.0
13	16	1	37.0	24 48.5	122 0.1	9.4	1.6
13	16	17	22.2	24 47.5	121 56.3	2.7	2.3
13	16	19	26.8	24 47.9	121 57.5	5.0	1.9
13	16	56	54.2	24 47.8	121 58.4	5.0	2.1
13	20	26	5.2	24 26.5	121 47.5	5.0	1.4
14	5	22	59.6	24 43.1	121 45.4	8.3	2.1
14	5	37	7.4	24 43.1	121 46.0	8.2	2.1
14	5	53	7.4	24 43.2	121 46.2	7.7	2.1

underneath the alluvial layer in the Ilan Plain area. The portion of the Median fault which lies to the southwest of the Ilan is also found to be potentially active as judged from the microearthquakes taking place on its northwestern side. It is evident that the Median fault is the most extensive and potentially the most active fault in Northeastern Taiwan.

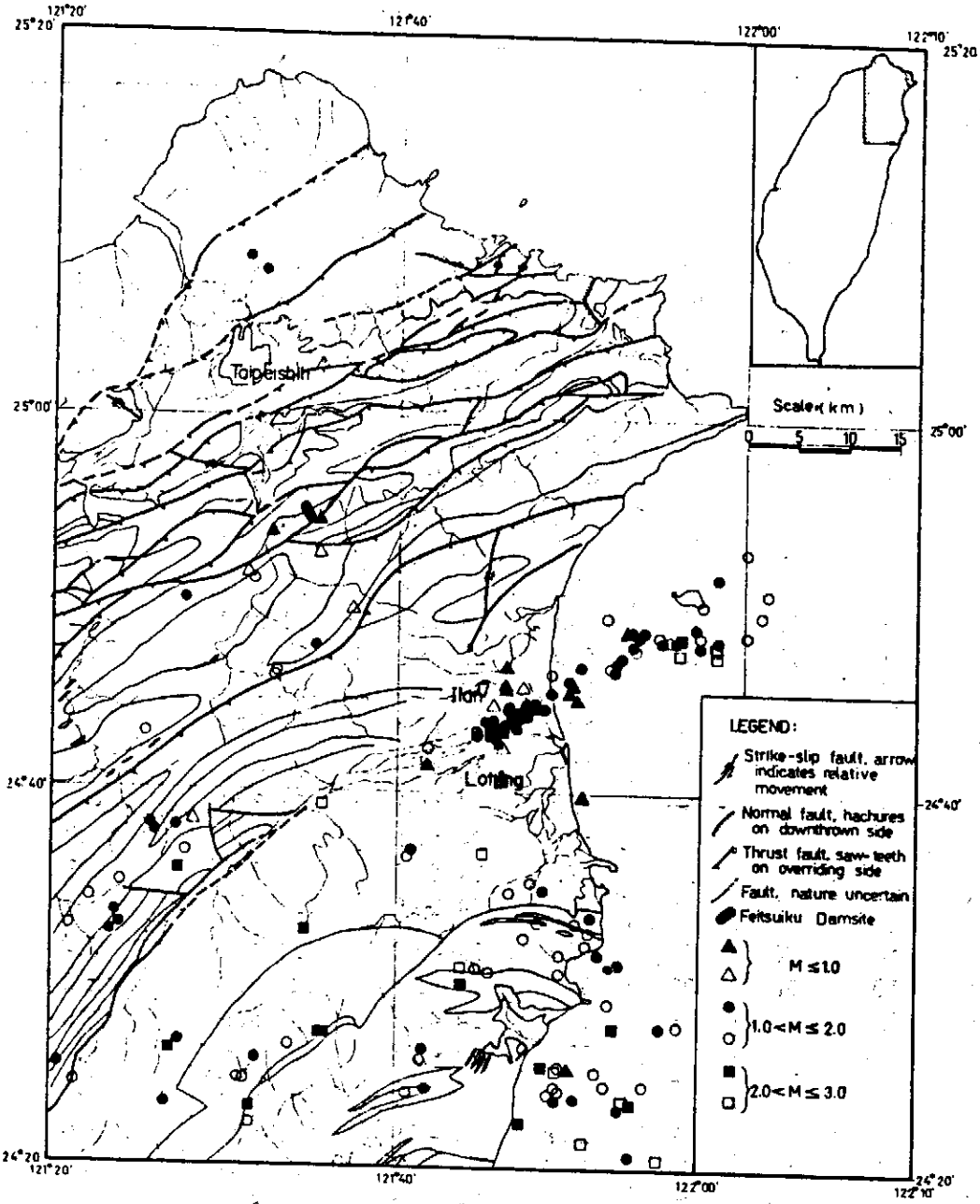

Figure 5. Epicenters of microearthquakes in the Hsintien-Ilan area (20 August to 14 October 1974).

Projections of hypocenters onto the vertical planes parallel and perpendicular to the northeasterly microeathquake zone in the Ilan-Lotung area are shown in Figure 6. These projections clearly show that the concealed Median fault extends essentially vertically downward from the ground surface to a depth of about 20 km.

(5) South of the Ilan Plain there lies the Pre-Tertiary metamorphic belt of Tananao Schist. The microearthquake activity in this area was found to be rather diffused.

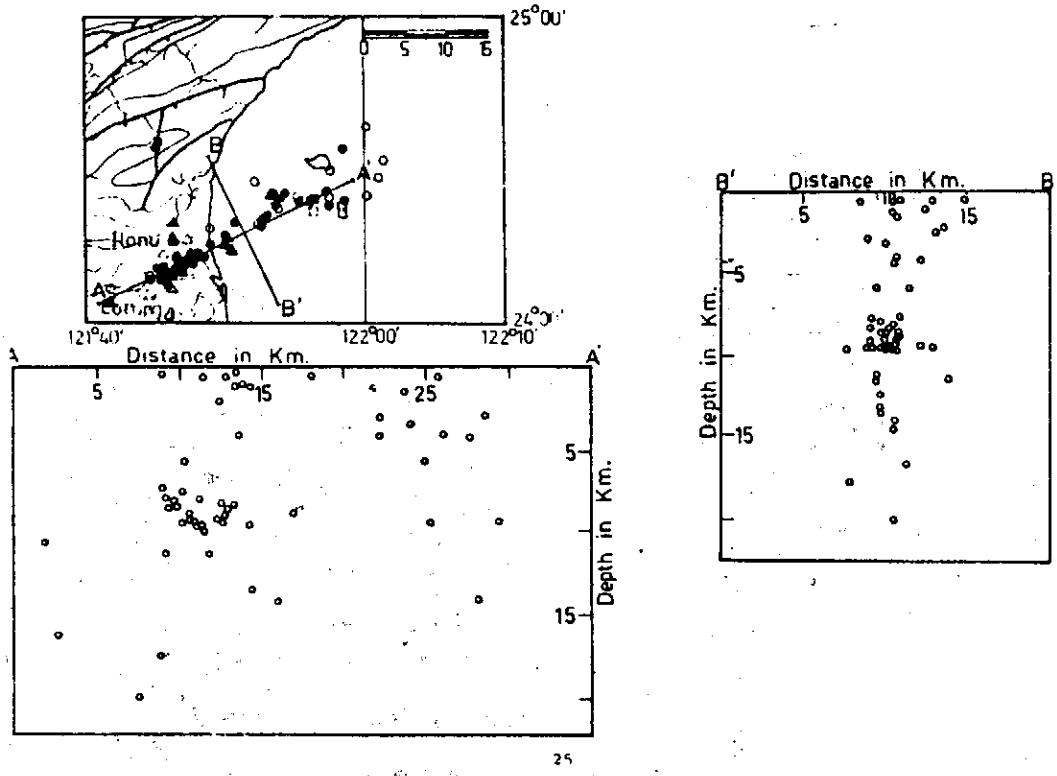

Figure 6. Vertical distribution of microearthquake foci in the Ilan area.

Meanwhile, the fault traces in this area have not been well recognized. Thus, it is difficult to correlate between these two phenomena. Nevertheless, there should be no doubt that the area is seismically active.

(6) Unlike the area southeast of the Houshaochang fault, the area northeast of it is marked by a total absence of microearthquakes even though there are numerous known thrust faults in the area. This appears to suggest that the geologic faults lying between Hsintien and Taipei may be more stable than those lying between Hsintien and Ilan.

The third set of earthquake data was obtained by means of the islandwide telemetered network of twenty S–P seismograph stations maintained by the Chinese Earthquake Research Center. The epicenters located during the first three months of 1975 are illustrated on the new geologic map of Taiwan (Ho, 1975) as shown in Figure 7. The spatial distribution of these earthquakes having magnitudes between 2.0 and 4.0 further reinforces the remarks made previously when the microearthquake data gathered by the temporary seismograph stations were discussed.

The discovery of a potentially active subsurface geologic fault in the Ilan Plain obviously has very important practical as well as academic implications. Prior knowledge of the whereabout of this fault can be utilized in land-use planning to minimize seismic hazards of the Ilan Plain, especially of the Ilan-Lotung area. Academically, the existence of this fault shows that the Median fault which bisects longitudinally the whole length of Taiwan into halves actually extends northeastward through the Ilan Plain and continues into the offshore area beyond the Kueishan Island. It appears to join the boundary between the Okinawa Trough and the Ryukyu Folded Zone, as illustrated in Figure 8. Two additional telemetered seismograph stations are being

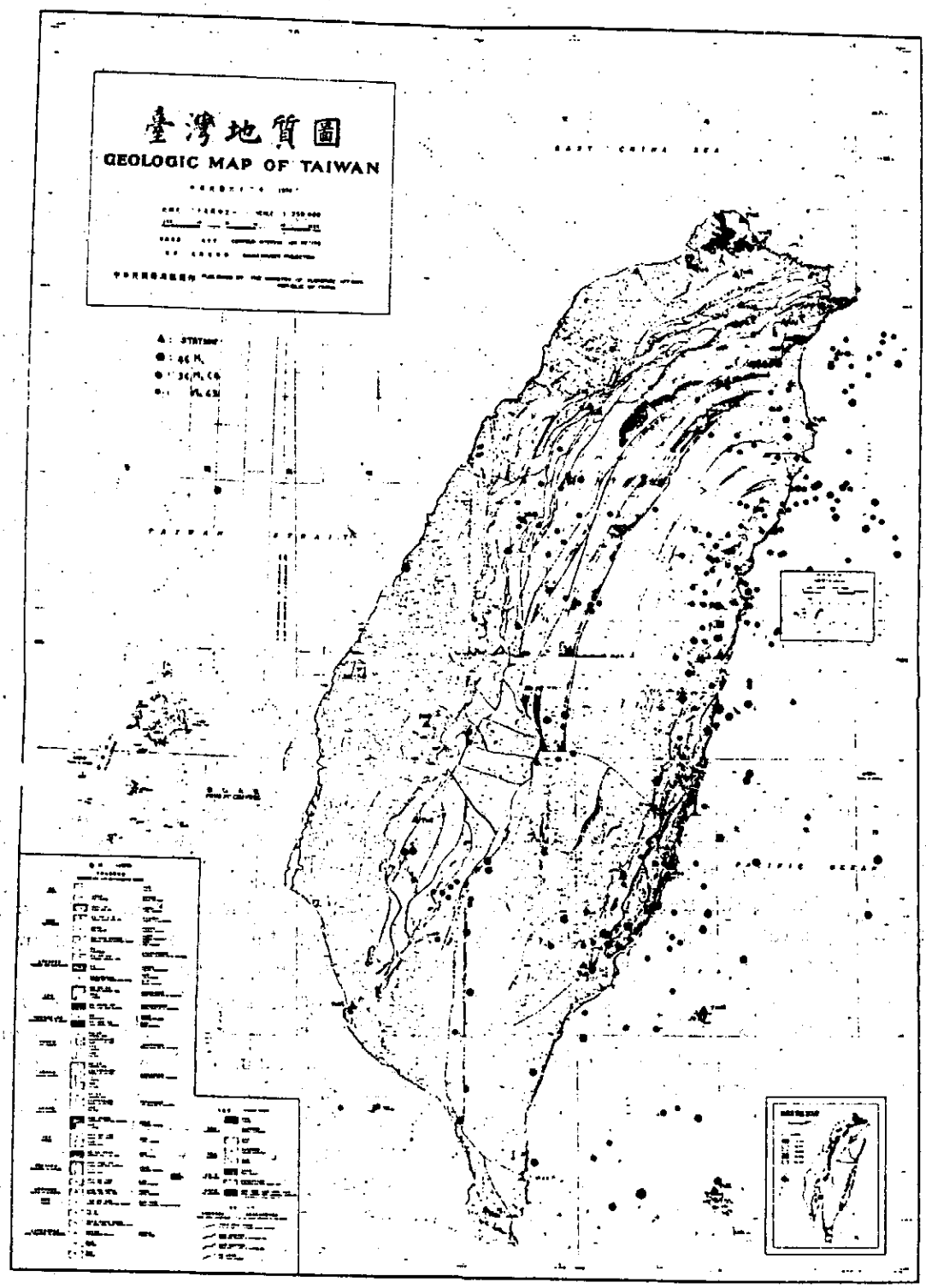

Figure 7. Epicenters of earthquakes in Taiwan (January - March 1975).

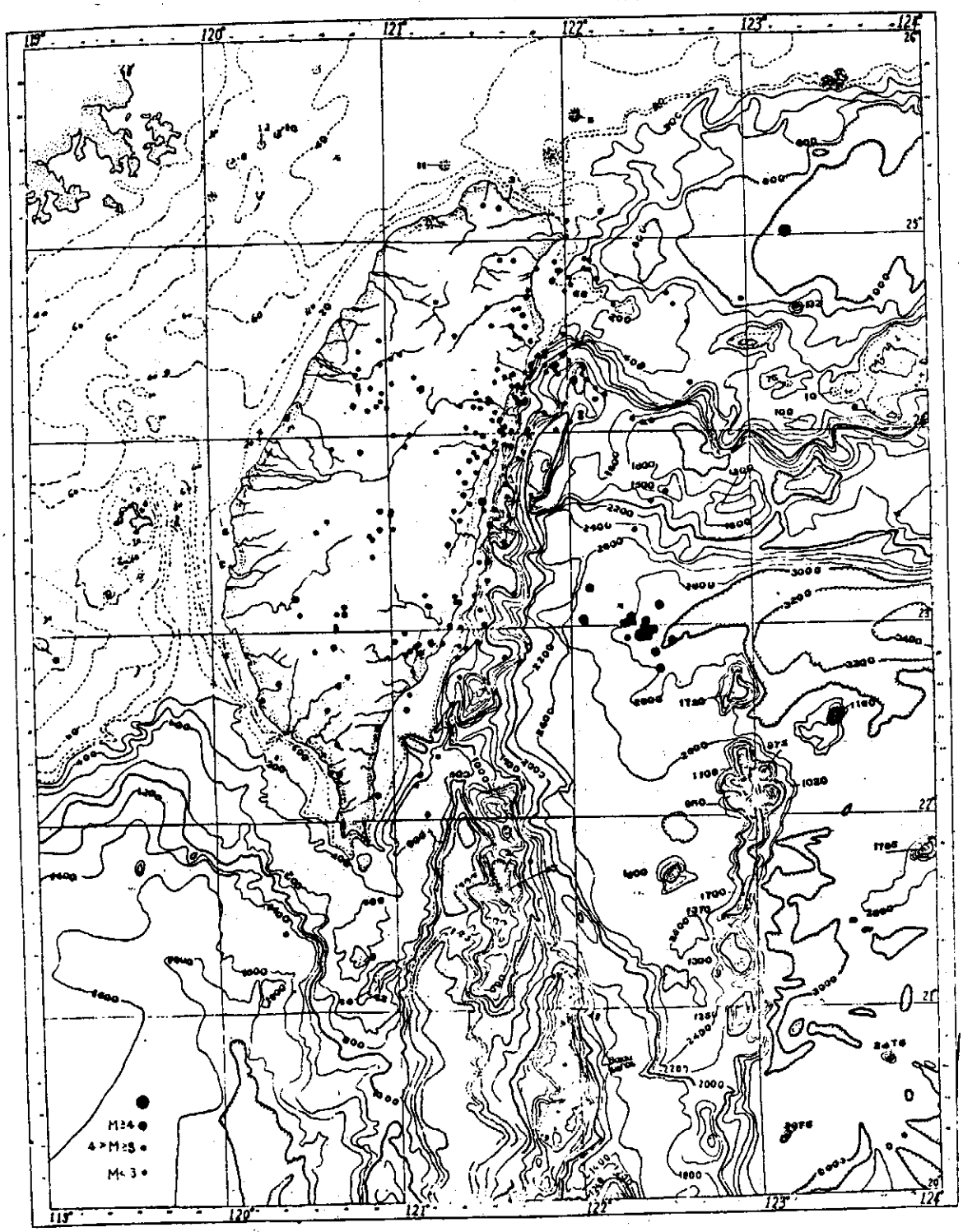

Figure 8. Epicenters of earthquakes in Taiwan and its vicinity (January-March 1975).

installed in the Ilan area to facilitate a long-term monitoring of the microearthquake activity along this fault. It is hoped that additional high-quality data will enable us to understand the tectonic environment of this area. It is also interesting to point out from Figure 8 that a trend of earthquake epicenters extends southeasterly from the Tananao Schist Formation offshore into the Pacific Ocean. This trend seems to coincide with the southern boundary of the Ryukyu Folded Zone.

ACKNOWLEDGMENTS

We thank Messrs. Y. S. Cheng, S. Y. Chen, C. C. Hsu and P. H. Kao for their assistance in the field operations. The study was supported partly by the National Science Council and partly by the Taipei Area Water Supply and Sewerage Development Commission.

REFERENCES

Eaton, J. P., 1969, Hypolayr - a computer program for determining hypocenters of local earthquakes in an earth consisting of uniform flat layers over a half space: *U. S. Geological Survey*, Open File Report, 155 p.

Ho, C. S., 1975, Geologic Map of Taiwan (1:250,000); The Ministry of Economic Affairs, Republic of China.

Hsu, M. T., 1971, Seismicity of Taiwan and some related problems, Bulletin of International Institute of Seismology and Earthquake Engineering, v. 8, p. 41-160.

Lee, W. H. K. and J. C. Lahr, 1972, HYPO71 - a computer program for determining hypocenter, magnitude and first motion pattern of local earthquakes, *U. S. Geological Survey*, Open File Report, 100 p.

Tsai, Y. B., T. L. Teng, Y. M. Hsiung and C. M. Lo, 1974, New seismic data of Taiwan region: *1973 Annual Report of the Institute of Physics, Academia Sinica*, 223-238.

CORRELATION BETWEEN MICROEARTHQUAKES AND GEOLOGIC FAULTS IN THE HSINTIEN-ILAN AREA

新店—宜蘭地區微震活動與斷層之關係

蔡義本　馮至津　邱哲明　廖鴻彬

節　　要

本文根據微小地震之震央分佈以研判新店—宜蘭地區活性斷層之位置。所使用之資料包括：(1)民國六十三年二月六日至三月四日以九部可攜型地震儀在新店—大屯山地區所測定之12次微震。(2)民國六十三年八月二十日至十月十四日以十九部可攜型地震儀在新店—宜蘭地區所測定之181次微震。及(3)民國六十四年一月一日至三月三十一日由中央研究院全省測震系統所測定，發生於新店—宜蘭地區約六十次之地震。根據這些經準確測定之微震震央位置即可發現可能有下述數條活性斷層潛伏於新店—宜蘭地區：

1. 大屯火山區之微震活動集中於地熱現象較顯著地帶附近之斷層上。
2. 東北—西南走向之大燒樟斷層自大燒樟以南約十五公里長之一段可能是活性斷層。
3. 位於新店與宜蘭之間另一東北—西南走向之石碇斷層自石碇以南約三十公里長之一段可能是活性斷層。
4. 在宜蘭與羅東之間新發現有一近乎垂直而深度不超過二十公里之活性斷層。這一斷層自宜蘭平原向東北延伸入海通過龜山島南方而與琉球褶皺帶之北緣相銜接，它顯然是將臺灣縱分為東西兩半之中斷層之延長，也是新店—宜蘭地區最具活性的斷層。今後宜蘭及羅東地區之發展與建設應顧及此一斷層可能引起大地震之潛在威脅而採取適當之對策。
5. 位於宜蘭平原南方之大南澳片岩地帶之微震震央較分散，同時地質資料亦較不詳，因此目前尚無法判研本地區之斷層位置。不過值得注意的乃是本地區之微震活動不但頻繁而且顯有向東南延伸進入太平洋而與琉球褶皺帶之南緣相銜接之趨勢。
6. 位於臺北與新店之間的數條斷層均未發現有微震現象，這可能表示此一地帶之斷層較上述新店—宜蘭之間的斷層為穩定。

ANNUAL REPORT OF THE INSTITUTE OF PHYSICS,
ACADEMIA SINICA, 1974

Gas Well Pressure Fluctuation as an Earthquake Precursor

FRANCIS T. WU

Department of Geological Sciences, Binghamton, New York State University

and

C. C. FENG

Academia Sinica

ABSTRACT

A significant rise in well head pressure in Niushan gas field was detected 9 days prior to the Tainan-Chiayi earthquake (January 18, 1964; 0:12:04:40.0 GMT, Magnitude 6.3 depth = 18 km). This phenomenon may relate to the opening of cracks in the reservoir during the accelerating creep stage of the earthquake and may be used for prediction.

INTRODUCTION

Changes in water level, flow rate, radon emission in water well electrical resistivity, Vp/Vs ratio together with other observations such as changes in tilts, elevation, creep rate, seismicity etc. were found to preceed earthquakes. While changes in tilts, elevation, creep rate, and so on relate obviously directly to the strain of the ground, changes in water level, flow rate, etc. involve the motion of water through the strained medium. Theories have recently been advanced to explain all these observations. In general there are two schools, one school requires the flowing of water in and out of the system; the other allows the presence of water but does not require significant water flow. Both schools however require the opening and closing of cracks (most probably in the form of joints). Scholz *et al.* (1973) and, Nur (1972) among others are proponents for the "wet" theory. The "dry" theories have been advanced by W. Stuart and B. Brady in U.S.A. and Myachkin in Russia; but not much has been published as yet.

The precursors mentioned above have been widely accepted as "long term" precursory phenomena. The type of changes and their time scale are shown in figures 1a and 1b. Although more drastic changes in some of these together with less orthodox observations such as the barking and migration of animals and lightening are mentioned as possible short term precursors, with time scale far shorter than the straight line in 1b predicts (Fig. 1c). Both types of precursors are useful. Thus long term precursors can be used for long term planning while short term precursors are useful for final emergency purposes.

At this stage, geophysicists are searching for more observations to include in a more comprehensive theory and to use as practical means for prediction. One single observation may not mean much but with several others we may increase our confidence in the prediction.

* This paper has been published in Petroleum Geology of Taiwan No. 12, p. 141–148, 7 Figs., June 1975.

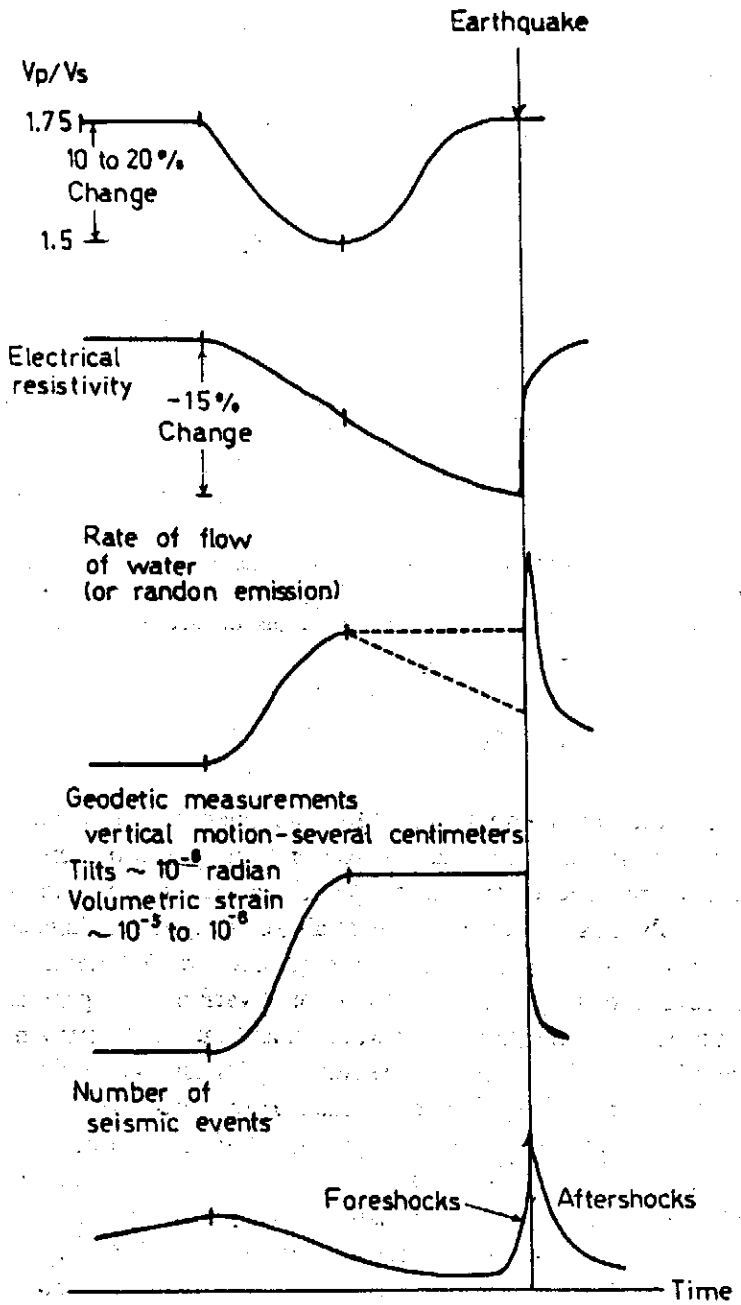

Figure 1a. Schematic earthquake precursors (after Scholz *et al.*, 1973).

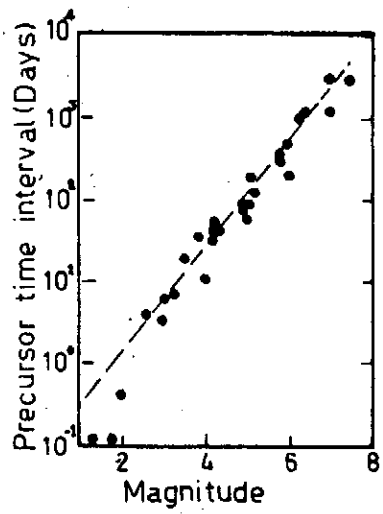

Figure 1b. Magnitude-duration relationship for long-term precursors.

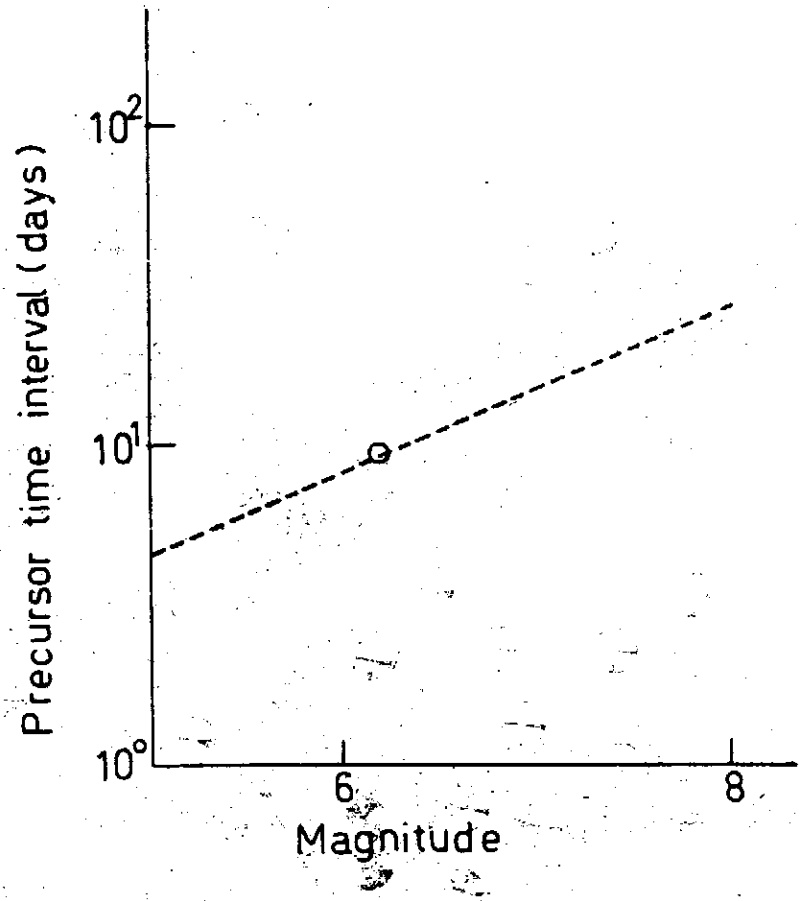

Figure 1c. Schematic magnitude-duration relation for short term precursors.

Oil or gas production data in the vicinity of hypocentral zone are obvious candidates for earthquake precursor studies. The reservoir permeability is likely to be affected by the regional strain and the results may be recorded routinely as pressure fluctuations of a gas well & the production rate of a gas or oil well. Lacking the need to be precise the recorded data may not be always usable. One has to screen the data carefully. Here we are describing a clear example of pressure change in three wells in a gas field prior to the 1964 Tainan[1]-Chiayi[2] earthquake, It is hoped that such an example will lead to awareness in the future of such changes in the ever expanding oil and gas production areas. Especially when earthquake safety is important to the drilling platform in the ocean, or production facilities on land.

DATA

Figure 2 indicates the location of the gas fields we have studied, the earthquake epicenter and the possible causative fault. The area that sustains substantial damage is also shown. Niushan[3] and Chutouchi[4] gas fields are the only two production field in this area between 1957-1970.

1.臺南 2.嘉義 3.牛山 4.竹頭崎

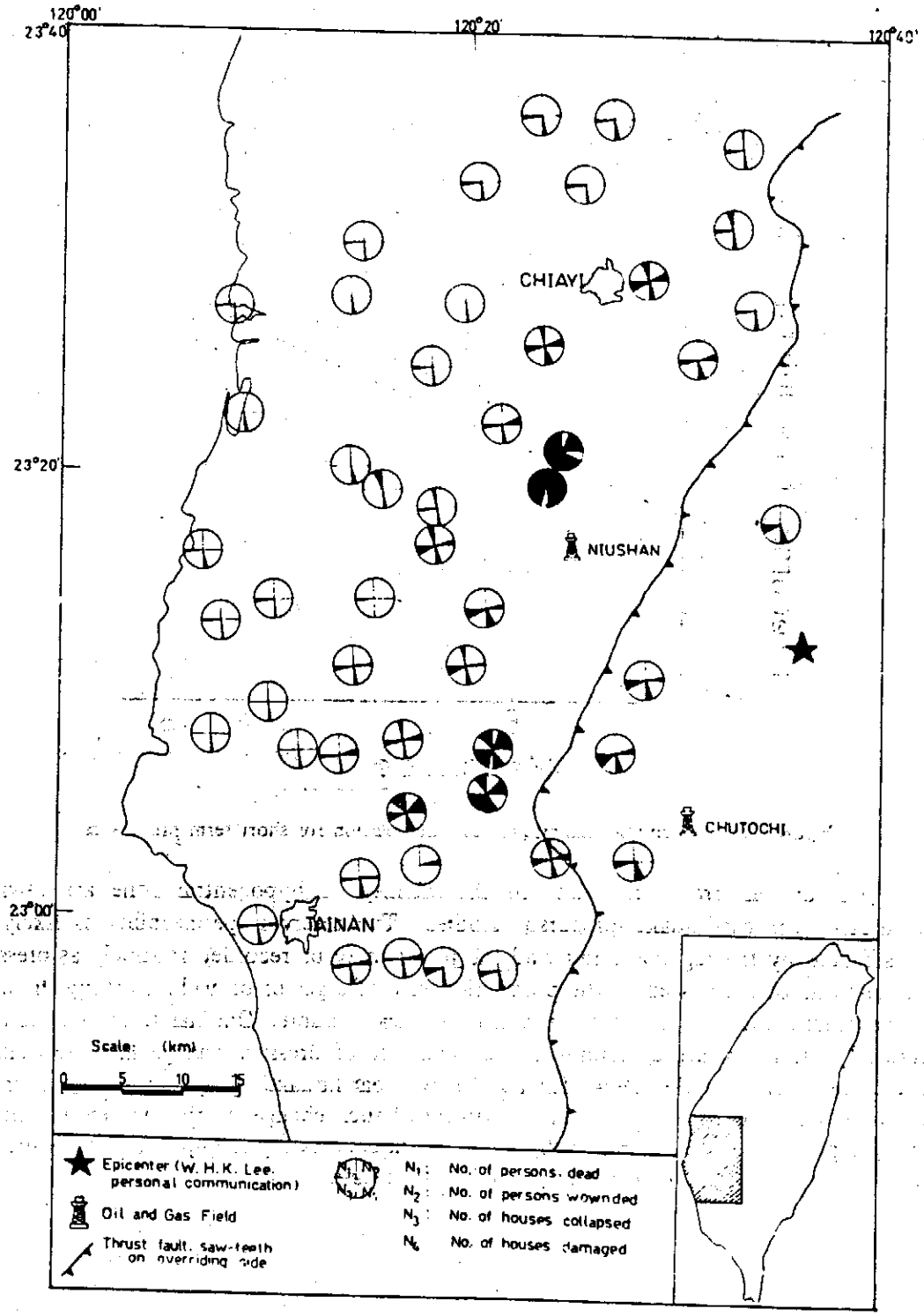

Figure 2. Location map for the gas fields, earthquake epicenter, possible causative fault (Chukou fault), and damage areas. The shaded areas in each quadrant is proportional to the normalized (to the maximum) of the damage figures. Notice that population concentration is much higher to the west of the fault than to the east.

Of the more than 10 wells in Niushan gas field, only three wells are not pumped. Pumped wells are not useful for our purpose because of the artificial regulation imposed by the pump. For all the wells, the production rate at each well (in terms of km^3/day) was found not to be dependable; apparently the total production of the field recorded at one gauge was usually distributed to each individual wells in an approximate manner.

The pressure readings at each well has a high and low everyday related to the presence of water in the well and the resulting bubbling of gas in the well. The long term stability of these readings is usually within $\pm .1$ kg/cm^2, although occasionally at one well the pressure may double the ordinary value. On January 10, 1964, the pressure at all three unpumped wells showed a sudden increase in pressure (Fig. 3). The pressure stayed high, with some variations until January 18, when the Tainan-Chiayi earthquake took place. Subsequently the surface pipings were damaged and these wells were left to exclude by themselves while the pumped wells were shut off; and the pressure dropped from more than 1.2 kg/cm^2 to 0.1-0.3 kg/cm^2. After the pipes were repaired the pressure at two operating wells returned to values prior to January 10.

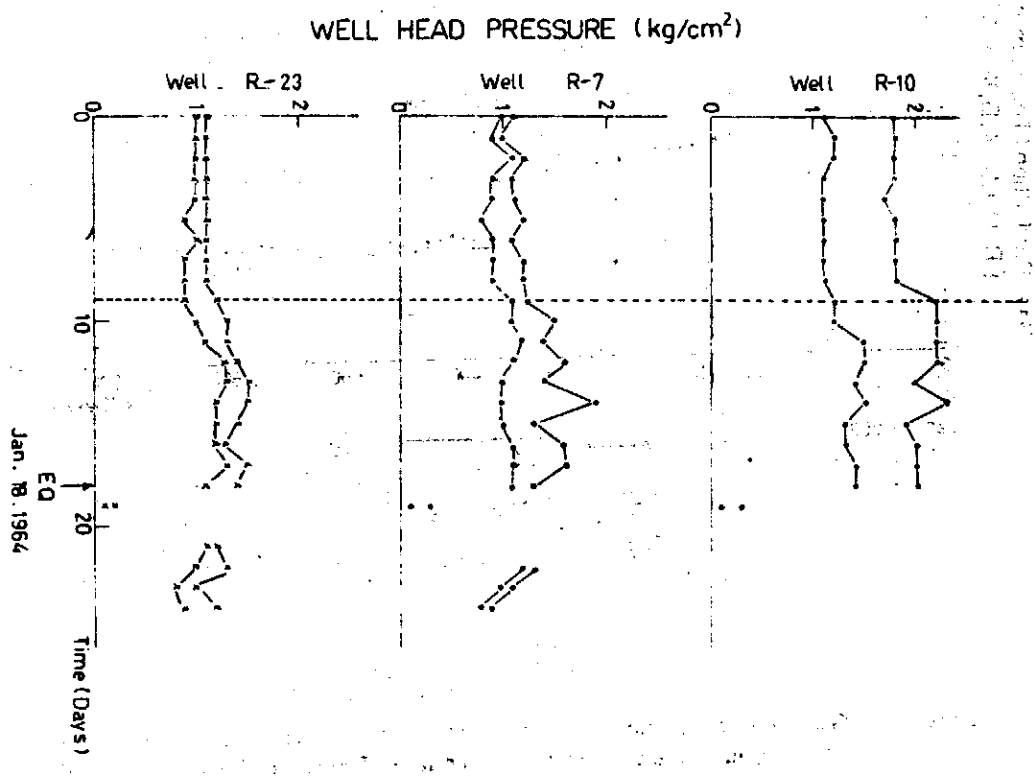

Figure 3. Pressure fluctuations in three self-exuding wells in Niushan gas field. There are two readings at each well every day, representing the maximum and minimum values. Values immediately after the earthquake may be caused by open flow in the pipe resulting from broken surface pipings.

Apparently, the rise in pressure in all three wells is precursory to the January 18 earthquake.

We have tried to collaborate this result with wells in Chutouchi field. There are altogether three continuously producing wells and one intermittently producing well. The pressure reading and the production rate data only showed slight changes during the period of January 1 to January 18. We then looked at the production rate data/10 days beginning from January 1, 1963 (Fig. 4). A slight drop had been observed starting from 1963 up to the time of the earthquake, the trend then steadied itself. Notice the DC offset before and after the earthquake; it is caused by the stoppage of one of the wells. Since the wells were tapping the same reservoir, the production of the remaining two wells increased but never reached the level with three wells.

Although Chutouchi result does not match that from Niushan, it may not be surprising as we shall explain in the next section.

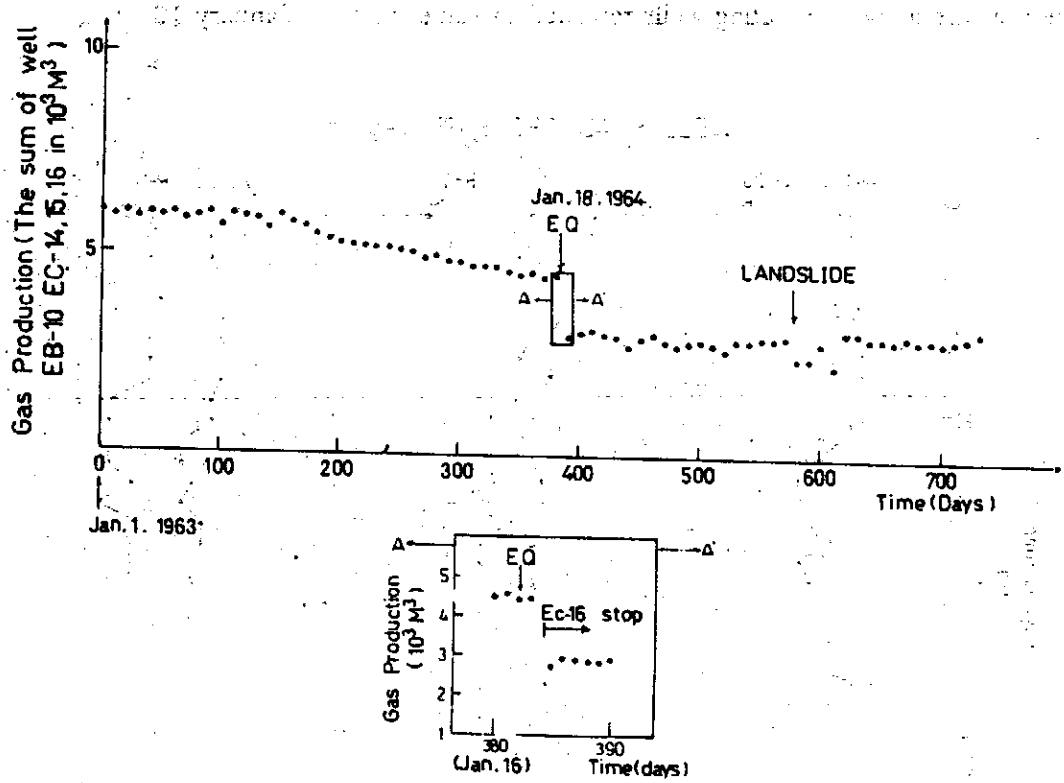

Figure 4. Gas production rate (km^3/day) at Chutouchi gas field. Inset shows details around the time of the earthquake. During the landslide, the wells were temporarily shut off.

DISCUSSION AND CONCLUSION

From the Niushan data we are hopeful that we have found a short term precursor for a magnitude 6.3 earthquake. The absence of an identical feature for wells in the Chutouchi field can perhaps be explained by the fact that these two fields are on two

different sides of the possible causative thrust fault, the Chukou[1] fault, and are therefore under different stresses (Fig. 5). On the Chutouchi side the reservoir may experience compression in the vertical and EW directions while on the Niushan side, tension prevails in the same directions. During the final accelerating creep stage of the fault, the fractures in the Niushan reservoir were opened under tension. Also, Chutouchi field is more distant from the section of maximum activity as shown by the damage data in Figure 2.

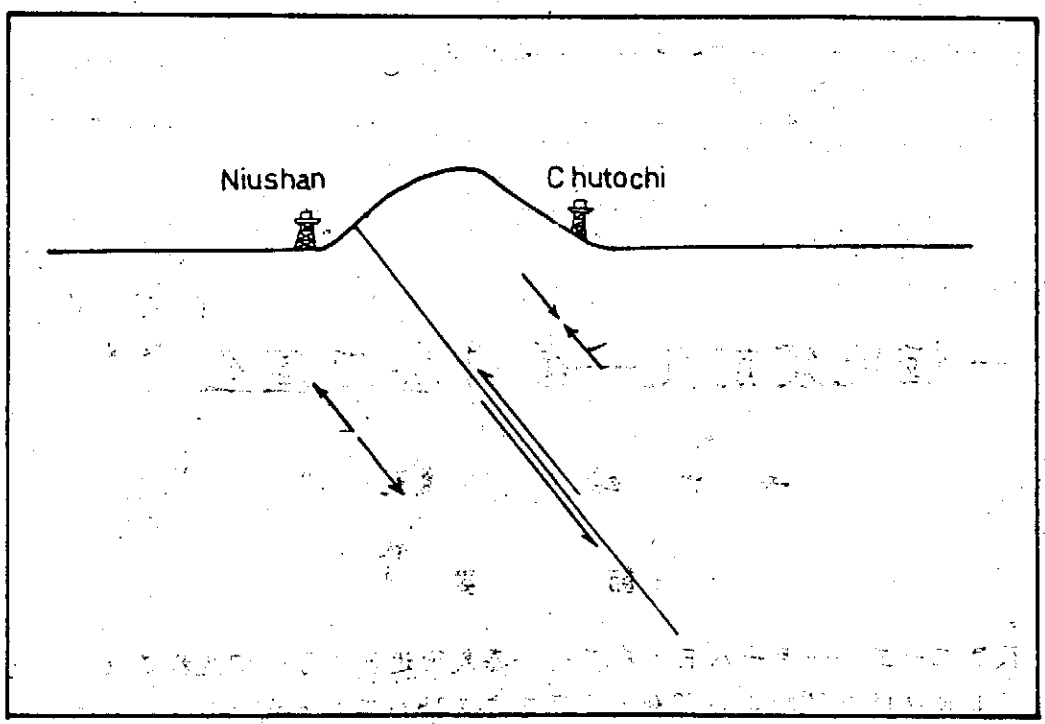

Figure 5. Direction of motion and maximum compression in the vicinity of Chukou fault prior to the earthquake.

It is unfortunate that both fields are now suspended, consequently they cannot be used for earthquake prediction purposes in the future. The other large earthquake on the island occurred north of Taichung[2]. Both Chinshui[3] and Chuhuangkeng[4] fields might be monitored for future prediction.

In many other countries in the world earthquakes and oilfields coexist. Such work should be carried out there.

Chinese Petroleum Coporation (CPC) is contemplating telemetering its well data to a central location. During this major modification, it can perhaps be taken into consideration that such data are useful for purposes other than production monitoring.

ACKNOWLEDGMENTS

This work was carried out in Taiwan while the senior author is supported by an United States NSF grant OIP-75-02712. The authors wish to specially thank Dr.

1.烏口 2.竪中 3.錦水 4.出磧坑

C. Y. Meng, Mr. T. M. Wu, Mr. H. T. Chiu, Mr. C. H. Tang and Mr. C. F. Huang of CPC for their generous assistance in many aspects of the work.

The hospitality of Dr. Yi-Ben Tsai, Director of Seismology Division, Institute of Physics, Academia Sinica is much appreciated.

REFERENCES

Nur, A., 1972, Dilatancy, pore fluids, and premonitory variations of t_s/t_p travel times, *Bull. Seism. Soc. Amer.*, no. 62, p. 1217.

Scholz, C. H., Sykes, L. and Aggarwal Y. R., 1973, The physical basis for earthquake prediction, *Science*, no. 181, p. 803-810.

一個地震前兆—氣井壓力產生變化

吳 大 銘　　馮 至 津

節　　要

民國五十三年一月十八日，在臺南—嘉義附近發生了一個規模為 6.3 的地震（格林威治時間12時4分40秒，震源深度為18公里）。我們發現，在這個地震發生的前九天，牛山氣田氣井的井口壓力有顯著增加的現象。這個現象可能是由地震發生前斷層帶加速滑移，引起氣層附近裂隙影響造成的。由是推之，觀測氣井壓力的變化亦可能用於預測地震。

ANNUAL REPORT OF THE INSTITUTE OF PHYSICS,
ACADEMIA SINICA, 1974

A Study of Microearthquakes in the Miaoli-Fengyuan Area in Central Taiwan

Y. M. Hsiung and Y. B. Tsai

Chinese Earthquake Research Center
Institute of Physics
Academia Sinica

I. Introduction

Several long highway bridges will be built in the next few years in the Miaoli-Fenguyan area in Central Taiwan as parts of the North-South Freeway Construction Project. Since the area is known as one of the most active seismic regions in Taiwan, an investigation of potential seismic hazards is highly desirable so that appropriate earthquake-resistant measures may be incorporated in the design and construction of these bridges. The Chinese Earthquake Research Center was entrusted to make such an investigation in late 1973. This article reports the results from a part of the investigation which involved observations of microearthquakes in the area for eight weeks.

The Miaoli-Fenguyan area in Central Taiwan as referred to in this article is meant to cover an area north of $24^{\circ}00'$N, south of $24^{\circ}50'$N, west of $121^{\circ}00'$E and southeast of the northeasterly trending coastal line of western Taiwan. According to past earthquake data shown in Figures 1 and 2 it is evident that the area was seismically active. In particular, a magnitude 7.1 earthquake on 21 April 1935 plus a series of strong aftershocks killed 3276 lives, injured 12053 persons, destroyed 17907 homes and damaged 36781 houses in the area. In fact, this sequence of earthquakes caused more fatality and property loss than any other past earthquakes in Taiwan. Besides, the 1935 earthquake also left a number of surface faulting traces

totalling several tens of kilometers. Moreover, according to geologic maps published by the Chinese Petroleum Company (1971) and by the Ministry of Economic Affairs (1974), several faults are known to exist in the area. The locations of all these faults are shown in Figure 3. The recent microearthquake study was primarily intended to identify which of these faults would be potentially active.

II. Field Operations and Data Analysis

Field recordings of microearthquakes in the Miaoli-Fengyuan area were made for eight weeks. Because the study area was elongated in the north-south direction, it was decided to carry out the field operations in two stages. The first stage covered the Miaoli area for four weeks starting on 17 October 1973. Then followed the second stage of recordings in the Fengyuan area beginning on 13 November 1973. In each stage six temporary seismograph stations were deployed to form a network covering the area under study. In total, eleven stations were established with a common station operating through-out the eight-week recording period. The coordinates of these stations are given in Table 1. The locations of these stations are further shown in Figure 3. The common station was situated in Sanyi between the northern and southern areas.

Each station was equipped with a short-period vertical seismometer, a smoke-paper drum recorder, a chronometer and a pack of batteries for power supply. normally, the internal timing of each temporary seismograph was checked with the standard time broadcasting at the beginning and the end of each seismogram so as to put the whole network on a common time base. A block diagram for the portable seismographs used in the present study is shown in Table 2.

In order to determine the hypocenter, origin time and the magnitude of an earthquake, the first arrival times of P and S waves and the total signal durations were read from the records collected at

different stations. In most cases a high precision of 0.05 second was attainable in reading the P-wave first arrival times. On the other hand, readings of the S-wave first arrival times were significantly less precise than the P-wave readings. The arrival times were subsequently fed into the computer program HYP071 which determined the hypocentral coordinates and the origin time of the earthquake by minimizing the residuals between the observed and the expected arrival times by the Geiger's method (Eaton, 1969; Lee and Lahr, 1972). The expected travel times from a trial hypocenter to individual recording stations and the associated partial derivatives of travel times were calculated by assuming a horizontally layered crustal model. The crustal model used for the present study is given in Table 3.

Finally, the earthquake magnitude M is determined according to the following formula:

$$M = -0.87 + 2.0 \log \tau + 0.0035 \Delta$$

where τ represents the total signal duration in seconds and Δ is the eipcentral distance in kilometers. Most events located during the eight-week recording period had magnitudes smaller than 3.0.

Because a minimum of four simultaneous readings of P-or S-wave arrival times were required for an earthquake to be locatable, the number of actually located earthquakes was somewhat less than the number of recorded events at individual stations.

The error in epicentral location was believed to be less than 2.0 kilometers, especially for earthquakes located inside the recording seismograph network. The error in focal depth determination was usually greater than that of the epicentral location. The results from the present survey are discussed in the following section.

III. Microearthquakes in the Miaoli-Fengyüan Area

A total of 100 microearthquakes were located during the eight-week recording period. The epicenters of these events are shown in Figure 3. Also shown in the same figure are the epicenters of the main shock and aftershocks of the 1935 sequence. It is seen from this figure that by and large current microearthquake activity takes place in those areas where the epicenters of the 1935 earthquake sequence were located. One notable exception was the area about five kilometers to the south of the 1935 main shock epicenter. The area happens to locate on the southward extension of the northern branch of the 1935 earthquake fault. Clustering of microearthquakes in this area suggests that crustal stresses may be building up there.

In order to determine the nature of faulting mechanisms of these microearthquakes, we divide them into four groups. Group A consists of 38 microearthquakes located within a narrow stripe running in the north-south direction. The stripe is bounded from $24^{\circ}10'$N to $24^{\circ}30'$N and from $120^{\circ}45'$ to $120^{\circ}50'$. Group B includes 23 microearthquakes along the southwestern branch of the 1935 earthquake fault zone. Group C includes 13 microearthquakes in the area northeast of the 1935 main shock epicenter. Group B and C form a northeasterly trending linear zone intersecting the northerly trending zone of Group A near the 1935 main shock epicenter and at an angle of about 60°. Finally, Group D consists of six microearthquakes centering at $24^{\circ}34'$N and $120^{\circ}43'$E. Before discussing the composite fault-plane solutions of these four groups of microearthquakes, a composite fault-plane solution of the 1935 earthquake sequence based on the polarities of P-wave initial motions is presented first in Figure 4. This fault-plane solution represents a right-lateral strike-slip fault trending in the N64°E direction, consistent with the southwestern branch of the 1935 earthquake fault. Now let us look into the composite fault-plane solutions of the four groups of microearthquakes observed in the present study. Figure 5 shows the composite fault-plane solution of Group A events. It is somewhat similar to the

one shown in Figure 4. However, the northwesterly striking nodal plane is favored for representing the actual fault plane because the events were located in a narrow north-south Band which is coincident with a continuous section of ground breakage followed by the 1935 earthquake sequence. Thus, the northwesterly-striking left-lateral fault might be considered as a conjugate fault of the 1935 earthquake fault. The composite fault-plane solution for the Group B events as shown in Figure 6 is almost identical to the one shown in Figure 4. Therefore, Group B events can be definitely associated with north-easterly striking right-lateral strike-slip Tuntzuchiao fault of the 1935 earthquake. Figure 7 shows the composite fault plane solution of the Group C events which is in direct contrast to all other four fault-plane solutions obtained in this study. If we take the north-easterly-striking nodal plane as the fault plane, then the sense of faulting would be left-lateral which is just opposite to that of Group B. This is rather difficult to comprehend, but erratic change of fault-plane solutions of microearthquakes in small areas has been elsewhere in Taiwan. Finally, Figure 8 represents the composite fault-plane solution of the six events in Group D which were located in the northern-most part of the Miaoli-Fengyuan area. It is again similar to that of the 1935 earthquake fault. These microearthquakes and the several shocks of the 1935 earthquake sequence seem to cluster along the two faults known in the area. From the present fault-plane solution we may infer that these faults are likely right-lateral strike-slip faults.

IV. Conclusions

A survey of microearthquakes in the Miaoli-Fengyuan area in central Taiwan was made for eight weeks in late 1973. A total of 100 earthquakes with magnitude greater than 0 were located. Most of these microearthquakes took place in the areas where the after-shocks and the surface faulting traces of the 1935 earthquake (M=7.1)

were located. The area south of the epicenter of the 1935 main shock was an exception. A group of microearthquakes were located in this area where no aftershock or surface faulting trace was observed previously. Since the area is located right on the southward extension of the northern branch of the 1935 earthquake fault, it is likely that crustal stress may be building up there.

Four composite fault-plane solutions based on polarities of the P-wave initial motions due to the observed microearthquakes were obtained. Three of them were found to be similar to the composite fault-plane solutions of the 1935 sequence of earthquakes. Among these three, two are inferred to represent right-lateral strike-slip faults striking in the northeast direction. The third one is inferred to represent a left-lateral strike-slip fault trending in the north-northwest direction. Finally, the fourth fault-plane solution which is opposite to the other three is inferred to represent a left-lateral strike-slip fault trending in the northeast direction extending to the northeast from the epicentral area of the 1935 main shock.

Acknowledgement

We thank Messrs. W. S. Liu, S. Y. Chen and T. K. Lee for their assistance in the field operations. The study was supported partly by the National Science Council and partly by the Taiwan area Freeway Construct n Bureau.

Reference

Hsu, Ming-Tung, 1971, Seismicity of Taiwan & some related problems, Bull. Intern. Inst. Seismol. and Earthq. Eng. Vol. 8, p. 41-160.

Lee, W.H.K. and J.C. Lahr, HYP071; a computer program for de-

termining hypocenter, magnitude, and first motion pattern of Local Earthquakes, U. S. Geological Survey, Open File Report, 100 p., 1972.

Geiger, L., Probability method for the determination of earthquake epicenters from the arrival time only, Bull. St. Louis Univ., 8, 56-72, 1912.

Chinese Economic Affairs, Geological map of Taiwan, 1974.

Taipei Seismic Observatory, Shinchu-Taichung Earthquake Report, 1936.

Table 1 Station Data

Station	Site	Latitude (N)	Longitude (E)	Gain db
1	Yenghuikeng	120° 53.53'	24° 29.23'	72
2	Sun Yi	120° 45.83'	24° 24.62'	72
3	Wumeikeng	120° 42.82'	24° 30.96'	66
4	Mirgdechun	120° 52.22'	24° 35.00'	66
5	Chinshuichun	120° 52.12'	24° 38.07'	66
6	Nanchuang	120° 59.51'	24° 36.04'	72
7	Shihshuikeng	120° 50.28'	24° 18.66'	66
8	Nan Shi	120° 42.32'	24° 22.07'	66
9	Hou Li	120° 44.50'	24° 18.50'	66
10	Kechuang	120° 36.88'	24° 18.43'	66
11	Peikeng	120° 45.85'	24° 10.41'	66

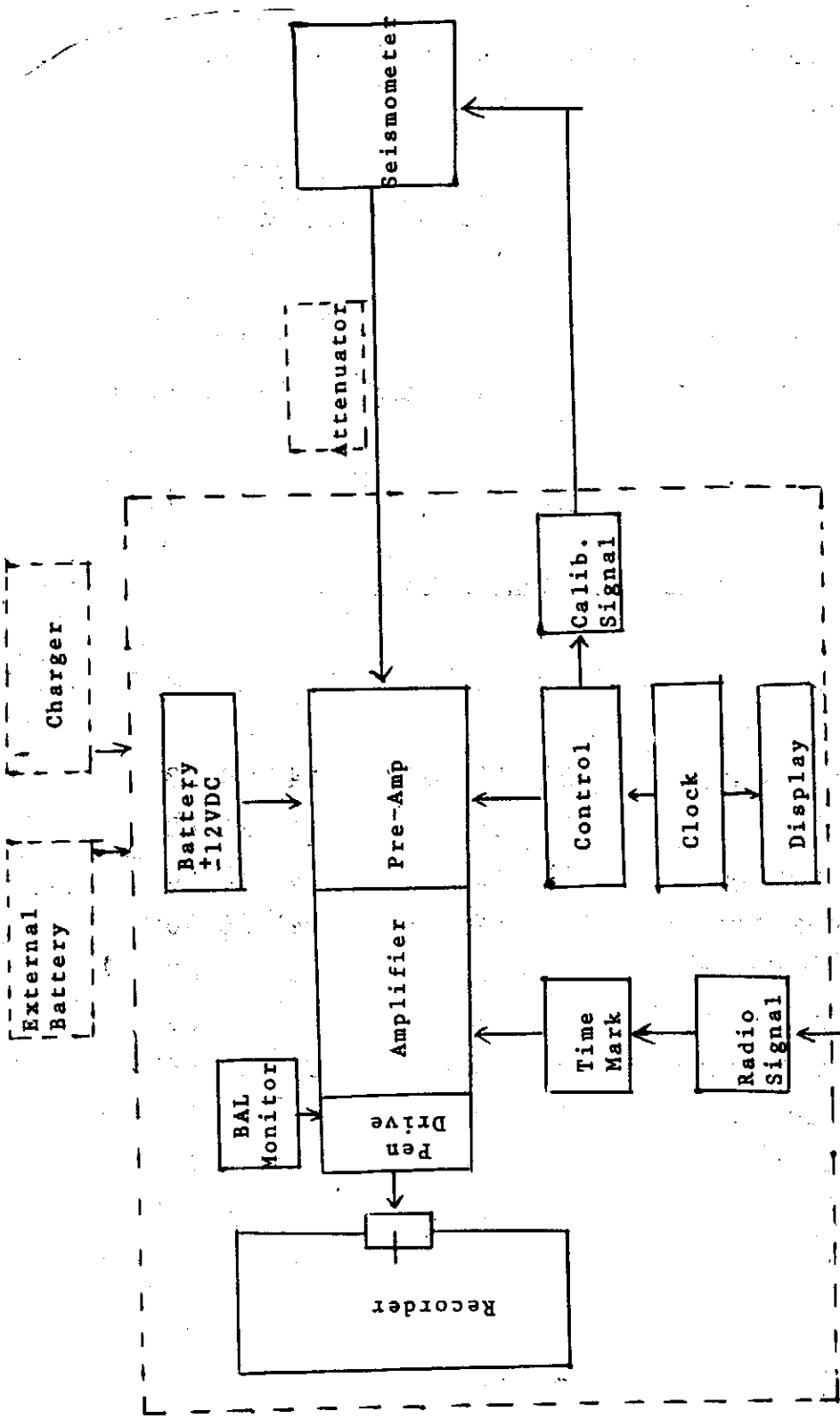
Seismometer
Attenuator
Calib. Signal
Charger
Battery ±12VDC
Pre-Amp
Control
Clock
Display
External Battery
Amplifier
Time Mark
Radio Signal
Radio
BAL Monitor
Pen Drive
Recorder

Table 2

Table 3 Crustal Model

Depth (km)	P-Vel km/sec	S-Vel km/sec
0-4	4.0	2.2
4-15	6.0	3.4
15-35	6.8	3.8
35 below	8.1	4.5

List of Microearthquake

1973	HR	MN	SEC	LAT-N	LON-E	DEPTH	MAG	NO	DMIN	GAP	RMS	ERH	ERZ	Q
10 21	11	35	7.50	24-31.42	120-56.25	6.07	0.96	8	6.1	125	0.18	1.0	1.6	B
10 21	13	29	14.54	24-10.64	120-54.77	28.78	2.13	12	13.3	115	0.28	1.1	1.4	B
10 23	3	22	32.64	24-29.33	120-53.63	5.69	0.86	5	0.2	235	0.13	1.7	1.1	C
10 25	2	30	17.51	24-16.02	120-57.22	14.67	1.91	8	12.0	180	0.21	3.4	1.6	D
10 26	5	55	59.87	24-22.49	120-50.04	7.84	0.33	6	8.1	154	0.14	1.3	2.1	C
10 28	15	50	33.81	24-20.20	120-53.92	5.50	1.48	10	9.4	115	0.18	0.8	5.3	C
10 29	12	5	6.65	24-23.94	120-51.36	13.32	0.57	4	9.4	257	0.07			C
10 30	16	48	56.42	24-19.43	120-46.63	32.19	1.57	8	8.1	211	0.19	3.3	2.3	D
10 31	15	26	3.72	24-19.30	120-53.36	25.55	1.56	12	7.5	122	0.17	1.1	1.6	B
11 1	20	50	07.67	24-32.89	120-42.91	8.07	1.58	12	3.6	236	0.16	1.0	0.9	C
11 1	21	12	2.20	24-32.96	120-42.50	8.12	0.66	8	3.7	248	0.11	1.5	1.1	C
11 1	21	12	28.19	24-32.86	120-42.91	7.65	1.16	8	3.5	236	0.17	2.2	1.7	C
11 1	21	13	10.15	24-34.91	120-42.91	6.41	0.78	6	7.1	299	0.08	1.0	1.4	C
11 1	23	22	35.43	24-20.28	120-50.96	4.80	0.94	6	11.8	298	0.10	0.9	6.7	D
11 2	2	54	10.18	24-33.79	120-42.91	5.72	0.89	6	5.2	241	0.26	3.4	6.7	D

List of Microearthquake

1973	HR	MN	SEC	LAT-N	LON-E	DEPTH	MAG	NO	DMIN	GAP	RMS	ERH	ERZ	Q
11 2	9	27	19.07	24-35.08	120-40.91	8.92	0.91	5	8.3	320	0.05	1.6	1.0	C
11 4	19	53	57.17	24-22.82	120-56.50	0.40	0.75	9	12.9	109	0.33	1.5	2.2	C
11 5	4	3	0.60	24-24.72	120-48.73	8.52	0.77	4	4.9	224	0.01			C
11 5	21	11	31.12	24-14.29	120-49.29	12.12	0.89	5	4.3	323	0.11	3.5	1.2	D
11 5	21	51	23.09	24-23.26	120-50.94	11.35	0.67	6	9.0	265	0.07	0.9	1.0	C
11 7	21	0	25.41	24-29.81	120-49.37	11.17	0.55	5	7.1	178	0.02	0.5	0.4	C
11 11	2	44	52.34	24-20.53	120-50.25	14.26	0.77	5	7.5	162	0.24	4.5	4.5	D
11 12	15	57	45.00	24-19.63	120-50.85	8.13	1.39	11	5.9	126	0.14	0.9	1.9	B
11 12	16	21	18.47	24-20.35	120-47.46	16.09	0.62	4	8.3	193	0.02			C
11 16	15	44	29.11	24-18.76	120-50.38	8.04	1.31	8	0.2	221	0.17	1.7	2.3	C
11 16	16	6	36.89	24-18.76	120-50.38	7.31	1.05	7	0.2	221	0.19	2.0	3.0	C
11 17	23	55	47.32	24-20.94	120-50.38	5.00	1.14	6	4.2	231	0.18	2.3	5.3	D
11 17	6	46	37.82	24-19.56	120-46.89	9.85	0.92	5	4.5	147	0.06	1.2	1.9	C
11 17	15	0	1.86	24-16.58	120-46.67	7.61	0.76	7	5.1	222	0.09	1.1	1.0	C
11 17	23	1	10.88	24-16.60	120-41.54	7.69	1.32	9	6.1	146	0.13	0.7	1.3	B

List of Microearthquake

1973	HR	MN	SEC	LAT-N	LON-E	DEPTH	MAG	NO	DMIN	GAP	RMS	ERH	ERZ	Q
11 19	5	24	9.61	24-14.46	120-38.95	3.81	1.47	9	8.1	212	0.14	0.7	0.8	C
11 19	8	15	0.78	24-23.26	120-50.38	7.58	1.10	6	8.5	280	0.24	7.2	9.0	D
11 19	12	48	50.89	24-17.23	120-50.75	9.73	0.93	7	1.7	233	0.11	1.4	1.5	C
11 20	0	18	22.14	24-17.73	120-47.17	5.21	0.98	8	4.7	118	0.08	0.4	0.7	B
11 21	2	41	10.18	24-28.88	120-52.47	4.07	2.34	10	13.7	255	0.25	2.4		D
11 21	3	8	12.32	24-18.00	120-49.99	10.57	1.34	5	1.3	254	0.04	1.9	0.6	C
11 21	11	43	13.00	24-10.66	120-48.15	7.93	2.71	8	11.3	229	0.12	2.1	4.2	C
11 21	12	2	50.17	24- 8.35	120-47.54	6.03	1.18	7	15.7	324	0.03	0.7	3.0	C
11 22	4	48	40.80	24-22.76	120-50.11	12.29	1.29	5	8.0	295	0.11	3.7	3.5	D
11 22	4	52	43.62	24-12.47	120-43.88	8.91	1.50	7	11.2	305	0.08	1.2	1.6	C
11 22	6	39	10.70	24-13.24	120-49.77	7.90	1.32	6	10.0	313	0.05	0.9	1.3	C
11 22	7	34	15.40	24-11.82	120-47.63	4.84	1.51	6	4.0	203	0.15	0.5	1.2	C
11 22	15	48	18.69	24-15.40	120-51.83	8.48	1.65	8	6.5	137	0.19	1.2	2.5	C
11 23	7	44	18.51	24-13.52	120-45.95	7.57	1.18	5	5.7	197	0.07	7.3	1.3	D
11 23	10	29	59.60	24-13.16	120-48.56	10.65	1.24	6	6.7	301	0.07	1.7	0.9	C

List of Microearthquakes

1973	HR	MN	SEC	LAT-N	LON-E	DEPTH	MAG	NO	DMIN	GAP	RMS	ERH	ERZ	Q
11 23	13	50	16.32	24-21.03	120-51.80	10.27	0.75	6	5.1	267	0.13	2.1	2.1	C
11 24	1	38	50.49	24-19.56	120-46.13	5.13	1.47	7	3.4	185	0.12	1.1	1.4	C
11 24	3	37	22.97	24-23.73	120-49.00	10.86	1.33	6	5.6	240	0.09	1.6	1.7	C
11 24	5	34	28.31	24-17.08	120-47.01	7.31	1.55	5	5.0	239	0.04	0.1	0.1	C
11 25	8	7	36.71	24-18.76	120-50.38	7.62	1.10	8	0.2	136	0.18	1.8	1.9	C
11 25	16	4	24.25	24-19.92	120-50.79	12.51	0.56	7	2.5	244	0.12	1.6	1.1	C
11 25	18	16	52.62	24-19.19	120-43.39	7.44	1.22	10	2.3	97	0.19	1.0	1.0	B
11 25	20	9	23.44	24-14.34	120-42.77	6.60	0.37	6	8.2	163	0.02	0.3	0.8	B
11 26	6	46	57.47	24-19.40	120-46.22	10.72	1.02	11	3.4	105	0.08	0.4	0.5	B
11 26	21	48	17.51	24-18.60	120-43.40	7.86	0.36	6	1.9	173	0.15	1.6	2.0	C
11 27	8	57	46.86	24-18.53	120-33.61	15.35	2.20	11	5.5	241	0.37	3.8	1.8	D
11 27	14	51	14.02	24-14.81	120-49.89	10.00	0.10	7	3.2	212	0.07	0.9	1.1	C
11 27	15	4	34.70	24-15.75	120-48.53	6.81	0.38	7	3.1	141	0.10	0.7	1.3	B
11 27	20	53	53.54	24-19.60	120-43.53	10.96	0.20	6	2.6	195	0.04	0.6	0.6	C
11 27	21	45	23.42	24-15.06	120-49.91	12.14	0.67	8	2.6	210	0.14	1.2	1.1	C

List of Microearthquake

1973	HR	MN	SEC	LAT-N	LON-E	DEPTH	MAG	NO	DMIN	GAP	RMS	ERH	ERZ	Q
11 29	0	8	53.92	24-29.81	120-45.93	17.71	1.18	6	9.6	338	0.09	3.1	1.2	D
11 29	6	9	53.93	24-18.76	120-52.52	28.48	1.73	11	3.8	148	0.13	1.8	1.2	C
11 29	18	39	25.65	24-20.35	120-47.29	10.06	0.55	6	5.8	252	0.07	1.0	1.0	C
11 29	20	17	52.17	24-13.44	120-47.07	9.08	0.58	7	6.0	157	0.14	1.5	2.0	C
11 29	21	2	6.21	24-23.78	120-56.03	11.59	0.60	9	13.6	208	0.09	0.9	1.8	C
11 29	22	49	59.09	24-13.45	120-48.28	5.51	0.92	6	6.4	187	0.05	0.4	1.0	C
11 30	8	8	59.10	24- 9.50	120-56.35	10.00	2.00	10	16.6	145	0.12	1.0	1.4	B
11 30	11	25	56.26	24-22.21	120-49.53	5.92	0.73	7	6.7	224	0.18	1.6	4.6	C
11 30	19	29	35.37	24-9.48	120-54.95	14.44	1.77	13	15.3	142	0.25	1.2	0.6	C
11 30	19	35	21.01	24- 9.56	120-54.52	10.00	1.13	11	14.8	207	0.13	0.9	1.7	C
12 1	0	45	29.73	24-21.48	120-50.04	11.48	0.20	5	9.2	159	0.01	0.3	0.5	C
12 1	2	14	52.21	24-24.72	120-53.53	10.00	0.60	7	13.0	212	0.63	8.3	26.0	D
12 1	2	15	15.42	24-26.73	120-48.69	1.13	0.84	10	6.2	247	0.22	2.6	0.8	D
12 1	3	57	15.55	24-15.15	120-48.53	13.29	1.17	9	3.7	159	0.21	1.8	1.9	C
12 1	14	48	25.27	24-20.73	120-44.76	10.01	0.45	10	4.1	98	0.16	0.9	1.0	B

List of Microearthquake

1973		HR	MN	SEC	LAT-N	LON-E	DEPTH	MAG	NO	DMIN	GAP	RMS	ERH	ERZ	Q
12	1	16	5	1.47	23-58.62	120-32.75	15.74	0.69	4	41.7	342	0.00			C
12	1	19	9	9.63	24- 9.07	120-53.71	15.28	0.75	8	13.5	212	0.17	2.0	2.1	C
12	2	19	26	8.43	24-10.09	120-57.56	10.00	1.27	10	17.2	205	0.14	1.4	3.2	C
12	3	1	1	1[illegible] 53	24-14.60	120-48.51	9.36	0.10	5	8.1	188	0.07	1.2	1.9	C
12	3	5	0	28.05	24-12.52	120-43.66	7.91	0.80	7	5.4	177	0.07	0.9	1.3	B
12	3	8	32	13.04	24-11.49	120-51.54	6.14	1.23	12	9.5	180	0.20	0.9	2.9	C
12	3	12	6	18.59	24-17.36	120-35.88	35.55	1.36	8	2.6	273	0.07	1.9	1.1	C
12	3	12	30	48.90	24-15.83	120-53.36	26.41	1.25	10	5.6	139	0.10	1.2	1.2	C
12	4	9	32	35.75	24-21.04	120-46.58	8.15	0.59	7	5.9	155	0.10	0.9	1.3	B
12	4	17	23	57.9[illegible]	24- 9.61	120-57.50	4.15	1.27	8	17.8	209	0.13	1.4		D
12	4	17	52	57.08	24-30.56	120-48.85	12.23	1.20	7	12.1	312	0.17	2.8	4.1	D
12	[illegible]	7	35	46.19	24-13.82	120-47.60	10.53	1.24	11	6.5	164	0.17	0.8	1.1	C
12	5	19	25	7.59	24-21.69	120-53.33	4.07	0.58	4	13.8	315	0.07			C
12	5	20	14	46.67	24-18.76	120-50.38	14.15	0.35	4	0	257	0.36			D
12	6	2	31	3.55	24-20.30	120-48.90	7.86	0.56	5	8.2	279	0.01	0.6	0.5	C

List of Microearthquake

1973	HR	MN	SEC	LAT-N	LON-E	DEPTH	MAG	NO	DMIN	GAP	RMS	ERH	ERZ	Q
12 6	17	25	4.33	24-17.55	120-46.61	6.57	0.40	8	4.0	114	0.21	1.4	1.8	B
12 7	7	43	56.18	24-17.45	120-47.21	6.72	1.01	9	5.0	120	0.15	0.8	1.2	B
12 7	9	43	24.39	24-18.51	120-43.96	13.33	1.11	9	7.1	101	0.23	1.4	2.4	B
12 7	14	43	26.79	24-20.10	120-46.05	9.42	0.59	5	3.9	224	0.01	0.2	0.3	C
12 7	15	53	54.45	24-19.90	120-45.21	11.32	0.55	4	2.9	198	0.00			C
12 7	18	36	10.02	24-15.72	120-46.20	8.46	0.35	4	5.9	253	0.01			C
12 8	16	57	4.84	24-15.72	120-44.60	29.93	1.02	9	5.1	251	0.11	1.6	1.0	C
12 8	18	2	44.84	24- 9.68	120-57.14	10.00	0.96	3	17.3	208	0.13	1.6	5.2	D
12 8	18	59	36.30	24-18.60	120-44.60	7.09	0.55	4	0.2	211	0.14			C
12 9	23	44	12.69	24-14.54	120-48.03	9.78	0.92	6	8.5	179	0.19	2.7	3.4	C

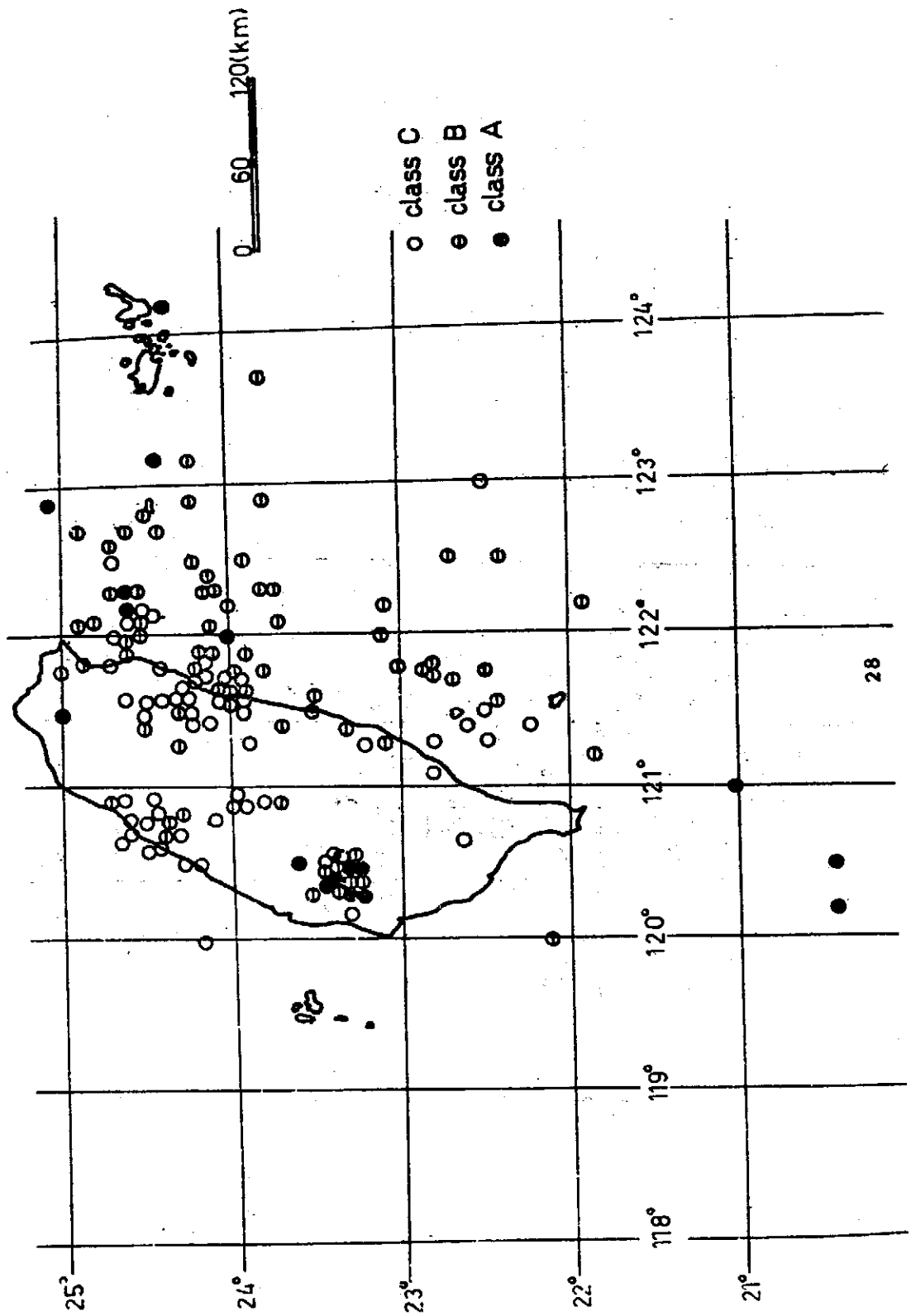

Fig 1. Distribution of earthquakes in Taiwan region (1900-1935)

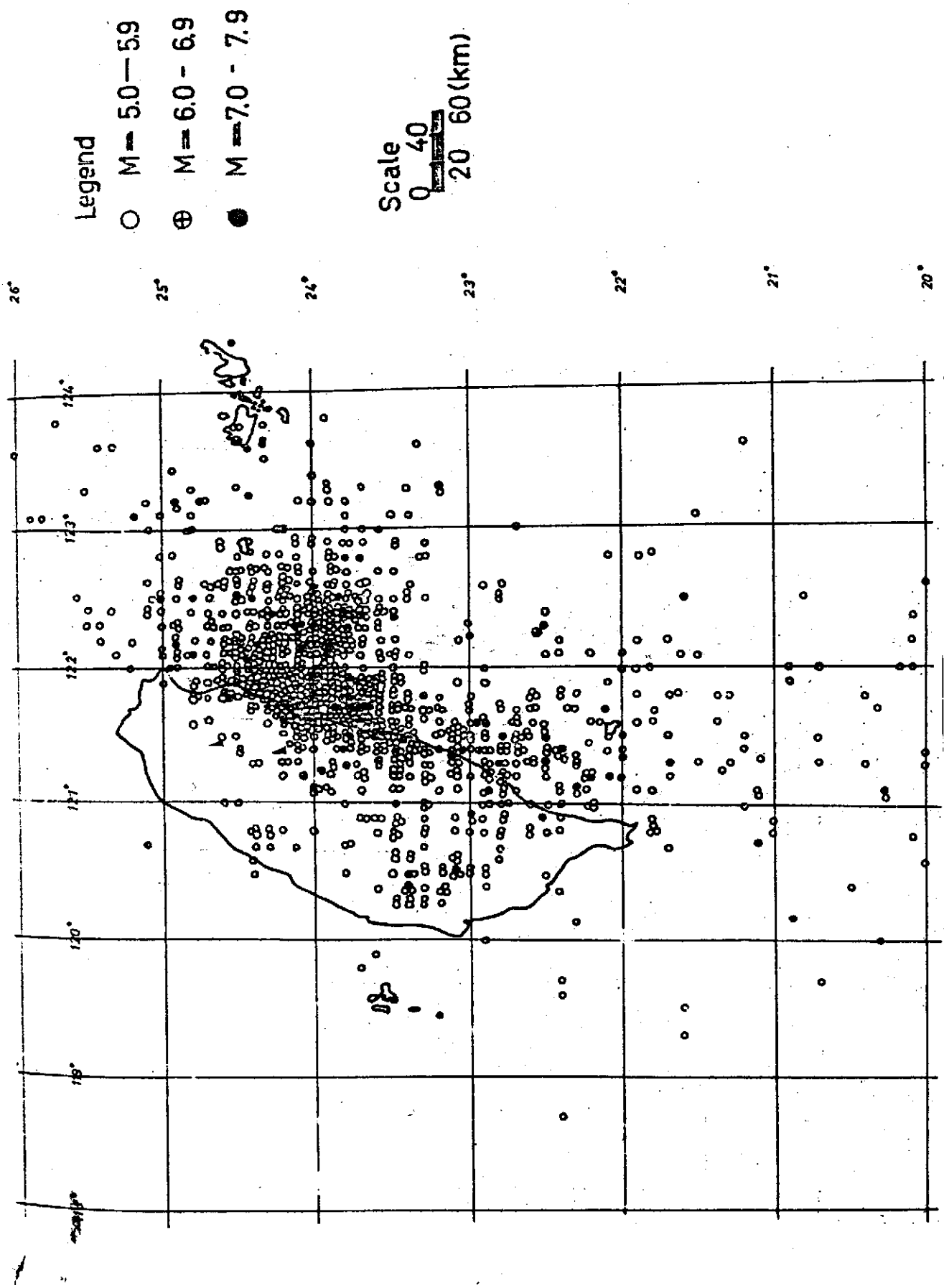

Fig 2. Distribution of earthquakes in Taiwan region (1936-1973)

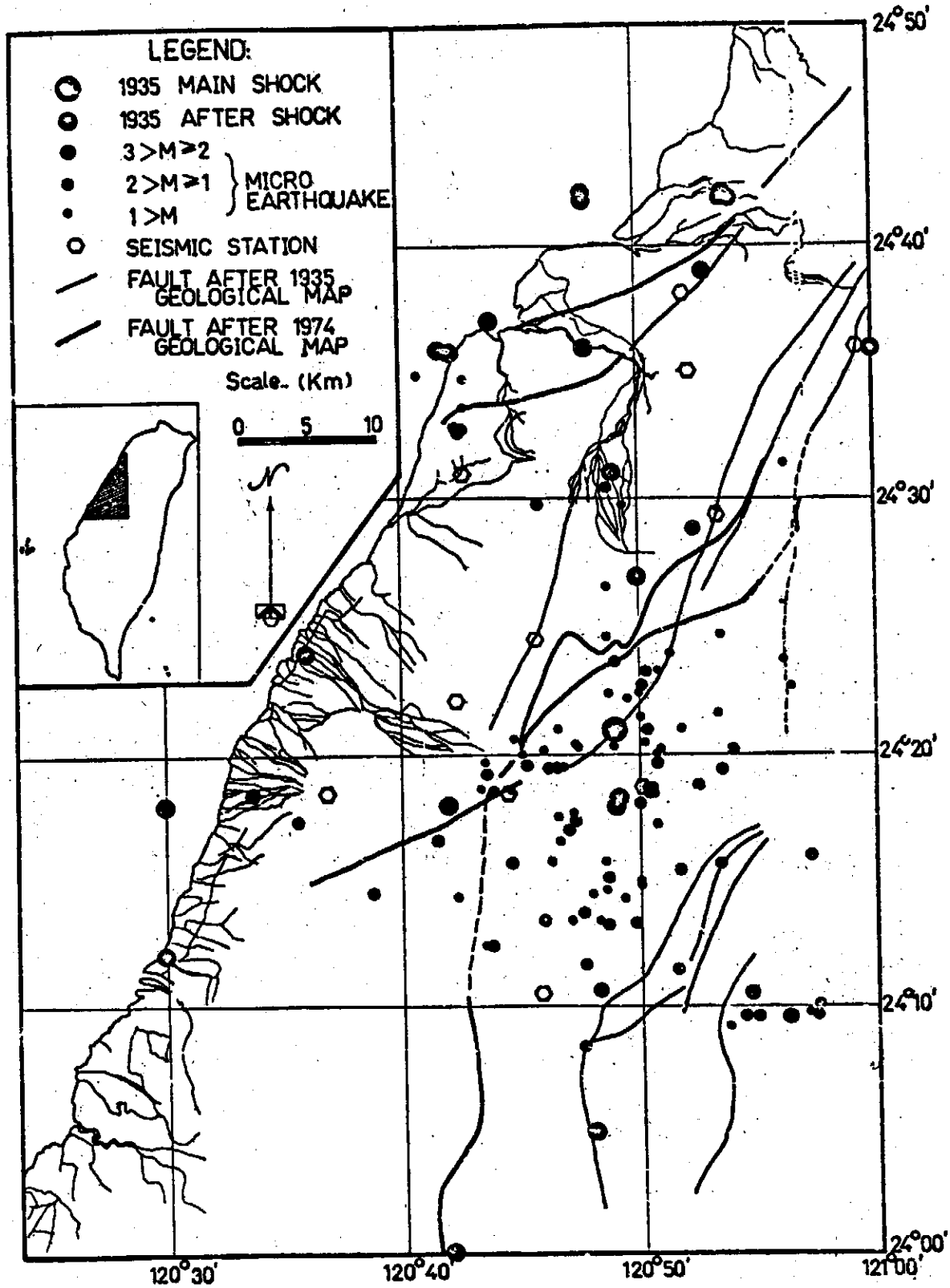

Fig 3. Location of fault, station, epicenters of microearthquake and aftershock of 1935 earthquake

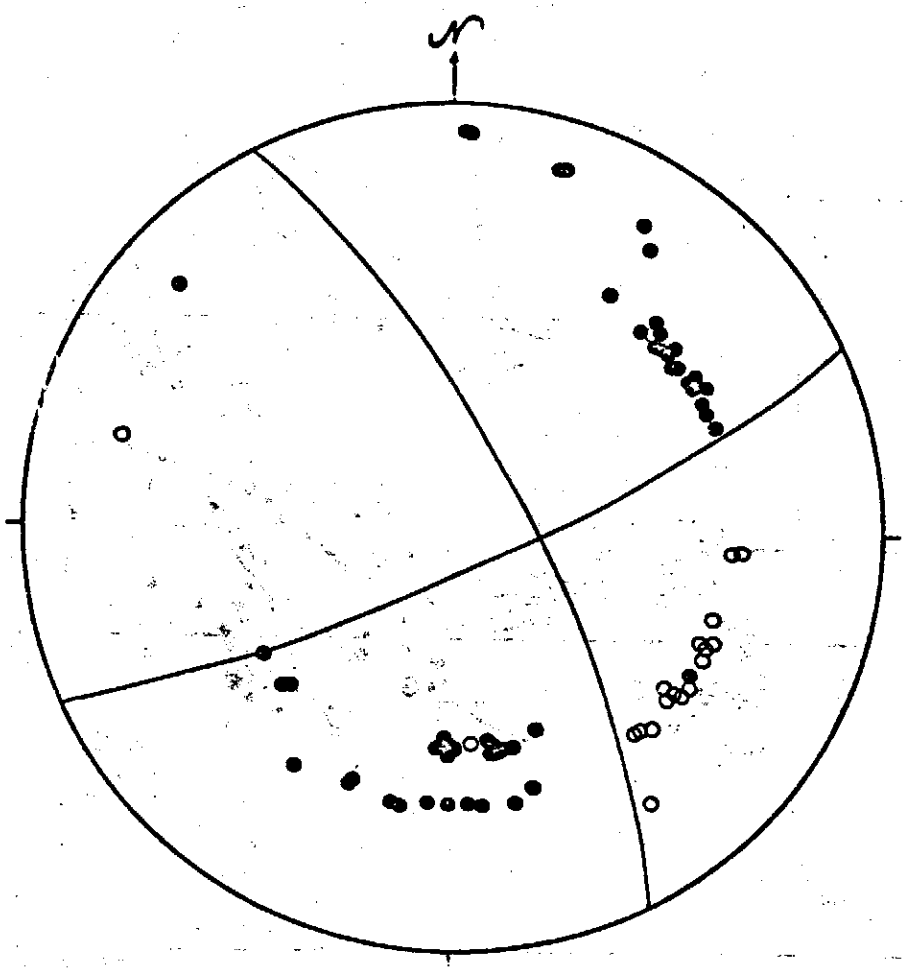

Fig 4. Fault plane solution of main shock & aftershocks in 1935 earthquake

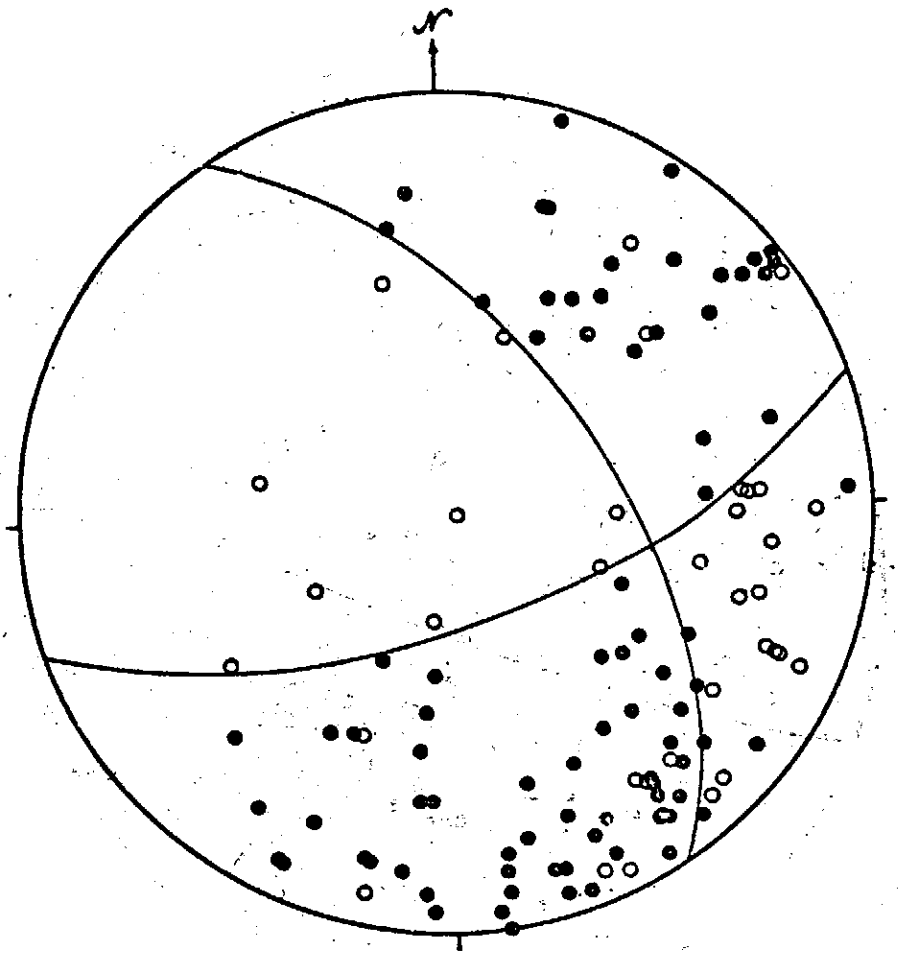

Fig 5. Fault-plane solution of microearthquakes of Group A

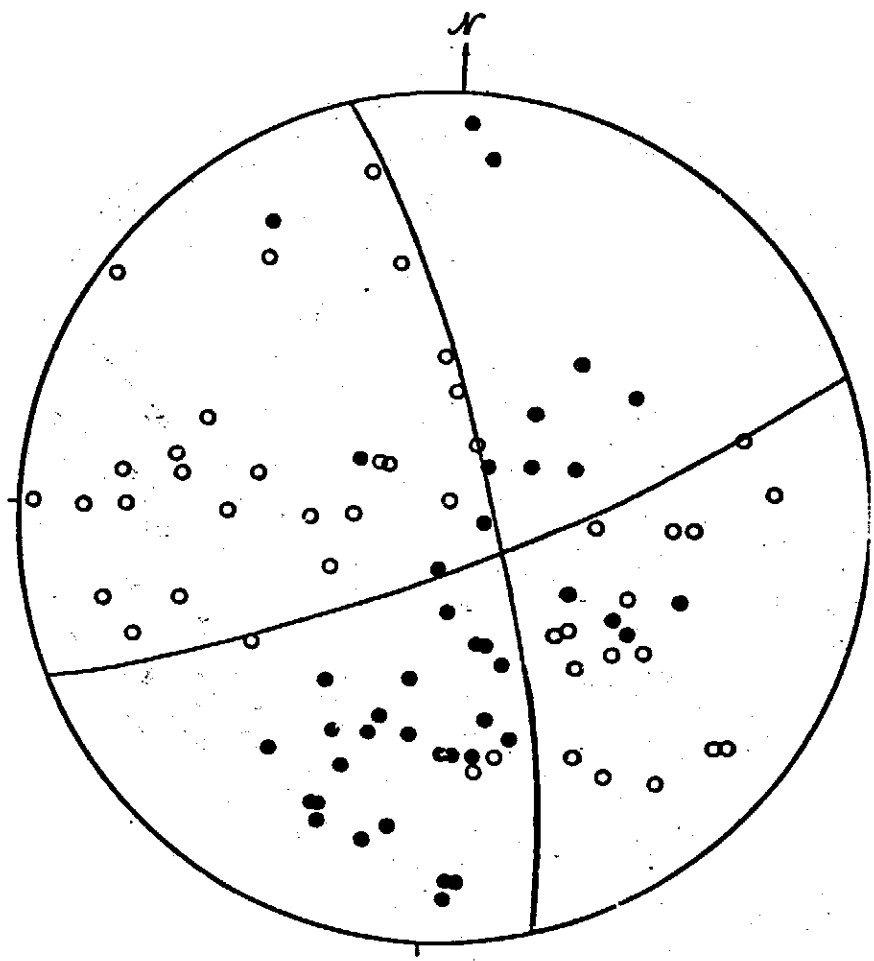

Fig 6. Fault- plane solution of microearthquakes Group B

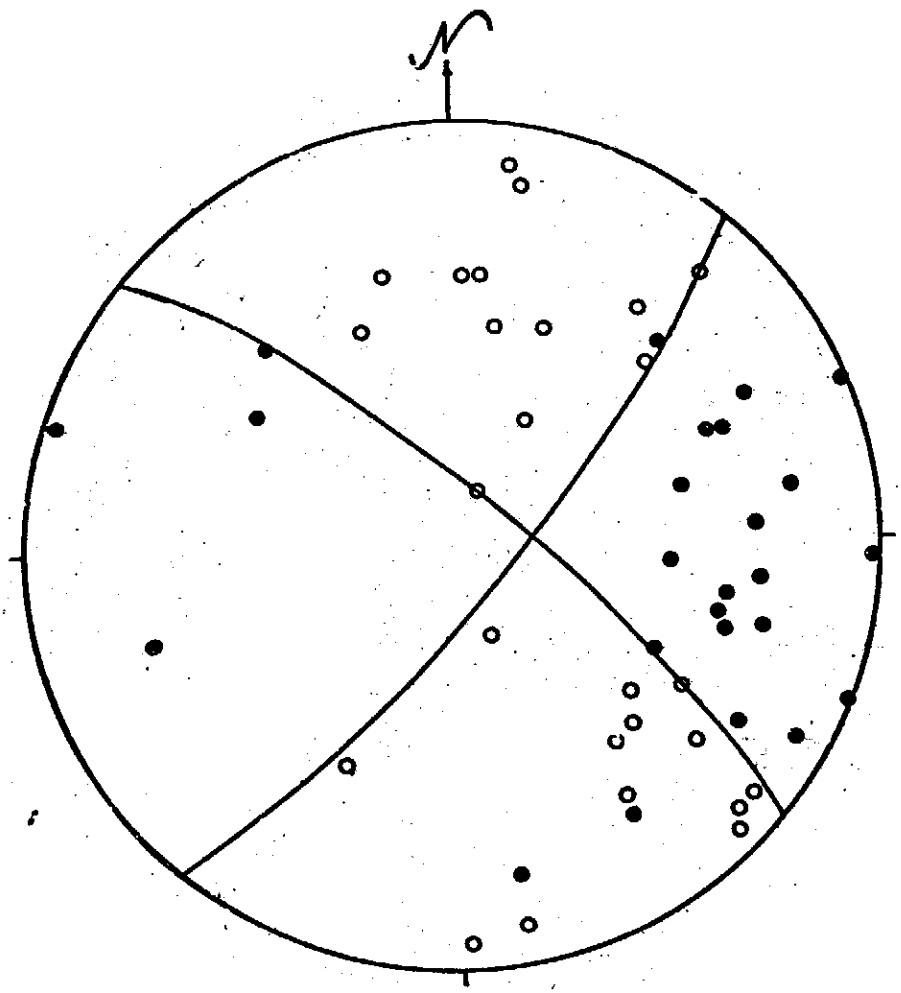

Fig 7. Fault-plane solution of microearthquakes Group C

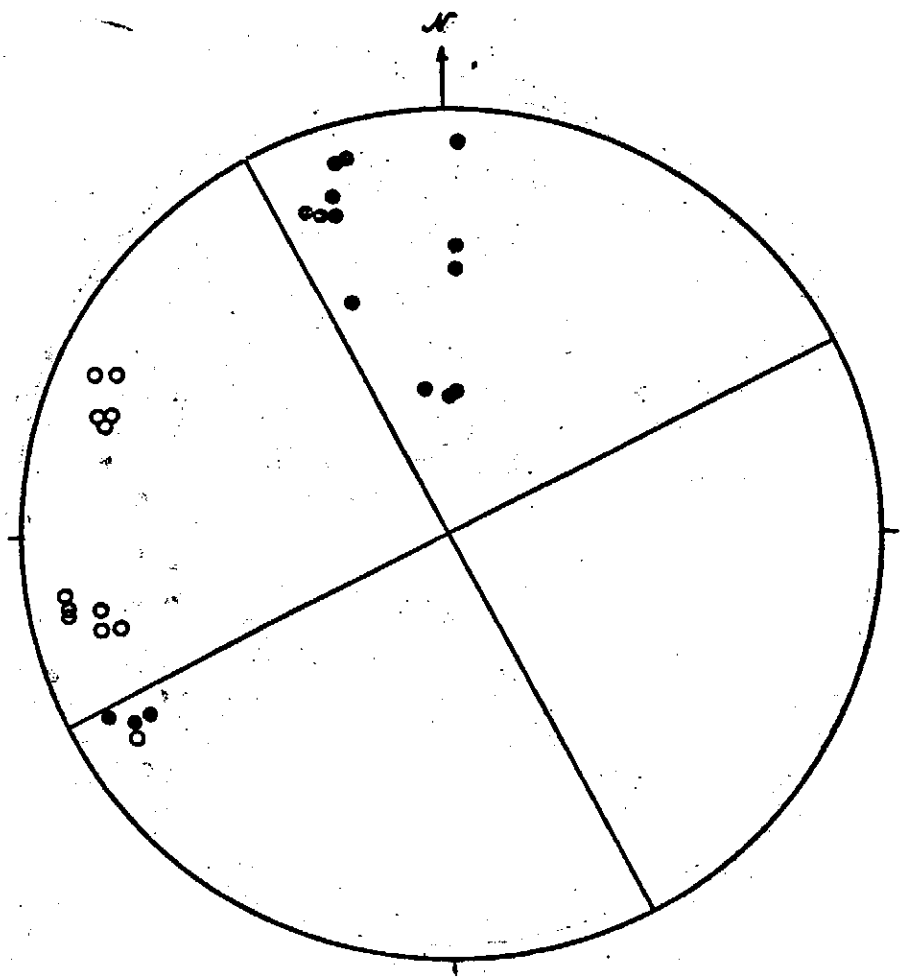

Fig 8. Fault-plane solution of microearthquakes Group D

ANNUAL REPORT OF THE INSTITUTE OF PHYSICS,
ACADEMIA SINICA, 1974

A SEISMOLOGICAL STUDY OF TAICHUNG HARBOR AREA

J. M. CHIU, H. P. LUENG AND Y. B. TSAI

CHINESE EARTHQUAKE RESEARCH CENTER
INSTITUTE OF PHYSICS
ACADEMIA SINICA
REPUBLIC OF CHINA

SPONSORS

NATIONAL SCIENCE COUNCIL
TAICHUNG HARBOR CONSTRUCTION BUREAU

JULY 31, 1975

Table of Contents

Chapter 1 introduction

A seismological study aimed to identify the potentially active faults and to evaluate the seismic risk in Taichung Harbor has been made recently by the Chinese Earthquake Research Center of Institute of Physics, Academia Sinica. This study was sponsored partly by the National Science Council and partly by the Taichung Harbor Construction Bureau.

Fig. I-1 shows the epicenters of 1935 Hsinchu-Taichung earthquake series. Two of the major aftershocks (No 13, 16) was located in the Taichung Harbor area. An surface fault trace was observed from Houli to Chingshui which is only a few kilometers northeast of the Taichung Harbor. Fig. I-1 suggests that the earthquake risk in this area may be high and should be evaluated carefully. According to Ho (1975), a series of north-south trending thrust faults has been recognized in the nearby foothill zone. So presence of potentially active faults at or close to Taichung Harbor calls for special considerations in its engineering designs. This task has been performed by means of a detailed microearthquake study in this area. The outcome is discussed in Chapter 2.

An evaluation of seismic risk at Taichung Harbor by performing statistical analyses upon the past seismic data in Taiwan is discussed in Chapter 3.

Chapter 2 A Microearthquake Survey in the Taichung Harbor Area

2-1 Introduction

Microearthquakes, reflecting the tectonic processes within the earth, can provide information with greater resolution in both time and space than what can be obtained by relying only large shocks over any reasonable interval of time. Thus information from microearthquakes can serve as a valuable supplement to that from larger shocks and can provide the means for promoting man's knowledge of the earth's tectonic processes.

From 12 May to 20 June, a detailed microearthquake survey was made around the Taichung Harbor area to study the seismic activity of recent faults of this area.

2-2 Geological Condition

In the studied area, the widely exposed formations are Lateritic deposit and Terrace deposit of Pleistocen. The former unit might belong to Tientzehou Formation, which consists of pebbles in the upper part. Both of the two parts are laterized. The sandstone is fine to medium grained, hight brownish to grayish, with muddy, losen and soft, having ripple marks on the bedding. Carbonized driftwoods, sandpipes are common. Shale is dark in color, Pebble beds sometimes are intersected with thin to lenticular sandstone beds. At the southern bank along the foothill of Tichchan Shan, the sandstone formation was slightly deformed. Minor faults and folds are present. The bedding planes become steeper than the lower part of the same formation upstream. It seems to be deformed during but not after the deposit was formed because the overlying younger terrace deposit which might be of the Chungli Formation shows no evidence of deformation.

At the northern bank of Tachia-Chi, 800m downstream from the Houli railway bridge, Kuantaoshan Sandstone which trends northeast and dips southeast is clearly exposed, and is in contact with Lateritic deposit by San-Yi overthrust. Although the overthrust is hidden, the exposed part of Kuantaoshan Sandstone has been greatly deformed, forming numerous minor folds and ruptures. The bedding planes suddenly change their altitudes and become more irregular. Just downstream from this place, in the Pleistocene Formation there reveals a fault scarplet. The apparent dip angle of the minor fault trace is 20° to the east. In the present view this fault is a low angle thrust. No further evidence is available to indicate whether it extends into the bedrock or is confined only in the Lateritic deposit. But undoubtedly it is close by the San-Yi overthrust. It might be caused by tension due to faulting in the San-Yi overthrust. Thus, it is concluded that active tectonic movement has been occurred in recent past in this area.

As to the 1935 Hsinchu-Taichung earthquake, the surface fault trace was almost completely obliterated by intensive farming activities in the area. Following descriptions of local populace some slight evidence is found at two places. One is at a point north of the Houli railway station, the northwestern side of the rupture has been lifted by a few meters up than that of southeastern side, but the rupture itself was gone. The other at Liyuten near Koeikeng, beds of Nanchuang Formation are in contact with the overlying Kuantaoshan Formation by a fault, which trends northeast and is considered to be right-handed strike slip. According to past records, this fault is probably the most active fault in this area.

2-3 Field Work

Portable seismographs of high sensitivity were operated at nine temporary stations for one month from 12 May to 20 June (Table II-1 and Fig. II-1). These stations were placed to cover the fault trace

of the 1935 Hsinchu-Taichung earthquake (Fig. I-1). Each station was equipped with a short period vertical seismometer, a smoke-paper drum recorder, a battery and a chronometer. Magnification of individual station was adjusted according to the background noise level in steps of 6 decibels. Regional background noise was very high as it was expected because (a) the study area is not far from the coast; (b) a relative thick alluvium covers the full area, (c) the density of motor roads is high, (d) the rainy weather during the recording time interval was unfavorable. Generally, the filter band was limited from 5 Hz to 30 Hz. But owing to the high frequency noise caused by taking off and landing of airplanes in a nearby airport, the filter band in TH02, TH03 and TH04 was confined from 5 Hz to 10 Hz. Time keeping was checked daily at every station with respect to standard time of radio broadcasting both at the beginning and at the end of the record.

2-4 Data Analysis

Once identification of events from the record of every station was made, the following data of each earthquake was taken, when possible, from the record (a) P-wave arrival time, (b) first motion of P-wave, (c) P-S time interval, (d) approximate signal duration. For this prospective area only those events with P-S time interval less than 5 sec was selected and located. Ocacsionally the precision of the reading of P-wave arrival time was less than ± 0.05 sec. The precision of the reading of S-wave arrival time was less than that of P. These data were subsequently fed into the computer program HYP071 which locate the hypocenter, the origin time and the magnitude of the earthquake through minimizing the residuals between observed and theoretical P and S wave arrivals by the Geiger's method (Eaton, 1969; Lee and Lahr 1972). Theoretical travel time was calculated based on a trial hypocenter and an assumed horizontally-layered crust model. The crust model used for this study is listed as follows:

Layer	Depth (km)	P-Velocity (km/sec)	S-Velocity (km/sec)
1	0-4.3	3.7	2.1
2	4.3-15.0	5.6	3.1
3	15.0-35.0	6.8	3.8
4	below 35.0	8.1	4.5

The magnitude of an earthquake was obtained by averaging magnitudes estimated at individual station. Station magnitude was derived from the recorded signal duration (τ) in sec and the epicentral distance (Δ) in km by the following equation:

$$M = -0.87 + 2.0 \log(\tau) + 0.0035\Delta$$

Uncertainty in the epicentral location was believed to be less than 2km. The uncertainty in focal depth determination was usually greater than that in epicentral location.

2-5 Discussions and Conclusions

Data concerning 46 microearthquakes which was located in the nearby area of Taichung Harbor during one month from 12 May to 20 June are listed in Table II-2 and plotted in Fig. II-2. Also shown in Fig. II-2 the geologic faults was taken from the recently published geologic map of Taiwan (Ho, 1975). It was clear that the occurrence of microearthquakes was by no means random in space but rather clustered along some linear geological structures. Although the faults in the study area was concealed under the alluvial layer, it was possible to delineate the active fault zones from these microearthquake data. Some interesting points can be made of the data. They are the following:

(a) A dense cluster of epicenters was found to extend from Houli toward southwest in direction of Taichung Harbor. It is in close coincidence with the fault trace of the 1935 Hsinchu-Taichung earth-

quakes shown in Fig. I-1. It is evident from Fig. II-2 that this underground fault was relatively active especially in the segment from Houli to Dunzuchiao. A profile along DD' (Fig. II-2) is plotted in Fig. II-3. A composite fault plane solution is plotted in Fig. II-4. Fig. II-3, II-4 show that this fault was a high angle right-lateral strike-slip fault with some thrust component.

(b) A group of epicenters were distributed to the right side of the San-Yi fault. A focal depth profile along CC' (in Fig. II-2) is plotted in Fig. II-5. A composite fault plane solution was plotted in Fig. II-6. A fault plane with dip angle about 60^{o} was shown from Fig. II-5. Therefore, in Fig. II-6 the nodal plane with a north-south strike is considered as representing the fault plane of the San-Yi fault. This fault was a right-lateral strike-slip fault with a thrust component.

(c) Local microearthquake records at each station also show something interesting. Among nine stations, TH01 and TH18 were the two stations closest to the epicenter of the main shock of the 1935 Hsinchu-Taichung earthquake series (see Fig. I-1). About five to ten local events at TH18 and three to five local events at TH01 could be found daily on records. Unfortunately not all microearthquakes recorded at TH18 and TH01 could be located because other stations failed to record them due to rather high background noise level. Nevertheless it was unmistakable that the area near TH01 and TH18 was a potentially active area.

(d) It can be said from past records and present survey that earthquake hazards are present in the Taichung Harbor area. The most likely source of earthquake threat to the Taichung Harbor may come from the active area mentioned above. As it is known that earthquake damages are caused mainly from the earth motion due to shear wave vibrations. Shaking of shear wave is perpendicular to the direction of wave propagation. Considering the direction from Houli to Taichung Harbor, the possible direction of shear-wave shaking is south-

east to northwest. It is prudent to design major engineering structures in the Taichung Harbor so as to have maximum resistance to earthquake shaking in the southeast to northwest direction.

Fig 1-1 EPICENTERS OF HSINCHU-TAICHUNG EARTHQUAKES (1935)

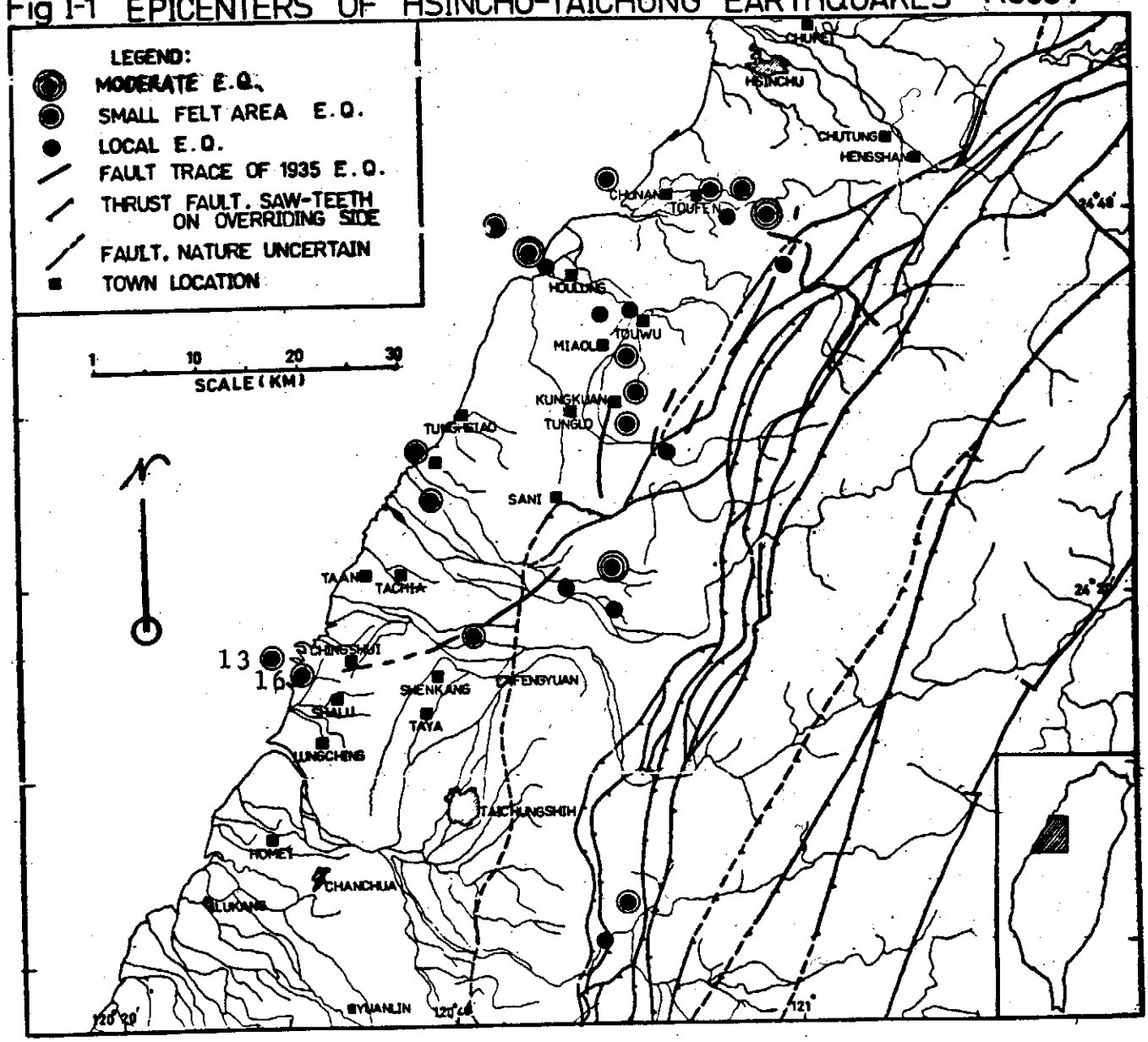

Table II-1 Station Data

STATION NO.	LATITUDE(E)	LONGITUDE(E)	ALTITUDE(m)	GAIN(db) & FILTER(Hz)	
TH01	24-19.94	120-39.22	230	78	5/30
TH02	24-13.11	120-36.76	200	78	5/10
TH03	24-16.96	120-38.23	220	78	5/10
TH04	24-17.93	120-36.29	230	72	5/10
TH05	24-15.74	120-36.06	210	66	5/30
TH06	24-09.91	120-34.07	250	72	5/30
TH07	24-10.41	120-45.85	230	78	5/30
TH08	24-03.73	120-43.89	100	78	5/30
TH18	24-18.46	120-44.83	400	78	5/30

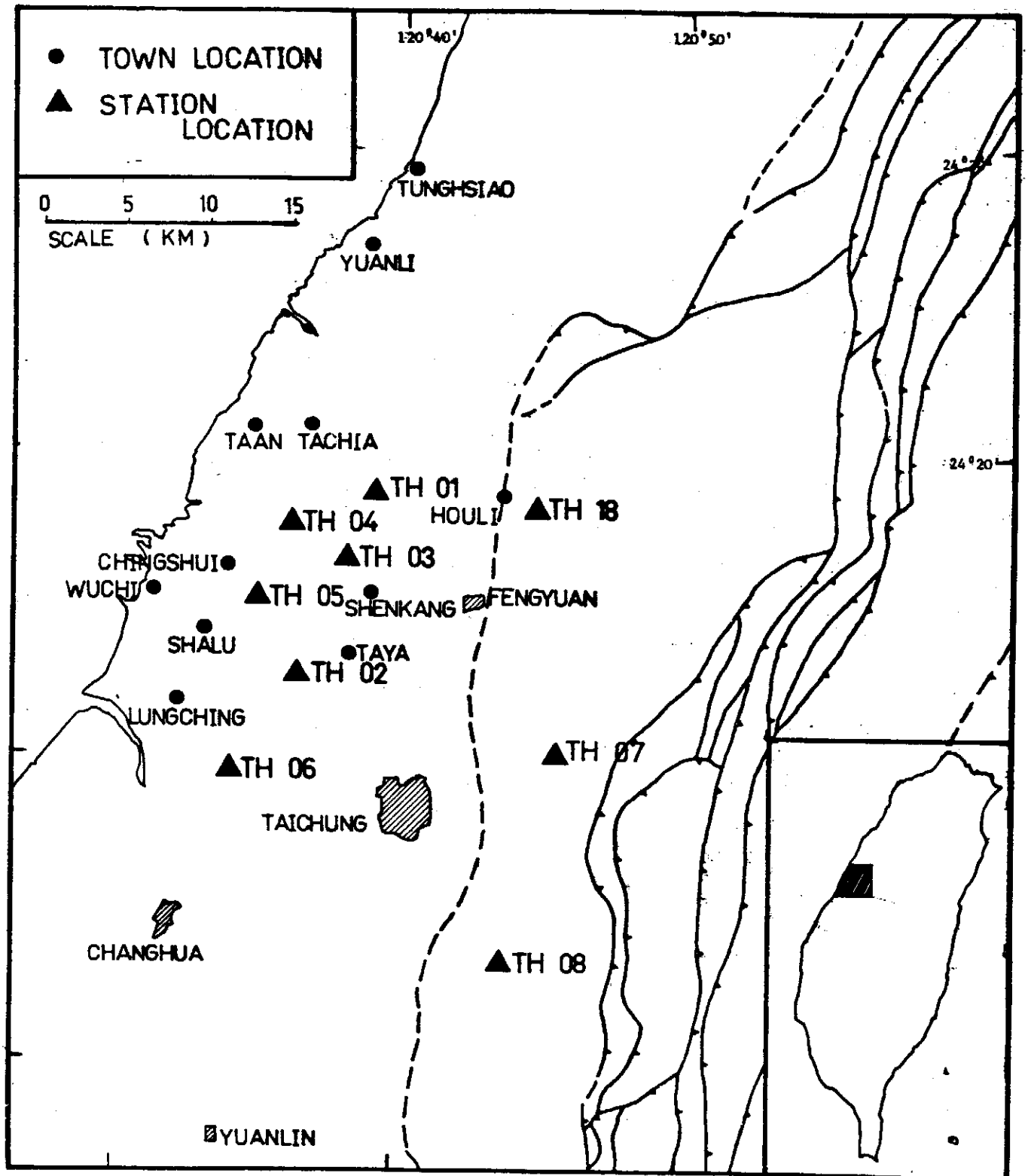

Fig II-1 LOCATION OF SEISMOGRAPH STATIONS DURING 12 MAY TO 20 JUNE

Table II-2 Listing of Earthquake in Taichung Harbor nearby area during 12 May to 20 June

1975	DAY	HR	MN	SEC	LAT-N	LONG-E	DEPTH	MAG
MAY	15	19	45	06.31	24-16.36	120-40.95	4.31	0.69
	18	15	55	15.65	24-18.62	120-40.79	5.97	1.40
	22	17	48	05.00	24-12.76	120-42.57	2.21	1.59
	23	05	20	46.62	24-11.08	120-44.87	4.38	1.97
	24	13	54	54.79	24-10.38	120-44.23	12.35	1.66
	25	21	00	07.93	24-17.35	120-38.32	9.19	0.85
	26	03	26	04.87	24-17.33	120-41.82	4.15	1.32
	27	11	51	45.04	24-17.76	120-42.53	15.37	1.78
	27	19	42	32.78	24-16.96	120-41.95	25.44	1.70
	28	11	15	12.18	24-18.56	120-41.13	6.11	1.83
	29	02	43	59.81	24-17.57	120-43.73	4.26	1.59
	31	04	57	56.73	24-18.56	120-46.29	7.84	1.62
	31	12	49	26.07	24-15.52	120-45.54	7.29	1.17
JUN	1	06	08	48.34	24-11.99	120-41.72	21.53	1.40
	1	14	40	13.04	24-13.94	120-45.64	3.77	1.28
	1	19	47	19.82	24-14.66	120-48.94	11.43	1.26
	2	10	13	23.49	24-15.53	120-48.37	8.26	1.60
	2	11	43	52.61	24-18.07	120-40.85	8.87	1.11
	2	16	39	18.03	24-20.73	120-45.59	6.93	1.17
	3	11	50	50.82	24-17.78	120-43.95	6.44	1.46
	4	00	16	06.78	24-15.93	120-42.02	7.73	1.18
	4	04	57	54.37	24-20.53	120-43.30	4.96	1.40
	4	18	26	35.63	24-13.11	120-48.28	5.77	1.26
	5	11	24	26.65	24-16.64	120-42.71	10.13	1.41
	6	07	39	49.50	24-15.91	120-42.73	27.02	1.78
	7	08	56	43.32	24-21.14	120-43.36	3.37	1.68
	8	23	23	10.15	24-21.15	120-47.84	6.71	1.32
	11	01	46	27.34	24-21.93	120-44.45	6.79	2.17

1975	DAY	HR	MN	SEC	LAT-N	LONG-E	DEPTH	MAG
JUN	11	15	39	15.01	24-17.29	120-41.68	4.76	0.96
	11	16	09	08.64	24-20.99	120-44.21	3.03	1.41
	11	20	18	18.71	24-18.39	120-40.51	5.00	0.96
	11	20	54	49.72	24-12.57	120-47.57	10.71	1.66
	11	22	38	58.01	24-21.70	120-44.77	3.78	1.56
	12	18	16	15.81	24-23.79	120-46.09	1.78	1.80
	13	00	47	38.46	24-17.31	120-41.01	5.79	1.34
	14	00	0-	47.19	24-22.45	120-48.21	26.32	1.87
	14	21	45	50.44	24-16.29	120-44.01	7.76	1.49
	15	05	10	27.50	24-15.53	120-41.02	22.99	1.04
	15	06	40	48.93	24-17.47	120-47.13	1.12	1.67
	15	20	22	15.11	24-19.04	120-40.68	7.53	1.12
	15	20	46	33.24	24-12.17	120-48.67	7.51	1.60
	16	01	57	57.33	24-16.94	120-41.38	3.95	1.65
	18	02	42	23.61	24-18.61	120-43.04	9.88	1.45
	19	08	39	35.81	24-10.51	120-42.31	4.15	1.34
	19	16	20	32.69	24-18.56	120-45.20	6.39	1.35
	19	17	58	57.14	24-18.83	120-45.34	6.60	1.43

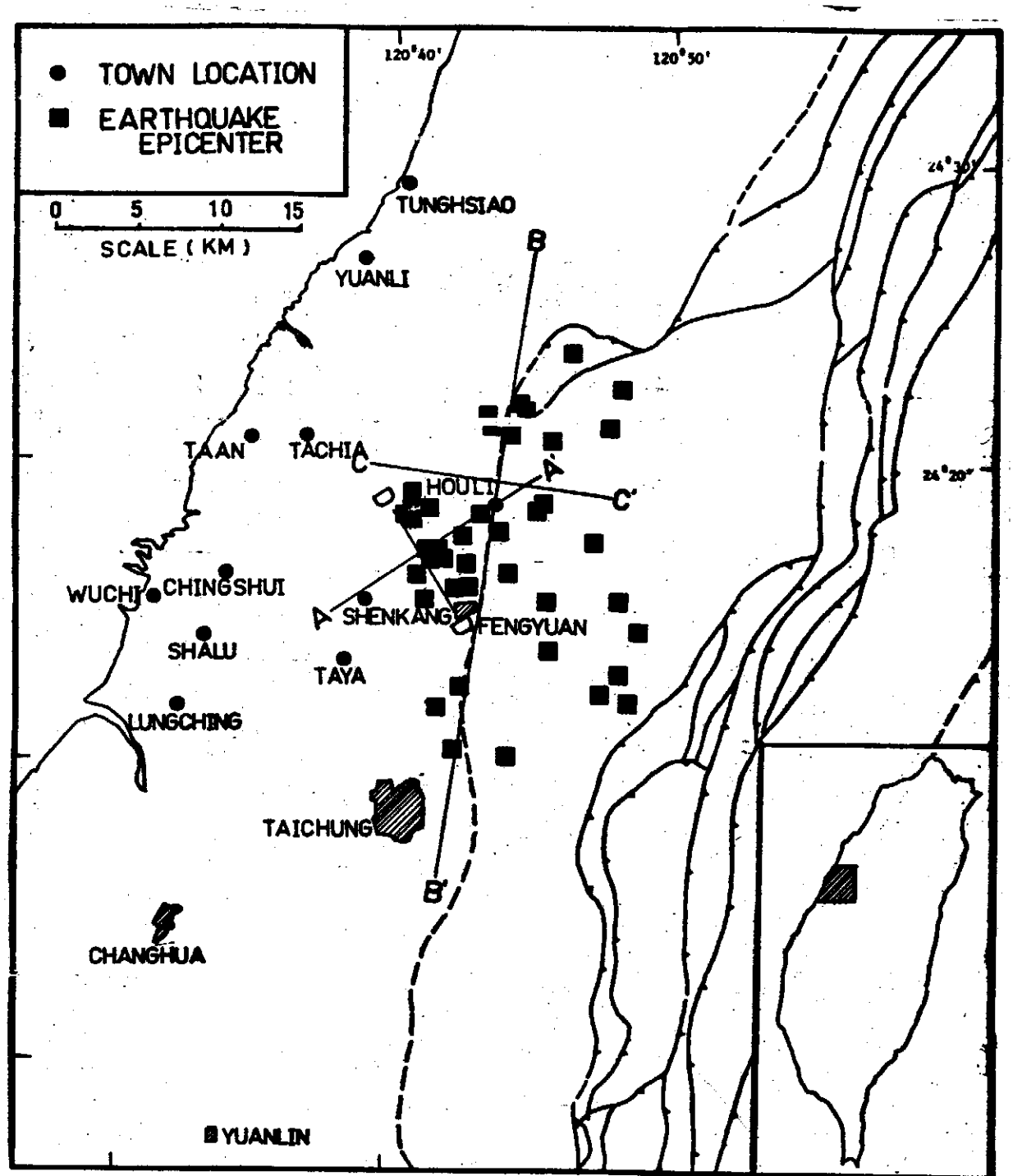

Fig II-2 EPICENTERS OF MICROEARTHQUAKES IN THE TAICHUNG-HARBOR NEARBY AREA DURING 12 MAY TO 20 JUNE

(EPICENTER MAP)

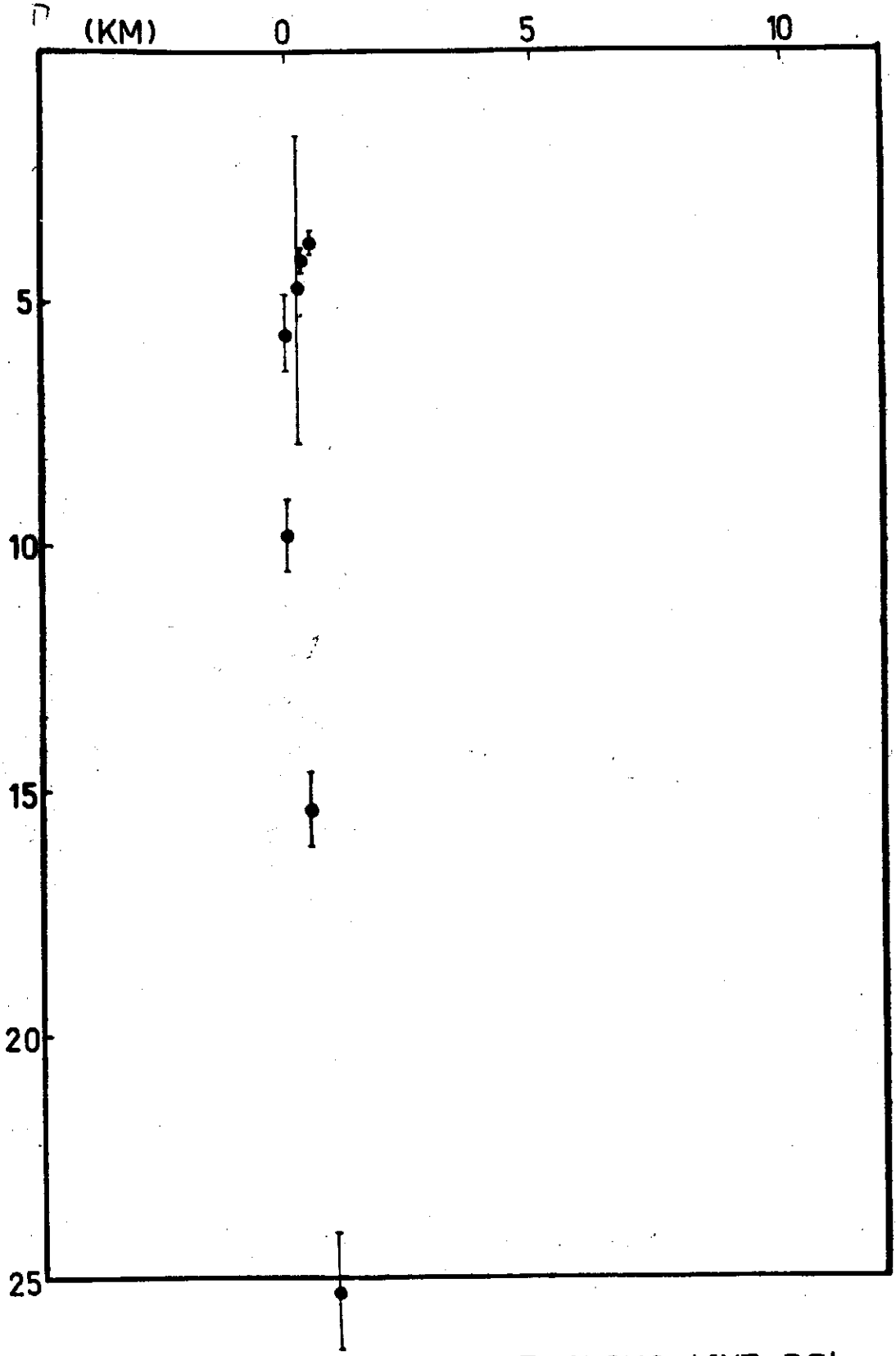

Fig II-3 FOCAL DEPT PROFILE ALONG LINE DD'
IN Fig I-2

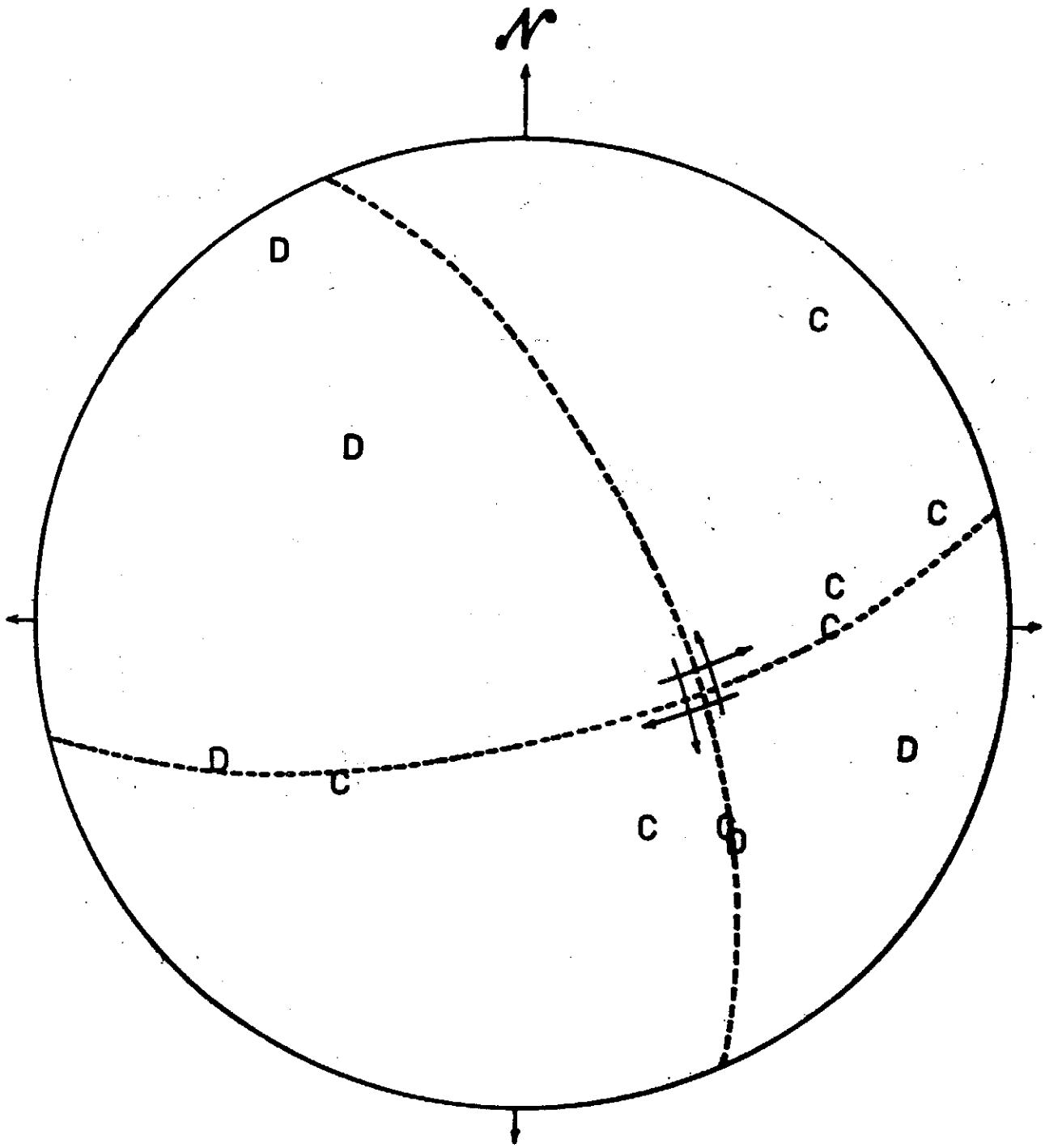

Fig II-4 FAULT PLANE SOLUTION OF MICROEARTHQUAKE ALONG AA' IN Fig I-2

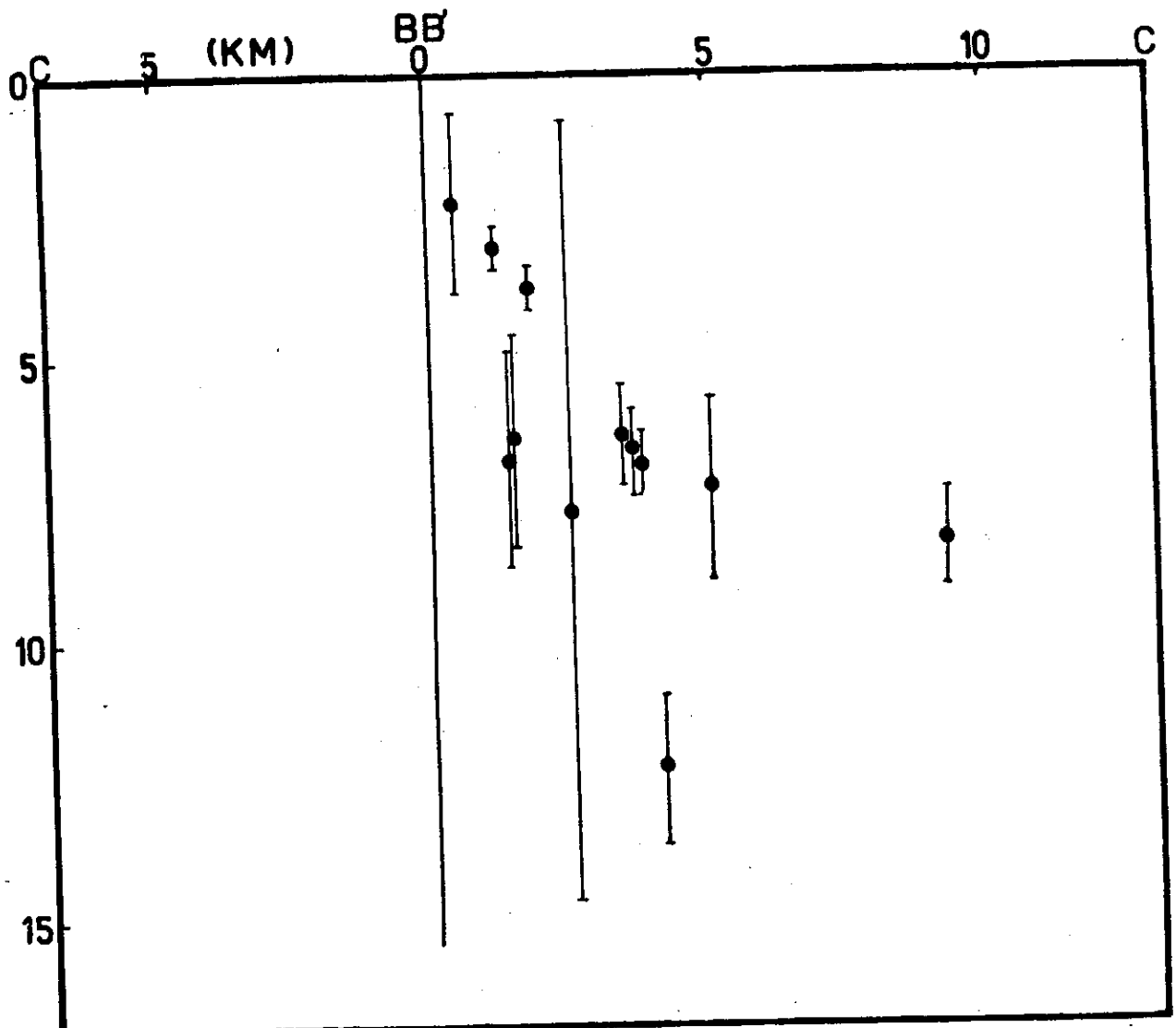

Fig II-5 FOCAL DEPTH PROFILE ALONG LINE CC' IN Fig II-2

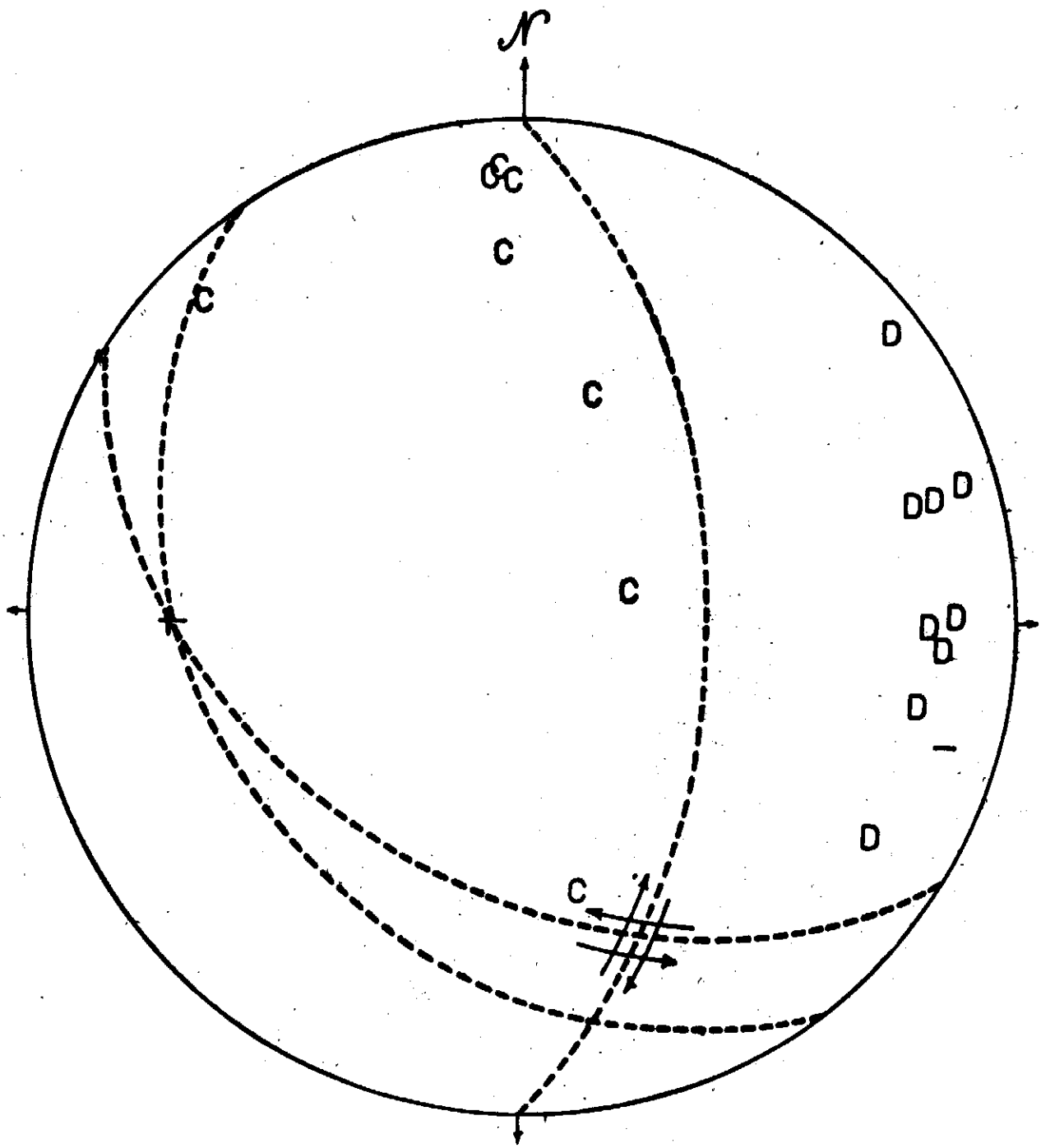

Fig II-6 FAULT PLANE SOLUTION OF MICROEARTHQUAKE ALONG BB IN Fig 2

Chapter 3

Estimation of Possible Maximum Horizontal Seismic Acceleration at the Taichung Harbor Area.

3-1 Introduction

For a member of applications, in particular those of structural engineering, there is a need for a definition of earthquake risk in Taiwan. At the present this is done by dividing Taiwan into three zones according to the maximum seismic intensity records in the past. As shown in Fig. III-1, these zones are labeled Zone IV, Zone V and Zone VI which correspond to the following horizontal ground accelerations:

Zone IV: 0.025 to 0.080 g
Zone V: 0.080 to 0.250 g
Zone VI: 0.250 to 0.800 g

According to this map the Taichung Harbor is located in Zone V.

Although this approach to seismic risk has the merit of simplicity, it nevertheless presents marked discontinuities at zone boundaries which have no physical counterparts. Even within the same risk zone there exists a wide range of seismic acceleration values which tends to make the choice of a seismic coefficient for individual engineering construction projects somewhat arbitrary. More seriously this zoing method does not reflect the statistical nature of seismic risk. A more realistic approach which does away with the shortcomings of the existing method is developed in order to estimate the possible maximum lateral seismic forces with certain return periods at the Taichung Harbor.

3-2 Estimation of possible maximum seismic accelerations at the Taichung Harbor

In order to make a quantitative estimation of seismic risk at Taichung Harbor, statistical analyses are performed upon the earthquakes occurred in Taiwan during 1935 to 1973.

For the present study we use a relationship between acceleration amplitude, earthquake magnitude and epicentral distance derived by Schnabel and Seed (1973) from peak ground accelerations recorded instrumentally from earthquakes in the Western United States (Fig. III-2). The acceleration amplitude established by this relationship at a specific location due to any given earthquake refers to the rock foundation. This relationship is preferred for the present application because it is based directly on instrumentally recorded acceleration data and so presumably is more reliable than other similar relationship derive from macroseismic intensity data. Its applicability to areas outside of the United States, such as Taiwan, is justifiable on the ground that it is established on data representing a great variety of earthquakes and geological conditions of recording sites. As such it may be taken as an averaged relationship between acceleration amplitude, earthquake magnitude and epicentral distance.

An ordered set of acceleration amplitudes is subsequently computed for the Taichung Harbor by applying this relationship to individual earthquakes. Two different statistical analyses are then performed upon the calculated acecleration data.

The first analysis makes use of the amplitude distribution. The amplitude distribution can be expressed as follows. Let N(A) be the number of earthquakes occurring per annum in which the acceleration amplitude exceed A. This is determined by dividing the total number in the set exceeding A by the number of years covered by the data set. It is found that N(A) may be expressed by an equation of the form

$$\log_e A = \log_e C_p + \frac{1}{\alpha p} \log (N_p(A)) \text{ --------- (1)}$$

where C_p and α_p are constants, representative of the point p, α_p has a negative value. By this equation the acceleration amplitude of certain return periods can be found.

The result of this analysis is shown in Fig. III-3. It is evident that the data point can be fitted better by two straight line segments with different sets of C_p and α_p values for the lower and upper ranges of $\log_e A$ than by a single straight line for the whole range of $\log_e A$. The peak amplitudes of horizontal seismic accelerations corresponding to return periods of 50 and 100 years at the Taichung Harbor are found from Fig. III-3 to be 0.15g and 0.21g respectively.

The second analysis makes use of the distribution of annual extremes of acceleration amplitudes. This is done by using extreme value analysis directly following procedures such as that suggested by Gumbel (1954). In this analysis the largest acceleration amplitudes for each year of record are extracted from the total set of earthquake acceleration amplitudes for a given location. These are ranked and expressed by an equation of the form:

$$\log_e A_m = U - 1/a \log_e (-\log_e (m/N+1)) \text{ -------- } (2)$$

where A_m is the value of m^{th} largest amplitude and N is the total number of years of record. By this equation the acceleration amplitudes of specific return periods at a given point can be found.

The result of this analysis is shown in Figure III-4. Like the first analysis it is found again that the data points can be fitted better by two straight line segments with different sets of U and a values for the lower and upper ranges of $\log_e A_m$. The accleration amplitudes corresponding to return periods of 50 and 100 years at the Taichung Harbor are found from this figure to be 0.16g and 0.22g, respectively. These values are essentially identical to those found earlier from the first analysis.

3-3 Conclusions

In summing up the results of these two analyses, it is concluded that the maximum amplitudes of horizontal seismic acceleration in rock foundation at the Taichung Harbor with return periods of 50 and 100 years should be set at about 0.15g and 0.22g, respectively.

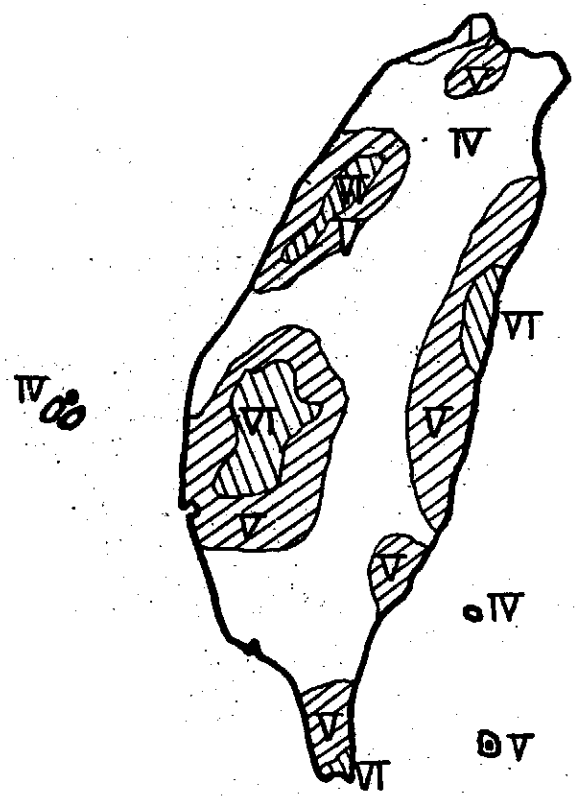

Fig. III-1 Map of maximum intensities in Taiwan

Acknowledgements

We thank Mr. D. A. Lee, Mr. Y. S. Cheng, Mr. P. H. Kao for their assistance in the field operations. The study was supported partly by the National Science Council and partly by the Taichung Harbor Construction Bureau.

References

1. Eaton, J. P., Hypolayr - A computer program for determining hypocenters of local earthquakes in an earth consisting of uniform flat layers over a half space, U.S. Geological Survey, Open File Report, 155 p., 1969.
2. Gumbel, E.J., Statistical theory of extreme values and some practical applications, Applied mathematics Series 33, National Bureau of Standards, 1954.
3. Ho, C.S., Geologic Map of Taiwan (1:250,000), The Ministry of Economic Affairs, Republic of China, 1975.
   Jack Oliver, Alan Ryall, James N. Brune and David B. Slemmons - Microearthquake Activity Recorded by Portable Seismographs of High Sensitivity, B.S.S.A. Vol. 56, No. 4, pp. 889-924, August, 1966.
5. Lee, W.H.K. and J.C. Lahr, HYP071 - A computer program for determining hypocenter, magnitude and first motion pattern of local earthquakes, U.S. Geological Survey, Open File Report, 100 p., 1972.
6. Schnabel, P.B. and H.B. Seed, Accelerations in rock for earthquakes in the Western United States, Bull. Seism. Soc. Am., 63, 510-516, 1973.
7. Tsai, Y.B., T.L. Teng, Y.M. Hsiung and C.M. Lo, New seismic data of Taiwan region, Annual Report of the Institute of Physics, Academia Sinica 1973, 223-238, 1974.
8. 新竹台中烈震報告（昭和10年4月21日）台北觀測所。
9. 昭和10年台灣震災誌，台灣總督府。

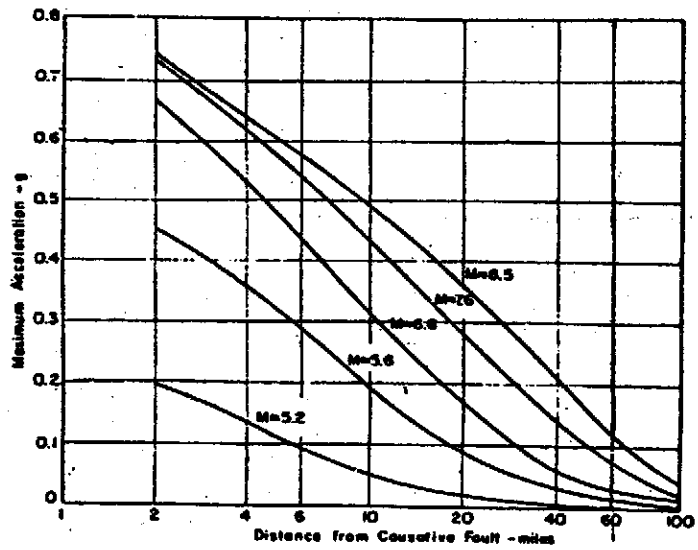

Average values

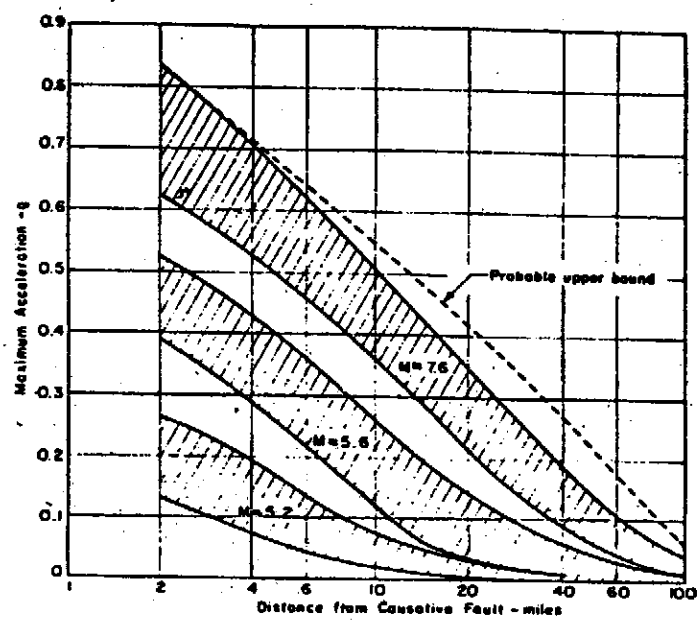

Ranges of maximum accelerations in rock.

Fig. III-2 Maximum accelerations in rock due to earthquakes in Western United States

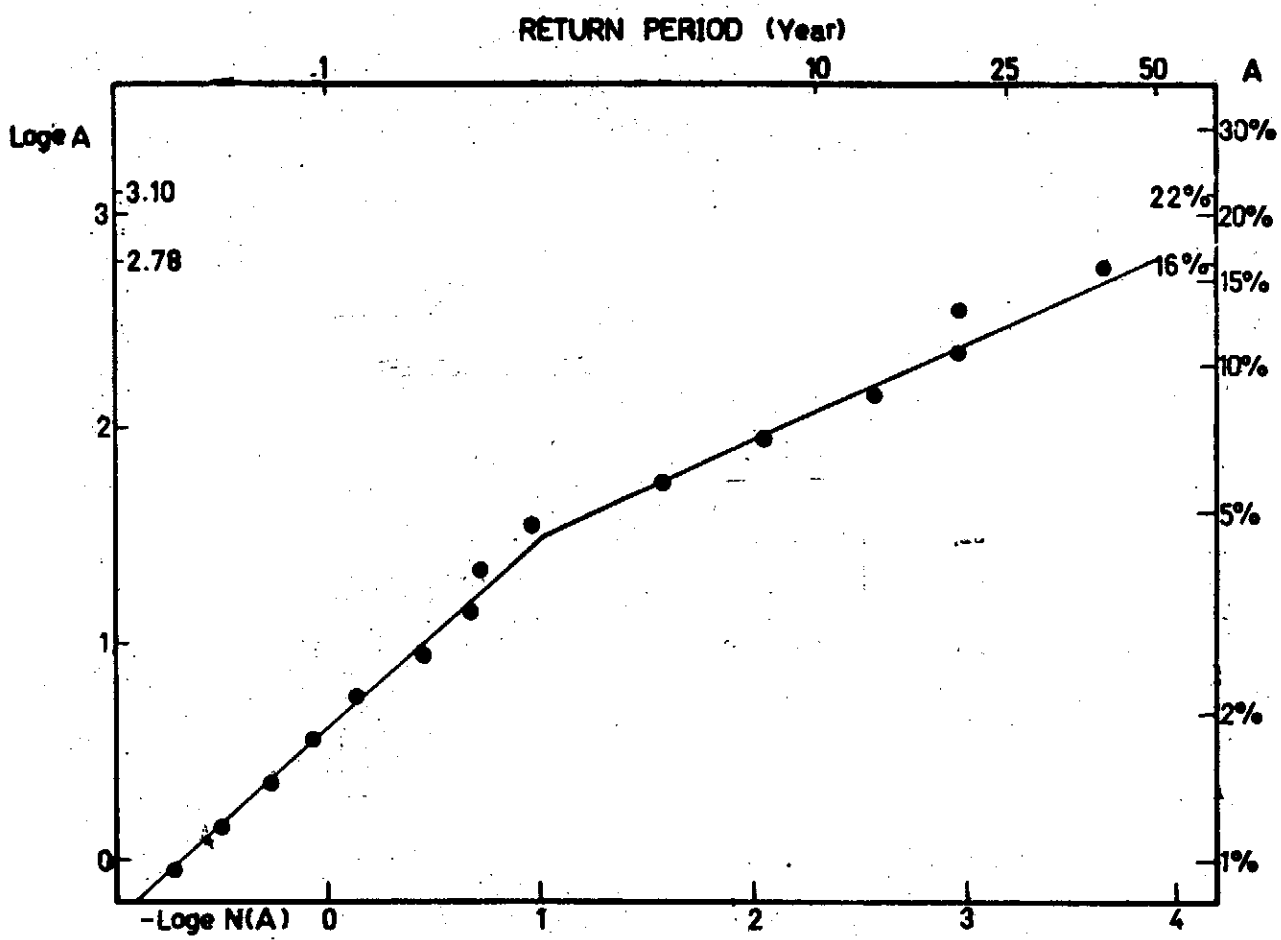

Fig III-3 MAXIMUM ACCELERATION AMPLITUDE VERSUS RETURN PERIOD AT TAICHUNG HARBOR BASED UPON AMPLITUDE DISTRIBUTION

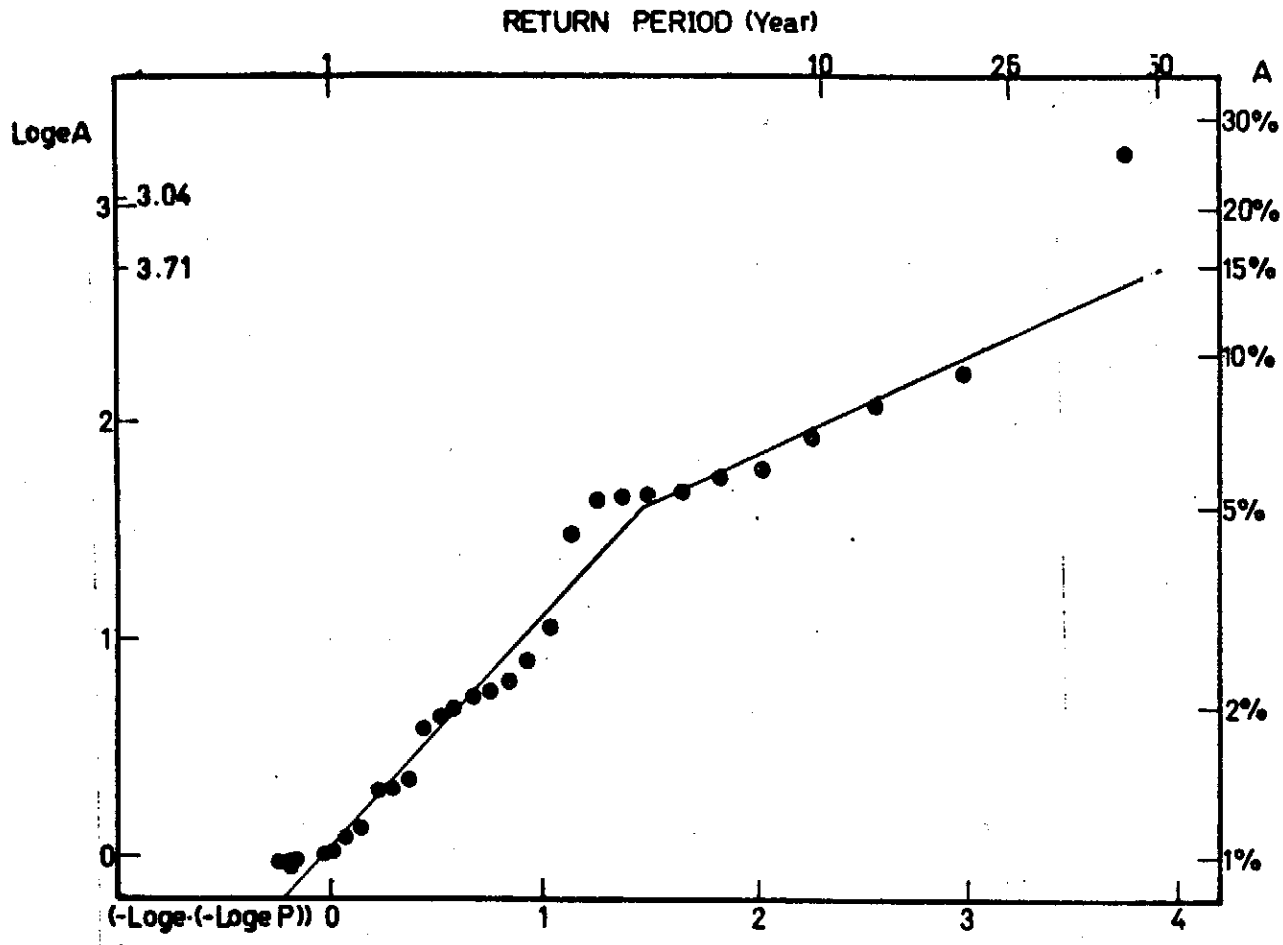

Fig Ⅲ 4 MAXIMUM ACCELERATION AMPLITUDE VERSUS RETURN PERIOD AT TAICHUNG HARBOR BASED UPON ANNUAL EXTREME VALUES

ANNUAL REPORT OF THE INSTITUTE OF PHYSICS,
ACADEMIA SINCA, 1974

DISPLACEMENT AND STRESS IN A THREE DIMENSIONAL WEDGE SHAPED MEDIUM

Yu-chiung Teng (鄧玉瓊)
Seismology Division, Institute of Physics
Academia Sinca
The Republic of China

Abstract

The case of an elastic wedge of arbitrary wedge angle subjected to an inclined point load on the free surface of the wedge is investigated. The Papokovitchfunction approach used by the author previously for two-dimensional wedge problem is extented here for three dimensional case. The formal solutions of both displacement and stress to the problem satisfying the prescribed boundary conditions may be obtained by means of the Kontorovich-Lebedev transform. These three dimensional solutions may reduce to the solutions of the two dimensional case. The formal solutions can be evaluated.

I. Introduction

Although some of the two dimensional wedge problems have been solved successfully, very little, however, has been done in the three-dimensional wedge problems. The well-known Boussinesq's problem[1]*. of a normal force acting on the boundary of a semi-infinite solid may be considered as a special case of the three-dimensional wedge problems with a wedge angle $2\alpha = \pi$. The stress distribution obtained by Hetényi [2] numerically for the elastic quarter space

* Numbers in brackets refer to References at end of paper.

through the algorithmic procedure, is but another special case of the three-dimensional wedge problems with $2\alpha = \pi/2$

Except for the aforementioned special cases, the three-dimensional wedge problem has not been much considered in the literature. In the two previous papers, the author and Kuo [3,4], starting with the Papkovitch functions, obtained the two-dimensional displacement and stress distribution for the case of an elastic wedge-shaped medium with a concentrated line load acting on (i) one of the wedge surfaces, (ii) a plane inside the elastic medium. This Papkovitch-functions approach, together with the use of Kontorovich-Lebedev transform, is extended in this paper to the case of the three-dimensional wedge problem, that is, an ealstic wedge, with an arbitrary wedge angle, subjected to a point load on one of the free surfaces.

II. Brief Review of Papkovitch Displacement-Stress Functions[5,6]

In an isotropic, elastic and homogeneous medium, the equation of equilibrium is

$$\mu \nabla^2 \vec{u} + (\lambda + \mu) \nabla \nabla \cdot \vec{u} + \rho \vec{f} = 0 \tag{1}$$

Where λ and μ are Lame constants, ρ is the density, $\vec{f}$ is the body force per unit mass, $\vec{u}$ is the displacement.
Resolving the displacement $\vec{u}$ to

$$\vec{u} = \vec{\nabla}\phi + \vec{\nabla} \times \vec{\psi} \tag{2}$$

with

$$\vec{\nabla} \cdot \vec{\psi} = 0 \tag{3}$$

equation (1) becomes

$$\mu \nabla^2 \left[\left(\frac{\lambda + 2\mu}{\mu} \right) \vec{\nabla}\phi + \vec{\nabla} \times \vec{\psi} \right] + \rho \vec{f} = 0 \tag{4}$$

Define

$$\vec{B} = [(\lambda + 2\mu)/\mu]\vec{\nabla}\phi + \vec{\nabla} \times \vec{\phi} \tag{5}$$

From (4), we have

$$\nabla^2\vec{B} = -\rho\vec{f}/\mu \tag{6}$$

And define

$$B_o = 2[(\lambda + 2\mu)/\mu]\phi - \vec{R} \cdot \vec{B} \tag{7}$$

where $\vec{R}$ is the position veotor. Operating on (7) with $\nabla^2 2$ and using the relations

$$\nabla \cdot \vec{B} = [(\lambda + 2\mu)/\mu]\nabla^2\phi \tag{8}$$

and

$$\nabla^2(\vec{R} \cdot \vec{B}) = 2\vec{\nabla} \cdot \vec{B} + \vec{R} \cdot \nabla^2\vec{B} \tag{9}$$

we find

$$\nabla^2 B_o = (\rho/\mu)\vec{R} \cdot \vec{f} \tag{10}$$

From equation (5) and (7)

$$\phi = [\mu/2(\lambda + 2\mu)][\vec{R} \cdot \vec{B} + B_o] \tag{11}$$

$$\vec{\nabla} \times \vec{\phi} = \vec{B} - [(\lambda + 2\mu)/\mu]\vec{\nabla}\phi = \vec{B} - \tfrac{1}{2}\vec{\nabla}(\vec{R} \cdot \vec{B} + B_o) \tag{12}$$

Substituting (11) and (12) into (2), we obtain

$$\vec{u} = \vec{B} - [(\lambda + \mu)/2(\lambda + 2\mu)]\vec{\nabla}(\vec{R} \cdot \vec{B} + B_o) \tag{13}$$

The stress $\underset{\sim}{\tau}$ is related to the displacement $\vec{u}$ by

$$\underset{\sim}{\tau} = \lambda\vec{\nabla} \cdot \vec{u}\underset{\sim}{I} + \mu(\vec{\nabla}\mathbf{u} + \mathbf{u}\vec{\nabla}) \tag{14}$$

where $\underset{\sim}{I}$ is the unit dyadic. Substituting (13) into (14), we find

$$\underset{\sim}{\tau} = \frac{\mu}{\lambda + 2\mu}[\lambda \underset{\sim}{I}\,\vec{\nabla} \cdot \vec{B} + \mu(\vec{\nabla}\vec{B} + \vec{B}\vec{\nabla}) - (\lambda+\mu)[(\vec{\nabla}\vec{\nabla}\vec{B}) \cdot \vec{R} + \vec{\nabla}\vec{\nabla} B_o]] \tag{15}$$

Therefore, from (6) and (10), if the body force is prescribed, the Laplacians of $\vec{B}$ and B_o will be known and then the stress $\underset{\sim}{\tau}$ and the displacement $\vec{u}$ may be determined. The functious, $\vec{B}$, B_o, are known as Papkovitch functions; the former is a vector and the latter is a scalar.

III. General Expressions for Stresses and Displacements in Cylindrical Coordinates

In cylindrical coordinates, $\underset{\sim}{\tau}$ and $\vec{u}$ are

$$\underset{\sim}{\tau} = \hat{r}\hat{r}\,\tau_{rr} + \hat{r}\hat{\theta}\,\tau_{r\theta} + \hat{r}\hat{z}\,\tau_{rz} + \hat{\theta}\hat{r}\,\tau_{\theta r} + \hat{\theta}\hat{\theta}\,\tau_{\theta\theta} + \hat{\theta}\hat{z}\,\tau_{\theta z} + \hat{z}\hat{r}\,\tau_{zr} + \hat{z}\hat{\theta}\,\tau_{z\theta} + \hat{z}\hat{z}\,\tau_{zz} \tag{16}$$

$$\vec{u} = \hat{r}\,u_r + \hat{\theta}\,u_\theta + \hat{z}\,u_z \tag{17}$$

From equations (15) and (13), we have

$$\tau_{rr} = \frac{\mu}{\lambda+2\mu}\left\{\begin{array}{l}(\lambda+2\mu)\dfrac{\partial B_r}{\partial r} + \lambda\left[\dfrac{1}{r}\dfrac{\partial B_\theta}{\partial\theta} + \dfrac{B_r}{r} + \dfrac{\partial B_z}{\partial z}\right] \\ -(\lambda+\mu)\left[r\dfrac{\partial^2 B_r}{\partial r^2} + \dfrac{\partial^2 B_o}{\partial r^2} + z\dfrac{\partial^2 B_z}{\partial r^2}\right]\end{array}\right\} \tag{18}$$

$$\tau_{\theta\theta} = \frac{\mu}{\lambda+2\mu}\Big\{-\mu\frac{\partial B_r}{\partial r} + (3\lambda+4\mu)\frac{1}{r}\frac{\partial B_\theta}{\partial\theta} + (2\lambda+3\mu)\frac{B_r}{r} - (\lambda+\mu)\frac{1}{r}\frac{\partial^2 B_r}{\partial\theta^2} + \lambda\frac{\partial B_z}{\partial z} - (\lambda+\mu)\Big[\frac{1}{r^2}\frac{\partial^2 B_o}{\partial\theta^2} + \frac{1}{r}\frac{\partial B_o}{\partial\theta^2} + \frac{z}{r^2}\frac{\partial^2 B_z}{\partial\theta^2} + \frac{z}{r}\frac{\partial B_z}{\partial r}\Big]\Big\} \tag{19}$$

$$\tau_{zz} = \frac{\mu}{\lambda + 2\mu}\Big\{ \lambda \Big[\frac{\partial B_r}{\partial r} + \frac{1}{r}\frac{\partial B_\theta}{\partial \theta} + \frac{B_r}{r}\Big] + (\lambda + 2\mu)\frac{\partial B_z}{\partial z} - (\lambda + \mu)\Big[r\frac{\partial^2 B_z}{\partial z^2} + z\frac{\partial^2 B_z}{\partial z^2} + \frac{\partial^2 B_o}{\partial z^2}\Big] \Big\} \tag{20}$$

$$\tau_{r\theta} = \frac{\mu}{\lambda + 2\mu}\Big\{(\lambda + 2\mu)\Big[\frac{1}{r}\frac{\partial B_r}{\partial \theta} - \frac{B_\theta}{r} + \frac{\partial B_\theta}{\partial r}\Big] - (\lambda + \mu)\Big[\frac{1}{r}\frac{\partial^2 B_r}{\partial r \partial \theta} + \frac{1}{r}\frac{\partial^2 B_o}{\partial r \partial \theta} - \frac{1}{r^2}\frac{\partial B_o}{\partial \theta} + \frac{z}{r}\frac{\partial^2 B_z}{\partial r \partial \theta} - \frac{z}{r^2}\frac{\partial B_z}{\partial \theta}\Big] \Big\} \tag{21}$$

$$\tau_{\theta z} = \frac{\mu}{\lambda + 2\mu}\Big\{(\lambda + 2\mu)\frac{\partial B_\theta}{\partial z} + \mu\frac{1}{r}\frac{\partial B_z}{\partial \theta} - (\lambda + \mu)\Big[\frac{\partial^2 B_r}{\partial \theta \partial z} + \frac{z}{r}\frac{\partial^2 B_z}{\partial \theta \partial z} + \frac{1}{r}\frac{\partial^2 B_o}{\partial \theta \partial z}\Big] \Big\} \tag{22}$$

$$\tau_{rz} = \frac{\mu}{\lambda + 2\mu}\Big\{ \mu\Big[\frac{\partial B_z}{\partial r} + \frac{\partial B_r}{\partial z}\Big] - (\lambda + \mu)\Big[r\frac{\partial^2 B_r}{\partial r \partial z} + z\frac{\partial^2 B_z}{\partial r \partial z} + \frac{\partial^2 B_o}{\partial r \partial z}\Big] \Big\} \tag{23}$$

$$u_r = B_r - \frac{\lambda + \mu}{2(\lambda + 2\mu)}\Big(B_r + r\frac{\partial B_r}{\partial r} + z\frac{\partial B_z}{\partial r} + \frac{\partial B_o}{\partial r}\Big) \tag{24}$$

$$u_\theta = B_\theta - \frac{\lambda + \mu}{2(\lambda + 2\mu)}\Big(\frac{\partial B_r}{\partial \theta} + \frac{z}{r}\frac{\partial B_z}{\partial \theta} + \frac{1}{r}\frac{\partial B_o}{\partial \theta}\Big) \tag{25}$$

$$u_z = B_z - \frac{\lambda + \mu}{2(\lambda + 2\mu)}\Big(r\frac{\partial B_r}{\partial z} + \frac{\partial B_z}{\partial z} + B_z + \frac{\partial B_o}{\partial z}\Big) \tag{26}$$

IV. Statement and Boundary Conditions

Consider a wedge shaped, elastic, isotropic and homogeneous medium as shown in Figure 1. The origin of the cylindrical coordinates is placed at the vertex of the wedge, and the wedge surfaces are bounded by $\theta = -\alpha$ and $\theta = +\alpha$. A point load P_o is located at the point $(r_o, \alpha, 0)$ and makes an angle β with respect to the wedge surface $\theta = +\alpha$ (P_o is assumed to be in the x-y plane for convinience.). $P(r, \theta, z)$ is the observation point.

The boundary conditions for the wedge surfaces are

$$\tau_{\theta\theta}\Big|_{\theta=-\alpha} = \tau_{\theta r}\Big|_{\theta=-\alpha} = \tau_{z\theta}\Big|_{\theta=\pm\alpha} = 0 \tag{27}$$

$$\tau_{\theta\theta}\Big|_{\theta=+\alpha} = -P_o \sin\beta \quad \delta(r-r_o) \quad \delta(z) \tag{28}$$

$$\tau_{\theta r}\Big|_{\theta=+\alpha} = -P_o \cos\beta \quad \delta(r-r_o) \quad \delta(z) \tag{29}$$

The z and r delta funstions can be written in terms of orthonormal functions. By taking a Kontorovich-Lebedev transform [7], equations (28) and(29) can be written as

$$\tau_{\theta\theta}\Big|_{\theta=\alpha} = \frac{-2P_o \sin\beta}{\pi^3}\int_0^\infty \cos kz\, dk \int_0^\infty \frac{s \sinh(s\pi) K_{is}(kr) K_{is}(kr_o)\, ds}{r} \tag{30}$$

$$\tau_{\theta r}\Big|_{\theta=\alpha} = \frac{-2P_o \cos\beta}{\pi^3}\int_0^\infty \cos kz\, dk \int_0^\infty \frac{s \sinh(s\pi) K_{is}(kr) K_{is}(kr_o)\, ds}{r} \tag{31}$$

where $K_{is}(kr)$ and $K_{is}(kr_o)$ are the modified Bessel functions. From the relation

$$\frac{K_{is}(kr)}{r} = \frac{k}{2is}\left[K_{is+1}(kr) - K_{is-1}(kr)\right] \qquad (32)$$

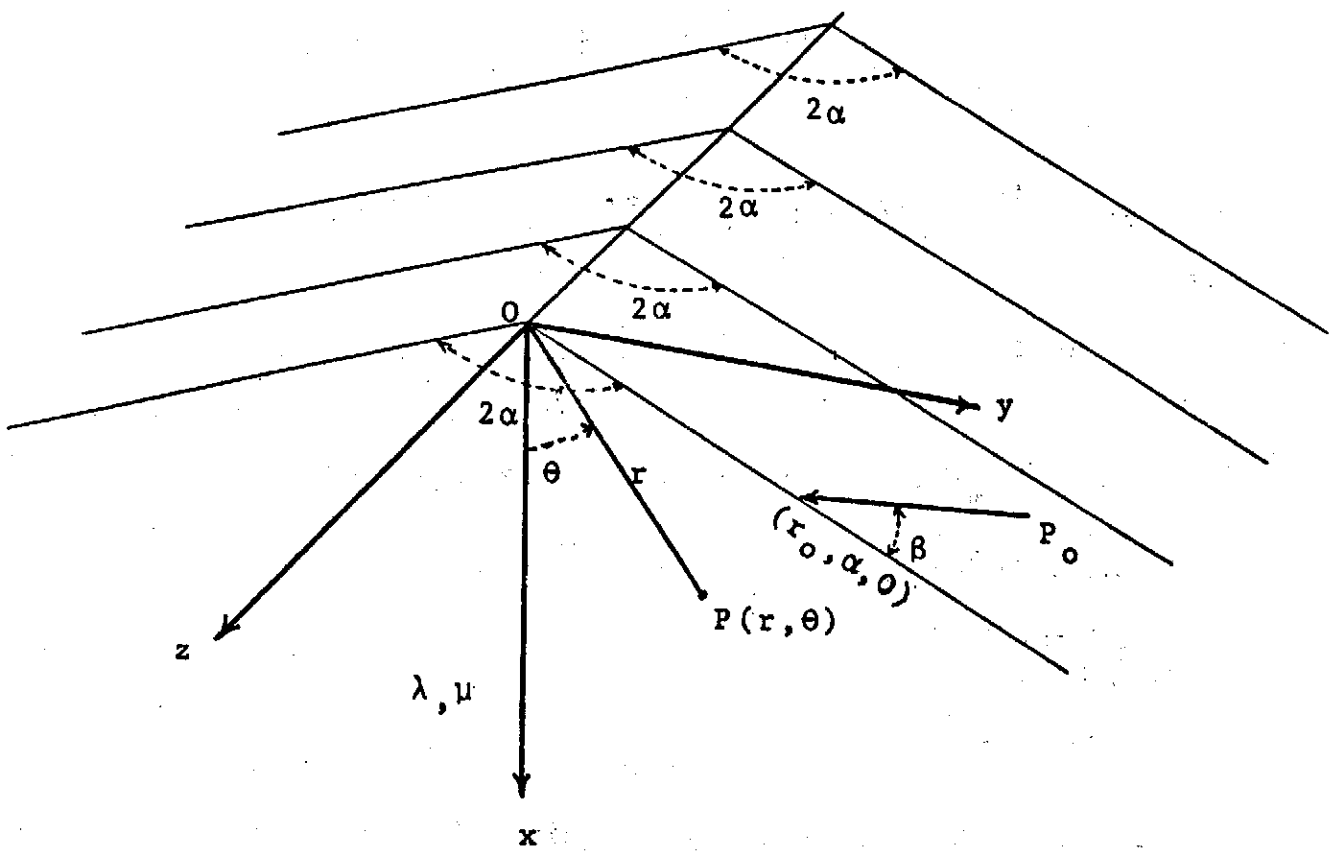

Figure 1. The Geometry of the Problem.

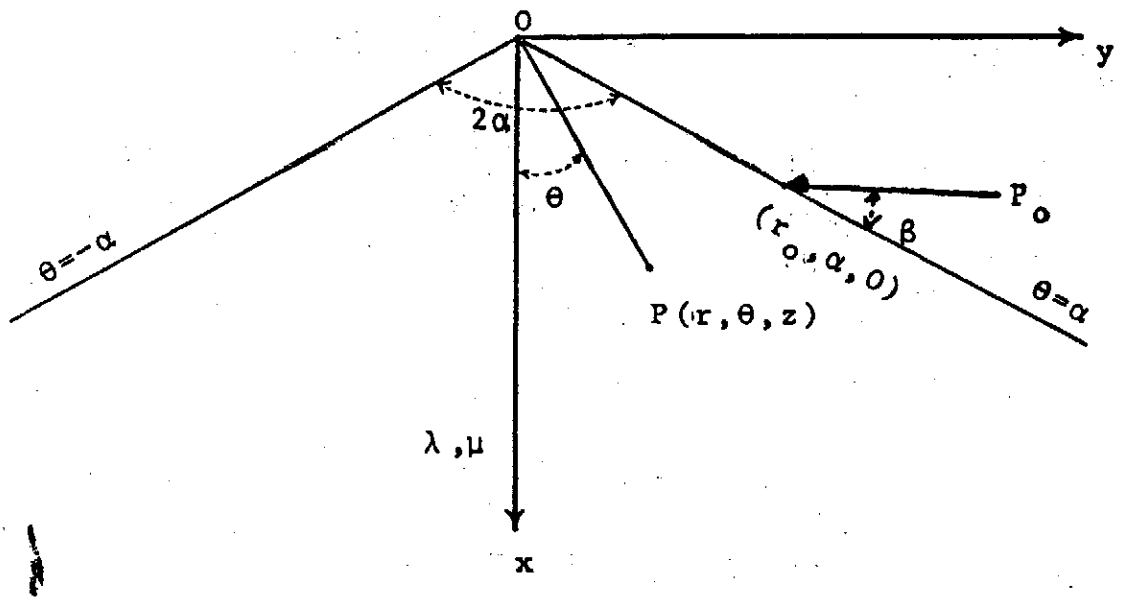

Figure 2. Cross section of Figure 1. in the plane of z=0.

equations (30) and (31) can be written as

$$\tau_{\theta\theta}\Big|_{\theta=+\alpha} = \int_0^\infty \cos kz\, dk \int_{-\infty}^{\infty} C_o \sin\beta\, [K_{is+1}(kr) - K_{is-1}(kr)]\, ds \quad (33)$$

$$\tau_{\theta r}\Big|_{\theta+\alpha} = \int_0^\infty \cos kz\, dk \int_{-\infty}^{\infty} C_o \cos\beta\, [K_{is+1}(kr) - K_{is-1}(kr)]\, ds \quad (34)$$

$$\text{where} \quad C_o = \frac{-P_o\, k \sinh(s\pi)\, K_{is}(kr_o)}{2i\pi^3} \quad (35)$$

V. Formal Solutions of Stresses and Displacement

In the absence of the body force $\vec{f}$, equations (6) and (10) give

$$\nabla^2 \vec{B} = 0 \quad (36)$$

$$\nabla^2 B_o = 0 \quad (37)$$

We can obtain the solutions of equations (36) in cylindrical coordinates as follows. Write $\vec{B}$ in the form

$\vec{B} = \hat{i}\, B_x + \hat{j}\, B_y + \hat{k}\, B_z = \hat{r}\, B_r + \hat{\theta}\, B_\theta + \hat{k}\, B_z$. Since $\nabla^2 B_x = 0$

$\nabla^2 B_y = 0$, and $\nabla^2 B_z = 0$, we use the general cylindrical harmonic solutions of B_x and B_y along with the relatinns

$$B_r = B_x \cos\theta + B_y \sin\theta \quad (38)$$

$$B_\theta = -B_x \sin\theta + B_y \cos\theta \quad (39)$$

The expressions of B_r, B_θ and B_z can be obtained. The expressions of B_o may have the forms of (i) the general cylindrical harmonic solutions, because $\nabla^2 B_o = 0$ (ii) $\vec{R} \cdot \vec{B}$, because equation (7). In order to match the expressions of the point load, we choose

$$B_r = \int_0^\infty \cos kz\, dk \int_0^\infty [A_s \cos(is-1)\theta + B_s \cos(is+1)\theta + E_s \sin(is-1)\theta + F_s \sin(is+1)\theta\,] K_{is}(ir)\, ds \tag{40}$$

$$B_\theta = \int_0^\infty \cos kz\, dk \int_0^\infty [A_s \sin(is-1)\theta - B_s \sin(is+1)\theta - E_s \cos(is-1)\theta + F_s \cos(is+1)\theta] K_{is}(kr)\, ds \tag{41}$$

$$B_z = 0 \tag{42}$$

$$B_o = \int_0^\infty \cos kz\, dk \int_0^\infty [P_s \cos(is+1)\theta + Q_s \sin(is+1)\theta + R_s \cos(is-1)\theta + T_s \sin(is-1)\theta] r\, K_{is}(kr)\, ds \tag{43}$$

In equations (40), (41), (42), and (43), As , B_s, E_s, F_s, P_s, Q_s, R_s, and T_s are unknown coefficients. Letting

$$A_s(s) = A_1(s) + A_2(s) \tag{44}$$

$$E_s(s) = E_1(s) + E_2(s) \tag{45}$$

$$B_s(s) = B_1(s) + B_2(s) \tag{46}$$

$$F_s(s) = F_1(s) + F_2(s) \tag{47}$$

$$P_s(s) = P_2(s) \tag{48}$$

$$Q_s(s) = Q_2(s) \tag{49}$$

$$R_s(s) = R_1(s) \tag{50}$$

$$T_s(s) = T_1(s) \tag{51}$$

and substituting equations (40) to (43) into equations (18) to (26), we have

$$\tau_{\theta\theta} = \frac{\mu}{\lambda+2\mu}\int_0^{\infty}\cos kz\, dk\int_{-\infty}^{\infty}\left[N_1 K_{is+1}(kr)+N_2 K_{is-1}(kr)\right] ds \tag{52}$$

$$\tau_{r\theta} = \frac{\mu}{\lambda+2\mu}\int_0^{\infty}\cos kz\, dk\int_{-\infty}^{\infty}\left[N_3 K_{is+1}(kr)+N_4 K_{is-1}(kr)\right] ds \tag{53}$$

$$\tau_{\theta z} = \frac{\mu}{\lambda+2\mu}\int_0^{\infty}\sin kz\, dk\int_{-\infty}^{\infty} N_5\, k\, K_{is}(kr)\, ds \tag{54}$$

$$\tau_{rr} = -\frac{\mu}{\lambda+2\mu}\int_0^{\infty}\cos kz\, dk\int_{-\infty}^{\infty}\left[\begin{array}{l} N_6 K_{is+}(kr)+N_7 K_{is-1}(kr)+N_8\, r\, K_{is+2}(kr) \\ +N_9\, r\, K_{is-2}(kr)+N_{10}\, r\, K_{is}(kr)\end{array}\right] ds \tag{55}$$

$$\tau_{zz} = \frac{-\mu}{\lambda+2\mu}\int_0^{\infty}\cos kz\, dk\int_{-\infty}^{\infty}\left[\begin{array}{l} k\, X_2\, K_{is+1}(kr) \\ +k\, Y_1\, K_{is-1}(kr) \\ -\frac{k^2}{2}(X_6+Y_5)\, ir\, K_{is}(kr)\end{array}\right] ds \tag{56}$$

$$\tau_{rz} = \frac{\mu}{\lambda+2\mu}\int_0^{\infty} k\sin kz\, dk\int_{-\infty}^{\infty}\left[N_{11} K_{is}(kr)+N_{12}\, r\, K_{is+1}(kr) + N_{13}\, r\, K_{is-1}\right] ds \tag{57}$$

$$u_r = \frac{1}{4(\lambda+2\mu)}\int_0^{\infty}\cos kz\, dk\int_{-\infty}^{\infty}\left\{\begin{array}{l} \left[\begin{array}{l} 2(\lambda+3\mu)\,(X_1+X_2+Y_1+Y_2) \\ -2(\lambda+\mu)\,(X_6+Y_5)\end{array}\right] K_{is}(kr) \\ -k(\lambda+\mu)\,(X_1+X_2+X_6)\, r\, K_{is+1}(kr) \\ -k(\lambda+\mu)\,(Y_1+Y_2+Y_5)\, r\, K_{is-1}(kr)\end{array}\right\} ds \tag{58}$$

$$u_\theta = \frac{1}{2(\lambda+2\mu)} \int_0^\infty \cos kz\, dk \int_{-\infty}^{\infty} \begin{Bmatrix} [(\lambda+\mu)\,is + \lambda+3\mu)]\, X_3 \\ -[(\lambda+\mu)is-(\lambda+3\mu)]\, X_4 \\ -(\lambda+\mu)\,[(is-1)X_8+(is+1)\,Y_7 \end{Bmatrix} \quad (59$$

$$K_{is}(kr) \quad (60$$

$$u_z = \frac{1}{2(\lambda+2\mu)} \int_0^\infty \cos kz\, dk \int_{-\infty}^{\infty} \begin{Bmatrix} X_1+X_2+X_6 \\ +Y_1+Y_2+Y_6 \end{Bmatrix} \quad r\, K_{is}(kr)\, ds \quad (61)$$

where

$$N_1 = \frac{k}{2} \begin{Bmatrix} [(\lambda+\mu)\,is + (\lambda+3\mu)]\; X_1 + (\lambda+\mu)\,(is-1)X_2 \\ +(\lambda+\mu)\;(is-1)\;X_6 \end{Bmatrix} \quad (62)$$

$$N_2 = \frac{k}{2} \begin{Bmatrix} -(\lambda+\mu)\,(is+1)\,Y_1 - [(\lambda+\mu)\,is-(\lambda+3\mu)]\;Y_2 \\ -(\lambda+\mu)\,(is+1)\,Y_5 \end{Bmatrix} \quad (63)$$

$$N_3 = \frac{k}{2} \begin{Bmatrix} -(\lambda+\mu)\,is+(\lambda+3\mu)]\,X_3 + (\lambda+\mu)\,(is+1)\;X_4 \\ +(\lambda+\mu)\,(is-1)\,X_8 \end{Bmatrix} \quad (64)$$

$$N_4 = \frac{k}{2} \begin{Bmatrix} -(\lambda+\mu)\,(is-1)\,Y_3 + [(\lambda+\mu)\,is-(\lambda+3\mu)]\;Y_4 \\ +(\lambda+\mu)\,(is+1)\;Y_7 \end{Bmatrix} \quad (65)$$

$$N_5 = \begin{Bmatrix} -[(\lambda+\mu)\,is+u]\,X_3 + [(\lambda+\mu)\,is-\mu]\,X_4 + (\lambda+\mu)(is-1)\,X_8 \\ -[(\lambda+\mu)\,is+\mu]\;Y_3 + [(\lambda+\mu)\,is-\mu]\,Y_4 + (\lambda+\mu)\,(is+1)\,Y_7 \end{Bmatrix} \quad (66)$$

$$N_6 = k\left[-\mu\,X_1 - (\lambda+\mu)\,X_2 + (\lambda+\mu)\right] X_6 \quad (67)$$

$$N_7 = k\,[-(\lambda+\mu)\,Y_1 - \mu\,Y_2 + (\lambda+\mu)\;Y_5] \quad (68)$$

$$N_8 = \frac{-k^2}{4} (\lambda + \mu) [X_1 + X_2 + X_6] \quad (69)$$

$$N_9 = \frac{-k^2}{4} (\lambda + \mu) [Y_1 + Y_2 + Y_5] \quad (70)$$

$$N_{10} = \frac{-k^2}{4} (\lambda + \mu) [X_1 + X_2 + X_6 + Y_1 + Y_2 + Y_5] \quad (71)$$

$$N_{11} = -\mu (X_1 + X_2) + (\lambda + \mu) X_6 - \mu (Y_1 + Y_2) + (\lambda + \mu) Y_5 \quad (72)$$

$$N_{12} = \frac{-k}{2} (\lambda + \mu) [X_1 + X_2 + X_6] \quad (73)$$

$$N_{13} = \frac{-k}{2} (\lambda + \mu) [Y_1 + Y_2 + Y_5] \quad (74)$$

$$X_1 = A_1 \cos(is-1)\theta + E_I \sin(is-1)\theta \quad (75)$$

$$X_2 = B_1 \cos(is+1)\theta + F_1 \sin(is+1)\theta \quad (76)$$

$$X_2 = A_1 \sin(is-1)\theta - E_1 \cos(is-1)\theta \quad (77)$$

$$X_4 = -B_1 \sin(is+1)\theta + F_1 \cos(is+1)\theta \quad (78)$$

$$X_6 = R_1 \cos(is-1)\theta + T_1 \sin(is-1)\theta \quad (79)$$

$$X_8 = -R_1 \sin(is-1)\theta + T_1 \cos(is-1)\theta \quad (80)$$

$$Y_1 = A_2 \cos(is-1)\theta + E_2 \sin(is-1)\theta \quad (81)$$

$$Y_2 = B_2 \cos(is+1)\theta + F_2 \sin(is+1)\theta \quad (82)$$

$$Y_3 = A_2 \sin(is+1)\theta - E_2 \cos(is-1)\theta \quad (83)$$

$$Y_4 = -B_2 \sin(is+1)\theta + F_2 \cos(is+1)\theta \tag{84}$$

$$Y_5 = P_2 \cos(is+1)\theta + Q_2 \sin(is+1)\theta \tag{85}$$

$$Y_7 = -P_2 \sin(is+1)\theta + Q_2 \cos(is+1)\theta \tag{86}$$

In the branch $\int_{-\infty}^{0} ds$ of equations (52) to (61) (86)

$$A_2(s) = B_1(-s) \tag{87}$$

$$A_1(s) = B_2(-s) \tag{88}$$

$$B_2(s) = A_1(-s) \tag{89}$$

$$B_1(s) = A_2(-s) \tag{90}$$

$$P_2(s) = R_1(-s) \tag{91}$$

$$R_1(s) = P_2(-s) \tag{92}$$

$$E_2(s) = - F_1(-s) \tag{93}$$

$$E_1(s) = - F_2(-s) \tag{94}$$

$$F_2(s) = - E_1(-s) \tag{95}$$

$$F_1(s) = - E_2(-s) \tag{96}$$

$$Q_2(s) = - T_1(-s) \tag{97}$$

$$T_1(s) = - Q_2(-s) \tag{98}$$

Substituting equations (52) to (61) into the boundary conditions, that is, equations (27), (33), and (34), we obtain four sets of simultaneous equations as follows

$$A_1 [(\lambda + \mu) is + (\lambda + 3\mu)] C_- + B (\lambda + \mu) (is-1) C_+ \tag{99}$$

$$+ R_1(\lambda + \mu) (is-1) C_- = -A_o \sin \beta$$

$$A_1[(\lambda+\mu)\,is+(\lambda+3\mu)]\,S_- + B_1(\lambda+\mu)(is+1)\,S_+ + R_1(\lambda+\mu)(is-1)\,S_- = A_o\cos\beta \tag{100}$$

$$A_1[(\lambda+\mu)\,is+\mu]\,S_- + B_1[(\lambda+\mu)\,is-\mu]\,S_+ + R_1(\lambda+\mu)(is-1)\,S_- = 0 \tag{101}$$

$$A_2(\lambda+\mu)(is+1)\,C_- + B_2[(\lambda+\mu)\,is-(\lambda+3\mu)]\,C_+ + P_2(\lambda+\mu)(is+1)\,C_+ = -A_o\sin\beta \tag{102}$$

$$A_2(\lambda+\mu)(is-1)\,S_- + B_2[(\lambda+\mu)\,is-(\lambda+3\mu)]\,S_+ + P_2(\lambda+\mu)(is+1)\,S_+ = -A_o\cos\beta \tag{103}$$

$$A_2[(\lambda+\mu)\,is+u]\,S_- + B_2[(\lambda+\mu)\,is-\mu]\,S_+ + P_2(\lambda+\mu)(is+1)\,S_+ = 0 \tag{104}$$

$$E_1[(\lambda+\mu)\,is+(\lambda+3\mu)]\,S_- + F_1(\lambda+\mu)(is-1)\,S_+ + T_1(\lambda+\mu)(is-1)\,S_- = -A_o\sin\beta \tag{105}$$

$$E_1[(\lambda+\mu)\,is+(\lambda+3\mu)]\,C_- + F_1(\lambda+\mu)(is+1)\,C_+ + T_1(\lambda+\mu)(is-1)\,C_- = -A_o\cos\beta \tag{106}$$

$$E_1[(\lambda+\mu)\,is+\mu]\,C_- + F_1[(\lambda+\mu)\,is-\mu]\,C_+ + T_1(\lambda+\mu)(is-1)\,C_- = 0 \tag{107}$$

$$E_2(\lambda+\mu)(is+1)\,S_- + F_2[(\lambda+\mu)\,is-(\lambda+3\mu)]\,S_+ + Q_2(\lambda+\mu)(is+1)\,S_+ = -A_o\sin\beta \tag{108}$$

$$E_2(\lambda+\mu)(is-1)\,C_- + F_2[(\lambda+\mu)\,is-(\lambda+3\mu)]\,C_+ + Q_2(\lambda+\mu)(is+1)\,C_+ = A_o\cos\beta \tag{109}$$

$$E_2[\,(\lambda+\mu)\,is+\mu\,]\,C_- + F_2[\,(\lambda+\mu)\,is-\mu\,]\,C_+ + Q_2\,(\lambda+\mu)\,(is+1)\,C_+ = 0 \tag{110}$$

From equations (99) to (110), we have

$$A_1 = -A_o\,w_9 \tag{111}$$

$$B_1 = A_o\,D_3 \,/\, (\lambda+\mu) \tag{112}$$

$$R_1 = -A_o\,W_5 \tag{113}$$

$$A_2 = A_o\,D_5 \,/\, (\lambda+\mu) \tag{114}$$

$$B_2 = -A_o\,W_{11} \tag{115}$$

$$P_2 = -A_o\,W_7 \tag{116}$$

$$E_1 = -A_o\,W_{10} \tag{117}$$

$$F_1 = -A_o\,D_4 \,/\, (\lambda+\mu) \tag{118}$$

$$T_1 = -A_o\,W_6 \tag{119}$$

$$E_2 = -A_o\,D_6 \,/\, (\lambda+\mu) \tag{120}$$

$$F_2 = -A_o\,W_{12} \tag{121}$$

$$Q_2 = -A_o\,W_8 \tag{122}$$

where $S_+ = \sin(is+1)\alpha$, $S_- = \sin(is-1)\alpha$, $C_+ = \cos(is+1)\alpha$, $C_- = \cos(is-1)\alpha$ and

$$A_o = \frac{(\lambda+2\mu)\,P_o \sinh(s\pi)\,K_{is}(kr_o)}{2\,\mu\,i\,\pi^3} \tag{123}$$

$$D_1 = [\,(is-1)\,C_+\cos\beta + (is+1)\,S_+\sin\beta\,] \;/\; a_1 \tag{124}$$

$$D_2 = [\,(is-1)\,S_+\cos\beta - (is+1)\,C_+\sin\beta\,] \;/\; a_2 \tag{125}$$

$$D_3 = \cos[\,(is-1)\alpha - \beta\,] \;/ a_1 \tag{126}$$

$$D_4 = \sin [\ (is-1)\alpha - \beta\ ] / a_2 \tag{127}$$

$$D_5 = \cos [\ (is+1)\alpha + \beta\ ] / a_1 \tag{128}$$

$$D_6 = \sin [\ (is+1)\alpha + \beta\ ] / a_2 \tag{129}$$

$$D_7 = [\ (is+1)\, C_- \cos\beta - (is-1)\, S_- \sin\beta\ ] / a_1 \tag{130}$$

$$D_8 = [\ (is+1)\, s_- \cos\beta + (is-1) C_- \sin\beta\ ] / a_2 \tag{131}$$

$$W_5 = \frac{b_1 \cos\beta}{(\lambda + 2\mu)(is-1)\, S_-} - \frac{2\mu D_3\, S_+}{(\lambda+\mu)^2 (is-1)\, S_-} \tag{132}$$

$$W_6 = \frac{-B_1 \cos\beta}{(\lambda + 2\mu)(is-1)\, C_-} + \frac{2\mu D_4\, C_+}{(\lambda+\mu)^2 (is-1)\, C_-} \tag{133}$$

$$W_7 = \frac{b_2 \cos\beta}{(\lambda + 2\mu)(is+1)\, S_+} + \frac{2\mu D_5\, S_-}{(\lambda+\mu)^2 (is+1)\, S_+} \tag{134}$$

$$W_8 = \frac{-B_2 \cos\beta}{(\lambda + 2\mu)(is+1)\, C_+} + \frac{2\mu D_6\, C_-}{(\lambda+\mu)^2 (is+1)\, C_+} \tag{135}$$

$$W_9 = \frac{-\cos\beta}{(\lambda + 2\mu)\, S_-} + \frac{D_3\, S_+}{(\lambda+\mu)\, S_-} \tag{136}$$

$$W_{10} = \frac{\cos\beta}{(\lambda + 2\mu)\, C_-} - \frac{D_4\, C_+}{(\lambda+\mu)\, C_-} \tag{137}$$

$$W_{11} = \frac{-\cos\beta}{(\lambda + 2\mu)\, S_+} + \frac{D_5\, S_-}{(\lambda+\mu)\, S_+} \tag{138}$$

$$W_{12} = \frac{\cos\beta}{(\lambda+2\mu)\,C_+} - \frac{D_6\,C_-}{(\lambda+\mu)\,C_+} \tag{139}$$

$$a_1 = \sin 2is\alpha + is\sin 2\alpha \tag{140}$$

$$a_2 = \sin 2is\alpha - is\sin 2\alpha \tag{141}$$

$$b_1 = [\,(\lambda+\mu)\,is + u\,] \,/\, (\lambda+\mu) \tag{142}$$

$$b_2 = [\,(\lambda+\mu)\,is - u\,] \,/\, (\lambda+\mu) \tag{143}$$

$$b_3 = [\,(\lambda+\mu)\,is + (\lambda+3\mu)\,] \,/\, (\lambda+\mu) \tag{144}$$

$$b_4 = [\,(\lambda+\mu)\,is - (\lambda+3\mu)\,] \,/\, (\lambda+\mu) \tag{145}$$

substituting equations (111) to (122) into (52) to (61), the formal solutions of stresses and displacements are obtained as

$$\tau_{\theta\theta} = \frac{P_o}{4i\pi^3}\int_0^\infty \cos kz\,dk \int_{-\infty}^{\infty} \sinh(s\pi)\left[Z_1 K_{is+1}(kr)+Z_2 K_{is-1}(kr)\right] k\,K_{is}(kr_o)\,ds \tag{146}$$

$$\tau_{r\theta} = \frac{P_o}{4i\pi^3}\int_0^\infty \cos kz\,dk \int_{-\infty}^{\infty} \sinh(s\pi)\left[Z_3 K_{is+1}(kr)+Z_4 K_{is-1}(kr)\right] k K_{is}(kr_o)\,ds \tag{147}$$

$$\tau_{\theta z} = \frac{P_o}{2i\pi^3}\int_0^\infty \cos kz\,dk \int_{-\infty}^{\infty} \sinh(s\pi) \begin{bmatrix} Z_5\sin(is-1)\theta \\ +Z_6\cos(is-1)\theta \\ +Z_7\sin(is+1)\theta \\ +Z_8\cos(is+1)\theta \end{bmatrix} k\,K_{is}(kr)\,K_{is}(kr_o)\,d \tag{148}$$

$$\tau_{rr} = \frac{P_0}{4i\pi^3}\int_0^{\infty}\cos kz\,dk\int_{-\infty}^{\infty}\sinh(s\pi)\begin{bmatrix} Z_9 K_{is+1}(kr) \\ +Z_{10} K_{is-1}(kr) \\ +Z_{11}\,kr\,K_{is}(kr)\end{bmatrix} kK_{is}(kr_0)ds \tag{149}$$

$$\tau_{zz} = \frac{P_0}{4i\pi^3}\int_0^{\infty}\cos kz\,dk\int_{-\infty}^{\infty}\sinh(s\pi)\begin{bmatrix} Z_{12} K_{is+1}(kr) \\ +Z_{13} K_{is-1}(kr) \\ +Z_{14}\,kK_{is}(kr)\end{bmatrix} kK_{is}(kr_0)ds \tag{150}$$

$$\tau_{rz} = \frac{P_0}{4i\pi^3}\int_0^{\infty}\sin kz\,dk\int_{-\infty}^{\infty}\sinh(s\pi)\begin{bmatrix} 2Z_{15} K_{is}(kr) \\ +Z_{16}\,kr\,K_{is+1}(kr) \\ +Z_{17}\,kr\,K_{is-1}(kr)\end{bmatrix} kK_{is}(kr_0)ds \tag{151}$$

$$u_r = \frac{P_0}{8\mu i\pi^3}\int_0^{\infty}\cos kz\,dk\int_{-\infty}^{\infty}\sinh(s\pi)\begin{bmatrix} Z_{18} K_{is}(kr) \\ +Z_{19}\,kr\,K_{is+1}(kr) \\ +Z_{20}\,kr\,K_{is-1}(kr)\end{bmatrix} K_{is}(kr_0)ds \tag{152}$$

$$u_\theta = \frac{P_0}{8\mu i\pi^3}\int_0^{\infty}\cos kz\,dk\int_{-\infty}^{\infty}\sinh(s\pi)\begin{bmatrix} (b_3D_5 - D_1)\sin(is-1)\theta \\ +(b_3D_6 - D_2)\cos(is-1)\theta \\ +(b_4D_3 - D_7)\sin(is+1)\theta \\ +(b_4D_4 - D_8)\cos(is+1)\theta\end{bmatrix} \cdot K_{is}(kr)K_{is}(kr_0)\,ds \tag{153}$$

$$u_z = \frac{P_o}{8\mu i \pi^3}\int_0^{\infty} \sin kz\, dk \int_{-\infty}^{\infty} \sin h(s\pi) \cdot \left[\begin{array}{l} (\frac{D_5}{\lambda+\mu} - W_9 - W_5)\cos(is-1)\theta \\ +(\frac{-D_6}{\lambda+\mu} - W_{10} - W_6)\sin(is-1)\theta \\ +(\frac{D_3}{\lambda+\mu} - W_{11} - W_7)\cos(is+1)\theta \\ +(\frac{-D_4}{\lambda+\mu} - W_{12} - W_8)\sin(is+1)\theta \end{array}\right] \quad (154)$$

$$\cdot krK_{is}(kr)K_{is}(kr_o)\, ds$$

where

$$Z_1 = -D_1 \cos(is-1)\theta + D_2 \sin(is-1)\theta + D_3 (is-1) \cos(is+1)\theta = D_4(is-1) \sin(is+1)\theta \quad (155)$$

$$Z_2 = -D_5(is+1)\cos(is-1)\theta + D_6(is+1)\sin(is-1)\theta + D_7 \cos(is+1)\theta - D_8 \sin(is+1)\theta \quad (156)$$

$$Z_3 = D_1 \sin(is-1)\theta + D_2 \cos(is-1)\theta - D_3(is+1)\sin(is+1)\theta - D_4(is+1)\cos(is+1)\theta \quad (157)$$

$$Z_4 = -D_5(is-1)\sin(is-1)\theta - D_6(is-1) \cos(is-1)\theta + D_7 \sin(is+1)\theta + D_8 \cos(is+1)\theta \quad (158)$$

$$Z_5 = -b_1 D_5 - b_2 S_+ D_3/S_- \quad (159)$$

$$Z_6 = -b_1 D_6 + b_2 C_+ D_4/C_- \quad (160)$$

$$Z_7 = -b_2 D_3 - b_1 S_- D_5/S_+ \quad (161)$$

$$Z_8 = -b_2 D_4 + b_1 C_- D_6/C_+ \quad (162)$$

$$Z_9 = D_1 \cos(is-1)\theta - D_2 \sin(is-1)\theta - D_3(is+3)\cos(is+1)\theta + D_4(is+3)\sin(is+1)\theta \quad (163)$$

$$Z_{10} = D_5(is-3)\cos(is-1)\theta - D_6(is-3)\sin(in-1)\theta - D_7\cos(is+1)\theta + D_8 \sin(is+1)\theta \quad (164)$$

$$Z_{11} = W_1 \cos(is-1)\theta + W_2 \sin(is-1)\theta + W_3 \cos(is+1)\theta + W_4 \sin(is+1)\theta \quad (165)$$

$$W_1 = -D_5 + \frac{S_+ b_4 D_3 + \cos\beta}{(is-1)\ S_-} \quad (166)$$

$$W_2 = D_6 - \frac{C_+ b_4 D_4 + \cos\beta}{(is-1)\ C_-} \quad (167)$$

$$W_3 = -D_3 + \frac{S_- b_3 D_5 - \cos\beta}{(is+1)\ S_+} \quad (168)$$

$$W_4 = D_4 - \frac{C_- b_3 D_6 - \cos\beta}{(is+1)\, C_+} \tag{169}$$

$$Z_{12} = 2\,[\, -D_3 \cos(is+1)\theta + D_4 \sin(is+1)\theta]/\,(\lambda + u) \tag{170}$$

$$Z_{13} = [\, -D_5 \cos(is-1)\theta + D_6 \sin(is-1)\theta\,]\,/\,(\lambda + u) \tag{171}$$

$$Z_{14} = W_5 \cos(is-1)\theta + W_6 \sin(is-1)\theta + W_7 \cos(is+1)\theta + W_8 \sin(is+1)\theta \tag{172}$$

$$\begin{aligned} Z_{15} = {} & [\, \mu\,(W_9 - \frac{D_5}{\lambda+\mu}) - (\lambda+\mu)\, W_5\,] \cos(is-1)\theta \\ & + [\, \mu\,(W_{10} + \frac{D_6}{\lambda+\mu}) - (\lambda+\mu)\, W_6\,] \sin(is-1)\theta \\ & + [\, \mu\,(W_{11} - \frac{D_3}{\lambda+\mu}) - (\lambda+\mu)\, W_7\,] \cos(is+1)\theta \\ & + [\, \mu\,(W_{12} - \frac{D_4}{\lambda+\mu}) - (\lambda+\mu)\, W_8\,] \sin(is+1)\theta \end{aligned} \tag{173}$$

$$\begin{aligned} Z_{16} = {} & (\lambda+\mu)\,[\,(W_9 + W_5)\cos(is-1)\theta + (W_{10}+W_6)\sin(is-1)\theta] \\ & - D_3 \cos(is+1)\theta + D_4 \sin(is+1)\theta \end{aligned} \tag{174}$$

$$\begin{aligned} Z_{17} = {} & -D_5 \cos(is-1)\theta + D_6 \sin(is-1)\theta \\ & + (\lambda+\mu)\,[\,(W_{11}+W_7)\cos(is+1)\theta + (W_{12}+W_8)\sin(is+1)\theta] \end{aligned} \tag{175}$$

$$\begin{aligned} Z_{18} = {} & [\,(\lambda+3\mu)\,(\frac{D_5}{(\lambda+\mu)} - W_9) + (\lambda+\mu)W_5\,] \cos(is-1)\theta \\ & + [\,(\lambda+3\mu)\,(-\frac{D_6}{\lambda+\mu} - W_{10}) + (\lambda+\mu)\, W_6\,] \sin(is-1)\,\theta \\ & + [\,(\lambda+3\mu)\,(\frac{D_3}{\lambda+\mu} - W_{11}) + (\lambda+\mu)\, W_7\,] \cos(is+1)\theta \\ & + [\,(\lambda+3\mu)\,(-\frac{D_4}{\lambda+\mu} - W_{12}) + (\lambda+\mu)\, W_8\,] \sin(is+1)\theta \end{aligned} \tag{176}$$

$$Z_{19} = (\lambda+\mu)\,[(W_9+W_5)\cos(is-1)\theta+(W_{10}+W_6)\sin(is-1)\theta] - D_3\cos(is+1)\theta + D_4\sin(is+1)\theta \tag{177}$$

$$Z_{20} = -D_5\cos(is-1)\theta + D_6\sin(is-1)\theta +(\lambda+\mu)\,[(W_{11}+W_7)\cos(is+1)\theta + (W_{12}+W_8)\sin(is+1)\theta] \tag{178}$$

VI. Evaluation of Streeses and Displacements

Here the displacement component u_θ, equation (153), is evaluated as an example. The other displacement components and stresses may similarly be obtained.

Let $r_>$ be the larger of r and r_o; $r_<$ be the smaller of r and r_o. By virtue of the relation

$$K_n(z) = \frac{\pi}{2\sin(n\pi)}\,[I_{-n}(z) - I_n(z)] \tag{179}$$

it follows that equation (153) may be transformed into a two-sided integral with respect to s

$$u_\theta = \frac{-P_o}{8\mu\pi^2}\int_0^\infty \cos kz\, M_o\, dk \tag{180}$$

where

$$M_o = \int_0^\infty \begin{bmatrix} (-D_1 + b_3D_5)\sin(is-1)\theta \\ +(-D_2 + b_3D_6)\cos(is-1)\theta \\ +(-D_7 + b_4D_3)\sin(is+1)\theta \\ +(-D_8 + b_4D_4)\cos(is+1)\theta \end{bmatrix} K_{is}(kr_>)\,I_{-is}(kr_<)\,ds \tag{181}$$

By setting equations (140) and (141), a_1 and a_2, to zero, we have

$$\sin(2is\alpha) + is \sin 2\alpha = 0 \tag{182}$$

$$\sin(2is\alpha) - is \sin 2\alpha = 0 \tag{183}$$

where s is complex. The integral (181) may be evaluated by means of the residue theorem. The residues can be found by integrating around each pole in the positive direction. The path of integration in (181) can be taken along the real axis and the infinite half circles above the real axis, and the origin is indented by a small semicircle in the upper half plane, the radius of the semicircle is an infitesimal quantity. Then the integral (191) may be represented in the form of an infinite series

$$M_o = \frac{-4\pi(\lambda+2\mu)}{(\lambda+\mu)\sin 2\alpha} \sin(\theta+\alpha+\beta) K_o(kr_>) I_o(kr_<)$$

$$+2\pi \sum_{n=1}^{\infty} \begin{bmatrix} (N_1+C_3N_5)\sin(\mu_n+1)\theta \\ +(-N_2+c_3N_6)\cos(\mu_n+1)\theta \\ +(-N_7+c_4N_3)\sin(\mu_n-1)\theta \\ +(N_8+c_4N_4)\cos(\mu_n-1)\theta \end{bmatrix} K_{\mu_n}(kr_>) \quad I_{\mu_n}(kr_<) \tag{184}$$

$$N_1 = [(\mu_n-1)\sin(\mu_n-1)\alpha \sin\beta - (\mu_n+1)\cos(\mu_n-1)\alpha\cos\beta]/\Delta_1 \tag{185}$$

$$N_2 = [(\mu_n+1)\sin(\mu_n-1)\alpha\cos\beta + (\mu_n-1)\cos(\mu_n-1)\alpha\sin\beta]/\Delta_2 \tag{186}$$

$$N_3 = \cos[(\mu_n+1)\alpha+\beta]/\Delta_1 \tag{187}$$

$$N_4 = \sin[(\mu_n+1)\alpha+\beta]/\Delta_2 \tag{188}$$

$$N_5 = \cos[(\mu_n-1)\alpha-\beta]/\Delta_1 \tag{189}$$

$$N_6 = \sin\ [\ (\mu_n - 1)\ \alpha\ -\ \beta\ ]\ \ /\ \Delta_2 \tag{190}$$

$$N_7 = [\ (\mu_n-1)\cos(\mu_n+1)\ \alpha\ \cos\beta + (\mu_n+1)\sin(\mu_n+1)\ \sin\beta\ ]\ /\Delta_1 \tag{191}$$

$$N_8 = -[(\mu_n-1)\sin(\mu_n+1)\ \alpha\ \cos\beta + (\mu_n+1)\cos(\mu_n+1)\ \sin\beta\ ]\ /\Delta_2 \tag{192}$$

$\mu_n = is_n$ are the roots of the transcendental equations (250) and (251), and

$$\Delta_1 = 2\alpha\cos\ (\ 2\mu_n\ \alpha\ )\ + \sin\ 2\alpha \tag{193}$$

$$\Delta_2 = 2\alpha\cos\ (2\mu_n\ \alpha\ )\ -\ \sin\ 2\alpha \tag{194}$$

Now we have

$$u_\theta = \frac{(\lambda+2\mu)\ P_o\sin(\theta+\alpha+B)}{2\pi\ \mu\ (\lambda+\mu)\ \sin\ 2\alpha}\int_0^\infty \cos(kz)\ K_o(kr)\ I_o(kr)\quad dk$$

$$-\frac{P_o}{4\mu\pi}\sum_{n=1}^{\infty}\begin{bmatrix}(N_1+c_3N_3)\sin(\mu_n+1)\theta\\ +(-N_2+c_3N_6)\cos(\mu_n+1)\theta\\ +(-N_7+c_4N_8)\sin(\mu_n-1)\theta\\ +(N_5+c_4N_4)\cos(\mu_n-1)\theta\end{bmatrix}\int_0^\infty \cos(kz)K_{\mu_n}(kr_>)\ I_{\mu_n}(kr_<)\ dk \tag{195}$$

$$c_3 = [\ (\lambda+\mu)\ \mu_n - (\lambda+3\mu)\ ]\ /\ (\lambda+\mu) \tag{196}$$

$$c_4 = [\ (\lambda+\mu)\ \mu_n + (\lambda+3\mu)\ ]\ /\ (\lambda+\mu) \tag{197}$$

The two integrals in equations (195) can be obtained (see [8]) as

$$\int_0^\infty \cos(kz)K_o(kr_>)\ I_o(kr_<)\ dk = [z^2+(r+r_o)]^{-\frac{1}{2}}\ k\left(\frac{(2rr_o)^{\frac{1}{2}}}{[z^2+(r+r_o)^2]^{\frac{1}{2}}}\right) \tag{198}$$

$$\int_0^\infty \cos(kz) K_{\mu_n}(kr_>)\, I_{\mu_n}(kr_<)\, dk = \frac{1}{2(rr_o)^{\frac{1}{2}}} Q_{\mu_n - \frac{1}{2}}(w)$$

$$w = (z^2+r^2+r_o^2)/(2rr_o),\ \mathrm{Re}(\mu_n) > -\tfrac{1}{2} \qquad (199)$$

where $K(\xi)$ is the complete elliptic integral

$$K(\xi) = \int_0^{\pi/2} (1-\xi^2\sin^2\phi)^{-\frac{1}{2}}\, d\phi = \tfrac{1}{2}\pi\, {}_2F_1(\tfrac{1}{2}, \tfrac{1}{2}; 1; \xi^2) \qquad (200)$$

$Q(w)$ is the Legendre functions of the second kind.

VIII. Remarks

Taking the limit $k \longrightarrow 0$, and integrating equations (146) to (154) from 0 to $+\infty$ with respect to z, we obtain the stresses and displacements of the two dimensional solutions. These recuced solutions are exactly the same as those obtained by the author and Kuo [3] previously.

The transcentental equations (182) and (183) for the three dimensional surface loading wedge problem, which determine the possible values of the roots s_n (or μ_n) and therefore give the various forms of the leading terms of the displacements and stresses are the same as those obtained for the two dimensional case. However, the stresses, different from the two dimensional case, are no longer independent of the elastic properties of the medium.

In the two dimensional case, the characteristic peculiarity of the logarthmic singularity at infinity for the displacements can be not removed. The present three dimensional case does not have such a peculiarity. It can easily be seen from equation (199).

REFERENCES

1. Boussinesq, J., "Applications des potentiels à l'étude de l'équilibre et du mouvement des solides elastique." Paris: Gauthier-Villars, 1885.
2. Hetényi, M., "A General Solution for the Elastic Quarter Space." JOURNAL OF APPLIED MECHANICS, Vol. 37, TRAMS. ASME, Vol., 92, Series E, 1970. PP. 70-76.
3. Teng, Y.C., and J.T. Kuo "Displacements and Stresses in a Two-Dimensional Wedge Shaped Medium," JOURNAL OF APPLIED MECHANICS, Vol. 41, No. 3, 1974, PP. 719-724.
4. Teng, Y.C., "A Concentrated Line Load Acting in the interior of an Elastic Wedge Shaped Medium," Annual Report of the Institute of Physics, Academia Sinica, Taiwan, The Republic of China, Vol. 4, 1973, PP. 271-294.
5. Papkovitch, P.F., "Solution générale des equations differentielles fondamentales d'élasticité, exprimée par trois fonctions harmoniques," Comptes Rendus. Hebdomaires des Seances, Vol. 1975, 1932, PP. 513-515.
6. Mindlin, R. D., "Note on the Galerkin and Papkovitch Stress Functions," Bulletin of the American Mathematical Society, Vol. 42, 1936, PP. -373-376.
7. Kontorovich, M.J. and N.N. Lebedev, "On a Method of Solution of Some Problems in the Deffraction Theory," Journal of Physicsm Moscow, Rol. 1, 1939, PP. 229-241.
8. Erdelyi, A., et al., "Tables of Integral Transform", Bateman Manuscript Project, Mcgraw Hill, 1954.